UNIVERSIDAD DE SANTIAGO DE COMPOSTELA

Facultad de Física

Departamento de Física de la Materia Condensada

Grupo de Física de Coloides y Polímeros

Development of Hybrid Nanoplatforms for Theranostic Applications

---

Memoria para optar al

Grado de Doctor.

Antonio Topete Camacho

Santiago de Compostela, Noviembre 2013

Víctor Mosquera Tallón, Catedrático del Departamento de Física de la Materia Condensada, Pablo Taboada Antelo, Profesor Titular del Departamento de Física de la Materia Condensada y Silvia Barbosa Fernández, Investigador Doctor del Programa Ramón y Cajal en el Departamento de Física de la Materia Condensada de la Universidad de Santiago de Compostela

INFORMAN:

Que la presente memoria titulada **"Development of Hybrid Nanoplatforms for Theranostic Applications"** ha sido realizada bajo nuestra dirección por el Ingeniero Químico con Maestría en Ciencias en Ingeniería Química D. Antonio Topete Camacho, en el Grupo de Investigación "Física de Coloides y Polímeros" del Departamento de Física de la Materia Condensada de la Universidad de Santiago de Compostela, y reúne los requisitos de calidad y rigor científicos necesarios para optar al grado de Doctor.

Santiago de Compostela, Septiembre de 2013

Prof. Dr. Víctor Mosquera Tallón

Prof. Dr. Pablo Taboada Antelo

Dra. Silvia Barbosa Fernández

I dedicate this thesis to my parents, Antonio and Elba. They taught me to believe in myself and to never give up of my goals. Their continuous support was essential to me during this period. I learned from them that life is a school and that each experience is a valuable lesson. Thank you.

Antonio Topete Palomera

In Memoriam

Acknowledgements

"Science is always a quest, never a real discovery. It's a trip, never an arrival".

Karl Popper.

First and foremost I offer my sincerest gratitude to my supervisors, Dr. Pablo, Dr. Víctor and Dr. Sílvia, I learned a lot from them and I thank them for their time and their assistance. I must also acknowledge my labmates: Josué (you are like a brother to me), Adriana, Dolores, Mateo, Alberto, Sonia and Eva. Not only you are great work colleagues, but you are also good friends. I would like to thank Manolo, Toyis and Bárbara for their support during this project and their sincere friendship.

Very special thanks go out to Dr. José Angel Costoya and Pablo Iglesias from the Molecular Oncology Group for all their assistance, and also to the Institute of Orthopaedics and Musculoskeletal Tissues of USC for their support and facilities. I want to thank Raquel, Merche and Ramiro, from Microscopy Services.

My sincere thanks to CONACYT that gave me all the support I needed to make this project a reality and to the University of Santiago de Compostela for accepting me and giving me all the equipment and human assistance to complete it.

I am really thankful to Prof. Dr. Wolfgang Parak and his Biophotoniks group from the Philipps-Universität of Marburg for offering me an unforgettable internship and leading me during that period. I would like to thank the entire group and especially to Susana Carregal Romero, Beatriz Pelaz, Dorleta Jiménez, Xiang Yu, Karsten Katner and Raimo Hartman, who helped me in Germany, not only in the lab group, but also with my adaptation to a new country.

My life in Santiago de Compostela would not be so unforgettable without my friends: Bieito, Naty, Irais, Fernando, Alejandra, Susana, Édgar, René, Karen, Ríos, Tere and Ceila. You were my family in Spain and I thank you for all the good times that we spent together.

At last, but not least, I want to thank my family. My mum, Elba, who is also my best friend. Thank you for supporting me with this aim and for everything that you have

taught me during my life. Thank you for all your love and for being always there, taking care of me no mattering about the distance or the hour. Thanks for being here in the presentation of this work; it means a lot to me. I also want to thank my siblings: Soraya, Ireri, Lariza and Juan for their love, their friendship, their help and their encouragement. My aunt Emilia. A special thanks to my nephews, José Carlos and María José, for their fullest trust. Finally, I thank my girlfriend, Keyla, for her love, her support, her advice, without her help the conclusion of this work would have been enormously harder. I love you amore, thank you.

Table of Contents

Resumen

La nanociencia y la nanotecnología tratan principalmente con la síntesis, caracterización, exploración y explotación de materiales nanoestructurados. Estos materiales se caracterizan por tener al menos una de sus dimensiones en el rango nanométrico (1 nm = 10^{-9} m). Los nanomateriales constituyen un puente entre las moléculas y los sistemas macroscópicos. Las propiedades físicas y químicas de los nanomateriales pueden diferir considerablemente de la de los átomos/moléculas simples o de los materiales macroscópicos de la misma composición. La particularidad de sus características nos conduce a la obtención de nuevos dispositivos y a su aplicación en la mejora de tecnologías ya existentes o en el desarrollo de unas nuevas.

La nanociencia y la nanotecnología han crecido explosivamente en las últimas dos décadas debido a la creciente disponibilidad de nuevos métodos de síntesis de nanomateriales así como de herramientas para su caracterización y manipulación. De igual manera, el nivel de entendimiento y conocimiento de las propiedades eléctricas, ópticas y magnéticas de las nanoestructuras de materiales semiconductores, metales y poliméricos ha avanzado significativamente.

Las herramientas de caracterización tales como las miscroscopías electrónicas, cristalografía, espectroscopía, entre otras, han permitido seguir y controlar el tamaño, la forma y la estructura de los nanomateriales. Sin embargo, la nanociencia y nanotecnología aún cuentan con un enorme campo de investigación y perfeccionamiento en lo que concierne al diseño, síntesis, caracterización y aplicación de sistemas nanométricos.

Una de las áreas de la nanotecnología que aún se encuentra en una etapa de desarrollo inicial es la nanomedicina. Ésta nueva rama de la nanotecnología involucra su aplicación al cuidado de la salud humana y se encuentra actualmente en una etapa de crecimiento. El uso de la nanotecnología ha permitido crear nuevos sistemas que revolucionarán la forma en que se diagnostica y se trata un gran número de enfermedades. Entre los nuevos nanomateriales que se han utilizado para estos fines podemos encontrar nanopartículas y nanocápsulas poliméricas, liposomas, micelas, nanopartículas magnéticas, nanopartículas semiconductoras (*quantum dots*), nanopartículas metálicas de diferentes geometrías, nanotubos de carbono, grafeno, nanodiamantes, dendrímeros, nanoestructuras basadas en biomoléculas (ácidos

nucléicos, proteínas, cápsides víricas), por mencionar algunos. Estas nanoestructuras ofrecen propiedades diferentes, y podríamos decir mejoradas con respecto a la forma macroscópica del material que las compone debido a su tamaño nanométrico.

Por ejemplo, nanopartículas poliméricas y liposomas se han venido utilizando en el tratamiento de enfermedades para transportar fármacos y liberarlos de manera controlada específicamente en el sitio del tumor. Nanopartículas magnéticas modificadas se han utilizado como agentes de contraste en imagen por resonancia magnética con excelentes resultados. De igual forma, también se han utilizado nanopartículas de oro como agentes fototerapéuticos, un nuevo tipo de terapia contra el cáncer en la cual las células malignas son destruidas gracias a la capacidad de las nanopartículas de oro de absorber energía lumínica y convertirla en calor.

Algunos ejemplos de nanotransportadores que han sido aprobados para su aplicación médica son:

- Doxil, liposomas cargados con doxorubicina, que fue el primer sistema basado en liposomas que recibió la aprobación de la Agenica del Medicamente americana (FDA en sus siglas en inglés).
- Abraxane, conjugados de albúmina y paclitaxel de 130 nm de tamaño, también aprobado por la FDA como tratamiento de segunda línea contra el cáncer de mama.
- Combidex (ferumoxtran-10), agente de contraste basado en nanopartículas de óxido de hierro, que está siendo utilizado para la diferenciación de ganglios linfáticos cancerosos y normales.
- DaunoXome, liposomas cargados con el agente quimioterapéutico daunorubicina.
- Ambisome, liposomas cargados con el antifúngicida amfotericina.
- Genexol-PM, partículas poliméricas formadas por el copolímero PEG-PLGA cargaas con el fármaco anticancerígeno paclitaxel.
- DE-310, complejo de dextrano y camptotecina para el tratamiento de tumores de pulmón, colon y mama.

Por otra parte, las formas tradicionales de suministrar fármacos en muchas ocasiones no son las más eficientes, pudiendo llegar a ser bastante agresivas con los pacientes, prolongadas y costosas. El uso de nanomateriales en el área médica permitirá

reducir las dosis, los tiempos y los costes de los tratamientos. De igual forma, la incorporación de nuevas formas de contraste para imagen y diagnóstico permitirá realizar una evaluación en tiempo real de la eficiencia del régimen de tratamiento que se ha elegido, facilitando de esta forma modificar y ajustar las dosis de acuerdo a la respuesta de cada paciente (medicina personalizada), así como la detección temprana de enfermedades.

La combinación de agentes terapéuticos y diagnósticos en un solo sistema da origen a un nuevo concepto, la llamada ***teragnóstica***. Un sistema teranóstico es capaz de tratar la enfermedad al mismo tiempo que sirve como agente de diagnóstico y de visualización de la misma.

Además de la combinación de las dos funcionalidades, terapia y diagnosis, también es deseable la incorporación de múltiples elementos que permitan abordar la enfermedad desde varios ángulos, de tal forma que las debilidades que presenta un agente terapéutico/diagnóstico sean subsanadas con las fortalezas de otro y viceversa (la denominada multiterapia o terapia multimodal).

La principal característica que deben cumplir estos nuevos sistemas teragnósticos es su capacidad de dirigirse y acumularse específicamente en el lugar donde se espera que realicen su función y, así, evitar un diagnóstico errado o daños a tejidos sanos. Por ejemplo, la doxorubicina, uno de los fármacos más utilizados en el tratamiento de varios tipos de cáncer, puede causar mielodepresión y cardiotoxicidad además de potenciar la toxicidad de otros agentes anticancerígenos. Su vía de administración es estrictamente intravenosa, puesto que toda extravasación puede producir necrosis del tejido circundante y se requieren altas dosis para lograr concentraciones en el organismo que sean terapéuticamente efectivas. Por lo tanto, es deseable un sistema capaz de transportar el fármaco por el torrente sanguíneo de forma protegida, que disminuya su contacto con cualquier otro órgano o tejido sano, que se dirija al sitio del tumor, que nos indique su localización y distribución, y que sea activable remotamente para liberar su carga y ejercer su actividad terapéutica.

Un sistema teragnóstico dirigible supondría un avance enorme en el tratamiento de enfermedades como el cáncer y, sin lugar a dudas ,la nanotecnología ofrece múltiples herramientas para hacer realidad estas ideas.

Por todo ello, el objetivo de esta Tesis Doctoral ha sido diseñar, sintetizar, caracterizar y probar la eficiencia de nuevos sistemas nanoteragnósticos multifuncionales capaces de efectuar eficientemente el tratamiento, diagnóstico y visualización de células tumorales Para ello, se han sintetizado una serie de nanoplataformas que combinan múltiples terapias y varios métodos de visualización y diagnóstico.

Por un lado, se han incorporado la doxorubicina (**DOXO**) como agente quimioterapéutico, el verde-indocianina (**ICG**, *indocyanine green*) como fotosensibilizador para terapia fotodinámica (*photodynamic therapy*, ***PDT***) y nanoestructuras de oro, que combinan las propiedades ópticas de las nanocorazas (***nanoshells***) y de las **nanostrellas** de oro, como agentes para terapia fototérmica (*photothermal therapy*, ***PTT***) y transportadores del principio activo quimiterapétutico. Por otra parte, se han incorporado nanopartículas superparamágneticas de óxido de hierro (**SPIONs** - *Superparamagnetic Iron Oxide Nanoparticles*) como agentes de visualización por resonancia magnética y, además, se ha tomado ventaja de la posibilidad de guiar las nanoplataformas mediante la aplicación de un campo magnético externo. La DOXO y la ICG además de agentes terapéuticos son moléculas fluorescentes, por lo que es posible utilizarlas como agentes de contraste ópticos, especialmente la ICG cuyas longitudes de onda de excitación y emisión (780 y 820 nm, respectivamente) caen dentro del rango de la llamada “ventana biológica” del espectro electromagnético, la región en la cual la absorción del agua y de la hemoglobina, principal cromóforo de la sangre, presentan su máxima transmitancia. Ambas, DOXO e ICG, han sido utilizadas como agentes de contraste *in vitro*, y la ICG también se ha probado *in vivo* en modelos animales. De igual forma, las estructuras de oro obtenidas permitirían utilizar nuestras nanoplataformas como agentes de contraste en técnicas de visualización *in vitro* e *in vivo* como la tomografía computerizada o en imágenes fotoacústicas. En este trabajo se tomó ventaja para una visualización directa de las plataformas de la alta dispersión de luz y densidad que presentan las nanoestructuras metálicas empleadas para visualizar su internalización celular por medio de microscopía confocal láser y microscopía de transmisión electrónica.

Otro aspecto importante fue la incorporación de una molécula guía, el ácido fólico (***FA***), en nuestro caso con la finalidad de dotar a las nanoplataformas con especificidad hacia las células cancerosas. Un gran número de células tumorales

sobreexpresan ciertos receptores de moléculas específicas, como lo son los receptores de ciertos factores de crecimiento, péptidos y del ácido fólico. Las razones por las que se ha utilizado el ácido fólico son debido a su estabilidad, la relativa facilidad con la que se puede conjugar a otras moléculas y su bajo coste.

Por otra parte, otro objetivo del presente trabajo fue la de desarrollar rutas sintéticas que permitieran la escalabilidad de los sistemas obtenidos. Al final de este trabajo fue posible producir las nanoplataformas a la escala de decenas de miligramos y, además, fue posible liofilizarlas para su conservación. Este es un aspecto importante en vistas a su posible producción a mayor escala, en la que se sigue trabajando.

Después de su producción estas nanoplataformas fueron caracterizadas por diversas técnicas experimentales. Se determinaron sus propiedades fisicoquímicas más importantes, sus propiedades ópticas y magnéticas, su capacidad y eficiencia de incorporación y liberación de fármaco, SPIONs, ICG y ácido fólico, además de su estabilidad a corto plazo. De igual forma, se realizaron estudios de liberación fotoactivada por medio de iluminación con luz láser, se comprobó la efectiva internalización celular de las nanoplataformas y la eficiencia de moléculas guías para mejorar esta inclusión, su eficiencia terapéutica, el efecto sinergético de la aplicación simultánea de varias formas de terapia, y se realizaron estudios preliminares de biodistribución *in vivo*.

Así, esta tesis se divide en siete capítulos. En el capítulo I se da una introducción general a algunos de los conceptos, términos y fundamentos más importantes de la nanotecnología, dando una breve descripción de los nanomateriales de mayor aplicación, que clasificamos en tres grupos: inorgánicos, orgánicos/poliméricos y biológicos. De cada grupo se dan algunos ejemplos, se explican brevemente sus propiedades más importantes y se dan ejemplos de aplicaciones. En general, se ha puesto mayor atención en aquellos materiales que tienen mayor aplicación en el área biomédica. Posteriormenten se describen más detalladamente las nanoestructuras de oro, las nanopartículas superparamagnéticas de óxido de hierro y las nanopartículas poliméricas de ácido poliláctico-*co*-ácido glicólico (PLGA). En cada una de estas secciones se ofrece una descripción de las propiedades especiales que poseen y de las técnicas más comunes para la síntesis/producción de cada tipo de nanopartícula. En la parte final del capítulo se introducen conceptos importantes en nanomedicina, como la biofuncionalización, el direccionamiento pasivo y activo o los materiales terágnosticos.

En el capítulo II se da una breve descripción de los materiales especiales que se han utilizado para la síntesis de las nanoplataformas multifuncionales. También se describen las técnicas experimentales de caracterización que se han empleado, entre otras, la dispersión de luz dinámica (DLS), potencial zeta, microscopías electrónicas de barrido y de trasmisión (SEM y TEM, respectivamente), espectroscopías de UV-visible y de fluorescencia, magnetometría, imagen por resonancia magnética (MRI), microscopía de fluorescencia, microscopía confocal o la difracción de rayos X.

En el capítulo III trata se realiza la síntesis de nanoplataformas multifuncionales basadas en nanopartículas de PLGA cargadas con DOXO y SPIONs, y funcionalizadas con chitosano, un polisacárido biocompatible que debido a su gran número de cargas positivas se utilizó como medio para adsorber moléculas de ICG en la superficie de la nanoplataforma mediante interacción electrostática. Se observó que la estabilidad de la ICG es favorecida al encontrarse conjugada a la nanoplataforma. En este capítulo se presenta un estudio detallado de los efectos de los diferentes parámetros de síntesis, como son la composición de las fases orgánica y acuosa, los volúmenes de las mismas o las cantidades iniciales de DOXO y SPIONs en el tamaño, potencial zeta, y la capacidad (%DL, *drug loading*) y eficiencia de carga (%EE, *entrapment efficiency*) de la estructura interna de la nanoplataforma. También se determinaron los perfiles de liberación de DOXO y de ICG a pH neutro y ácido. Por otro lado, se determinó la capacidad como agente de contraste de imagen magnética del nanodispositivo mediante la realización de pruebas de visualización por MRI en células HeLa en “phantoms” de agar. Además, se comprobó con éxito la posibilidad que presentan las nanoplataformas de ser movilizadas y guiadas mediante un campo magnético externo gracias a la presencia de SPIONs en su estructura. Por otro lado, se demostró mediante ensayos *in vitro* que las nanoplataforma diseñadas para ejercer simultáneamente acciones quimi y foto-terapéuticas presentan una citotoxicidad muy mejorada respecto a aquellas diseñadas para ejercer una única acción de tratamiento. Finalmente, se realizaron estudios *in vivo* preliminares para determinar la localización y biodistribución de estas plataformas en un modelo animal de ratón en el que se indujo un tumor de mama. Los resultados obtenidos mostraron una eficiente acumulación en la zona del tumor, en el bazo y en el hígado, eliminándose en estos dos últimos casos a las pocas horas. Sorprendentemente, también se observó una cierta acumulación en la zona del cerebro lo que sugiere que las nanoplataformas lograron pasar la barrera hematoencefálica,

abriendo nuevas posibilidades para su aplicación en el tratamiento y visualización de enfermedades cerebrales como Alzheimer.

El capítulo IV trata específicamente de la síntesis de nanocorazas de oro utilizando las nanopartículas de PLGA como núcleo en un proceso de crecimiento por semillas (*seeded-growth method)* en ausencia de tensioactivos (surfactant-less). En este caso, se ha utilizado un método de crecimiento usando pequeñas nanopartículas de oro como semillas conjugadas a la superficie de las nanopartículas de PLGA previamente modificadas con chitosano para, posteriormente, realizar el crecimiento de la coraza usando una disolución de crecimiento compuesta por $HAuCl_4/K_2CO_3$ y ácido ascórbico (AA) como agente reductor, a concentraciones superiores a la estequiométrica. Las estructuras que se obtuvieron presentaron una topografía ramificada, típica de las llamadas "nanoestrellas" y que se asemeja a la estructura de algunos virus. El estudio demostró que es posible regular el tamaño (desde 150 a 240 nm) y el grado de ramificación de las nanoestructuras simplemente modificando las relaciones de los tres reactivos: disolución de crecimiento, precursor de NP-seed y AA, así como la forma en que se adiciona el AA, ya sea en una sola adición o en múltiples adiciones seguidas, obteniéndose de esta última manera nanoestructuras de tamaños menores (~100 nm). Finalmente, se realizó un estudio de viabilidad celular en el rango de concentraciones $2\cdot10^8$-$2\cdot10^{11}$ NP/mL, obteniéndose valores por encima del 90% para todo el rango. También se presentan imágenes de microscopía diferencial de contraste de interferencia, demostrando la eficiente internalización de la nanoplataforma híbrida en células.

En el capítulo V se presenta la síntesis de nanoplataformas híbridas de PLGA y oro, como las preparadas en el capítulo anterior, pero que ya incorporan el fármaco (DOXO) y las nanopartículas magnéticas (SPIONs) en su núcleo polimérico. Además, estas nanoplataformas fueron funcionalizadas con ácido fólico (FA) previamente conjugado a un poli(etilenglicol) (PEG) hetero-bifuncionalizado que consta de un grupo tiol en uno de sus extremos y un grupo amino en el otro. La conjugación del FA al SH-PEG-NH_2 se realizó mediante química de carbodiimida; posteriormente el SH-PEG-FA obtenido se conjugó a la estructura de oro mediante el enlace de grupo tiol a la superficie de oro de la nanoplataforma. El tamaño de estas nanoplataformas fue de alrededor de 180 nm con un grado de ramificación bajo. Se realizaron estudios de liberación controlada mediante iluminación con láser con longitud de onda en el infrarrojo cercano, en la llamada "ventana biológica". Se demuestró la capacidad que

presentan nuestros sistemas para liberar de manera controlada la carga que llevan en su núcleo después de ser iluminadas mediante un pulso corto de 1 segundo de duración (superficie irradiada 6 μm^2) con un láser de 820 nm de longitud de onda acoplado a un microscopio óptico. De esta forma, se obtuvieron imágenes de microsopía confocal de células HeLa (previamente incubadas con nanoplataformas) antes y después de iluminar a diferentes potencias del láser, en la cuales se observa la liberación de la carga solo después haber irradiado la célula que contiene las nanoplataformas. Con esta configuración del láser se obtuvieron también imágenes de TEM antes y después de irradiar las nanoplataformas con el fin de observar el efecto de la irradiación en su estructura y, de esta forma, correlacionar los patrones de liberación de fármaco con los cambios estructurales de los nanosistemas a diferentes potencias del láser. Debido a la alteración estructural de las nanoplataformas bajo irradiación láser pulsante, se empleó otro tipo de configuración para realizar ensayos de liberación. En este caso, se empleó un láser de iluminación continua a 808 nm, con una superficie irradiada de 0.13 cm^2 y tiempos de iluminación en el rango de los 5-10 minutos. Así, se comprobó que la liberación de DOXO se ve estimulada por la acción lumínica de la irradiación, aunque de forma más suave que en el caso del láser pulsante debido a la menor acumulación de energía de un tiempo corto de exposición. Las plataformas, asimismo, también presentaron una potencial aplicación como agentes de contraste para visualización de imágenes por resonancia magnética. Finalmente, se realizaron pruebas de citotoxicidad *in vitro* que demostraron la acción sinergística de la aplicación simultánea de las terapias quimio- y fototérmica gracias a la multifuncionalidad terapéutica de las plataformas diseñadas y a la eficacia en la combinación de los sistemas de direccionamiento específicos basados en la presencia de una molécula gúia (FA) en la estructura de la plataforma y el guiado magnético.

En el capítulo VI, se presenta la preparación de un sistema basado al producido en el capítulo V pero funcionalizado con un complejo de albúmina de suero humano (HSA), ICG y FA. Este complejo se obtuvo mediante la conjugación no-covalente de ICG con la HSA por simple incubación. Posteriormente, se conjugó el FA al complejo HSA-ICG mediante química de cabodiimida. Una vez obtenido el complejo HSA-ICG-FA, este se adsorbió sobre la superficie de las nanoplataformas híbridas de PLGA/DOXO con coraza de oro. Este tipo de nanoplataformas presentó un tamaño alrededor de los 100 nm. La incorporación de ICG en la superficie de la nanoplataforma

originó la posibilidad de aplicar tres tipos de terapia diferentes combinados en un solo sistema, pues la ICG puede actuar como fotosensibilizador en terapia fotodinámica (PDT). Esta terapia se basa en la generación de oxígeno singlete, altamente citotóxico, capaz de reaccionar con la membrana plasmática de las células cancerígenas y, por lo tanto, destruirlas. Por otra parte, también se observó una mejora en la estabilidad de la ICG conjugada a la nanoplataforma que en estado libre, principal limitación de esta molécula para su amplia aplicación en la práctica clínica. Mediante la incorporación de los tres tipos de terapia (PDT, quimio y fototerapia), aunados a la capacidad del FA como molécula guía, en una nanoplataforma única se obtuvieron efectos citotóxicos superiores a aquellos originados con un solo tipo de terapia o en ausencia de molécula guía. Estos resultados se reprodujeron en diferentes líneas celulares. De igual forma, se probó también la capacidad de esta nanoplataforma como agente de contraste fluorescente *in vitro* e *in vivo* en un modelo animal. Los resultados obtenidos de las pruebas de biodistribución *in vivo* mostraron una eficiente acumulación en la zona del tumor y en el bazo.

En el capítulo VII presentamos la síntesis de nanoplataformas multiterapéuticas basadas en nanoestrellas de oro (NS). Estas NS fueron funcionalizadas con DOXO por medio de un enlace escindible (puente disulfuro) que permite su liberación bajo la acción de enzimas reductoras. La nanoplataforma también fue funcionalizada con ácido fólico (FA) para asegurar la liberación específica del fármaco de la nanoplataforma y aumentar la eficiencia de internalización en células HeLa. Al modificar sintéticamente el plasmón de resonancia superficial, la presente nanoplataforma también fue capaz de actuar como agente fototerapéutico. De esta forma, se combinaron dos tipos de terapia en un solo sistema. También fue posible visualizar la internalización celular de las nanoplataformas gracias a la autofluorescencia de la DOXO. Se observó una mejora en la internalización cuando la nanoplataforma presentaba en su estructura la molécula guía, presentando una menor viabilidad celular en células HeLa gracias a una mejor eficiencia citotóxica de las terapias fototérmica y química combinadas.

En resumen, se ha logrado sintetizar diferentes nanoplataformas multifuncionales teranósticas aplicables en el tratamiento, diagnóstico y visualización de cáncer. Los procesos que se utilizaron para su preparación han sido de bajo consumo de energía y con materiales, en su mayoría, biocompatibles. Los resultados obtenidos de su caracterización fisicoquímica y de la evaluación de su desempeño *in vitro* e *in vivo*

sugieren que estas nanoplataformas podrían ser utilizadas como tratamientos anticancerígenos con resultados más efectivos, permitiendo disminuir las dosis y los tiempos de tratamiento, y realizar terapias combinadas de forma simultánea y localizada.

Summary

Nanoscience and nanotechnology deal mainly with the synthesis, characterization, exploration and exploitation of nanostructured materials. These materials are characterized by having at least one of its dimensions in the nanometre range (1 nm = 10^{-9} m). Nanomaterials are a bridge between the molecules and the macroscopic systems. The physical and chemical properties of nanomaterials may differ considerably from that of the atoms/molecules or simple macroscopic materials of the same composition. The particularity of their features leads us to the development of new devices and their application in the improvement of existing technologies or in the development of new ones.

Nanoscience and nanotechnology have grown explosively in the last two decades due to the increasing availability of new methods for the synthesis of nanomaterials as well as tools for their characterization and manipulation. Similarly, the level of understanding of the electrical, optical and magnetic propeties of semiconductor, metals and polymer nanostructures has advanced significantly in last years.

Also, characterization tools such as the electronic miscroscopies, crystallography, spectroscopy, among others, have allowed us to follow and control the size, shape, and structure of nanomaterials. However, nanoscience and nanotechnology still have a huge field of research and development to be done with regard to the design, synthesis, characterization and application of nanoscale systems.

One of the fields of nanotechnology that is still in an initial development stage is nanomedicine. This new area of nanotechnology is just the application of nanotechnology concepts and techniques to the biomedical field and it is currently in a great growing phase. The use of nanotechnology has enabled us to create new systems that may revolutionize the way in which a large number of diseases can be diagnosed and treated. Among the new nanomaterials that have been use for these purposes, we can find polymeric nanoparticles and nanocapsules, liposomes, micelles, magnetic nanoparticles, semiconductor nanoparticles (*quantum dots*), metal nanoparticles of different shapes, carbon nanotubes, grapheme, nanodiamonds, dendrimers, biomolecule-based nanostructures (nucleic acids, proteins, viral capsides) just to mention a few. These nanostructures offer different properties and we could even say improved

characteristics respect to the macroscopic-composing bulk material due to its nanometer size.

For example, polymeric nanoparticles and liposomes have been used in drug delivery treatments of several diseases. They can be controlled to transport drugs and release them specifically at the tumor site. Modified magnetic nanoparticles have been used as contrast agents in resonance magnetic imaging with excellent results. Also, gold nanoparticles have been applied as phototherapeutic agents, a new type of therapy against cancer in which malignant cells are destroyed by the ability of gold nanoparticles to absorb light and convert it into heat.

Some examples of nanocarriers that have been approved for medical applications in clinical practice are:

- Doxil, doxorubicin-loaded liposomes, which was the first liposomal system approved by the Federal Drug Administation (FDA) of USA.
- Abraxane, paclitaxel-loaded albumin nanoparticles of 130 nm in size, also approved by the FDA as a second-line treatment against breast cancer.
- Combidex (ferumoxtran-10), contrast agent based on iron oxide nanoparticles, which is being used for differentiation of lymphatic cancerous and healthy nodes.
- DanoXome, liposomes loaded with the chemotherapeutic agent daunorubicin.
- Ambisome, amphotericin-loaded liposomes for antifungal treatment.
- Genexol-PM, polymeric particles made by the block copolymer PEG-PLGA and loaded with the chemotherapeutic drug paclitaxel.
- DE-310, a camptothecin-dextran complex for treatment of lung, colon and breast tumors.

On the other hand, in general the traditional forms of drug administration are not the most efficient many times, which can be quite aggressive with the patients, lengthy and costly. The use of nanomaterials in the medical area would reduce the dose, frequency and economical costs of disease treatments. Similarly, the incorporation of new forms of contrast agents for imaging and diagnosis should not only allow to perform a real-time monitoring about the treatment´s efficiency chosen facilitating. in this way, to change and adjust the therapeutic dose according to the response of each patient (personalized medicine), but also the early detection of diseases.

Then, the combination of therapeutic and diagnostic agents in one system creates a new concept called ***theranostics***; hence, a theranostic system can treat the disease and, at the same time, work as a diagnostic and imaging agent.

In addition to the combination of these two features, therapy and diagnosis, it is also desiderable the incorporation of other elements in theranostic nanosystems which enable to address the disease from multiple angles, so that the weaknesses of one therapeutic or diagnostic agent can be remedied with the strengths of another and vice versa (the so-called multimodal treatment or therapy).

The main feature that must be complied with these new theranostic systems is their ability to target and accumulate specifically in the site where it is expected to carry out their function and, thus, avoid misdiagnosis or damage to healthy tissues. For example, doxorubicin, one of the most widely used drugs in the treatment of several types of cancer, can cause myelosupression and cardiotoxicity besides enhancing the toxicity of other anti-cancer agents. Its administration route is strictly parenteral since any extravasation can produce necrosis of the surrounding tissue and require high doses to achieve concentrations in the body that are therapeutically effective. Therefore, it is desirable to have a system capable of i) transporting and protecting a drug in the bloodstream; ii) diminishing interactions with any other organ or healthy tissue, iii) specifically targeting the tumor site; iv) indicating its localization and biodistribution; and finally v) being remotely activated to release its payload and exercise its therapeutic activity.

Hence, a targeted teranostic system would be a great advance in diseases treatments such as in cancer and, with no doubts, nanotechnology offers several tools to make these ideas completely real.

The main goal of this PhD thesis has been to design, synthesize, characterize and test the efficiency of new multifunctional nanotheranostics systems capable of imaging, diagnosing and treating cancer tumor cells. To accomplish this aim, we have synthesized a series of nanoplatforms that combine multiple therapies and several visualization and diagnosis methods.

On one hand, we have incorporated doxorubicin (**DOXO**) as a chemotherapeutic agent, indocyanine green (**ICG**) as a photosensitizer for photodynamic therapy (**PDT**) and gold nanostructures that combine the optical properties of nanoshells and gold

nanostars for photothermal therapy (**PTT**), and also serve as carriers for the chemotherapeutic agent. On the other hand, we have incorporated superparamagnetic iron oxide nanoparticles (**SPIONs**) as magnetic resonance imaging (MRI) contrast agents, taking also advantage of the possibility of magnetic guiding of the nanoplatforms by applying an external magnetic field. Besides their therapeutic functions, DOXO and ICG are also fluorescent molecules, being possible to use them as fluorescent optical contrast agents, in particular ICG, whose excitation and emission wavelengths (780 and 820 nm, respectively) lye within the range of the so-called "biological window" of the electromagnetic spectrum, the region in which the light absorption of water and hemoglobin (the main cromophore in blood) is minimal. Both DOXO and ICG have been used as contrast agents *in vitro*, and ICG has also been tested in *in vivo* animal models. In the same way, the obtained gold structures would allow our nanoplatforms to be used as contrast agents in other optical imaging techniques *in vitro* and *in vivo* such computed tomography or photoacoustic imaging. In this work, we took advantage of the high light dispersion and density shown by nanoshells to visualize its cellular internalization by confocal laser microscopy and TEM microscopy.

Another important factor has been the incorporation of a targeting molecule, folic acid **(FA**), with the objective of providing the platforms specificity towards cancer cells. A large number of tumor cells overexpress certain receptors of specific molecules, such as growth factors receptors, peptides and folic acid. We have used folic acid due to its stability, its relatively ease to be conjugated with other molecules and its low cost.

On the other hand, other objetive of the present has been to develop new synthetic procedures to be able to scale the produced nanoplatforms. At the end of this works tens of milligrams were able to be obtained in simple and easy steps, and stored after lyophilization for extended preservation. This latter aspect is key in order to extend production to the gram-scale, which I am working on.

After their obtention, these nanoplatforms were characterized through different experimental techniques. We determined their main physicochemical properties, their optical and magnetic properties, their capacity and efficiency to incorporate and release DOXO, SPIONS, ICG and folic acid and, finally, their short-term stability. Likewise, we performed detailed studies on photo-triggered laser cargo released, nanoplatform´s cellular uptake and internalization, multiple tests on the therapeutic effectiveness of the

synthesized nanoconstructs, the synergistic cytotoxic effect created upon the simultaneous application of different types of therapy, the positive effects of targeting ligands on cellular internalization, and preliminary *in vivo* nanoplatform biodistribution studies.

This thesis is divided into seven chapters. Chapter I is an introduction to some of the main concepts, terms and fundamentals of nanotechnology. It briefly describes the most common and applied nanomaterials, which we classify into three groups: inorganic, organic/polymeric and biological ones. We give examples for each group and explain their main properties and applications. Mostly, we have focused our attention on those materials that have greatest applications in biomedicine. Later, we detail the description of gold nanostructures, superparamagnetic iron oxide nanoparticles and polymeric poly(lactic-*co*-glycolic acid) (PLGA) nanoparticles. In each of these sections we describe their special properties and the most common techniques used for their synthesis/production. At the end of the chapter, we introduce some important concepts in nanomedicine such as which is biofunctionalization, passive and active targeting or theranostics materials.

Chapter II is a brief description of the special materials we have used for the synthesis of multifunctional nanoplatforms. We also illustrate the experimental characterization techniques we have employed throughout the work such as dynamic light scattering (DLS), zeta potential, scanning electronic microscopy (SEM), transmission electronic microscopy (TEM), UV-visible and fluorescence spectroscopies, magnetometry, magnetic resonance imaging (MRI), fluorescence microscopy, confocal laser scanning microscopy or X-ray diffraction amongst others.

In chapter III, we explain the synthesis of multifunctional nanoplatforms based on DOXO and SPIONs-loaded PLGA NPs which are subsequently functionalized with chitosan, a biocompatible polysaccharide used as a medium to adsorb ICG molecules on the nanoplatform surface by electrostatic interaction due to its large number of positive charges. It was observed that the stability of ICG dye was improved while conjugated to the nanoplatform. Here, a detailed study on the influence of the different synthetic parameters such as the aqueous and organic phase volumes or the initial DOXO and SPIONs feeding ratios on the size, potential zeta, and drug loading (% DL) and entrapment efficiency (%EE) of the nanoplatform cores. We have also determined the release profiles of DOXO and ICG at neutral and acidic pH. On the other hand, the

ability of these nanoplatforms as MRI contrast agents was performed *in vitro using* Hela cells phantoms. Moreover, the ability of nanoplatforms to be guided by an external magnetic field was verified under application of an external magnetic field. *In vitro* studies demonstrated that these nanoplatforms specially designed to simultaneously act as chemo and photo-therapeutic agents possess an enhanced cytotoxicity regarding those designed for single therapeutic activity. Finally, preliminary *in vivo* studies in a breast tumor-bearing mice model were performed in order to analyze the localization and biodistribution of the present nanoplatforms. The results showed that these nanoconstructs efficiently accumulate in/close to the tumor site, in the spleen and liver, being cleared from the two latter after a few hours. Surprisingly, the present nanoplatforms were also retained in the brain area overcoming the blood brain barrier, which opens up new possibilities to use these nanosystems for visualization and treatment of brain diseases such as Alzheimer´s.

In chapter IV we deal with the synthesis of gold nanoshells using PLGA nanoparticles as cores through a seeded-growth surfactant-less method. In this case, we have used a growth method using small gold nanoparticles as seeds conjugated to the surface of chitosan-modified PLGA nanoparticles to allow the growth of the shell using a growth solution consisting only of $HAuCl_4/K_2CO_3$ and ascorbic acid (AA) as reducing agent at concentrations above the stoichiometric one. The as-obtained structures a branched morphology, typically of the so-called “nanostars”, and resemble the structure of some viruses. This study demonstrated that it is possible to fit the size (from 150 to 240 mn) and the degree of branching of the nanostructures by simply changing the relations among the three reagents: the growth solution, the NP-seed precursor and AA reducing agent, and how AA is added, either in a single or in multiple additions; in this manner, smaller nanostructures (less than 100nm) are obtained. To conclude, we conducted a cell viability study of the as-obtained nanostructures in the concentration range $2\cdot10^8$-$2\cdot10^{11}$ NP/mL, obtaining viability values above 90% in all cases. We also demonstrate by differential interference contrast (DIC) microscopy the efficient cell uptake and internalization of the hybrid nanoplatforms.

In Chapter V we report the synthesis of hybrid nanoplatforms oconstutited of PLGA and gold nanoshells, as those elaborated in a previous chapter, but incorporating a chemotherapeutic drug (DOXO) and magnetic nanoparticles (SPIONs) in their polymeric nuclei. Furthermore, these nanoplatforms were functionalized with folic acid

(FA), previously conjugated to a hetero bifunctional thiol-amino poly (ethylene glycol) (PEG). The conjugation between the FA and the SH-PEG-NH_2 was made by carbodiimide chemistry and, later, the SH-PEG-FA obtained was conjugated to the gold structure by binding the thiol group with the gold surface of the nanoplatform. The size of these nanoplatforms was around 180 nm with a low degree of branching. We performed near infrared (NIR) laser–triggered controlled release studies in the so-called "biological window". In this chapter we demonstrate the ability of our systems to release their cargo in a photocontrolled manner after being illuminated by a short laser light pulse of 1 s and with a spot size of 6 μm^2 using a 820 nm laser (within the "biological window") coupled to a microscope. As a result, we obtained confocal images of HeLa cells (previously incubated with nanoplatforms) where it was possible to observed how the nanoplatform cargo is released to the cell only when applying the external light stimulus. We also obtained TEM images before and after irradiating the nanoplatforms with this laser configuration to observe the effect of laser illumination on their structure and correlate drug release patterns with their structural changes at different laser powers. Provided that structural changes of the platforms were observed under pulsed light irradiation, we also used other type of laser configuration to perform additional release experiments. Hence, we used continuous wave laser illumination at 808 nm, with a spot size of 0.13 cm^2 for 5-10 minutes. We checked that DOXO release was also triggered by this light irradiation but smoother (if compared with pulsed irradiation) due to the lower energy light density accumulated. Moreover, nanoplatforms were also tested as MRI imaging contrast agents. Finally, *in vitro* cytotoxicity tests proved the cytotoxic synergism upon combined application of chemo- and photothermal therapies provided by these nanoconstructs, and the successful specific targeting of these when functionalized with folic acid ligand and magnetic guidance.

In chapter VI a modification of platforms developed in chapter V was performed. In this case, the platforms are additionally functionalized with a complex of human serum albumin (HSA), ICG and FA. This complex was obtained through non-convalent conjugation of ICG to HSA by simple incubation. Later on, FA was covalently conjugated to the HSA-ICG complex by carbodiimide chemistry. Once obtained the HSA-ICG-FA complex, this was adsorbed onto the surface of the PLGA/DOXO hybrid nanoplatforms with a gold shell. This type of nanoplatforms presented a size around 100 nm. The incorporation of ICG on the nanoplatform surface

allowed simultaneously applying three different types of therapies with one unique system. In this way, ICG dye acts as a photosensitizer for photodynamic therapy (PDT). This therapy consists in the generation of highly cytotoxic singlet oxygen capable of reacting with the cytoplasmatic membrane of cancerous cells and destroying them. We also observed an improvement in the ICG stability when conjugated to the nanoplatform if compared with that of free dye, which is the main drawback fro the widespread use of this molecule in the clinical practice. Upon incorporation of these three types of therapy (PDT, chemo and phothermal therapies) and the ability of FA as targeting ligand in a single nanoplatform, we obtained enhanced cytotoxic effects than single therapy-based platforms, or in the absence of the targeting molecule. These data were reproduced when using different cancer cell lines. We also tested the ability of these nanoplatforms as fluorescent contrast agents *in vitro* and *in vivo*. The experimental data obtained in the biodistribution tests *in vivo* showed an efficient accumulation in the tumor and in the spleen.

In chapter VII, we present the development of another novel multimodal therapy platform based on gold nanostars (Au NS) as core particles. These NS are functionalized with the chemotherapeutic drug DOXO, which is conjugated to the NS surface by means of a cleavable heterofunctional crosslinker (sulfo-LC-SPDP) to allow its relase under breakage of a disulfide bond under the action of reducing enzymes. To ensure a specific delivery of the chemotherapeutic drug, the nanoplatoform is additionally functionalized with FA as targeting ligand and cellular uptake adjuvant. By synthetically modifying the plasmon band of Au NS to the near infrared (NIR) region of the electromagnetic spectrum, the present nanoplatform are able to simultaneously combine the capability of photototthermal therapy (PTT), through the conversion of absorbed light energy into localized heat, and chemotherapy, enabling their monitoring by means of optical fluorescence imaging thanks to DOXO autofluorescence. The cellular uptake was observed to be enhanced when the targeting ligand was bound to the nanoplatform. In addition, the therapeutic efficiency of the nanoplatform tested in HeLa cells demonstrated the larger cytotoxicity efficiency of the combined chemo and photothermal therapies if compared to individual ones, as observed in the other nanoplatforms studied throughout the present PhD thesis.

In summary, we have successfully synthesized different multifunctional theranostic nanoplatforms that can be applied in cancer treatment, diagnosis and

imaging. The processes used to prepare them have involved low energy consumption and most of the materials were biocompatible. The results obtained from their physicochemical characterization and performance *in vitro* and *in vivo* suggest that these nanoplatforms could be used in as anticancer treatments with more effective results, allowing lower doses, treatment times, and combined therapies applied locally and simultaneously.

CHAPTER I – INTRODUCTION

1.1 Nanoscience and nanotechnology

Nanoscience and nanotechnology are relatively new areas of knowledge that study the synthesis, characterization and applications of nanostructured materials, which are characterized by having at least one of their dimensions in the nanometric range (1 nm = 10^{-9} m). Nanomaterials are considered to be the transition between atomic and macroscopic systems. Their physical and chemical properties can considerably differ from those of the atoms/molecules or bulk materials of the same composition [1]. There are two main approaches for the production of new nanomaterials: top-down and bottom-up methodologies [2] (Figure 1.1).

1.1.1 The top-down approach

The top-down approach relies on the concept that nanostructured materials can be obtained from macroscopic materials by extracting the excess of material by physical, chemical and mechanical means. Amongst the different top-down methodologies we can mention, for example, *photolithography*, which is used to obtain micro- and nanometer sized patterns of semiconductor materials using a positive or negative patterned mask, a photoresist and UV light; *electron beam lithography (EBL)*, which consists of a scanning electron microscope (SEM) in which the beam can be turned on and off by a computer and directed to draw a prearranged pattern over the surface of a resist-coated substrate; *molecular beam epitaxy*, which is based on the epitaxial growth of atomic layers on a single crystal substrate; *focused ion beam milling*, which is essentially identical to EBL but instead of electrons, ions are used to eject atoms from the sample substrate and generate micro- and nanometric patterns and structures [3].

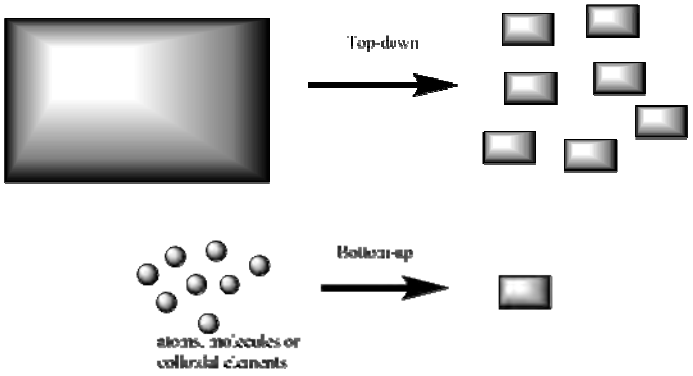

Figure 1.1: Nanotechnology approaches: top-down and bottom-up methodologies.

1.1.2 The bottom-up approach: self-assembly as a strategy to produce nanomaterials

The bottom-up approach is based on the self-assembly of building blocks of nanometric size. By assembling these sub-units in a controlled manner, the desired nanostructure can be obtained. The same scheme of self-assembly processes can directly or indirectly be adapted to the production of nanomaterials. The bottom-up approach makes use of the self-assembly of numerous building blocks to construct nanostructures. Based on their size, these building blocks can be atomic, molecular or colloidal. Moreover, the consideration of self-assembly process can be expanded depending on the nature of the process: thermodynamic or kinetic [2]. In self-assembly processes directed by thermodynamics, entropy plays a central role. The final structures obtained by these methods are equilibrium structures formed after achieving the right balance between entropy and the binding enthalpies of the various components at a given temperature [3].

On the other hand, kinetic self-assembly methods rely on trapping the system in some non-equilibrium (metastable) configuration by rapidly changing the reactant´s concentrations, the solvent, or the temperature of the system [3]. The simplest self-assembly process is the chemical reaction between two or more atoms to form a molecule. More complex self-assembly processes are driven by different forces, weaker than covalent bonds but strong enough to form stable structures.

There are five representative forces that govern the binding/interaction of atoms and molecules: covalent, metallic, ionic, hydrogen bonding and van der Waals forces.

The *covalent* force acts when two atoms bind to form a molecule, with a bonding energy of ca. 200 – 800 kJ/mol (~$100k_BT$) [3]. A *metallic* bond acts in the same manner than a covalent one but it takes place between metals that possess a "sea of electrons". These both are short range forces. Each atom or molecule involved in one of these bonds lost their identity after the bonding. In this sense, they are known as "chemical forces" that produce "chemical bonds". The electronic density of each atom or molecule is modified completely. On the other hand, *hydrogen bonds* and *van der Waals forces* are usually weak (a bond is called "weak" when it is in the order of k_BT at room temperature so the bond rapidly breaks and reforms as a result of thermal fluctuations [2]) and act at longer range distances; the result of these forces doesn't change the identity of atoms or molecules involved. In contrast to chemical forces, these are known as "physical forces" that generate "physical bonds". In general, in self-assembly processes weaker forces of longer range of action than chemical ones become more important.

The typical example of a self-assembly is the formation of micelles from amphiphilic molecules in aqueous medium. When amphiphilic molecules, with both hydrophilic and hydrophobic moieties, are dissolved in an aqueous medium they will spontaneously assembly in such a way that the hydrophobic parts avoid contact with water molecules, and the hydrophilic ones are exposed to water, leading to the formation of micelles. The driving force for the self-assembly of these structures is the hydrophobic interaction. Another example of self-assembly is provided by nature with the specific assembly of DNA strands with their complementary ones by hydrogen bonding. The nature of DNA molecules also leads to the formation of higher order structures driven by the combination of electrostatic, hydrophobic and hydrogen bond forces. Another example is the layer-by-layer assembly technique, which consists in the alternating deposition of oppositely charged poly-ions onto a substrate. After the deposition of the first layer, a second one of opposite charge is assembled and so on until the desired thickness is achieved. The substrate can be removed by chemical or thermal decomposition. This method is based on the coulombic (electrostatic) interaction between opposite charges and has been used, for example, to produce polymeric nanocapsules [4, 5]. pH and ionic strength of the medium where the assembly process is being done are crucial parameters, as the charge of polyelectrolytes are determined by these factors. In conclusion, if appropriate conditions and elements are

chosen, nanostructures with almost any shape, size and physicochemical characteristics can be constructed by employing the tool provided by nanoscience and nanotechnology.

1.2 Nanomaterials

Nanomaterials are defined by the European Commission as: *A natural, incidental or manufactured material containing particles, in an unbound state or as an aggregate or as an agglomerate, and where for 50 % or more of the particles in the number size distribution, one or more external dimensions is in the size range 1 – 100 nm* [6]. Nowadays a large number of nanomaterials can be produced and the number of synthetic processes for their obtention has been exponentially growing during last years [1, 7-9] , and the range of their potential application seems to be far from limits. Accordingly to their composition, we can classify nanomaterials in three main groups: inorganic, organic/polymeric and biological ones [10]. In next sections, we will give a brief description of those most important with a special focus on those intended for biomedical applications.

1.2.1 Inorganic nanomaterials

Inorganic nanomaterials are fabricated from metals, semiconductor and rare earth elements in their neutral valence state and/or with their oxides, chalcogenides, pnictides, alloys and their combinations [9]. The unique properties of inorganic nanomaterials arise from the different behavior of electrons confined in a nanometered region [1]. Most used and studied inorganic nanomaterials are noble metal [11], iron oxide [12], semiconductor and silica nanoparticles (NPs) [13], mesoporous materials [14], semiconductor and oxide nanosheets [15] and nanowires [16], etc. In this section, we will focus on gold and iron oxide nanoparticles because they are primary elements in biomedical nanoplatforms as those synthesized and applied in the present work. We describe also semiconductor nanoparticles, known as *quantum dots* [17], because they are a representative example of how nanometered size affects the physical, chemical, electronic and optical properties of nanomaterials and, although not studied here, also display remarkable properties for biomedical applications.

1.2.1.1 Metallic nanoparticles

Metallic nanoparticles are synthesized mainly from noble metals as Au, Ag, Pt and Pd and can have different shapes, from spheres, rods, shells, stars, etc. Their optical response depends closely on their size, shape, composition and surrounding medium [18]. They present a localized surface plasmon resonance (LSPR) which makes them very attractive as contrast agents [19], biosensors [20], fluorescence enhancers [21], SERS substrates [22] or photothermal therapy agents [23], amongst others. The LSPR peak in the visible and near infrared region (NIR) of the electromagnetic spectrum can be tuned just by varying their geometry, size and/or composition. Their surface chemistry allows easy conjugation of molecules, for example hydrophilic polymers, which improve their stability and/or biodistribution [24], or specific groups/ligands for example, to specifically target certain molecules, cells or tissues [23, 25, 26]. Despite their great potential applicability in biomedical applications thanks to their exciting optical properties and excellent stability and inertness, they also display very promising uses as catalysts, and as building blocks in electronic and energy storage and transformation devices [8].

1.2.1.2 Magnetic nanoparticles

They are synthesized mainly by thermal decomposition or coprecipitation of Fe^{+3} and Fe^{+2} salts to generate Fe_3O_4 and γ-Fe_2O_3 magnetic nanoparticles. Their size spans from few to tenths of nanometers and they can be stabilized with biocompatible polymers [27]. They can be manipulated by external magnetic fields and have been found used in biomedical applications as imaging contrast agents for magnetic resonance imaging (MRI) and/or stimuli responsive drug/protein delivery vehicles, as hyperthermia agents or energy storage devices [28].

1.2.1.3 Quantum dots

Quantum dots (QDs) are nanocrystals of semiconducting materials with sizes ranging from 2 to 120 nm. They consist of a number of atoms ranging from a few hundreds to a few thousands, with their crystalline structure being the same as the bulk materials they form. When synthesized in solution they form colloidal NPs stabilized by

amphiphilic organic molecules. Their shape can be spherical, cubic, rod or tetrapod [29]. They present novel properties due to the space confinement of charge carriers (electrons and holes) within the physical dimensions of the nanocrystals in opposition to the free diffusion of charge carriers in the bulk material. One of the most studied and understood confinement effects is the broadening of the band gap as the size of the nanocrystals is decreased. This effect manifests as a blue shift of the first absorption peak and the photoluminescence maximum, together with the appearance of higher discrete energy states in the valence and conduction bands. Varying the combination of the components (binary: CdSe and CdS; tertiary: ZnCdSe and CdSeTe) is possible to broaden the accessible wavelengths in the optical spectrum. As the metallic nanoparticles, quantum dots have been found application in optics, electronics, light emitting diodes, photovoltaic devices and, recently, there has been an increasing interest in their potential biomedical applications as cell markers and contrast agents due to their outstanding photostability, much better than common organic fluorophores [17, 29].

1.2.2 Organic/Polymeric nanomaterials

In this category we find two important groups, carbon based nanomaterials such as carbon nanotubes [30], fullerenes [31] and nanodiamonds [32], and polymeric/surfactant based nanomaterials [33, 34]. Fullerenes are carbon hollow clusters, being C_{60} the most thoroughly studied. Fullerenes have been applied as artificial photosynthetic systems to transform light into chemical energy in the fabrication of plastic solar cells in combination with polymers, and as therapeutic products of several diseases [35].

Carbon nanotubes were discovered in 1991 as a minor byproduct of fullerenes synthesis. Carbon nanotubes are perfect hollow cylinders and can be single walled (SWNT) or multiwall tubes (MWNT). Carbon nanotubes present outstanding physical properties derived from their single tube structure, preferred orientation, network connectivity, carbon-carbon bonds etc. The most significant properties of carbon nanotubes are their outstanding mechanical strength, high thermal and electrical conductivity and special optical properties such as absorption in the NIR region, photoluminescence and special Raman spectroscopy [36]. Potential applications of carbon nanotubes are numerous and are currently being incorporated into hundreds of

different applications from textiles, construction materials for vehicles as a due to their mechanical strength, and medicine [30, 31].

Nanodiamonds are diamond-based materials at the nanoscale, including pure phase diamond films, diamond particles and their structural assemblies. There is a special class of nanodiamond material called “ultrananocrystalline” diamonds, with a size in the order of a few nanometers; their applications include polishing, engine oil additives, dry lubricants, and as chemotherapeutic delivery devices [37].

Polymeric/surfactant nanomaterials have found numerous applications in biomedical areas as therapeutics and diagnostics carriers. They can be produced from natural or biocompatible synthetic surfactants and block copolymers by exploiting the self-assembling properties of these special molecules, thus, they can be used as biocompatible carriers for toxic or dangerous drugs in order to prevent unspecific action and damage of healthy cells and tissues [38] and as delivery agents for labile or sensitive substances such as fluorescent dyes [39], proteins [40] or DNA [41]. Micellization is the typical self-assembly process of surfactant molecules. Starting from the simplest spherical micelles, as the solutions conditions (concentration, pH, temperature, ionic strength, etc) are changed, it is possible to induce the self-assembly of these primary spherical micelles into more complex structures such as vesicles, cylinders, worm-like micelles, lamellar structures consisting of surfactant bi-layers, and bicontinuous structures with surfactant molecules assembled into connected films [2, 42]. This behavior is sometimes also observed with amphiphilic block copolymers [42]. Polymeric/surfactant nanomaterials can also be used as substrates and/or templates to build more complex nanoplatforms, as those synthesized for this research. In this section, we mention three examples: micelles, polymeric nanoparticles and liposomes, since we consider them some of the most representative examples of this group of nanomaterials

1.2.2.1 Micelles

They are self-assembled aggregates usually composed of surfactant or amphiphilic copolymers. They are formed by a lyophobic part surrounded by a lyophilic one that stabilizes the supramolecular structure in the solvent. The concentration at which appears the first aggregate/micelle is known as the critical micellar concentration

(CMC). Usually micelles have spherical geometries, although depending on the conditions they can also have rod-like and worm-like shapes [43]; vesicles or mesophases with cubic, hexagonal and lamellar structure can be also formed depending on solution conditions. Micelles are capable to solubilize lyophobic substances [44] but present an important disadvantage, which is their inherent instability at long periods of time due to their dynamic nature.

1.2.2.2 Polymeric nanoparticles

Polymeric NPs possess sizes ranging from 10 – 1000 nm. They are produced from non-degradable (polystyrene) or biodegradable polymers such as the poly (lactic acid) (*PLA*), poly (lactic-co-glicolic acid) (PLGA), polycaprolactones, chitosan, gelatin, sodium alginate, etc. They are mainly used for targeted delivery and release of drugs [45], although they are capable to transport other cargo molecules such as nucleic acids [41], proteins [46], peptides [33] and even inorganic nanoparticles of smaller size, such as magnetic nanoparticles [47]. Their geometry is usually spherical, even though they have been produced with ovoid or prism geometries, for example, through photolithography techniques. They are generally produced by emulsion-evaporation, emulsion-diffusion, or nanoprecipitation techniques [48], but lately nanofluidic NP assembly methodologies are gaining great interest due to the large monodisperse nature of the resulting NPs and the easy scalability of the Np production process [49]. The polymeric NP structure is a monolithic matrix with the cargo-substance (if present) solubilized and uniformly distributed within the NP core. The cargo is released mainly by diffusion and erosion processes of the polymeric matrix [50], although different stimuli responsive (pH, temperature, light, sound…) cargo delivery NP systems have been developed in recent years [51-53]. Polymeric NPs are very stable and many of them biocompatible, being eliminated basically by metabolic or enzymatic excretion pathways [54].

1.2.2.3 Liposomes

They are biocompatible and biodegradable structures produced form natural and synthetic lipids. They consist of an aqueous core surrounded by single or multiple lipidic bilayers; they are biologically inert, and very slightly immunogenic with a very

low intrinsic toxicity. They are capable to transport drugs with different lipophilicities: highly lipophilic cargos accumulate almost completely in the lipidic bilayer and poorly lipophilic ones localized in the aqueous compartment; drugs with middle characteristics can be localized in both regions. Unilamellar liposomes have sizes ranging 50 – 250 nm and multilamellar ones up to 1 – 5 μm. The former are used for transport hydrophilic drugs as they posses big aqueous compartments, and the latter ones for the transport of lipophilic drugs. However, this type of particles posses several disadvantages such as poor entrapment efficiencies and low solution stabilities [55].

1.2.3 Biological nanomaterials

Living systems can produce nanostructured materials *e.g.* in the biomineralization process, where calcium carbonate, calcium phosphate particles and microstructures in the nanometer size range are produced [56]. Nature has been an inspiration to produce materials with outstanding properties, *e.g.* gecko-inspired adhesives [57] or urchin-like nanoparticles [58]. A different approach is to manipulate biological materials to produce nanomaterials. Biomolecules, such as nucleic acids or proteins, have been used as building blocks to obtain materials with complex structures taking advantage of their self-assembly abilities [59]. Viral capsides, protein-based nanostructures, have been used as gene delivery vectors as well as drug and contrast agents carriers [60, 61]. In this section, we will mention two types of nanomaterials produced using biomolecules as building blocks, DNA complexes and protein based nanoparticles. We consider both of them good examples of clever manipulation of materials provided by nature in order to obtain biocompatible and biostable nanostructures. We will also give a brief description of virus capsides in order to highlight the importance of bio-shape in efficient drug delivery.

1.2.3.1 DNA complexes

Nucleic acids are polyanions that can adopt diverse structures, and their conformation can respond to different external stimuli such as pH, temperature or ionic strength [62]. DNA is easy to synthesize (by polymerase chain reaction, PCR), functionalize and manipulate. It has been used to form complexes with cationic surfactants, lipids, peptides and cationic polymers (the latter known as “polyplexes”)

[63]. These complexes can be used as vectors to introduce nucleic acids, plasmid DNA, antisense oligonucleotides or siRNA (small interfering RNA) to living cells for therapeutic purposes, for example, to fight against hereditary diseases, multigenetic disorders or cancer [63-65].

1.2.3.2 Protein-based structures

Physicochemical properties of proteins make them very attractive for the construction of nanomaterials [59] by exploiting their structural complexity and the great number of functionalities they bear. For example, amyloid fibrils made from proteins are excellent candidates for the construction of nanobiomaterials such as nanowires, nanolayers, gels, scaffolds, templates and liquid crystals, using the bottom-up approach as a result of their outstanding physicochemical properties (rigidity, stability against heat and destabilizing agents, resistance against proteases, amongst others), structural compatibility, nanometric dimensions and efficient self-assembling in well defined ultrastructures [66]. Nanoparticles are another example of protein based structures. Albumin based nanoparticles bound to paclitaxel (Abraxane), an anticancer drug, already approved by FDA for the treatment of metastatic breast cancer. These nanostructures take advantage of the natural properties of albumin to reversibly bind paclitaxel, transport it across endothelial cells and concentrate it in areas of tumor [67].

1.2.3.3 Viral capsides

Viral capsides are nanosized protein shells whose main functions are to protect, transport and deliver their genome inside a host cell [68]. They are typically built from several copies of one or a few different proteins often clustered into multimers called capsomers or five (pentamers) or six (hexamers) proteins. Viral capsides can adopt several shapes from roughly spherical with icosahedral symmetry to rod-like and prolate shapes. These nanostructures are promising candidates in nanoscience and nanotechnology applications, they have been successfully applied in gene therapy [69], encapsulation and attachment of specific materials (e.g. drugs [60], quantum dots [61]) and as biotemplates for the fabrication of nano-wires [70].

1.3 Gold Nanoparticles

The use of metal colloids, mainly of noble metals, dates back from more than 1000 years ago as, for example, Lycurgus cup, which contains Au and Ag particles of 50 -70 nm distributed in the glass. When the cup is illuminated from outside a green color is observed whilst when illuminated from the inside it has a red color. Michael Faraday, in 1857, was the first to describe that optical properties of colloidal gold are different from those of the bulk material, and was the first in evaluating the preparation and outstanding properties of gold nanoparticles [71].

1.3.1 Optical properties of gold Nanoparticles.

The optical properties of gold nanoparticles (Au NPs) depend on their size and shape, as well as on the medium they are dispersed. Intense brilliant colors of colloidal metallic NPs are an evident example of their interesting optical properties that arise from their special interaction with light. In the presence of an oscillating electromagnetic field, such as light, free electrons from a metallic nanoparticle have a coherent collective oscillation respect to the metal. This process is known as the localized surface plasmon resonance (LSPR) [18] (Figure 1.2). This electronic oscillation can be visualized in a simple way as one photon confined in the reduced space of the NP forming an intense electric field around the nanoparticle. The LSPR is manifested with a strong extinction whose maximum wavelength is placed exactly at the resonance frequency. Some of the absorbed photons will be dispersed in all directions at the same frequency in a process known as *scattering*. Other part of the absorbed photons will be converted into phonons or vibrations of the metal lattice, this process is called *absorption* [11]. The absorption and scattering contributions to the total extinction cross section depends strongly on the dimensions of the Au NPs. Another unique property of these is the possibility to adjust the LSPR by changing the size, shape, composition and the surroundings of the nanoparticle. In the case of spherical Au NPs, they have a red color with an absorption peak localized at ca. 530 nm, while triangular and branched nanoparticles have a blue color with an absorption peak that can be tuned from 600 to 1000 nm [72].

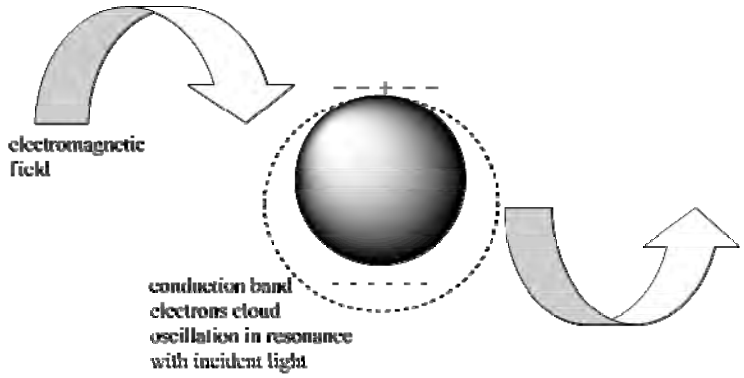

Figure 1.2: Surface plasmon resonance in an Au NP: The cloud of the conduction band electrons oscillates in resonance with the incident light.

The LSPR of Au NPs is described by Mie´s theory of scattering [72], which is the exact solution to Maxwell's electromagnetic field equations for a plane wave interacting with a homogenous sphere of radius R with the same dielectric constant as the bulk metal. The extinction cross section (C_{ext}) of the spheres can be obtained as a series of multipole oscillations if the boundary conditions are given. When the diameter of the sphere is much smaller than the wavelength of the incident light and only dipole oscillations contribute, higher order terms can be ignored in the calculations, so C_{ext} for spherical particles can be expressed as [72]:

$$C_{ext} = \frac{24\pi^2 R^3 \varepsilon_m^{3/2}}{\lambda} \frac{\varepsilon_2}{(\varepsilon_1+\varepsilon_m)^2+\varepsilon_2^2} \qquad \text{(Eq 1.1)}$$

where ε_m is the dielectric constant of the surrounding medium; $\varepsilon = \varepsilon_1 + i\varepsilon_2$ is the complex dielectric constant of the particle. From equation (1), a resonance peak occurs whenever the condition $\varepsilon_1 = -2\varepsilon_m$ is satisfied. NPs with non-spherical shapes (rods, prisms, core-shell NPs) have a C_{ext} that is strongly dependent on the aspect ratio and the NP size. This fact is exploited to generate NPs for biomedical applications, of which details will be given in further sections [72].

1.3.2 Synthesis of Au NPs

Colloidal gold has been used for more than thousand years as mentioned previously. Au NPs can be obtained by top-down and bottom-up methods. In top-down´s methodology, bulk Au is systematically broken until the desired nanoparticles

are obtained. However, this method is limited in controlling NP size, shape and further functionalization. The bottom-up methodology is based on the assembly of Au atoms by chemical or biological reduction. The chemical reduction involves two steps: the nucleation and the subsequent NP growth. When both steps are completed in the same process this is called a *in situ* synthetic procedure, otherwise it is referred to a *seed-growth method* [71].

In 1857, Faraday reported the formation of deep red gold solution upon reduction of chloroaurate ($AuCl_4^-$) with white phosphorous in a two-phase CS_2-water mixture. Since then, many different synthetic wet chemical routes have been developed to date to obtain Au NPs with well-defined sizes and shapes. In 1951, Turkevich [73] synthesized 20 nm Au NPs by reduction of $HAuCl_4$ with trisodium citrate. In 1971, Frens [74] refined the method to control the size of the resulting NPs. Schmid [75] in 1981 reported the synthesis of clusters of Au_{55} and phosphine and the notion of quantum dots. In 1993, Mulvaney and Giersig [76] were the first to synthesize thiolate capped NPs by substituting the citrate for a thiol compound. In 1994, the Brust-Schiffrin´s [77] method was developed, also using thiolated stabilizer to control NP size and stability but in a biphasic reaction, obtaining smaller NPs.

1.3.2.1 In situ synthesis

This method consists in the reduction of a gold salt solution, for example $HAuCl_4$, with a reducing agent and then being stabilized by a ligand with affinity to gold. In some cases, the reducing agent can also act as the stabilizer. Some of the reducing agents that have been used include ascorbic acid, sodium citrate, sodium borohydride, alcohols, hydrogen, hydroxylamine, formaldehyde, ozone, carbon monoxide, hydrazine, etc [71]. The reduction process can also be done electrochemically, photochemically and sonochemically [71]. During reduction, capping agents such as surfactants, polymers ions or organic acids are used to confine the NP size in the nanometer range, to direct the growth and/or to stabilize the nanoparticles. Stabilization can be accomplished, for example, by electrostatic repulsion and/or steric hindrance [71].

1.3.2.1.1 Turkevich method

The Turkevich´s method, published in 1951, is one of the first reported methods for spherical gold nanoparticles production based on a single phase water-based reduction of gold salt by citrate ions. In the standard method, the reduction of a boiling gold hydrochlorate solution by tri-sodium citrate added quickly under vigorous stirring takes place. After a few minutes, a wine-red AuNPs colloid is formed with sizes ca. 20 nm. In this method, the citrate acts as both reducing agent and stabilizer [78].

In 1970, Frens made some changes to the Turkevich's method to obtain nanoparticles with sizes from 15 to 150 nm by varying the citrate: Au ratio, although obtained NPs larger than 20 nm were always polydisperse [74]. In later years, many groups have examined in detail this method in order to elucidate the mechanism of nanoparticle formation. For example, it was determined that higher concentrations of citrate ions stabilize more rapidly the NPs, leading to smaller sizes, while lower concentrations give larger NPs and even lead to aggregation. It has also been elucidated that the "true" stabilizing molecule is the dicarboxy acetone, the oxidized product of citrate. Variations of the reaction pH and temperature also allow extra control over the NPs size. NPs of 5 nm were obtained by Puntes' group [79] using D_2O instead of water. Also, changing the order of addition (Au solution to citrate) leads to 10 nm NPs. In conclusion, the final characteristics of spherical NPs obtained by Turkevich's method can be controlled by manipulating the kinetic and thermodynamic reaction parameters e.g. the relative reactant concentrations, temperature, pH…

1.3.2.1.2 Brust-Schiffrin's method

The Brust-Schiffrin's method, published in 1994, is used for the synthesis of thiolate protected nanoparticles. This synthesis uses a biphasic (an aqueous and organic phase solution) and tetraoctylammonium bromide (TOAB) as a phase-transfer agent to reduce the $[AuCl_4]^-$ anion with $NaBH_4$ in the presence of alkanethiols [77]. The pros of this synthesis are that it is carried out at ambient conditions, the high stability of the resulting NPs, the absence of NP aggregation after isolation and redispersion, small NP sizes with narrow distributions, and ease of functionalization and ligand modification.

The particle size can be controlled between 2 and 5 nm by adjusting the temperature, reduction rate and thiol to Au ratio. Larger S:Au ratios give smaller NPs due to the growth inhibition by the sulfur containing agents. Fast addition of $NaBH_4$ and low temperature conditions also produce NPs with narrower size distributions. This method has been also modified, for example, by changing the solvent to methanol, where both the $HAuCl_4$ and p-mercaptophenol are soluble, avoiding the phase-transfer of TOAB impurities. Any thiol that is soluble in the same solvent (methanol, ethanol or water) than $HAuCl_4$ can be used to obtain NPs in single phase reactions. The reducing agent used in Brust-Schiffrin method is stronger than the citrate used in Turkevich's method, therefore, the reaction rate is faster and much smaller NP sizes are obtained.

1.3.2.2 Seed-growth methods

The seed-mediated growth is another approach to produce well defined nanoparticles. This method is used to prepare nanoparticles with different morphologies and aspect ratios (Figure 1.3). In a typical seed-mediated growth synthesis, a precursor solution of small and highly stable nanoparticles between 3 – 5 nm is prepared. These nanoparticles, called seeds, act as nucleation sites to generate larger nanoparticles in the presence of a gold salt growth solution, and a capping/directing agent (e.g. CTAB, sodium citrate trihydrate, polymers). A mild reducing agent (ascorbic acid, formaldehyde) is used to reduce Au^{+3} to Au^0 only in the presence of Au seeds as catalysts; thus, the newly reduced Au^0 can only assemble on the seeds and no new particle nucleation occurs in solution. The growing process is slow due to the mildness of the reducing agents, and subsequent growing steps can be done.

This method has also been used to obtain non-spherical particles such as, for example, nanorods, branched nanoparticles, or gold nanoshells. These nanoparticles, with a non-spherical shape, are quite interesting because they present a surface plasmon resonance located at different wavelengths depending on their size and aspect ratio. In contrast to spherical nanoparticles whose surface plasmon resonance peak is positioned around 520 nm and is barely modified with size changes (approximately only 20 nm for sizes ranging from 5 nm to 100 nm), non-spherical nanoparticles have a plasmon peak (or multiple plasmon peaks in some cases) that can be readily tuned from the visible to

the NIR region of the electromagnetic spectrum by simply modifying their aspect ratios and dimensions.

1.3.2.2.1 Spherical nanoparticles

The seed growth-method provides additional control to produce spherical or quasi-spherical nanoparticles of large sizes. The first method based on seeded-growth was patented by Natan and co-workers [80]. They synthesized NPs from 20 – 100 nm by adding citrate capped seeds to a Au growth solution. This method provided a better control over NPs characteristics than Turkevich's and Frens' methods. Later, Murphy et al. [81] improved this methodology by using ascorbic as the reducing agent and CTAB as the stabilizer, obtaining highly monodispersed (deviation < 10%) 40 nm NPs. In 2006, Liz-Marzán's group [82] obtained NPs up to 200 nm by a seed-growth method. Recently, NPs with sizes up to 300 nm have been synthesized using hydroquinone [83] and ascorbic acid [84] as reducing agents. In summary, temperature, pH, growth solution to seed ratios and type and concentration of the reducing agent are variables that affect the size distribution and shape of spherical nanoparticles prepared by seed-growth methods.

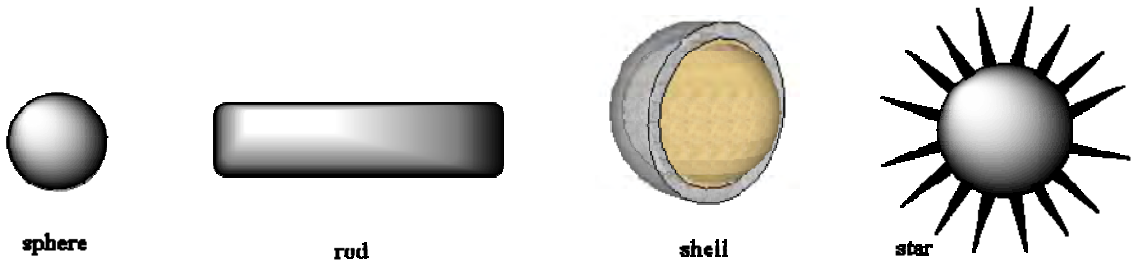

Figure 1.3: Different shapes of Au NPs.

1.3.2.2.2 Au nanorods (Au NRs)

Gold nanorods exhibit two distinct plasmon resonance modes: one associated with electron oscillations parallel to the longitudinal axis and the other with electron oscillations parallel to the transverse axis (Figure 1.4). The longitudinal plasmon mode can be tuned by adjusting the aspect ratio of the nanorod, making it a particularly useful structure for different applications in the fields of photonics and/or biotechnology.

The first seeded-growth method used in nanorod synthesis was published by Murphy's group [81]. In this method, a citrate-capped seed solution is firstly prepared.

Then, the seeds are added to a solution containing a $HAuCl_4$ growth solution, CTAB and freshly prepared ascorbic acid. This method generated Au NRs with aspect ratios (longitudinal axis/transversal axis) from 4 – 20. Later, Mulvaney's and Liz-Marzán's [85] groups made modifications in the solution temperature and CTAB concentration to obtain better yields of nanorods and less secondary nucleation of NPs with spherical shapes. The synthesis was much improved when $AgNO_3$ is introduced in the growth solution [86]. The role of Ag ions in the directional growth of AuNRs was explained by Liu and Guyot-Sionnet [87] in terms of the underpotential deposition of metallic silver on the different crystal facets of gold, leading to symmetry breaking and rod formation. Nikoobakht and El Sayed [88] improved the method using CTAB-capped seeds instead of citrate-capped seeds, and using $AgNO_3$ in the growth solution they obtained up to 99 % yield of nanorods with aspect ratios ranging from 1.5 – 5 and generating only traces of spherical NPs.

Au NPs have an extinction cross-section composed by an absorptive component and a scattering component. Among Au NPs, Au NRs have a very large absorption cross-section, and provided that they possess a longitudinal LPSR band that can be finely tuned in the NIR region, these characteristics makes them a promising photothermal therapy agent. A pitfall for biomedical use of Au NRs is the relative toxicity they can present as a consequence of using CTAB as the capping agent. To solve this issue, they have been functionalized with silica, iron oxide or polymeric coatings such as polyethylene glycol, PEG, or bioactive molecules [24, 89-92].

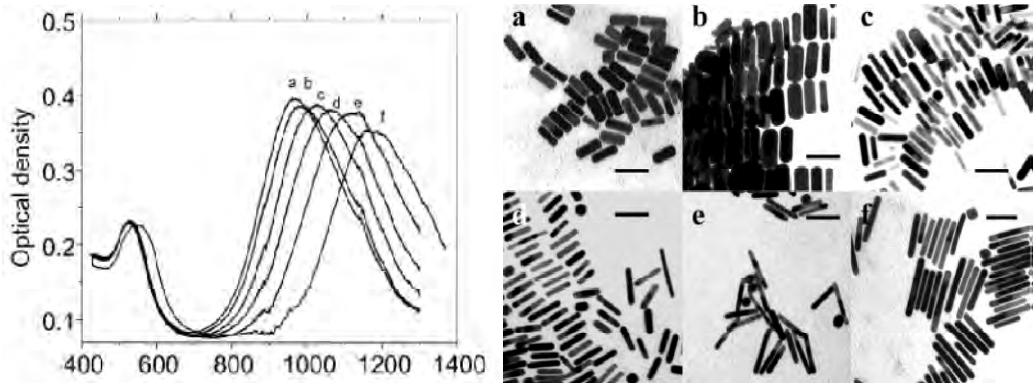

Figure 1.4: UV-vis spectra and TEM images of AuNRs with and different aspect ratios. The first peak at 520 nm in the UV-Vis spectra corresponds to the transverse plasmon band and the second peak at 900-1200 nm corresponds to the longitudinal plasmon one (images used with permission from [88]. Copyright® 2003, American Chemical Society).

1.3.2.2.3 Au nanoshells (Au NShs)

Au nanoshells (Au NShs) (Figure 1.5a) are another type of metal nanostructures which have highly tunable plasmon resonances in the NIR region of the electromagnetic spectrum (700-1200 nm), known as the "biological window" due to the high light penetration in human tissues and low energy absorption by water and hemoglobin present in human body. This fact makes them quite interesting for biomedical applications since they can be used simultaneously as therapeutic and diagnostic devices. Halas and coworkers [93] formed such core-shell structures for first time by a seeded metallization of colloidal silica spheres. The silica particles are functionalized with a monolayer of aminopropyltriethoxysilane molecules (APTES), which is subsequently used to bind small colloidal Au seeds by electrostatic attraction. Silica-seed nanoparticles are mixed with a plating solution of $HAuCl_4$ and K_2CO_3 growing solution, and, subsequently, a reducing agent is added to reduce Au^{+3} ions to Au^0. The seeds act as nucleation sites, and after a few minutes the mixture takes a bluish-greenish color indicating the shell formation. The thickness of the final Au shell can be controlled by adjusting the ratios of seed-decorated SiO_2 NPs, reductant and plating solutions. The plasmon resonance frequency is tuned by adjusting the relative sizes of the core and shell dimensions.

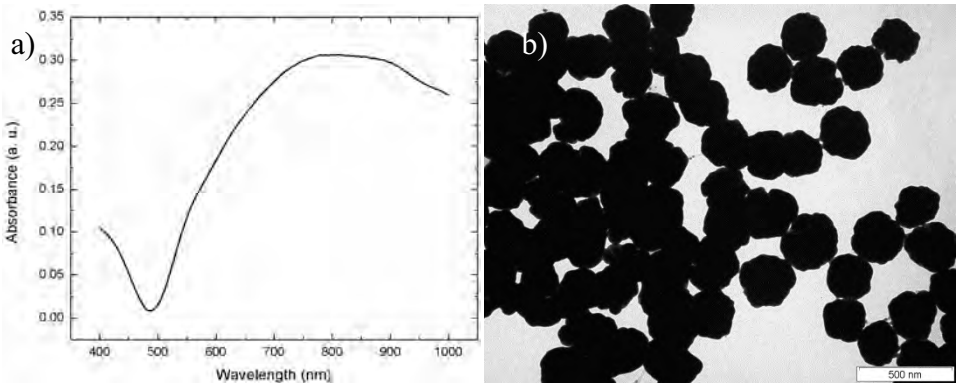

Figure 1.5. a) UV-Vis spectrum and b) TEM image of Au NShs. The broadening of the plasmon band can be attributed to NP polydispersity and to the nature of the dielectric function of gold shell.

The UV-Vis spectrum of Au NShs presents a broad single peak due to the nature of the synthesis, which generates not uniform sizes. As a result, the plasmon resonance peak becomes a weighted average of the contributions of the resonance peaks of

individual nanoshells (Figure 1.5b); a second contribution arises from the nature of the dielectric function of gold shell, which is modified by electron scattering at the gold interface [94].

1.3.2.2.4 Au nanostars

Another interesting group of Au NPs are Au nanostars (Figure 1.6), which are branched structures with star, flower or sea-urchin shapes. These structures are quite interesting due to their special response toward optical illumination. Like AuNSh and Au NRs, Au nanostars present a LSPR tunable in the NIR region providing them with potential biomedical applications as therapeutic and diagnosis devices. The position and energy of the LSPR band can be tuned by modification of their total size as well as the number, size and aperture angle of tips.

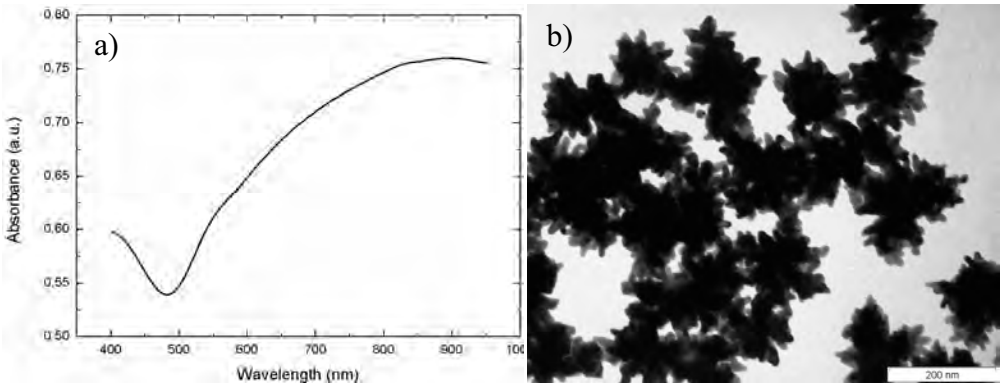

Figure 1.6: a) UV-Vis spectrum and b) TEM image of Au nanostars.

An interesting feature of anisotropic Au NPs, in general is the generation of very high electromagnetic fields at the nanoparticles' surface. Electromagnetic enhancements due to LSPR are considered the main effects behind of surface enhanced Raman scattering (SERS). SERS spectroscopy is one of the most powerful analytical techniques for identification of molecular species [95]. Coupling of plasmons, for example, at the gap between nanospheres dimers, are known as "hot spots" due to the high electromagnetic field enhancements, reaching at these sites, the single molecule detection limit. Au NPs can therefore be regarded as nanoamplifiers and, since the discovery of this effect, SERS spectroscopy has been studied intensively [96]. In particular, Au nanostars present "hot spots" localized at the tips with extraordinary field enhancements, with calculated enhancement factors up to 10^8, much larger than those of

sphere dimers. It has also been observed experimentally that Au nanostars display stronger SERS activity than spheres and rods, and similar to sphere dimers [95]. The advantage of Au nanostars is the possibility to observe in solution single molecules adsorbed on the tips with no need for the formation of hot spots within nanoparticle aggregates, which makes Au nanostars prospects for Raman imaging applications [95, 97].

Synthetic methods for obtention of Au nanostars can be classified in seeded-growth and one-pot methods. In seeded-growth methods preformed seeds act as nucleation sites on which additional material can be deposited for subsequent growth, usually leading to monodisperse particles with different sizes. One of the most popular methods was inspired by the seeded growth process employed in the synthesis of Au NRs. In this method, a chloroauric acid ($HAuCl_4$) solution is reduced with ascorbic acid at room temperature in the presence of one or more cationic surfactants (typically CTAB). Many reported methods based on this approach suggest that the use of capping agents, (i.e. surfactants or polymers), which seem to display preferential adsorption on certain crystalline facets of the metal seed surface, is the responsible of the anisotropic growth process through the alteration of the growth rates along specific crystallographic directions [98]. The nature of the reducing agent has also significant influence in the final Au nanostars. For example, poly-crystalline branched Au NPs with sizes ranging 47-185 nm were produced using hydroxylamine sulfate as reducing agent [99]. A successful protocol used N,N dimethylformamide (DMF) as reducing agent and poly(vinylpyrrolidone) as protecting polymer with 100% production of nanoparticles with multiple sharp spikes at room temperature [100]. Au nanostars suitable for biological systems were obtained using gelatin as capping ligand, silver 4 nm seeds and a growth solution containing K_2CO_3, which was claimed to provide optimal conditions for the kinetic control reduction by ascorbic acid [101]. In these nanoparticles, gelatin molecules tend to bind onto the 100 planes of the initial seeds, giving rise to a slow growth in the <100> direction and, thus, promoting anisotropic growth in the <111> direction.

In non-seeded methods, nuclei evolve *in situ* to form nanocrystals seeds and subsequently bigger spiky particles through the direct addition of metal atoms. Controlling the formation of nuclei at these one-pot synthetic conditions is complicated and usually leads to wider distributions of particle sizes and shapes. Ascorbic acid has

been used as reducing agent to obtain multiple-twinned crystals with preferential growth on the <111> facets [102]. HEPES, which performed both as reducing and stabilizing agent, was used to obtain branched nanocrystals with high yield (> 90%) in a "green" chemical synthesis [103]. In a different approach, high yields of polydisperse branched gold nanoparticles with one, two or three single crystalline tips were obtained using hydrogen peroxide (H_2O_2) and sodium citrate as reducing agents, in combination with bis(p-sulfonatophenyl) phenylphosphinedihydrate dipotassium as stabilizer [104]. Multi-branched urchin-like Au NPs were also obtained using thiolated capping molecules, with significant improvements in terms of solubility and stability in organic solvents [58].

1.3.3 Biomedical applications of Au NPs

Thanks to their especial optical properties and their inertness and low toxicity [105], Au NPs have found many applications in the biomedical area. Despite they have been used since ancient Romans for example, in glass staining, it is just recently they have received a significant attention in biology and medicine research and praxis. The conjugation of biomolecules to NPs surface has opened a wide range of applications. The first applications of Au NPs bioconjugates were as biosensors. Au NPs dispersions suffer a visible color change when they aggregate. For example, this property was used by Mirkin *et al.* [20] to detect oligonucleotides. Au NPs were functionalized with single strands of DNA. When the complementary strands coupled to the functionalized NPs, a change in color from ruby red to blue occurred due to NP aggregation. On the other hand, the SPR of Au NPs is very sensitive to the dielectric constant of the surrounding medium, especially in the proximity of the surface as already commented previously. When the nanoparticles are functionalized with certain ligands (*e.g.* antibodies) they show a shift in their SPR peak when the ligand counterpart is attached. The SPR shift is closely correlated to the concentration of counter-ligand allowing its quantification if a sort of calibration curve is created. The nanoparticles can be functionalized to observe only the attachment of the desired target molecules, and the binding can be observed as a color change of the NPs dispersion or a shift in the SPR wavelength.

Au NPs can be also used as contrast agents in biological systems thanks to their enhanced scattering cross section, which increases with the AuNP size. An example of

this application was demonstrated by El Sayed *et al*. [25], who used anti-EGFR conjugated Au NPs to distinguish between cancerous and normal tissue. The scattering of Au NPs was observed by a simple optical microscope, with a 600 % greater binding ratio to cancerous cells than to normal ones, enabling the detection of cancerous cells by a dark field microscope.

Another application of Au NPs is as drug carriers and delivery systems. Therapeutic biomolecules have been delivered to cells using Au NPs. Solid Au NPs only have one possible way to transport cargos, this is by attachment on their surface. Although it has certain advantages when compared to "free" drug treatments, a major pitfall is that the payload is exposed to the environment. This could lead to drug loss before the carrier reaches the target tissue/cells. At this respect, hollow structures present a notorious advantage over solid NPs. Nanoshells have the ability of carrying the payload in the core, protecting it from losses, enzymatic attack and premature clearance from the body.

The use of Au NPs as photothermal therapy agents has also been exploited. This therapy consists in the accumulation in the tumor cells/tissues of light-absorbing NPs and subsequent illumination of the tumor region with a NIR laser of low power. Optimal wavelengths are in the range of 800 – 1000 nm because of the previously mentioned "biological window", the region of the electromagnetic spectrum where water and tissue light absorption is minimal. El Sayed *et al*. [23] demonstrated the effective tumor destruction after 514 nm-laser visible illumination of citrate stabilized 40 nm Au NPs functionalized with anti-EGFR. Caruso's group [106] used AuNPs in a different approach. They incorporated Au NPs in layer-by-layer-assembled microcapsules. The Au NPs, entrapped in the layers of polyelectrolytes served as triggering agents for cargo release after irradiation with NIR laser due to localized temperature increases and subsequent capsule disruption.

1.3.3.1 Au NShs in biomedical applications

Au NShs present a surface plasmon resonance, a phenomena occurring on metallic nanoparticles in which the valence electron cloud oscillates collectively upon excitation with light at the same frequency of the surface plasmon. The surface plasmon resonance position wavelength of gold nanoshells can be tuned from the visible to the

near-infrared region of the electromagnetic spectrum by varying their dimensions and the shell thickness [93, 107]. Au NShs can be strong photoabsorbers and scatters depending on their dimensions: smaller and thinner nanoshells will be better absorbers and larger and thicker will be better scatters. Au NShs have absorbing cross-sections several orders of magnitude higher than those of the commonly used fluorescent dyes such as indocyanine green (commonly used in cancer photothermal cancer therapy that presents photobleaching and short plasma half-life) or rhodamine 6G. Absorbing and scattering cross-sections of gold nanoshells are comparable and even higher than those of solid Au nanospheres and Au NRs.

The total extinction cross-section of Au NSh is composed by two components, an absorption cross-section and a scattering cross-section. Absorption cross-section is not as large as the Au NRs, but if the size is tuned correctly, Au NSh with acceptable absorption and scattering properties can be synthesized. According to El Sayed *et al.* [18], nanoshells with a core radius of 60 nm and a total radius of 70 nm will have both acceptable scattering and absorbing cross-sections with optical resonances lying in the NIR region, where transmissivity of biological tissue is the highest [108] and away from oxyhemoglobin's visible absorption at 500-600 nm [109]. Nanoparticle with these characteristics would have both abilities, as phototherapeutic agents and as imaging agents for dark field microscopy [110], photoacoustic imaging [111], confocal scanning optical microscopy [25], light scattering microscopy [112] and optical coherence tomography, [112]. Also, for biomedical applications Au NShs possess the interesting property of enabling double-carrying capacity: they can transport payloads in the inner core and attached on their surface, and can release the cargo in a controlled manner by light stimuli, for example. In this way, Au NShs have been tested in canine *in vivo* models for brain tumor ablation [113], and *in vitro* in different cells lines combined with chemotherapeutics agents, showing very promising results [114, 115].

1.3.3.2 Au nanostars in biomedical applications

Like Au NShs, Au nanostars possess a LSPR tunable in the NIR region of the electromagnetic spectrum. This characteristic makes Au nanostars very valuable for biomedical applications. Optical response of Au nanostars is also dependent on their size and shape. Sizes of Au nanostars are generally smaller as compared to Au

nanoshells. The position of Au nanostars LSPR can be controlled by modification of their whole size but in it has also been observed by many researchers that tuning the LSPR position can be achieved by the modification of the branching degree, the distance between tips/branches and sharpness of the tips/branches [116-118]. In this way it is possible to obtain Au nanostars with LSPR located at different NIR wavelengths with minimal changes in total size, therefore and study the effect of light absorption without changing significantly the dimensions of the nanostructure.

Generally, Au nanostars are smaller than AuNShs, so higher cellular uptake efficiencies are expected (see section 1.6.1.1). Au nanostars can be surface functionalized easily and it is possible to conjugate drugs [119], targeting ligands [119] and photosensitizers [120] to their surface. Their optical response to NIR light illumination makes them also good contrast agents and photothermal therapy agents. Like Au NShs. Au nanostars can be used as multifunctional nanoplatforms as they are able to combine multiple imaging and multiple therapeutic strategies in a single device. Nevertheless, an important disadvantage of Au nanostars is the single carrying capability on their surface, unlike Au NShs which can carry loads in their dielectric core.

1.3.3.3 Photothermal therapy

Traditional methods against cancer, chemotherapy and radiotherapy are unspecific and must be applied for long periods of time and with high and toxic doses of anticancer therapeutics or high energy X rays. This involved important side effects upon treatment such as structural and functional morbidity, skin redness, cosmetic defects (deformations), vomiting, hair loss, and many other without the guarantee of the tumor being fully eradicated. Another type of therapies are non-surgical ablation methods. Tumor ablation refers to the complete destruction of the tumor by direct application of chemical or thermal energy while sparing nearby vital and healthy structures [121]. These methods, also known as hyperthermia, consist in the moderate heating of the tissue, up to 42 – 47 ºC, for tens of minutes to induce cell membrane damage and protein denaturation. Radiofrequency, microwaves and ultrasound are some of the heating sources used in hyperthermia [122-124]. The difference with traditional surgery

is that these therapies can be applied in a minimal or non-invasive manner. Nevertheless, the accuracy and efficacy of these methods are yet to be improved.

Photothermal therapy is a method that uses light absorbing elements, such as dyes, for achieving thermal damage to tumors. When photothermal agents absorb light, electrons make transitions from the ground state to the excited state. The electronic excitation energy subsequently relaxes through non, for example, radioactive decay channels. This results in the increase in the kinetic energy leading to overheating of the local environment around the light absorbing species. The heat produced can be employed for local cell or tissue destruction. The photoabsorbing agents can be natural chromophores in the tissue or externally added dye molecules such as indocyanine green, naphthalocyanines and porphyrins coordinated with transition metals [125]. An innovative approach to accomplish this goal is the use of nanoparticles that are able to focus the energy on the desired spot or zone. Au NPs seem to be the ideal materials to this purpose thanks to their optical properties (intense LSPR-enhanced absorption), size, functionalizability with targeting ligands, stability and non-toxicity. The photothermal properties of Au NPs have been studied by Link and El-Sayed [96], who have shown that the photoexcitation of metal nanostructures results in the formation of a heated electron gas that subsequently cools rapidly within one picosecond by exchanging energy with the nanoparticle lattice. This is followed by phonon-phonon interactions where the nanoparticle lattice cools rapidly by exchanging energy with the surrounding medium on the timescale of 100 picoseconds. This fast energy dissipation and conversion can be readily used for the heating of the local environment by using light radiation with a frequency strongly overlapping with the NP's SPR absorption band [125].

As a consequence of their unique optical properties, Au nanoshells have been used as cancer photothermal therapy agents. The ability to increase temperature of the surrounding medium after NIR laser illumination makes them effective photothermal agents for cancer cell killing. Functionalization of nanoshells with polyethylene glycol (PEG) have been demonstrated to enhance their colloidal stability [126] and to improve their residence times in the bloodstream, providing an effective means to reduce macrophage phagocytosis and increasing chances of nanoshells to reach the tumor site.

1.3.3.4 Photodynamic therapy

Photodynamic therapy (PDT), also known as photochemotherapy, involves cell destruction caused by means of toxic singlet oxygen (the metastable excited state of triplet molecular oxygen, in which all electrons are paired) and/or free radicals that are produced from a sequence of photochemical and photobiological processes [125]. These processes are initiated by the reaction of a photosensitizer with tissue oxygen upon exposure to a specific wavelength of light in the visible or near-infrared (NIR) region following the process:

$$\text{Sens} + h\nu \rightarrow {}^{1}\text{Sens}^*$$

$${}^{1}\text{Sens}^* \rightarrow {}^{1}\text{Sens}^*$$

$${}^{3}\text{Sens}^* + {}^{3}O_2 \rightarrow {}^{2}O_1 + \text{Sens}$$

$${}^{2}O_1 + \text{substrate} \rightarrow \text{Oxidation}$$

where Sens is the sensitizer; ${}^{1}\text{Sens}^*$ is the excited singlet state of sensitizer; ${}^{3}\text{Sens}^*$ is the excited triplet state of the sensitizer; ${}^{3}O_2$ is ground state triplet oxygen; and ${}^{2}O_1$ is excited singlet state of oxygen [127].

PDT is already approved by the U.S. government to treat solid tumors (lung, esophagus, bladder and cervix), age related macular degeneration, actinic keratosis, and is under trials for brain, ocular melanoma, ovarian, prostate, renal cell, pancreas, bone, head and neck cancers, papilloma, rheumatoid arthritis, cosmesis, psoriasis, endometrial ablation, localized infection (bacterial and fungal) and prophylaxis of arterial restenosis, with highly positive results [109]. The major disadvantages of PDT are its limited light penetration in tissues; dependency on the oxygen concentration in the tumor (numerous tumors present hypoxia [128, 129]), short blood half-life and limited target specificity of photosensitizers.

However, PDT also present several important advantages such as the possibility to be applied several times without apparent induction of cell resistance (unlike radiation therapy, DNA is not targeted so there is no opportunity for treatment-induced mutation or selection) or exceeding tissue tolerance (since there is preservation of the collagen [130] and, hence, of the tissue architecture). The principal requirements for efficient PDT are that the light source matches the activation wavelength of the photosensitizer. In particular, the two main chromophores in the organism are water and

hemoglobin. The absorption coefficient of hemoglobin changes upon binding to oxygen (oxy-hemoglobin) (Figure 1.7); hence, the minimum absorption of tissue is between 700 and 1000 nm, so the use of photosensitizers with maximum absorption in this range of wavelengths are the optimal for PDT.

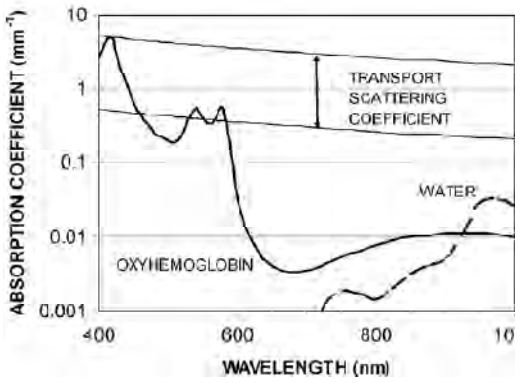

Figure 1.7: Absorption coefficient of oxy-hemoglobin and water as a function of wavelength.

1.4 Superparamagnetic iron oxide nanoparticles (SPIONs)

When the size is reduced to nanoscale, as with metallic and semiconducting nanoparticles, metal oxide nanoparticles start to show different properties to those of the bulk material. At this size scale, the thermal fluctuations are sufficient to induce a rotation on the direction of the nanometric nanoparticle magnetization. This phenomenon is called superparamagnetism. Superparamagnetic nanoparticles, especially iron oxide, have been used as magnetic resonance imaging contrast agents for disease diagnosis and, also, as hyperthermia agents. In this section a brief introduction to the subject will be given.

1.4.1 Introduction to magnetic parameters

All materials interact with a magnetic field, and this interaction can be either attractive toward a magnetic pole (ferro- and paramagnetism) or repulsive (diamagnetism). The application of a magnetic field (*H*) results in magnetization *(M*) of a sample, which can be measured by, for example, a superconductive quantum interference device (SQUID), one of the most popular and sensitive methods of investigating magnetic properties. When a ferromagnetic material is magnetized by an increasing applied field and, subsequently, the field is decreased, the magnetization does

not follow the initial magnetization curve obtained during the field increase. This irreversibility is called hysteresis [8] (Figure 1.8).

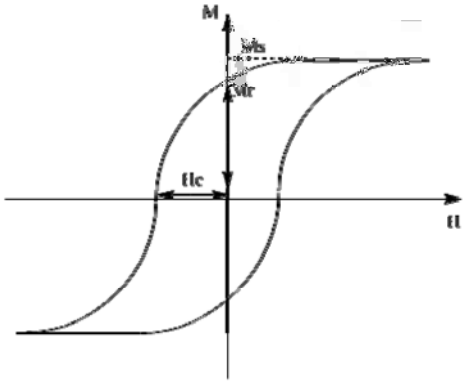

Figure 1.8: Typical hysteresis loop for a ferromagnetic material and the important magnetic parameters which can be obtained from the hysteresis loop. Dashed line shows the first scan.

At large fields, the magnetization approaches the maximum value, called the saturation magnetization (M_s). Magnetic materials in a ferromagnetic state have a residual magnetization at zero external field, called the remanent magnetization (M_r). Coercivity (H_c) characterizes the reverse-field strength needed to reduce the magnetization to zero. Thus, hysteresis measurements allow us to obtain information about coercivity, remanent magnetization, and saturation magnetization of a given material [8].

1.4.2 Size-dependent magnetic properties: superparamagnetism

The magnetic properties of a material result mainly from electron motion: spin motion and orbital motion. The electronic structure of a nanometric material is strongly dependent on its size; therefore, the behavior of magnetic nanoparticles is dependent on their size. Many physical phenomena (magnetic domain size, exchanging coupling effects, etc.) which determine magnetic properties experimentally observable have natural length scales at the nano- and micrometer range, so that the magnetic properties of the nanomaterial will be different from those of the bulk material. A bulk ferromagnetic material presents multiple magnetic domains. Magnetic domains are regions where magnetic moments orient in one direction while the alignment of spins in neighboring magnetic domains is usually anti-parallel. The oppositely aligned magnetic

domains are separated from each other by a domain wall known as the *Bloch wall*. The length of the Bloch wall depends on the material, for example for Fe is approximately 14 nm and for γ-Fe_2O_3 is approximately 170 nm, thus, magnetic nanoparticles normally consist of a single domain [8].

The main property of magnetic nanoparticles is that they show *superparamagnetism* at ambient temperature. Under a magnetic field with zero magnitude, there is an energetic barrier ΔE that must be overcome in order to turn the magnetization of a single-domain particle. This energetic barrier, $\Delta E = KV$, is proportional to the particle volume (K is the magnetic anisotropy constant). As the size of the particle decreases, ΔE may become comparable to the thermal energy (k_BT, where k_B is the Boltzmann's constant). In this case, the energy barrier can no longer pin the direction of magnetization to the time scale of observation, and rotation of the magnetization direction occurs due to thermal fluctuations. Such a particle is said to be superparamagnetic. The coercivity of a superparamagnetic particle is zero ($Hc = 0$), because thermal fluctuations prevent the existence of a stable magnetization. Cooling of a superparamagnetic particle reduces the energy of thermal fluctuations and, at a certain temperature, the free movement of magnetization becomes blocked by anisotropy. The temperature of the transition from the superparamagnetic to the ferromagnetic state is called the blocking temperature (T_B). The blocking temperature is related to the particle volume and the anisotropy constant. The latter can be calculated as $K = 25k_BT_B/V$. For Fe_3O_4 and γ-Fe_2O_3 NPs the size limit at which superparamagnetism occurs is around 20-30 nm [8].

1.4.3 Magnetic Resonance Imaging (MRI)

Magnetic resonance imaging (MRI) is a real time technique that allows the non-invasive visualization of cellular functions and tissues in living organisms. It is frequently used to diagnose diseases such as cancer, neurodegenerative diseases, as well to provide biological function information in preclinical stages. Recently, nanotechnology has led to the development of new types of contrast agents based on superparamagnetic NPs. MRI is nowadays one of the most powerful diagnosis techniques employed by medical science and it has become the favorite tool for

visualization of brain and central nervous system, to evaluate cardiac function, tumor detection, and early detection of lesions [12].

MRI is based on the basic principle of nuclear magnetic resonance (NMR) together with the relaxation of proton spins under a magnetic field. When the proton nuclei are exposed to a strong magnetic field, their spins align either in a parallel or antiparallel manner to the magnetic field. During the alignment the spins come under a specific frequency known as Larmor frequency (ω_o) [8]. When a "resonance" frequency, in the radiofrequency range, is introduced to the nuclei, protons absorb energy and are excited to their antiparallel state. After the RF pulse disappears the excited nuclei relax to their initial lower energy level. There are two possible relaxation pathways. The first one, known as longitudinal or T_1 relaxation which involves the decreased net magnetization (M_z) recovering the initial state, is the time needed to get back at the 63% of equilibrium magnetization. The second pathway, called the transverse relaxation or T_2, involves the induced magnetization of the perpendicular plane (M_{xy}) disappearing by the dephasing of spins. Transverse magnetization decays rapidly due to the non-uniformities in the main magnetic field (Figure 1.9).

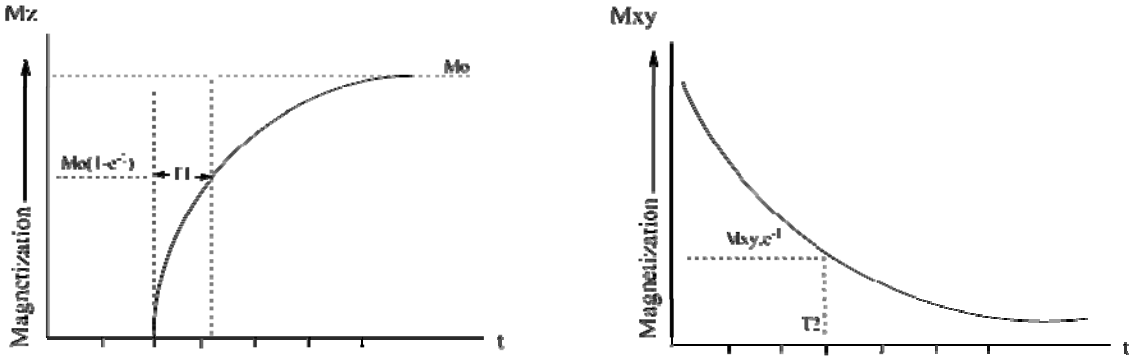

Figure 1.9: Magnetization diagrams showing T_1 and T_2 relaxations.

As these protons get out of phase (i.e. lost phase coherence) transverse magnetization (and induced signal) is lost exponentially. Typically, in soft tissues T_1 is around 1 s while T_2 is a few tenths of milliseconds. However, these values vary widely amongst different tissues and depend on the external magnetic field providing to MRI its tremendous soft tissues contrast. Based on the relaxation process, MRI contrast agents are classified as T_1 or T_2 contrast agents [12, 131].

MRI contrast agents work by shortening the T_1 or T_2 relaxation times of protons located nearby. Reduction of the T_1 relaxation time results in a hypersignal and, consequently, gives rise to a positive contrast, while reduced T_2 relaxation time reduces both T_2 and T_2* (describing the decay of the transverse magnetization taking into account the inhomogeneity of local static magnetic fields) signals, leading to a negative contrast.

$$\frac{1}{T2^*} = \frac{1}{T2} + \gamma B_s \qquad \text{(Eq 1.2)}$$

where the term γB_S represents the relaxation by the field inhomogeneity and is referred to susceptibility effect. Typically, elements with unpaired electron spins such as gadolinium, manganese, and iron can effectively reduce the T_1 relaxation time [12, 131].

1.4.4 Synthesis of SPIONs

The synthetic routes for SPIONs can be classified in two categories: physical methods such as mechanical grinding and biomineralization, and chemical methods such as coprecipitation, microemulsion, hydrothermal, sol-gel, electrochemical, polyol, flame assisted, sonochemical, thermal decomposition synthesis, etc. [12] Chemical methods offers certain advantages over the physical methods when the nanoparticles are intended to be used as MRI contrast agents because of important parameters such as particle size, size distribution, crystallinity degree and phase purity can be readily controlled. These parameters are the most critical for achieving a good MRI contrasting performance [132].

In turn, accordingly to chemical principles, solution-based methods can be classified into two categories: the hydrolytic routes and non-hydrolytic routes. In the first category, we find coprecipitation method, microemulsion, hydrothermal synthesis, electrochemical method, sol-gel synthesis and sonochemical method. These routes rely on the hydrolysis of ferrous and ferric ions, while the thermal-decomposition method, the main non-hydrolytic method, relies on the pyrolysis of iron-organic compounds.

1.4.4.1 Co-precipitation method

The co-precipitation method is the most important and used hydrolytic method for the production of iron-oxide based MRI contrast agents. The first synthetic routes for the production of magnetite are based on the co-precipitation of Fe(II)/Fe(III) in aqueous medium, and the reduction of Fe(III) salts with KNO_3 at 90 °C under alkaline conditions [133]. Based on these first works, further synthetic routes for the production of magnetite and maghemite were developed. Magnetite has higher magnetization than maghemite and is more used for MRI, although the latter is more chemical stable under ambient conditions [12].

In order to control the size of magnetic nanoparticles, it is necessary to use capping agents to inhibit their growth. There exist two approaches when polymers (either biopolymers or synthetic polymers) are used as stabilizers and size controlling agents: by coating the particles after precipitation or adding the polymer directly during the synthesis. Elmore in 1936 [134] and Cox in 1965 [135] used dextrane to obtain stable ferromagnetic colloids following the first and second approaches, respectively. Based on the foundations of these pioneering works, many of the MRI contrast agents used nowadays were developed. Massart [136] pioneering work´s demonstrated that colloidal stable magnetic nanoparticles can be synthesized under alkaline conditions in the absence of organic capping agents. He studied the effect on size, polydispersity and yield of the base type (ammonia, CH_3NH_2 or NaOH), cations ($N(CH_3)_4^+$, $CH_3NH_3^+$, NH_4^+, Na^+, Li^+, K^+) and Fe(II)/Fe(III) ratios. Massart's work served as a founding base for the development of synthetic routes of aqueous magnetic fluids making coprecipitation method one of the most recurred.

For example, magnetite (Figure 1.10) is an amphoteric solid and presents an isoelectric pH (pH_{PZC}) of 6-8 as determined by potentiometric titration [137, 138] . Below pH_{PZC}, protonation of the particle surface leads to the formation of $Fe–OH_2^+$ moieties, while deprotonation occurring above the isoelectric point gives rise to $Fe–O^-$ surface moieties which affect the electrostatic attachment of polymers on the magnetic iron oxide particle surfaces [137]. Apart from the electrostatic interaction, ligand exchange (surface complexation), hydrophobic interactions, entropic effects, hydrogen bonding, and cation bridging were also reported to be responsible for the adsorption of stabilizing agents on the surface of iron oxides. Carboxylic acid moieties and hydroxyl groups of organic acids have a strong affinity for the iron oxide surface [12]. Dextran is

the most commonly used biopolymer in commercialized MRI contrast agents [12]. Oleic acid has been also used to synthesize hydrophobic magnetite NPs with narrow size distributions and high stability [139].

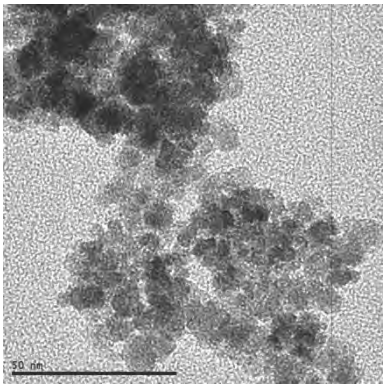

Figure 1.10: Magnetite (Fe_3O_4) stabilized with dextrane. Size is ca. 10 nm.

1.4.5 SPIONs as MRI contrast agents

In contrast to T_1 probes, superparamagnetic nanoparticles such as maghemite (γ-Fe_2O_3) and magnetite (Fe_3O_4) nanocrystals can produce predominantly spin–spin relaxation effects due to the induced local field inhomogeneities, consequently resulting in shorter T_1 and T_2 relaxation times. Magnetic iron oxide nanoparticles are predominately used as T_2 contrast agents, producing negative enhancement effects on T_2 and T_2^* weighted images, as commented previously. Iron oxide nanoparticles have revolutionize disease detection methods due to their remarkable interactions with blood proteins, mononuclear phagocytic cells, macrophage in tissues, cancer cells, biological barriers, etc. As a matter of fact, all these interactions are determined not only by the particle size but also by the particle physicochemical surface characteristics, leading to different fates for various types of iron oxide contrast agents; hence, different diagnostic methodologies are being developed. Therefore, the magnetic susceptibility, hydrodynamic size, size distribution, and surface physiochemical properties of the particle contrast agents are the most important parameters regarding their potential biomedical applications [12].

The contrast enhancing efficacy of T_2 contrast agents is characterized by their relaxivity coefficient (r_2), which is related to T_2 through the equation [12]:

$$\frac{1}{T2} = \frac{1}{T2^{\circ}} + Cr_2 \qquad \text{(Eq 1.3)}$$

where C is the contrast agent concentration and $T_2°$ is the relaxation rate of pure water.

Iron oxide nanoparticles are classified in two categories; SPIONs, with hydrodynamic radius larger than 40 nm and USPIONs (ultra small) with sizes below 40 nm. The former are quickly taken up by the reticuloendothelial system (RES) and eventually accumulate in the liver or spleen; therefore, they have been widely used for lesion detection and tumors in the liver. It has been proved that pegylation of Fe_3O_4 enables nanoparticles to escape the RES system opening new possibilities of functionalization with numerous targeting molecules (proteins, aptamers, peptides) for an active cancer detection and treatment [12]. On the other hand, USPIONs present longer blood circulation times and tend to accumulate in lymph nodes producing hypointense signals. Unlike normal lymph nodes, metastatic nodes lack macrophages, they appear isointense in comparison to the pre-contrast stage. Therefore, USPIONs are potentially useful to detect lymph node metastases. Taking advantage of their long blood circulation time, USPIONs conjugated to Herceptin molecules have been used to detect breast tumor and to detect human colon carcinoma after labeling with monoclonal antibody [140].

1.5 PLGA nanoparticles

Entrapment of hydrophilic and hydrophobic drugs and bioactive molecules (proteins, DNA, siRNA, etc.) in biodegradable polymer nanoparticles present great advantages over the direct administration of therapeutic agents. Biodegradable polymer nanoparticles increases the solubility, biodisponibility and retention time of drugs, making possible to lower doses and diminish secondary adverse side effects in patients. Entrapping drugs in polymeric nanoparticles avoids probable drug degradation in biological media, and allows a controlled and sustained release. By modifying the nanoparticle surface with suitable molecules, targeted delivery to a specific site of action can be achieved, reducing the interaction of drugs with healthy tissues [141].

Some of the most used biodegradable polymers for nanoparticle preparation and subsequent drug loading and delivery are the family of aliphatic polyesters such as poly(lactic-co-glycolic acid) (PLGA), poly(lactic acid) (PLA), poly(glycolic acid) (PGA); poly-ε-caprolactone, poly (alkyl cyanoakrylates), chitosan and gelatin [48, 54].

PLGA is a polymer formed by a block of poly(lactic acid) and another of poly(glycolic acid) (Figure 1.11). PLGA has been widely used for the preparation of nanoparticles provided that it is easily hydrolyzed into their two forming monomers, lactic acid and glycolic acid, which are degraded and eliminated without difficulty by the organism [48, 54].

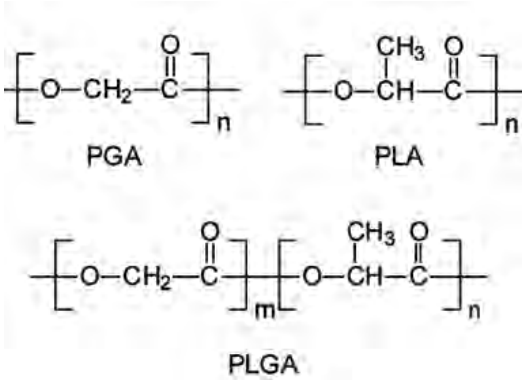

Figure 1.11: PLGA chemical formula. Monomers product of hydrolysis PGA and PLA are metabolized by human body.

1.5.1 Synthesis of PLGA-based drug delivery systems

Besides controlled release, PLGA NPs are capable to protect the therapeutic cargo from possible attacks during the track through blood stream before reaching its site of action. Many researchers have obtained biodegradable PLGA polymer nanoparticles through multiple techniques. Although with different variation on processing parameters, almost all of them are based on the same principles of emulsion, coacervation or conventional polymer processing techniques adapted to obtain nano- and micrometric materials. PLGA nanoparticles have been used to carry hydrophilic and hydrophobic drugs, fluorophores, magnetic nanoparticles, quantum dots and biomolecules [48, 142-145].

Some techniques for the production of PLGA nanoparticles are based on the emulsion of an organic solution of the polymer and the load in to an aqueous phase containing an emulsifier or stabilizer. Once the emulsion is formed, the organic solvent is evaporated or extracted, either by agitation at ambient conditions or at low pressure conditions. Higher temperatures can be used to accelerate evaporation although temperatures above the T_g of the used PLGA are not recommended. Finally, the dispersion is purified/washed to eliminate the excess emulsifiers and lyophilized for

conservation. The double emulsion (explained with detail later) technique consists of an aqueous solution emulsion containing a hydrophilic substance into an organic solution containing the polymer and further processing as previously described [48].

1.5.2 Emulsions

Emulsions are liquid-liquid dispersions thermodynamically unstable of immiscible or partially miscible substances. Natural evolution of an emulsion leads to a complete phase separation. This evolution can be retarded using additives (surfactants or fine solids). Emulsions are more stable if the size distribution of the dispersed drops is narrow. High viscosity of the dispersant phase also favors the emulsion, retarding rupture processes such as coalescence and creaming. The thermodynamic instability of an emulsion is intimately related to its history and, in particular, to the preparation process. Emulsions can be classified in single and double emulsions. Single ones are, at the same time, classified in oil-in-water (o/w) and water-in-oil (w/o), and double ones in water-in-oil-in-water (w/o/w) and oil-in-water-in-oil (o/w/o).

During emulsification, small drops in the micro and nanometric order are formed by breaking one of the phases after an energy supply. Under drop braking conditions, an enhanced coalescence rate can be expected. From a dynamic point of view, the emulsion formed (by agitation or shearing) will be that in which the coalescence rate is the lowest. Emulsion-based methods follow the main steps represented in the following scheme:

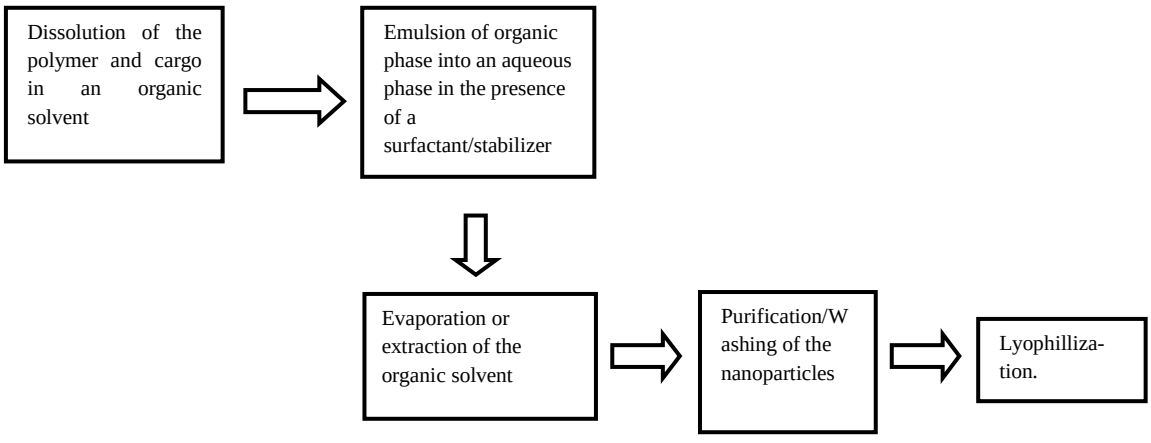

Figure 1.12: Basic steps for emulsion-based techniques to produce PLGA nanoparticles.

1.5.2.1 Single emulsion method (o/w)

In the single emulsion (or emulsion-evaporation) process the PLGA is dissolved in a volatile organic solvent (*e.g.* dichloromethane), together with the cargo molecules. The organic phase is added to the aqueous phase containing a stabilizer (*e.g.* poly (vinyl alcohol), Pluronic F127…) and sonicated or homogenized to produce an emulsion. Once the emulsion is formed it is necessary to remove the organic solvent by evaporation to obtain stable solid spheres. The next step consists of the NP purification, also known as washing. It is important to consider that the excess of surfactant that is not protecting the emulsion droplets can form micelles in the continuous phase, and with some organic phase solubilized inside, which can decrease the entrapment efficiency; hence, it is important to eliminate this excess. Finally, the product is lyophilized to avoid payload leakages and stored.

This process has been used to encapsulate hydrophobic substances such as drugs, fluorescent dyes, and nanocrystals, among others, with the only requirement that the solubility of the cargo must be greater in the organic phase than in the aqueous one, in this way, cargos stay inside the PLGA/solvent droplets during the processing phase.

1.5.2.2 Double emulsion method (w/o/w)

The double emulsion process is used to encapsulate hydrophilic substances such as hydrosoluble drugs, proteins, peptides, etc. in polymeric nanoparticles. It consists of two emulsion processes. In the first step, the hydrophilic substance is dissolved in a small volume of water or buffer containing a stabilizer (*e.g.* a protein or a polymer, for example). This first emulsion is identified as phase W_1; on the other hand, PLGA chains are dissolved in an organic solvent, known as phase *O*. Then, phase W_1 is emulsified in the phase *O* with the aid of a homogenizer or a sonicating tip. At this point of the process small droplets of aqueous phase have been formed inside the organic phase. Subsequently, the phase *O* is added to a second aqueous phase, W_2, containing a stabilizer (e. g. poly (vinyl alcohol), Pluronic F127…) and is again emulsified with a homogenizer or sonicating tip. This further process is similar to that of the single emulsion method [48]. This methodology enables the incorporation of two compounds with a different solubility profile in one highly stable system. The polar or hydrophilic substance can be entrapped in the first emulsion step, and the second compound would

be incorporated in the organic phase together with the PLGA. Generally, the nanoparticle sizes obtained by the double emulsion method are larger than those obtained with the single emulsion one [48].

1.5.2.3 Nanoprecipitation

This technique presents numerous advantages regarding the former ones, in that it is a straightforward technique, fast and easy to perform. The nanoparticle formation is instantaneous and the entire procedure is carried out in only one step. Briefly, it requires two solvents that are miscible. Ideally, both the polymer and the drug must be dissolved in the first one (the solvent), but not in the second system (the non-solvent).

Nanoprecipitation occurs by a rapid desolvation of the polymer when the polymer solution is added to the non-solvent solution. Indeed, as soon as the polymer-containing solvent has diffused into the dispersing medium, the polymer precipitates, involving immediate drug entrapment. The rapid nanoparticle formation is governed by the so-called Marangoni effect, which originates from interfacial turbulences that take place at the interface of the solvent and the non-solvent and result from complex and accumulated phenomena such as flow, diffusion and surface tension changes.

Nanoprecipitation often enables the production of small nanoparticles (100–300 nm) with narrow unimodal distribution and a wide range of preformed polymers can be used, such as poly(d,l-lactic-*co*glycolic acids), cellulose derivatives or poly(caprolactones) [146]. This method does not require extended shearing/stirring rates, sonication or very high temperatures, and is characterized by the absence of oily-aqueous interfaces, conditions that might damage, for example a protein structure. Moreover, surfactants are not always needed and unacceptable toxic organic solvents are generally excluded from this procedure.

However, the original nanoprecipitation method suffers from some drawbacks. This technique is mostly suitable for cargo compounds having a hydrophobic nature such as indomethacin, which is soluble in ethanol or acetone, but displays very limited solubility in water. Consequently, reduced or even zero drug leakage toward the outer medium led to nanoparticles with entrapment efficiency values reaching 100% [49, 146, 147].

1.6 Surface functionalization and bioconjugation of nanoparticles

As previously mentioned, the synthesis of NPs involves stabilizing molecules which prevent aggregation and, in many cases, also control the growth in terms of final size and geometrical shape. Stabilization of NPs can be due to electrostatic repulsion, steric exclusion or hydration layer on the NP surface. The nature of the stabilizing molecules will determine the physicochemical surface properties of the nanoparticle. For example, hydrophobic NPs can be transferred to hydrophilic or aqueous solvents if the initial hydrophobic stabilizing agent is exchanged by hydrophilic ligand molecules.

Surface stabilizing agents can be additionally modified with molecules of different nature; for example, hydrophobic nanoparticles stabilized with mercaptocarboxylic acid can be modified by molecules covalently bound to the terminal carboxylic acids. Another way to change NPs properties is by adding a molecular layer that adsorbs on the original ligand molecules and changes the surface properties accordingly [148]. No matter the chemical nature of NPs, their surface can be modified to change hydrophobicity, surface charge or attach functional groups at the NP surface in order to increase stability, enhance interaction with specific surfaces or molecules, or target NPs to specific sites of interest.

1.6.1 Influence of NPs physicochemical properties on biodistribution and cellular uptake.

The surface physicochemical properties of NPs play an important role on their biological performance as surface is the region of NPs that interacts with the surroundings. When strange elements enter the organism, the mononuclear phagocyte system (MPS), also known as reticulendothelial system (RES), is activated. This is the mechanism by which the human body fights against external elements such as bacteria, fungi or viruses. First, the foreign material is identified by opsonines, followed by phagocytosis by macrophages. Opsonines are proteins that help the RES to identify strange materials [149]. Most of nanoparticles are recognized by RES within minutes after intravenous injection. The main factors that determine RES uptake are the size, shape, surface charge [150]. Most of nanoparticles used in biomedical applications have

sizes and hydrophobic surfaces that make them very susceptible to activate the RES, preventing them to reach the desired site of action. After reaching the tumor, organ or tissue of interest, NPs must be efficiently internalized by cells, a process also affected by NPs surface properties. Herein, we briefly comment some aspects on the effects of size, shape and surface charge of NPs on biodistribution and cellular uptake.

1.6.1.1 Effect of NPs size

Size is a key factor in determining the biodistribution and cellular uptake and therefore the efficacy of nanoparticles. The first barriers that nanoparticles must overcome before reaching the target site are the liver, spleen and the kidneys. NPs with sizes < 10 nm are filtrated and eliminated by kidneys while NPs with sizes > 200 nm are eliminated by phagocytic uptake clearance and hepatic filtration [151]. An *in vivo* biodistribution study with polystyrene NPs with sizes ranging 50-500 nm have demonstrated that larger NPs accumulate with higher levels in the liver [152]. It was also shown that size substantially affects protein adsorption, showing a direct correlation between size and degree of adsorption. After 2 h of incubation in serum protein, 100 nm pegylated poly(cyanoacrylate-co-n-hexadecyl) cyanoacrylate NPs had 6% of protein adsorption while for 171 and 234 nm NPs was 23 and 34% respectively [153]. Sonavane *et al.* [154] studied the biodistribution in mice after intravenous administration of citrate-capped Au NPs of 15, 50, 100 and 200 nm. Their results showed a size dependent biodistribution with higher accumulation of smaller NPs in tissues, mainly accumulated in liver, followed by lung, spleen and kidney; interestingly, 15 and 50 nm NPs were able to trespass the blood brain barrier. Similar results were obtained by De Jong *et al.* [155] for AuNPs of 10, 50, 100 and 250 nm injected intravenously to rats, showing a size dependent distribution with the most widespread distribution of the smallest NPs in blood, heart, liver, lungs, spleen, kidneys, thymus, reproductive organs and a very low but detectable concentration of gold in the brain for 10 nm NPs. Chithrani *et al.* [156] studied the size dependency of cellular uptake of citrate-capped AuNPs with sizes ranging from 14 to 100 nm; their results indicate a maximum cellular uptake of 50 nm NPs. De Santos *et al.* [157] studied the effect of size on cellular uptake of carboxyl terminated poly(styrene) NPs with sizes ranging from 40 nm-2000 nm in five different cell lines. Although all NPs, even the larger ones, entered

all kinds of cells, the cell uptake rate was highly size dependent with a dramatic uptake decrease as the size of NPs increased.

1.6.1.2 Effect of NPs shape

Chithrani *et al.* [156] also reported the shape effect by comparing cellular uptake of Au NRs and spherical Au NPs. Their results showed that the uptake of Au NRs is lower than their spherical counterparts. For example, cells took up to more 500 and 375% 74 and 14 nm spherical Au NPs than 74·14 nm Au NRs, respectively. Cellular uptake of citrate-capped Au NRs with lower aspect ratio (1:3) was greater than higher aspect ratio (1:5). Gratton *et al.* [158] reported the cellular uptake of cationic PEG hydrogel nanoparticles fabricated by a top-down lithographic method. Their results differ from Chithrani's for cylindrical nanoparticles with similar volumes but different aspect ratios, 200 · 200 nm and 150 · 450 nm, the higher aspect ratio were internalized in HeLa cells ~ 4 times faster than lower aspect ratio ones. Interestingly, cylindrical NPs of 100 nm of diameter and aspect ratio of 3 showed lesser internalization that 150 nm-NPs with the same aspect ratio. This result is also different from Chithrani's and could be explained by the different surface charge of NPs.

1.6.1.3 Effect of NPs surface charge

Surface charge is undoubtedly an important factor in the biodistribution and cellular uptake of NPs. Cell membrane is formed by a lipid bilayer with a negative surface charge due to the phosphate head groups of phospholipid molecules. Therefore, positively charged NPs will be taken up more efficiently than neutral and negatively charged NPs. Positively charged NPs are also expected to have higher nonspecific internalization rate and shorter blood circulation half-times [151]. Nevertheless, there is evidence of uptake of negatively charged NPs despite the unfavorable interactions of NPs with the negatively charged cell membrane [159, 160]. The internalization of negatively charged NPs is believed to occur through nonspecific binding and clustering of the NPs on cationic sites on the plasma membrane (that are relatively scarcer than negatively charged domains) [159]. For example, Hirn *et al.* [161] have studied the biodistribution of Au NPs 24 h after intravenous administration in mice for aminated or carboxylated 2.8 nm Au NPs. After 24 h both types of NPs were accumulated mostly in

the liver, with an 81% of negative NPs and 72% of positive NPs. In contrast, positively charged NPs were accumulated in a greater extent in the spleen, heart, kidneys and remaining organs, and a higher amount of negative NPs in urine was detected. Balogh *et al.* [162] reported that positive Au/poly(amidoamine) (PAMAM) nanocomposites showed a greater accumulation in kidneys while negative and non-charged were accumulated preferentially in the liver. He *et al.* [163] reported the *in vitro* cellular uptake by murine macrophages and non-phagocytic cells and the biodistribution in tumor bearing mice of chitosan NPs with zeta potentials ranging from -40 mV to +35 mV. Their results indicated that NPs bearing higher positive or negative charges were more attractive to macrophages; non-phagocytic cellular uptake was charge dependent with greater internalization of less negative NPs. Biodistribution results indicated that NPs with slight negative charge were more efficiently accumulated in tumor, probably due to the longer blood circulation time than highly negative and positive NPs.

1.6.2 Pegylation

Different methods have been used to increase nanoparticles biostability and blood circulation half-life by several orders of magnitude. Polyeters, poloxamers (Pluronics), poloxamines and chitosan have been tested to decrease the opsonines attachment to nanoparticles surface [144]. The most used polymer for functionalization of nanoparticles is poly(ethylene glycol) (PEG), an ethylene oxide polymer, with hydrophilic and biocompatible characteristics. Owing to its simple structure and chemical stability is the prototype of an inert, biocompatible polymer [148]. Pegylation (functionalization of NP's surface with PEG) provides the nanoaparticles with steric stability and a hydrophilic coating that minimizes macrophage recognition. Nowadays, is possible to find PEG with numerous molecular weights and multiple combinations of terminal end functional groups, *e.g.* thiols (-SH), amines ($-NH_2$), carboxylic acids (-COOH), N-hydroxisuccinimides (NHS), maleimides, etc (Figure 1.13).

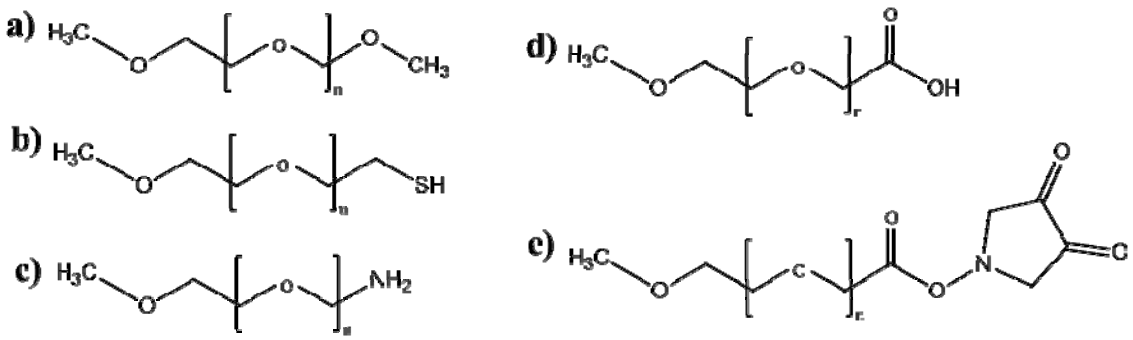

Figure 1.13: (a) methyl-terminated PEG, (b) thiol-terminated PEG, (c) amino-terminated PEG, (d) carboxy-termintaded PEG, (e) N-hydroxysuccinimide-terminated PEG.

PEG molecular weights used for nanoparticle pegylation ranges from 2000 Da (45 -OCH_2CH_2- repeating units) to 20000 Da (454 OCH_2CH_2- repeating units). PEG chains can attach to NPs surface in two different conformations depending on the grafting density. The mushroom conformation takes place when the distance between the attachment points (*D*) is larger than the Flory radius (*F*) of the polymer (eq. 1.4) [164]:

$$F = \alpha n^{\frac{3}{5}} \qquad \text{(Eq 1.4)}$$

where *n* is the number of repeating units of monomers; α is the monomer length monomer in Å. For PEG, α = 3,5 Å.

In this configuration, the PEG chain is attached by one terminal end and the rest of the molecule coil in a half sphere conformation with radius similar to the Flory radius. When $D < F$, the polymer acquires a "brush" conformation, with a dense layer of extended chains attached to the NP by one terminal end (Figure 1.14). The change between the two conformations depends on the type of PEG and the nanoparticle [164].

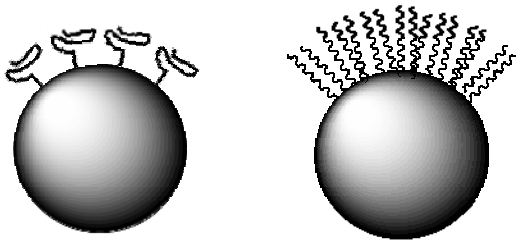

Figure 1.14: Scheme of mushroom configuration and brush configuration of PEG grafted to nanoparticles.

Gref *et al.* [165] studied the effect of PEG chain length in preventing protein adsorption on the surface of NPs. Their results showed that an optimal molecular mass (*M*w) range exists (between 2 and 5 kDa) in order to reduce plasma protein adsorption. The amount of protein adsorbed on 5kDa PLA-PEG was substantially reduced (~80%) compared to the amount of non-pegylated PLA NPs. NP size is altered by the PEG shell, that can be in the order of a few to tenths of nanometers, while the shell thickness is of same magnitude as the hydrodynamic diameter of a free PEG molecule in a random coil configuration [166].

The circulation half-time ($t_{1/2}$) describes the blood pool residence and is the period over which the concentration of circulating nanoparticles remains above 50% of the injected dose, and it is equivalent to drug's half-life. The required circulation half-time depends on the intended application but, in general, it must be long enough to let nanoparticles get the desired site before elimination by the RES system. Many studies have demonstrated that pegylation of nanoparticles surface with different compositions (SPIONs, quantum dots, gold NPs, polymeric NPs) [24, 40, 126, 151, 167-174] minimizes non-specific adsorption of proteins through its hydrophilicity and steric repulsion reducing opsonization and complement activation, as well as reduction in uptake by the liver and increases the circulation half-time.

1.6.2.1 Pegylation of polymeric nanoparticles

Polymeric nanoparticles can be pegylated by two main approaches: adsorption on preformed polymeric nanoparticles of PEG homopolymers or PEG-containing block copolymers, *e.g.* Pluronics composed of poly(propylene oxide) (PPO) hydrophobic blocks and poly(ethylene oxide) PEO hydrophilic blocks; or the synthesis of copolymers with a PEG block and the hydrophobic biodegradable moiety eg. PLGA, poly(caprolactone), poly(cyanoacrylate) to generate the polymeric NP.

1.6.2.2 Pegylation of inorganic nanoparticles

In order to pegylate metallic and semiconductor nanoparticles, a thiol terminated PEG (SH-PEG) is the most used approach. Thiol-containing molecules can interact with metal ions and metal surfaces to form dative Au-S bonds (47 kcal/mol) [175]. Dative

bonds also are known as coordinate covalent bonds. They differ from normal covalent linkages because they are formed by two electrons coming from a single atom, instead of two atoms each sharing one electron. In a coordinate bond formed with a thiol, the unshared pair of electrons on the sulfur atom is able to form a dative bond with a metal atom. In this sense, even disulfides are able to datively link to a metal surface without their prior reduction to thiol (Figure 1.15).

SH-PEG has been used to create water soluble gold nanoparticles and quantum dots having reduced non-specific binding character and able to form required surface groups for coupling proteins and other affinity molecules. Reaction of thiol groups and gold surfaces under slightly alkaline aqueous conditions is favored. Pegylated gold nanoparticles with different sizes and shapes, spherical, rods and nanoshells have been proved to exhibit longer circulation times *in vivo* upon systemic injections [176].

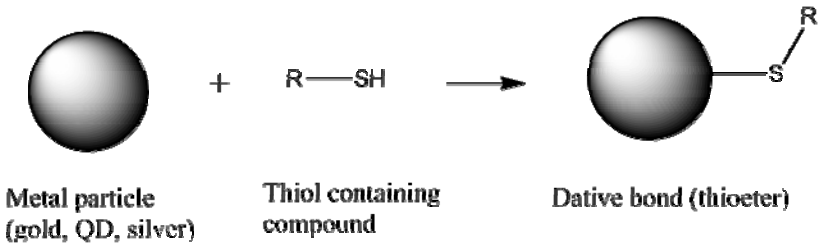

Figure 1.15: Dative bond between a thiolated molecule and a metal nanoparticle.

1.6.2.3 Conjugation of biomolecules by carbodiimide chemistry

Conjugation of molecules to NPs is relatively easy when NPs have been functionalized with bifunctional PEG molecules, especially Au NPs due to the high affinity of thiol to gold surface. If the SH-PEG has the adequate functionality in the free end, it is possible to conjugate molecules of interest by carbodiimide chemistry. Carbodiimides are zero-length crosslinking agents used to mediate the formation of an amide or phosphoramidate linkage between a carboxylate group and an amine, or a phosphate and an amine, respectively. They are called zero-length reagents because in forming these bonds no additional chemical structure is introduced between the conjugating molecules. N-substituted carbodiimides can react with carboxylic acids to form highly reactive, *o*-acyloisoruea derivatives that are extremely short lived. This active species, then, can react with a nucleophile such as a primary amine to form an amide bond (Figure 1.16). Other nucleophiles also are reactive. Sulfhydryl groups attack

the active species and form thioester linkages, although these are not as stable as the bond formed with an amine [177].

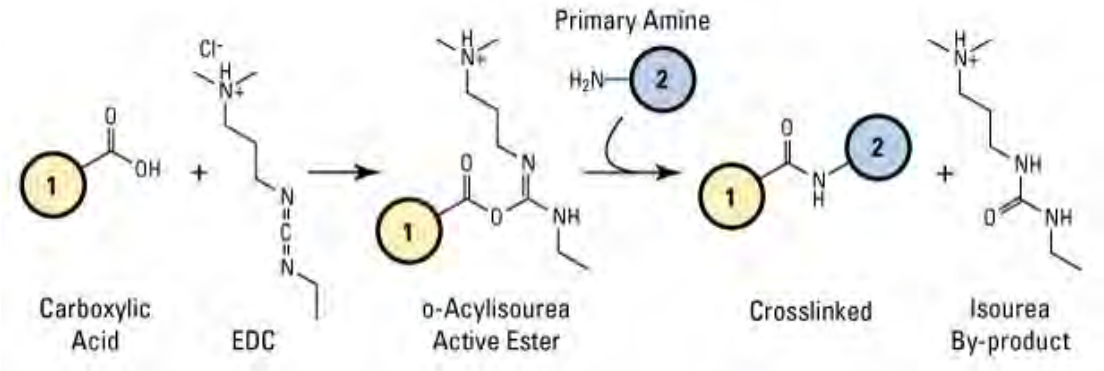

Figure 1.16: Reaction between EDC and a carboxylated molecule or particle (1) to form the amide bond (peptide bond) with the aminated ligand (2) (image taken from [178]).

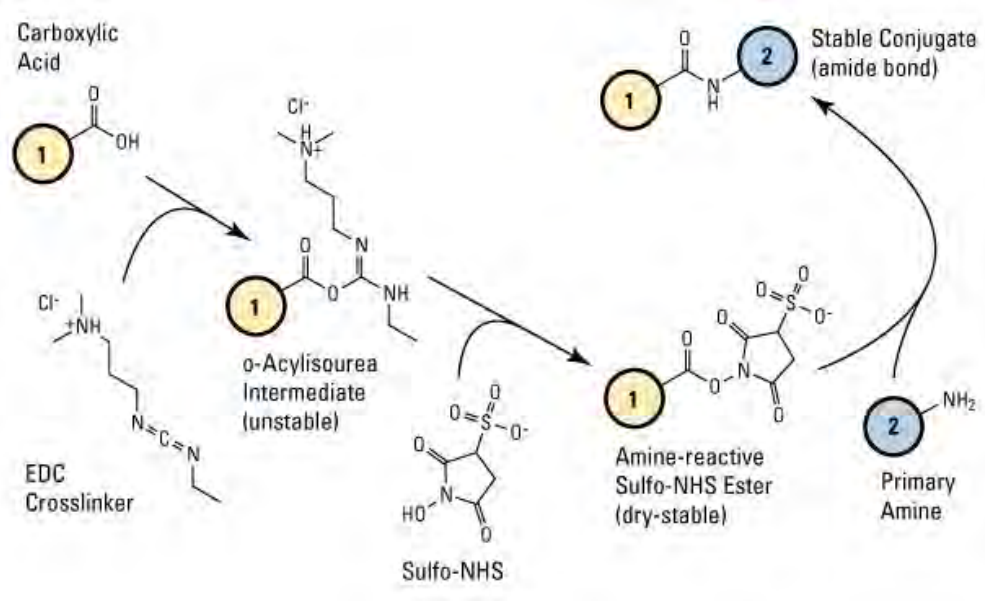

Figure 1.17: Reaction of EDC and sulfo-NHS with a carboxylated molecule (1) to produce the semi-stable active intermediate. The aminated molecule (2) attacks this intermediate to form the amide bond (image taken from [178]).

EDC (1-ethyl-3-(3-dimethylaminopropyl) carbodiimide hydrochloride) is the most popular carbodiimide used for conjugating biological substances bearing carboxylates and amines. Its application in particle and surface conjugation procedures

along with NHS (N-hydroxysuccinimide) and sulfo-NHS (N-hydroxysulfosuccinimide) is nearly universal, and this fact makes it the most common bioconjugation reagent in use today. EDC is water soluble, which allows for its direct addition to a reaction without prior organic solvent dissolution. Both the reagent itself and the isourea formed as by-product of the crosslinking reaction are water soluble, and may be removed easily by dialysis or gel filtration. The advantage of adding sulfo-NHS to EDC reactions is to increase the solubility and stability of the active intermediate, which ultimately reacts with the attacking amine (Fig. 17). Carbodiimide chemistry is a simple way to biofunctionalize NPs with biomolecules with interesting properties such as nucleic acids, proteins, peptides or antibodies [177].

1.6.3 Passive adsorption of proteins

Another way to biofunctionalize NPs is through passive adsorption of proteins which tend to adsorb onto NPs due to electrostatic attraction if both parts are oppositely charged, by van der Waals forces, hydrogen bridges, gold-thiol bonds (from cysteine residues) or by hydrophobic interactions, *e.g.* when the pH is near the protein or NPs isoelectric point so that the electrostatic repulsion is reduced. After adsorption, protein can be irreversibly immobilized by those forces, or a combination of them [148]. After intimate contact of protein and the NPs surfaces the protein can suffer conformational changes, which may lead to complete denaturation of the first protein layer adsorbed on NPs. The subsequent protein molecules are adsorbed onto the first layer through protein-protein interactions, which finally results in an external layer of protein with more of a native activity and conformation. If done in a controlled manner, protein passive adsorption could provide NPs with colloidal stability and provide the possibility to travel undetected by RES largely extending blood circulation times [148, 179].

1.6.4 Passive targeting: the EPR effect

There are two mechanisms for nanoparticle targeting to cancerous tissues: passive and active targeting. These mechanisms are responsible of increased efficiencies and reduction of adverse side effects with nanoparticle-based therapies in contrast to the direct administration of free chemotherapeutics. Passive targeting is based on the enhanced permeation and retention (EPR) effect that cancerous tissues displayed due to

their abnormal physiology compared to healthy ones. Many of the drugs used nowadays against cancer do not discriminate between healthy tissues and cancerous tissues: they reach and exert their function by a free diffusion-dependent equilibrium in both normal and tumor tissues without distinction.

Maeda and co-workers, who coined the EPR concept, were the first researchers to devised a nano-sized targeted anticancer drug to tumor tissues by using the EPR effect [180]. Characteristics of the EPR effect include extensive angiogenesis and, hence, enhanced vascular density, extensive extravasation (vascular permeability) and impaired lymphatic drainage/recovery system of the tumors. The vascular permeability is induced by factors such as: bradykinin, a peptide that causes blood vessels to dilate, nitric oxide (NO), vascular permeability factor (VPF) and vascular endothelial growth factor (VEGF), prostaglandins, collagenase (matrix metalloproteinase MMP) and peroxynitrite ($ONOO^-$).

The enhanced production of these permeability mediators augments the permeability of tumor tissues in comparison to normal ones, thereby also contributing to the EPR effect. Solid and rapidly growing tumors suffer from an inadequate supply of nutrients and oxygen. Accordingly, they possess an extensive angiogenesis, resulting in a high vascular density. The formation of tumor blood vessels proceeds in a chaotic manner and, hence, a defective architecture of the vascular endothelium with large gaps in endothelium cell–cell junctions takes place, leading to hyperpermeability. The EPR effect provides an opportunity for more selective targeting of NPs. Size and surface of the nanoparticle carrier play a very crucial role with respect to uptake by the tumor. Particles of size < 200 nm with hydrophilic surfaces tend to exhibit an improved EPR effect, which has been attributed to the increased residence time of the carrier in blood [145].

Most normal drugs have a plasma half-life of 20 min. The minimum time necessary to exert the EPR effect is 6 h. To take advantage of the EPR effect, it is critical for the nanocarriers to evade immune vigilance and circulate for a prolonged period. Therefore, the targeting efficacy of nanocarriers is achieved as long as they remain in the bloodstream where the vessel structure is normal, but would extravasate through the leaky vasculature at the tumor site. Upon arrival at the target sites, the nanocarriers release the drug in the vicinity of the tumor cells. The absence of lymphatic

drainage from the tumors contributes to retention of the nanocarriers, ultimately leading to the accumulation of high concentrations of drug [181].

On the other hand, the kidneys are capable of filtering particles smaller than 10 nm and the liver can capture particles larger than 100 nm. Therefore, the ideal nanocarrier size is somewhere between 10 and 100 nm. Clearance organs (such as kidneys) can filter nanocarriers not only based on their size, but also by their surface charge. Ideally, the nanocarriers should not be positively charged but either neutral or negatively charged because the luminal surface in the endothelium possesses highly negative surface charges; thus, positively charged nanocarriers would be adsorbed and decrease their *in vivo* half-life [145].

1.6.5 Active targeting

The alternative mechanism, active targeting, is based on the biofunctionalization of nanoparticles with targeting ligands that have an enhanced affinity to cancer cells as a consequence of the overexpression of receptors of these targeting ligands on the cell membrane. These targeting moieties act as “keys” to open “cell doors” that allow their specific accumulation and enhanced internalization inside cells [182] into cancerous cells without entering into the healthy cells. On the following section we will mention some of the most important targeting ligands that have been used for cancer diagnosis, imaging and therapy.

1.6.5.1 Antibodies

Antibodies are immunoglobulin proteins produced by B-cells. They have the function of recognizing foreign materials circulating in the bloodstream. Toxins and pathogenic bacteria have surfaces that present antigens. The antigen is recognized by antibodies which form an antigen-antibody complex. This complex, then, attracts the attention of other components of the immune system, such as macrophages, which have antibody receptors on their surfaces, facilitating destruction of pathogens (Figure 1.18). Antibody functions also include neutralization and blocking of pathogens and toxins, activation of the complement system, response to parasites, allergic responses and mucosal protection [183].

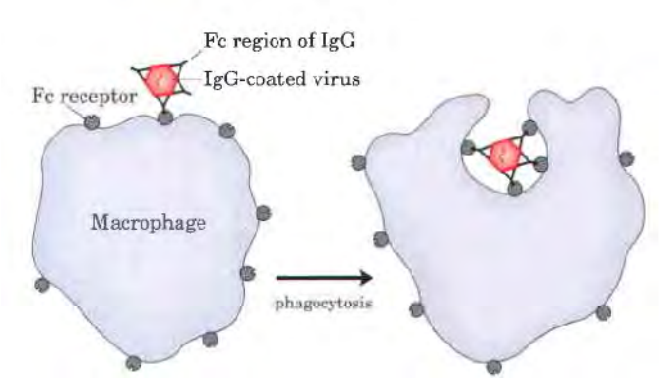

Figure 1.18: Phagocytosis of an antibody-bound virus by a macrophage (taken from [62]).

Growth factors are polypeptides that stimulate cell proliferation by binding to their specific high-affinity cell membrane receptors, activating tyrosine kinase, signaling cell division [184]. In all types of cancer, the normal regulation of cell division has become dysfunctional due to defects in one or more genes. For example, genes encoding proteins that normally send intermittent signals for cell division become oncogenes, producing constitutively active signaling proteins; or genes encoding proteins that normally restrain cell division (tumor suppressor genes) mutate to produce proteins that lack this breaking function. In many tumors, both kinds of mutation have occurred [62]. Mutations are also believed to be responsible of another characteristic of tumor cells, the overexpression of certain growth factor receptors. The molecular mechanisms of overexpression are not fully understood but some studies indicate that are correlated to aneuploidy, an abnormal number of chromosomes that occurs during cell division when the chromosomes do not separate properly between the two cells [185], and overexpression of certain genes such as human papilloma virus 16 *E6* [186]. For example, EGFR is overexpressed in cervical and pancreatic cancers [186]; KIT (a member of the tyrosine kinase family of growth factor receptors), PDGFR (platelet derived growth factor receptor); HER2 GFR (human epidermal growth factor receptor 2) are overexpressed in breast cancers [187]; and KGFR (keratinocyte growth factor receptor) is overexpressed in colorectal cancer [188]. Other growth factor receptors frequently overexpressed in cancer cells are human epidermal growth factor receptors 3 and 4 (HER3 and HER4), vascular endothelial growth factor receptor (VEGFR), basic fibroblast growth factor receptor (BFGFR), transforming growth factor β (TGFR-β), amongst others [184].

Monoclonal antibodies (mAbs) are produced *in vitro* using hybridomas, a fusion of B cells and tumoral cells. mAbs can besynthesized with a great selectivity for their receptors. mAbs are designed to bind to extracellular portions of growth factor receptor competing with growth factors for receptor binding, blocking autocrine and paracrine growth factor loops, and induce receptor dimerization and downregulation, as in the case of antiEGFR mAbs [187]. Another example is anti-HER2 mAb, which can reduce tumor cell proliferation and sensitize them to chemotherapeutic agents [189]. Numerous monoclonal antibodies have been approved by the FDA for clinical use to treat tumors and can be conjugated to nanoparticles. Table 1.1 gives a brief list of mAbs approved for human therapy and some of their applications. Nanoparticles of different nature have been functionalized with antibodies for therapeutic and diagnosis applications [23, 190-193] resulting in improved efficiencies and specificity (Figure 1.19).

Table 1.1: Antibodies approved by FDA for cancer therapy [183].

Antibody	**Brand name**	**Target**	**Cancer type**
Bevacizumab	Avastin	Vascular endothelial growth factor (VEGF)	Colorectal, non-small cell lung, breast,
Trastuxumab	Herceptin	HER2 receptor	Breast
Tositumomab	Bexxar	CD20	Lymphoma
Rituximab	Rituxan	CD20	Lymphoma
Nofetumomab	Verluma	Glycoprotein 40 kD	Several tumors
Gemtuzumab	Mylotarg	CD33	Myeloid leukaemia
Ibritumomab	Zevalin	CD20	Non-Hodgkin lymphoma

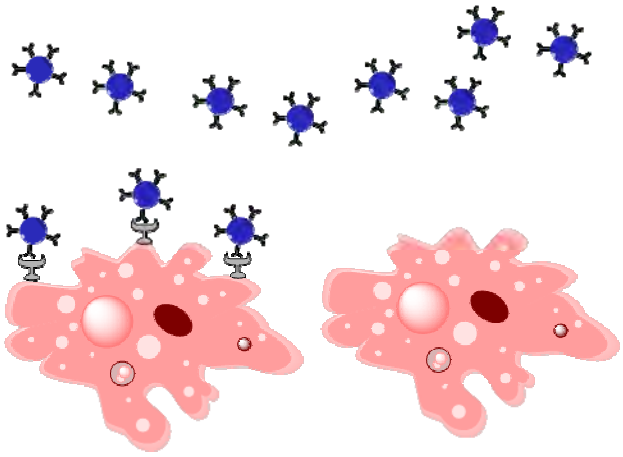

Figure 1.19: Antibody-functionalized nanocarriers bind specifically to tumor cells, which overexpress antigen (antibody receptor) and "ignore" normal cells (without antigen).

1.6.5.2 Aptamers

Aptamers are single stranded DNA, RNA or unnatural oligonucleotides that have been selected *in vitro* from a pool (~10^{14}-10^{15}) of random oligonucleotides for their ability to bind to a target molecule. Aptamers have molecular weights in the order of 10-15 kDa, one order of magnitude lower than that of antibodies. Aptamers fold in tertiary conformations with specific binding pockets which bind to their target molecules with high specificity and affinity. Due to their small size and similarity to endogenous molecules, aptamers exhibit superior penetration and are believed to be less immunogenic than antibodies. Aptamers are highly stable and may tolerate a wide range of temperature, pH (4-9) and organic solvents without loss of activity, but are susceptible to nuclease degradation [194]. Aptamers have been used as targeting moieties conjugated to quantum dots [195], magnetic nanoparticles [196] and drug delivery polymeric nanoparticles [197, 198],

1.6.5.3 Peptides

There are two types of peptides used for enhanced cellular uptake and active targeting of NPs. Cell-penetrating peptides (CPP) and cell-targeting peptides (CTP). CPP are small proteins that translocate spontaneously through the plasma membrane when incubated in the extracellular medium [199]. Studies determined that peptide domains responsible for cellular uptake contain six arginines and two lysine residues

and these positively charged residues have been identified as key determinants of cellular uptake as they mediate the initial interactions of the peptide with the negatively charged cell surface [200]. Peptides with domains rich in positive residues (*e.g.* polyarginine and polylysisne) have found great utility as mediators of NP cellular uptake [201]. One example is the 86 aminoacid Tat protein from HIV-1 virus. Tat HIV-1 peptide has been conjugated to gold nanoparticles resulting in rapid intracellular uptake and particle localization to the nucleus [202].

Cell-targeting peptides (CTP) are composed of a few aminoacids (from 3 to 10) and show high cell specificity and strong affinity for a given targeted cell line upon interactions with a receptor that is exclusively overexpressed by these cells. The most studied CTP is RGD peptide, which targets the αvβ-3 integrin receptor and plays a role in angiogenesis of solid tumors, cell migration, invasion and also metastatic activity [199, 203]. Polymeric NPs [204], Au NPs [205], SPIONS [206] have been functionalized with RGD peptide to target cancer cells with imaging and therapeutic purposes. Another example is CTX, a peptide derived from the venom of the giant Israeli scorpion which targets the protein matrix metalloproteinase-2 overexpressed on the cell surface of cancers such as malignant glioma, medulloblastoma, prostate cancer, intestinal cancer, and sarcoma [207]. CTX-activated iron oxide NPs have demonstrated an improved pharmacokinetics and biodistribution, and also show excellent targeting of cancer cells both *in vitro* and *in vivo* [208].

1.6.5.4 Folic acid

Folic acid, also known as vitamin B9, is a molecule which plays a fundamental role in nucleotide and DNA synthesis and is essential for rapidly proliferating cells and tissues, which includes advanced stages of cancer. In many cells, the intracellular acquisition of folates is mediated through folate receptors alpha, beta and gamma (FOLR1-3), which bind to folates with a very high affinity (K_d ~ 100 pM). In particular, folate receptors alpha or FOL1, and many of the folate-cycle related genes are highly expressed in rapidly proliferating cells. FOLR1 and FOLR3 are considerably overexpressed in a subset of cancers of the breast, pleural mesothelioma, endometrium/uterine, and particularly the ovary, while folate receptor beta or FOLR2 is a promising target in myeloid leukemia [209]. Different NPs have been functionalized

with folic acid in order to specifically target cancerous cells with enhanced internalization rates and larger amounts. For example, iron oxide NPs coated with a monolayer of PEG activated with folic acid show cancer cell specific uptake in human adenocarcinoma cells, process which can be monitored by using MRI [210]. Mansoori *et al.* [211] have reported the synthesis of two folate conjugated Au NPs and the analysis of folate receptor tissue distribution and particle endocytosis in cells with both high and low folate receptor expression (HeLa and MCF-7, respectively).

1.7 Theranostic nanomaterials

1.7.1 Nanomedicine: objectives and challenges

Nanotechnology offers a tremendous potential in applications such as biomedical diagnosis and therapy giving rise to a new field named Nanomedicine which nowadays constitutes one of the priority areas in most of the developed countries. For example, the National Institute of Health of USA created a budget of 1443M$ for the period 2006-2011 to encourage and develop projects in this research field.

The main applications of nanomaterials in the biomedical field can be split in imaging diagnosis and therapeutics. A majority of the imaging and therapeutic compounds widely used in clinical practice are composed of small molecules as, for example, the gadolinium complexes employed as T_1 imaging contrasts in nuclear magnetic resonance imaging (MRI), or the anticancer drugs used in oncology. The main drawbacks of this kind of small-sized molecules are their too short blood circulating times, lack of enough image resolution for an early detection of diseases like cancer, unspecific biodistribution, non-controlled release, unavailability to overcome biological barriers, cytotoxity...

To solve some of these problems, nanotechnology enabled the design and obtention of the so-called drug delivery vehicles, also known as nanoplatforms or nanovectors, nanoparticles capable of carrying and delivering one or more bioactive molecules [182, 212]. Amongst the most well-known representatives of this type of nanomaterials in clinical use, for example for cancer treatment, we can find liposomes (for example, DOXIL™, liposomes loaded with the anticancer drug doxorubicin

approved in 1995 for the treatment of Kaposi´s sarcoma) [213]; albumin nanoparticles (as ABRAXANE™, approved in 2005 for the treatment of methastatic breast cancer) [67]; or polymer nanoparticles (as GENEXOL-PM, a formulation of polymeric micelles loaded with the anticancer drug paclitaxel and free of Cremophor-El, which is in phase II trial for treating pancreatic tumours in USA) [214]. However, the generation of nanovectors based on nanoparticles in the market nowadays, around a couple of dozens, are non-targeting passive systems whose biodistribution along the human body cannot be traced [215]. The localization of these systems is only directed by their size (in particular, by the enhanced retention and permeation effect, EPR, which leads to the nanovehicle to be localized in areas with uncontrolled increases of vascularity, as ocurred in solid tumours [216], and is not related with a specific recognition by the targeted cell or tissue.

Moreover, a shared characteristic of all commercialized nanoplatforms is that they are designed for only one specific application (either diagnosis or therapy), and a vast majority of them are only developed to look for an improvement in the drug dosage process or pharmaceutical efficacy of previously approved drug compounds for clinical use. In addition, most of the studies performed in research labs are also still only focused on the obtention of monofunctional nanoparticle systems which improve the properties of the commercialized products for their applications in therapeutics, diagnosis, as biomarkers, biosensors...[34, 217, 218], as commented before, or which allow the incorporation of additional functionalities as the molecular recognition of the target-tissue and/or the controlled release of drugs. The best examples among the former type of systems are liposomes and nanoparticles functionalized with antibodies [219], aptamers and small peptides [198, 202, 220] which bind to over-expressed specific markers in the misfunctional area. Amongst the nanovectors in the second category we can find pH-responsive [34] or enzimatycally-activated [221] polymers, as well those systems which are active when an external stimulus is applied: For example, Au NSh's [170], Au NRs [222] and carbon nanotubes [223], which are activated by infrared light generating a local heat release used for photothermal therapy, superparamagnetic iron oxide nanoparticles (SPION) guided by magnetic fields which can be employed as imaging contrast agents in MRI [217] and magnetic hyperthermia [224]; or semiconductor quantum dots (QDs), which can emit fluorescent light of different

wavelengths, and with a suitable functionalization can bind to tumor cells to obtain clear images of these cells *in vivo* [218].

1.7.2 Theranosis: therapeutics + diagnosis

However, there is no a response to other of the most important challenges in clinical practice: the independent performance of diagnosis and therapeutical phases in the treatment of diseases like cancer, which involves a time delay which may lead to a worsening of the disease and the subsequent risk for the patient´s health. Thus, Nanomedicine is called to solve the lack of a system based on nanoparticles which would be able to simultaneously posess the capability of acting as a diagnosis element and of exhibiting a therapeutical action. This is the subject of theragnosis (theragnosis = therapeutics + diagnosis). The suitable combinations of different nanostructured materials should give rise to the development of these multifunctional nanomedical platforms (*theragnostic platforms*) and their commercialization. To achieve this goal, it is necessary to assemble the different components of the nanoplatform, to analyze their properties and to check if they fulfill all necessary requirements about biostability and biocompatibility.

In this regard, first attempts to create theragnostic nanoplatforms at lab scale can be found in the studies of Kopelman *et al.* [225], who synthesize polyacrylamide nanoparticles loaded with photosensible molecules and magnetic contrast agents for their simultaneous use in MRI detection and photodynamic therapy (PDT) treatment of brain cancer in rats. Viese *et al.* [226] covered SPIONs with polyethylene glycol (PEG) and conjugated the nanoparticles with an antibiotic (chlortoxin) and the chromophore fluorescein, thus obtaining a system capable of marking and eliminating gliome cancerous cells. Cheon *et al.* developed SPIONs functionalized with antibodies to improve the nanoparticle targeting [132]. They also attached radionuclide to SPIONS for the simultaneous obtention of images by MRI and positon emission tomography (PET) [227]. Kim *et al.* [228] and Sukhorukov *et al.* [4] developed polymeric nanocapsules through the layer by layer technique (LbL). These capsules posses fluorescent groups and paramagnetic complexes to enable their detection through MRI and fluorescence imaging; or they are simultaneously loaded with a drug and metallic nanoparticles with photothermal activity for a combined therapeutical action against

cancer cells, respectively. Hyeon *et al* [229, 230] Haam *et al.* [142, 190] and Salgueiriño-Maceira *et al.* [231] synthesized multifunctional nanoparticles (silicon oxide-based or polymer-based) able to be used as contrast agents in MRI and/or fluorescence imaging, with the possibility of achieving a combined therapeutical action through the pharmacological activity of an anticancer drug (doxorubicin, for example) and the phothermal capability of a gold layer deposited on the nanoplatform surface. Also, porous silicon oxide nanoparticles have been used very recently as nanovectors for the combined action of the loaded anticancer drug paclitaxel and attached small-interfering RNA (si-RNA) constructs on different cell lines [232]. On the other hand, docetaxel-loaded polymeric nanoparticles functionalized with fluorescent aptamers which recognize the extracellular domain of the prosthatic membrane antigen (PSMA) were used by Langer´s group to localize and kill prosthatic cancerous cells in animal models [198, 233].

1.7.3 Unsolved handicaps of theranosis

Nevertheless, in sipte of the evident progresses achieved, all these systems display different inconvinients such as:

a) The necessity of obtaining previously special molecules through laborious synthetic routes to achieve the desired properties of the construct, which implies larger manufacture costs, formation of by-products, biocompatibility issues...

b) Cytotoxicity of some of the constituent elements of these platforms, as ocurred, for example with QDs.

c) Reduced contrast imaging resolution in MRI for an early detection of very small tumours.

d) Reduced efficacy *in vitro* and *in vivo* of the nanoplatforms with photothermal capabilities due to the quality of the metal nanoparticles/shells obtained (inhomogeneities, roughness), and the deformation experienced by these nanomaterials after a short exposure to radiation.

e) Reduced efficacy *in vivo* of those platforms which employed photodynamic therapy.

f) Unavailability of systematic studies which enable an optimization of the platform design.

Unefficient platform sizes and shapes: Recent theoretical and experimental modelizations applied to analyze the nanoparticle behavior in the blood current demonstrated that spherical nanovectors with sizes around ~ 100 nm (most of the commercial available nanovectors nowadays) display the worst lateral movement through the blood vessel walls, that is, they have a complete unsuitability to find the conjugated antigen at the target-endotelium, and also the worst penetration through blood vessels which would difficult their accumulation, for example, in solid tumours.

1.7.4 PLGA/Au theranostic nanoplatforms as a solution

For the previously mentioned reasons, in this research we have synthesized a theragnostic multifunctional nanoplatform injectable via parenteral and which can be simultaneously used in cancer diagnosis and therapy by combining:

a) diagnosis capacity through optical (fluorescence) and magnetic (MRI) imaging.
b) therapeutical capacity through the combination of chemical, photothermal and photodynamic therapy. <

with which we try to overcome, at least in part, the weakness of the different systems studied up to now. This nanoplatform was constructed with biocompatible and biodegradable materials (PLGA, F127, chitosan) through a method composed of easy and scalable steps. In this way, all elements are enclosed (or supported) in a polymeric nanoparticle with such characteristics. At the same time, this polymeric nanovector ensures long circulating times and controlled drug release in human body. Nanovectors of different architecture were tested in order to define the best structure with optimal properties. Moreover, to allow specific recognition in tumor sites, this ensembles were functionalized with specific molecules which easily bind to over-expressed membrane receptors in cancerous cells. To achieve this goal, the nanoplatform was composed of:

1. Iron oxide superparamagnetic nanoparticles (SPIONs) with high enhanced R_2 relaxitivity, which makes them excellent candidates as MRI contrats agents. In addition, the presence of these NPs as part of the nanodevice can be also

exploited as a guiding mechanism for the whole nanodevice under the presence of suitable applied external magnetic fields.

2. Biocompatible FDA-approved fluorochrome indocyanine green (ICG), with absorption and emission at the near infrared (NIR) biological window, for fluorescence optical imaging, as photosensitizer for photodynamic therapy and as photothermal agent.
3. A potent chemotherapeutic agent: doxorubicin.
4. Gold nanoshells (AuNShs) with near infrared (NIR) absorption capacity to enable the use of the device as a photothermal agent too, and which would complement both chemotherapeutic effects.
5. Spherical nanoparticles formed by biodegradable, biocompatible and FDA-approved polymer, PLGA, which encapsulates (or holds) part or all of the previous components, and also regulates the nanovector size, its circulating time and drug delivery release profile.
6. Attached guiding molecules, folic acid and anti-HER2 monoclonal antibody Herceptin, for an efficient site-directed targeting of the nanoplatform to receptors overexpressed on abnormal cell membranes.

Important issues such as size and shape control, polydispersity, solubilization capacity, drug delivery release rate and efficacy as MRI and optical contrast agent were fitted when developing these nanodevices.The therapeutical efficacy of the nanodevice takes place through several mechanisms as:

a) Targeted controlled release of the antitumoral drug due to the presence of the guiding molecules on the nanovector surface and the additional guiding effect provided by SPIONs upon application of suitable external magnetic fields.

b) Drug release assisted by both diffusion through the nanovector walls and by the exposition to NIR. The latter involves a local heating in the areas where the nanovectors, surrounded by ICG/chitosan or gold shell, are localized giving rise to a fracture of the nanovector and subsequent release.

c) This local temperature increase through optical excitation might also help in killing tumoral cells (phothermal effect), and could be combined with the chemotherapeutic effect of the drug compound and the magnetothermal effect created by application of external magnetic fields (in the same way as the photothermal effect).

These multifunctional nanoparticles have the additional advantage that the therapeutic efficacy might be evaluated *in situ* and would enable to define their mechanism of action much more precisely. Furthermore, the design of these systems would also serve for a) achieving the needed action specificity to decrease the affectation of healthy cells and tissues and thus, diminishing the toxic side effects; b) reducing of the necessary dose levels to reach the desired therapeutically response; c) combining chemo, photothermal and/or photodynamic therapies to increase malign cell mortality; d) increasing the blood circulating time by avoiding recognition by RES through protection offered by polymeric nanomatrixes, which would also help to decrease the needed drug concentration in dosages; e) decreasing the time needed for a correct diagnosis and treatment; f) diminishing the associated economical cost to diagnosis and therapy upon integration of all functionalities an unique system. Finally these theranostic nanoplatforms would also allow their easy modification to offer new funtionalities through: a) conjugation of, for example, DNA or siRNA for gene therapy; b) conjugation of radionuclide for their use in computerized tomography, etc.

1.8 Bibliography

[1] Rao CNR, Cheetham AK. Materials Science at the Nanoscale. In: Gogotsi Y, editor. Nanomaterials Handbook. Boca Raton: Taylor and Francis Group; 2006.

[2] Lee SY. Self-assembly and Nanotechnology: A Force Balance Approach. Hoboken, New Jersey: Jon Wiley and Sons; 2008.

[3] Lindsay SM. Introduction to Nanoscience. New York: Oxford University Press; 2010.

[4] Sukhorukov GB, Donath E, Lichtenfeld H, Knippel E, Knippel M, Budde A, et al. Layer-by-layer self assembly of polyelectrolytes on colloidal particles. Colloids and Surfaces A: Physicochemical and Engineering Aspects. 1998;137:253-66.

[5] Muñoz Javier A, del Pino P, Bedard MF, Ho D, Skirtach AG, Sukhorukov GB, et al. Photoactivated Release of Cargo from the Cavity of Polyelectrolyte Capsules to the Cytosol of Cells. Langmuir. 2008;24:12517-20.

[6] http://ec.europa.eu/environment/chemicals/nanotech/.

[7] Agasti SS, Rana S, Park M-H, Kim CK, You C-C, Rotello VM. Nanoparticles for detection and diagnosis. Advanced Drug Delivery Reviews. 2010;62:316-28.

[8] Schmid G. Nanoparticles: From Theory to Application. Weinheim: Wiley-VCH; 2004.

[9] Rao CNR, Ramakrishna Matte HSS, Voggu R, Govindaraj A. Recent progress in the synthesis of inorganic nanoparticles. Dalton Transactions. 2012;41:5089-120.

[10] Guozhong C. Nanostructures and Nanomaterials. London: Imperial College Press; 2007.

[11] Eustis S, El-Sayed MA. Why gold nanoparticles are more precious than pretty gold: Noble metal surface plasmon resonance and its enhancement of the radiative and nonradiative properties of nanocrystals of different shapes. Chemical Society Reviews. 2006;35:209-17.

[12] Qiao R, Yang C, Gao M. Superparamagnetic iron oxide nanoparticles: from preparations to in vivo MRI applications. Journal of Materials Chemistry. 2009;19:6274-93.

[13] Tarn D, Ashley CE, Xue M, Carnes EC, Zink JI, Brinker CJ. Mesoporous Silica Nanoparticle Nanocarriers: Biofunctionality and Biocompatibility. Accounts of Chemical Research. 2013;46:792-801.

[14] Li W, Zhao D. An overview of the synthesis of ordered mesoporous materials. Chemical Communications. 2013;49:943-6.

[15] Osada M, Sasaki T. Two-Dimensional Dielectric Nanosheets: Novel Nanoelectronics From Nanocrystal Building Blocks. Advanced Materials. 2012;24:210-28.

[16] Kempa TJ, Day RW, Kim S-K, Park H-G, Lieber CM. Semiconductor nanowires: a platform for exploring limits and concepts for nano-enabled solar cells. Energy & Environmental Science. 2013;6:719-33.

[17] Klimov VI. Nanocrystal Quantum Dots. Los Alamos: Taylor and Francis Group; 2010.

[18] Jain PK, Huang X, El-Sayed IH, El-Sayed MA. Noble Metals on the Nanoscale: Optical and Photothermal Properties and Some Applications in Imaging, Sensing, Biology, and Medicine. Accounts of Chemical Research. 2008;41:1578-86.

[19] Loo C, Hirsch L, Lee M-H, Chang E, West J, Halas N, et al. Gold nanoshell bioconjugates for molecular imaging in living cells. Opt Lett. 2005;30:1012-4.

[20] Reynolds RA, Mirkin CA, Letsinger RL. Homogeneous, Nanoparticle-Based Quantitative Colorimetric Detection of Oligonucleotides. Journal of the American Chemical Society. 2000;122:3795-6.

[21] Bardhan R, Grady NK, Cole JR, Joshi A, Halas NJ. Fluorescence Enhancement by Au Nanostructures: Nanoshells and Nanorods. ACS Nano. 2009;3:744-52.

[22] Jackson JB, Halas NJ. Surface-enhanced Raman scattering on tunable plasmonic nanoparticle substrates. Proceedings of the National Academy of Sciences. 2004;101:17930-5.

[23] El-Sayed IH, Huang X, El-Sayed MA. Selective laser photo-thermal therapy of epithelial carcinoma using anti-EGFR antibody conjugated gold nanoparticles. Cancer letters. 2006;239:129-35.

[24] Niidome T, Yamagata M, Okamoto Y, Akiyama Y, Takahashi H, Kawano T, et al. PEG-modified gold nanorods with a stealth character for in vivo applications. Journal of Controlled Release. 2006;114:343-7.

[25] El-Sayed IH, Huang X, El-Sayed MA. Surface Plasmon Resonance Scattering and Absorption of anti-EGFR Antibody Conjugated Gold Nanoparticles in Cancer Diagnostics: Applications in Oral Cancer. Nano Letters. 2005;5:829-34.

[26] Bardhan R, Chen W, Perez-Torres C, Bartels M, Huschka RM, Zhao LL, et al. Nanoshells with Targeted Simultaneous Enhancement of Magnetic and Optical Imaging and Photothermal Therapeutic Response. Advanced Functional Materials. 2009;19:3901-9.

[27] Gao J, Gu H, Xu B. Multifunctional Magnetic Nanoparticles: Design, Synthesis, and Biomedical Applications. Accounts of Chemical Research. 2009;42:1097-107.

[28] Frey NA, Peng S, Cheng K, Sun S. Magnetic nanoparticles: synthesis, functionalization, and applications in bioimaging and magnetic energy storage. Chemical Society Reviews. 2009;38:2532-42.

[29] Mattoussi H, Palui G, Na HB. Luminescent quantum dots as platforms for probing in vitro and in vivo biological processes. Advanced Drug Delivery Reviews. 2012;64:138-66.

[30] Fisher JE. Carbon Nanotubes: Structure and Properties. In: Gogotsi Y, editor. Nanomaterials Handbook. Boca Raton: Taylor & Francis; 2006.

[31] Lacerda L, Bianco A, Prato M, Kostarelos K. Carbon nanotubes as nanomedicines: From toxicology to pharmacology. Advanced Drug Delivery Reviews. 2006;58:1460-70.

[32] Krueger A. New Carbon Materials: Biological Applications of Functionalized Nanodiamond Materials. Chemistry – A European Journal. 2008;14:1382-90.

[33] Soppimath KS, Aminabhavi TM, Kulkarni AR, Rudzinski WE. Biodegradable polymeric nanoparticles as drug delivery devices. Journal of Controlled Release. 2001;70:1-20.

[34] Bromberg L. Polymeric micelles in oral chemotherapy. Journal of Controlled Release. 2008;128:99-112.

[35] Mateo-Alonso A, Tagmatarchis N, Maurizio P. Fullerenes and Their Derivatives. In: Gogotsi Y, editor. Nanomaterials Handbook Boca Raton: Taylor & Francis; 2006

[36] Dresselhaus MS, Dresselhaus G, Charlier JC, Hernández E. Electronic, thermal and mechanical properties of carbon nanotubes. Philosophical Transactions of the Royal Society of London Series A: Mathematical, Physical and Engineering Sciences. 2004;362:2065-98.

[37] Shenderova O, McGuire G. Nanocrystalline Diamond. In: Gogotsi Y, editor. Nanomaterials Handbook. Boca Raton: Taylor & Francis; 2006.

[38] Tan WB, Zhang Y. Surface modification of gold and quantum dot nanoparticles with chitosan for bioapplications. Journal of Biomedical Materials Research Part A. 2005;75A:56-62.

[39] Manchanda R, Fernandez-Fernandez A, Nagesetti A, McGoron AJ. Preparation and characterization of a polymeric (PLGA) nanoparticulate drug delivery system with simultaneous incorporation of chemotherapeutic and thermo-optical agents. Colloids and Surfaces B: Biointerfaces. 2010;75:260-7.

[40] Li Y-P, Pei Y-Y, Zhang X-Y, Gu Z-H, Zhou Z-H, Yuan W-F, et al. PEGylated PLGA nanoparticles as protein carriers: synthesis, preparation and biodistribution in rats. Journal of Controlled Release. 2001;71:203-11.

[41] Ravi Kumar MNV, Bakowsky U, Lehr CM. Preparation and characterization of cationic PLGA nanospheres as DNA carriers. Biomaterials. 2004;25:1771-7.

[42] Alexandridis P, Lindman B. Amphiphilic Block Copolymers: Self - assembly and Applications

Applications. Amsterdam: Elsevier; 2000.

[43] Dalhaimer P, Engler AJ, Parthasarathy R, Discher DE. Targeted Worm Micelles. Biomacromolecules. 2004;5:1714-9.

[44] Zhang W, Shi Y, Chen Y, Hao J, Sha X, Fang X. The potential of Pluronic polymeric micelles encapsulated with paclitaxel for the treatment of melanoma using subcutaneous and pulmonary metastatic mice models. Biomaterials. 2011;32:5934-44.

[45] Dinarvand R, Sepehri N, Manoochehri S, Rouhani H, Atyabi F. Polylactide-co-glycolide nanoparticles for controlled delivery of anticancer agents. International journal of nanomedicine. 2011;6:877-95.

[46] Panyam J, Dali MM, Sahoo SK, Ma W, Chakravarthi SS, Amidon GL, et al. Polymer degradation and in vitro release of a model protein from poly(d,l-lactide-co-glycolide) nano- and microparticles. Journal of Controlled Release. 2003;92:173-87.

[47] Jia Y, Yuan M, Yuan H, Huang X, Sui X, Cui X, et al. Co-encapsulation of magnetic Fe3O4 nanoparticles and doxorubicin into biodegradable PLGA nanocarriers for intratumoral drug delivery. International journal of nanomedicine. 2012;7:1697-708.

[48] Jain RA. The manufacturing techniques of various drug loaded biodegradable poly(lactide-co-glycolide) (PLGA) devices. Biomaterials. 2000;21:2475-90.

[49] Karnik R, Gu F, Basto P, Cannizzaro C, Dean L, Kyei-Manu W, et al. Microfluidic Platform for Controlled Synthesis of Polymeric Nanoparticles. Nano Letters. 2008;8:2906-12.

[50] Zolnik BS, Burgess DJ. Effect of acidic pH on PLGA microsphere degradation and release. Journal of Controlled Release. 2007;122:338-44.

[51] Lee ES, Na K, Bae YH. Polymeric micelle for tumor pH and folate-mediated targeting. Journal of Controlled Release. 2003;91:103-13.

[52] Little SR, Kohane DS. Polymers for intracellular delivery of nucleic acids. Journal of Materials Chemistry. 2008;18:832-41.

[53] Timko BP, Dvir T, Kohane DS. Remotely Triggerable Drug Delivery Systems. Advanced Materials. 2010;22:4925-43.

[54] Kumari A, Yadav SK, Yadav SC. Biodegradable polymeric nanoparticles based drug delivery systems. Colloids and Surfaces B: Biointerfaces. 2010;75:1-18.

[55] Immordino ML, Dosio F, Cattel L. Stealth liposomes: review of the basic science, rationale, and clinical applications, existing and potential. International journal of nanomedicine. 2006;1:297-315.

[56] Dickinson DPE. Nanomaterials: Syntheis, Properties and Applications. New York: Taylor and Francis Group; 1996.

[57] Mahdavi A, Ferreira L, Sundback C, Nichol JW, Chan EP, Carter DJD, et al. A biodegradable and biocompatible gecko-inspired tissue adhesive. Proceedings of the National Academy of Sciences. 2008;105:2307-12.

[58] Bakr OM, Wunsch BH, Stellacci F. High-Yield Synthesis of Multi-Branched Urchin-Like Gold Nanoparticles. Chemistry of Materials. 2006;18:3297-301.

[59] Doshi N, Mitragotri S. Designer Biomaterials for Nanomedicine. Advanced Functional Materials. 2009;19:3843-54.

[60] Wu W, Hsiao SC, Carrico ZM, Francis MB. Genome-Free Viral Capsids as Multivalent Carriers for Taxol Delivery. Angewandte Chemie International Edition. 2009;48:9493-7.

[61] Dixit SK, Goicochea NL, Daniel M-C, Murali A, Bronstein L, De M, et al. Quantum Dot Encapsulation in Viral Capsids. Nano Letters. 2006;6:1993-9.

[62] Nelson LD, Cox MM. Lehninger Principles of Biochemistry. 5th ed. New York: W. H. Freeman and Company; 2008.

[63] Mao S, Sun W, Kissel T. Chitosan-based formulations for delivery of DNA and siRNA. Advanced Drug Delivery Reviews. 2010;62:12-27.

[64] Dachs GU, Dougherty GJ, Stratford IJ, Chaplin DJ. Targeting gene therapy to cancer: a review. Oncology research. 1997;9:313-25.

[65] Friedmann T. Progress toward human gene therapy. Science. 1989;244:1275-81.

[66] Juárez J, Cambón A, Topete A, Taboada P, Mosquera V. One-Dimensional Magnetic Nanowires Obtained by Protein Fibril Biotemplating. Chemistry – A European Journal. 2011;17:7366-73.

[67] Gradishar WJ. Albumin-bound paclitaxel: a next-generation taxane. Expert Opinion on Pharmacotherapy. 2006;7:1041-53.

[68] Roos WH, Ivanovska IL, Evilevitch A, Wuite GJL. Viral capsids: Mechanical characteristics, genome packaging and delivery mechanisms. Cell Mol Life Sci. 2007;64:1484-97.

[69] Xu Z, Zhou X, Shi W, Qian Q. Capsid modification of adeno-associated virus and tumor targeting gene therapy. Chin Sci Bull. 2008;53:3790-7.

[70] Luque A, Zandi R, Reguera D. Optimal architectures of elongated viruses. Proceedings of the National Academy of Sciences. 2010.

[71] Zhao P, Li N, Astruc D. State of the art in gold nanoparticle synthesis. Coordination Chemistry Reviews. 2013;257:638-65.

[72] Hu M, Chen J, Li Z-Y, Au L, Hartland GV, Li X, et al. Gold nanostructures: engineering their plasmonic properties for biomedical applications. Chemical Society Reviews. 2006;35:1084-94.

[73] Turkevich J, Stevenson PC, Hillier J. A study of the nucleation and growth processes in the synthesis of colloidal gold. Discussions of the Faraday Society. 1951;11:55-75.

[74] Frens G. Controlled Nucleation for the Regulation of the Particle Size in Monodisperse Gold Suspensions. Nature: Phys Sci. 1973;241:20-2.

[75] Schmid G, Pfeil R, Boese R, Bandermann F, Meyer S, Calis GHM, et al. Au55[P(C6H5)3]12CI6 — ein Goldcluster ungewöhnlicher Größe. Chemische Berichte. 1981;114:3634-42.

[76] Giersig M, Mulvaney P. Preparation of ordered colloid monolayers by electrophoretic deposition. Langmuir. 1993;9:3408-13.

[77] Brust M, Walker M, Bethell D, Schiffrin DJ, Whyman R. Synthesis of thiol-derivatised gold nanoparticles in a two-phase Liquid-Liquid system. Journal of the Chemical Society, Chemical Communications. 1994;0:801-2.

[78] Kimling J, Maier M, Okenve B, Kotaidis V, Ballot H, Plech A. Turkevich Method for Gold Nanoparticle Synthesis Revisited. The Journal of Physical Chemistry B. 2006;110:15700-7.

[79] Ojea-Jiménez I, Romero FM, Bastús NG, Puntes V. Small Gold Nanoparticles Synthesized with Sodium Citrate and Heavy Water: Insights into the Reaction Mechanism. The Journal of Physical Chemistry C. 2010;114:1800-4.

[80] Brown KR, Natan MJ. Hydroxylamine Seeding of Colloidal Au Nanoparticles in Solution and on Surfaces. Langmuir. 1998;14:726-8.

[81] Jana NR, Gearheart L, Murphy CJ. Wet Chemical Synthesis of High Aspect Ratio Cylindrical Gold Nanorods. The Journal of Physical Chemistry B. 2001;105:4065-7.

[82] Rodríguez-Fernández J, Pérez-Juste J, García de Abajo FJ, Liz-Marzán LM. Seeded Growth of Submicron Au Colloids with Quadrupole Plasmon Resonance Modes. Langmuir. 2006;22:7007-10.

[83] Perrault SD, Chan WCW. Synthesis and Surface Modification of Highly Monodispersed, Spherical Gold Nanoparticles of 50−200 nm. Journal of the American Chemical Society. 2009;131:17042-3.

[84] Ziegler C, Eychmu ller A. Seeded Growth Synthesis of Uniform Gold Nanoparticles with Diameters of 15−300 nm. The Journal of Physical Chemistry C. 2011;115:4502-6.

[85] Pérez-Juste J, Liz-Marzán LM, Carnie S, Chan DYC, Mulvaney P. Electric-Field-Directed Growth of Gold Nanorods in Aqueous Surfactant Solutions. Advanced Functional Materials. 2004;14:571-9.

[86] Jana NR, Gearheart L, Murphy CJ. Seed-Mediated Growth Approach for Shape-Controlled Synthesis of Spheroidal and Rod-like Gold Nanoparticles Using a Surfactant Template. Advanced Materials. 2001;13:1389-93.

[87] Liu, Guyot-Sionnest P. Mechanism of Silver(I)-Assisted Growth of Gold Nanorods and Bipyramids. The Journal of Physical Chemistry B. 2005;109:22192-200.

[88] Nikoobakht B, El-Sayed MA. Preparation and Growth Mechanism of Gold Nanorods (NRs) Using Seed-Mediated Growth Method. Chemistry of Materials. 2003;15:1957-62.

[89] Gole A, Murphy CJ. Polyelectrolyte-Coated Gold Nanorods: Synthesis, Characterization and Immobilization. Chemistry of Materials. 2005;17:1325-30.

[90] Gole A, Stone JW, Gemmill WR, zur Loye H-C, Murphy CJ. Iron Oxide Coated Gold Nanorods: Synthesis, Characterization, and Magnetic Manipulation. Langmuir. 2008;24:6232-7.

[91] Pastoriza-Santos I, Pérez-Juste J, Liz-Marzán LM. Silica-Coating and Hydrophobation of CTAB-Stabilized Gold Nanorods. Chemistry of Materials. 2006;18:2465-7.

[92] Huang Y-F, Sefah K, Bamrungsap S, Chang H-T, Tan W. Selective Photothermal Therapy for Mixed Cancer Cells Using Aptamer-Conjugated Nanorods. Langmuir. 2008;24:11860-5.

[93] Oldenburg SJ, Averitt RD, Westcott SL, Halas NJ. Nanoengineering of optical resonances. Chemical Physics Letters. 1998;288:243-7.

[94] Averitt RD, Westcott SL, Halas NJ. Linear optical properties of gold nanoshells. J Opt Soc Am B. 1999;16:1824-32.

[95] Guerrero-Martínez A, Barbosa S, Pastoriza-Santos I, Liz-Marzán LM. Nanostars shine bright for you: Colloidal synthesis, properties and applications of branched metallic nanoparticles. Current Opinion in Colloid & Interface Science. 2011;16:118-27.

[96] Link S, El-Sayed MA. Shape and size dependence of radiative, non-radiative and photothermal properties of gold nanocrystals. International Reviews in Physical Chemistry. 2000;19:409-53.

[97] Allgeyer ES, Pongan A, Browne M, Mason MD. Optical Signal Comparison of Single Fluorescent Molecules and Raman Active Gold Nanostars. Nano Letters. 2009;9:3816-9.

[98] Kuo C-H, Huang MH. Synthesis of Branched Gold Nanocrystals by a Seeding Growth Approach. Langmuir. 2005;21:2012-6.

[99] Zou X, Ying E, Dong S. Seed-mediated synthesis of branched gold nanoparticles with the assistance of citrate and their surface-enhanced Raman scattering properties. Nanotechnology. 2006;17:4758-64.

[100] Barbosa S, Agrawal A, Rodríguez-Lorenzo L, Pastoriza-Santos I, Alvarez-Puebla RnA, Kornowski A, et al. Tuning Size and Sensing Properties in Colloidal Gold Nanostars. Langmuir. 2010;26:14943-50.

[101] Lu L, Ai K, Ozaki Y. Environmentally Friendly Synthesis of Highly Monodisperse Biocompatible Gold Nanoparticles with Urchin-like Shape. Langmuir. 2008;24:1058-63.

[102] Burt JL, Elechiguerra JL, Reyes-Gasga J, Martin Montejano-Carrizales J, Jose-Yacaman M. Beyond Archimedean solids: Star polyhedral gold nanocrystals. Journal of Crystal Growth. 2005;285:681-91.

[103] Xie J, Lee JY, Wang DIC. Seedless, Surfactantless, High-Yield Synthesis of Branched Gold Nanocrystals in HEPES Buffer Solution. Chem Mater. 2007;19:2823-30.

[104] Hao E, Bailey RC, Schatz GC, Hupp JT, Li S. Synthesis and Optical Properties of "Branched" Gold Nanocrystals. Nano Letters. 2004;4:327-30.

[105] Connor EE, Mwamuka J, Gole A, Murphy CJ, Wyatt MD. Gold Nanoparticles Are Taken Up by Human Cells but Do Not Cause Acute Cytotoxicity. Small. 2005;1:325-7.

[106] Angelatos AS, Radt B, Caruso F. Light-Responsive Polyelectrolyte/Gold Nanoparticle Microcapsules. The Journal of Physical Chemistry B. 2005;109:3071-6.

[107] Averitt RD, Sarkar D, Halas NJ. Plasmon Resonance Shifts of Au-Coated Au_{2}S Nanoshells: Insight into Multicomponent Nanoparticle Growth. Physical Review Letters. 1997;78:4217-20.

[108] Weissleder R. A clearer vision for in vivo imaging. Nat Biotech. 2001;19:316-7.

[109] Wilson CB, Patterson SM. The physics, biophysics and technology of photodynamic therapy. Physics in Medicine and Biology. 2008;53:R61.

[110] Khanadeev VA, Khlebtsov BN, Staroverov SA, Vidyasheva IV, Skaptsov AA, Ileneva ES, et al. Quantitative cell bioimaging using gold-nanoshell conjugates and phage antibodies. Journal of Biophotonics. 2011;4:74-83.

[111] Sokolov K, Follen M, Aaron J, Pavlova I, Malpica A, Lotan R, et al. Real-Time Vital Optical Imaging of Precancer Using Anti-Epidermal Growth Factor Receptor Antibodies Conjugated to Gold Nanoparticles. Cancer Research. 2003;63:1999-2004.

[112] Gobin AM, Lee MH, Halas NJ, James WD, Drezek RA, West JL. Near-Infrared Resonant Nanoshells for Combined Optical Imaging and Photothermal Cancer Therapy. Nano Letters. 2007;7:1929-34.

[113] Schwartz JA, Shetty AM, Price RE, Stafford RJ, Wang JC, Uthamanthil RK, et al. Feasibility Study of Particle-Assisted Laser Ablation of Brain Tumors in Orthotopic Canine Model. Cancer Research. 2009;69:1659-67.

[114] Park H, Yang J, Lee J, Haam S, Choi I-H, Yoo K-H. Multifunctional Nanoparticles for Combined Doxorubicin and Photothermal Treatments. ACS Nano. 2009;3:2919-26.

[115] Yang J, Lee J, Kang J, Oh SJ, Ko H-J, Son J-H, et al. Smart Drug-Loaded Polymer Gold Nanoshells for Systemic and Localized Therapy of Human Epithelial Cancer. Advanced Materials. 2009;21:4339-42.

[116] Nehl CL, Liao H, Hafner JH. Optical Properties of Star-Shaped Gold Nanoparticles. Nano Letters. 2006;6:683-8.

[117] Hao F, Nehl CL, Hafner JH, Nordlander P. Plasmon Resonances of a Gold Nanostar. Nano Letters. 2007;7:729-32.

[118] Sau TK, Rogach AL, Döblinger M, Feldmann J. One-Step High-Yield Aqueous Synthesis of Size-Tunable Multispiked Gold Nanoparticles. Small. 2011;7:2188-94.

[119] Chen H, Zhang X, Dai S, Ma Y, Cui S, Achilefu S, et al. Multifunctional Gold Nanostar Conjugates for Tumor Imaging and Combined Photothermal and Chemo-therapy Theranostics. 2013;3:633-49.

[120] Wang S, Huang P, Nie L, Xing R, Liu D, Wang Z, et al. Single Continuous Wave Laser Induced Photodynamic/Plasmonic Photothermal Therapy Using Photosensitizer-Functionalized Gold Nanostars. Advanced Materials. 2013;25:3055-61.

[121] Manthe RL, Foy SP, Krishnamurthy N, Sharma B, Labhasetwar V. Tumor Ablation and Nanotechnology. Molecular Pharmaceutics. 2010;7:1880-98.

[122] Eikesdal HP, Bjerkvig R, Raleigh JA, Mella O, Dahl O. Tumor vasculature is targeted by the combination of combretastatin A-4 and hyperthermia. Radiotherapy and oncology : journal of the European Society for Therapeutic Radiology and Oncology. 2001;61:313-20.

[123] Nelson BK, Conover DL, Krieg EF, Snyder DL, Edwards RM. Interactions of radiofrequency radiation-induced hyperthermia and 2-methoxyethanol teratogenicity in rats. Bioelectromagnetics. 1997;18:349-59.

[124] Diederich CJ, Hynynen K. Ultrasound technology for hyperthermia. Ultrasound in medicine & biology. 1999;25:871-87.

[125] Huang X, Jain P, El-Sayed I, El-Sayed M. Plasmonic photothermal therapy (PPTT) using gold nanoparticles. Lasers Med Sci. 2008;23:217-28.

[126] Kah JCY, Wong KY, Neoh KG, Song JH, Fu JWP, Mhaisalkar S, et al. Critical parameters in the pegylation of gold nanoshells for biomedical applications: An in vitro macrophage study. Journal of Drug Targeting. 2009;17:181-93.

[127] Weishaupt KR, Gomer CJ, Dougherty TJ. Identification of Singlet Oxygen as the Cytotoxic Agent in Photo-inactivation of a Murine Tumor. Cancer Research. 1976;36:2326-9.

[128] Höckel M, Schlenger K, Aral B, Mitze M, Schäffer U, Vaupel P. Association between Tumor Hypoxia and Malignant Progression in Advanced Cancer of the Uterine Cervix. Cancer Research. 1996;56:4509-15.

[129] Sundfor K, Lyng H, Rofstad EK. Tumour hypoxia and vascular density as predictors of metastasis in squamous cell carcinoma of the uterine cervix. Br J Cancer. 1998;78:822-7.

[130] Barr H, Tralau CJ, Boulos PB, MacRobert AJ, Tilly R, Bown SG. THE CONTRASTING MECHANISMS OF COLONIC COLLAGEN DAMAGE

BETWEEN PHOTODYNAMIC THERAPY and THERMAL INJURY. Photochemistry and Photobiology. 1987;46:795-800.

[131] Na HB, Song IC, Hyeon T. Inorganic Nanoparticles for MRI Contrast Agents. Advanced Materials. 2009;21:2133-48.

[132] Lee J-H, Huh Y-M, Jun Y-w, Seo J-w, Jang J-t, Song H-T, et al. Artificially engineered magnetic nanoparticles for ultra-sensitive molecular imaging. Nat Med. 2007;13:95-9.

[133] David I, Welch AJE. The oxidation of magnetite and related spinels. Constitution of gamma ferric oxide. Transactions of the Faraday Society. 1956;52:1642-50.

[134] Elmore WC. Ferromagnetic Colloid for Studying Magnetic Structures. Physical Review. 1938;54:309-10.

[135] Ricketts CR, Cox JSG, Fitzmaurice C, Moss GF. The Iron Dextran Complex. Nature. 1965;208:237-9.

[136] Massart R. Preparation of aqueous magnetic liquids in alkaline and acidic media. Magnetics, IEEE Transactions on. 1981;17:1247-8.

[137] Sun Z-X, Su F-W, Forsling W, Samskog P-O. Surface Characteristics of Magnetite in Aqueous Suspension. Journal of Colloid and Interface Science. 1998;197:151-9.

[138] Tombácz E, Illés E, Majzik A, Hajdú A, Rideg N, Szekeres M. Ageing in the Inorganic Nanoworld: Example of Magnetite

Nanoparticles in Aqueous Medium. Croatia Chemical Acta. 2007;80:503-15.

[139] Jain TK, Morales MA, Sahoo SK, Leslie-Pelecky DL, Labhasetwar V. Iron oxide nanoparticles for sustained delivery of anticancer agents. Mol Pharm. 2005;2:194-205.

[140] Huh Y-M, Jun Y-w, Song H-T, Kim S, Choi J-s, Lee J-H, et al. In Vivo Magnetic Resonance Detection of Cancer by Using Multifunctional Magnetic Nanocrystals. Journal of the American Chemical Society. 2005;127:12387-91.

[141] Uchegbu FI, Schätzlein GA. Polymers in Drug Delivery: Taylor and Francis; 2006.

[142] Yang J, Lee C-H, Ko H-J, Suh J-S, Yoon H-G, Lee K, et al. Multifunctional Magneto-Polymeric Nanohybrids for Targeted Detection and Synergistic Therapeutic Effects on Breast Cancer. Angewandte Chemie International Edition. 2007;46:8836-9.

[143] Saxena V, Sadoqi M, Shao J. Polymeric nanoparticulate delivery system for Indocyanine green: Biodistribution in healthy mice. International Journal of Pharmaceutics. 2006;308:200-4.

[144] Danhier F, Ansorena E, Silva JM, Coco R, Le Breton A, Préat V. PLGA-based nanoparticles: An overview of biomedical applications. Journal of Controlled Release. 2012;161:505-22.

[145] Acharya S, Sahoo SK. PLGA nanoparticles containing various anticancer agents and tumour delivery by EPR effect. Advanced Drug Delivery Reviews. 2011;63:170-83.

[146] Bilati U, Allémann E, Doelker E. Development of a nanoprecipitation method intended for the entrapment of hydrophilic drugs into nanoparticles. European Journal of Pharmaceutical Sciences. 2005;24:67-75.

[147] Fessi H, Puisieux F, Devissaguet JP, Ammoury N, Benita S. Nanocapsule formation by interfacial polymer deposition following solvent displacement. International Journal of Pharmaceutics. 1989;55:R1-R4.

[148] Sperling RA, Parak WJ. Surface modification, functionalization and bioconjugation of colloidal inorganic nanoparticles. Philosophical Transactions of the Royal Society A: Mathematical, Physical and Engineering Sciences. 2010;368:1333-83.

[149] Lewin B. Genes. Upper Saddle River: Pearson Prentice Hall; 2004.

[150] Kievit FM, Zhang M. Cancer Nanotheranostics: Improving Imaging and Therapy by Targeted Delivery Across Biological Barriers. Advanced Materials. 2011;23:H217-H47.

[151] Alexis F, Pridgen E, Molnar LK, Farokhzad OC. Factors Affecting the Clearance and Biodistribution of Polymeric Nanoparticles. Molecular Pharmaceutics. 2008;5:505-15.

[152] Nagayama S, Ogawara K-i, Fukuoka Y, Higaki K, Kimura T. Time-dependent changes in opsonin amount associated on nanoparticles alter their hepatic uptake characteristics. International Journal of Pharmaceutics. 2007;342:215-21.

[153] Fang C, Shi B, Pei Y-Y, Hong M-H, Wu J, Chen H-Z. In vivo tumor targeting of tumor necrosis factor-α-loaded stealth nanoparticles: Effect of MePEG molecular weight and particle size. European Journal of Pharmaceutical Sciences. 2006;27:27-36.

[154] Sonavane G, Tomoda K, Makino K. Biodistribution of colloidal gold nanoparticles after intravenous administration: Effect of particle size. Colloids and Surfaces B: Biointerfaces. 2008;66:274-80.

[155] De Jong WH, Hagens WI, Krystek P, Burger MC, Sips AJAM, Geertsma RE. Particle size-dependent organ distribution of gold nanoparticles after intravenous administration. Biomaterials. 2008;29:1912-9.

[156] Chithrani BD, Ghazani AA, Chan WCW. Determining the Size and Shape Dependence of Gold Nanoparticle Uptake into Mammalian Cells. Nano Letters. 2006;6:662-8.

[157] dos Santos T, Varela J, Lynch I, Salvati A, Dawson KA. Quantitative Assessment of the Comparative Nanoparticle-Uptake Efficiency of a Range of Cell Lines. Small. 2011;7:3341-9.

[158] Gratton SEA, Ropp PA, Pohlhaus PD, Luft JC, Madden VJ, Napier ME, et al. The effect of particle design on cellular internalization pathways. Proceedings of the National Academy of Sciences. 2008;105:11613-8.

[159] Verma A, Stellacci F. Effect of Surface Properties on Nanoparticle–Cell Interactions. Small. 2010;6:12-21.

[160] Sobhan MA, Sreenivasan VKA, Withford MJ, Goldys EM. Non-specific internalization of laser ablated pure gold nanoparticles in pancreatic tumor cell. Colloids and Surfaces B: Biointerfaces. 2012;92:190-5.

[161] Hirn S, Semmler-Behnke M, Schleh C, Wenk A, Lipka J, Schäffler M, et al. Particle size-dependent and surface charge-dependent biodistribution of gold nanoparticles after intravenous administration. European Journal of Pharmaceutics and Biopharmaceutics. 2011;77:407-16.

[162] Balogh L, Nigavekar SS, Nair BM, Lesniak W, Zhang C, Sung LY, et al. Significant effect of size on the in vivo biodistribution of gold composite nanodevices in mouse tumor models. Nanomedicine: Nanotechnology, Biology and Medicine. 2007;3:281-96.

[163] He C, Hu Y, Yin L, Tang C, Yin C. Effects of particle size and surface charge on cellular uptake and biodistribution of polymeric nanoparticles. Biomaterials. 2010;31:3657-66.

[164] Levin CS, Bishnoi SW, Grady NK, Halas NJ. Determining the Conformation of Thiolated Poly(ethylene glycol) on Au Nanoshells by Surface-Enhanced Raman Scattering Spectroscopic Assay. Analytical Chemistry. 2006;78:3277-81.

[165] Gref R, Lück M, Quellec P, Marchand M, Dellacherie E, Harnisch S, et al. 'Stealth' corona-core nanoparticles surface modified by polyethylene glycol (PEG): influences of the corona (PEG chain length and surface density) and of the core

composition on phagocytic uptake and plasma protein adsorption. Colloids and Surfaces B: Biointerfaces. 2000;18:301-13.

[166] Fee CJ, Van Alstine JM. Prediction of the Viscosity Radius and the Size Exclusion Chromatography Behavior of PEGylated Proteins. Bioconjugate Chemistry. 2004;15:1304-13.

[167] Bazile D, Prud'homme C, Bassoullet M-T, Marlard M, Spenlehauer G, Veillard M. Stealth Me.PEG-PLA nanoparticles avoid uptake by the mononuclear phagocytes system. Journal of Pharmaceutical Sciences. 1995;84:493-8.

[168] Peracchia MT, Fattal E, Desmaële D, Besnard M, Noël JP, Gomis JM, et al. Stealth® PEGylated polycyanoacrylate nanoparticles for intravenous administration and splenic targeting. Journal of Controlled Release. 1999;60:121-8.

[169] Peracchia MT, Harnisch S, Pinto-Alphandary H, Gulik A, Dedieu JC, Desmaële D, et al. Visualization of in vitro protein-rejecting properties of PEGylated stealth® polycyanoacrylate nanoparticles. Biomaterials. 1999;20:1269-75.

[170] Hirsch LR, Stafford RJ, Bankson JA, Sershen SR, Rivera B, Price RE, et al. Nanoshell-mediated near-infrared thermal therapy of tumors under magnetic resonance guidance. Proceedings of the National Academy of Sciences. 2003;100:13549-54.

[171] Butterworth MD, Illum L, Davis SS. Preparation of ultrafine silica- and PEG-coated magnetite particles. Colloids and Surfaces A: Physicochemical and Engineering Aspects. 2001;179:93-102.

[172] Walling M, Novak J, Shepard JRE. Quantum Dots for Live Cell and In Vivo Imaging. International Journal of Molecular Sciences. 2009;10:441-91.

[173] Otsuka H, Nagasaki Y, Kataoka K. PEGylated nanoparticles for biological and pharmaceutical applications. Advanced Drug Delivery Reviews. 2003;55:403-19.

[174] Xie J, Xu C, Kohler N, Hou Y, Sun S. Controlled PEGylation of Monodisperse Fe3O4 Nanoparticles for Reduced Non-Specific Uptake by Macrophage Cells. Advanced Materials. 2007;19:3163-6.

[175] Felice RD, Selloni A. Adsorption modes of cysteine on Au(111): Thiolate, amino-thiolate, disulfide. The Journal of Chemical Physics. 2004;120:4906-14.

[176] Zhang G, Yang Z, Lu W, Zhang R, Huang Q, Tian M, et al. Influence of anchoring ligands and particle size on the colloidal stability and in vivo biodistribution of polyethylene glycol-coated gold nanoparticles in tumor-xenografted mice. Biomaterials. 2009;30:1928-36.

[177] Hermanson GT. Bioconjugate Techniques. USA: Academic Press; 2008.

[178] Scientific T. http://www.piercenet.com/browse.cfm?fldID=F3305493-0FBC-93DA-2720-4412D198A9C9.

[179] Goy-López S, Juárez J, Alatorre-Meda M, Casals E, Puntes VF, Taboada P, et al. Physicochemical Characteristics of Protein–NP Bioconjugates: The Role of Particle Curvature and Solution Conditions on Human Serum Albumin Conformation and Fibrillogenesis Inhibition. Langmuir. 2012;28:9113-26.

[180] Maeda H. The enhanced permeability and retention (EPR) effect in tumor vasculature: the key role of tumor-selective macromolecular drug targeting. Advances in Enzyme Regulation. 2001;41:189-207.

[181] Maeda H. Macromolecular therapeutics in cancer treatment: The EPR effect and beyond. Journal of Controlled Release. 2012;164:138-44.

[182] Farokhzad OC, Langer R. Impact of Nanotechnology on Drug Delivery. ACS Nano. 2009;3:16-20.

[183] Arruebo M, Valladares M, #243, nica, Gonz, #225, et al. Antibody-Conjugated Nanoparticles for Biomedical Applications. Journal of Nanomaterials. 2009;2009.

[184] Goustin AS, Leof EB, Shipley GD, Moses HL. Growth Factors and Cancer. Cancer Research. 1986;46:1015-29.

[185] Sen S. Aneuploidy and cancer. Current Opinion in Oncology. 2000;12:82-8.

[186] Schrevel M, Gorter A, Kolkman-Uljee SM, Trimbos JBMZ, Fleuren GJ, Jordanova ES. Molecular mechanisms of epidermal growth factor receptor overexpression in patients with cervical cancer. Mod Pathol. 2011;24:720-8.

[187] Nahta R, Hortobágyi GN, Esteva FJ. Growth Factor Receptors in Breast Cancer: Potential for Therapeutic Intervention. The Oncologist. 2003;8:5-17.

[188] Watanabe M, Ishiwata T, Nishigai K, Moriyama Y, Asano G. Overexpression of keratinocyte growth factor in cancer cells and enterochromaffin cells in human colorectal cancer. Pathology International. 2000;50:363-72.

[189] Nahta R, Esteva FJ. Herceptin: mechanisms of action and resistance. Cancer Letters. 2006;232:123-38.

[190] Yang J, Lee C-H, Park J, Seo S, Lim E-K, Song YJ, et al. Antibody conjugated magnetic PLGA nanoparticles for diagnosis and treatment of breast cancer. Journal of Materials Chemistry. 2007;17:2695-9.

[191] Carpin L, Bickford L, Agollah G, Yu T-K, Schiff R, Li Y, et al. Immunoconjugated gold nanoshell-mediated photothermal ablation of trastuzumab-resistant breast cancer cells. Breast Cancer Res Treat. 2011;125:27-34.

[192] Loo C, Lowery A, Halas N, West J, Drezek R. Immunotargeted Nanoshells for Integrated Cancer Imaging and Therapy. Nano Letters. 2005;5:709-11.

[193] Melancon MP, Lu W, Yang Z, Zhang R, Cheng Z, Elliot AM, et al. In vitro and in vivo targeting of hollow gold nanoshells directed at epidermal growth factor receptor for photothermal ablation therapy. Molecular Cancer Therapeutics. 2008;7:1730-9.

[194] Farokhzad OC, Jeffrey CM, Langer R. Nanoparticle–aptamer bioconjugates for cancer targeting. Expert Opinion on Drug Delivery. 2006;3:311-24.

[195] Chan WCW, Nie S. Quantum Dot Bioconjugates for Ultrasensitive Nonisotopic Detection. Science. 1998;281:2016-8.

[196] Harisinghani MG, Barentsz J, Hahn PF, Deserno WM, Tabatabaei S, van de Kaa CH, et al. Noninvasive Detection of Clinically Occult Lymph-Node Metastases in Prostate Cancer. New England Journal of Medicine. 2003;348:2491-9.

[197] Farokhzad OC, Jon S, Khademhosseini A, Tran T-NT, LaVan DA, Langer R. Nanoparticle-Aptamer Bioconjugates: A New Approach for Targeting Prostate Cancer Cells. Cancer Research. 2004;64:7668-72.

[198] Farokhzad OC, Cheng J, Teply BA, Sherifi I, Jon S, Kantoff PW, et al. Targeted nanoparticle-aptamer bioconjugates for cancer chemotherapy in vivo. Proceedings of the National Academy of Sciences. 2006;103:6315-20.

[199] Vivès E, Schmidt J, Pèlegrin A. Cell-penetrating and cell-targeting peptides in drug delivery. Biochimica et Biophysica Acta (BBA) - Reviews on Cancer. 2008;1786:126-38.

[200] Vives E. Cellular utake of the Tat peptide: an endocytosis mechanism following ionic interactions. Journal of Molecular Recognition. 2003;16:265-71.

[201] Delehanty JB, Boeneman K, Bradburne CE, Robertson K, Bongard JE, Medintz IL. Peptides for specific intracellular delivery and targeting of nanoparticles: implications for developing nanoparticle-mediated drug delivery. Therapeutic Delivery. 2010;1:411-33.

[202] de la Fuente JM, Berry CC. Tat Peptide as an Efficient Molecule To Translocate Gold Nanoparticles into the Cell Nucleus. Bioconjugate Chemistry. 2005;16:1176-80.

[203] Zitzmann S, Ehemann V, Schwab M. Arginine-Glycine-Aspartic Acid (RGD)-Peptide Binds to Both Tumor and Tumor-Endothelial Cells in Vivo. Cancer Research. 2002;62:5139-43.

[204] Graf N, Bielenberg DR, Kolishetti N, Muus C, Banyard J, Farokhzad OC, et al. αVβ3 Integrin-Targeted PLGA-PEG Nanoparticles for Enhanced Anti-tumor Efficacy of a Pt(IV) Prodrug. ACS Nano. 2012;6:4530-9.

[205] Scarì G, Porta F, Fascio U, Avvakumova S, Dal Santo V, De Simone M, et al. Gold Nanoparticles Capped by a GC-Containing Peptide Functionalized with an RGD Motif for Integrin Targeting. Bioconjugate Chemistry. 2012;23:340-9.

[206] Lin R-Y, Dayananda K, Chen T-J, Chen C-Y, Liu G-C, Lin K-L, et al. Targeted RGD nanoparticles for highly sensitive in vivo integrin receptor imaging. Contrast Media & Molecular Imaging. 2012;7:7-18.

[207] Veiseh M, Gabikian P, Bahrami S-B, Veiseh O, Zhang M, Hackman RC, et al. Tumor Paint: A Chlorotoxin:Cy5.5 Bioconjugate for Intraoperative Visualization of Cancer Foci. Cancer Research. 2007;67:6882-8.

[208] Kievit FM, Veiseh O, Fang C, Bhattarai N, Lee D, Ellenbogen RG, et al. Chlorotoxin Labeled Magnetic Nanovectors for Targeted Gene Delivery to Glioma. ACS Nano. 2010;4:4587-94.

[209] Garcia-Bennett A, Nees M, Fadeel B. In search of the Holy Grail: Folate-targeted nanoparticles for cancer therapy. Biochemical Pharmacology. 2011;81:976-84.

[210] Sun C, Sze R, Zhang M. Folic acid-PEG conjugated superparamagnetic nanoparticles for targeted cellular uptake and detection by MRI. Journal of Biomedical Materials Research Part A. 2006;78A:550-7.

[211] Mansoori GA, Brandenburg KS, Shakeri-Zadeh A. A Comparative Study of Two Folate-Conjugated Gold Nanoparticles for Cancer Nanotechnology Applications. Cancers. 2010;2:1911-28.

[212] Riehemann K, Schneider SW, Luger TA, Godin B, Ferrari M, Fuchs H. Nanomedicine—Challenge and Perspectives. Angewandte Chemie International Edition. 2009;48:872-97.

[213] Allen TM, Chonn A. Large unilamellar liposomes with low uptake into the reticuloendothelial system. FEBS Letters. 1987;223:42-6.

[214] Lee KS, Chung HCI, A. S, Park YH, Kim SB, S. KC, et al. Multicenter phase II study of a cremophor-free polymeric micelle-formulated paclitaxel in patients (pts) with metastatic breast cancer (MBC). J Clin Oncol. 2006;24:10520.

[215] Wagner V, Dullaart A, Bock A-K, Zweck A. The emerging nanomedicine landscape. Nat Biotech. 2006;24:1211-7.

[216] Park J. Liposome-based drug delivery in breast cancer treatment. Breast Cancer Res. 2002;4:95 - 9.

[217] Jun Y-w, Lee J-H, Cheon J. Chemical Design of Nanoparticle Probes for High-Performance Magnetic Resonance Imaging. Angewandte Chemie International Edition. 2008;47:5122-35.

[218] Liu W, Howarth M, Greytak AB, Zheng Y, Nocera DG, Ting AY, et al. Compact Biocompatible Quantum Dots Functionalized for Cellular Imaging. Journal of the American Chemical Society. 2008;130:1274-84.

[219] Brannon-Peppas L, Blanchette JO. Nanoparticle and targeted systems for cancer therapy. Advanced Drug Delivery Reviews. 2004;56:1649-59.

[220] Allen TM. Ligand-targeted therapeutics in anticancer therapy. Nat Rev Cancer. 2002;2:750-63.

[221] Thornton PD, Mart RJ, Ulijn RV. Enzyme-Responsive Polymer Hydrogel Particles for Controlled Release. Advanced Materials. 2007;19:1252-6.

[222] Huang X, Neretina S, El-Sayed MA. Gold Nanorods: From Synthesis and Properties to Biological and Biomedical Applications. Advanced Materials. 2009;21:4880-910.

[223] Welsher K, Liu Z, Daranciang D, Dai H. Selective Probing and Imaging of Cells with Single Walled Carbon Nanotubes as Near-Infrared Fluorescent Molecules. Nano Letters. 2008;8:586-90.

[224] Fortin J-P, Wilhelm C, Servais J, Ménager C, Bacri J-C, Gazeau F. Size-Sorted Anionic Iron Oxide Nanomagnets as Colloidal Mediators for Magnetic Hyperthermia. Journal of the American Chemical Society. 2007;129:2628-35.

[225] Kopelman R, Lee Koo Y-E, Philbert M, Moffat BA, Ramachandra Reddy G, McConville P, et al. Multifunctional nanoparticle platforms for in vivo MRI enhancement and photodynamic therapy of a rat brain cancer. Journal of Magnetism and Magnetic Materials. 2005;293:404-10.

[226] Veiseh O, Sun C, Gunn J, Kohler N, Gabikian P, Lee D, et al. Optical and MRI Multifunctional Nanoprobe for Targeting Gliomas. Nano Letters. 2005;5:1003-8.

[227] Choi J-s, Park JC, Nah H, Woo S, Oh J, Kim KM, et al. A Hybrid Nanoparticle Probe for Dual-Modality Positron Emission Tomography and Magnetic Resonance Imaging. Angewandte Chemie International Edition. 2008;47:6259-62.

[228] Kim JS, Rieter WJ, Taylor KML, An H, Lin W, Lin W. Self-Assembled Hybrid Nanoparticles for Cancer-Specific Multimodal Imaging. Journal of the American Chemical Society. 2007;129:8962-3.

[229] Kim J, Lee JE, Lee SH, Yu JH, Lee JH, Park TG, et al. Designed Fabrication of a Multifunctional Polymer Nanomedical Platform for Simultaneous Cancer- Targeted Imaging and Magnetically Guided Drug Delivery. Advanced Materials. 2008;20:478-83.

[230] Kim J, Piao Y, Hyeon T. Multifunctional nanostructured materials for multimodal imaging, and simultaneous imaging and therapy. Chemical Society Reviews. 2009;38:372-90.

[231] Salgueiriño-Maceira V, Correa-Duarte MA. Increasing the Complexity of Magnetic Core/Shell Structured Nanocomposites for Biological Applications. Advanced Materials. 2007;19:4131-44.

[232] Xia T, Kovochich M, Liong M, Meng H, Kabehie S, George S, et al. Polyethyleneimine Coating Enhances the Cellular Uptake of Mesoporous Silica Nanoparticles and Allows Safe Delivery of siRNA and DNA Constructs. ACS Nano. 2009;3:3273-86.

[233] Gu F, Zhang L, Teply BA, Mann N, Wang A, Radovic-Moreno AF, et al. Precise engineering of targeted nanoparticles by using self-assembled biointegrated block copolymers. Proceedings of the National Academy of Sciences. 2008;105:2586-91.

CHAPTER II – Materials and Characterization Techniques

2.1 Materials

2.1.1 Doxorubicin

Doxorubicin (DOXO) is a drug used against a great number of cancers. It is a DNA intercalating molecule. The action mechanism of DOXO is complex and it is not completely clarified, although it is believed that acts by intercalation of the plane cromophore group of anthracycline between to base pairs of DNA. It is known that when it intercalates, inhibits biosynthesis of macromolecules as it hinders the progression of the enzyme topoisomerase II, which uncoils DNA during transcription. Topoisomerases I and II are enzymes that modify topological state of DNA. DOXO poisons these enzymes, stabilizing a DNA –topoisomerase II complex, an intermediate called the cleavable complex in a reaction where the topoisomerase remains covalently attached to a single strand (I) or both strands (II) of the double helix, avoiding liberation of the double helix and stopping in this way the replication process. Other suggested mechanisms of DOXO cytotoxicity include free radical formation, lipid peroxidation, and direct membrane effects. DOXO binding to cell membranes ultimately results in production of active oxygen species, especially hydroxyl radicals generated in DOXO enzymatic reduction catalyzed by iron and/or copper ions; this results in a decline of mitochondrial oxidative phosphorylation. The attack of reactive oxygen species on the myocytes has been implicated as the main cause of a severe DOXO cardiotoxicity. DOXO is used against certain leukemias, Hodgkin lymphoma, bladder, breast, stomach, lung, ovarian and thyroids cancer, soft tissue sarcoma, multiple myeloma, amongst others. DOXO is also administered in a liposome encapsulated form called Doxil. Some of the secondary effects are nausea, vomit, arrhythmia, neutropenia, complete alopecia [1].

DOXO is a photoactive molecule with absorption maxima at 484 nm and emission maxima at 594 nm. pKa of the amine in the 3’ position varies from 7,2 to 8,6

depending on the concentration, ionic strength and measurement method. pKa of the phenol group at position 11' is 9,5. At low pH = 4 – 6, amino sugar moiety is protonated and has a positive charge. Over pH = 6 DOXO has a neutral charge. Above pH = 7,5 the neutral DOXO fraction is reduced due to the deprotonation of its phenol group. Commercially available DOXO is in its hydrochloride salt form with water solubility of 30 g/L. The most favorable form of DOXO for encapsulation in polymeric nanoparticles is the neutral form, therefore is necessary to hydrophobize it eliminating the hydrogen chloride by reaction with triethylamine (Figure 2.1) and extracting hydrophobic form with dichloromethane. Despite its hydrophobicity DOXO has certain water solubility due the presence of the glycolic group.

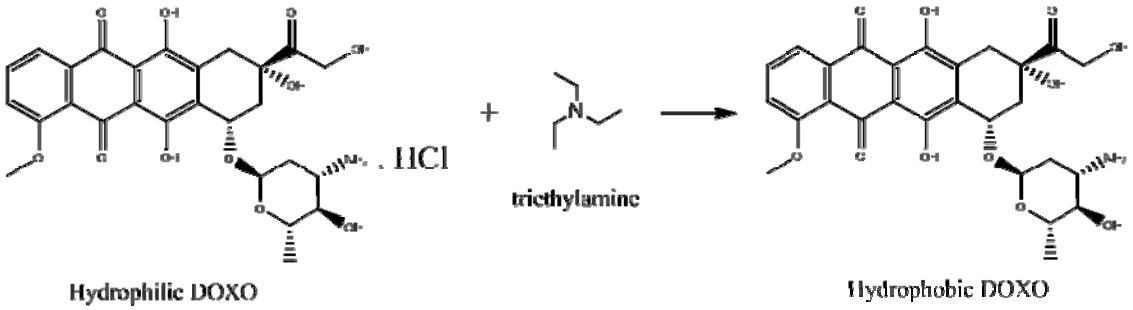

Figure 2.1: Hydrophilic and hydrophobic forms of doxorubicin. Hydrophobization of DOX is done by reacting it with three molar equivalents of triethylamine.

2.1.2 PLGA

PLGA is a polyester composed by poly(lactic acid) and poly(glycolic acid) blocks (Figure 2.2). It is biodegradable and biocompatible with low immunogenicity and toxicity. Synthesis of PLGA is obtained by the rupture of lactic acid ring and glycolic acid ring and linked via ester bonds.

Poly (lactic acid) can present two isomeric forms, L-poly(lactic acid), optically active, and the racemic form D,L-poly(lactic acid). The former is semi-crystalline due the structure regularity while the latter is amorphous. Poly (glycolic acid) is crystalline due to the lack of methyl group. PLGA copolymers with dextro form of PLA are crystalline while those containing the D,L-PLA form are amorphous [2].

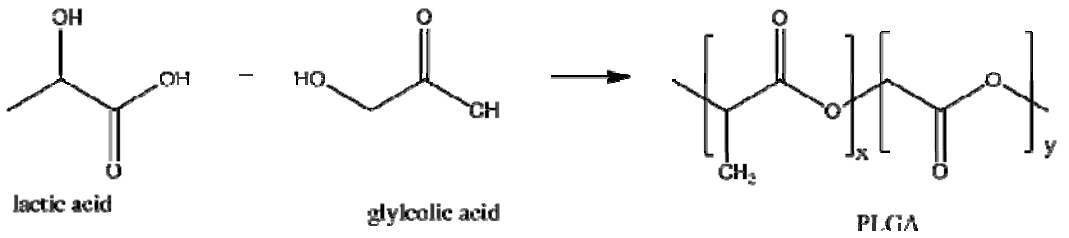

Figure 2.2: Lactic acid and glycolic acid are the monomers of PLGA polymer.

Molar ratio and sequence arrangement of lactic acid al glycolic acid determine the physicochemical properties of PLGA copolymer. Poly(D,L-lactic acid) and PLGA with less than 85 % of glycolic acid are amorphous while poly(glycolic acid) and poly(L-lactic acid) are crystalline. Solvation of PLGA depends on the lactic:glycolic ratio as lactic is more hydrophobic than glycolic. For nanoparticle fabrication the most used ratio is 50:50. In aqueous medium PLGA is degraded by hydrolysis. Both products are eliminated by metabolic route or in combination with kidney excretion [3].

Degradation and release of substances from PLGA nanoparticles can be controlled by modifying the molecular weight and the PLA:PGA ratio of the copolymer. PLGA with more PLA content will be more hydrophobic, therefore absorbs less water and will degrade more slowly. Glass transition temperature (T_g) of PLGA decreases as the proportion of PLA as well as the molecular weight of copolymer decrease. Another way to modify release kinetics is by changing the terminal group of PLGA, either with a CH_3O (metoxi) group or with a COO^- (carboxi) group. Release of cargo is mainly driven by two mechanisms: diffusion of cargo through the polymeric matrix and by surface and volume erosion of polymeric matrix. Generally, release kinetics profiles shoe two steps, a first burst release followed by a slow prolonged release. Surface of PLGA nanoparticles can be tailored with hydrophilic polymers to increase their residence time or with targeting molecules conjugated to carboxyl groups of PLA [3].

About the environment in the nanoparticle matrix during degradation, the entrapped drug experiments a considerable drop in pH. Hydrolisis of PLGA increases as the amorphous content of copolymer increases. If the temperature around the polymer nanoparticle is above Tg of copolymer degradation accelerates. Tg of PLGA ranges from 42 – 60° C depending on the amorphous content. PLGA has been approved by the European Medicines Agency (EMA) and the United States Food and Drug Administration (FDA) for pharmacological formulations porpoises [3].

2.1.3 Indocyanine green (ICG)

ICG is a water soluble fluorescent tricarbocyanine dye approved by US FDA with attractive features of low toxicity a high absorbance in the wavelength range of 600 – 900 nm, which is known as the biological window because of the minimal absorption of tissues and water.

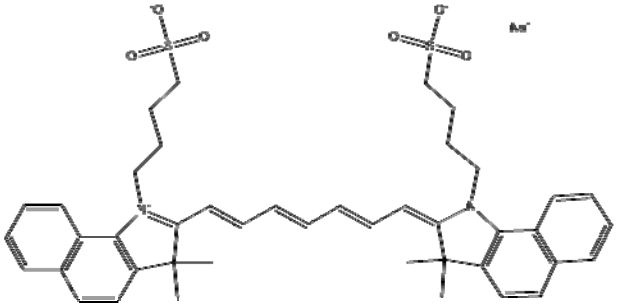

Figure 2.3: ICG molecule.

ICG has been widely applied in medical diagnosis for cardiac output measurements, blood volume determinations, liver function studies, pharmacokinetic analysis, choroidal angiography, object localization in tissue and fluorescence probing enzymes and proteins. It is also applied in tissue welding with near IR light sealing (joining of tissues using albumin as solder [4]), in photosclerosis of venous varicosities and photodynamic therapy studies. Absorption and emission behavior of ICG is concentration dependent due to the formation of dimmers and higher number oligomers and self-quenching, and also changes in its optical properties are observed in different solvents such as water, plasma, serum albumin [5, 6]. A relationship between the emission strength and ICG concentration and observed a maximum value of emission strength in plasma or blood solvent has been reported [7]. The ICG concentration at which the emission strength reaches a maximum is 0,1 mg/ml (~129 μM) in plasma and 0,05 mg/ml (~64,5 μM) in blood . Major pitfalls of ICG are its poor photostability, rapid clearance by the liver, insufficient stability in aqueous solutions and poor fluorescence quantum yields. ICG has been also encapsulated with doxorubicin in PLGA NPs [8] and in lipid-polymeric NPs [9] in order to combine chemo- and photothermal therapies within a single system.

2.1.3.1 Indocyanine green (ICG) as photosensitizer

Photophryn is the prototypical photosensitizer. It is a combination of many different porphyrin molecules derived from blood. Photophryn presents several absorption peaks being the longest at 630 nm, where hemoglobin absorption is still large. A new generation of photosensitizers has emerged with better properties and, amongst them, it is indocyanine green (ICG), a FDA approved fluorescent dye with maximum absorption peak at 783 nm and emission at 820 nm. ICG has been used mainly as a contrast agent and for cardiac output diagnosis. Recently, ICG has been used as photothermal therapeutic agent and PDT photosensitizer due to its very low toxicity, optimal absorption wavelength peak and its photoluminescence which allows monitoring its biodistribution [5-7]. The photothermal effect originates from internal conversion (heat) of absorbed photons instead of being emitted as fluorescence. In order to improve its biodistribution, specific targeting ability and optical properties, ICG has been incorporated to different nanocarriers such as polymeric NPs, liposomes, micelles, Au NPs, etc [8-13]. The organic nanocarriers (polymeric, liposome, micelle) enhance the targeting efficiency of ICG either by passive targeting or active targeting, and protect the molecule from degradation [8, 10]. Au NPs can act as transporters by attaching the ICG molecule to their surface along with a targeting ligand for specific accumulation in tumor [13]. An important fact is that both Au nanoshells and Au NRs can act as fluorescence enhancers [14], making it possible to track the NP-ICG conjugate by fluorescence imaging. A new class of PDT nanoparticle is the use of quantum dots-photosensitizer conjugates, where the QD serves as the primary light absorber and then, through FRET, activates the photosensitizer [15], The potential advantage of this approach is that the NP can be selected to have a very high photon cross-section at an optimal wavelength for the specific application, while the photosensitizer can be selected in the basis of, for example, its highly singlet oxygen yield.

2.2. Characterization techniques

2.2.1 Dynamic light scattering

When light impinges on matter, the electric field of the light induces an oscillating polarization of the electrons in the molecules. The molecules they serve as secondary sources of light and subsequently radiate (scatter) light. The frequency shifts, the angular distribution, the polarization, and the intensity of the scattered light are determined by the size, shape and molecular interactions in the scattering material. Thus form the light-scattering characteristics of a given system it should be possible with the aid of electrodynamics and the theory of time-dependent statistical mechanism, to obtain information about the structure and molecular dynamics of the scattering medium [16].

For molecules or particles equal or larger than $\lambda/20$, being λ the wavelength of the incident radiation, several of these oscillating dipoles are created simultaneously within one given particle. As a consequence, some of the emitted light waves possess a significant phase difference. Accordingly, interference of the scattered light emitted from such individual particles leads to a non-isotropic angular dependence of the scattered light intensity. The interference pattern of intra-particular scattered light, also called the particle form factor, is characteristic of the geometry of the scattering particle. Hence, this provides a quantitative means for the structural characterization of particles in very dilute solutions by light scattering. On the other hand, for particles smaller than $\lambda/20$, regarded as point-dipole oscillators, only a negligible phase difference exists between light emitted from various scattering centres within a given particle; in this case, the detected scattered intensity will be independent of the scattering angle, and it only will depend on the particle mass, which is proportional to the total number of scattering centers one particle contains. [17].

So far, we have considered light scattering as a purely elastic process where the emitted light has exactly the same wavelength as the incident light. Particles in solution, however, usually show a random motion (Brownian motion) caused by thermal density fluctuations of the solvent. This theory known as *fluctuation theory of light scattering* was developed by Smoluchowski [16] in 1908 and Einstein [16] in 1910. As a consequence of temporal changes in inter-particle positions and the corresponding

temporal concentration fluctuations, both the interference pattern and the resulting scattered intensity detected at a given scattering angle also change with time, reflecting the Brownian motion of the scattering particles [17]. This phenomenon provides the basis of dynamic light scattering, an experimental procedure which yields a quantitative measure for the mobility of scattering particles in solution, characterized by their self-diffusion coefficients. Most modern particle size analyzers used to determine the size of particles in solution are based on this principle [16-18]. General standard light scattering setups consist of the following components:

1. The incident light source, typically a laser source. This provides coherent and monochromatic light with intensity between some few miliwatts (mW) and several watts (W). In practice, the light intensity needed for a successful scattering experiment depends on the sensitivity of the optical detector and on the scattering power of the sample itself, as determined by its size, concentration, and refractive index increment. As shown in Figure 23, typically, the primary laser beam is guided and focused onto the sample by optical mirrors and lenses. The laser beam diameter within the sample is well below 1 mm, which defines the scattering volume.

2. The light scattering cell, in most cases a cylindrical quartz glass cuvette of outer diameter between 10 and 30 mm, embedded within an index matching and thermostating bath. Using an index matching bath around the cylindrical light scattering cuvette is important to suppress unwanted diffraction effects of the incident and the scattered light at the sample-air interfaces.

3. The detector, either a photo-multiplier tube or a very sensitive avalanche photo diode (APD) and its associated optics (pinhole or optical fiber) mounted on the arm of a goniometer. The detector optics determines the horizontal and vertical dimensions of the scattering volume, whereas its depth is defined by the incident laser beam width. Band pass filters with high transmission at the incident laser light wavelength are often used in front of the detector to suppress undesired contributions of stray light or fluorescence from the sample.

4. The electronic hardware components associated with the detector used for signal processing. The scattered intensity I (q,t), which is monitored by the optical detector, is typically digitalized and stored in a computer. These raw data have to be further processed: In the case of static light scattering, particle form

factor models can be used to fit the experimental data; in a dynamic light scattering experiment, the raw data have to be converted into the time intensity correlation function g_2 (q, τ). This is done during the measurement using a very fast hardware correlator as, for example, the ALV 5000 from ALV, Langen, Germany.

Light scattered by a set of mesoscopic particles produces a random interference pattern on a screen. This pattern, generally possess the form of irregularly spaced and sized bright spots called speckles. The scattered light intensity pattern remains unchanged as long as the particles do not change their position. Particle motion naturally leads to a temporal evolution of the scattered speckle field since one interference pattern is continuously replaced by another. In a single speckle spot, this evolution is observed as strong temporal intensity fluctuations, with a certain well-defined temporal correlation. The intensity fluctuations are inherently related to the scatter dynamic and, therefore, the temporal correlation function depends on the particles shift. Thus, the measurable correlation properties of light can be linked to the dynamical properties of particles which, in turn, can provide information about their flow velocity and direction, particle size, density of moving scatters, etc.

In dynamic light scattering, also known as photon correlation spectroscopy (PCS) or quasi-elastic light scattering (QELS), the diffusive motions of particles in solution gives rise to fluctuations in the scattered light intensity on the microsecond timescale. This technique is one of the most popular methods used to determine the particles size by measuring the temporal fluctuations of the scattered light intensity. Roughly, this is made by focusing a monochromatic light beam, such a laser, on a solution with particles in Brownian motion; this causes a Doppler shift when the light "hits" the moving particle, changing the light wavelength. This change is related to the size particle [19, 20].

In the scope of DLS, temporal fluctuations are usually analyzed by means of the intensity autocorrelation function (ACF). In the time domain, the correlation function usually decays with time (Figure 2.4), and faster dynamics leads to faster decorrelation of the scattered intensity trace. It can be shown that for a random process the intensity ACF is the Fourier transform of the power spectrum and, therefore, DLS measurements can be equally well-performed in the spectral domain. In fact, DLS experiments were initially discussed in terms of the broadening of the spectrum peak of monochromatic

light due to Doppler shifts experienced by propagating light waves scattered by moving particles [21].

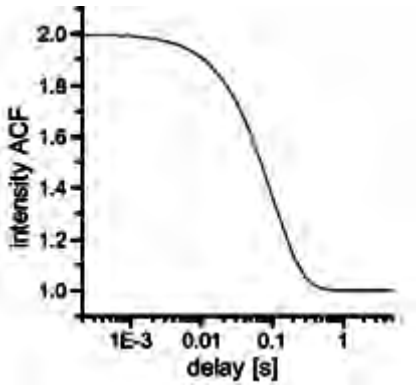

Figure 2.4: Illustration of autocorrelation function (Image taken from [21]).

To detect the intensity fluctuation with time, a DLS system requires an autocorrelator on top of a regular SLS system, as shown in Figure 2.5.

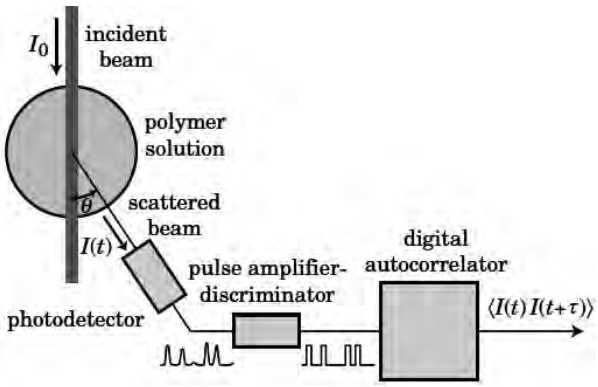

Figure 2.5: Sketch of a dynamic light scattering system. The pulse amplifier discriminator converts the analogic signal of the photodetector, $I(t)$, in a digitalized signal, which is further processed by the autocorrelator into the autocorrelation function.

As commented above, Figure 2.6a illustrates how the intensity (I) varies with time (t). $I(t)$ fluctuates around its mean value, $<I>$. It may appear completely random and, therefore, meaningless, but it is not. Motions of particles (i.e. polymer molecules) and solvent molecules contribute to the change of $I(t)$ with time. This apparently noisy signal carries the information about particles motions.

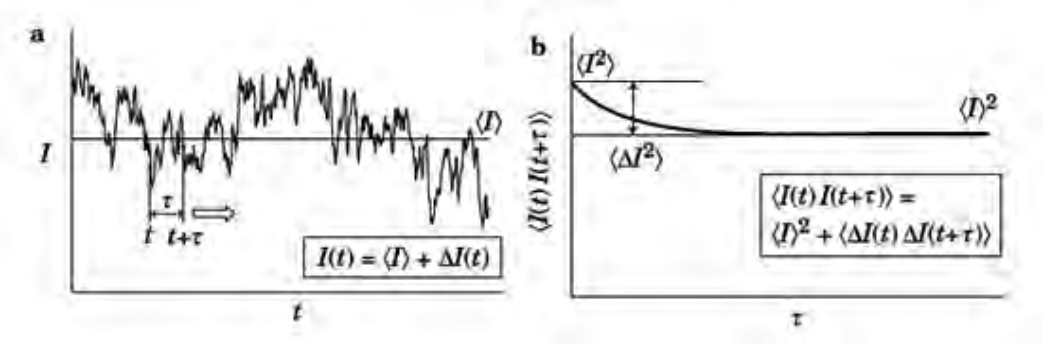

Figure 2.6: (a) Light scattering intensity $I(t)$ fluctuates around its mean value $\langle I\rangle$. (b) Autocorrelation function $\langle I(t)I(t+\tau)\rangle$ is obtained as the long-time average of $I(t)I(t+\tau)$ for various delay times τ. The aurocorrelation function decays from $\langle I^2\rangle$ to $\langle I\rangle^2$ over time. The amplitude of the decaying component is $\langle \Delta I^2\rangle$.

The autocorrelator calculates the product average of two scattering intensities $I(t)$ and $I(t+\tau)$ measured at two different times separated by τ, the delay time. The average product $\langle I(t)I(t+\tau)\rangle$ is a function of τ and is called the correlation function of $I(t)$, or the intensity-intensity correlation function. The correlator converts $I(t)$ into $\langle I(t)I(t+\tau)\rangle$. Hence, the intensity-intensity correlation function is the average of $I(t)I(t+\tau)$ over a long period T. Hence, assuming that the long time average is equal to the ensemble average, we can write [16]:

$$\langle I(t)I(t+\tau)\rangle = \lim_{T\to\infty} \frac{1}{T}\int_0^T I(t)I(t+\tau)dt \qquad \text{(Eq 2.1)}$$

Note that, if the system is at equilibrium, the ensemble average does not change with time and, therefore, $\langle I(t)I(t+\tau)\rangle = \langle I(t0)I(\tau)\rangle$. The autocorrelation function of $I(t)$ (Figure 2.6a) is shown in Figure 2.6b. When $\tau = 0$, $\langle I(t)I(t+\tau)\rangle = \langle I^2\rangle$. With increasing τ, $\langle I(t)I(t+\tau)\rangle$ decays to an asymptotic level (baseline), $\langle I\rangle^2$.

Because the scattering intensity $I(t)$ fluctuates around a mean value $\langle I\rangle$, it is convenient to separate its fluctuating component, $\Delta I(t)$, as $I(t) = \langle I\rangle + \Delta I(t)$. By definition, $\langle \Delta I(t)\rangle = 0$. Then, the correlation function can be rewritten as:

$$\langle I(t)I(t+\tau)\rangle = \langle I\rangle^2 + \langle \Delta I(t)\Delta I(t+\tau)\rangle \qquad \text{(Eq 2.2)}$$

The autocorrelation of $\Delta I(t)$is zero upon increases of τ. When $\tau \to \infty$, $\langle \Delta I(t)\Delta I(t+\tau)\rangle = \langle \Delta I(t)\rangle\langle \Delta I(t+\tau)\rangle = 0$. The decaying componet in $\langle I(t)I(t+\tau)\rangle$ is $\langle \Delta I(t)\Delta I(t+\tau)\rangle$. The initial height of the decaying component is $\Delta I^2 = \langle I^2\rangle - \langle I\rangle^2$. Division of $\langle I(t)I(t+\tau)\rangle$ by $\langle I\rangle^2$ leads to the intensity autocorrelation function as:

$$\langle I(t)I(t+\tau)\rangle/\langle I\rangle^2 = 1 + \langle \Delta I(t)\Delta I(t+\tau)\rangle/\langle I\rangle^2 = 1 + f_c g_2(\tau) \quad \text{(Eq 2.3)}$$

where $f_c \equiv \langle \Delta I^2\rangle/\langle I\rangle^2$ (the coherent factor), and the second factor is the baseline-subtracted, normalized intensity autocorrelation function:

$$g_2(\tau) \equiv \langle \Delta I(t)\Delta I(t+\tau)\rangle/\langle \Delta I\rangle^2 \quad \text{(Eq 2.4)}$$

The coherent factor depends on the coherence of the light reaching the photodetector. The measured intensity correlation function is related to the field correlation function by the Siegert relation:

$$g_1(\tau) = 1 + b|g_2(\tau)|^2 \quad \text{(Eq 2.5)}$$

where $g_1(\tau)$ is:

$$g_1(\tau) = |E^*(t)E(t+\tau)|/\langle |E(t)|^2\rangle \quad \text{(Eq 2.6)}$$

where $E^*(t)$ is the electric field conjugate function. For monodisperse spherical particles:

$$g_1(t) = exp(-\Gamma\tau) \quad \text{(Eq 2.7)}$$

where Γ is the characteristic delay rate, which is related to the translational diffusion coefficient, *D*, of a solute by means of the expression:

$$\Gamma = q^2 D \quad \text{(Eq 2.8)}$$

The diffusion coefficient is frequently used to determine the hydrodynamic radius, R_H, of the constituent particles by using the Stokes-Einstein equation [22]:

$$D = \frac{K_B T}{6\pi\eta R_H} \quad \text{(Eq 2.9)}$$

where K_B is the Boltzmann constant, T the absolute temperature and η the liquid viscosity. The hydrodynamic radius obtained by DLS represents an ideal hard sphere that diffuses with the same speed as the particle under examination. Actually, particles are solvated and the radius calculated from the particle diffusion corresponds to the size of the dynamic solvated particle.

2.2.2 Zeta potential

When a charge is present on the surface of a particle, the distribution of ions in the surrounding interfacial region is affected, resulting in an increased concentration of counter ions (ions with opposite charge) in the proximity of the particle's surface. In this way an electrical double layer exists around each particle.

The liquid layer surrounding the particle is divided in two regions: one inner region known as Stern layer where the ions are strongly attached to the surface; and a second external diffuse region where the ions are less firmly attached. Within the diffuse layer there is a certain type of boundary where the particle and the ions form a stable entity. When the particle moves, for example by gravity, the ions inside this boundary travel together with the particle, buy any other ion beyond this boundary does not move with the particle. This boundary is called the surface of hydrodynamic shear or slipping plane (Figure2.7). The potential existing in this boundary is known as the *zeta potential* [23]. The magnitude of the zeta potential gives an indication of the colloidal system potential stability. A colloidal system is when one of the three states of matter: gas, liquid and solid, are finely dispersed in one of the others. For this technique we are interested in the two states of: a solid dispersed in a liquid, and a liquid dispersed in a liquid, i.e. an emulsion [23].

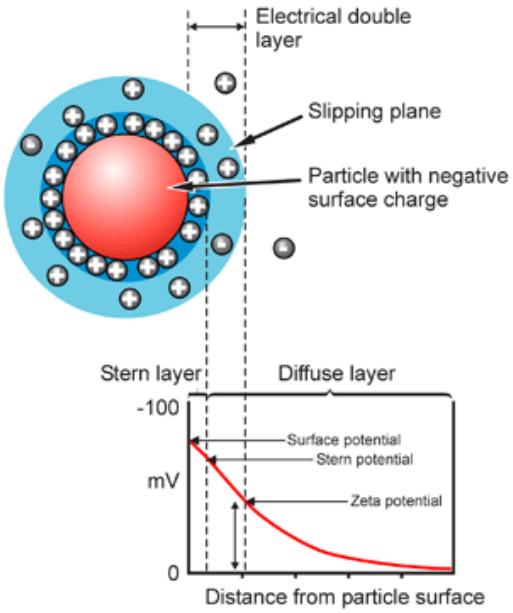

Figure 2.7: The surface of hydrodynamic shear or slipping plane is the distance from the surface at which ions become bound (essentially immobile), beyond this boundary ions do not travel with the particle when the particle moves (image taken from [23]).

If all the particles in suspension have a large negative or positive zeta potential then they will tend to repel each other and there is no tendency to flocculate. However, if the particles have low zeta potential values then there is no force to prevent the particles coming together and flocculating. The general dividing line between stable and unstable suspensions is generally taken at either +30 mV or -30 mV. Particles with zeta potentials more positive than +30 mV or more negative than -30 mV are normally considered stable [23].

The most important factor affecting the zeta potential is pH (Figure2.8). A zeta potential value on its own without a quoted pH is virtually meaningless. At acid pH zeta potential will be positive and at alkaline pH it will be negative. The point at which the sign of zeta potential switches is known as the isoelectric point, at this point the colloidal system is less stable [23].

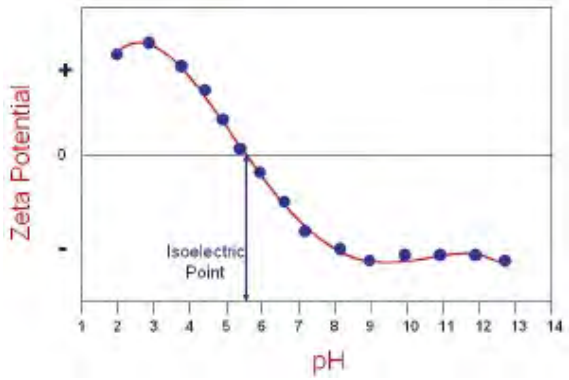

Figure 2.8: Zeta potential as a function of pH. The point of zero zeta potential is known as the isoelectric point (image taken from [23]).

When an electric filed is applied trough an electrolyte, the charged particles suspended on it are attracted to oppositely charged electrode. The viscous forces will oppose to this movement and when the equilibrium between both forces is reached the particles move with a constant velocity, known as electrophoretic mobility [23].

The velocity of particles depends of the following parameters:

- Force of the electric field
- Dielectric constant.
- Viscosity of the medium.
- Zeta potential of particles.

The zeta potential of the particle can be calculated if the electrophoretic mobility is known by means of the Henry's equation [24]:

$$U_E = \frac{2\varepsilon z f(Ka)}{3\eta} \qquad \text{(Eq 2.10)}$$

where z is the zeta potential, U_E is the electrophoretic mobility, ε is the dielectric constant, η is the viscosity, $f(ka)$ is the Henry´s function, whose extended form is [24]:

$$f(ka) = 1 + \frac{1}{16}(ka)^2 - \frac{5}{48}(ka)^3 - \frac{1}{8}(ka)^4 \times \left[\frac{1}{12}(1-ka) - \left(1 - \frac{1}{12}(ka)^2\right) e^{ka} E_1(ka)\right] \qquad \text{(Eq 2.11)}$$

where $E_1(ka)$ is the exponential integral of order one, k is the reciprocal of the thickness of the electrical double layer also commonly referred to as the "Debye length", and a is the particle radius.

Zeta potential determinations based on electrophoretic measurements are performed usually in aqueous medium with a moderate electrolyte concentration. For these conditions, a Henry's function value of 1.5 is used, known as the Smoluchowski approximation [24]. Therefore, the determination of zeta potential from U_E is straightforward for systems that fit the Smoluchowski model: particles larger than 200 nm dispersed in electrolyte with a concentration of ca. 10^{-3} M [23]. For small particles in a medium with a low dielectric constant, *f(ka)* assumes the value of 1.0, which also enables an easy calculation of the potential [24]. This is known as the Hückel approximation. Measurements in non-aqueous medium commonly use the Hückel approximation [23].

Zeta potential is measured using a combination of two measurement techniques: *Electrophoresis* and *Laser Doppler Velocimetry*, sometimes called *Laser Doppler Electrophoresis*. Velocity of particles is measured in a classical microelectrophoresis system consisting of a cell with electrodes at either end to which a potential is applied (Figure 2.9). Particle moves towards the electrode of opposite charge, their velocity is measured and expressed in unit field strength as their mobility.

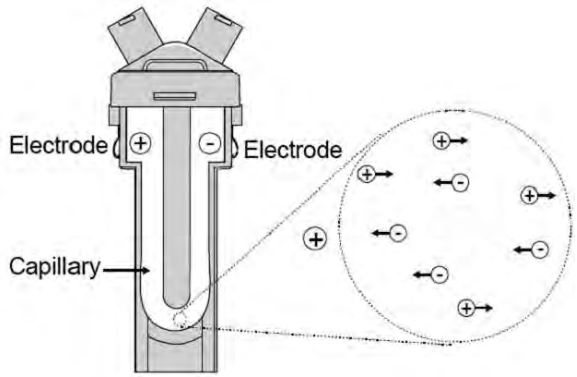

Figure 2.9: Capillary folded cell used for zeta potential measurements.

In laser Doppler velocimetry a laser (Figure 2.10-1) is used to illuminate the particles within the sample. The light source is split to provide an incident and reference beam. The reference beam is "modulated" to provide the Doppler effect necessary. The laser beam passes through the centre of the sample cell (Figure 2.10-2), and the scattering at an angle of 17° is detected. When an electric field is applied to the cell, any particle moving through the measurement volume will cause the intensity of light detected to fluctuate with a frequency proportional to the particle speed. A (Figure 2.10-

3) detector sends this information to a digital signal processor (Figure 2.10-4). This information is then passed to a computer (Figure 2.10-5) where the equipment software produces a frequency spectrum form which the electrophoretic mobility and hence the zeta potential is calculated. The intensity of the scattered light within the cell must be within a specific range to be successfully measured by the detector. If too much light is detected then the detector will become overloaded. To overcome this, an "attenuator" (Figure 2.10-6) is used to reduce the intensity of the laser and hence the intensity of the scattering. To correct for any differences in the cell wall thickness and dispersant refraction, compensation optics (Figure 2.10-7) are installed within the scattering beam path to maintain alignment of the scattering beams.

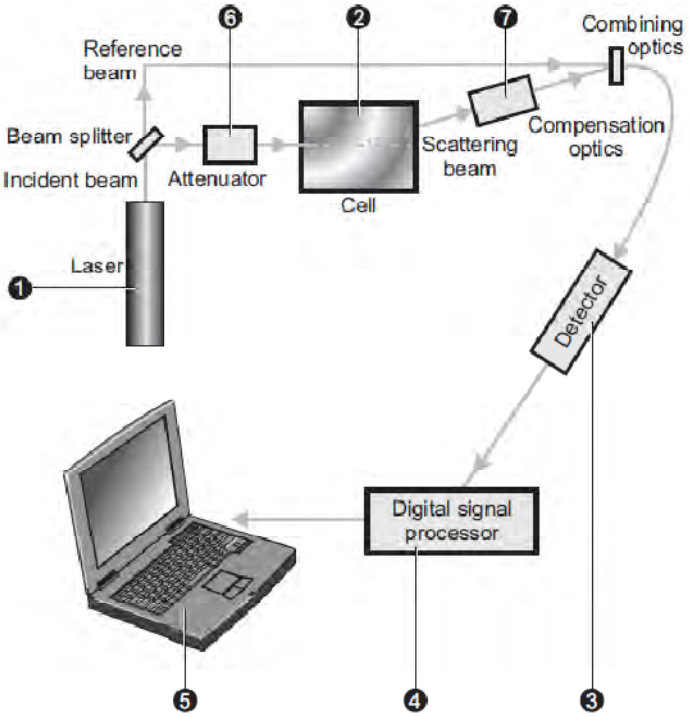

Figure 2.10: Setup of a zeta potential measurement system.

2.2.3 Electron microscopy

Microscopy is an important tool for the characterization of nanomaterials structure. For example, this set of imaging techniques may be used to examine the detailed shape, size and distribution of a wide range of nanoscopic objects. There are different available classes of microscopic techniques, such as the traditional optical microscopy, or more powerful ones such as scanning electron microscopy (SEM),

transmission electron microscopy (TEM), and scanning probe microscopy (SPM), amongst others.

2.2.3.1 Transmission electron microscopy (TEM)

Transmission electron microscopy (TEM) involves the transmission of an electron beam through a sample in a high-vacuum environment. The images and their associated contrasts arise from regional differences in electron densities in such sample. TEM has a resolution of ca. 1 to 100 nm and can provide very detailed structural information of polymeric materials. The TEM specimens need to be very thin in order to enable the transmission of electron beams through the sample.

A transmission electron microscope (Figure 2.11a) is constituted by an electron source (electron gun) which emits electrons travelling through the vacuum created into the microscope column. A condenser lens focus the electron beam on the sample, and several objective lenses are used to form the diffraction pattern at the back focal plane and the sample image at the image plane; there are also some intermediate lenses to magnify the image or the diffraction screen. To obtain an improved contrasted image, an objective diaphragm is inserted in the back focal plane to select the transmitted beam. At the bottom of the microscope, the non-scattered electrons reach a fluorescent screen, which provides a contrasted image of the specimen, with a darkness distribution corresponding to its different electron densities.

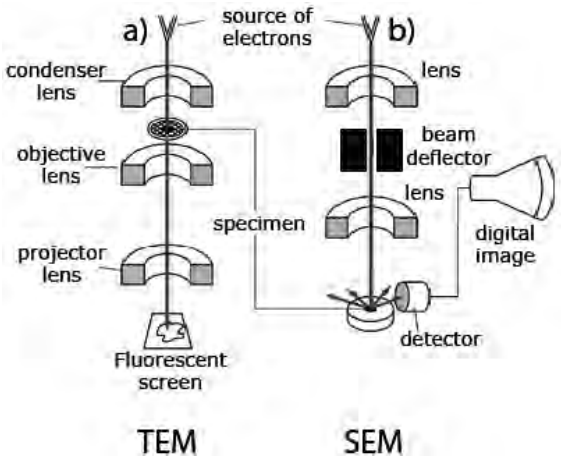

Figure 2.11: Schematic diagram of electron microscopes: a) TEM; b) SEM.

In order to solve the material´s structure on the mesoscopic scale at even high resolutions comparable to interatomic distances, high-resolution transmission electron

microscopes (HRTEM) emerge as a powerful tool. HRTEM uses the transmitted and scattered electron beams directed to a sample to create a diffraction image, in contrast to conventional TEM that only uses the transmitted beams. The high resolution image recorded can be interpretable directly in terms of projections of individual atomic positions. In this way, defects and other inhomogeneities present in a material specimen can be accurately determined. A great advantage of the HRTEM microscope is the capability to observe both electron microscope images and diffraction patterns for determined selected area electron diffractions from a sample [25-27]. The selected area electron diffraction in an electron microscope is formed by setting an aperture in the imaging plane of the objective lens. Only rays passing through this aperture contribute to the diffraction pattern at the far field. For a perfect lens without aberrations, the diffracted rays come from an area that is defined by the back-projected image of the selected aperture. The aperture image is typically a factor of 20 times smaller because of the objective lens magnification. The smallest area that can be selected in SAED is limited by the objective aberration. [28].

2.2.3.2 Scanning electron microscopy (SEM)

Scanning electron microscopy (SEM) is another valuable electron microscopy technique for the examination and analysis of the microstructural characteristics of solid objects, with a resolution of ca. 5 nm. SEM can also be used to obtain compositional information of nanomaterials by coupling an electron diffraction X-ray scattering detector. SEM enables the observation of heterogeneous organic and inorganic materials on the mesoscopic scale [29]. In a typical SEM experiment, an electron beam is focused to obtain a very fine spot size that is rastered over the surface, and an appropriate detector collects the electrons emitted from each point. In this way, an image having a great field depth and a remarkable three-dimensional appearance is built up line by line. The specimen is usually coated with a conducting film prior to examination to enhance electron conductivity and, thus, improving image contrast.

A scanning electron microscope (Figure 2.11b) consists of an electron gun at the top of the column, which creates a divergent electron beam. In the column, which is under vacuum, a series of magnetic apertures focuses the electron beam, and an electrostatic field drives the electrons through a small spot called crossover and

accelerates them through the column until the sample chamber, where the electron beam interacts with the sample. The signals resulting from the beam-sample interaction are monitored. Finally, SEM constructs a virtual image from the signal emitted from the sample by scanning the electron beam line by line through a rectangular (raster) pattern on the sample surface. The scan pattern defines the area represented in the image. At any time, the beam illuminates only a single point in the pattern. As the beam moves, the signals it generates vary in strength, reflecting structural/morphological differences in the sample.

2.2.4 Optical spectroscopy

The three most important types of optical spectroscopies are ultraviolet and visible (UV-Vis), fluorescence and infrared (IR) spectroscopy. They differ only in the selection of the incident light wavelength. Both UV-Vis and fluorescence describe the phenomenon of electron excitation; namely, a valance electron of a molecule is excited upon absorbing energy from the electromagnetic radiation and is, thereby, transferred from one energy level to other more energetic level. The spectra are electronic. In contrast, IR spectra describe the vibration of atoms (not electrons) around a chemical bond.

2.2.4.1 UV-vis absorption spectroscopy

An electron transition consists of the promotion of an electron from a molecular orbital in the ground state to an unoccupied orbital by absorption of a photon. The molecule is, then, said to be in an excited state. Let us recall first the various types of molecular orbitals. A σ orbital can be formed either from two *s* atomic orbitals, from one *s* and one *p*, or from two *p* atomic orbitals having a collinear symmetry axis. The bond formed in this way is called a σ bond. A π orbital is formed from two *p* atomic orbitals overlapping laterally. The resulting bond is called a π bond. For example, in ethylene (CH_2=CH_2) the two carbon atoms are linked by one σ and one π bond. Absorption of appropriate energy can promote, for example, one of the π electrons to an anti-bonding orbital denoted by π^*. The transition is, then, called $\pi \rightarrow \pi^*$.

A molecule may also possess non-bonding electrons located on heteroatoms such oxygen or nitrogen. The corresponding molecular orbitals are called n orbitals. Promotion of a non-bonding electron to an anti-bonding orbital is possible, and the associated transition is denoted by $n \rightarrow \pi^*$. Hence, molecules containing a non-bonding electron, such as oxygen, nitrogen, sulphur, or halogens, often exhibit absorption in the UV region. To illustrate these energy levels, Figure 2.12 shows the molecule formaldehyde as an example with all their possible transitions. In particular, the $n \rightarrow \pi^*$ transition deserves further attention: Upon excitation, an electron is removed from the oxygen atom and goes into the π^* orbital localized half-partially on both the carbon atom and the oxygen atom. The $n \rightarrow \pi^*$ excited state, thus, has a charge transfer character, as shown by the increase observed in the dipole moment regarding the ground state dipole moment of C=O [30, 31].

In summary, the electronic transitions observed in UV-Vis spectroscopy are $n \rightarrow \pi^*$, $\pi \rightarrow \pi^*$, $n \rightarrow \sigma^*$, $\pi \rightarrow \sigma^*$, $\sigma \rightarrow \pi^*$, and $\sigma \rightarrow \sigma^*$. The energy of these electronic transitions is, generally, in the following order: $n \rightarrow \pi^* < \pi \rightarrow \pi^* < n \rightarrow \sigma^* < \pi \rightarrow \sigma^* < \sigma \rightarrow \pi^* < \sigma \rightarrow \sigma^*$. Of the six transitions outlined, only the two lowest energetic ones ($n \rightarrow \pi^*$ and $\pi \rightarrow \pi^*$) are achieved by energies available in the 200 to 800 nm. The last four types of electronic transitions required higher energy inputs, below 200 nm, corresponding to the far ultraviolet region of the electromagnetic spectrum. For instance, most $\sigma \rightarrow \sigma^*$ transitions for individual bonds take place below 200 nm and a compound containing only σ bonds is transparent (near zero absorption) in the near-UV-Vis region. For example, methane (which has only C-H bonds) the transition $\sigma \rightarrow \sigma^*$ takes place at 125 nm.

In absorption and fluorescence spectroscopy, two important types of orbitals are considered: the Highest Occupied Molecular Orbitals (HOMO) and the Lowest Unoccupied Molecular Orbitals (LUMO). Both of these refer to the ground state of the molecule. For instance, in formaldehyde, the HOMO is the n orbital and the LUMO is the π^* orbital.

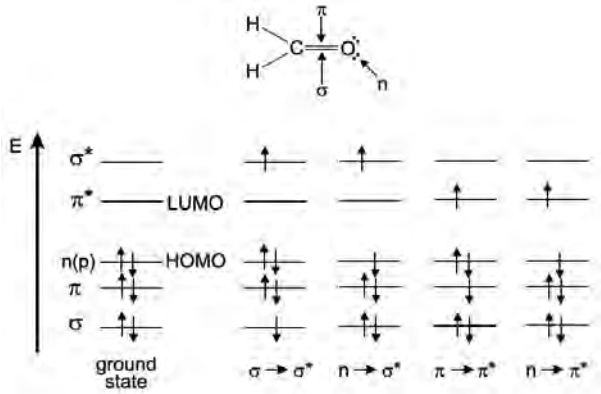

Figure 2.12: Energy levels of molecular orbitals in formaldehyde and possible electronic transitions.

When one of the two electrons of opposite spins (belonging to a molecular orbital of a molecule in the ground state) is promoted to a molecular orbital of higher energy, its spin is, in principle, unchanged so the total spin quantum number ($S = \sum s_i$ with $s_i = +\frac{1}{2}$ or $s_i = -\frac{1}{2}$) is zero. Because of the multiplicities of both the ground and excited states ($M = 2S + 1$) are equal to 1, both are called singlet states (usually denoted S_0 for the ground state, and S_1, S_2,... for the excited states (Figure 2.13). The corresponding transition is called a singlet-singlet transition. A molecule in a singlet excited state may undergo conversion into a state where the promoted electron has changed its spin; therefore, there are two electrons with parallel spins, and the total spin quantum number is 1 and the multiplicity is 3. Such state is called a triplet state because it corresponds to three states of equal energy. According to Hund's rule, the triplet state has lower energy than the singlet state of the same configuration [32].

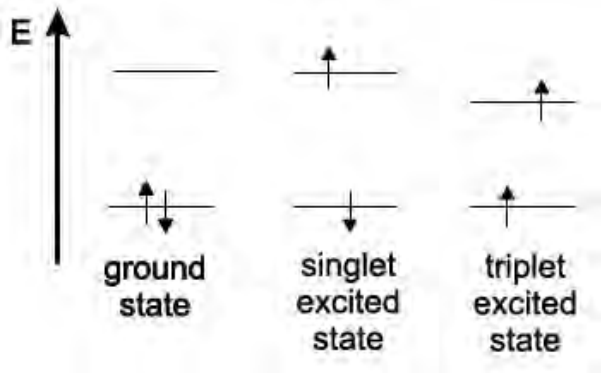

Figure 2.13: Distinction between singlet and triplet states.

An instrument for measuring the absorption of UV and visible radiation is built of one or more light sources, a wavelength selector, a sample container, radiation transducers, a signal processors and readout devices. Figure 2.14 shows a scheme of a single-beam instrument for absorption measurements. Single beam instruments vary widely in their complexity and performance characteristics. The simplest ones consist of a tungsten bulb as the source, a set glass filter for wavelength selection, a test tube for sample holders, a photovoltaic cell as the transducer, and an analogmeter as the readout device. Other sophisticated instruments have interchangeable tungsten and deuterium lamp sources, use a rectangular silica cell, and are equipped with a high-resolution grating monochromator with variable slit. Photomultiplier tubes are used as transducers, and the output is often digitalized, processed and stored in a computer so that it can be printer or plotted in several forms [33].

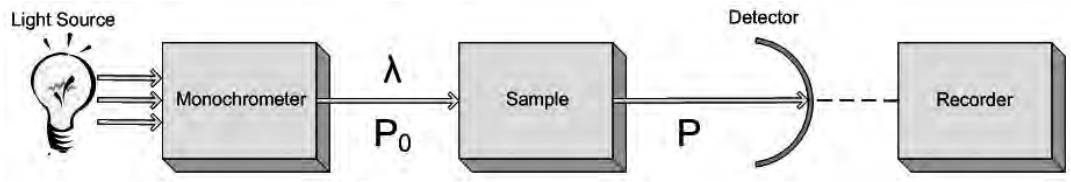

Figure 2.14: General scheme of a single-beam instrument for UV-Vis absorption measurements.

2.2.4.2 Fluorescence spectroscopy

Once a molecule is excited by the absorption of a photon, this can return its ground state through either fluorescence emission, internal energy conversion (i.e. direct return to the ground state without fluorescence emission for example, by heat radiation), intersystem crossing (possibly followed by phosphorescence emission), intramolecular charge transfer and/or conformational change. All these processes can be visualized in the Perrin-Jablonski diagram (Figure 2.15). The singlet electronic states are denoted as S_0 (fundamental electronic state), S_1, S_2, ... and the triplet states as, T_1, T_2, ..., with different vibrational levels associated with each electronic state. It is important to note that energy absorption is very fast ($\approx 10^{15}$ s) with respect to all other processes (so that there is no concomitant displacement of the nuclei according to the Franck-Codon principle) [30, 32]. The vertical arrows corresponding to the energy absorption process start from the 0 vibrational energy level, S_0, since most of molecules are in this state at

room temperature. Absorption of a photon, hence, can bring a molecule to one of the vibrational levels of S_1, S_2.

Emission of photons accompanying the $S_1 \rightarrow S_0$ relaxation is called fluorescence. It should be emphasized that, apart from a few exception, fluorescence emission occurs from S_1 and, therefore, its characteristics (except polarization) do not depend on the excitation wavelength (of course only one species exists in the ground state). The transition between the ground state and the excited stated (0-transition) is usually the same for absorption and fluorescence. However, the fluorescence spectrum is located at higher wavelengths than the absorption one because of the energy loss in the excited state due to vibrational relaxation (Figure 2.16). According to the Stokes rule the fluorescence emission wavelength should be always higher than that of absorption. However, in most cases the absorption spectrum partly overlaps the fluorescence spectrum, i.e. a fraction of light is emitted at shorter wavelengths than the absorbed light. Such an observation seems to be, at first, in contradiction with the energy conservation principle. However, such energy defect is compensated by the fact that a small fraction of molecules is in a higher vibrational level in the ground state as well as in the excited state at room temperature [32].

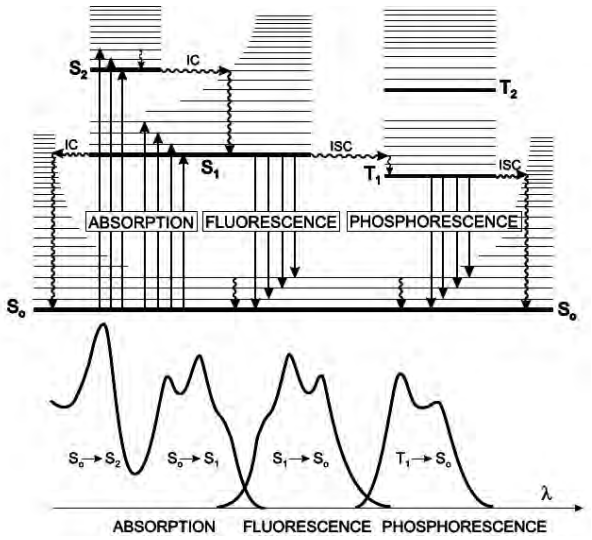

Figure 2.15: Perrin-Jablonski diagram and illustration of the relative positions of absorption, fluorescence and phosphorescence processes.

In general, differences between the vibrational levels are similar in the ground

and excited states, so that the fluorescence spectrum often resembles the first absorption band. The gap, expressed in wavenumber, between the maximum of the first absorption band and the maximum of fluorescence is called the Stokes shift. It should be noted that photon emission is as fast as photon absorption. However, excited molecules remain in the S_1 state for a certain time (a few tens of picoseconds to a few hundreds of nanoseconds, depending on the type of molecule and its surrounding medium) before emitting a photon or undergoing other relaxation processes. Thus, after excitation of a population of molecules by a very short light pulse, the fluorescence intensity decreases exponentially with a characteristic time, reflecting the average lifetime of the molecules in the S_1 excited state.

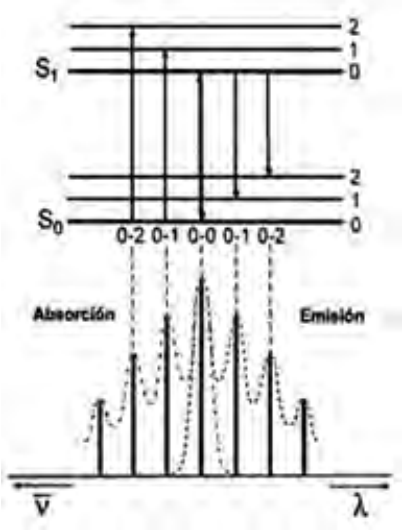

Figure 2.16: Illustration of the vibrational bands in the absorption and fluorescence spectra.

As a consequence of the strong influence of the local environment or surrounding medium on fluorescence emission, fluorescent molecules are currently used for physicochemical, biochemical and biological investigation. For example, fluorescence spectroscopy can be employed as a highly sensitive method for protein analysis. Intrinsic protein fluorescence deriving from the naturally fluorescent amino acid tryptophan (and to a lesser extent from tyrosine and phenylalanine) can provide information on the protein conformational structure and it changes.

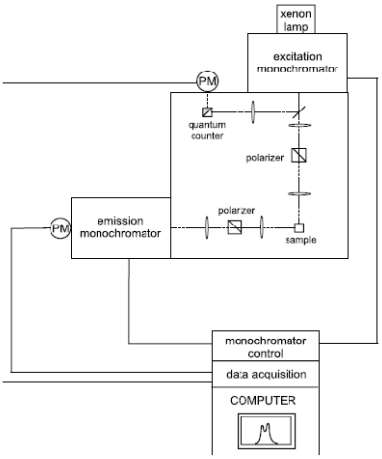

Figure 2.17: Schematic representation of a spectrofluorometer.

Fluorescence Resonance Energy Transfer (FRET) is a process that occurs whenever the emission spectrum of a fluorophore, called the donor, overlaps with the absorption spectrum of another molecule, called the acceptor. In this process, an energy transfer from the donor to the acceptor occurs. The extent of energy transfer is determined by the distance between the donor and the acceptor, and the extent of spectral overlap. The spectral overlap is described in terms of the Förster distance (the distance at which FRET is 50% efficient) which is comparable in size to biological macromolecules (3-6 nm) [34]. Some examples of the vast number of applications of FRET include the development of biosensors [35], the monitoring of the release of molecules from drug delivery nanosystem [36], and real time monitoring of DNA [37] and RNA [38] intracellular processes.

Figure 2.17 shows the components of a conventional spectrofluorometer. The light source is commonly a high-pressure xenon arc lamp, which offers the advantage of a continuous emission from 250 nm to the infrared. A monochromator is used to select the excitation wavelength. Fluorescence is collected at right angles with respect to the incident beam and detected through a monochromator by a photomultiplier. Automatic scanning of wavelengths is achieved by motorized monochromators, which are controlled by the electronic devices and the computer, in which the data are stored [30, 32]. The optical module contains various parts: a sample holder, shutters, polarizers if necessary, and a beam splitter consisting of a quartz plate reflecting a few per cent of

the exciting light towards a quantum counter or a photodiode. A quantum counter usually consists of a triangular cuvette, containing a concentrated solution of a dye whose fluorescence quantum yield is independent of the excitation wavelength.

2.2.4.3 Infrared spectroscopy

Molecules consist of atoms which have a certain mass and are connected by elastic bonds. As a result, they can perform periodic motions, i.e. they have vibrational degrees of freedom. All motions of the atoms in a molecule relative one each other are a superposition of the so-called normal frequencies. These are described by a normal coordinate. For polyatomic molecules, the number of characteristic frequencies is $3N-6$ for non-linear molecules and $3N-5$ for linear molecules, where N is the number of atoms in the molecule, which define their vibrational spectra. These spectra depend on atoms mass, their geometrical arrangement, and the strength of their chemical bonds. Molecular aggregates such as crystals or complexes behave like "super-molecules" in which the vibrations of the individual components are coupled. As a first approximation the normal vibrations are considered not coupled, i.e. they do not interact. However, the bonds elasticity does not strictly follow Hooke's law. Therefore, overtone and combinations of normal vibrations may appear [30, 39].

Infrared (and RAMAN) spectrometers are the most important tools for observing vibrational spectra. Depending on the nature of the vibration, which is determined by the symmetry of the molecule, vibration may be active or forbidden in the infrared (or RAMAN) spectrum.

From basic theory, it is easy to understand that a molecule can take up an amount of energy, $h\nu$, to reach a vibrationally excited state only when the frequency of the incident radiation on a molecule is the same as the vibrational frequency of the latter. This phenomenon involves either a change of the molecule's dipole moment or a change in its polarizability. If the former phenomenon takes place, we will observe an IR band; if the second one occurs, we will observe a RAMAN band. The absorption wavelength range of IR spectroscopy is from 2.5 to 1000 μm, which corresponds to the energy $h\nu = hc\tilde{\upsilon}$ with $\tilde{\upsilon}$ = 4000-10 cm^{-1}, with c the light velocity.

According to classical mechanics, the vibrating atoms groups in a molecule can be modelled as balls joined by springs (the molecular bonds). To take the simplest

example, let us consider two balls joined by one spring representing a diatomic molecule. In this approximation, two atoms and the connecting bond are treated as a simple harmonic oscillator composed of 2 masses (atoms or balls). These two balls can vibrate with a characteristic frequency that depends on the mass of the balls and on the spring force (spring force can be approximated by Hooke's law). Matematically, the equation $\nu = (1/(2\pi))\sqrt{\kappa/\mu}$, describes the characteristic oscillation frequency ν and how it depends on mass μ and spring constant force κ. According to this equation, stiffer spring constant (stronger bonds) result in a higher frequency, whereas heavier atoms result in lower frequencies. This simple system possess only a single characteristic frequency. The balls can only vibrate with this characteristic frequency or an integer multiple of this frequency. A more complex molecule can still be modelled quite accuarately as balls of different massess joined by springs of different tensions (representing different atoms with different bonds). Figure 2.18 shows a diagram representing the vibration of a diatomic molecule or one vibrational degree of freedom of a polyatomic molecule, which is excited by a transition from energy level $\upsilon = 0$ to $\upsilon = 1$ [30, 39, 40].

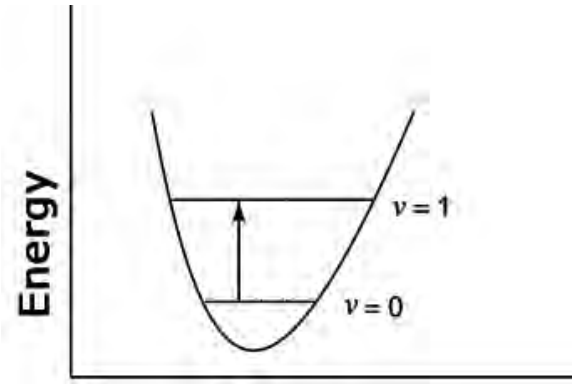

Figure 2.18: Observation of the excitation of a vibrational state in the electronic ground state by infrared absorption.

In the classical harmonic oscillator, $E = \frac{1}{2}\kappa x^2 = h\nu$, where x is the displacement of the spring. Thus, the energy or frequency is dependent on how far one stretches or compresses the spring. If this simple model were true, a molecule could absorb energy of any wavelength. However, vibrational motion is quantized and, therefore, the molecules can only exist in finite energy states. In the case of harmonic

potentials, these states are equidistant, i.e. $E_i = h\nu(n_i + 1/2), n_i = 0, 1, 2, ...$ where the energy levels are numbered as n_i. At n_i = 0, the potential energy has its lowest value, which is not the potential minimum energy [39, 40]. According to the selection rules, only transitions to the next energy level are allowed; therefore, molecules will absorb an amount of energy equal to $h\nu$. This rule is not inflexible and, occasionally, transitions of $2h\nu$, $3h\nu$, or higher are observed. These correspond to bands called overtones in an IR spectrum. They are of lower intensity than the fundamental vibration bands.

As mentioned above, infrared spectra cover the near infrared(0.75-3 μm), middle infrared (3-30 μm) and far infrared (30-300 μm) range. In this region, most molecules show absorption or emission bands arising from symmetry-allowed interaction with the radiatio. The energy of the absorbed and emitted light is equivalent to the energy difference between the lowest vibrational states of the electronic ground state of a molecule.

Three types of instruments for IR absortion measurements are commonly available: dispersive spectrophotometers with a grid monochormator, Fourier thansform spectrometers employing an interferometer, and non-dispersive photometers using a filter or absorbing gas (typically used for analysis of atmospheric gases at specific wavelengths).

Until 1980s, the most widely used instruments for IR measurements were dispersive spectrometers. Nowadays, this type of instruments has been displaced by Fourier transform (FT) spectrometers because of their speed, reability, enhanced signal-to-noise ratio. Infrared spectrometers (Figure 2.19) usually combine a radiation source, collimator, fixed mirror, moving mirror, a sample holder, a device for spectral dispersion or selection of radiation (beam splitter), and a radition detector, all connected to appropiate recording and evaluation facilities. An ideal spectrometer records completely resolved spectra with a maximum signal-to-noise ratio. It requires a minimum amount of sample which is measured nondestructively in a minimum time, and it provides facilities for storing and evaluating the spectra. FTIR spectrometers can be single-beam or double-beam instruments. A typical procedure for determining transmittance or absorbance with this type of instrument is to first obtain a reference

interferogram by scanning a reference (usually air) twenty or thirty times coadding the data, and storing the results in the computer. A sample is inserted in the radiation path and the process repeated. The ratio of the sample to reference spectral data is, then, computed to obtain the transmittance at various frequencies.

Infrared spectroscopy (IR) has long been used to determine molecular structures and to identify unknown compounds. IR data have been used to obtain information about the chemical composition, configuration, and crystallinity of polymeric and biological materials [30].

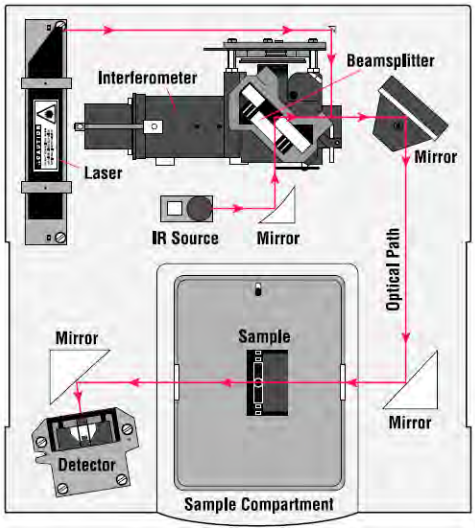

Figure 2.19: Scheme of a FTIR instrument.

2.2.4.4 Inductively coupled-plasma emission spectroscopy

Inductively coupled plasma-atomic emission spectroscopy (ICP-AES) is a widespread technique for elemental analysis of a sample [41]. Most of the substances in gas state decompose in atoms when heated to a sufficiently high temperature. Unlike optical spectra of condensed matter, spectra of atoms in gas state consist of very narrow lines which originate from state transitions of each atom. Each element has its own characteristic spectrum, and spectral lines of different elements in one sample are barely superposed, which makes this technique very precise and sensitive [42]. In Figure 2.20, a scheme of an ICP-AES instrument is shown. A plasma source is used to make specific elements to emit light, after which a spectrometer separates this light in their

characteristic wavelengths. This technique is especially suited for direct analysis of liquid samples. The sample solution is transformed into an aerosol by a nebuliser. Small droplets (1-10 μm) are transferred by argon plasma. When the aerosol droplets enter the hot area of plasma, they are converted into salt particles. These salt particles are split into individual molecules that will subsequently fall apart to atoms and ions. In the plasma, even more energy is transferred to the atoms and ions, promoting the excitation of their electrons. When these excited atoms and ions back to a lower excitation state or to their ground state they will emit electromagnetic radiation in the ultra-violet/visible range of the spectrum. The classical approach for ICP-AES measurement is to collect and measure the emitted radiation radially, i.e. the optical axis is orthogonal to the central channel of the ICP. The limit of detection is in de order of ca. ng/ml.

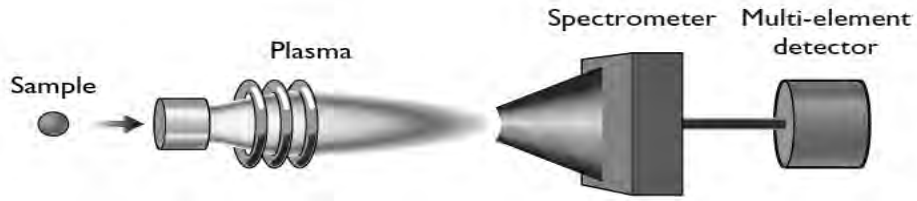

Figure 2.20: Scheme of an ICP-AES instrument.

2.2.5 Superconducting quantum interference device (SQUID)

A SQUID magnetometer is a sensitive device for measuring magnetic fields. SQUID magnetometers are used to characterize materials when the highest detection sensitivity over a broad temperatures range and application of magnetic fields up to several Tesla is needed. The main application of this instrument is the study of magnetic properties of materials by measuring the induced or remnant magnetic moment, usually as a function of applied magnetic field and temperature (Figure 2.21). A SQUID magnetometer combines several superconducting components, including the proper SQUID device, a superconducting magnet, detection coils, a flux transformer, and superconducting shields (Figure 2.22). To make a measurement, a sample is first attached to a sample rod. The sample is then scanned through the centre of a first-order or second-order superconducting gradiometer. The gradiometers form a closed flux transformer that is coupled to a SQUID. The shape and magnitude of the response curve can be then analyzed using a computer to obtain a corresponding magnetic moment

[43]. In particular, we use SQUID to measure the magnetic properties of magnetic nanoparticles (superparamagnetic materials, see section *5.2*) and hybrids.

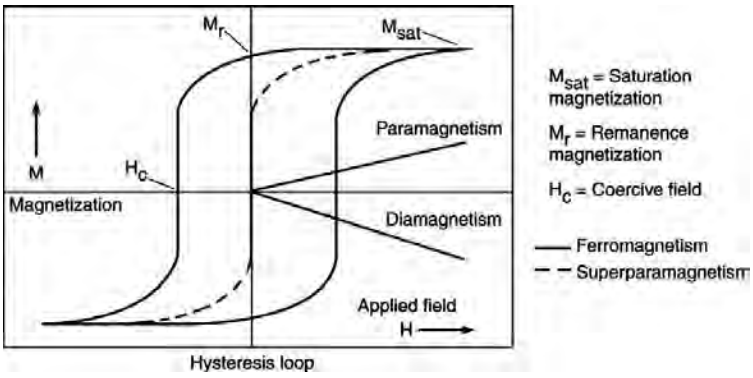

Figure 2.21: Hysteresis loops (magnetization *vs.* applied magnetic field) characteristic of ferromagnetic and superparamagnetic NPs. For comparison, *para-* and *diamagnetic* behavior are also shown. The Figure indicates the remanence, M_r, and coercive field, H_c, values.

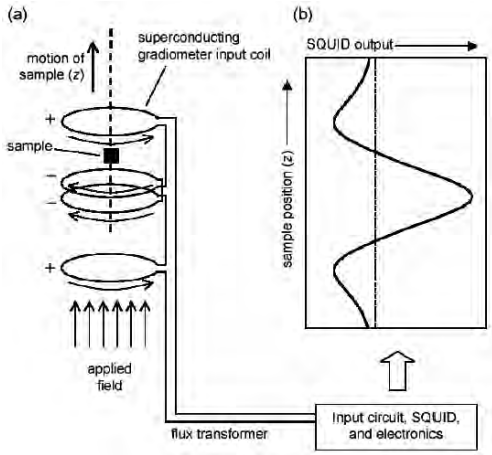

Figure 2.22: Scheme of a SQUID magnetometer.

2.2.6 Magnetic resonance imaging (MRI)

One of the most valuable and widely used imaging methods in medical diagnostic is the Magnetic Resonance Image (MRI). Though the diagnostic potential of conventional MRI is immense and a variety of different contrast modes are well established, further improvements of the method have been pursued in past years by application of magnetic nanoparticles for contrast enhancement based on functional site specificity.

In MRI, the nuclear magnetic moment of protons is used as a sensitive probe of the chemical neighbourhood of protons in different tissues and organs of human body. Nuclear moments are aligned by means of an external magnetic bias field (commonly in the range of 0.2-3 T) and the precession of the spins is excited by transverse RF pulses at a proton resonance frequency of about 42.58 MHz T^{-1}. After applying the pulse sequence, the induced magnetization decays and the longitudinal (T_1) and transverse (T_2) relaxation times of the precessing nuclear magnetic moments show tissue-specific differences that are used to generate the required image contrast. Imaging is performed by controlling external field gradients so that the resonance condition is fulfilled only in a restricted local region and, then, by scanning the resonant volume the image is built. Magnetic response signals are detected by pick-up coils. In this way, the tissue-specific differences of the relaxation time T_1 and/or T_2 may be used for construction of the T_1- and T_2.weighted images showing optimal contrast of special tissue features. In practice, for optimization of tissue contrast a variety of different pulse sequences (e.g., the widely applied spin-echo methods) may be used [44, 45].

Generally, a magnetic resonance scanner (Figure 2.23) is essentially defined by three hardware groups and their parameters: a) the main magnet with its homogeneity over imaging volume; b) the magnetic field gradient system with its linearity over the imaging volume; and c) the radiofrequency (RF) system with its RF signal homogeneity and signal sensitivity over the imaging volume. Whole-body MRI imposes very special demands on these system components [46, 47]:

The main magnet. Magnetic resonance imaging requires a very strong magnetic field that has precisely the same magnitude and direction everywhere in the region we want to image. One of the key properties used to describe the quality of a MRI system is the uniformity, or homogeneity, of the applied magnetic field. For example, high-quality MRI systems made for clinical use in hospitals will have magnetic fields that vary less than 5 parts per million (ppm) over a 40 cm diameter spherical volume in the region desired for imaging.

The magnetic field gradient. As mentioned earlier, a key property of the static magnetic field of a MRI system is its homogeneity, but anything we place inside the magnetic field tends to change the magnetic field slightly. To make the magnetic field as uniform as possible and to compensate for changes caused by different objects in the field, we shim the field. Shimming is typically handled by placing small amounts of

iron at specific locations within long trays that line the cylindrical magnetic field coil; or by several set of wire coils. Once the shimming is complete, the magnetic field is highly uniform over a central region where the imaging takes place.

The radio frequency system. Radio frequency systems suitable for MRI are characterized by RF excitation with homogeneous signals over an examination volume as large as possible. Here, it is important that the excitation flip angle remains as constant as feasible, as the image contrast is fundamentally influenced by this parameter.

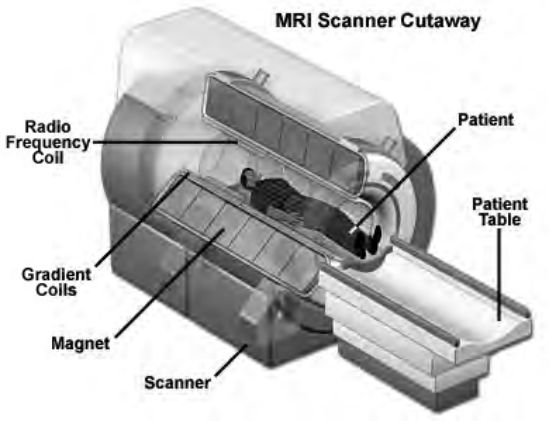

Figure 2.23: MRI scanner diagram. The main magnet aligns nuclear magnetic moments. The gradient coils in conjunction with the radio frequency coil flip the protons magnetic moments away from the direction of the main magnetic field. When the radiofrequency pulse is turned off, protons will tend to return to the least energy position. This process is called decay or precession. As protons magnetic orientation strives to realign with the main magnetic field, the proton emits a radio frequency of its own. The intensity of this signal is collected by receiving coils is stored in a matrix. Fourier transformed is applied to the data and used to generate 3D images [48, 49].

2.2.7 Fluorescence microscopy

Fluorescence microscopy is the most frequently employed light microscopy used in biomedical research today. Fluorescence microscopes contain special filters and employ a unique method of illumination to produce images of fluorescent light emitted from excited molecules in a specimen. The filters are designed to isolate and manipulate

two distinct sets of excitation and fluorescence wavelengths. A band of shorter excitation wavelengths from the illuminator and filters is directed to the specimen, while a band of longer fluorescence wavelengths emitted from the specimen forms an image of the specimen in the image plane [50].

2.2.7.1 Fluorochromes

To perform fluorescence microscopy effectively, it is necessary to select the proper fluorochrome, filters, and illuminator for a given application, and evaluate the quality of fluorescence signals. Fluorescence microscopy allows visualization of specific molecules that fluoresce in the presence of excitatory light. Thus, the amount, intracellular location, and movement of macromolecules, small metabolites, and ions can be studied using this technique. Typically, non-fluorescent molecules are tagged with a fluorochrome in order to make them visible. Fluorochromes, also known as fluorescent dyes or fluorescent molecules, are molecules capable of fluorescing. Examples of these are DAPI and the Hoechst dyes used to directly label nuclear DNA, or rhodamine-labeled phalloidin used to indirectly label cytoplasmic actin filaments [50]. If a fluorochrome is conjugated to a large macromolecule (through a chemical reaction or by simple adsorption), the tagged macromolecule is said to contain a fluorophore, the chemical moiety capable of producing fluorescence. Fluorochromes exhibit distinct excitation and emission spectra that depend on their atomic structure and electron resonance properties. Fluorescent dyes usually contain several unconjugated double bonds. Fluorochrome-labeled antibodies can be used to label fixed, permeabilizer cells in a method known as immunofluorescence microscopy. These techniques are commonly used to visualize the distribution of certain proteins in a cell or to make visible specific organelles, filaments, and biochemically distinct membrane regions [50].

2.2.7.2 Important parameters of fluorochromes

Two important parameters of fluorochromes are the Stokes shift, which is the difference between the excitation wavelength and emission wavelength, fluorochromes with large stoke shifts are advantageous for fluorescence microscopy as they permit to isolate the emission light by interference filters; the second parameter is the Quantum

efficiency of fluorescence emission, which is the fraction of absorbed photon quanta reemitted by a fluorochrome as fluorescence photons. Quenching is a phenomenon that reduces the quantum efficiency of a fluorochrome without altering the emission spectra. This phenomenon occurs by interaction with other molecules including other fluorochrome molecules. Fluorochromes are desired to be water soluble, chemically stable and resistant to photobleaching. Photobleaching is the loss of fluorescence due to photon-induced chemical damage and covalent modification.

2.2.7.3 Fluorescence microscope

A fluorescence microscope consists of the following parts (Figure 2.24):

Light source: it must be a bright light source, such as a mercury or xenon arc lamp, because only a narrow band of wavelengths and, in consequence, a small portion of the illuminator output is used to excite the fluorochromes in the specimen.

Epi-illuminator: the epi-illuminator consists of the lamp and its collector lens plus a connector tube fitted with a field stop diaphragm, a relay lens, and slots for additional filters. It is attached to the lamp at one end and is mounted at the other end to the microscope in the vicinity of the fluorescence filter cube. The lamp housing should contain a focusable collector lens to fill the back aperture of the objective as required for Koehler illumination. On most research microscopes the epi-illuminator is a built-in component of the microscope setup. Apart from proper adjustment and focus of the lamp, little other manipulation of the illumination pathway is required, for example, the field stop diaphragm is centered and is opened to provide optimal framing of the specimen. Epi-illumination is much more efficient than transmitted mode (or diascopic) illumination because there is much less background in the fluorescence image.

Filters: Filters used to isolate bands of wavelengths in fluorescence microscopy include colored glass filters, thin film interference filters, or a combination of them. The filters include long- or short-pass edge filters and narrow or broad bandpass filters. The filters must be selected in accordance with the absorption and emission of the fluorochromes to be observed. An appropriate selection of the filters sets can improve considerably the quality of the images obtained by fluorescence microscopy.

Dichroic mirror: The dichroic mirror or beam splitter is a special long-pass filter coated with multiple layers of dielectric materials similar to those contained in thin film

interference filters, but specially designed for reflection and transmission at certain boundary wavelengths. The mirror is mounted at a 45° angle with respect to the optic axis within a filter cube and faces the light source. At this angle, the dichroic mirror reflects short excitation wavelengths at a 90° angle along the optic axis to the specimen, but transmits long fluorescence wavelengths that are collected by the objective and directed to the image plane. The transition from near total reflection to maximal transmission can be remarkably sharp, occurring over 20–30 nm, allowing the mirrors to act as precise discriminators of excitation and fluorescence wavelengths. The specifications for a dichroic mirror assume a 45° angle between the axis of the incident beam and the plane surface of the mirror. Dichroic mirrors should be handled with extreme care, because the exposed dielectric layers can be scratched and damaged during handling and cleaning.

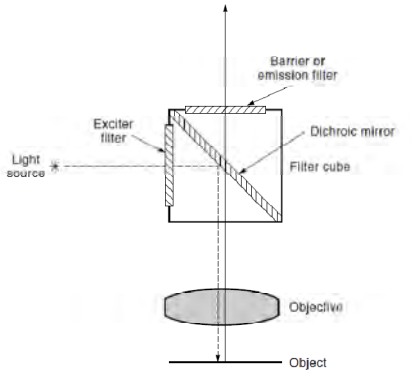

Figure 2.24: Scheme of the fluorescence microscope optics.

Objective lenses: Proper selection of an objective lens is important, especially for imaging dim fluorescent specimens. High-numerical aperture (H-NA), oil immersion plan-fluorite lenses and planapochromatic objective lenses are ideal, because at NA = 1.3 or 1.4 their light-gathering ability is especially high. These lenses give excellent color correction, so different fluorescent wavelengths are brought to the same focus in the focal plane. They are also transparent to UV light, a requirement for examining UV-excitable dyes such as DAPI, Hoechst…. In addition, they contain low-fluorescence glass, a feature that minimizes background fluorescence and gives high contrast. Since image brightness (photon flux per unit area and time) is proportional to NA^4/M^2, where *NA* is the numerical aperture and *M* is the magnification at 60X, 1.4 NA planapochromatic objective is among the brightest objectives and is very well suited for

fluorescence imaging. The spatial resolution *d* for two noncoherent fluorescent point objects is the same as in bright-field microscopy with incoherent light, and is given as $d = 0.61\lambda/NA$, where λ is the mean wavelength of fluorescent light transmitted by the barrier filter.

2.2.8 Confoncal laser scanning microscopy (CLSM)

CLSM produces optical sections by scanning the specimen point-by-point with a laser beam focused in the specimen, using a spatial filter (usually a pinhole or a slit) to remove unwanted fluorescence from above and below the focal plane of interest. The term "optical section" refers to the instrument's ability to produce sharper images of fluorescently labeled tissues than those produced using a standard epifluorescence microscope and, in most cases, without resorting to physical sectioning of the tissue. Optical paths of the various commercially available CLSMs are designed so that when the laser beam is focused in the specimen, it is confocal with the point of light focused at the pinhole in front of the photodetector. Thus, only information from the focal plane of interest reaches the photodetector. The power of this approach lies in its ability to image structures at discrete levels within an intact biological specimen with a theoretical lateral resolution of 0.14 μm and a vertical resolution of 0.23 μm with a lens of 1.4 NA [50].

2.2.8.1 Confocal laser scanning microscope

The confocal microscope is an integrated microscope system consisting of a fluorescence microscope, multiple laser light sources, a confocal box or scans head with optical and electronic equipment, a computer and monitor for display, and software for acquiring, processing, and analyzing images. The scan head generates the photon signals required to reconstruct the confocal image and contains the following devices: inputs from one or more external laser light sources, fluorescence filter sets, a galvanometer-based rater scanning mechanism, one or more variable pinhole apertures for generating the confocal image, and photomultiplier tube (PMT) detectors for different fluorescent wavelengths (Figure 2.25).

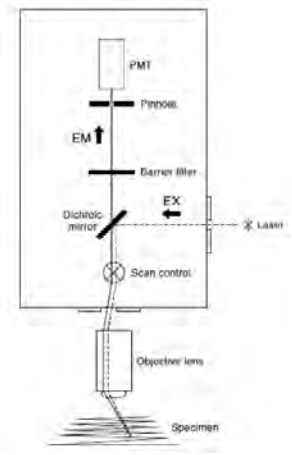

Figure 2.25: Scan head components.

2.2.8.2 Optical principle of CLSM

The optical principle in which CLSM is bases is described as follows: Epi-illumination is used, where the light source and detector are both on the same side of the specimen plane and separated by the objective lens, which operates as both a condenser and objective. The components of the fluorescence filters set (exciter, dichroic and emission filters) perform the same functions as in wide-filed fluorescence microscopy. A laser beam is expanded to fill the back aperture of the objective, and it forms an intense diffraction-limited spot that is scanned form side to side and from top to bottom over the specimen in a pattern called raster. This procedure is called point scanning.

The heart of the confocal optics is the pinhole aperture, which accepts fluorescent photons from the illuminated focused spot in the raster, but largely excludes fluorescence signals from objects above and below the focal plane, which being out of focus, are focused on the pinhole as disks of much larger diameter. Because the size of the disk of an out-focus object is spread out over such large area, only a fraction of light from out-of-focus objects passes through the pinhole. The pinhole also eliminates much of the stray light in the optical system. The combination of point scanning and the use of a pinhole as a spatial filter at the conjugate image plane are essential for producing the confocal image (Figure 2.26).

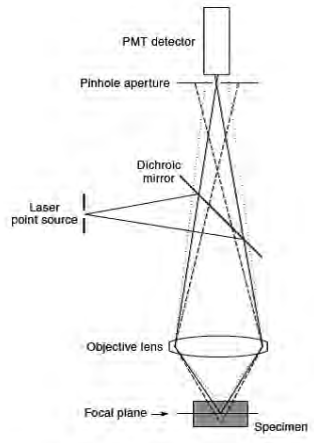

Figure 2.26: Scheme of a CLSM optics.

Fluorescent wavelengths emanating from an excited point in the specimen at any time *t* are collected by the same objective and focused as a small diffraction spot that just fills the diameter of a variable pinhole aperture placed in front of the PMT detector in a plane that corresponds to the image one in a wide-field fluorescence microscope. The pinhole is optically confocal with and conjugate to the specimen plane. Thus, the PMT does not "see" an image, but receives a constant stream of changing photon fluxes; the computer, in turn, sees a constantly changing voltage signal from the PMT, digitilizes it, and displays the signal on the monitor.

To generate an image of an extended specimen, the laser beam is scanned across the object by a raster scanning mechanism that is typically based on two high-speed vibrating mirrors driven by galvanometer motors (Figure 2.27). One mirror oscillates left-right while the other moves up and down. Fluorescent photons emitted from an excited point in the specimen are collected by the objective. Because the speed of the galvanometer mirrors is inconsequential relative to the speed of light, fluorescent light follows the same light path on its return and is brought to the same position on the optic axis as the original exciting laser beam. This process is called *descanning*. The fluorescent light, then, passes through a dichroic mirror and becomes focused at the confocal pinhole. Because descanning is instantaneous, the image in the pinhole always remains steady and does not move back and forth like the beam in the specimen plane; however, the focused spot varies in intensity over time as the spot excites different locations in the specimen.

Fluctuations in light intensity are converted into a continuously changing voltage (an analogue signal) by the PMT detector. The analogue signal is digitalized at regular time intervals by an analogue-to-digital converter to generate pixels that are stored in an image frame buffer board and displayed on a computer monitor. Thus, a confocal image of an object is reconstructed from photon signals and is displayed by a computer; the confocal image never exists as a real image that can be seen by the eye in the microscope.

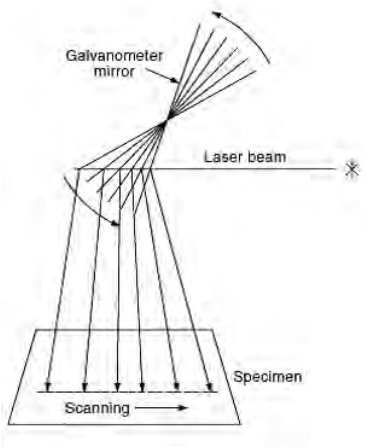

Figure 2.27: Scheme of a galvanometer mirror that allows the scanning process.

2.2.8.3 Advantages of CLSM over wide-field fluorescence systems

The principal advantage of CLSM is the possibility to obtain optical sections of 10 – 50 µm thick of fluorescent objects. With a stack of images representing different focal planes spaced at regular intervals along the optic axis (z-axis), the object can be displayed in a variety of ways:

- A composite projection view, where all the information contained in a stack or series of images taken at a series of focal planes along the z- axis is projected into a songle focused image.
- Three dimensional views of an object which can be obtained from a z-stack of confocal images with the help of computer software for imge display.
- Transverse x-z or y-z cross sectional views, where the object appears as being been transversely cut, that is, in a plane oriented parallel to the z-axis.

- Time sequences of three dimensionally images with multiple colors, which can be displayed as three-dimensional color movies in real time or in time-lapse mode.

An additional advantage is the possibility to use confocal microscopy in *reflection* mode, in which a laser beam scans the three-dimensional surface of a reflective object. Fluorescence filter sets are not used for this mode of imaging; rather the focused spot of the laser is reflected off the surface. Reflections from features lying in the confocal plane pass through the confocal pinhole aperture, wheras light from reflections above and below of the focal plane is largely excluded.

2.2.9 X-ray diffraction

X-ray diffraction (XRD) is a versatile, powerful and non destructive technique that reveals detailed information about the chemical crystallographic structure of natural and manufactured materials. Diffraction effects are observed when an electromagnetic radiation impinges on periodic structures with geometrical variations on the length scale of the radiation wavelength. The inter-atomic distances in crystal and molecules is around to 0.15 – 0.5 nm, which correspond in the electromagnetic spectrum with the wavelength of X-rays, having photon energies between 3 and 8 keV [51].

There are three different types of interactions between X-rays and matter. First, the photoionization, where electrons may be liberated from their bound atomic states during the process, and which falls into the group of inelastic processes. In addition, other inelastic scattering process that incoming X-ray beams may undergo upon interaction with matter is the energy transfer to an electron but, in this case, without a release of the electron from the atom (phenomenon known as Compton scattering). Finally, X-rays may be elastically scattered by electrons, process known as Thomson scattering. In this process, the electron oscillates at the frequency of the incoming beam so the wavelength of the scattered radiation is conserved.

There are many theories and equations to correlate the diffraction pattern and the material structure. The Bragg law is a simple way to describe the diffraction of X-rays by a crystal. In Figure 2.28a, the incident X-rays reach the crystal planes with an incident angle θ and are diffracted at an angle θ. The diffraction peak is observed when

the Bragg condition is satisfied [31, 51]:

$$n\lambda = 2d \sin\theta \qquad \text{(Eq 2.12)}$$

where λ is the wavelength of the incident X-rays, d is the distance between each adjacent crystal plane (d-spacing), θ is the Bragg angle at which a diffraction peak is observed, and n (1, 2, ...) is an integer number, called the reflection order; this means that the Bragg condition can be satisfied by various X–ray wavelengths. The Bragg law gives a simple relationship between the diffraction pattern and the crystal structure, and many X-ray diffraction applications can be easily explained by this law.

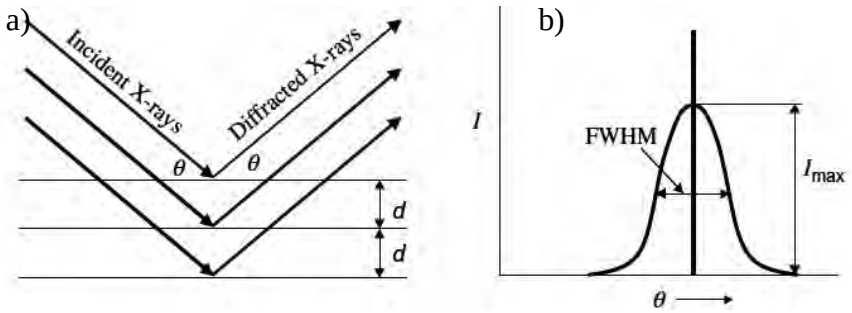

Figure 2.28: (a) Incident and reflected X-rays form an angle θ which is symmetric to the crystal normal plane; (b) The diffraction peak is observed at a Bragg angle θ [31].

In X-ray diffraction using a single wavelength, the Bragg equation is typically expressed with n = 1 for the first order of diffraction because higher order reflections can be considered as resulting from different lattice planes. For instance, the second-order reflection from (*hkl*) planes is equivalent to the first-order reflection from (*2h, 2k, 2l*) planes. The diffraction peak is displayed as diffracted intensities at a range of 2θ angles. For perfect crystals, the peak is a delta function, the dark straight vertical line shown in Figure 2.28b [31].

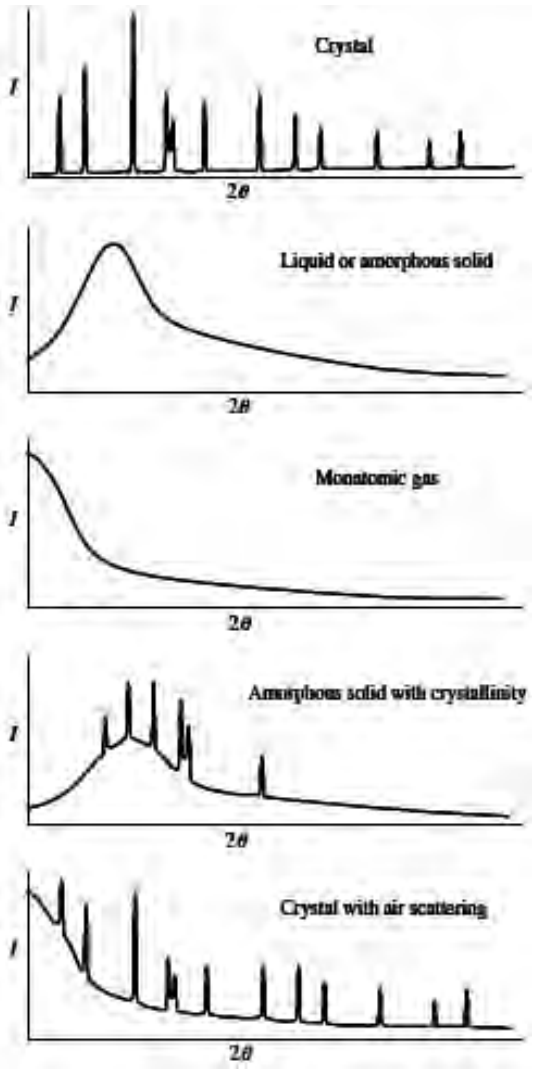

Figure 2.29: Diffraction patterns from crystalline solids, liquids, amorphous solids, and monoatomic gases as well as their mixtures [31].

A typical diffraction peak is a broadened peak displayed by the curved line in Figure 2.28b. The peak broadening can be due to many effects, including imperfect crystal conditions, such strain, mosaic structures, and finite sizes; ambient conditions, such as atomic thermal vibrations; and instrumental conditions, such as X-ray beam size, beam divergence, beam spectrum distribution, and detector resolution. The curved line gives a peak profile, which is the diffracted intensity distribution of the Bragg angle. The highest point on the curve gives the maximum intensity of the peak, I_{max}. The width of the peak is typically measured by its full width at half maximum (FWHM). The total diffracted energy can be measured by the area under the peak, which is referred to as integrated intensity. The integrated intensity is a more consistent value for measuring the diffracted intensity of a reflection since it is less affected by all

peak broadening factors [31, 51].

The Bragg diffraction condition is based on the existence of a long periodicity of crystalline materials. As mentioned above, X-rays diffraction can provide information on the atomic arrangement in material with long-range order, short-range order, or no order at all, like gases, liquid, and amorphous solids, and a material may have one or to be a mixture of the former atomic arrangement types. Figure 2.29 gives a schematic comparison of the diffraction patterns for crystalline solids, liquids, amorphous solids, and monatomic gases as well as their mixtures. The diffraction patterns shown in this Figure are displayed as diffracted intensity versus 2θ assuming that the diffracted intensity is a unique function of the diffraction angle. The diffraction pattern from crystals has many sharp peaks corresponding to various crystal planes based on the Bragg law. The peaks at low 2θ angles are from crystal planes of large d-spacing and, vice versa, at high 2θ angles. To satisfy the Bragg condition at all crystal planes, the crystal diffraction pattern is actually generated from polycrystalline materials or powder materials. Therefore, the diffraction pattern is also called powder diffraction pattern. A similar diffraction pattern can be collected with a single crystal if this has been rotated at various angles during data collection so that the Bragg law can be satisfied when the crystal is at the right orientation.

Both amorphous solid and liquid materials do not have the long-range order of crystals, but their atomic distances have a narrow distribution because of atoms are tightly packed. In this case, the intensity of the scattered X-rays forms one or two maxima with a very broad distribution in the 2θ range. The intensity *vs.* 2θ distribution, thus, reflects the distribution of the atomic distances. In the case of a gas there is no order at all, i.e. the atoms are distributed randomly in space. The scattering curve is featureless except that the scattered intensity drops continuously with the increase of 2θ. On the other hand, the diffraction pattern from a material containing both amorphous and crystalline features has a broad background from the amorphous phase and sharp peaks from the crystalline phase. For example, many polymer materials have an amorphous matrix with crystallized regions. The diffraction pattern may contain air-scattering background in addition to sharp diffraction peaks. The air-scattering can be generated from the incident beam or diffraction beam. If the air-scattering is not removed by the diffractometer, the diffraction pattern contains a high background at low 2θ angle and the background gradually decreases with increasing 2θ angle [51].

On the other hand, X-ray diffraction phenomena can also be explained in reciprocal space by the reciprocal lattice and the Ewald sphere. Reciprocal lattice is a transformation of the crystal lattice in real space to reciprocal space. The shape and size of a unit cell in real space can be defined by three vectors, **a**, **b**, and **c,** all starting from any single lattice point. The unit cell of the corresponding reciprocal lattice is, then, given by three vectors **a***, **b***, and **c*** (also referred to as reciprocal lattice axes), and:

$$\begin{aligned} \boldsymbol{a}^* &= \frac{1}{V}(\boldsymbol{b} \times \boldsymbol{c}), \\ \boldsymbol{b}^* &= \frac{1}{V}(\boldsymbol{c} \times \boldsymbol{a}), \\ \boldsymbol{c}^* &= \frac{1}{V}(\boldsymbol{a} \times \boldsymbol{b}) \end{aligned} \qquad \text{(Eq 2.13)}$$

where V is the volume of the crystal unit cell in the real space and

$$V = \boldsymbol{a} \cdot \boldsymbol{b} \times \boldsymbol{c} \qquad \text{(Eq 2.14)}$$

Since each reciprocal lattice axis is the vector product of two lattice axes in real space, these are perpendicular to the plane defined by the two lattice axes. The original lattice axes and reciprocal lattice axes maintain the following relations:

$$\boldsymbol{a} \cdot \boldsymbol{b} = \boldsymbol{b} \cdot \boldsymbol{b} = \boldsymbol{c} \cdot \boldsymbol{c} = \mathbf{1} \qquad \text{(Eq 2.15)}$$

and

$$\boldsymbol{b} \cdot \boldsymbol{a}^* = \boldsymbol{c} \cdot \boldsymbol{a}^* = \boldsymbol{a} \cdot \boldsymbol{b}^* = \boldsymbol{c} \cdot \boldsymbol{b}^* = \boldsymbol{b} \cdot \boldsymbol{c}^* = \boldsymbol{a} \cdot \boldsymbol{c}^* = 0 \qquad \text{(Eq 2.16)}$$

Figure 2.30 illustrate the relationship between the original lattice in real space and the reciprocal lattice. The unit cell of the original lattice is drawn in dotted lines. The three reciprocal lattice axes define a unit cell of the reciprocal lattice (solid lines). The origin of the reciprocal lattice axes, denoted by O, is the origin of the reciprocal lattice. The repeat translation of the reciprocal lattice unit cell in three dimensions forms the complete reciprocal lattice. Except the origin, each lattice point is denoted by a set

of three integers (*hkl*), which are the number of translations of the three reciprocal lattice axes, respectively, to reach the lattice point. In other words, the vector drawn from the origin of the lattice point (*hkl*) is given by:

$$\mathrm{H}_{hkl} = h\mathbf{a}^* + h\mathbf{b}^* + l\mathbf{c}^* \qquad \text{(Eq 2.17)}$$

and the direction of the vector H_{hkl} is normal to the lattice planes (*hkl*) in real space. The magnitude of the vector H_{hkl} is given by the *d*-spacing of the (*hkl*) planes:

$$|\mathrm{H}_{hkl}| = 1/d_{hkl} \qquad \text{(Eq 2.18)}$$

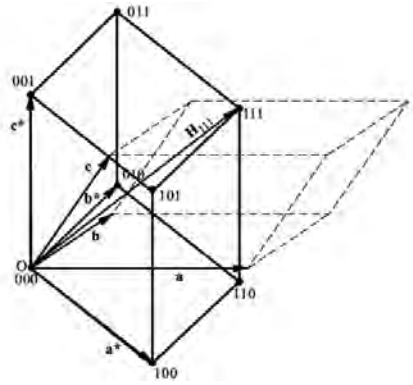

Figure 2.30: Relationship between the original lattice in real space and the reciprocal lattice [52].

Therefore, each point (*hkl*) in the reciprocal lattice represents a set of lattice planes (*hkl*) in the real space lattice. The position of the point in the reciprocal lattice defines the orientation and *d*-spacing of the lattice planes in the real space lattice. The farther away a reciprocal lattice point is from the origin, the smaller is the *d*-spacing of the corresponding lattice planes. For example, the reciprocal lattice point (111) represent the (111) lattice planes in the real apace lattice, and the lattice vector is given by $\mathrm{H}_{111} = \mathbf{a}^* + \mathbf{b}^* + \mathbf{c}^*$ and $d_{111} = 1/|H_{111}| = 1/\mathbf{a}^* + \mathbf{b}^* + \mathbf{c}^*$.

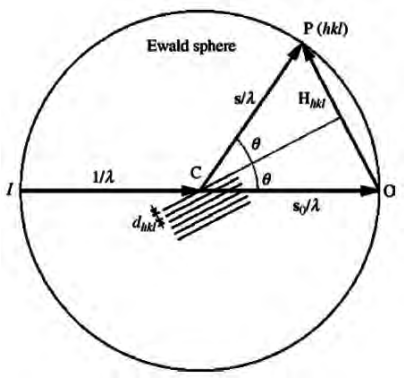

Figure 2.31: The Ewald sphere and Bragg condition in reciprocal space.

On the other hand, the relationship between the Bragg condition and the reciprocal lattice can be explained visually by the Ewald sphere, also referred as reflection sphere. Ewald came up with a geometrical construction to help the visualization of which Bragg planes are in the correct orientation to diffract. In Figure 2.31, the diffracting crystal is located in the centre of the Ewald sphere, *C*. The radius of the Ewald sphere is defined as $1/\lambda$. The incident beam can be visualized as the vector from *I* to *C*, and the diffracted beam is the vector from *C* to *P*. Both the incident and diffracted beams form an angle θ from a set of crystal planes (*hkl*). The *d*-spacing of the crystal planes is d_{hkl} In the Ewald sphere; both incident beam vector s_0/λ and diffracted beam vector s/λ start at the poin *C* and end at the point *O* and *P*, respectively. The vector from *O* to *P* is the reciprocal lattice vector H_{hkl} and is perpendicular to the crystal planes. The three vectors have the following relationship:

$$\frac{s-s_0}{\lambda} = H_{hkl} = h\mathbf{a}^* + h\mathbf{b}^* + l\mathbf{c}^* \qquad \text{(Eq 2.19)}$$

and their magnitude can be expressed based on the Bragg law as:

$$\frac{s-s_0}{\lambda} = \frac{2\sin\theta}{\lambda} = |H_{hkl}| = \frac{1}{d_{hkl}} \qquad \text{(Eq 2.20)}$$

The point O is the origin of the reciprocal lattice, and the point P is the reciprocal point (*hkl*). The Bragg condition is satisfied only when the reciprocal lattice point falls on the Ewald sphere. For a single crystal, the chance to have a reciprocal lattice point on the Ewald sphere is very small if the crystal orientation is fixed.

Multiplying both ends of equation 2.48 by the three lattice axes in real space, respectively, the Laue equations are obtained:

$$\begin{aligned} \boldsymbol{a} \cdot (s - s_0) &= h\lambda \\ \boldsymbol{b} \cdot (s - s_0) &= k\lambda \\ \boldsymbol{c} \cdot (s - s_0) &= h\lambda \end{aligned} \qquad \text{(Eq 2.21)}$$

The Laue equations establish that a periodic three-dimensional lattice produces diffraction maxima at specific angles depending on the incident beam direction and the wavelength. The Laue equations are suitable to describe the diffraction geometry of a single crystal. The Bragg law is more conveniently used for powder diffraction. Both the Bragg law and Laue equations define the diffraction condition in different formats.

On the other hand, the distance between the origin of the reciprocal lattice O and the lattice point P is reciprocal to the *d*-spacing. The largest possible magnitude of the reciprocal lattice vector is given by $2/\lambda$. This means that the smallest d-spacing satisfying the Bragg condition is $\lambda/2$. In powder X-ray diffraction, the random orientation of all crystallites can take all possible orientations assuming an infinite number of crystallites. The trace of the reciprocal lattice points from all crystallites can be considered as a series of spherical surfaces with origin O as the centre point. Therefore, the condition to satisfy the Bragg law is only if the *d*-spacing is greater than half of the wavelength. In other words, the Bragg condition can be satisfied if a reciprocal lattice point falls in a sphere of 2λ from the origin O. This sphere is called the limiting sphere for powder diffraction.

X-ray diffraction systems have a variety of configurations and component options to fulfil requirements of different samples and applications. As shown in Figure 2.32, a typical XRD system normally consist of five basic components:

- The X-ray source produces X-rays with the required radiation energy, focal spot size, and intensity;
- The X-ray optics establish the primary X-ray beam to the required wavelength, beam focus size, beam profile, and divergence;
- The Goniometer and sample stage establish and tune the geometric relation

between primary beam, sample, and detector;

- The sample alignment and monitor assist users about sample positioning into the instrument and monitors the sample state and position;
- The area detector intercepts and records the scattering X-rays from a sample, and it saves and displays the diffraction pattern into a frame.

Each of the former basic components may have several options suitable for various application and functions. The whole system is controlled by a computer equipped with a software for instrument control, data acquisition, and data analysis. In addition to the five basic components, there are some other accessories, such as a low and high-temperature stages, helium or vacuum beam path for SAXS, beam stop, and alignment and calibration fixtures.

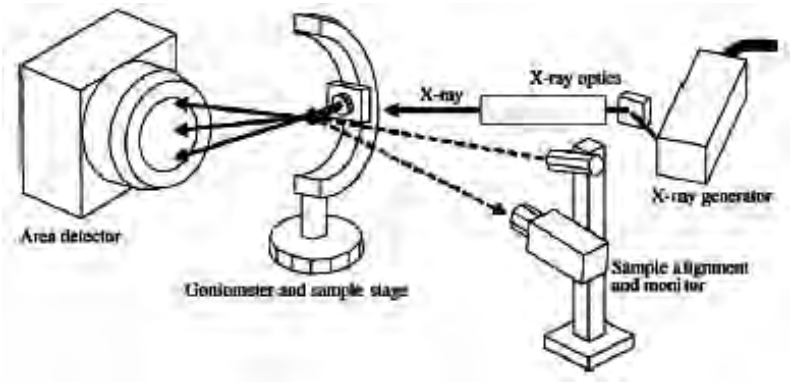

Figure 2.32. Scheme of a X-ray diffractometer.

2.3 Bibliography

[1] Mohan P, Rapoport N. Doxorubicin as a Molecular Nanotheranostic Agent: Effect of Doxorubicin Encapsulation in Micelles or Nanoemulsions on the Ultrasound-Mediated Intracellular Delivery and Nuclear Trafficking. Molecular Pharmaceutics. 2010;7:1959-73.

[2] Dinarvand R, Sepehri N, Manoochehri S, Rouhani H, Atyabi F. Polylactide-co-glycolide nanoparticles for controlled delivery of anticancer agents. International journal of nanomedicine. 2011;6:877-95.

[3] Uchegbu FI, Schätzlein GA. Polymers in Drug Delivery: Taylor and Francis; 2006.

[4] McNally-Heintzelman KM, Sorg BS, Welch AJ, Dawes JM. ICG-doped albumin protein solders for improved tissue repair. 1999. p. 99-110.

[5] Gathje J, Steuer RR, Nicholes KR. Stability studies on indocyanine green dye. Journal of Applied Physiology. 1970;29:181-5.

[6] Landsman ML, Kwant G, Mook GA, Zijlstra WG. Light-absorbing properties, stability, and spectral stabilization of indocyanine green. Journal of Applied Physiology. 1976;40:575-83.

[7] Biesen P, Jongsma F, Tangelder G, Slaaf D. Yield of fluorescence from indocyanine green in plasma and flowing blood. Ann Biomed Eng. 1995;23:475-81.

[8] Manchanda R, Fernandez-Fernandez A, Nagesetti A, McGoron AJ. Preparation and characterization of a polymeric (PLGA) nanoparticulate drug delivery system with simultaneous incorporation of chemotherapeutic and thermo-optical agents. Colloids and Surfaces B: Biointerfaces. 2010;75:260-7.

[9] Zheng M, Yue C, Ma Y, Gong P, Zhao P, Zheng C, et al. Single-Step Assembly of DOX/ICG Loaded Lipid–Polymer Nanoparticles for Highly Effective Chemo-photothermal Combination Therapy. ACS Nano. 2013;7:2056-67.

[10] Saxena V, Sadoqi M, Shao J. Polymeric nanoparticulate delivery system for Indocyanine green: Biodistribution in healthy mice. International Journal of Pharmaceutics. 2006;308:200-4.

[11] Lee C-H, Cheng S-H, Wang Y-J, Chen Y-C, Chen N-T, Souris J, et al. Near-Infrared Mesoporous Silica Nanoparticles for Optical Imaging: Characterization and In Vivo Biodistribution. Advanced Functional Materials. 2009;19:215-22.

[12] Zheng X, Zhou F, Wu B, Chen WR, Xing D. Enhanced Tumor Treatment Using Biofunctional Indocyanine Green-Containing Nanostructure by Intratumoral or Intravenous Injection. Molecular Pharmaceutics. 2012;9:514-22.

[13] Bardhan R, Chen W, Perez-Torres C, Bartels M, Huschka RM, Zhao LL, et al. Nanoshells with Targeted Simultaneous Enhancement of Magnetic and Optical Imaging and Photothermal Therapeutic Response. Advanced Functional Materials. 2009;19:3901-9.

[14] Bardhan R, Grady NK, Cole JR, Joshi A, Halas NJ. Fluorescence Enhancement by Au Nanostructures: Nanoshells and Nanorods. ACS Nano. 2009;3:744-52.

[15] Samia ACS, Dayal S, Burda C. Quantum Dot-based Energy Transfer: Perspectives and Potential for Applications in Photodynamic Therapy. Photochemistry and Photobiology. 2006;82:617-25.

[16] Berne JB, Pecora R. Dynamic light scattering with applications to chemistry, biology and physics. Toronto: Dover Publications; 2000.

[17] Schärtl W. Light Scattering from Polymer Solutions and Nanoparticles Dispersions. Berlin: Springer; 2007.

[18] Xu R. Particle characterization: light scattering methods. New York: Kluwer Academic Publisher; 2002.

[19] Holoubek J. Some applications of light scattering in materials science. Journal of Quantitative Spectroscopy and Radiative Transfer. 2007;106:104-21.

[20] Murphy RM. Static and dynamic light scattering of biological macromolecules: what can we learn? Current Opinion in Biotechnology. 1997;8:25-30.

[21] Kokhanovsky AA. Light Scattering Reviews 4: single light scattering and radiative transfer.: Chichester: Praxis Publishing; 2009.

[22] Sperling LH. Introduction to Physical Polymer Science. New Jersey: Jon Wiley & Sons; 2006.

[23] Malvern. Zetasizer Users Manual2004.

[24] Swan JW, Furst EM. A simpler expression for Henry's function describing the electrophoretic mobility of spherical colloids. Journal of Colloid and Interface Science. 2012;388:92-4.

[25] Wang ZL. Handbook of Microscopy for Nanotechnology. Boston: Kluwer Academic Publishers; 2005.

[26] Bendersky LA, Gayle FW. Electron Diffraction Using Transmission Electron Microscopy. J Res Natl Inst Stand Technol. 2001;106:997-1012.

[27] van Dyck SA, van Landuyt DJ, van Tendeloo G. Electron Microscopy: Principles and Fundamentals. . Weinheim: VCH; 1997.

[28] Yao N, Wang ZL. Handbook of Microscopy for Nanotechnology. Boston: Kluwer Academic Publishers; 2005.

[29] Goldstein JI, Newbury DE, Echlin P, Joy DC, Lyman CE, Lifshin E, et al. Scanning Electron Microscopy and X-Ray Microanalysis. New York: Kluwer Academic/Plenum Publishers; 2003.

[30] van Holde KE, Johnson WC, Ho PS. Principles of Physical Biochemistry. Upper Saddle River: Pearson Prentice Hall; 2006.

[31] He BB. Two-dimensional X-Ray diffraction. New Jersey: John Wiley & Sons; 2009.

[32] Valeur B. Molecular fluorescence principles and application. Weinheim: Wiley-VCH; 2002.

[33] Buchner J, Kiefhaber T. Protein folding handbook. Weinheim: Wiley-VCH; 2005.

[34] Lakowicz JR. Principles of Fluorescence Spectroscopy: Springer; 2006.

[35] Awais M, Sato M, Sasaki K, Umezawa Y. A Genetically Encoded Fluorescent Indicator Capable of Discriminating Estrogen Agonists from Antagonists in Living Cells. Analytical Chemistry. 2004;76:2181-6.

[36] Chen H, Kim S, He W, Wang H, Low PS, Park K, et al. Fast Release of Lipophilic Agents from Circulating PEG-PDLLA Micelles Revealed by in Vivo Fo rster Resonance Energy Transfer Imaging. Langmuir. 2008;24:5213-7.

[37] Kuznetsov SV, Sugimura S, Vivas P, Crothers DM, Ansari A. Direct observation of DNA bending/unbending kinetics in complex with DNA-bending protein IHF. Proceedings of the National Academy of Sciences. 2006;103:18515-20.

[38] Xie Y, Dix AV, Tor Y. FRET Enabled Real Time Detection of RNA-Small Molecule Binding. Journal of the American Chemical Society. 2009;131:17605-14.

[39] Vedantham G, Sparks HG, Sane SU, Tzannis S, Przybycien TM. A Holistic Approach for Protein Secondary Structure Estimation from Infrared Spectra in H2O Solutions. Analytical Biochemistry. 2000;285:33-49.

[40] Schrander B. Infrared and Raman Spectroscopy: Methods and Applications. Weinheim: VCH; 1995.

[41] Skoog DA, Holler FJ, Crouch SR. Principles of instrumental analysis. Canada: Thomson Brooks/Cole; 2007.

[42] Harris D, C. Análisis Químico Cuantitativo. Barcelona: Reverté; 2007.

[43] Clarke J, Braginski AI. The SQUID handbook. Weinheim: Wiley-VCH; 2004.

[44] Mørup S, Hansen MF. Handbook of Magnetism and Advanced Magnetic Materials. New York: Jon Wiley & Sons; 2007.

[45] Andrä W, Häfeli U, Hergt R, Misri R. Handbook of Magnetism and Advanced Magnetic Materials. New York: Jon Wiley & Sons; 2007.

[46] Goyen M. Real whole-body MRI: requirements, indications, perspectives. New York: The McGraw-Hill Companies Inc; 2008.

[47] Stroman PW. Essentials of functional MRI. Boca Raton: CRC Press.

[48] Tabassi R. http://www.quora.com/Magnetic-Resonance-Imaging/How-does-an-MRI-scan-work.

[49] Berger A. Magnetic resonance imaging. BMJ. 2002;324:35.

[50] Murphy DP. Fundamentals of light microscopy and electronic imaging. New York: Wiley-Liss; 2001.

[51] Sun SF. Physical Chemistry of Macromolecules: Basic Principles and Issues. New York: John Wiley & Sons; 2004.

[52] Two-dimensional X-Ray diffraction. New Jersey: John Wiley & Sons; 2009.

CHAPTER III - NIR-Light-Active Hybrid Polymeric Nanoparticles for Simultaneous Cancer Monitoring and Multimodal Therapy

3.1 Summary

In this chapter, we report the synthesis of a multifunctional biocompatible nanotheranostic nanoplatform consisting of a biodegradable PLGA matrix co-loaded with superparamagnetic iron oxide nanoparticles (SPIONs) and the anticancer drug doxorubicin (DOXO), and additionally surface-functionalized with indocyanine green (ICG), a NIR fluorescent dye. A detailed study of the different parameters involved in the synthetic process was done in order to achieve the optimal physicochemical properties of the nanoplatforms in terms of size, zeta potential, SPIONs/DOXO co-loadings and release profiles. Chemo- and photothermal therapeutic efficacy as well as magnetic resonance and optical fluorescence imaging performance were tested in vitro on a tumoral cervical HeLa cell line. Magnetic guided targeting of the present nanoplatforms was also proven with this cell line. The in vivo biodistribution of the nanoplatforms in a mice model was assessed. An effective nanoplatform accumulation in the tumor and, unexpectedly, in the brain area was observed, whilst lower presence of particles was noted in the rethiculo endotelyal system. The present obsevrations suggest the NPs ability to possibly overcome the blood brain barrier. These results open up new possibilities to use our multifunctional nanoplatforms to treat brain-located tumors and diseases.

3.2 Introduction

The advances provided by nanotechnology have offered new opportunities to develop novel nanocarriers able to improve the pharmacokinetics and the local bioavailability of a variety of drugs as well as providing additional functionalities including imaging, diagnosis or targeting with the final objective of obtaining true multifunctional nanomedical platforms through exploiting clever combinations of nanostructured materials in a single nanodevice [1-4]. These multifunctional nanoplatforms open new windows to overcome the different and still unresolved impediments in clinical practice and, in particular, in cancer therapeutics such as the substantial toxicity to normal tissues of drug doses required to completely eliminate the tumors, creating undesirable side effects; the poor effectiveness of drug treatments against multi-drug resistant cancer cells; the impossibility of early detection of very

small tumors or blood circulating malignant cells; or the spatial-temporal separation of diagnosis and therapeutic clinical phases, amongst others [2, 3].

To construct multifunctional nanoplatforms, biodegradable polymeric nanoparticles (NPs) are an interesting approach provided that they are frequently used to improve the therapeutic impact of different types of drugs and bioactive molecules by enhancing their solubilization, their interaction with the biological environment, their absorption into a selected tissue, their bioavailability, their retention time and their intracellular penetration [5, 6], while simultaneously reducing the patient expenses and the risks of toxicity.

To this end, poly-D,L-lactide-co-glycolide (PLGA) copolymer is one of the most successfully used biodegradable polymers for the development of nano- and micro-particle-based drug delivery systems and scaffolds for tissue engineering [7, 8] provided that it undergoes hydrolysis in the body to produce biodegradable and biocompatible metabolite monomers, lactic acid and glycolic acid, and with the additional advantage of being commercially available in a wide range of molecular weights and compositions. Because of the two former monomers are endogenous and easily metabolized by the body *via* the Krebs cycle, a minimal systemic toxicity is associated with the use of PLGA for drug delivery and biomaterial applications [9].

For these reasons, PLGA nanoparticles (PLGA NPs) have been used for the encapsulation of a wide range of active compounds, ranging from hydrophilic and hydrophobic drugs, vaccines, proteins, or nucleic acids, amongst others, [10] exhibiting a high stability and loading capacity, and offering various feasible routes of administration. These characteristics have led to its approval by the US FDA and European Medicines Agency (EMA) to be used in several drug delivery systems in humans. PLGA NPs were also selected in some previous prospective studies to construct new multifunctional systems allowing simultaneous diagnosis and therapy (*e.g.* nanotheranostics devices). For example, the anticancer drug doxorubicin (DOXO) was bound to magnetic NPs that were embedded in a PLGA matrix by means of hydrophobic interactions. DOXO was sustainably released without inhibition due to the presence of the magnetic particles, which additionally provided the ability of magnetically-guided targeting through the application of an external magnetic field, as tested in mice, rats and humans [11, 12]. In a similar approach, Yang *et al.* [13] also co-loaded DOXO and superparamagnetic iron oxide NPs

(SPIONs NPs) inside PLGA NPs surface-functionalized by a monoclonal antibody (Herceptin, HER) to serve as an active targeting moiety on SK-BR3 cells, which overexpress the human epidermal growth factor receptor-2 (HER2). More recently, Kim *et al.* [14] also synthesized DOXO/SPION or DOXO-quantum dots (QDs) co-loaded PLGA NPs stabilized with a polylysine-PEG-folate polymer to provide the nanoplatform with simultaneous chemotherapeutic, imaging (magnetic resonance, MRI, or fluorescence optical, FOI, imaging) and active targeting capabilities against KB cells, which overexpress folate receptors on their membrane. Also, SPIONs embedded in PLGA NPs were designed as a dual drug delivery and imaging system able to encapsulate both hydrophilic (carboplatin) and hydrophobic drugs (paclitaxel and rapamycin). Both *in vitro* and *in vivo* MR imaging showed that these NPs possess a better image resolution than commercial contrast agents [15, 16]. On the other hand, DOXO-loaded Au half-shelled-metallized PLGA NPs were obtained to achieve a synergistic tumor cytotoxicity by the simultaneous combination of chemo- and photo-thermal therapies by exploiting the near-infrared (NIR) plasmonic properties of the metal layer. This nanoconstruct was additionally surface-functionalized with a monoclonal antibody (Herceptin) to dually ensure specific cell targeting and additional therapeutic activity as tested both *in vitro* and *in vivo* [17-19].

Here, we report on a magnetically-targeted multifunctional nanoplatform able to be used for simultaneously perform magnetic resonance and optical imaging, and to enable, at the same, chemo- photothermal therapeutic activities with the advantage of avoiding additional chemical synthetic steps as the *in situ* growth process of a metal layer as done in previous works [17-19]. The present nanoplatform is composed of four different components. Firstly, PLGA NPs were used as a core matrix for co-loading of DOXO as a chemotherapeutic agent, and hydrophobic SPIONs employed for both magnetically-guided targeting and as a T_2-MRI contrast agent. Finally, indocyanine green (ICG), a tricarbocyanine dye with absorbing properties exclusively in the NIR electromagnetic spectrum, and currently used as a diagnostic compound for blood volume determination, ophthalmic angiography, cardiac output and hepatic function [20, 21], was complexed to the chitosan-functionalized surface of the PLGA NPs to provide the system with the capabilities of optical imaging and photo-thermal therapy under NIR light irradiation of suitable wavelength and power. Since these nanoplatforms are NIR-resonant, the simultaneous effect of targeted NIR-induced

hyperthermia and chemotherapy results in larger cell toxicities in a HeLa cervical cancer cell line at low drug concentrations, elucidating a synergistic effect. Furthermore, magnetic targeting additionally enhanced the therapeutic efficacy of the nanoplatforms. The cancerous cells were also imaged through MRI and confocal microscopy. Finally, preliminary *in vivo* studies using a mice-model highlighted the high accumulation of the nanoplatforms in the tumor area and, to much lesser extent, in the reticuloendothelium system (RES), as detected by fluorescence optical imaging. Strikingly, a relatively unexpected concentration of multifunctional nanoplatforms was also observed in the brain, which can open up the possibility of using these types of nanomaterials as specific theranostic nanodevices for diagnosis and treatment of brain diseases.

3.3 Materials and methods

3.3.1 Materials

Poly(D,L-lactide-*co*-glycolide) (PLGA) of different molecular weights (7-17 kDa; 24-38 kDa; 38-54 kDa and 40-75 kDa with 50:50 lactide–glycolide ratio; 4-14 kDa and 66-107 kDa with 75:25 lactide–glycolide ratio), poly-vinyl alcohol (PVA) with 88% hydrolyzation degree, Pluronic F127, hydrogen tetrachloroaurate (III) trihydrate ($HAuCl_4$), ascorbic acid, trisodium citrate dihydrate, sodium borohydride ($NaBH_4$, 99%), $FeCl_2$, $FeCl_3$ and ICG were purchased from Sigma–Aldrich (St. Louis, MO, USA). Low molecular weight chitosan (LMW-chitosan, M_W = 111 kDa*)* was purchased from Fluka (St. Louis, MO, USA). Oleic acid with 90% purity was purchased from Alfa Aesar (Karlshrue, Germany). DOXO HCl and fetal bovine serum (FBS) were purchased from Fisher Scientific (Pittsburgh, PA, USA). ProLong® Gold antifade reagent with DAPI and Dulbecco's modified eagle medium, fetal bovine serum (FBS), L-glutamine, penicillin/streptomycin, sodium pyruvate, and MEM non-essential amino acids (NEAA) were purchased from Invitrogen (Carlsbad, USA). Dialysis membrane tubing (molecular weight cutoff ~3500) was purchased from Spectrum Laboratories, Inc. (Rancho Dominguez, California). All other chemicals and solvents were of reagent grade (purchased from Sigma–Aldrich). HeLa

cervical cancer cells were from Cell Biolabs (San Diego, CA, USA). All glassware was washed with aqua regia and HF 5% (v/v) and extensively rinsed with water. Milli-Q grade water were used in all preparations.

3.3.2 Synthesis of SPIONs

Oleic acid-stabilized SPIONs were synthesized by a coprecipitation method. Briefly, aqueous solutions of 0.1 M $FeCl_3$ (30 mL) and $FeCl_2$ (15 mL) prepared with N_2 purged-water were mixed; then, 3 mL of 5 M ammonia solution were added in small aliquots of 0.6 mL while stirring. A black precipitate was formed indicating the formation of SPIONs. After 20 min of stirring under N_2 atmosphere, 56.4 mg of oleic acid were added to the SPIONs and the temperature was raised to 80 °C and kept for 30 min while stirring to evaporate the ammonia. The magnetic NPs were washed twice by centrifugation at 9000 rpm for 20 minutes to eliminate excess of oleic acid, the supernatant was discarded and the precipitate was lyophilized and stored at 4 °C [22, 23].

3.3.3 DXSP-PLGA-ICG NPs preparation

PLGA NPs containing SPIONs and DOXO (DXSP-PLGA NPs) were prepared using a conventional nanoprecipitation method with modifications. In a typical preparation, PLGA (25 mg) was dissolved in a sealed vial containing acetone (4 mL) together with suitable amounts of DOXO (previously converted to its hydrophobic base form by addition of triethylamine as reported in literature) [24] and SPIONs dispersed in acetone by sonication with a probe type sonicator (20 kHz, Bandelin Sonopuls, Bandelin GmbH, Berlin, Germany) at 20 W for 10 min in an ice bath. Then, this organic solution was added dropwise with a syringe pump (0.166 mL/min) to an aqueous solution (50 mL) containing Pluronic F127 (typically 1 wt. % if not otherwise stated) while stirring at 10 °C. After sonication at 100 W for 10 min in an ice bath to homogenize the resulting dispersion, the organic solvent was completely evaporated under mechanical stirring overnight, the dispersion subsequently centrifuged twice at 9000 rpm for 30 min and 20 ºC. Subsequently, the supernatant was removed and the final precipitate was resuspended in 5 mL of water.

ICG was complexed to the DXSP-PLGA NPs by electrostatic interactions with positively charged low molecular weight -chitosan (LMW-chitosan) displayed on the surface of the DXSP-PLGA NPs. First, 5 mL of DXSP-PLGA NPs suspension were mixed with 0.25 mL of 1 wt. % LMW-chitosan previously dissolved in 1% (v/v) acetic acid. After stirring for 4 h, DXSP-PLGA NPs were centrifuged twice at 9000 rpm for 30 min to eliminate free and loosely adsorbed chitosan. Then, the DXSP-PLGA NPs were mixed with 5 mg of ICG previously dissolved in 5 mL water and stirred 4 h at ambient temperature. Then, the sample was washed by centrifugation three times at 9000 rpm for 30 min at 20 ºC to eliminate excess of ICG, whose concentration in the supernatant was spectrophotometrically measured ir order to have an initial estimation of the ampunt of complexed dye. Subsequently, the supernatant was discharged and the pellet of DXSP-PLGA NPs with electrostatically bound ICG (DXSP-PLGA-ICG NPs) was redispersed in 5 mL of water, lyophilized and stored at 4 ºC.

3.3.4 Characterization of the NPs

NP sizes were obtained by dynamic light scattering (DLS) at 25 °C by means of an ALV-5000F (ALV-GmbH, Germany) instrument with vertically polarized incident light (λ = 488 nm) supplied by a diode-pumped Nd:YAG solid-state laser (Coherent Inc., CA, USA) operated at 2 W, and combined with an ALV SP-86 digital correlator (sampling time 25 ns to 100 ms). Experiment duration was in the range 5-10 min, and each experiment was repeated at least three times. The correlation functions from DLS runs were analyzed by the CONTIN method to obtain the intensity distributions of decay rates (Γ), from which the apparent diffusion coefficients ($D_{app} = \Gamma/q^2$, $q = (4\pi n_S/\lambda)\sin(\theta/2)$) were derived (being n_S the refractive index of solvent and θ the scattering angle). Values of the apparent hydrodynamic radius ($rh_{,app}$) were calculated from the Stokes-Einstein equation

$$r_{h,app} = kT/(6\pi\eta D_{app}) \qquad \text{(Eq 3.1)}$$

where k is the Boltzmann constant and η is the viscosity of water at temperature T. Sizes and morphologies of the NPs were also acquired by transmission and scanning electron microscopy (TEM and SEM, respectively) by means of a Phillips CM-12 and a Carl Zeiss Libra 200 Fm Omega (TEM), and a FESEM Ultra Plus electronic microscopes operating at 120 and 20 kV, respectively. Samples were prepared for analysis by evaporating a drop of the NP dispersion on a carbon-coated cooper grid without staining (TEM) or on a silicon wafer (SEM). NPs zeta potential was measured by triplicate with a Zetasizer Nano ZS (Malvern, UK), using disposable folded capillary cells. UV-Vis and fluorescence spectroscopy spectra of the particles were performed in a Cary 100 Bio and Cary Eclipse spectrophotometers (Agilent Technologies, Santa Clara, CA, USA), respectively. Each sample was measured three times, to ensure reproducibility, and averaged to produce a single spectrum. X-ray diffraction (XRD) experiments were carried out with a rotating anode X-ray generator (Siemens D5005, Germany). Twin Göbel mirrors were used to produce a well-collimated beam of CuKa radiation (λ = 1.5418 Å). X-ray diffraction patterns were recorded with an imaging plate detector (AXS F.Nr. J2–394).

The concentration of NPs was determined by viscometry. Dynamic viscosities of deionized water and polymeric NPs were measured with a capillary/rolling ball automated microviscometer (AMVn Microviscometer, Anton Paar, Austria). A rolling-ball viscometer consists of a computer-controlled stepper motor that rotates a capillary containing a ball immersed in the test fluid. The resistance to the gravitational pull on the ball is due to the fluid density and viscosity. The viscosity is determined by timing the ball rolling down a slope with a defined angle. Based on the rolling-ball principle the dynamic viscosity is defined by:

$$\eta = K_1(\theta)(\rho_B - \rho_S)t \qquad \text{(Eq 3.2)}$$

where $K_1(\theta)$ is the cell calibration constant depending on the angle θ, t is the rolling ball time, and ρ_B and ρ_S are the densities of the ball and sample, respectively.

The concentration of NPs was calculated from the solvent's and the sample's specific viscosities (Eq 3.3) (measured in triplicate) and the hydrodynamic radius of the NPs using the Einstein's viscosity relationship for spheres (Eq 3.4):

$$\eta_{sp} = 1 - \frac{\eta}{\eta_0} \qquad \text{(Eq 3.3)}$$

$$\eta_{sp} = 2.5\left(\frac{n_2}{V}\right)V_e \qquad \text{(Eq 3.4)}$$

where η is the sample's dynamic viscosity, η_0 is the solvent viscosity, $\frac{n_2}{V}$ is the number of equivalent spheres per volume unit, $Ve = \frac{4}{3}\pi R_e^2$ is the volume of an equivalent sphere, and R_e is the hydrodynamic radius of an equivalent sphere. The UV-vis absorption (turbidity) of different dilutions of NPs was measured and plotted versus the calculated concentrations to prepare a calibration curve, thus, NP concentrations could be calculated from UV-vis measurements.

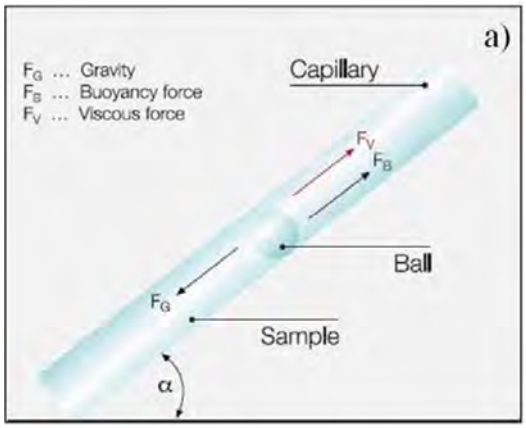

Figure 3.1: Diagram of the capillary/rolling ball measurement principle.

3.3.5 SPIONs, DOXO and ICG entrapment efficiency and loading/conjugation capacity

Content of SPIONs in DXSP-PLGA NPs was assessed by means of an inductively coupled plasma-mass spectroscopy (ICP-MS) equipment Varian 820-MS (Agilent Technologies). DXSP-PLGA NPs were dissolved in 500 µL of concentrated HNO_3 (68%) and the solution volume was raised to 5 mL with a 20% HNO_3 solution for total Fe quantification.

To exactly quantify the extent of DOXO loading and ICG conjugation, DXSP-PLGA-ICG NPs were weighted and dissolved in dimethylsulfoxide (DMSO). ICG

and DOXO fluorescence calibration curves were prepared prior to measurements to verify spectral characteristics, linearity range, and possible overlap between the spectra of the two compounds. Samples were placed in quartz-0.5 mL cuvettes, and measurements were performed immediately after preparation. DMSO was used as a blank for background correction. The excitation wavelengths were 760 nm for ICG and 490 nm for DOXO, respectively, and spectral emission readings were recorded in 1-nm intervals from 510 nm to 700 nm for DOXO and from 790 to 900 nm for ICG. All measurements and sample handling were done in reduced lighting conditions, and the instrument operating conditions were kept constant. The concentrations of ICG and DOXO were determined from the corresponding blank-subtracted reading at the peak emission wavelength, by using the previously obtained calibration curves of ICG and DOXO in DMSO. Drug loaded/conjugated, D.L., and entrapment efficiency, E.E., in the DXSP-PLGA-ICG NPs were calculated as follows:

$$D.L.\% = \frac{weight\ of\ DOXO,SPIONs\ or\ ICG\ in\ NPs}{weight\ of\ NPs} \times 100 \qquad \text{(Eq 3.5)}$$

$$E.E.\% = \frac{weight\ of\ DOXO,SPIONs\ or\ ICG\ in\ NPs}{weight\ of\ DOXO,SPIONs\ or\ ICG\ initially\ loaded} \times 100 \quad \text{(Eq 3.6)}$$

3.3.6 *In vitro* release kinetics

200 mg of DXSP-PLGA and PLGA/ICG NPs were resuspended either in 50 mL of phosphate-buffered saline (PBS), pH 7.4 or sodium citrate-citric acid buffer, pH 5.5, complemented with 10 % (v/v) of fetal bovine serum (FBS). For both ICG and DOXO, the total drug amount in the NPs was kept below 10% of the drug solubility limit in PBS in order to ensure sink conditions. The solubility limit of ICG in PBS is approximately 35 mg/mL, and for DOXO base below 1 mg/mL [25]. The suspension was divided into aliquots of 5 mL in tubes with a magnetic stirrer which were placed in a temperature controlled bath at 37 ºC and stirring speed of 100 rpm. The tubes were collected at regular time intervals and were centrifuged at 9000 rpm for 20 min, followed by lyophilization of the pellet for 36 h. Remaining drug (ICG and DOXO) in the polymeric NPs after release was measured by dissolving the nanoparticle pellet in DMSO for 24 h to release into solution. The percentage of ICG

and DOXO released from the NPs at a certain time interval was calculated by the following equation:

$$\% \text{ ICG or DOXO released} = 100 - (\% \text{ ICG or DOX remaining}) \quad \text{(Eq 3.7)}$$

3.3.7 Laser irradiation experiments

Temperature increment tests were performed with a continuous wave fiber-coupled diode laser source of 808 nm wavelength (50W, Oclaro Inc, San Jose, CA, USA). The laser was powered by a Newport 5700-80 regulated laser diode driver (Newport Corporation, Irvine, CA, USA). A 5 m-long, 200-μm-core optical fiber was used to transfer laser power from the laser unit to the target solution, and equipped with a lens telescope mounting accessory at the output, which allowed the tuning of the laser spot size in the range 1-10 mm. The output power was independently calibrated using an optical power meter (Newport 1916-C), and the laser spot size was previously measured with a laser beam profiler (Newport LBP-1-USB) placed at the same distance from the lens telescope output as the NP sample holder (8 cm). For measuring the temperature change mediated by the present hybrid NPs, 2 mL of hybrid DXSP-PLGA-ICG NPs were placed in a quartz cuvette and irradiated for determined time intervals and/or at different power intensities. The sample temperature was measured with a type J thermocouple linked to a digital thermometer inserted into the solution. Bare PLGA NPs in water were used as a control.

3.3.8 Magnetic resonance imaging and magnetic susceptibility

Transverse relaxation times were measured at 9.4 T (400 MHz) with 440 mT m^{-1} gradients and 25 ºC with a Bruker Biospin USR94/20 instrument (Ettlingen, Germany). MRI phantoms were constructed in 1.6 % (w/v) agarose solutions (Sigma–Aldrich) following a previously established experimental protocol [26]. Firstly, a 1.6% (w/v) agarose solution was heated and stirred at 80 ºC until complete dissolution of the solid agarose. Then, while the system was fluid, an array of seven centrifuge tubes (1.5 mL) were placed within the agarose, which was slowly cool down to room temperature. After solidification, the tubes were removed and an agarose mold with

seven holes was obtained. For cell imaging, HeLa cells ($2 \cdot 10^6$ cells) were seeded in 75 cm^2 flasks and cultured for 24 h at standard conditions (5% CO_2 at 37 ºC) in Dulbecco's Modified Eagle Medium (DMEM) supplemented with 10% (v/v) FBS, 2 mM L-glutamine, 1% penicillin/streptomycin, 1 mM sodium pyruvate, and 0.1 mM MEM Non-Essential Amino Acids (NEAA). Then, the medium was replaced with fresh one containing DXSP-PLGA-ICG NPs (4) and incubated for 6 h; then, the medium with NPs was removed and cells were washed with PBS and incubated for additional 18 h. Afterwards, cells were tripzinized and resuspended in 100 µL of PBS. In each hole of the phantom a mixture of cells labeled with DXSP-PLGA-ICG NPs and 2% (w/v) agarose was set. After a resting period, 1.6% (w/v) agarose was added to the mold to seal the phantom holes. Imaging of the phantoms was performed acquiring a 3D-gradient echo image (T_2-weighting) with the following parameters: field of view, 80×80×40 mm; matrix size: 512×512×256 points giving a spatial resolution of 156×156×156 µm; echo time TE = 7.89 ms and repetition time TR = 100 ms; flip angle 20 degree and 2 averages.

On the other hand, magnetic susceptibility measurements were carried out with a SQUID magnetometer (Quantum Design MPMS5, San Diego, CA, USA) at 5 and 300 K.

3.3.9 Cellular uptake

DXSP-PLGA-ICG NPs cellular uptake was followed by confocal microscopy by seeding HeLa cells on poly-L-lysine coated glass coverslips (12 ×12 mm) placed inside 6-well plates (3 mL, $5 \cdot 10^4$ cells/well) and grown for 24 h at standard culture conditions, as reported in the former section. Then, the DXSP-PLGA-ICG NPs at the desired concentration were added to cells (200 µL, ~ $5.0 \cdot 10^8$ particles/mL) and the incubation protocol was conducted as previously described. In some wells, a magnet of 0.5 T was placed below each individual well in order to study the possible effect of the applied magnetic field on partciles internalization. After 2 h of incubation the NP-containing cells were washed three times with PBS and, then, fixed with paraformaldehyde 4% (w/v) for 10 min, washed and stained with BODIPY Phalloidin (Invitrogen) in 0.2% (w/v) Triton X-100 (permeabilizer). The cells were washed again with PBS pH 7.4, mounted on glass slides and stained with ProLong Gold antifade

DAPI (Invitrogen) and cured for 24 h at -20 °C. Samples were visualized at 63X using a confocal spectral microscope Leica TCS-SP2 **(**LEICA Microsystems Heidelberg GmbH, Mannheim, Germany*;* green channel for DOXO, $\lambda_{exc.}$ 488 nm, and red channel for BODIPY Phalloidin, $\lambda_{exc.}$ 633 nm); blue channel for DAPI, $\lambda_{exc.}$ 355 nm,. A similar protocol was also performed to observe the internalization of the NPs following the fluorescence of ICG ($\lambda_{exc.}$ = 785 nm) without BODIPY Phalloidin to avoid overlapping of emissions.

3.3.10 *In vitro* cytotoxicity

Cytotoxicity induced by the nanoplatforms was determined by crystal violet staining as the inhibition of cellular growth. To this end, HeLa cells with an optical confluence of 80–90% were seeded into 96-well plates (100 µL, 1.5×10^4 cells/well) and grown for 24 h at standard culture conditions (5% CO_2 at 37 ºC) in Dulbecco's Modified Eagle Medium (DMEM) supplemented with 10% (v/v) FBS, 2 mM L-glutamine, 1% penicillin/streptomycin, 1 mM sodium pyruvate, and 0.1 mM MEM Non-Essential Amino Acids (NEAA). Afterwards, DXSP-PLGA-ICG NPs and corresponding controls (free DOXO, DOXO-loaded PLGA NPs and SP-PLGA-ICG NPs) were injected in the wells (100 µL) and incubated for 24 h and 48 h in the presence and absence of an apllied external field provided by a magnet (= 0.5 T) placed at the bottom of the wells. After incubation, the culture medium was discarded and the cells were washed with 10 mM PBS, pH 7.4, several times. The cells were shaken at room temperature (300 rpm, 15min) in the presence of 10 µL of a glutaraldehyde solution (11% (w/v) in water). The solution was discarded and cells were washed 3-4 times with milli-Q water. The cells were then shaken at room temperature (300 rpm, 15 min) in the presence of 100 µL of a crystal violet solution (0.1% (w/v) in 200 mM orthophosphoric acid, 200 mM formic acid, and 200 mM 2-N-morpholino-ethanesulfonic acid (MES), pH 6). The solution was discarded, and the cells were again washed 3-4 times with milli-Q water. Once washed, the cells were left for incubation at room temperature overnight for drying. Once dried, the cells were shaken at room temperature (300 rpm, 15 min) in the presence of 100 µL of acetic acid (10% (v/v) in water). Immediately after, the absorbance of the resulting solution was measured with a Microplate Reader (FLUOstar Optima, BMG Labtech

GmbH, Germany) operating at 595 nm. All experiments were triplicate carried out. The growth inhibition was quantified as:

$$\%\ \text{Inhibition} = 100 - \frac{100 * \text{OA}}{\text{TA}} \qquad \text{(Eq 3.8)}$$

where OA and TA stand for the absorbance of studied samples and negative controls (cells in the absence of NPs), respectively.

3.3.11 *In vivo* biodistribution

To assess the *in vivo* performance of the nanoparticles $3 \cdot 10^6$ cells from MDA-MB-231 adenocarcinome breast cell line [27] were injected in the dorsal flank of immunodeficient BALB/c nude mice. One week upon injection, cell implantation was checked by registering the fluorescent and bioluminescent activity of the cells. We next injected 10 mg/kg of either DXSP-PLGA-ICG NPs or free ICG in the tail vein and registered the *in vivo* fluorescent activity (λ_{exc} = 710 nm/λ_{em} = 840 nm) with a IVIS Spectrum imaging system (Caliper LifeSciences, Perkin-Elmer, USA) at 2, 4, 6, 24, 48 and 96 h upon NPs administration.

3.4 Results and discussion

3.4.1 Effect of synthesis variables on NPs characteristics

Factors such as particle size and surface properties could influence the circulation times, biodistribution, the interactions of NPs with cells and tissues and the ability to cross physiological drug barriers [28]. Hence, to design our nanoplatform we first establish the optimal physico-chemical properties of the PLGA core matrix. At this respect, the main aims are to control the PLGA NP size, their surface properties and the cargo release rate in order to achieve site-specific action of the active compound at the therapeutically optimal rate and dose regime, which are influenced by different parameters involved in the NP synthetic procedure (*i.e.*

molecular weight and concentration of PLGA chains, nature and concentration of the stabilizing agent, volumes of the oil and aqueous phases, and concentrations of cargo molecules, amongst others). Then, the influence of several of these parameters on the structural and physico-chemical properties of the bare PLGA NPs was firstly analyzed.

3.4.1.1 Effect of PLGA molecular weight and concentration

The effect of polymer molecular weight on the size and zeta potential of the resulting PLGA NPs was rather small, the NP diameters being largely determined by the primary size of the formed emulsion droplets (Table 3.1). On the other hand, an increase in PLGA concentration causes a significant increase in NPs diameters from 146 ± 4 nm at 10 mg/mL PLGA to 191 ± 5 nm at 100 mg/mL (Figure 3.2a) [29, 30]. Increasing the PLGA concentration enhances the viscous resistance of the emulsion mixture thereby absorbing the agitation energy which, in turn, leads to the reduction in shear stress and to droplets with larger size and, hence, to larger NPs. Also, a significant decrease in NP zeta potential values was noted from -23.5 ±0.9 mV at 10 mg/mL to −34.5 ±1.7 mV at 100 mg/mL, respectively. This decrease is consistent with the presence of more charged carboxylic groups of PLGA chains in the NPs, which ensures their colloidal stabilization.

Table 3.1: Sizes, polydispersity indexes (PDI) and zeta potential values of PLGA NPs obtained with several PLGA polymers of different molecular weights and composition at a polymer concentration of 10 mg/ml.

PL-GA Proportion	Mw (kDa)	r_h (nm)	PDI	Zeta Potential (mV)
50-50	7-17	82 ± 3	0.060	-28.3 ± 2.3
50-50	24-38	75 ± 4	0.045	-29.9 ± 1.4
50-50	38-54	81 ± 3	0.038	-31.5 ± 0.9
50-50	40-75	83 ± 2	0.061	-33.8 ± 1.9
75-25	4-15	75 ± 4	0.027	-22.0 ± 0.6
75-25	66-107	77 ± 4	0.021	-18.4 ± 1.1

3.4.1.2 Effect of organic and aqueous phases volumes

The effect of both organic and aqueous phase volumes (at constant polymer and stabilizer concentrations of 10 and 25 mg/mL, respectively) on the characteristics of the resulting NPs is shown in Fig. 3.2b-c.

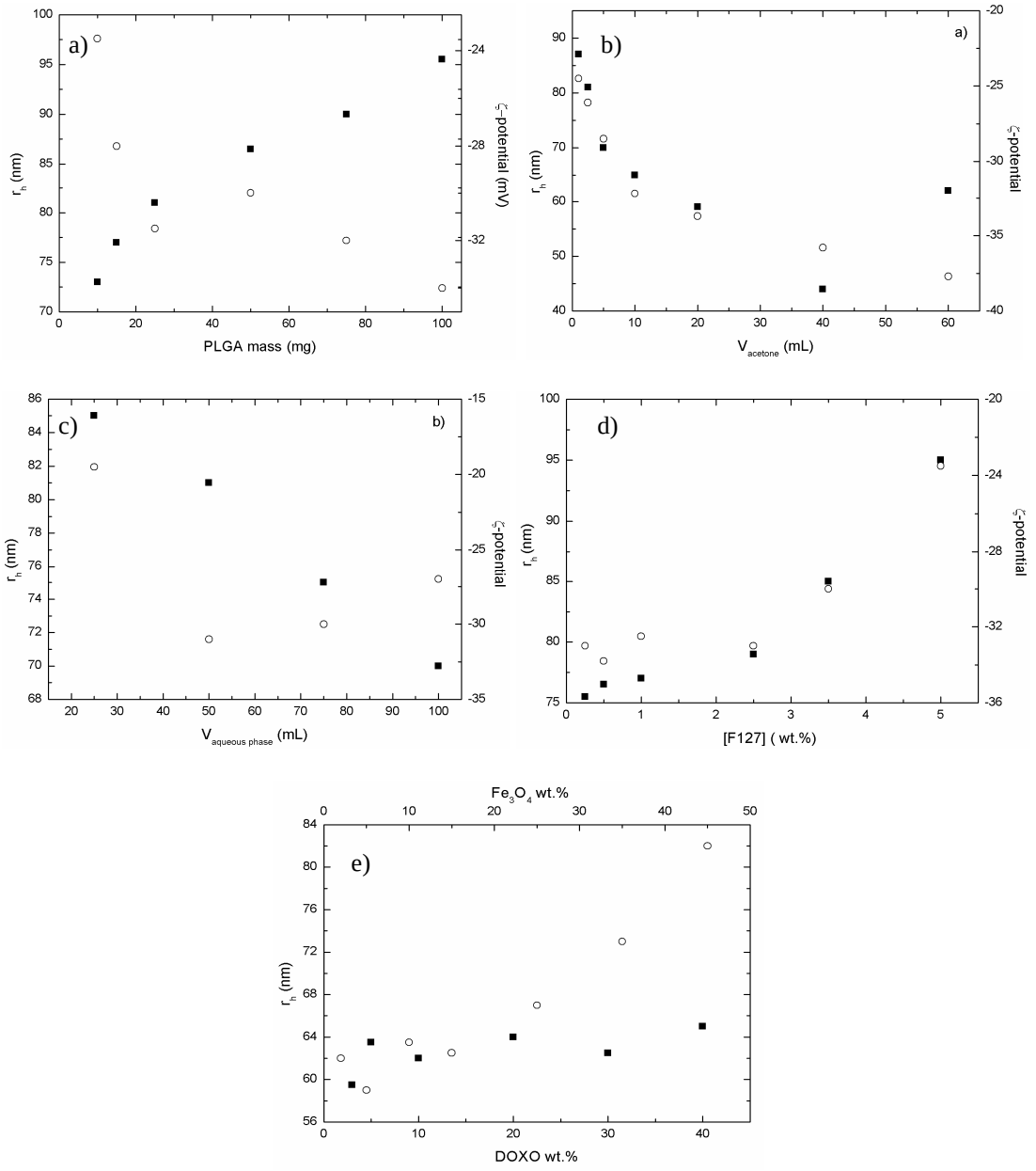

Figure 3.2: a) Effect of PLGA mass on the size (■) and zeta potential (○) of PLGA NPs. Effect of b) organic phase (acetone) and c) aqueous phase volumes on the size (■) and surface charge (○) of PLGA NPs. In b) $V_{aqueous\ phase}$ = 50 mL, and in c) $V_{acetone}$ = 2.5 mL. d) Effect of F127 stabilizer concentration on the size (■) and surface charge (○) of PLGA NPs ($V_{aqueous\ phase}$ = 50 mL, $V_{acetone}$ = 2.5 mL). e) Effect of DOXO (■) and SPIONs (○) loaded concentration on the size of the resulting DXSP-PLGA NPs.

An increase in both aqueous and organic phase volumes involved a reduction in both NP size and zeta potential. For the organic phase volume, the reduction in both size and zeta potential occurs up to a critical value (40 mL) provided the optimal diffusion of the PLGA polymer chains under such conditions, which favors the formation of smaller nanodroplets. Above such threshold value, the NP size started to increase from 90 ± 3 to 123 ± 6 nm due to the formation of reverse emulsion droplets of larger sizes.

3.4.1.3 Effect of type and concentration of stabilizer concentration

The increase in F127 stabilizer concentration slightly changed the average NP sizes from ca. 150 ± 9 to 162 ± 11 nm between 2.5 and 25 mg/mL of added F127; at larger F127 concentrations NP sizes increased up to ca. 190 ± 15 nm (Figure 3.2d). This effect can be ascribed to the enhancement of the aqueous solution viscosity, which results in a reduction of the net shear stress and the corresponding increase in particle size [31]. However, other researchers have reported the opposite effect [30-33] originated from the orientation of more stabilizer molecules in the interfacial area which decreases the interfacial tension and, hence, favours the formation of smaller droplets [34]. It seems clear that the observed effect must be a balanced of both opposite effects.

On the other hand, while increasing F127 concentration the zeta potential first slightly increases (from −33.8 ±1.8 mV at 2.5 mg/mL to −30.0 ±1.7 mV at 25 mg/mL) and, then, it steeply rises up to -23.5 ±1.2 mV at 50 mg/mL F127. This decrease in the net electric charge arises from the successive number of F127 layers on the PLGA NPs which progressively shield the carboxyl groups of PLGA chains (bare PLGA NPs have a zeta potential of ca. -45.0 ± 2.8 mV) [35, 36]. The type of stabilizer also had some influence on the physico-chemical properties of the resulting NPs. Under standard preparation conditions, F127-stabilized PLGA NPs display lower sizes than PVA-stabilized ones (Table 3.2). Such size reduction could stem from the amphiphilicity of the Pluronic copolymer, whose hydrophobic blocks might penetrate the core-shell NP interface and interact with the PLGA chains given rise to more compact NPs. As a consequence, the hydrophilic blocks would shield the carboxylic groups of PLGA chains to a lesser extent, as observed from the smaller

(more negative) zeta potential values found for F127-stabilized NPs. In addition, the purification process of the stabilizer excess also influenced the final size and charge of the resulting NPs (Table 3.2).

3.4.1.4 Effect of initially loaded DOXO and SPIONs

The particle size and zeta potential of PLGA NPs loaded with SPIONs and the chemotherapeutic drug DOXO (DXSP-PLGA NPs) was found to be smaller than that of bare polymeric NPs, and dependent on the molecular weight of the PLGA polymer (Table 3.3). The size NP reduction upon cargo incorporation can stem from a compactation of the PLGA core through the enhancement of hydrophobic interactions between PLGA chains, drug molecules and oleic acid chains anchored on the SPIONs surfaces [37]. This enhanced hydrophobic interactions inside the polymeric matrix might involve a PLGA chain reconfiguration while exposing additional hydrophilic charged carboxylic groups to the aqueous medium, giving rise to lower (more negative) zeta potential values [38].

Table 3.2: Effect of stabilizer type and purification process on the size and shape of DXSP-PLGA NPs at a stabilizer concentration of 10 mg/mL.

Stabilizer	Centrifugation cycle	r_h (nm)	Zeta Potential (mV)
F127	1	106 ± 6	-19.1 ± 1.2
F127	2	95 ± 5	-22.7 ± 1.5
PVA	1	114 ± 7	-8.8 ± 1.0
PVA	2	105 ± 6	-9.8 ± 0.7

On the other hand, the capability of the nanocarriers to entrap sufficient active drug concentration to exert their therapeutic activity is crucial for their clinical application. In this regard, as both the initial DOXO and SPIONs concentrations increase the entrapped amount of the respective cargos first rised and, then, reached a quasi-plateau region (Fig. 3.3). This behavior is favored by an enhanced cargo

miscibility inside the polymeric core promoting, at first, a larger incorporation in the organic phase.

Table 3.3: Sizes, polidispersities (PDI) and zeta potential values of DXSP-PLGA NPs obtained with several 50:50 PLGA polymers of different molecular weight and composition loaded with 10 wt.% DOXO and 2 wt.% Fe_3O_4 NPs at a polymer concentration of 10 mg/mL.

Mw (kDa)	**rh (nm)**	**PDI**	**Zeta Potential (mV)**
7-17	55.2 ± 0.7	0.030	-45.3 ± 3.2
24-38	60.7 ± 0.7	0.028	-47.6 ± 2.9
38-54	62.1 ± 1.0	0.030	-40.0 ± 2.1
40-75	77.0 ± 1.4	0.062	-33.9 ± 1.9

However, the increase in loading capacity (LC) is not proportional to the increase of initial drug content during formulation, thus, the entrapment efficiencies (EE) decreased. The maximum entrapped DOXO and SPIONs concentrations were found to be approximately of ca. 18 wt.% and ca. 9.5 wt.%, respectively. We have also noted an important increase in both LC and EE when co-loading both DOXO and SPIONs inside the PLGA matrix. For example, a drug EE of 95% and a LC of 8.9% was reached in the presence of 1.5 wt.% of oleic acid-stabilized SPIONs (as measured by ICP-MS), compared with a 39% EE and 3.2% LC when the SPIONs were not loaded inside the PLGA NPs. Provided that the drug content in NPs is affected by drug-polymer interactions and DOXO miscibility inside the polymeric matrix [39], it seems that the establishment of enhanced hydrophobic interactions between the different components inside the NPs would give rise to a synergistic effect which favours the enhanced solubilization ability of the present hybrid nanovehicle, as commented previously.

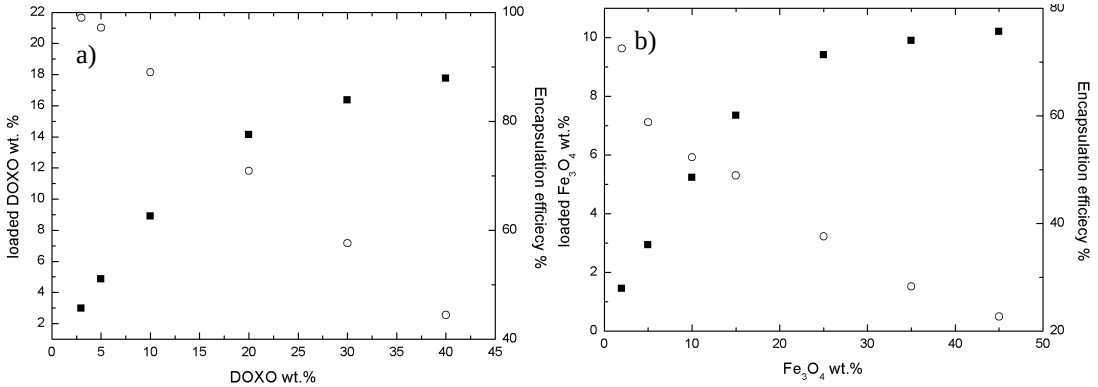

Figure 3.3: Loading capacity (■) and encapsulation efficiency (○) of PLGA NPs at different a) DOXO and b) SPIONs concentrations. In a), SPIONs concentration is kept constant at 5 wt.% whilst in b) DOXO concentration is fixed at 10 wt.%.

3.4.2 Standarization of DXSP-PLGA NPs

Based on previous results and looking for small particle sizes to enable a parenteral administration route of the NPs, avoidance of recognition by macrophages, elevated zeta potentials to ensure colloidal stability and high payloads when required, we standarized the preparation of DXSP-PLGA NPs. In this way, standardized NPs were usually prepared by taking 25 mg of PLGA, 2 and 10 wt. % initial SPIONs and DOXO concentrations, respectively, and dissolved in 5 mL of acetone. The organic phase was added dropwise in a 50 mL F127 solution (1 wt. %) under stirring. After a brief sonication step to homogenize the resulting dispersion, the organic solvent was left to evaporate under stirring, and the particles recovered and washed through several centrifugation cycles. Afterwards, by exploiting their negative surface charge the resulting particles were covered through electrostatic layer-by-layer attraction with a LMW-chitosan to reverse the net electrical charge of the particles (+15.2 ± 0.9 mV). Finally, ICG was complexed to the surface of the DXSP-PLGA NPs by electrostatic interactions too.

3.4.3 DXSP-PLGA-ICG NPs characterization

Oleic acid-stabilized SPIONs with a mean diameter of ca. 10 nm were obtained by a co-precipitation method (Figure 3.4a). The X-ray diffraction pattern of

the as-synthesized SPIONs clearly indicated that they are formed exclusively by magnetite (Fe_3O_4) (Figure 3.4b).

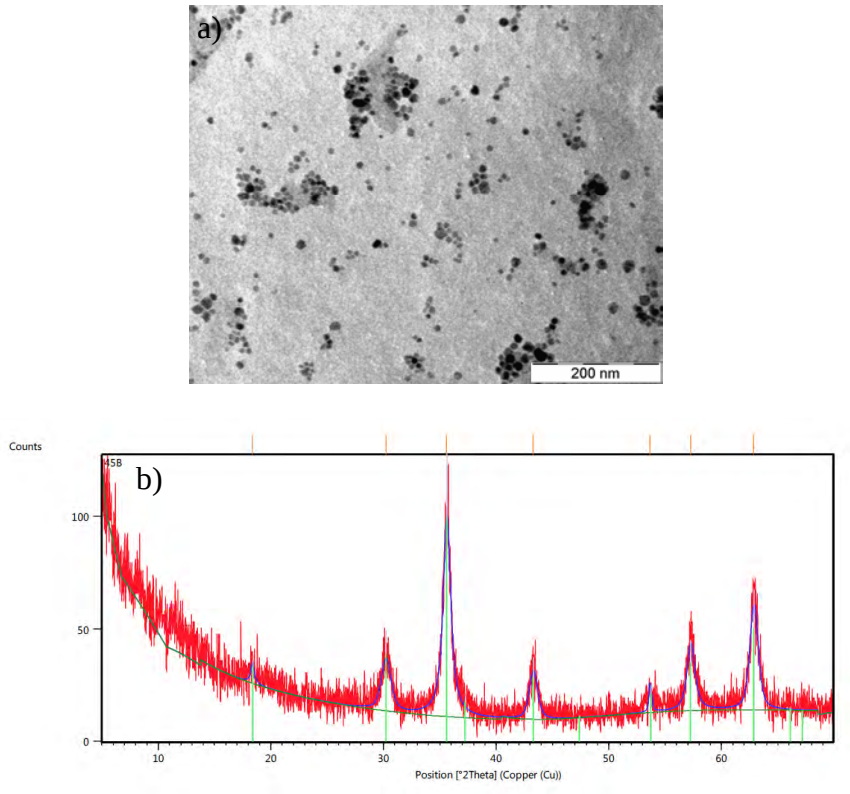

Figure 3.4: a) TEM image of oleic acid-stabilized Fe_3O_4 NPs; b) Powder X-ray diffractogram (XRD) of as-synthesised oleci acid stabilized Fe_3O_4 NPs. Green lines indicate the position of the characteristic peaks in the diffractogram whereas brown vertical lines denote the characteristic peaks of magnetite X-ray diffraction pattern.

The SPIONs appeared to uniformly assemble and distribute throughout the PLGA matrix (Figure 3.5a). This is believed to result from i) hydrophobic interactions between the oleic acid chains stabilizing the SPIONs, the drug molecules, and the PLGA chains; ii) hydrogen bonding between functional groups of the surfactant and polymeric chains, and/or iii) to existing dipole-dipole interactions between the entrapped SPIONs. The size of DXSP-PLGA NPs was estimated ca. 122 ± 11 nm by DLS with a surface electric charge of -35.3 ± 4.8 mV, which seems to be suitable for NPs passive tumor targeting through the enhanced permeability and retention effect (EPR) [40]. The successful incorporation of DOXO inside the hybrid NPs was corroborated by the appearance of absorption and fluorescence emission peaks at ca. 480 and 591 nm, respectively, consistent with the spectra of free DOXO (Figures 3.5b

and 3.5c). It is worth mentioning that the lower DOXO fluorescence in the NPs if compared to that of an equivalent amount of free DOXO stems from the self-quenching effect of the drug inside the polymeric matrix [41].

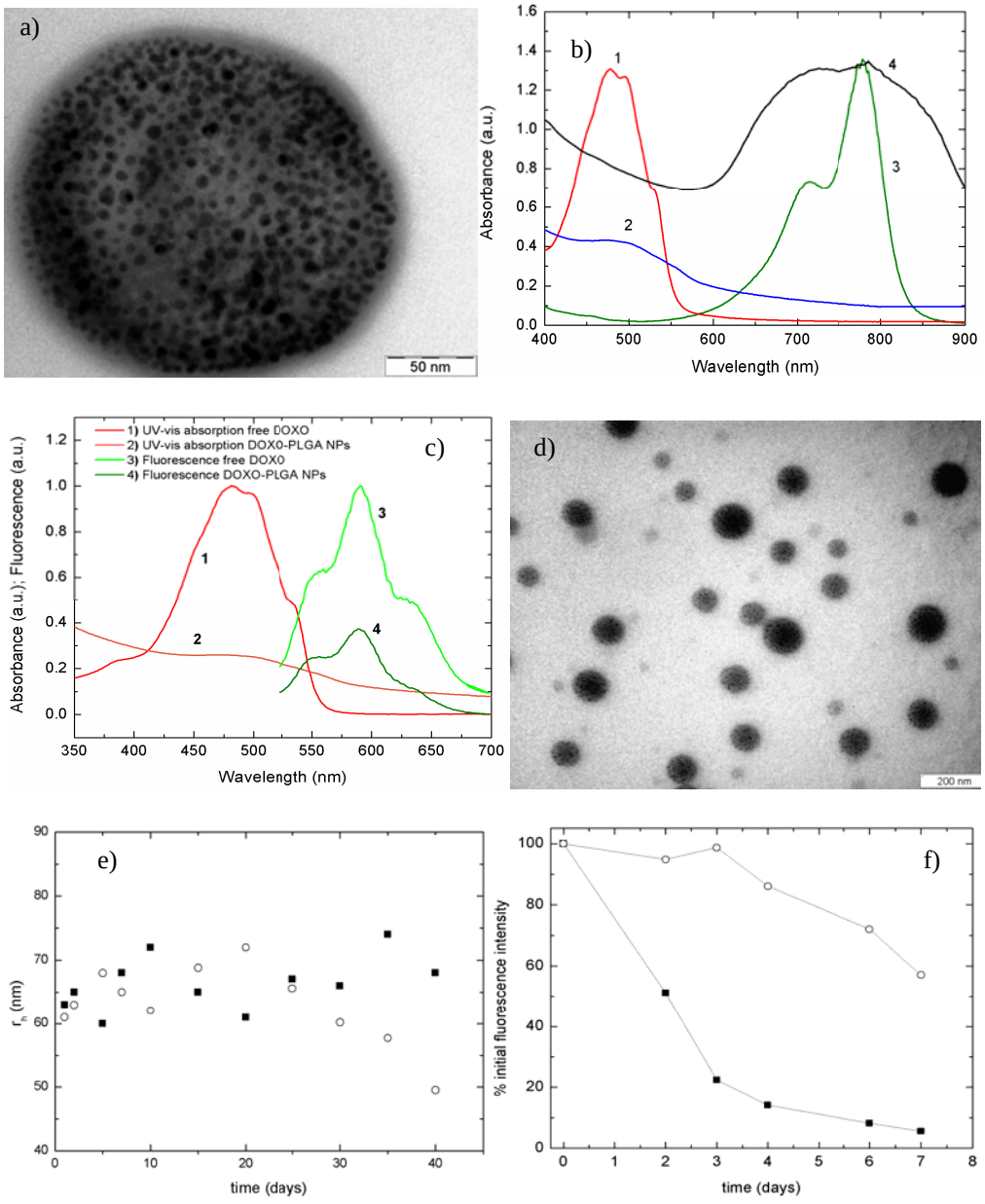

Figure 3.5: a) TEM image of a DXSP-PLGA NP. b) UV-Vis spectra of 1) free DOXO, 2) DXSP-PLGA NPs, 3) free ICG and 4) DXSP-PLGA-ICG NPs. c) Fluorescence emission spectra of free DOXO, free ICG, and DXSP-PLGA-ICG NPs at excitation wavelengths 490 nm and 760 nm. d) TEM image of DXSP-PLGA-ICG NPs. e) Size evolution of PLGA NPs in aqueous serum-containing (10% (v/v) FBS) medium of pH (■) 7.4 and (○) 5.5. f) Fluorescence stability of (■) free ICG and (○) ICG complexed to PLGA NPs. In f) lines are to guide the eye.

After coating the PLGA NP surface with LMW-chitosan, the estimated size of the hybrid NPs was ca. 135 ± 15 nm (114 ± 10 nm by TEM, Figure 3.5d), with a spherical shape and a zeta potential of ca. +15.2 ± 0.9 mV. The observed differences in size between DLS and TEM arise from the drying process and subsequent shrinkage polymeric chains underwent during TEM sample preparation. A negligible size variation was observed upon ICG complexation to give DXSP-PLGA-ICG hybrid NPs, which possessed a net zeta potential of -29.1 ± 2.5 mV pointing to the successful complexation of ICG molecules onto the NP surfaces. This was additionally corroborated by the appearance of a fluorescence emission peak for the hybrid NPs at ca. 820 nm, typical of ICG molecules (Figure 3.5c).

DXSP-PLGA-ICG NPs remained stable upon extensive incubation under serum containing medium of physiological pH as observed from the negligible changes in NP size which points to the capability of the F127 stealth layer to avoid protein binding and subsequent NP aggregation, in agreement with literature data [42]. By contrast, under acidic conditions the larger hydrolytic degradation rate of PLGA chains involved a slightly decrease in NP stability at the end of the incubation period as denoted by the decreases in NP sizes (Figure 3.5e). Additionally, we observed that the strong complexation of ICG to the nanoplatform surface protect ICG from degradation provided that after 7 days of incubation the fluorescence intensity of complexed ICG on the hybrid NPs remained nearly ca. 58 %, while the intensity of free ICG decreased up to 6 % of its initial intensity (Figure 3.5f) [43].

3.4.4 NIR-induced hyperthermia

Dyes that absorb energy in the near infrared region (NIR) will release heat following to exposure to the appropriate light wavelength, and this heat can contribute to malignant cell killing. Exposure of aqueous suspensions of DXSP-PLGA-ICG NPs to continuous NIR illumination at a laser power of 2.5 W/cm^2 for 5 min results in an elevation of solution mean temperature able to produce cytotoxic cell hyperthermia. No important temperature changes were observed when bare PLGA NPs were exposed to NIR light (Figure 3.6a). In contrast, aqueous dispersions of DXSP-PLGA-ICG NPs containing 1, 4 and 8 μM of ICG achieved temperature elevations of 4ºC, 8ºC and 14ºC, respectively. Due to photo- and thermal degradation, there existed a

slow temperature decline after 8 min of laser irradiation. Hence, at concentrations above 4 μM ICG hybrid NPs can be easily heated up above 45 ºC, which is sufficient to induce irreversible damage to tumor cells but not normal cells, probably as a consequence of protein denaturation and poor DNA synthesis and repair due to the comparatively lower oxygen level and pH in cancerous cells [44]. These results suggest that these nanoplatforms could act as efficient NIR-light absorbers for photothermal tumor therapy.

In addition, DXSP-PLGA-ICG NP dispersions achieved a more efficient laser-dependent temperature response than free ICG at similar concentrations [45]. The possible reasons for this behavior may arise from a higher condensed concentration of ICG molecules on the NP surfaces than free ICG, which results in a higher energy efficiency and lower heat dissipation after laser irradiation [46].

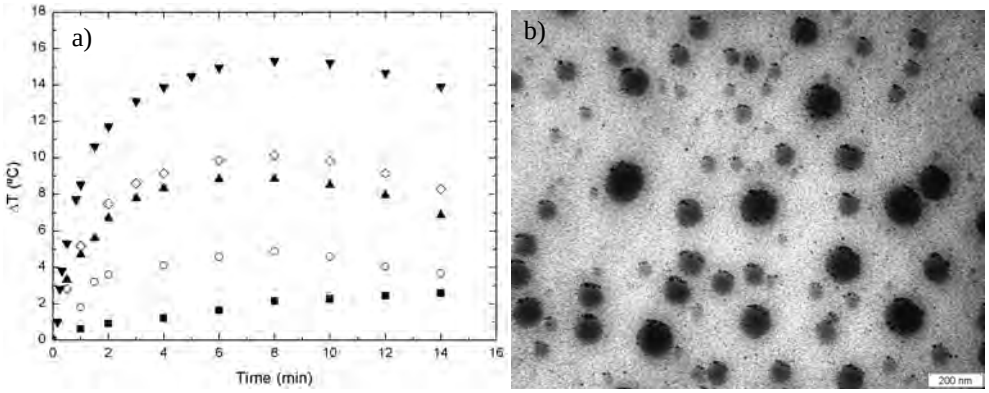

Fig. 3.6: a) Temperature increments as a function of time under NIR light irradition (2.5 W cm^{-2}, 5 min at 808 nm) for aqueous solutions of (■) bare PLGA NPs; (◇) 8 μM free ICG, and DXSP-PLGA-ICG NPs containing (○) 1, (▲) 4 (▼) and 8 μM conjugated-ICG. b) TEM image of DXSP-PLGA-ICG NPs after irradiation (2.5 W cm^{-2}, 5 min at 808 nm).

The morphology of the hybrid NPs after irradiation was, at least, partially conserved as observed by TEM images, where the nanoplatform morphology is still clearly observed (Figure 3.6b). Nevertheless, as a consequence of heating, drug molecules (see below) and some SPIONs were released; also, an enhaced SPIONs concentration near the PLGA matrix surface can be observed, probably as a result of partial melting of the polymeric core.

3.4.5 *In vitro* magnetic-resonance imaging

SPIONs have received great attention as T_2-contrast agents due to their capability to shorten spin-spin relaxation times which gives rise to decreases in the MRI signal intensity [47]. The specific weighted transverse-relaxivity (r_2) values can be greatly increased by clustering SPIONs in reservoirs, resulting in higher saturation magnetizations than individual particles owing to the interaction between the assembled nanocrystals [48,49]. In this line, the present nanoplatforms displayed robust magnetic properties. The magnetization as a function of the applied magnetic field at 5 and 300 K is shown in Figure 3.7a-b. At 5 K, the thermal energy is not sufficient to induce magnetic moment randomization, thus, the nanoconstructs show typical ferromagnetic hysteresis loops with a remanence of 17.5 emu g^{-1} and a coercivity of 254 ± 9 Oe. However, at 300 K the thermal energy is enough to randomize the magnetic moments leading to a decrease of the magnetization and to no remanence or coercivity, thereby, the hybrid NPs possess superparamagnetic behavior. The saturation magnetization μ_{sat} of the nanoplatforms at 300 K was 60.7 emu g^{-1}, which is higher than values reported for other Au-Fe_3O_4 or Au-γ-Fe_2O_3 [48, 49]. Also, the μ_{sat} of the nanoplatforms was observed to be lower than that of classical singly dispersed SPIONs possibly due to i) the diamagnetic mass of the polymer contributing to the total mass of the nanoplatforms, and ii) the presence of canted or noncollinear surface [50, 51].

To evaluate the potential T_2 enhancing capability of the present hybrid NPs, DXSP-PLGA-ICG NPs with various iron concentrations were investigated by T_2-weighted MR imaging at 9.4 T and 400 MHz. The Fe concentrations in the NPs were determined by ICP-MS. Fig. 3.7c shows the T_2-weighted MR images of the hybrid NPs in aqueous media at different Fe concentrations ranging from 0.01 to 0.17 mM. The signal intensity of the MR images decreased as the Fe concentration increased, as expected for T_2 contrast agents due to the shortening of spin-spin relaxation time of water, as commented previously. The specific relaxivity, r_2, a measure of the change in spin-spin relaxation rate (T_2^{-1}) per Fe unit concentration, was determined to be 255 mM $Fe^{-1}s^{-1}$ for DXSP-PLGA-ICG NPs. The relatively high r_2 value could be due to the large external magnetic field (9.4 T) applied to the nanoplatforms, as well as their superior magnetic properties due to the enhanced magnetic interactions between

clustered SPIONs inside the polymeric matrix. It is worth noting that the obtained r_2 value was higher than that of commercially T_2 MRI contrats agents based on functionalized Fe_3O_4 NPs such as Feridex/Endorem (r_2 = 160 mM $Fe^{-1}s^{-1}$), Resovist (r_2 = 151 mM $Fe^{-1}s^{-1}$) and Sinerem (r_2 = 160 mM $Fe^{-1}s^{-1}$) [54,55] and rather similar as that of other polymeric nanoplatforms embedding clustered SPIONs [13, 14, 52].

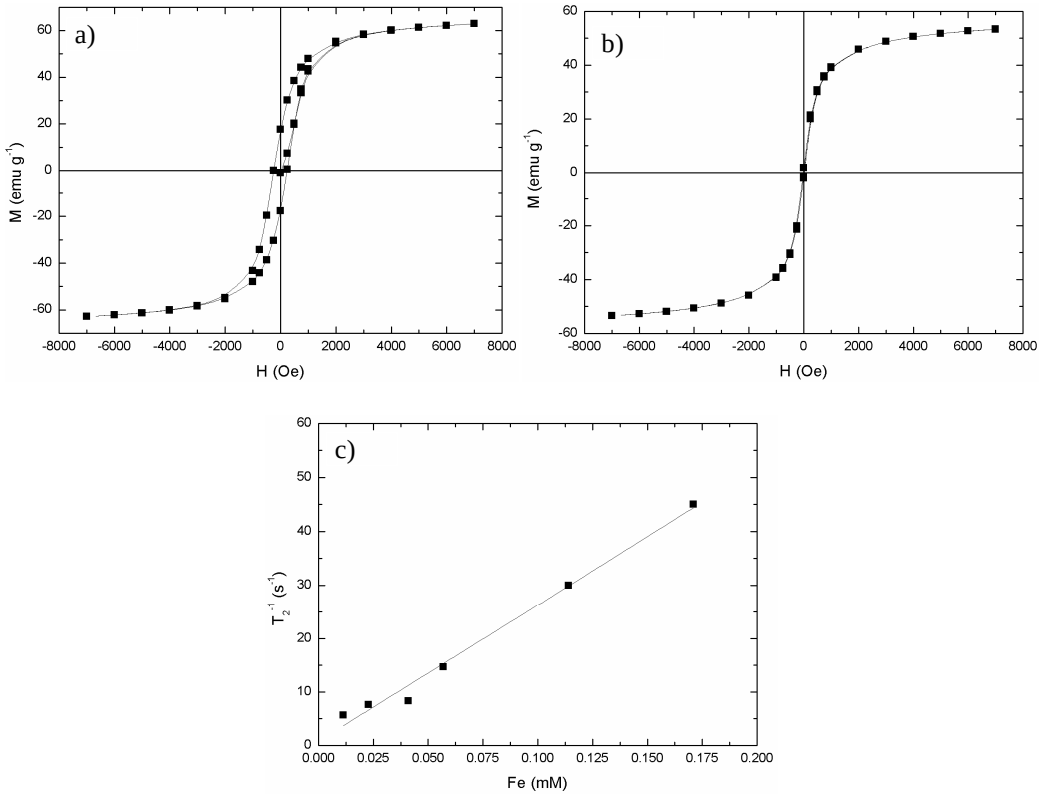

Figure 3.7: Magnetization as a function of applied magnetic field of DXSP-PLGA-ICG NPs at a) 5 K b) 300 K. c) Spin-spin relaxivity (r_2) of the hybrid NPs.

3.4.6 Release kinetics

DOXO release kinetics could be fine-tuned by simply changing the molecular weight of the PLGA core. The burst phase and, consequently, the amount of DOXO released at short incubation times may largely be increased by decreasing the molecular weight of the PLGA chains used to form the core of the polymeric NPs (Figure 3.8a). This behavior is related to the combination of several effects such as the decrease in the viscosity and compactation of the polymeric core, and a weakening of the hydrophobic interactions between PLGA chains and DOXO

molecules as the PLGA molecular weight decreases, which favors an enhanced mobility of drug molecules inside the PLGA core and a larger partition of DOXO molecules from the organic phase into the aqueous one. Hence, we decided to use PLGA NPs composed of a relatively large molecular weigth PLGA polymer (38-54000 Da) to reduce drug leakage during the burst phase. For this type of PLGA NPs, it has been shown that the cargo release typically occurs via a combination of diffusion and erosion [53] through hydrolysis of the ester bonds in the polymer backbone. Also, the PLGA copolymer configuring the reservoir for DOXO drug molecules shows a glass-transition temperature (T_g) of ca. 45 ºC, which reduces the drug leakage during circulation and release when needed, that is, in the vicinity of tumors where acidic hydrolysis of the polymeric matrix can be enhanced [54].

In vitro cumulative DOXO release profiles at both neutral and acidic conditions in the presence of 10% (v/v) FBS showed a burst followed by a much slower diffusion-inititated release pattern due to the concentration gradient (Figure 3.8b). At pH 7.4, ca. 17% DOXO was released from NPs during the first 5 h of incubation and, then, a more sustained release was observed, with ca. 38% released at 48 h. The DOXO release could be enhanced upon irradiation of the hybrid NPs with NIR light (2.5 W cm^{-2} for 5 min), achieving 21 and 54% after 5 and 48 h of incubation, respectively; this result confirmed that drug release from the present hybrid NPs can be controllable by NIR-laser irradiation. This enhancement can be a consequence of the larger diffusion of the drug through the polymeric matrix upon temperature elevation.

On the other hand, under acidic pH 5.5 DXSP-PLGA-ICG NPs released ca. 37% of the initially loaded DOXO during the first 5 h and ca. 58 % after 48 h of incubation, respectively. The faster release under acidic conditions is originated from the reprotonation of the amine group of DOXO, which involves an increase in its hydrophilicity and a decrease in the affinity for the hydrophobic chains. This, in turn, favors its escape from the NP core by an out-diffusion process through the core-shell structure whose diffusion rate depends on factors such as copolymer crystallinity, viscosity, and drug association state [55]. Also, the larger hydrolitic degradation rate of PLGA NPs at acidic pH might contribute to the faster release kinetics of DOXO observed under these conditions. The incomplete cumulative release of DOXO results from the combination of the relatively short time duration of the release study and an

enhancement of polymer–drug interactions, which make the NP matrix more rigid difficulting the drug release [56, 57].

It is plausible that polymeric NPs are passively targeted to the tumor tissue through the EPR effect with minimised DOXO release along circulation in the bloodstream. After accumulation in the vicinity of the tumor cells, DOXO could be selectively released from the DXSP-PLGA-ICG NPs in the acidic solid tumor microenvironment for passive cellular uptake [58]. More importantly, intact DXSP-PLGA-ICG NPs might be also taken up by tumor cells through nonspecific endocytosis and located preferentially at the acidic endosome compartments, in which the decreasing pH values might induce a faster DOXO release and a subsequent diffusion in the cytosol. This cellular uptake mechanism could bypass, to certain extent, the multidrug resistance (MDR) effect, which is often observed when free DOXO penetrates in the cell by passive diffusion.

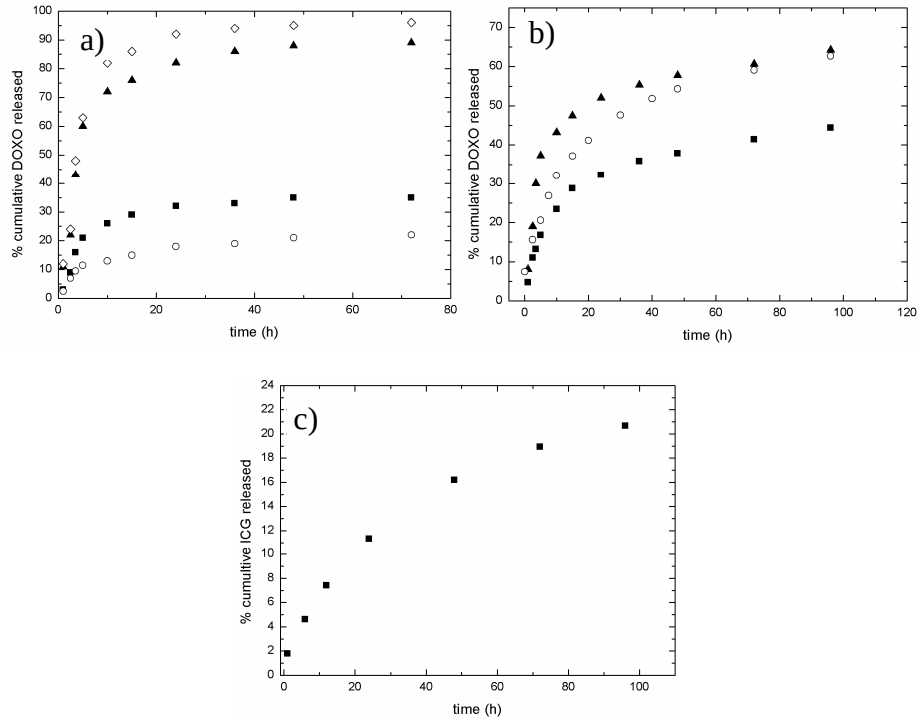

Figure 3.8: a) *In vitro* release kinetics of DOXO from DXSP-PLGA-ICG NPs of different copolymer molecular weight in aqueous serum-containing (10% (v/v) FBS) medium at pH 7.4. (○) 40-75; (■) 38-54; (▲) 24-38 and (◇) 7-17 kDa. b) *In vitro* release kinetics of DOXO from DXSP-PLGA NPs (PLGA M_w = 38-54000) in aqueous serum-containing (10% FBS) medium of pH 7.4 in the absence (■) and presence (○) of irradiation (2.5 W cm^{-2}, 5 min at 808 nm), and of pH (▲) 5.5. c) *In vitro* release kinetics of ICG from DXSP-PLGA-ICG NPs.

On the other hand, in the time course of the release experiments a low amount of ICG was noted to be released at either of the tested conditions, which points to the strength of the electrostatic interactions between the sulfonate and amine groups of the dye and LMW-chitosan chains adsorbed on the NP surface, respectively (Fig. 3.8c), as observed in related systems [59]. Meanwhile, a negligible release of SPIONs was observed under similar solution conditions.

3.4.7 *In vitro* cellular uptake

The uptake and cellular distribution of DXSP-PLGA-ICG NPs were analysed by confocal microscopy. After 2 h of cell incubation in the presence of DXSP-PLGA-ICG NPs gave rise to a granular fluorescence pattern mainly in the cytoplasm, in contrast to the continuous fluorescence pattern observed in cell nuclei upon administration of free DOXO [60, 61]. This observation might be originated, on one hand, from a relatively low amount of DOXO released from the hybrid NPs (as can be deduced from release studies, see Figure 3.8) and, on the other, from a different internalization pathway of the hybrid NPs if compared to free chemo-drug, in particular, through an endocytosis-mediated mechanism (Figure 3.9a-b). In this way, the DXSP-PLGA-ICG NPs would be initially located within the endosome vesicles and would release DOXO in the cytosol in a sustained manner due to the endosome acidic environment and the size limitation which prevents the NPs from traversing the nuclear pore complex and eventually impeding the drug to enter the cell nuclei afterwards.

The uptake of the hybrid NPs could be also easily followed by using the fluorescence emission of the complexed ICG dye in the nanoplatforms. The cell cytoplasm appears coloured due to the dye emission fluorescence signal, in this case in green due to the choice in the colour palette of the microscope. It is worth mentioning that a complete colocalization of both DOXO and ICG fluorescence signals is not uniformely present around cell nuclei. At this respect, it is necessary to bear in mind that DOXO fluorescence is largely enhanced when DOXO is released fropm the polymeric matix as a consequence of its self-quenching effect when inside the NPs [41]. In addition, some ICG molecules can be also released to the cytoplasm from the NPs and mainly bonded to intracellular proteins (glutathione S-transferase),

as observed from the more expanded green fluorescence pattern in some parts of the cell cytoplasm (Figure 3.9a-ii) [60]. Nevertheless, the present results fully demonstrated the possible use of the present hybrid nanoparticles as optical imaging agents [62].

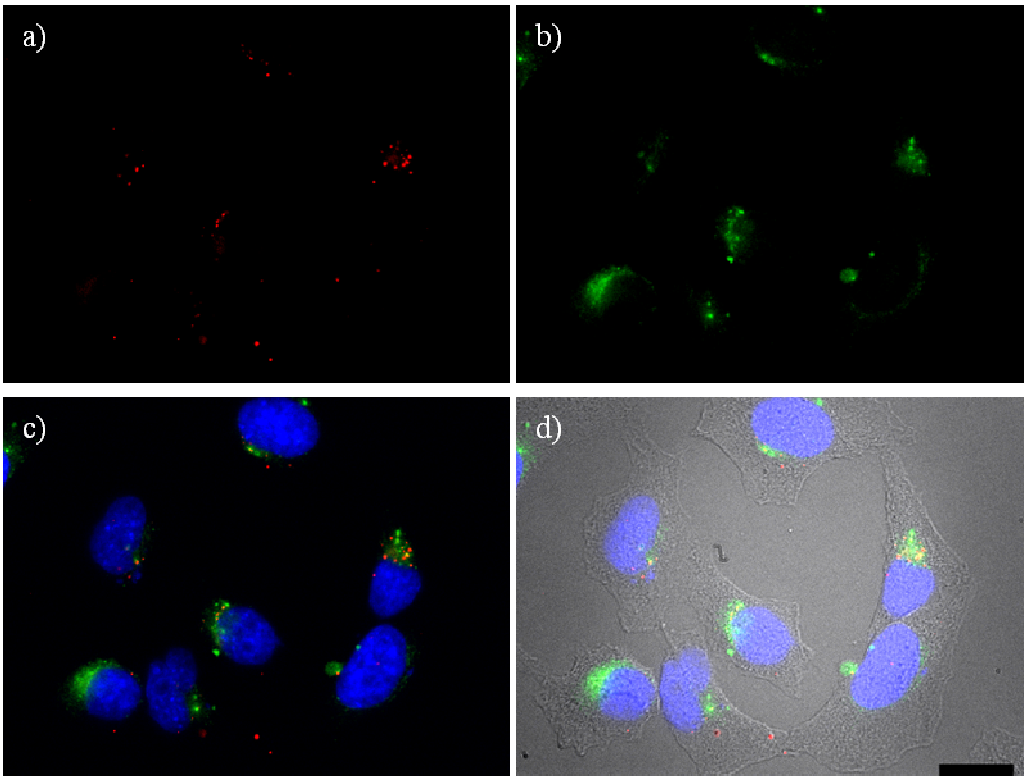

Figure 3.9: Fluorescence microscopy images of cellular uptake and intracellular distribution of DXSP-PLGA-ICG NPs. In all images HeLa cell nuclei is blue-stained with DAPI (λ_{exc} = 355 nm); a) DOXO fluorescence (red-coloured, λ_{exc} = 488 nm); b) ICG fluorescence (green-coloured, λ_{exc} = 712 nm); c) merged images of the three fluorescence channels; d) merged images plus bright field channel.

On the other hand, when an external magnetic field is applied to the cell culture an enhancement of DOXO fluorescence was also observed. The hybrid NPs then could be concentrated and attracted near the cancer cells by the external magnetic field, giving more chances to them to contact and internalize within the cells. The increase in fluorescence would then stem from the increase in NPs accumulated inside the cells, which effectively deliver larger amounts of the chemotherapeutic drug and increase its local concentration (Figure 3.10a). This fact is

additionally confirmed by T_2-weighted MR images obtained using a 9.4 T clinical MRI system on HeLa cells treated with the hybrid NPs in the presence of the applied external magnetic field. The image in the presence of the SPIONs-loaded hybrid NPs was darker than those obtained for untreated cells or cells treated with hybrid NPs in the absence of the applied magnetic field, further corroborating the efficacy of NP internalization by means of a magnetic-guided targeting strategy (Figure 3.10b).

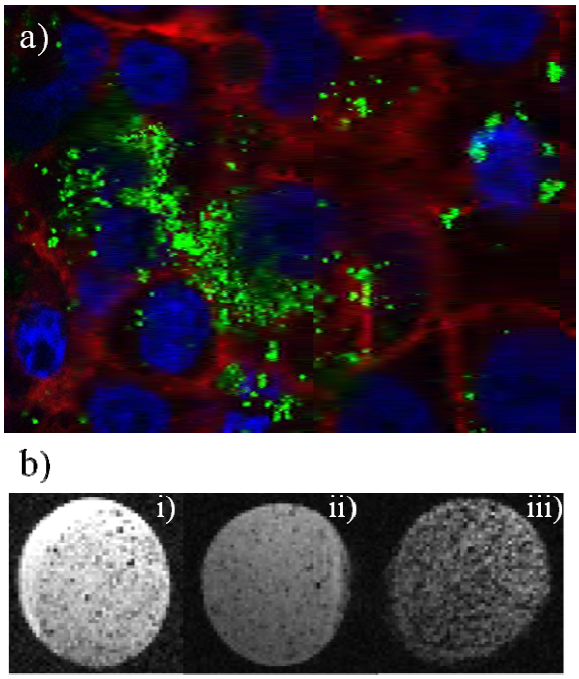

Figure 3.10: a) Confocal microscopy image of DXSP-PLGA-ICG NPs inside HeLa cells in the presence of an applied external magnetic field. Nuclei are blue-stained with DAPI, cystoplasm is stained with BODIPY-Phalloidin (in red), and DOXO fluorescence from the loaded NPs is colored in green. b) T_2-weighted MR images of i) untreated, and DXSP-PLGA-ICG NPs treated cells in the ii) absence and iii) presence of an external magnetic field.

3.4.8 *In vitro* cell viability

We further quantitatively evaluated the multidimensional therapeutic potential of the present hybrid NPs based on the combination of localized hyperthermia under ICG excitation by NIR laser irradiation and DOXO chemotherapy. HeLa cells were incubated with free DOXO, SPION-PLGA (SP-PLGA), SPION-PLGA-ICG (SP-PLGA-ICG), DOXO-SPION-PLGA (DXSP-PLGA) (as controls) and DXSP-PLGA-

ICG NPs for 24 and 48 h, and a crystal violet cell cytotoxicity assay was performed provided that DOXO can cause interferences with formazan crystals when using the standard MTT cell proliferation assay.

The concentration of free DOXO and DOXO loaded in the NPs was ca. 2.5 μM, and of ICG loaded in the NPs 4.0 μM, respectively. SP-PLGA NPs and SP-PLGA-ICG NPs exhibited negligible toxicity in HeLa cells in the absence of NIR irradiation. DXSP-PLGA NPs and DXSP-PLGA-ICG NPs displayed relatively similar cytotoxicities than free DOXO, being the former slightly more cytotoxic in the absence of irradiation after 48 h of incubation (Figure 3.11a). Intracellular NP-released DOXO concentration could be enhanced by circumventing the multidrug resistance (MDR) effect which can appear when administering as a free drug, hampering the drug action by pumping out drug molecules from cytosol to extracellular area [63]; also, an enhanced internalization of the hybrid NPs into cells through inespecific endocytosis migth be expected, while free DOXO is transported into cells by a passive diffusion mechanism [64]. In contrast, the DOXO concentration inside cells can be reduced by the sustained release of the drug from the NPs, which is more important at short incubation times. All of these opposite events then would led to a similar DOXO concentration in cells and close cytotoxicity of free DOXO, DXSP-PLGA and DXSP-PLGA-ICG NPs.

Cell cytotoxicity was significantly enhanced when NIR light of 2.5 W/cm^2 was irradiated for 5 min on HeLa cells treated with DXSP-PLGA-ICG NPs (60 and 74% after 24 and 48 h of incubation, respectively) compared with those cells bearing DXSP-PLGA or SP-PLGA-ICG NPs under similar illumination conditions (20 and 40% at 24 h of incubation, and 48 and 33% at 48 h, respectively, see Figure 3.11b). Therefore, it seems that the simultaneous combination of NIR hyperthermia ability provided by ICG and the chemotherapeutic action of DOXO can result in an enhanced cytotoxic effect. Apart for the inherent cytotoxicity provided by hyperthermia process (as denoted by the higher cytotoxicity found for SP-PLGA-ICG NPs in the presence of irradiation than in the absence), the observed larger cytotoxicity might be also caused by an altered kinetics, permeability and uptake of the chemotherapeutic agent during the heating process [65]. In this regard, the photothermal effect of ICG might help to partially melt the core of the PLGA polymeric matrix, releasing a larger amount of DOXO from DXSP-PLGA-ICG NPs (as observed in drug release

experiments, see Figure 3.8) for achieving an additional cytotoxic activity against the cancerous cell line. On the other hand, the cytotoxicity of DXSP-PLGA-ICG NPs was observed to be additionally enhanced (up to ca. 76 and 88% after 24 and 48 h of incubation) when an external magnetic field was applied to the cell culture, probably allowing concentration and NP attraction near the cells and, thereby, increasing the internalization of NPs and the localized release of DOXO inside cells inside cells and an enhanced photothermal response, as previously mentioned [66, 67].

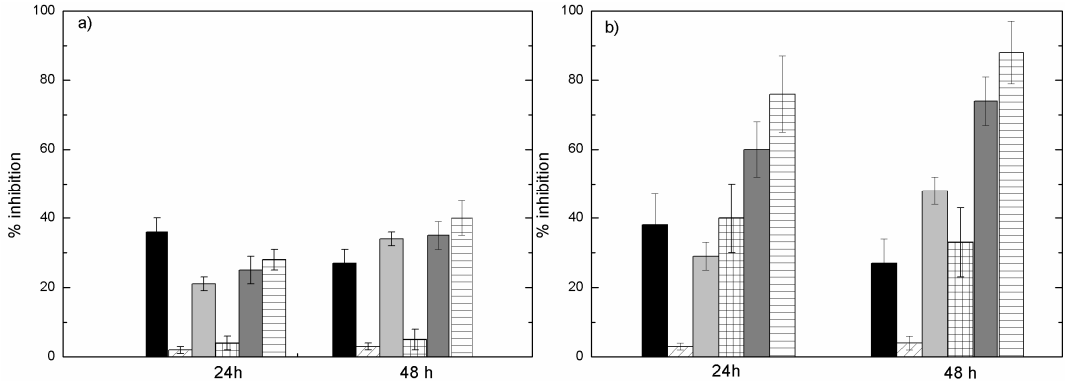

Figure 3.11: HeLa cell viabilities of free DOXO (black column), SP-PLGA NPs (stripped column), DXSP-PLGA NPs (light gray column), SP-PLGA-ICG NPs (squared column), DXSP-PLGA-ICG NPs (gray column) and DXSP-PLGA-ICG NPs in the presence of applied external magnetic field (sparse white column) a) in the absence and b) presence of continuous NIR light (808 nm) of 2.5 W cm^{-2} for 5 min. Data shown as mean ± SD (n=3).

3.4.9 Optical imaging *in vivo* and biodistribution

By exploiting the fluorescence imaging ability of the present hybrid NPs, we performed a first brief analysis of the *in vivo* biodistribution after intravenous injection (at the tail vein) of the present hybrid NPs in a tumor-bearing mice model through NIR fluorescence optical imaging utilizing the intrinsic and sensitive laser fluorescence of ICG. Accumulation of DXSP-PLGA-ICG NPs in the tumor region took place in a very short time interval (2 h) through the EPR effect. Surprisingly, a relatively important fluorescence intensity around the tumor area is still retained after 96 h post-injection (Figure 3.12); in contrast, a much lower fluorescence from free ICG administered as a control is observed due to its known blood instability and extremely short *in vivo* half-life (ca. 150-180 s)[68]. In fact, only traces of free ICG fluorescence were already detected after 48 h post-injection (image not shown).

Hence, it is clearly shown that the DXSP-PLGA-ICG NPs suitably stabilized ICG molecules avoiding their rapid photo-degradation and aqueous instability, and favoring a prolonged retention in the tumor through the EPR effect.

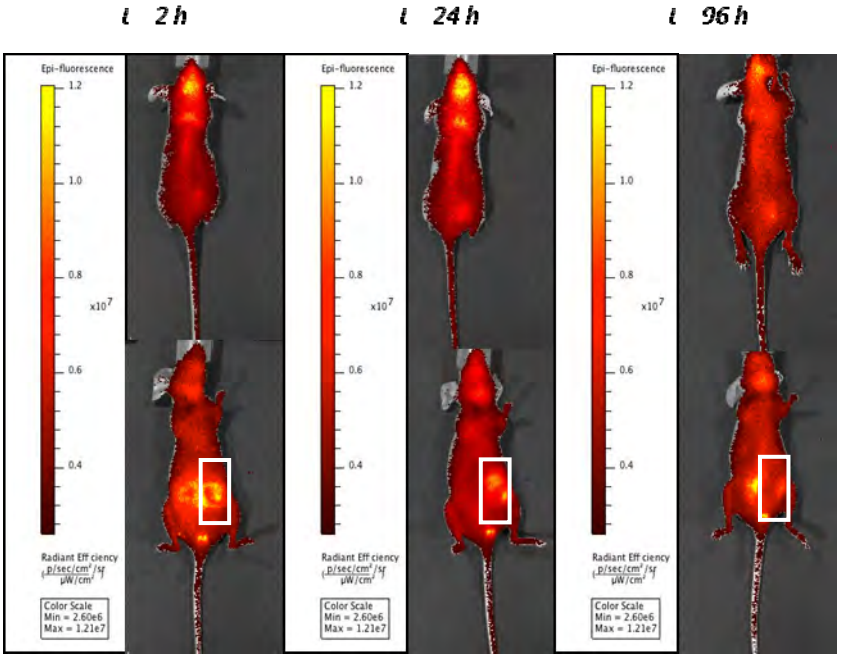

Figure 3.12: Time-lapse *in vivo* NIR images of MDA-MB-231 breast adenocarcinoma tumor-bearing mouse after intravenous tail injection of DXSP-PLGA-ICG NPs. The squared region denotes the tumor localization.

3-D image reconstruction of the fluorescence images also allowed to determine that the hybrid NPs are mainly eliminated through the reticulendothelial system (RES); in particular, NPs are observed to accumulated mainly in the spleen and, to lesser extent, in the liver (Fig. 3.13), with no traces in lungs at 6 h post-injection. At longer circulation times (96 h), the NP accumulation greatly reduces until completely disappear. From the fluorescence images, it can be also observed along the time interval analyzed some fluorescence in the bladder region. This might indicate that ICG can be partially dettached from the NPs by screening of electrostatic interactions between the dye and the polymeric NP surface; furthermore, it is also possible that some little fragments from the biodegraded NPs might be also excreted via renal clearance after polymer degradation in plasma and subsequent ICG released.

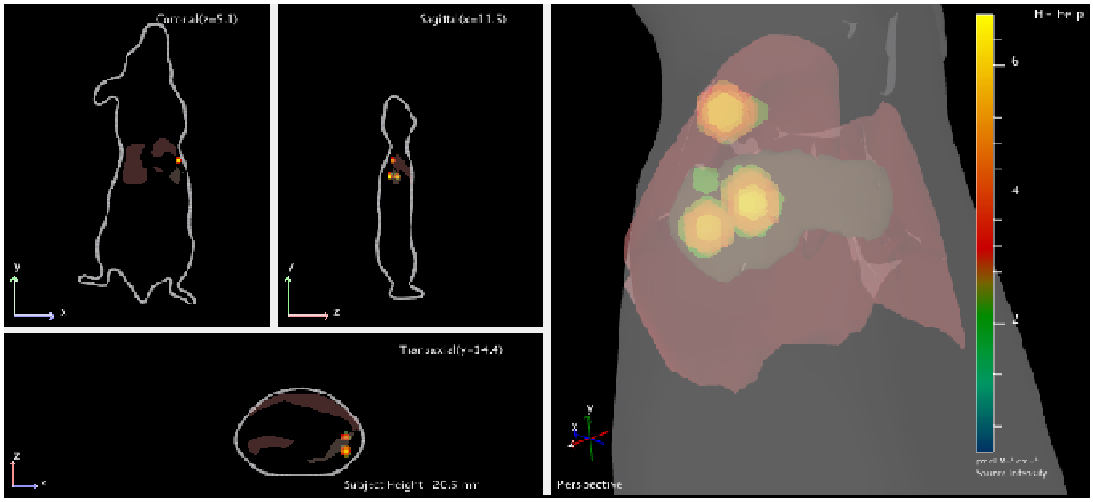

Figure 3.13: 3D-reconstructed fluorescence images of DXSP-PLGA-ICG NPs accummulation in the RES system after 6 h of incubation in a MDA-MB231 tumor-bearing mouse after intravenous tail injection of DXSP-PLGA-ICG NPs.

Finally, in the time scale of the experiments it can be also observed that there exists an important fluorescence signal from the hybrid NPs around the mice´s head which suggests they might accumulate in the brain area (Figure 3.12), thereby, possibly overcoming the blood brain barrier (BBB). Some previous studies have shown that surface NP coating is a key factor to overcome BBB and achieve successful brain delivery [69]. In this regard, Pluronic-F68 or polysorbate-coated PLGA NPs have been shown to effectively delivery DOXO to intracranial glioblastoma in rats [70]. through the enhanced adsorption of apolipoprotein A-I on the NP surface which interacts with the scavenger receptor SR-BI at the BBB endothelium, facilitating BBB crossing. By contrast, HSA or PVA-stabilized PLGA NPs were found to exert a negligible effect on tumor suppression [71]. Therefore, the surface F127/chitosan stabilizing adlayer of our hybrid NPs also seems to play an important role to promote brain accumulation in a similar way Pluronic F68 does, as might be expected due to the similar structural compositions of both Pluronic-type copolymers. However, a deeper study about the underlying mechanisms involving BBB overpassing and subsequent brain accumulation by the present hybrid NPs is being carried out, which might definitively opens up the possibility of using these type of particles not only as specific nanotheranostic nanodevices for diagnosis and treatment of brain tumors but also for their use in other brain pathologies such as as

Alzheimer´s or Parkinson´s neurodegenerative diseases, or cerebrovascular accidents as strokes.

3.5 Conclusions

In summary, the present results reveal that the possible combination of chemotherapy, magnetic targeting, and photothermal therapy through polymeric hybrid NPs is expected to significantly increase the likelihood and selectivity of cell killing and, potentially, to overcome resistance to chemotherapeutic agents making these particles a promising approach not only for cancer therapy but also for other neurodegenerative diseases such as Alzheimer´s or Parkinson´s diseases thanks to their ability to overcome the blood brain barrier. PLGA hybrid NPs might be guided to the tumor area by an applied magnetic field as observed *in vitro*, and the subsequent combination of NIR laser irradiation and chemotherapy at the tumor site would enhance their therapeutic effectiveness. The permeability of tumor vessels and the sensitivity of tumor cells toward chemotherapeutics should be greatly enhanced by hyperthemia, holding the promise of improving drug efficacy. Photothermal ICG-mediated therapy might facilitate triggered and instant drug release from the hybrid NPs, which is critical for achieving a high effective drug concentration in the tumor site. Moreover, one of the major advantages of NIR laser light as a source for localized hyperthermia is that light exposure is non-invasive and can be applied extracorporally compared with other types of hyperthermia like radiofrequency or microwave ablation. In addition, the magnetic and luminescent properties of the present hybrid NPs achieved through the simultaneous incoporation of Fe_3O_4 NPs and the fluorescent ICG dye in their nanostructure also allows, at the same time, their use as multimodal imaging diagnostic nanoplatforms able to follow their therapeutic response *in vivo*, configuring a good example of fully biocompatible and biodegradable theranostic nanodevices.

3.6 Bibliography

[1] Farokhzad OC, Langer R. Nanomedicine: Developing smarter therapeutic and diagnostic modalities. Advanced Drug Delivery Reviews. 2006;58:1456-9.

[2] Lee PY, Wong KYK. Nanomedicine: a new frontier in cancer therapeutics. . Current Drug Deliv. 2011;8:245-53.

[3] Heidel J, Davis M. Clinical Developments in Nanotechnology for Cancer Therapy. Pharm Res. 2011;28:187-99.

[4] Shen M, Huang Y, Han L, Qin J, Fang X, Wang J, et al. Multifunctional drug delivery system for targeting tumor and its acidic microenvironment. Journal of Controlled Release. 2012;161:884-92.

[5] Shenoy DB, Amiji MM. Poly(ethylene oxide)-modified poly(-caprolactone) nanoparticles for targeted delivery of tamoxifen in breast cancer. International Journal of Pharmaceutics. 2005;293:261-70.

[6] Alexis F, Pridgen E, Molnar LK, Farokhzad OC. Factors Affecting the Clearance and Biodistribution of Polymeric Nanoparticles. Molecular Pharmaceutics. 2008;5:505-15.

[7] Lü J-M, Wang X, Marin-Muller C, Wang H, Lin PH, Yao Q, et al. Current advances in research and clinical applications of PLGA-based nanotechnology. Expert Review of Molecular Diagnostics. 2009;9:325-41.

[8] Armentano I, Dottori M, Fortunati E, Mattioli S, Kenny JM. Biodegradable polymer matrix nanocomposites for tissue engineering: A review. Polymer Degradation and Stability. 2010;95:2126-46.

[9] Kumari A, Yadav SK, Yadav SC. Biodegradable polymeric nanoparticles based drug delivery systems. Colloids and Surfaces B: Biointerfaces. 2010;75:1-18.

[10] Danhier F, Ansorena E, Silva JM, Coco R, Le Breton A, Préat V. PLGA-based nanoparticles: An overview of biomedical applications. Journal of Controlled Release. 2012;161:505-22.

[11] Lübbe AS, Bergemann C, Huhnt W, Fricke T, Riess H, Brock JW, et al. Preclinical Experiences with Magnetic Drug Targeting: Tolerance and Efficacy. Cancer Research. 1996;56:4694-701.

[12] Lübbe AS, Bergemann C, Riess H, Schriever F, Reichardt P, Possinger K, et al. Clinical Experiences with Magnetic Drug Targeting: A Phase I Study with 4′-

Epidoxorubicin in 14 Patients with Advanced Solid Tumors. Cancer Research. 1996;56:4686-93.

[13] Yang J, Lee C-H, Park J, Seo S, Lim E-K, Song YJ, et al. Antibody conjugated magnetic PLGA nanoparticles for diagnosis and treatment of breast cancer. Journal of Materials Chemistry. 2007;17:2695-9.

[14] Kim J, Lee JE, Lee SH, Yu JH, Lee JH, Park TG, et al. Designed Fabrication of a Multifunctional Polymer Nanomedical Platform for Simultaneous Cancer- Targeted Imaging and Magnetically Guided Drug Delivery. Advanced Materials. 2008;20:478-83.

[15] Singh A, Dilnawaz F, Mewar S, Sharma U, Jagannathan NR, Sahoo SK. Composite Polymeric Magnetic Nanoparticles for Co-Delivery of Hydrophobic and Hydrophilic Anticancer Drugs and MRI Imaging for Cancer Therapy. ACS Applied Materials & Interfaces. 2011;3:842-56.

[16] Schleich N, Sibret P, Danhier P, Ucakar B, Laurent S, Muller RN, et al. Dual anticancer drug/superparamagnetic iron oxide-loaded PLGA-based nanoparticles for cancer therapy and magnetic resonance imaging. International Journal of Pharmaceutics. 2013;447:94-101.

[17] Lee S-M, Park H, Choi J-W, Park YN, Yun C-O, Yoo K-H. Multifunctional Nanoparticles for Targeted Chemophotothermal Treatment of Cancer Cells. Angewandte Chemie International Edition. 2011;50:7581-6.

[18] Lee S-M, Park H, Yoo K-H. Synergistic Cancer Therapeutic Effects of Locally Delivered Drug and Heat Using Multifunctional Nanoparticles. Advanced Materials. 2010;22:4049-53.

[19] Park H, Yang J, Lee J, Haam S, Choi I-H, Yoo K-H. Multifunctional Nanoparticles for Combined Doxorubicin and Photothermal Treatments. ACS Nano. 2009;3:2919-26.

[20] Watanabe Y, Kumon K. Assessment by pulse dye-densitometry indocyanine green (ICG) clearance test of hepatic function of patients before cardiac surgery: Its value as a predictor of serious postoperative liver dysfunction. Journal of cardiothoracic and vascular anesthesia. 1999;13:299-303.

[21] Desmettre T, Devoisselle JM, Mordon S. Fluorescence Properties and Metabolic Features of Indocyanine Green (ICG) as Related to Angiography. Survey of Ophthalmology. 2000;45:15-27.

[22] Li S, Ma Y, Yue X, Cao Z, Dai Z. One-pot construction of doxorubicin conjugated magnetic silica nanoparticles. New Journal of Chemistry. 2009;33:2414-8.

[23] Jain TK, Morales MA, Sahoo SK, Leslie-Pelecky DL, Labhasetwar V. Iron oxide nanoparticles for sustained delivery of anticancer agents. Mol Pharm. 2005;2:194-205.

[24] Jain TK, Richey J, Strand M, Leslie-Pelecky DL, Flask CA, Labhasetwar V. Magnetic nanoparticles with dual functional properties: Drug delivery and magnetic resonance imaging. Biomaterials. 2008;29:4012-21.

[25] Manchanda R, Fernandez-Fernandez A, Nagesetti A, McGoron AJ. Preparation and characterization of a polymeric (PLGA) nanoparticulate drug delivery system with simultaneous incorporation of chemotherapeutic and thermo-optical agents. Colloids and Surfaces B: Biointerfaces. 2010;75:260-7.

[26] Trekker J, Hodenius M, Soenen S, Van Roy W, De Cuyper M, Lagae L, et al. The effect of intracellular clustering on the stability and contrast generating properties of SPIOS: a comparison between PEGylated SPIOs and liposome SPIOs. Proc Intl Soc Mag Reson Med 2012. p. 4342.

[27] Iglesias P, Fraga M, Costoya JA. Defining hypoxic microenvironments by non-invasive functional optical imaging. European journal of cancer (Oxford, England : 1990). 2013;49:264-71.

[28] Feng S-S. New-concept chemotherapy by nanoparticles of biodegradable polymers: where are we now? Nanomedicine. 2006;1:297-309.

[29] Song X, Zhao Y, Hou S, Xu F, Zhao R, He J, et al. Dual agents loaded PLGA nanoparticles: Systematic study of particle size and drug entrapment efficiency. European Journal of Pharmaceutics and Biopharmaceutics. 2008;69:445-53.

[30] Song X, Zhao Y, Wu W, Bi Y, Cai Z, Chen Q, et al. PLGA nanoparticles simultaneously loaded with vincristine sulfate and verapamil hydrochloride: systematic study of particle size and drug entrapment efficiency. Int J Pharm. 2008;350:320-9.

[31] Benita S, Benoit JP, Puisieux F, Thies C. Characterization of drug-loaded poly(d,l-lactide) microspheres. Journal of Pharmaceutical Sciences. 1984;73:1721-4.

[32] Vandervoort J, Ludwig A. Biocompatible stabilizers in the preparation of PLGA nanoparticles: a factorial design study. International Journal of Pharmaceutics. 2002;238:77-92.

[33] Bilati U, Allémann E, Doelker E. Development of a nanoprecipitation method intended for the entrapment of hydrophilic drugs into nanoparticles. European Journal of Pharmaceutical Sciences. 2005;24:67-75.

[34] Galindo-Rodriguez S, Allémann E, Fessi H, Doelker E. Physicochemical Parameters Associated with Nanoparticle Formation in the Salting-Out, Emulsification-Diffusion, and Nanoprecipitation Methods. Pharm Res. 2004;21:1428-39.

[35] Sahoo SK, Panyam J, Prabha S, Labhasetwar V. Residual polyvinyl alcohol associated with poly (d,l-lactide-co-glycolide) nanoparticles affects their physical properties and cellular uptake. Journal of Controlled Release. 2002;82:105-14.

[36] Stolnik S, Dunn S, Garnett M, Davies M, Coombes AA, Taylor DC, et al. Surface Modification of Poly(lactide-co-glycolide) Nanospheres by Biodegradable Poly(lactide)-Poly(ethylene glycol) Copolymers. Pharm Res. 1994;11:1800-8.

[37] Ma Y, Liang X, Tong S, Bao G, Ren Q, Dai Z. Gold Nanoshell Nanomicelles for Potential Magnetic Resonance Imaging, Light-Triggered Drug Release, and Photothermal Therapy. Advanced Functional Materials. 2013;23:815-22.

[38] Astete CE, Kumar CSSR, Sabliov CM. Size control of poly(d,l-lactide-co-glycolide) and poly(d,l-lactide-co-glycolide)-magnetite nanoparticles synthesized by emulsion evaporation technique. Colloids and Surfaces A: Physicochemical and Engineering Aspects. 2007;299:209-16.

[39] Panyam J, Williams D, Dash A, Leslie-Pelecky D, Labhasetwar V. Solid-state solubility influences encapsulation and release of hydrophobic drugs from PLGA/PLA nanoparticles. Journal of Pharmaceutical Sciences. 2004;93:1804-14.

[40] Acharya S, Sahoo SK. PLGA nanoparticles containing various anticancer agents and tumour delivery by EPR effect. Advanced Drug Delivery Reviews. 2011;63:170-83.

[41] Savić R, Luo L, Eisenberg A, Maysinger D. Micellar Nanocontainers Distribute to Defined Cytoplasmic Organelles. Science. 2003;300:615-8.

[42] Zweers MLT, Engbers GHM, Grijpma DW, Feijen J. In vitro degradation of nanoparticles prepared from polymers based on dl-lactide, glycolide and poly(ethylene oxide). Journal of Controlled Release. 2004;100:347-56.

[43] Kirchherr A-K, Briel A, Ma der K. Stabilization of Indocyanine Green by Encapsulation within Micellar Systems. Molecular Pharmaceutics. 2009;6:480-91.

[44] Paiva M, Castro DJ, Bublik M, Sercarz J. Laser-Induced Thermal Therapy for Recurrent Head and Neck Cancer: A Comprehensive Review.: 50. Journal of Investigative Medicine. 2006;54:S381-S2 10.2310/6650.2005.x0015.

[45] Zheng X, Zhou F, Wu B, Chen WR, Xing D. Enhanced Tumor Treatment Using Biofunctional Indocyanine Green-Containing Nanostructure by Intratumoral or Intravenous Injection. Molecular Pharmaceutics. 2012;9:514-22.

[46] Zheng M, Yue C, Ma Y, Gong P, Zhao P, Zheng C, et al. Single-Step Assembly of DOX/ICG Loaded Lipid–Polymer Nanoparticles for Highly Effective Chemo-photothermal Combination Therapy. ACS Nano. 2013;7:2056-67.

[47] Weissleder R. A clearer vision for in vivo imaging. Nat Biotech. 2001;19:316-7.

[48] Kim J, Park S, Lee JE, Jin SM, Lee JH, Lee IS, et al. Designed Fabrication of Multifunctional Magnetic Gold Nanoshells and Their Application to Magnetic Resonance Imaging and Photothermal Therapy. Angewandte Chemie International Edition. 2006;45:7754-8.

[49] Gole A, Stone JW, Gemmill WR, zur Loye H-C, Murphy CJ. Iron Oxide Coated Gold Nanorods: Synthesis, Characterization, and Magnetic Manipulation. Langmuir. 2008;24:6232-7.

[50] Shevchenko EV, Bodnarchuk MI, Kovalenko MV, Talapin DV, Smith RK, Aloni S, et al. Gold/Iron Oxide Core/Hollow-Shell Nanoparticles. Advanced Materials. 2008;20:4323-9.

[51] Mørup S. Spin-canting and transverse relaxation at surfaces and in the interior of ferrimagnetic particles. Journal of Magnetism and Magnetic Materials. 2003;266:110-8.

[52] Niu C, Wang Z, Lu G, Krupka TM, Sun Y, You Y, et al. Doxorubicin loaded superparamagnetic PLGA-iron oxide multifunctional microbubbles for dual-mode US/MR imaging and therapy of metastasis in lymph nodes. Biomaterials. 2013;34:2307-17.

[53] Zolnik BS, Leary PE, Burgess DJ. Elevated temperature accelerated release testing of PLGA microspheres. Journal of Controlled Release. 2006;112:293-300.

[54] Göpferich A. Mechanisms of polymer degradation and erosion. Biomaterials. 1996;17:103-14.

[55] Forrest ML, Won C-Y, Malick AW, Kwon GS. In vitro release of the mTOR inhibitor rapamycin from poly(ethylene glycol)-b-poly(ε-caprolactone) micelles. Journal of Controlled Release. 2006;110:370-7.

[56] Budhian A, Siegel SJ, Winey KI. Production of haloperidol-loaded PLGA nanoparticles for extended controlled drug release of haloperidol. Journal of Microencapsulation. 2005;22:773-85.

[57] Ubrich N, Bouillot P, Pellerin C, Hoffman M, Maincent P. Preparation and characterization of propranolol hydrochloride nanoparticles: a comparative study. Journal of Controlled Release. 2004;97:291-300.

[58] Lee Y, Park SY, Mok H, Park TG. Synthesis, Characterization, Antitumor Activity of Pluronic Mimicking Copolymer Micelles Conjugated with Doxorubicin via Acid-Cleavable Linkage. Bioconjugate Chemistry. 2007;19:525-31.

[59] Lee C-H, Cheng S-H, Wang Y-J, Chen Y-C, Chen N-T, Souris J, et al. Near-Infrared Mesoporous Silica Nanoparticles for Optical Imaging: Characterization and In Vivo Biodistribution. Advanced Functional Materials. 2009;19:215-22.

[60] Zheng C, Zheng M, Gong P, Jia D, Zhang P, Shi B, et al. Indocyanine green-loaded biodegradable tumor targeting nanoprobes for in vitro and in vivo imaging. Biomaterials. 2012;33:5603-9.

[61] Cambon A, Rey-Rico A, Mistry D, Brea J, Loza MI, Attwood D, et al. Doxorubicin-loaded micelles of reverse poly(butylene oxide)-poly(ethylene oxide)-poly(butylene oxide) block copolymers as efficient "active" chemotherapeutic agents. Int J Pharm. 2013;445:47-57.

[62] Verdière AC, Dubernet C, Nemati F, Poupon MF, Puisieux F, Couvreur P. Uptake of doxorubicin from loaded nanoparticles in multidrug-resistant leukemic murine cells. Cancer Chemother Pharmacol. 1994;33:504-8.

[63] Minko T, Kopeckova P, Pozharov V, Kopecek J. HPMA copolymer bound adriamycin overcomes MDR1 gene encoded resistance in a human ovarian carcinoma cell line. Journal of controlled release : official journal of the Controlled Release Society. 1998;54:223-33.

[64] Yoo HS, Lee KH, Oh JE, Park TG. In vitro and in vivo anti-tumor activities of nanoparticles based on doxorubicin–PLGA conjugates. Journal of Controlled Release. 2000;68:419-31.

[65] Hauck TS, Jennings TL, Yatsenko T, Kumaradas JC, Chan WCW. Enhancing the Toxicity of Cancer Chemotherapeutics with Gold Nanorod Hyperthermia. Advanced Materials. 2008;20:3832-8.

[66] Silva AK, Silva EL, Carrico AS, Egito ES. Magnetic carriers: a promising device for targeting drugs into the human body. Current pharmaceutical design. 2007;13:1179-85.

[67] Oliveira H, Perez-Andres E, Thevenot J, Sandre O, Berra E, Lecommandoux S. Magnetic field triggered drug release from polymersomes for cancer therapeutics. Journal of controlled release : official journal of the Controlled Release Society. 2013.

[68] Saxena V, Sadoqi M, Shao J. Polymeric nanoparticulate delivery system for Indocyanine green: Biodistribution in healthy mice. International Journal of Pharmaceutics. 2006;308:200-4.

[69] Kreuter J, Ramge P, Petrov V, Hamm S, Gelperina SE, Engelhardt B, et al. Direct evidence that polysorbate-80-coated poly(butylcyanoacrylate) nanoparticles deliver drugs to the CNS via specific mechanisms requiring prior binding of drug to the nanoparticles. Pharm Res. 2003;20:409-16.

[70] Gelperina S, Maksimenko O, Khalansky A, Vanchugova L, Shipulo E, Abbasova K, et al. Drug delivery to the brain using surfactant-coated poly(lactide-co-glycolide) nanoparticles: influence of the formulation parameters. European journal of pharmaceutics and biopharmaceutics : official journal of Arbeitsgemeinschaft fur Pharmazeutische Verfahrenstechnik eV. 2010;74:157-63.

[71] Wohlfart S, Khalansky AS, Gelperina S, Maksimenko O, Bernreuther C, Glatzel M, et al. Efficient chemotherapy of rat glioblastoma using doxorubicin-loaded PLGA nanoparticles with different stabilizers. PLoS One. 2011;6:e19121.

CHAPTER IV - Simple Control of Surface Topography of Gold Nanoshells by a Surfactant-less Seeded-Growth Method

4.1 Summary

In this chapter, we report the synthesis of branched gold nanoshells (BGNS) through a seeded-growth surfactant-less method. This was achieved by decorating PLGA NPs with Au seeds (NP-seed), using chitosan as an electrostatic self-assembling agent. Branched shells with different degrees of anisotropy and optical response were obtained by modulating the ratios of $HAuCl_4/K_2CO_3$ growth solution, ascorbic acid (AA) and NP-seed precursor. Chitosan and AA were crucial in determining the BGNS size and structure, acting both as co-reductants and structure directing growth agents. Preliminary cytotoxicity experiments points to the biocompatibility of the obtained BGNS, allowing their potential use in biomedical applications. In particular, these nanostructures with "hybrid" compositions which combine the features of gold nanoshells and nanostars then can hold important potential applications as multifunctional nanoteranostic devices.

4.2 Introduction

The obtention of metal nanoparticles (NPs) through highly efficient and controlled synthetic methodologies has been a very active area of research during the past two decades due to their unique size- and shape- dependent properties [1-6]. In particular, gold (Au) NPs exhibit remarkable optical properties due to their localised surface plasmon resonance (LSPR) absorption with peak positions which are largely dependent on the NP size, shape, composition and the dielectric constant of the medium [7]. Also, the strong electromagnetic field generated by LSPR excitation can drastically enhance the fluorescence and Raman signals of nearby molecules [8-11]. Hence, all these extraordinary properties have increased the potential applications of these nanoscaled materials in different fields such as in catalysis [12, 13], photonics [14-16], sensing [17-20] or nanomedicine [21-24], amongst others.

Au NPs have been produced to different shapes, such as spheres [25-27], rods [28-30], prisms [31], cubes [32], plates [33], nanoshells [34], hollow [35, 36] and branched [6, 37, 38] NPs. Non-spherical NPs and nanoshells can exhibit, for example, important shifts of their LSPR bands to the red and near-infrared region (NIR) of the

electromagnetic spectrum. Thanks to their great energy absorption capabilities they can generate considerable heat under red and NIR irradiation becoming excellent photothermal agents; moreover, they possess unique catalytic and Surface Enhanced Raman Spectroscopy (SERS) properties in comparison to spherical NPs due to the their larger surface area, more availability of reactive metal sites, and the anisotropic distribution of the electromagnetic field near their surface, respectively. In addition to the former properties, the hollow architecture of Au nanoshells also enables the encapsulation of different cargo molecules to provide additional functionalities, which opens up their special utility in the fields of diagnosis and therapy [39-42].

On the other hand, both theoretical calculations and experimental data indicate that a large electromagnetic field enhancement exists at the tips of branched particles, leading to stronger SERS [9, 43] and photothermal activities relative to non-branched ones provided that the large specific surface areas of the former facilitate a higher photohermal transduction efficiencies and an easier penetration of the electric field in comparison to smoother nanostructures [44, 45].

Hence, the combination of a branched surface structure and cargo loading capability in a single nanostructure can open the door to develop a new class of exciting multifunctional nanomaterials for sensing and biomedical applications. In this regard, Halas *et al.* have synthesized nanoshells with a roughned surface by treating presynthesized nanoshells with an aqueous solution containing cetyltrimethylammonium bromide (CTAB), $HAuCl_4$ and ascorbic acid (AA) followed by chemical etching of the pre-synthesized nanoshells [46, 47]. However, this methodology did not give rise to highly surface anisotropic structures, and the far-field scattering properties of the roughened nanoshells were close to those of the smoothed ones except for small differences in the angular light scattering distributions; in addition, the used post-synthesis chemical etching approach is not ideal because it can lead to particle destabilization and does not allow control of the surface topography. To solve this issue, very recently Park *et al.* developed a high yield synthetic method to radially arrange gold spikes on the surface of polymeric NPs, so called “spiky nanoshells” [48, 49]. The synthetic procedure is based on the CTAB-assisted seed-growth method [29, 30] on negatively charged polymer templates in the presence of silver (Ag) ions. This metholodolgy leads to Au nanospikes organized at a radial positioned determined by the size of the polymer

template. The presence of CTAB and/or metal halide salts, in particular NaBr, play a key role in the formation and regulation of the spiky shell morphology [50]. However, this process has still several drawbacks as the use of toxic cationic surfactants (CTAB) during the particle synthesis (which can be a severe problem for intended biomedical applications if their complete elimination is not completelly achieved), or as being composed of several reduction steps, *i.e.* the reduction of deposited Ag ions on the surface of the polymeric template by $NaBH_4$ followed by the CTAB-assisted growth of branches/spikes on the Ag seeds by reduction of an Au growth solution by AA exploiting the preferential binding of bromide ions from CTAB to selective facets of Au NPs [51].

Here, we report an alternative methodology to synthesize branched gold nanoshells (BGNS) in high yield based on a simpler seed-reduction method. In this approach, pre-formed citrate-stabilized Au seeds were attached on the surface of chitosan-Pluronic F127 stabilized poly(lactic-*co*-gycolic) acid (PLGA) NPs and subsequently anisotropically grown by the addition of a growth solution exclusively formed by Au salt, potassium carbonate (K_2CO_3) and AA. By altering the feeding ratio of different raw components, the structure of the anisotropic metal nanoshells can be tuned and, thus, their associated optical properties. Finally, the biocompatibilty of the as-obtained nanoshells was tested *in vitro* to decipher future use in biological applications as biomedical nanoplatforms.

4.3 Materials and methods

Poly(D,L-lactic-*co*-glycolic) (PLGA) of 40-75 kDa with 50:50 lactide–glycolide ratio, Pluronic F127, hydrogen tetrachloroaureate (III) trihydrate ($HAuCl_3 \cdot 3H_2O$), low molecular weight chitosan (LMW-chitosan, M_W = 111 kDa), potassium carbonate anhydrous, sodium borohydride, sodium citrate tribasic, resazurin (7-Hydroxy-3*H*-phenoxazin-3-one 10-oxide) and ascorbic acid were purchased from Sigma–Aldrich (St. Louis, MO, USA). ProLong® Gold antifade reagent with DAPI, Dulbecco's modified eagle medium, fetal bovine serum (FBS), L-glutamine, penicillin/streptomycin, sodium pyruvate, and MEM non-essential amino acids (NEAA) were purchased from Invitrogen (Carlsbad, USA). Dialysis membrane tubing (molecular weight cutoff ~3500) was purchased from Spectrum Laboratories,

Inc. (Rancho Dominguez, California). Thiol-PEG (HS-PEG, molecular weight 5000 Da was from Polymer Source (Ontario, Canada). All other chemicals and solvents were of reagent grade (purchased from Sigma–Aldrich). Milli-Q water was used for all aqueous solutions. All glassware was washed with aqua regia and HF 5% (v/v) and extensively rinsed with water.

4.3.1 Preparation of PLGA NPs

PLGA NPs were synthesized by a modified nanoprecipitation method (see Chapter 3). Briefly, a 10 % (w/v) solution of PLGA in acetone was added dropwise at a flow ratio of 0.166 mL/min to 50 mL of a cooled (10° C, 1 % (w/v) aqueous solution of F127 copolymer (PEO_{98}-PPO_{67}-PEO_{98}) under moderate magnetic stirring (250 rpm). Then, the resulting emulsion was homogenized with a sonicating tip (100 W, 20 kHz) for 10 minutes in an ice cold bath. The emulsion was magnetically stirred 4 h and then centrifuged in 10 mL tubes at 9000 rpm for 30 min at 18 °C. The resulting pellets were dispersed in 5 mL of water, stirred 4 h, centrifuged and dispersed again under the same conditions. The final PLGA NP dispersion was translucent and homogenous with hydrodynamic size and zeta potential of 110 ± 20 nm and -39 ± 7 mV, respectively.

4.3.2 Synthesis of Au seed NPs

Citrate-capped gold seeds were prepared based on a method previously reported by Jana *et al.* [29]. Briefly, 10 mL of $2.56 \cdot 10^{-4}$ M tri-sodium citrate were mixed with 0.125 mL of 0.010 M $HAuCl_3 \cdot 3H_2O$. Next, 0.3 mL of 0.1 M ice cold $NaBH_4$ solution was added and the solution mixed. The solution turned orange-pink immediately, indicating particle formation. The seed dispersion was aged overnight to allow for decomposition of unreacted $NaBH_4$. The average particle size obtained from TEM was 4 ± 2 nm.

4.3.3 Preparation of NP-seed precursor

PLGA NPs have a negative surface charge (ca. – 40 mV in the present case) due to the carboxyl groups of the PLGA core; therefore, we used chitosan, a natural biocompatible polycation, to invert the surface charge of NPs to positive to allow the subsequent attachment of negatively charged Au seeds. Briefly, 25 mL of PLGA NPs were mixed with 1.25 mL of 1 % (w/v) chitosan (in 1% (v/v) acetic acid) and stirred for 4 h at room temperature, followed by centrifugation at 9000 rpm for 30 min at 18 °C and subsequent dispersion in 25 mL of water. Then, 5 mL of Au seeds were added and stirred for 4 h, followed by centrifugation at 7000 rpm for 20 min at 18 °C. The supernatant was discarded and the pellets were dispersed in 25 mL of water. The NP-seed dispersion was sonicated (20 W, 20 kHz) 5 s to avoid any kind of particle aggregation. Control samples without chitosan as seed-attaching element were prepared by mixing 4 mL of PLGA NPs with 21 µM of cisteamine, 21 µM of EDC and 21 µM of sulfo-NHS. This mixture was reacted 4 h followed by centrifugation at 9000 rpm for 30 min and 18 °C and subsequent dispersion in 2 mL of water. 0.1 mL of citrate-capped seeds were added. Incubation and washing steps were the same as those of NP-chitosan-seeds samples.

4.3.4 Preparation of Au growth solution.

Au growth solution was prepared by dissolving 0.05 g of K_2CO_3 in 98 mL of water. After 30 min of stabilization, 2 mL of 0.025 M $HAuCl_4 \cdot 3H_2O$ was added and the solution aged for 24 h. The solution had a pH = 9.87 right before the synthesis. At this pH the predominant species of Au are $[AuCl_x(OH)_{4-x}]^-$ (x = 0 - 4) , with predominance of $[Au(OH)_4]^-$ [52]. The final concentration of Au^{+3} in the growth solution was 0.6 mM.

4.3.5 Branched Gold Nanoshell growth (BGNS)

To obtain homogeneous BGNS sizes, NP-seed precursor was filtered with 1.2 µm filters (Merck Millipore, MA, USA) to eliminate large aggregates formed during centrifugation. In a typical synthesis, 1 mL of NP-seed precursor was mixed with 2.5 mL of the Au growth solution under moderate stirring (400 rpm). After 1 min, 50 µL

of fresh 0.5 M AA (pH = 1.95) was added. After a few seconds the mixture changed from colorless to blue indicating the formation of branched nanoshells. After completion of the reduction reaction, and in order to ensure water stability for long time, thiolated polyethylene glycol was linked to the surface of the nanoshells. Briefly, BGNS (optical density ~1), K_2CO_3 (20 mM) and SH-PEG-OCH_3 (0.5 mM) were mixed in a volume ratio of 2:1:2. The conjugation was carried out at 4 °C for 4 h under moderate stirring. Pegylated BGNs were centrifuged at 3500 rpm for 15 min at 20 °C to eliminate free SH-PEG-OCH_3, and subsequently dispersed in water.

4.3.6 Particle Characterization

Dynamic light scattering measurements were performed at 25 °C by means of an ALV-5000F (ALV-GmbH, Germany) instrument with λ = 488 nm wavelength, scattering angle to incident beam was θ = 90 ° and sampling time 120 s. Zeta potential measurements were performed at 25 °C in a Zetasizer Nano ZS (Malvern Instruments, UK) using folded capillary disposable cells and measured by triplicate. UV-Vis spectroscopy measurements were performed in a CARY 100 Bio UV-Visible (Agilent Technologies, Santa Clara, USA) spectrophotometer. UV-vis spectra of BGNS were recorded 30 min after the growth reaction without dilution. UV-vis kinetic experiments were recorded with a sampling time of 5 s at 25 °C. Transmission electron microscopy (TEM) images of PLGA NPs and BGNs were obtained with a Philips CM-12 (Philips, Netherlands) microscope operating at 120 kV. HR-TEM images and selected area electron diffraction (SAED) patterns were obtained with a transmission electron microscope (Carl-Zeiss Libra 200 FE-EFTEM, Germany) operating at 200 kV. Scanning electron microscopy (SEM) images were obtained with a FESEM Ultra Plus (Zeiss, Germany) microscope operating at 20 kV. X-ray diffraction (XRD) experiments were carried out with a rotating anode X-ray generator (Siemens D5005, Germany). Twin Göbel mirrors were used to produce a well-collimated beam of CuKa radiation (λ = 1.5418 Å). X-ray diffraction patterns were recorded with an imaging plate detector (AXS F.Nr. J2–394).

The concentration of BGNS was determined by viscometry, as previously described. Briefly, dynamic viscosities of deionized water and BGNS were measured with a capillary/rolling ball automated microviscometer (AMVn Microviscometer,

Anton Paar, Austria). The viscosity is determined by timing the ball rolling down a slope with a defined angle. Based on the rolling-ball principle, the dynamic viscosity is defined by:

$$\eta = K_1(\theta)(\rho_B - \rho_S)t \qquad \text{(Eq 4.1)}$$

where $K_1(\theta)$ is the cell calibration constant depending on the angle θ, t is the rolling ball time, and ρ_B and ρ_S are the densities of the ball and sample, respectively.

The concentration of BGNS was calculated from the solvent's and the sample's specific viscosities (Eq 4.2) (measured in triplicate) and the hydrodynamic radius of the BGNS using the Einstein's viscosity relationship for spheres (Eq 4.3):

$$\eta_{sp} = 1 - \frac{\eta}{\eta_0} \qquad \text{(Eq 4.2)}$$

$$\eta_{sp} = 2.5\left(\frac{n_2}{V}\right)V_e \qquad \text{(Eq 4.3)}$$

where η is the sample's dynamic viscosity, η_0 is the solvent viscosity, $\frac{n_2}{V}$ is the number of equivalent spheres per volume unit (the concentration of PGNHs), $Ve = \frac{4}{3}\pi R_e^2$ is the volume of an equivalent sphere, and R_e is the hydrodynamic radius of an equivalent sphere. The UV-vis absorption of different dilutions of BGNHS was measured and plotted versus the calculated concentrations to prepare a calibration curve, thus, concentrations of BGNS samples could be calculated from UV-vis measurements. Our results were compared with concentrations calculated by using the theoretical extinction coefficient of nanoshells of the same size [53]. The difference found was less than one order of magnitude, which could stand for the different topography; nevertheless, our results are in agreement with other values reported [21, 54-56].

4.3.7 Cell nanoparticle uptake

BGNS uptake was followed by confocal microscopy by seeding HeLa cells on poly-L-lysine coated glass coverslips (12×12 mm^2) placed inside 6-well plates (3 mL, $1.5 \cdot 10^5$ cells/well) and grown for 24 h at standard culture conditions, that is, 5% CO_2 at 37 ºC) in Dulbecco's Modified Eagle Medium (DMEM) supplemented with 10% (v/v) FBS, 2 mM L-glutamine, 1% penicillin/streptomycin, 1 mM sodium pyruvate, and 0.1 mM MEM Non-Essential Amino Acids (NEAA). Then, 400 μL of NP solution ($1 \cdot 10^9$ NPs/mL) in PBS were added to cells. After 6 h of incubation the NP-containing cells were washed three times with PBS pH 7.4 and, then, fixed with paraformaldehyde 4% (w/v) for 10 min, washed with PBS. Samples were visualized with an oil immersion 63X objective (NA 1.4) using a DMI6000B Leica microscope (Leica Microsystems, Germany) in differential interference contrast (DIC) and fluorescence modes.

Uptake of BGNS by HeLa cells was also investigated by TEM. HeLa cells were seeded in 6-well plates (3 mL, $1.5 \cdot 10^5$ cells/well) and grown for 24 h at standard culture conditions. Then, 400 μL ($1 \cdot 10^9$ NPs/mL) were added to cells. After 6 h of incubation the NP-containing cells were washed three times with PBS, trypsinized and centrifuged at 1500 rpm for 4 min. Cell pellets were fixed with 500 μL of 2.5 % (v/v) glutaraldehyde. The pellet was then included in agar, post-fixed with osmium tetraoxide in 0.1 M cacodylate buffer (1% (w/v)), and finally pelletized with Eponate (Ted Pella Inc, Redding, CA, USA). Ultra-thin cuts were obtained with an ultramicrotome (UltraCut S, Leica, Germany) and were analyzed by TEM (JEOL JEM 1011, Japan).

4.3.8 Resazurin cell cytotoxicity assay

HeLa cells were seeded in a 96-well-plate at 15000 cells/well (3 wells/sample) in 100 μL growth medium (Dulbecco's Modified Eagle Medium (DMEM) supplemented with 10% Fetal Bovine Serum (FBS), 2 mM L-glutamine, 1% penicillin/streptomycin, 1 mM sodium pyruvate, and 0.1 mM MEM Non-Essential Amino Acids (NEAA). After 24 h, cells were incubated 6 h with 50 μL of BGNS at different concentrations and some cells were left without BGNS as a control (blank).

Then, cells were washed with PBS and a solution out of 10% (v/v) of Resazurin (Sigma-Aldrich) and 90% of growth medium was added to each well (100 µL/well) and incubated for 3 h. Fluorescence spectra were recorded with a microplate fluorescence spectrometer (FluoroLog-3, Horiba, Japan). Spectra were recorded by exciting at 560 nm and recording fluorescence emission in the range 572-650 nm. The background signal (640-650 nm) was subtracted to the average maximal fluorescence of each sample. Values were normalized and plotted against concentration in logarithmic scale.

4.4 Results and discussion

The current synthesis of BGNS involved the preparation of Au seed-decorated PLGA NPs (NP-seed) and subsequent branched nanoshell growth by using a growth solution exclusively containing $HAuCl_4$, K_2CO_3 and AA; in this way, avoidance of using CTAB eliminates the inherent disadvantages of its use in the synthetic process such as difficulty of clearance and potential toxicity in biomedical applications [48, 49]. In particular, the solely reaction of $HAuCl_4$ and AA has been previously used to grow dendritic patches onto polystyrene nanospheres by exploiting the conformal surface growth of Au onto the polymeric NP surface regulated by AA surface adsorption [57], or to obtain flower-like gold NPs by using chitosan as stabilising agent [58]. Nevertheless, to the best of our knowledge this is the first work in which the present synthetic approach is used to obtain branched gold nanoshells. A relative similar approach was recently used to grow silver-polymer composites by using PLGA NPs to electrostatically attach silver ions which are subsequently photorreduced; capping agents such as polyvinyl alcohol (PVA) or sodium citrate are added prior the addition of the strong reductant agent (AA) to complete the reduction reaction [59]. However, in contrast to the methodology developed here, in the former approach the addition of the capping agents is key to attain the star-like structure; in its absence, only spheroidal-like particles are obtained.

As with most anisotropic particles, the present growth of the gold branched shell on top of chitosan/F127-functionalised PLGA NPs is a seed-mediated process. In a typical synthesis (see Figure 4.1), Au seeds with a diameter of ca. 4 nm were prepared by fast reduction with sodium borohydride in the presence of sodium citrate

as a capping agent (Figure 4.2a) [29]. Then, these seeds were electrostatically bound to chitosan-F127 stabilized PLGA NPs (Figure 4.2b) (ca. 125 nm in diameter as measured by dynamic light scattering, DLS) obtained by a nanoprecipitation method, which posses a net surface charge of + 15 ± 6 mV and served as cores in order to promote the heterogeneous nucleation onto the bound Au seeds.

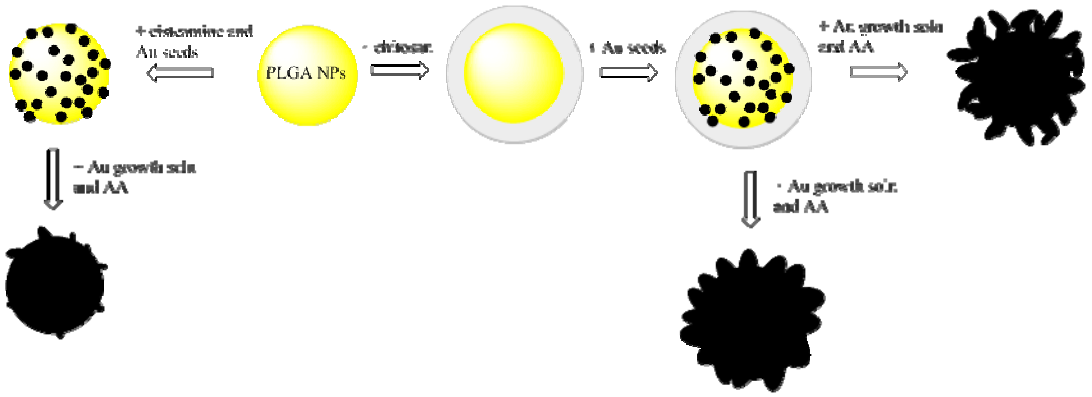

Figure 4.1: Growth of branched gold nanoshells over PLGA NPs using chitosan or cysteamine as binding linker.

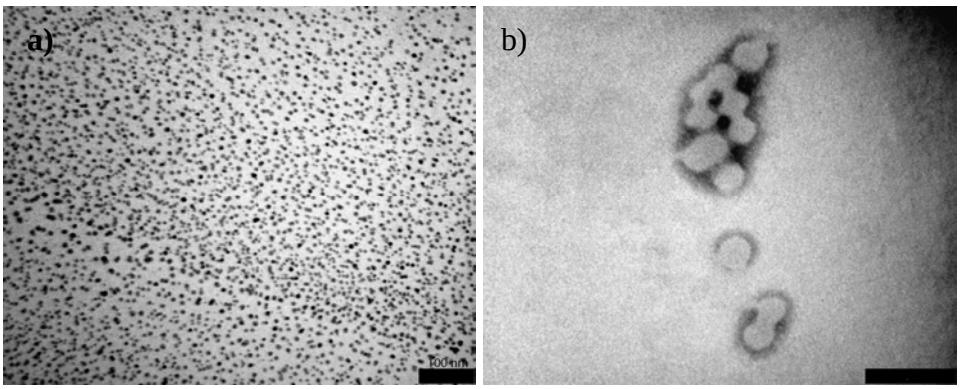

Figure 4.2: TEM images of a) citrate-capped Au seeds prepared by reduction with $NaBH_4$, and b) PLGA NPs stained with phosphotungstic acid. Scale bars are 200 nm.

To grow the branched gold nanoshells, the seed-decorated polymeric PLGA NPs were placed into a growth solution containing $HAuCl_4$ and K_2CO_3. Because of the pH-dependent weak reducing activity of AA, with values of -0.127 and -0.34 V for pH values of 4.0 and 7.0, respectively [60], this molecule could only reduce Au salt in the presence of previously formed Au seeds (with an standard reduction

potential, E^0 = 1.002 V) but not isolated Au^I to Au^0 (E^0 = -1.5 V) [61], hence, leading to a preferential reduction of Au salt on the seed surfaces. This should directly contribute to the formation of branches on the seed-decorated PLGA NPs used as nanotemplates presumably because of the slow and directional diffusion of gold precursors to the NP-attached seeds which, in the present case, is not regulated by the presence of halide ions, as reported in previous works [50].

Here, chitosan also plays an important role in the synthetic process: On one hand, chitosan chains contribute as a reducing agent in the redox reaction of $HAuCl_4$ [62, 63]. However, in the presence of chitosan solely, one day is needed at least to produce a partial roughened gold coverage around the polymeric NPs with an absorbance peak centered at ca. 570 nm, which is typical of aggregated Au NPs (Figure 4.3). The full metal coverage of the polymer core is not achieved indicating that chitosan does not act as a strong reducing agent. On the other hand, the electrostatic interactions between chitosan´s amine groups and primary Au seeds, and the scrolling and protrusion capacity of vicinal chitosan chains can triggered for agglomeration of primary seeds, which can serve as secondary nuclei for further growth of larger crystals which configure the nanoshell spikes, that is, the chitosan chains can act as a structure-directing agent supporting the growth of anisotropic gold shells [58, 64, 65]. TEM and HR-TEM images confirm this point (Figure 4.3b-c), where some agglomerates of small particles can be observed. The HR-TEM image exhibited regions of varying contrast starkly different from the uniformly dark particles of spherical Au nanocrystals. Also, the flat nature of these nanocrystals can be deduced by the presence of Moiré patterns arising from the presence of two superimposed, different crystal lattices [66].

TEM images (Figure 4.4) revealed that synthesized BGNs were covered with branches in high yield, and the final product was free of small particles and other nanostructures. The branches formed were stable and hardly changed after several months of storage at room temperature under common laboratory conditions. Resulting branched Au nanoshells prepared by this process possess the advantages of being quickly and easily obtained, enabling the control of their morphology without using non-toxic materials.

It is well known that the plasmon peak position of smooth shells can be readily controlled by changing the ratio between the core diameter and shell

thickness, and that the increased core/shell ratio results in strong red shifts of the nanoshell plasmon band [67]. However, very large cores are often not desirable as they significantly increase the overall particle diameter, and the preparation of very thin uniform shells can be synthetically challenging. Hence, coupling a shell with branches one can readily tune the plasmon band over a wide wavelength range without significantly changing the nanoshell size (or the amount of gold). Trying to decipher the mechanism/s involved in their formation, we here considered the systematic variation of different factors involved in the synthesis of these spiky gold nanoshells in order to test their influence on the reaction kinetics and on the size, shape and optical properties of the resulting particles.

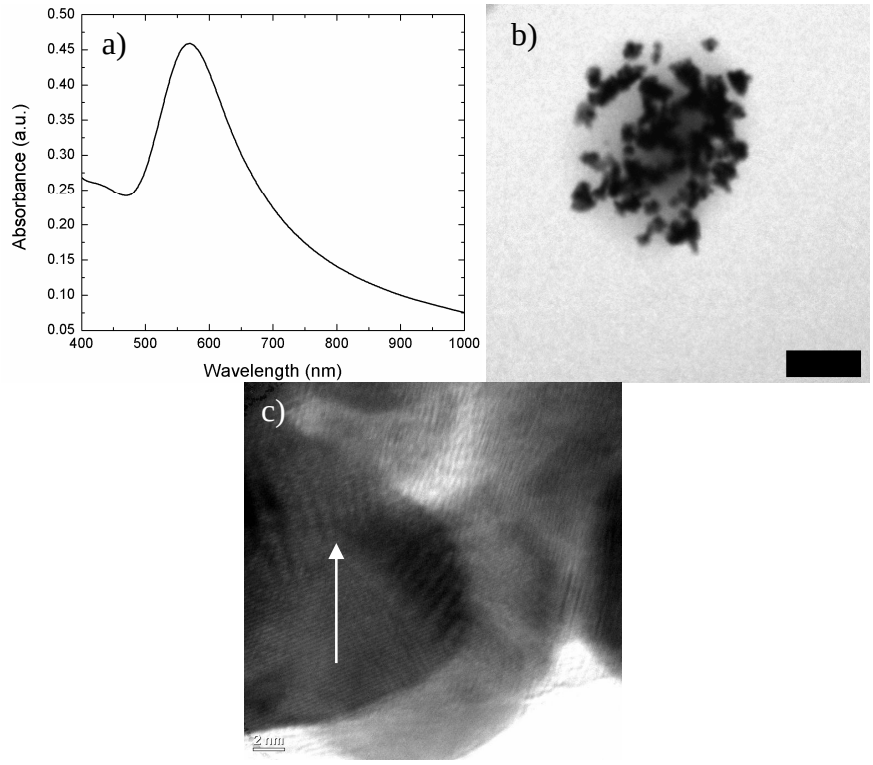

Figure 4.3: a) UV-vis absorption spectrum of NP-seed in the presence of Au growth solution and in the absence of AA after 1 day of reaction. Although chitosan by itself acts as reductant, its activity is not sufficient to generate fully-developed BGNS. b) TEM image of a NP-seed after 1 day under the aforementioned conditions (Scale bar is 50 nm). c) HR-TEM image showing the agglomeration of small flat crystals (as observed from the presence of Moiré patterns, see arrow) as precursors of branches.

4.4.1 Effect of ascorbic acid

Experimentally, the influence of AA concentration on the structure and properties of BGNS was studied by altering the amount of supplied AA. As already well known, the reduction of the auric ion by AA is stoichiometric at a molar ratio of ascorbic acid to gold ($AA:Au^{3+}$) of 1.5 [68]. All present experiments were performed at an $AA:Au^{3+}$ ratio above 1.97 so it is clear that the branched morphology results from an excess of AA. As shown in Figure 4.4, the increase of ascorbate ions from 5 to 75 μL of a 0.5 M solution led to a rapid change in solution color from colorless to blue-greenish in few seconds, indicating the main role of AA as a reducing agent.

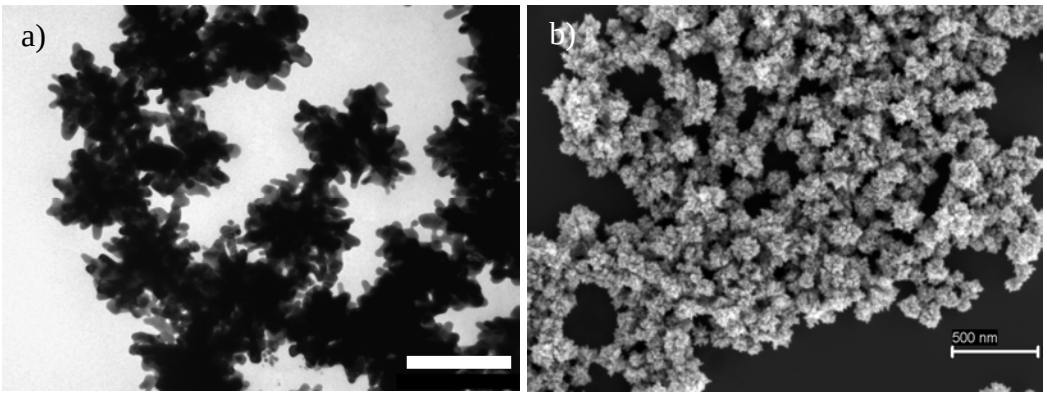

Figure 4.4: a) TEM images of BGNS showed the great anisotropy of these structures with spikes protruding from the core (AA solution = 5 μL, Au growth solution = 2.5 mL, and NP-seeds solution = 0.5 mL). b) SEM image showing a high yield production of BGNS and negligible undesired by-products. Scale bar is 200 nm in a) and 500 nm in b).

In fact, the widespread heterogeneous nucleation may result from the fact that both the gold precursor, $[Au(OH)_xCl_{4-x}]^-$, and AA could be expected to adsorb onto the seed-decorated core polymeric particles, further raising the probability of nucleation on the surface of NPs. In particular, AA could bind to the chitosan chains favoring the surface reduction of Au ions in the closest vicinity of gold seeds electrostatically-attached along the biopolymer chains, which would facilitate the anisotropic shell morphology. The changes in solution color correspond to variations in the position of the wide plasmon absorption band of Au nanoshells spreading over

ca. 500-1000 nm, as well as in the NP size and shape. The plasmon absorption peak first red shifted from ca. 680 nm to more than 1000 nm upon addition of 5 to 20 μL of AA solution, typical for the size increase of nanoshells and the emergence and growth of multiple spikes onto their surfaces (Figure 4.5). TEM images showed that the products of such reactions exhibited branched structures, with the number and length of branches increasing as the AA concentration does within this concentration range (Figure 4.6a-b). The appearance of a plasmon band at 700-1000 nm is not only coincidental with the appearance of the spikes but its intensity gradually enhances with the increase in the nanoshell size and count of branches.

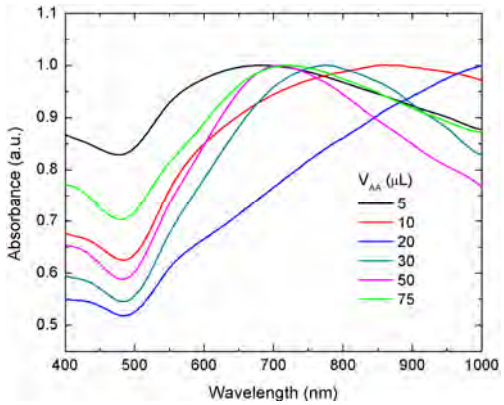

Figure 4.5: Effect of AA concentration on UV-vis absorption spectra of BGNs. Volumes of Au growth solution and NP-seed were kept constant at 2.5 mL and 0.5 mL, respectively.

In contrast, upon addition of larger volumes of AA solution (20 to 75 μL) a progressive slight blue-shift of the plasmon peak is observed as a consequence of the progressive formation of more spheroidal and less roughened nanoshells through the apparent growth of the nanoshell core and the reduction in the number and protrusion of spikes (Figure 4.6c-d), with the whole nanoshell diameters slightly decreasing from 210 to 190 nm as previously observed in the formation of pure gold star-shaped NPs in aqueous solution [58, 69]. Nevertheless, the apparent protrusion of these gold structures demonstrates that these are unlikely to have formed in the bulk and subsequently attached to the core-PLGA nanospheres by heterocoagulation but they have been, in fact, heterogeneously nucleated and grown in all accessible dimensions (laterally as well as towards the bulk solvent).

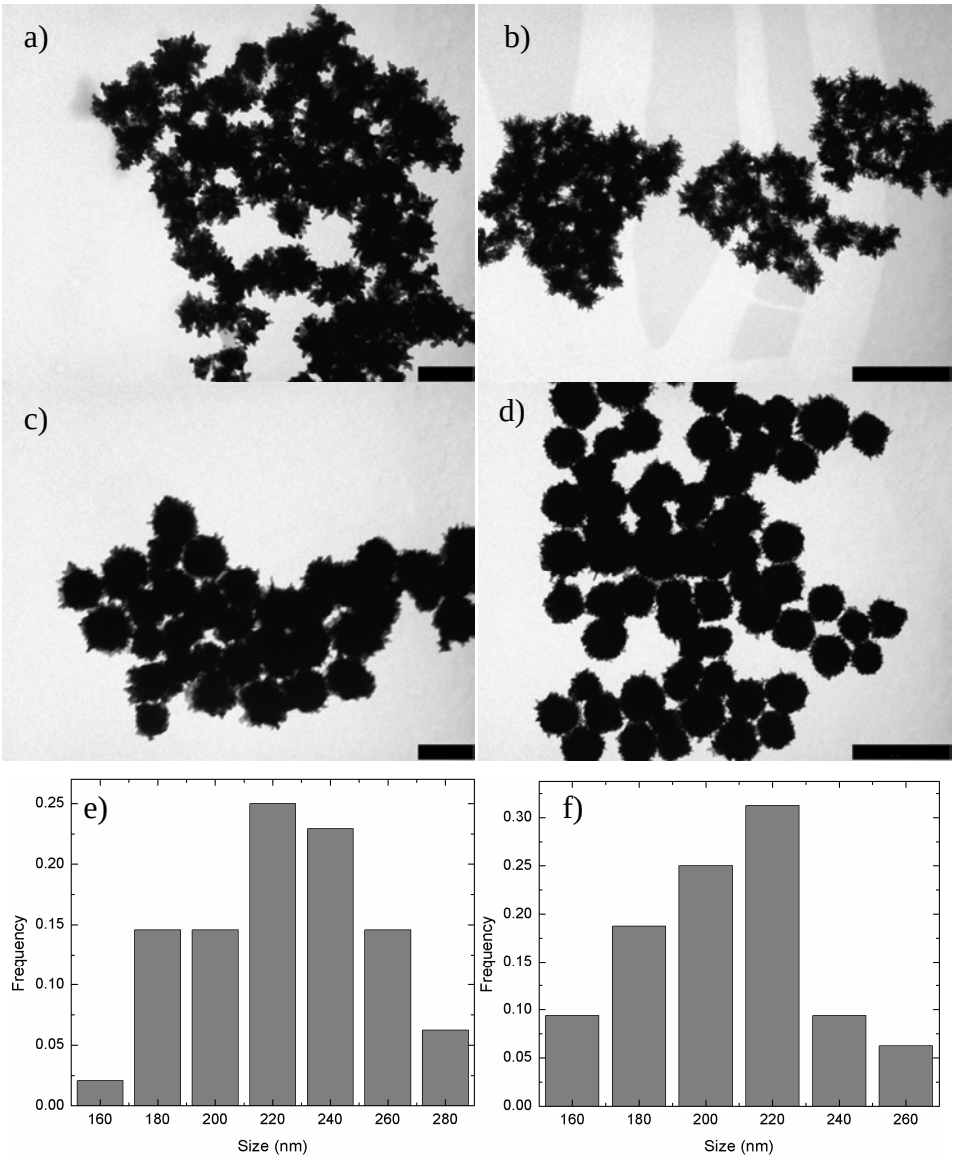

Figure 4.6: TEM images showing the effect of AA on NP size and structure. Added AA volumes were: a) 5 µL; b) 20 µL; c) 50 µL; and d) 75 µL. Au growth solution and NP-seed volumes were kept constant at 2.5 mL and 0.5 mL, respectively. e) Size distribution of BGNS observed in a). f) Size distribution of BGNS observed in d). Scale is 200 nm in a) and c), and 500 nm in b) and d).

Hence, the obvious variation of nanoshell size and morphology by controlling the AA concentration clearly involved that the supply of Au^0 in the reaction system was a key for generating branched nanoshells. In this regard, it is necessary to bear in mind that the nature of gold reduction strongly depends on the dissociation degree of the AA molecule. As indicated in Figure 4.7, the pH of the reduction reactions carried out in this work varied between 2.98 (for 75 µL AA) and 7.15 (for 5 µL AA). With

dissociation constants $pK_{a,1}$ = 4.17 and $pK_{a,2}$ = 11.58, it is therefore expected that mainly the non-dissociated (H_2Asc) and singly deprotonated ($HAsc^-$) forms of AA participate in the gold reduction reaction. As has been previously noted, the reducing strength of ascorbic acid increases with pH, *i.e.* with the prevalence of the $HAsc^-$ form [70].

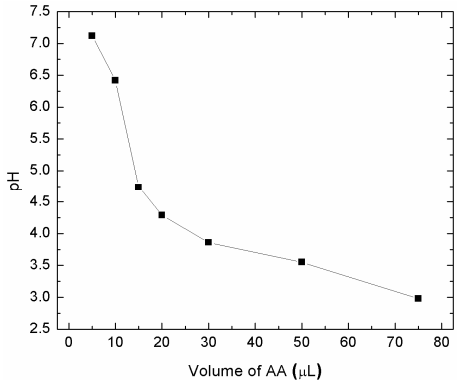

Figure 4.7: pH of the reaction mixtures with different initial volumes of AA. Initial pH of Au growth solution and AA were 9.87 and 1.95, respectively.

It can be deduced that even at low AA concentrations the transformation of Au^I to Au^0 is sufficiently fast, as observed with the naked eye and when measured the reaction kinetics by spectrophotometry (see below), to induce the branched coverage of the nanoshell surfaces, being the $HASc^-$ form of AA the main reductant species. This anisotropic coverage may be partially assisted: i) on one hand, by the concentration-dependent facet selectivity of Au^0 onto the seed surfaces which should allow the preferential growth along certain crystalline faces of the initial nuclei (polycrystalline citrate-Au seeds), in particular, along existent twin boundaries, in a kinetically controlled process as ocurred for pod and star-shaped single NPs [65, 67, 68] (Figure 4.8a); ii) on the other, by the presence of chitosan chains acting as nucleation centers and structure directing agents. In fact, when chitosan is absent in the reaction solution (for example, when substituted by cysteamine molecules covalently attached to PLGA carboxyl groups with EDC/sulfo-NHS) only slightly roughened nanoshell surfaces were obtained (Figure 4.8b).

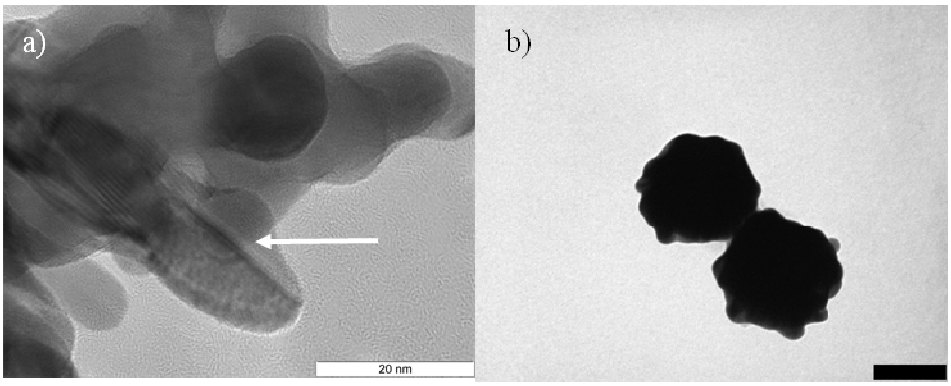

Figure 4.8: a) TEM image showung the presnece of twinning in branches (see arrow); b) TEM image of nanoshells grown in the absence of chitosan, in which only small protuberances appeared. Scale bar is 100 nm.

On the other hand, when the AA concentration is larger an additional pH decrease took place, indicating that the main reductant species would be the non-dissociated form of AA, H_2Asc. Despite this species posses lower reducing activity, the large reductant excess concentration would favor the formation of larger concentrations of Au^0 leading to a more uniform metal ion deposition. In addition, this AA excess might be also uniformly adsorbed on the surface of nanoshells by means of strong N-H···O-C hydrogen bonding between the amine groups of chitosan chains and the vinylogous carboxylate group of AA [71]; then, the partial suppression of the anisotropic growth in spite of the deposition of Au on the seeds would be still highly favored. Then, this would lead to a more uniform nanoshell growth with smaller-aspect-ratio spikes on their surface as observed. Hence, the behavior of AA as a ligand at large concentrations would partially prevent the selective deposition of the excess of Au^0 on higher energy facets, favoring an isotropic growth to give more uniform NP surface coverages and smoother nanoshells, as ocurred or single metallic branched NPs [67]. All this would highlight the multifunctional role of AA, acting as both as a reducing agent and as a stabilizer, being especially relevant at high concentration (ca. >30 μL).

The previous experimental data demonstrated the possibility to tune the morphology of as-prepared nanoshells by altering, at least partially, the reduction rate of Au^I to Au^0. Because the amount of seeds was fixed to 0.5 mL, the enhanced Au^0 concentration provided by excess of reductant, in turn, increased the Au^0/seed ratio,

which represented the reactivity of gold ions. This led us to investigate the influence of other experimental variables that could improve the Au^0/seed ratio, which also allowed for tailoring the properties of the present BGNs.

4.4.2 Influence of NP-seed precursor

The influence of NP-seed concentration on the properties of as-prepared BGNS was also studied. As the amount of NP-seed increased from 0.1 to 3 mL, with the amount of AA and Au growth solution fixed at 50 μL and 2.5 mL respectively, a progressive red shift of the wide plasmon absorption band maximum from 672 nm to > 1000 nm was observed (Figure 4.9).

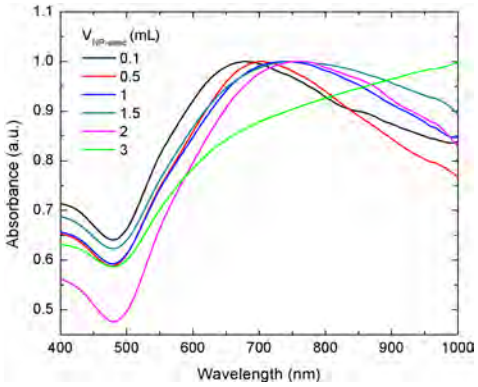

Figure 4.9: Effect of NP-seed concentration on the UV-vis absorption spectra of BGNS. Volumes of Au growth solution and AA were kept constant at 2.5 mL and 50 μL, respectively. As the number of NP-seed increases, the plasmon band maximum red-shifts.

Under TEM, complete nanoshell gold coverage is observed with increases in the size, number and length of the branches (Figure 4.10). Obviously, the addition of more seed-decorated polymeric NPs led to lower Au^0/seed ratios providing less Au^0 to supply the growth on each NP. A lower Au^0/NP seed ratio facilitated then a branched growth rather than an isotropic one, which also relied on the AA concentration as commented previously.

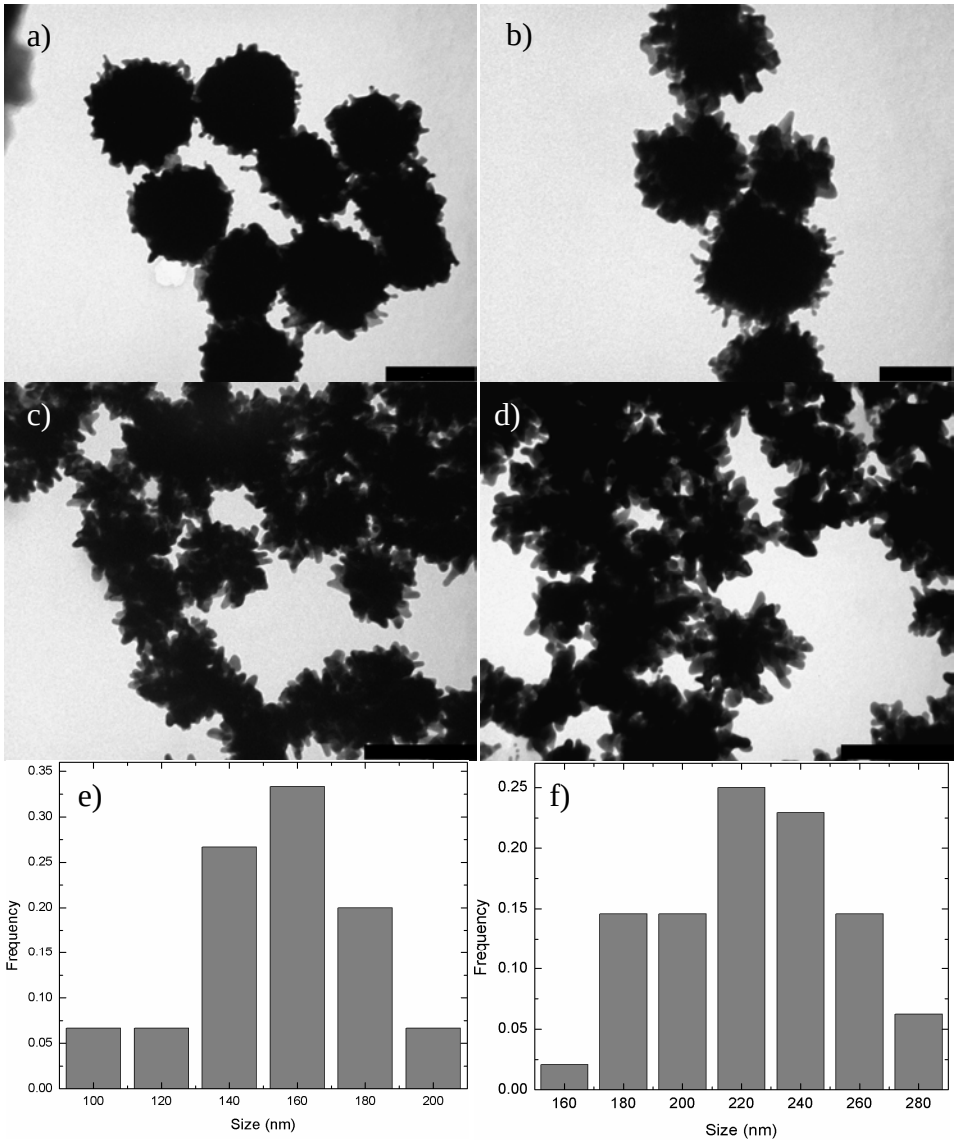

Figure 4.10: TEM images of BGNS showing the effect of added NP-seeds. Added volumes were: a) 0.5 mL; b) 1 mL; c) 2 mL; d) 3 mL. Au growth solution and AA volumes were kept constant at 2.5 mL and 50 μL, respectively. e) Size distribution of BGNS observed in a). f) Size distribution of BGNS observed in d). Scale bars are 100 nm in a-b) and 200 nm in c-d).

A control experiment indicated that at a relatively low added AA concentration (for example, after the addition of 10 μL of 0.25 M AA solution) the as-prepared nanoshells were even more branched in spite of NP sizes became larger with the increase of NP-seed particles (Figure 4.11). As mentioned previously, despite a relatively fast reduction of Au^{I} to Au^{0} was achievable even at low AA concentrations, which led to a high reactivity of gold ions in contrast with observations made, for example, when using hydroquinone as reductant (for which the opposite effect was

found during the obtention of urchin-like Au NPs [72]), the lower avavilability of metal ions seems to favour the deposition of Au on more energetically favorable directions, resulting in the anisotropic growth of the agglomerated nanocrystals around the chitosan chains. If the excess concentration of Au^0 was high enough in the reaction system, the deposition rate of Au^0 on higher energy facets would be faster than on lower ones resulting in branched nanoshells.

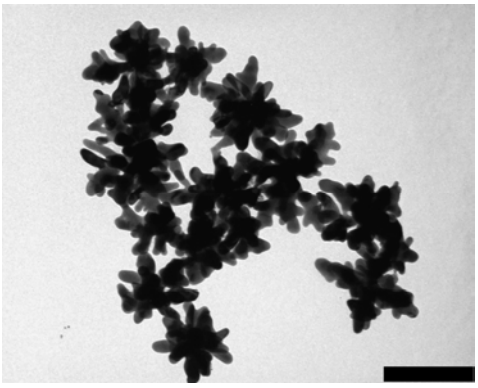

Figure 4.11: BGNS obtained after using 10 μL of 0.25 M AA with a more branched structure. Scale bar is 200 nm.

4.4.3 Influence of Au growth solution

Another factor that changes the plasmonic properties and structure of the BGNS was the variation of $HAuCl_4$ growth solution concentration relative to the amount of NP-seed precursor.

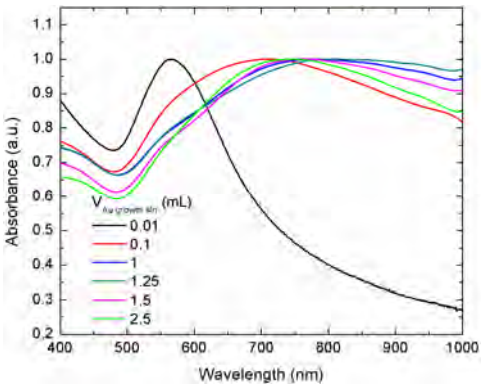

Figure 4.12: Effect of Au^{+3} growth solution volume on UV-vis absorption spectra of BGNS. Volumes of AA and NP-seed were kept constant at 50 μL and 1 mL, respectively.

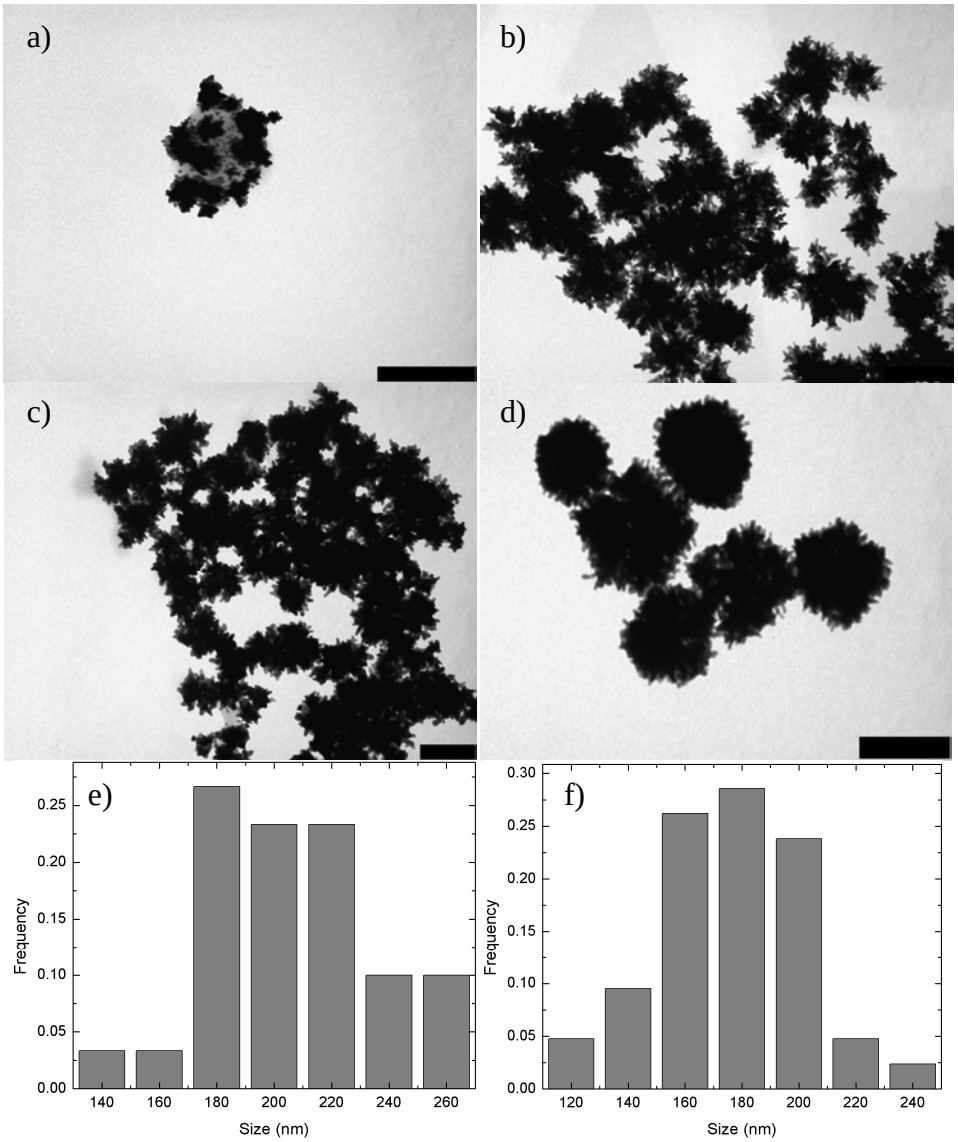

Figure 4.13: TEM images showing the effect of Au growth solution concentration. Added volumes of Au growth solution were: a) 0.01 mL; b) 0.1 mL; c) 1.25 mL; d) 2.5 mL. AA and NP-seed volumes were kept constant at 50 µL and 1 mL, respectively. e) Size distribution of BGNS observed in b). f) Size distribution of BGNS observed in d). Scale bars are 200 nm.

4.4.4 Reaction kinetics

The formation of branched-shell NPs was facilitated by a large gold reactivity under certain conditions which was deduced as a kinetics-favored process, as previously mentioned, since branching occurs regardless of the growth solution/NP-seed ratio. We failed to catch in most of the conditions the whole extension of the time-dependent kinetics of branched-shell growth provided that they are almost instantaneously formed after the addition of AA. However, when possible, the spectra

measured *in situ* during the shell growth denote, on one hand, gradual red-shifts of the plasmon bands into the NIR region and, on the other, increases in light absorbance with reaction time until reaching a plateau value due to the progressive increase in shell thickness and in the number and length of spikes (Figure 4.14). In particular, as the added AA concentration increases up to 20 μL, the plasmon band additionally red-shifts during the metal shell growth, and the reaction kinetics became faster. Above 20 μL, the reduction reaction takes place instantaneously but a red-shift of the plasmon band with time can be also noted; however, the absolute final position of the maximum blue-shifts regarding lower added AA concentrations due to the observed changes in structure of the resulting nanoshells, as mentioned previously in subsection 4.4.1.

For example, we could observe that upon injection of 5 μL of a 0.50 M AA solution the absorbance reached its maximum within ca. 120 s (Figure 4.14, row 1) and the plasmon peak is red-shifted ca. 100 nm from the first time point measured (at 5 s). However, TEM images obtained at a very short stage of the metal growth process under the former reaction conditions exceptionally allowed to observe that the formation of branches onto the electrostatically attached seeds might already occurred at the earliest stages of the gold nanolayer formation, that is, when this is not fully developed (Figure 4.15a-b) in contrast to previous observations by Wei *et al.* [73] and Park *et al.* [49], where a very fast isotropic growth of gold islands takes place first followed by anisotropic growth of sharp branches at low gold concentrations onto these islands. As the reaction carried on, the polymeric NPs were fully covered with a branched gold shell which became thicker and more branched with time after completion of the reduction reaction due to the progressive depletion of the gold ions which deposite on more energetically preferred directions (Figure 4.15c-d) [72]. This fact would be additionally facilitated through the role played by chitosan as agglomerating agent of crystal seeds in their vicinity to give intermediate particles crystal plane defects which would act as additional nucleation growth centers for branch formation [58, 74].

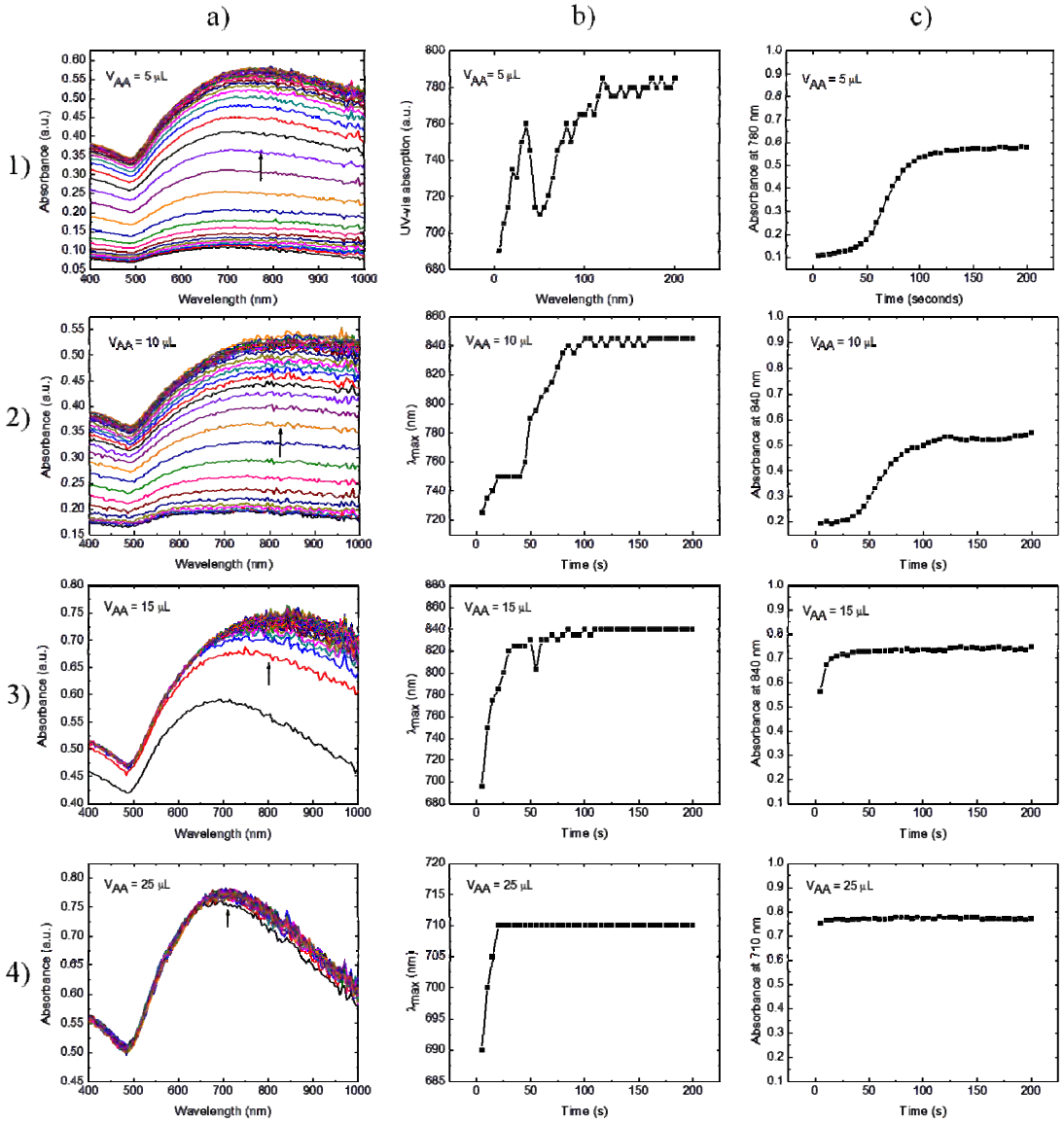

Figure 4.14: a) Time evolution of UV-vis absorption spectra upon addition of different volumes of AA. Au growth solution and NP-seed were kept constant at 1 mL each one, respectively. b) Time evolution of the plasmon peak wavelength position (λ_{max}). c) Time evolution of absorbance intensity at λ_{max}.

It is worth mentioning that a slight blue shift of the plasmon absorption band of ca. 30 nm is observed when maintaining the growth duration from 3 to 8 min, which kept constant during prolonged growth (Figure 4.16). Within this time period the nanoshell morphology was slightly tuned from spiky to smoother gold nanoshells (Figure 4.15e-f). These results would be consistent with a kinetic-favored growth mechanism of the anisotropic gold nanoshells [75, 76]. Namely, the kinetics-favored formation of the branched shells should be thermodynamically unstable and tended to

transform to isotropic shells [77]. Consequently, it seems that after ca. 8 min, a thermodynamic equilibrium of the NP surfaces structure was built up through the reorganization of their sizes of surface atoms which, in turn, suppressed the additional transformation of the NP morphology and, thereby, the blue shift of absorption spectra.

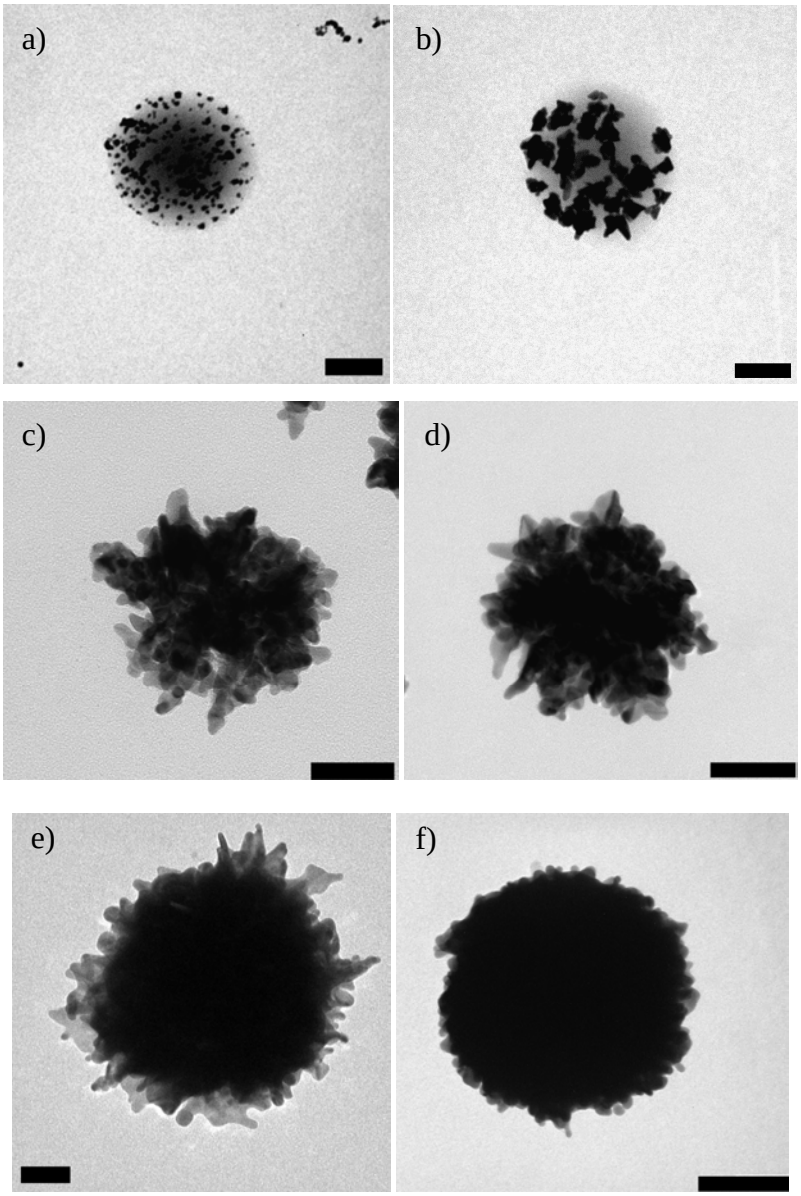

Figure 4.15: TEM images of BGNS growth. Reactants volumes were 2.5 mL of Au growth solution, 0.5 mL of NP-seed and 30 μL of AA, respectively. Aliquots (10 μL) of the reaction mixture were taken at: a) 0, b) 5 s, c) 60 s, d) 120 s, e) 180 s and f) 8 min. Scale bars are 50 nm in a), b) and e), and 100 nm in c), d) and f).

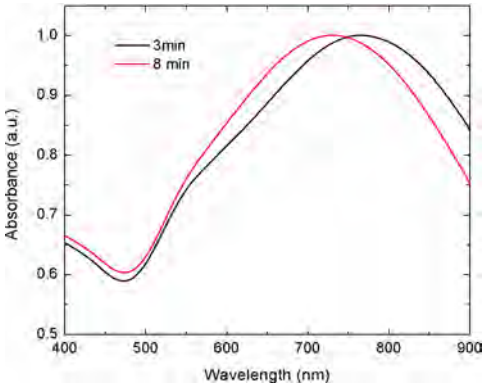

Figure 4.16: UV-vis absorption spectra of BGNs after 3 and 8 minutes of reaction. A slight blue shift of the plasmon peak is observed indicating that the structure undergoes a reshaping into a more thermodynamically stable geometry with a lower anisotropy degree. Reactants volumes were 2.5 mL of Au growth solution, 0.5 mL of NP-seed and 30 μL of AA, respectively.

The existence of highly active facets was confirmed by powder XRD and HRTEM observation of spiky nanoshells (Figure 4.17). XRD indicated that the lattice parameters of the spiky nanoshells fitted well to the face-centered-cubic structure of bulk gold crystal, showing reflections in the 2θ range of 25-70º indexable to the (111), (200) and (220) reflections of fcc Au (JCPDS, file nº 4-0784) [74] (Figure 4.17a). SAED patters also confirmed that these branched nanoshells were crystalline and randomly oriented, confirming the diffraction peaks obtained by XRD (Figure 4.17b). The appearance of these peaks meant that the spiky nanoshells were polycrystalline (in particular, formed by a polycrystalline core with a number of single crystal spikes branching out from the surface). Besides, the nanoshells possessed the strongest (111) diffraction peak indicating that the branched growth of these hybrid particles might be thought the deposition of Au^0 mainly on (111) lattice planes. This consideration was further proved by HRTEM (Figure 4.17c). Under HRTEM, interplanar distances in elongated single branches were found to be 0.236 nm corresponding to (111) lattice planes, whereas in some branches formed by several agglomerated crystals an interplanar spacing of 0.203 nm was also found, corresponding to (200) lattice planes. This result is reasonable since despite the XRD and SAED patterns show predominace of (111) lattice planes, peaks belonging to (200) and (220) crystal planes with sufficient intensity are also present. For the analyzed branches, the growth direction was vertical to the (111) plane, indicating

that this plane can be a high-energy facet and allowed preferential deposition of gold ions.

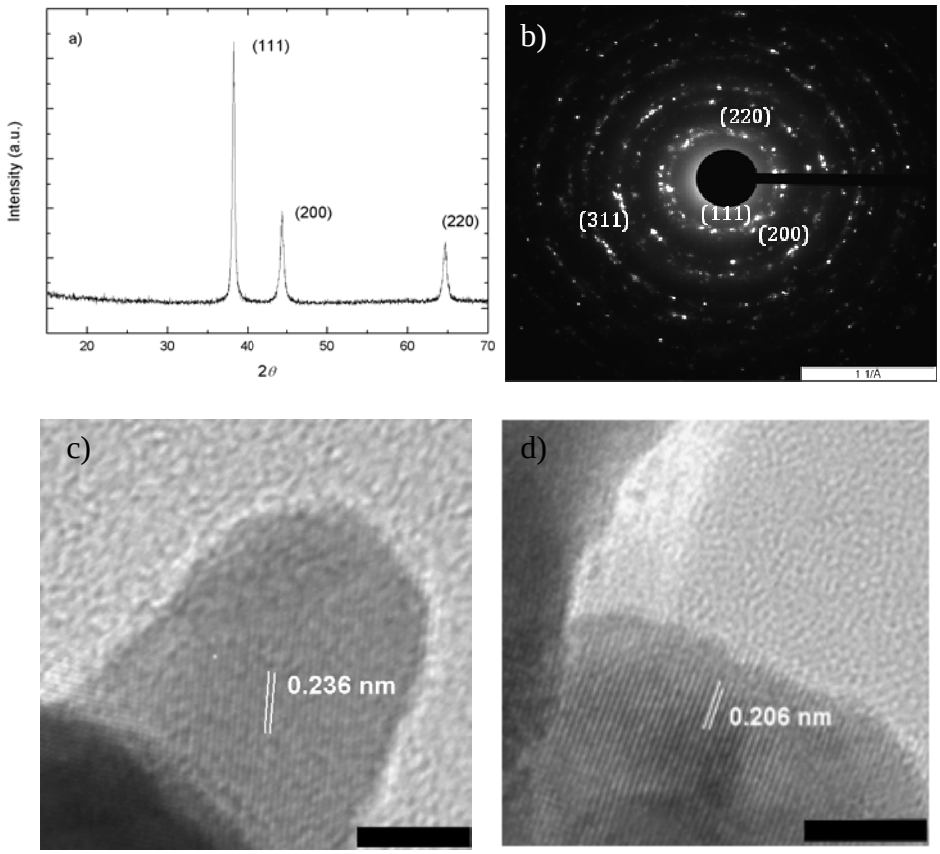

Figure 4.17: a) XRD pattern and b) SAED pattern of BGNS. c) HRTEM of one branch with an interplanar distance of 0.236 nm corresponding to (111) lattice planes and d) with 0.206 nm of interplanar distance corresponding to (200) lattice planes. Scale bars in c-d) are 5 nm.

The kinetics-favored profile of the spiky shell growth was further proved by a stepwise addition of AA. In general, the UV-vis spectra and, thus, the morphology of as-prepared nanoshells were partially determined by the AA amount of the primary addition, which did not relate to the total amount of AA (Figure 4.18a-d). The nanoshell size *via* stepwise addition of AA was smaller than those via one-off addition (from 200 to 180 nm, Figure 4.18e-f). This fact revealed that the formation of the branched shells was mostly favored by a sufficient initial concentration of Au^0 through AA reduction rather than its total concentration during the reaction, but always within the concentration range where the ligand role played by AA is minimal.

Interestingly, the time interval in between the two injection steps also influenced the plasmon absorption band and size of the nanoshells attributed to the different face activity of gold seeds and particles during the different growth time intervals (Figure 4.17d), as observed in previous works [72].

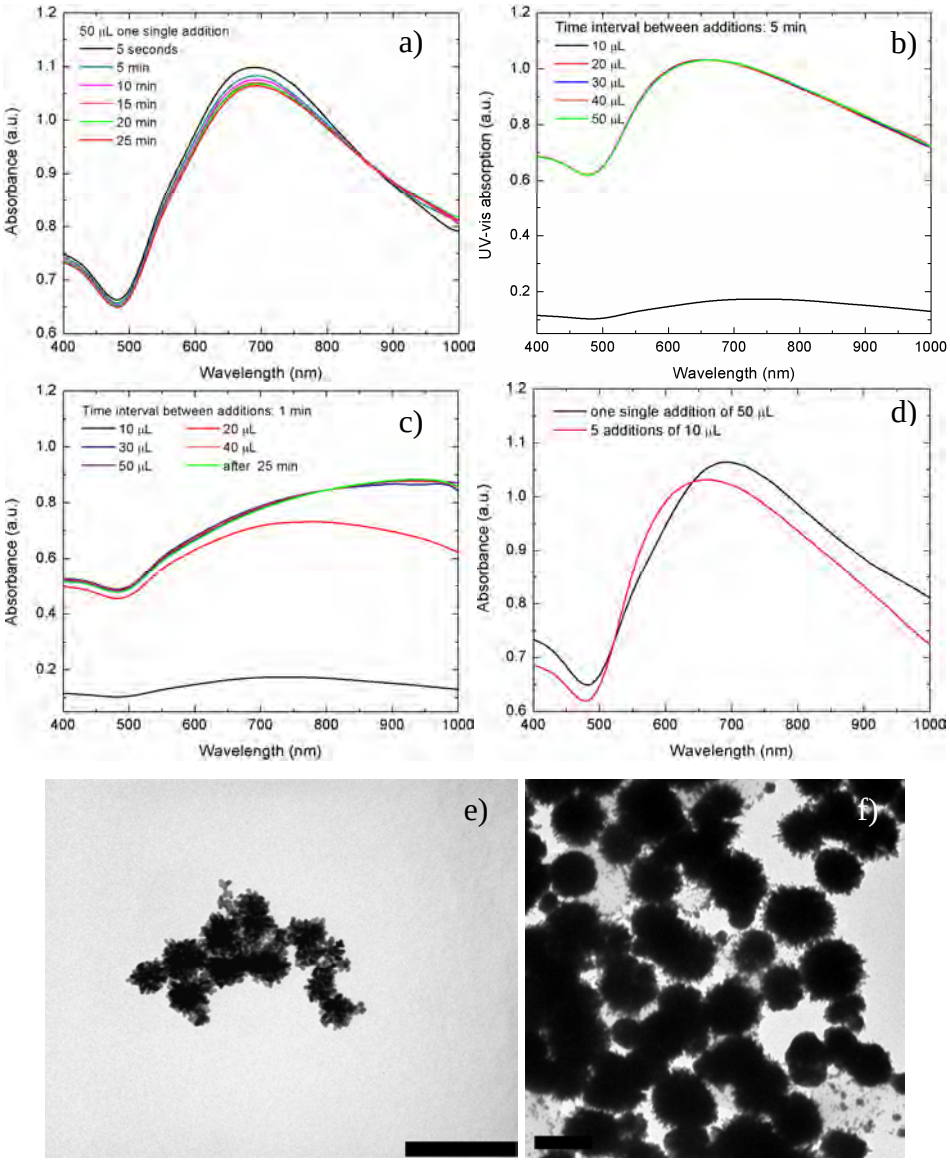

Figure 4.18: UV-vis spectra of BGNS: a) after one-off addition of 50 µL of AA (spectra were measured after 5 s, 5, 10, 15, 20 and 25 min); b) after stepwise addition of 10 µL each 5 min; c) after stepwise addition of 10 µL each 1 min. d) Comparison of the spectra obtained after a single 50 µL addition and 5 addition of 10 µL aliquots of AA added each 5 min. e) TEM images of BGNs obtained after multiple additions of 10 µL aliquots of AA and f) after a single addition of 50 µL. Scale bar is 200 nm in e) and f).

Similarly, it was also found that the use of seeds stored within 1 day after preparation resulted in more branched nanoshells than that over 1 day provided that the former possessed active facets with higher surface energy, facilitating the deposition of Au^0 along these facets and therefore, the branched growth of the shells.

4.4.5 Cell cytotoxicity assay

Here, we preliminary tested the potential biocompatibility of the as-obtained BGNS by using the resazurin cell viability assay in order to establish if the synthesized BGNS could be used in biomedical applications. Resazurin is a blue dye, itself weakly fluorescent until it is irreversibly reduced to the pink colored and highly red fluorescent resorufin. Resazurin is effectively reduced in mitochondria in the presence of diaphorase as the enzyme, and NADPH or NADH the reductant that converts resazurin to resorufin. Then, this conversion makes useful this test to analyze cell viability by assaying the cell mitochondrial metabolic activity.

Cell viability of pegylated BGNS was assayed in a HeLa cervical cell line in a wide range of particle concentrations (ca. $2\cdot10^8$-$2\cdot10^{11}$ NP/mL). As observed in Figure 4.19a the cell viability was above 90% in the whole concentration range except at the largest concentration, for which it decreases to ca. 83%. These data denote *a priori* an excellent biocompatibility of this kind of particles although additional experiments would be required to fully confirm this point.

On the other hand, to reject possible false positives and to confirm the effective incorporation of the NPs inside the cells, optical and transmission electron microscopies were performed. In this way, BGNS seem to be internalized by the cells, and are present to large extents in the cell cytoplasm but not in nuclei, as observed from differential interference contrast (DIC) optical microscopy images (Figure 4.19b). TEM images also confirmed the internalization of the present type of particles inside the cell cytoplasm (in particular, inside intracellular vacuoles, see Figure 4.19c-d), probably occurring via a non-specific endocytosis pathway.

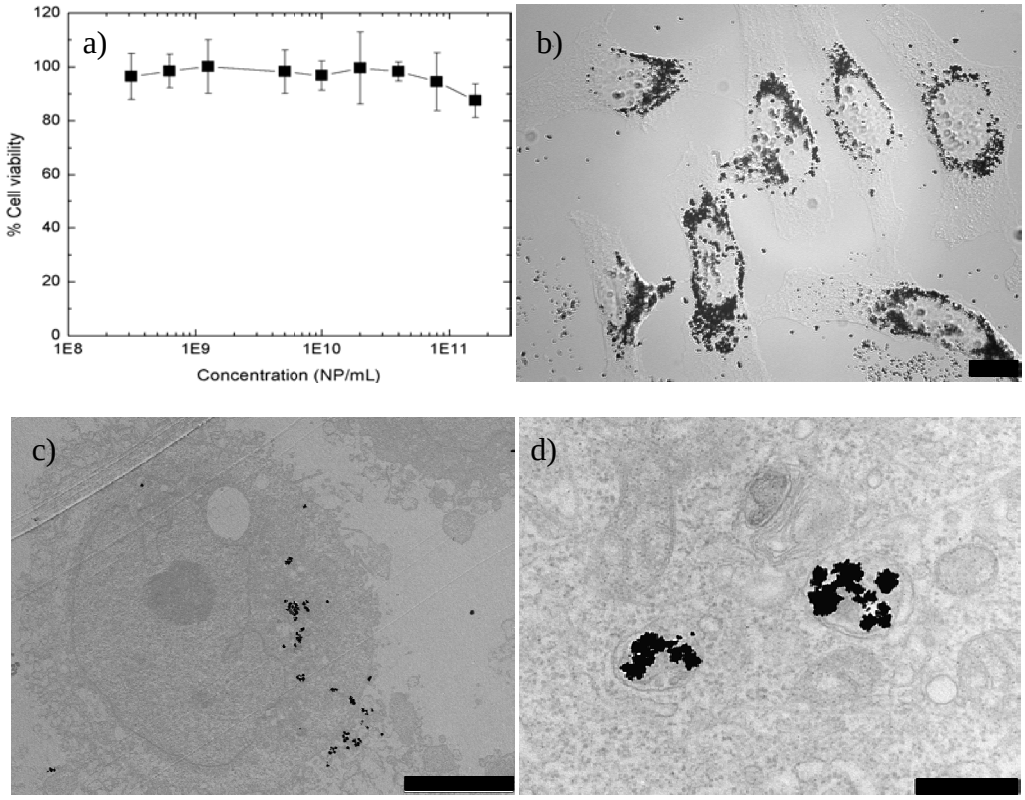

Figure 4.19 a) Cell viability of HeLa cells after incubation with pegylated BGNHS determined by the resazurin viability test. Cytotoxicity of BGNS was negligible in a wide concentration range ($2 \cdot 10^8$-$2 \cdot 10^{11}$ NP/mL). b) DIC microscopy image of HeLa cells after incubation with BGNS. c) Internalization of BGNS into HeLa cells as visualized by TEM. d) The formation of intracellular vacuoles suggests that BGNS are internalized via non-specific endocystosis. Scale bars are 20 μm in b), 5 μm in c), and 500 nm in d).

4.5 Conclusions

In summary, we have synthesized branched gold nanoshells (BGNS) with PLGA cores by means of a surfactant-less method, using an $HAuCl_4/K_2CO_3$ growth solution and concentrated ascorbic acid as reductant. Size and structure (anisotropy) and, in consequence, the optical properties of nanostructures were tuned by modulating the synthetic conditions (feed ratios of Au growth solution, AA and NP-seed precursor). Both chitosan and AA played an important role as co-reductants and directing agents, resulting in the growth of branched structures resembling geometries found in nature, such as viruses, sea-urchins or bushes. Among the diverse experimental variables, the concentration of AA was dominant to enhance the

reactivity of gold ions by reduction of Au^{I} to Au^{0} on the seed surfaces onto preferred facet via a kinetics-favored process. This process is additionally assisted by the presence of the chitosan chains which enable the formation of nanocrystal agglomerates, which can serve as secondary nuleation centers, and can directed the crystal growth through preferred orientations. A excessive amount of AA promotes an instant reduction of the particles, decreasing their anisotropy by the isotropic deposition of the gold ions and the adsorption of excess AA on the surface of nanoshells. Meaningfully, the as-prepared BGNS were stable in aqueous solution for several months, and were found to be internalised by cells in the cytoplasm and fully biocompatible, as deduced from a cell viability test. The hollow and branched architecture of BGNS is also advantageous because it adds another control characteristic (*i.e.* core size) to tune the plasmon band position to the near infrared region of the electromagnetic spectrum, and allowing their potential use as photothermal agents and/or surface enhanced Raman scattering (SERS) probes. In addition, other functional materials and molecules can be incorporated into the core to fabricate multifunctional materials. In this way, these branched hollow NPs hold potential applicability as multifunctional nanoteranostic agents due to their optical properties and core-carrying capacity.

4.6 Bibliography

[1] Sau TK, Rogach AL. Nonspherical Noble Metal Nanoparticles: Colloid-Chemical Synthesis and Morphology Control. Advanced Materials. 2010;22:1781-804.

[2] Zhao P, Li N, Astruc D. State of the art in gold nanoparticle synthesis. Coordination Chemistry Reviews. 2013;257:638-65.

[3] Pérez-Juste J, Pastoriza-Santos I, Liz-Marzán LM, Mulvaney P. Gold nanorods: Synthesis, characterization and applications. Coordination Chemistry Reviews. 2005;249:1870-901.

[4] Grzelczak M, Perez-Juste J, Mulvaney P, Liz-Marzan LM. Shape control in gold nanoparticle synthesis. Chemical Society Reviews. 2008;37:1783-91.

[5] Hao E, Schatz G, Hupp J. Synthesis and Optical Properties of Anisotropic Metal Nanoparticles. Journal of Fluorescence. 2004;14:331-41.

[6] Hao E, Bailey RC, Schatz GC, Hupp JT, Li S. Synthesis and Optical Properties of "Branched" Gold Nanocrystals. Nano Letters. 2004;4:327-30.

[7] Kelly KL, Coronado E, Zhao LL, Schatz GC. The Optical Properties of Metal Nanoparticles: The Influence of Size, Shape, and Dielectric Environment. The Journal of Physical Chemistry B. 2002;107:668-77.

[8] Kühn S, Håkanson U, Rogobete L, Sandoghdar V. Enhancement of Single-Molecule Fluorescence Using a Gold Nanoparticle as an Optical Nanoantenna. Physical Review Letters. 2006;97:017402.

[9] Guerrero-Martínez A, Barbosa S, Pastoriza-Santos I, Liz-Marzán LM. Nanostars shine bright for you: Colloidal synthesis, properties and applications of branched metallic nanoparticles. Current Opinion in Colloid & Interface Science. 2011;16:118-27.

[10] Bardhan R, Grady NK, Cole JR, Joshi A, Halas NJ. Fluorescence Enhancement by Au Nanostructures: Nanoshells and Nanorods. ACS Nano. 2009;3:744-52.

[11] Link S, El-Sayed MA. Shape and size dependence of radiative, non-radiative and photothermal properties of gold nanocrystals. International Reviews in Physical Chemistry. 2000;19:409-53.

[12] Jena BK, Raj CR. Seedless, Surfactantless Room Temperature Synthesis of Single Crystalline Fluorescent Gold Nanoflowers with Pronounced SERS and Electrocatalytic Activity. Chemistry of Materials. 2008;20:3546-8.

[13] Wang W, Pang Y, Yan J, Wang G, Suo H, Zhao C, et al. Facile synthesis of hollow urchin-like gold nanoparticles and their catalytic activity. Gold Bull. 2012;45:91-8.

[14] Loo C, Hirsch L, Lee M-H, Chang E, West J, Halas N, et al. Gold nanoshell bioconjugates for molecular imaging in living cells. Opt Lett. 2005;30:1012-4.

[15] Sun J, Zhang J, Jin Y. 11-Mercaptoundecanoic acid directed one-pot synthesis of water-soluble fluorescent gold nanoclusters and their use as probes for sensitive and selective detection of Cr3+ and Cr6+. Journal of Materials Chemistry C. 2013;1:138-43.

[16] Khanadeev VA, Khlebtsov BN, Staroverov SA, Vidyasheva IV, Skaptsov AA, Ileneva ES, et al. Quantitative cell bioimaging using gold-nanoshell conjugates and phage antibodies. Journal of Biophotonics. 2011;4:74-83.

[17] Li Z, Jin R, Mirkin CA, Letsinger RL. Multiple thiol-anchor capped DNA–gold nanoparticle conjugates. Nucleic Acids Research. 2002;30:1558-62.

[18] Shiang Y-C, Huang C-C, Chang H-T. Gold nanodot-based luminescent sensor for the detection of hydrogen peroxide and glucose. Chemical Communications. 2009:3437-9.

[19] Stewart ME, Anderton CR, Thompson LB, Maria J, Gray SK, Rogers JA, et al. Nanostructured Plasmonic Sensors. Chemical Reviews. 2008;108:494-521.

[20] Carregal-Romero S, Ochs M, Rivera-Gil P, Ganas C, Pavlov AM, Sukhorukov GB, et al. NIR-light triggered delivery of macromolecules into the cytosol. Journal of Controlled Release. 2012;159:120-7.

[21] Braun GB, Pallaoro A, Wu G, Missirlis D, Zasadzinski JA, Tirrell M, et al. Laser-Activated Gene Silencing via Gold Nanoshell−siRNA Conjugates. ACS Nano. 2009;3:2007-15.

[22] El-Sayed IH, Huang X, El-Sayed MA. Selective laser photo-thermal therapy of epithelial carcinoma using anti-EGFR antibody conjugated gold nanoparticles. Cancer letters. 2006;239:129-35.

[23] Hu M, Chen J, Li Z-Y, Au L, Hartland GV, Li X, et al. Gold nanostructures: engineering their plasmonic properties for biomedical applications. Chemical Society Reviews. 2006;35:1084-94.

[24] Huang X, El-Sayed IH, Qian W, El-Sayed MA. Cancer Cell Imaging and Photothermal Therapy in the Near-Infrared Region by Using Gold Nanorods. Journal of the American Chemical Society. 2006;128:2115-20.

[25] Turkevich J, Stevenson PC, Hillier J. A study of the nucleation and growth processes in the synthesis of colloidal gold. Discussions of the Faraday Society. 1951;11:55-75.

[26] Brust M, Walker M, Bethell D, Schiffrin DJ, Whyman R. Synthesis of thiol-derivatised gold nanoparticles in a two-phase Liquid-Liquid system. Journal of the Chemical Society, Chemical Communications. 1994;0:801-2.

[27] Bastús NG, Comenge J, Puntes Vc. Kinetically Controlled Seeded Growth Synthesis of Citrate-Stabilized Gold Nanoparticles of up to 200 nm: Size Focusing versus Ostwald Ripening. Langmuir. 2011;27:11098-105.

[28] Sau TK, Murphy CJ. Seeded High Yield Synthesis of Short Au Nanorods in Aqueous Solution. Langmuir. 2004;20:6414-20.

[29] Jana NR, Gearheart L, Murphy CJ. Wet Chemical Synthesis of High Aspect Ratio Cylindrical Gold Nanorods. The Journal of Physical Chemistry B. 2001;105:4065-7.

[30] Nikoobakht B, El-Sayed MA. Preparation and Growth Mechanism of Gold Nanorods (NRs) Using Seed-Mediated Growth Method. Chemistry of Materials. 2003;15:1957-62.

[31] Millstone JE, Métraux GS, Mirkin CA. Controlling the Edge Length of Gold Nanoprisms via a Seed-Mediated Approach. Advanced Functional Materials. 2006;16:1209-14.

[32] Wang Y, Black KCL, Luehmann H, Li W, Zhang Y, Cai X, et al. Comparison Study of Gold Nanohexapods, Nanorods, and Nanocages for Photothermal Cancer Treatment. ACS Nano. 2013;7:2068-77.

[33] Pelaz B, Grazu V, Ibarra A, Magen C, del Pino P, de la Fuente JM. Tailoring the Synthesis and Heating Ability of Gold Nanoprisms for Bioapplications. Langmuir. 2012;28:8965-70.

[34] Averitt RD, Sarkar D, Halas NJ. Plasmon Resonance Shifts of Au-Coated Au_{2}S Nanoshells: Insight into Multicomponent Nanoparticle Growth. Physical Review Letters. 1997;78:4217-20.

[35] You J, Zhang G, Li C. Exceptionally High Payload of Doxorubicin in Hollow Gold Nanospheres for Near-Infrared Light-Triggered Drug Release. ACS Nano. 2010;4:1033-41.

[36] Shevchenko EV, Bodnarchuk MI, Kovalenko MV, Talapin DV, Smith RK, Aloni S, et al. Gold/Iron Oxide Core/Hollow-Shell Nanoparticles. Advanced Materials. 2008;20:4323-9.

[37] Bakr OM, Wunsch BH, Stellacci F. High-Yield Synthesis of Multi-Branched Urchin-Like Gold Nanoparticles. Chemistry of Materials. 2006;18:3297-301.

[38] Kawamura G, Yang Y, Fukuda K, Nogami M. Shape control synthesis of multi-branched gold nanoparticles. Materials Chemistry and Physics. 2009;115:229-34.

[39] Yang J, Lee J, Kang J, Oh SJ, Ko H-J, Son J-H, et al. Smart Drug-Loaded Polymer Gold Nanoshells for Systemic and Localized Therapy of Human Epithelial Cancer. Advanced Materials. 2009;21:4339-42.

[40] Kim J, Park S, Lee JE, Jin SM, Lee JH, Lee IS, et al. Designed Fabrication of Multifunctional Magnetic Gold Nanoshells and Their Application to Magnetic

Resonance Imaging and Photothermal Therapy. Angewandte Chemie International Edition. 2006;45:7754-8.

[41] Hirsch LR, Stafford RJ, Bankson JA, Sershen SR, Rivera B, Price RE, et al. Nanoshell-mediated near-infrared thermal therapy of tumors under magnetic resonance guidance. Proceedings of the National Academy of Sciences. 2003;100:13549-54.

[42] Bardhan R, Chen W, Perez-Torres C, Bartels M, Huschka RM, Zhao LL, et al. Nanoshells with Targeted Simultaneous Enhancement of Magnetic and Optical Imaging and Photothermal Therapeutic Response. Advanced Functional Materials. 2009;19:3901-9.

[43] Schutz M, Steinigeweg D, Salehi M, Kompe K, Schlucker S. Hydrophilically stabilized gold nanostars as SERS labels for tissue imaging of the tumor suppressor p63 by immuno-SERS microscopy. Chemical Communications. 2011;47:4216-8.

[44] Hao F, Nehl CL, Hafner JH, Nordlander P. Plasmon Resonances of a Gold Nanostar. Nano Letters. 2007;7:729-32.

[45] Baffou G, Quidant R, Girard C. Heat generation in plasmonic nanostructures: Influence of morphology. Applied Physics Letters. 2009;94:153109.

[46] Wang H, Goodrich GP, Tam F, Oubre C, Nordlander P, Halas NJ. Controlled Texturing Modifies the Surface Topography and Plasmonic Properties of Au Nanoshells. The Journal of Physical Chemistry B. 2005;109:11083-7.

[47] Wang H, Fu K, Drezek RA, Halas NJ. Light scattering from spherical plasmonic nanoantennas: effects of nanoscale roughness. Appl Phys B. 2006;84:191-5.

[48] Sanchez-Gaytan BL, Swanglap P, Lamkin TJ, Hickey RJ, Fakhraai Z, Link S, et al. Spiky Gold Nanoshells: Synthesis and Enhanced Scattering Properties. The Journal of Physical Chemistry C. 2012;116:10318-24.

[49] Sanchez-Gaytan BL, Park S-J. Spiky Gold Nanoshells. Langmuir. 2010;26:19170-4.

[50] Sanchez-Gaytan BL, Qian Z, Hastings SP, Reca ML, Fakhraai Z, Park S-J. Controlling the Topography and Surface Plasmon Resonance of Gold Nanoshells by a Templated Surfactant-Assisted Seed Growth Method. The Journal of Physical Chemistry C. 2013;117:8916-23.

[51] Garg N, Scholl C, Mohanty A, Jin R. The Role of Bromide Ions in Seeding Growth of Au Nanorods. Langmuir. 2010;26:10271-6.

[52] Goia D, Matijević E. Tailoring the particle size of monodispersed colloidal gold. Colloids and Surfaces A: Physicochemical and Engineering Aspects. 1999;146:139-52.

[53] Jain PK, Lee KS, El-Sayed IH, El-Sayed MA. Calculated Absorption and Scattering Properties of Gold Nanoparticles of Different Size, Shape, and Composition: Applications in Biological Imaging and Biomedicine. The Journal of Physical Chemistry B. 2006;110:7238-48.

[54] Carpin L, Bickford L, Agollah G, Yu T-K, Schiff R, Li Y, et al. Immunoconjugated gold nanoshell-mediated photothermal ablation of trastuzumab-resistant breast cancer cells. Breast Cancer Res Treat. 2011;125:27-34.

[55] Melancon MP, Lu W, Yang Z, Zhang R, Cheng Z, Elliot AM, et al. In vitro and in vivo targeting of hollow gold nanoshells directed at epidermal growth factor receptor for photothermal ablation therapy. Molecular Cancer Therapeutics. 2008;7:1730-9.

[56] Nguyen HT, Tran KK, Sun B, Shen H. Activation of inflammasomes by tumor cell death mediated by gold nanoshells. Biomaterials. 2012;33:2197-205.

[57] Bao H, Bihr T, Smith A-S, Klupp Taylora RN. Facile colloidal coating of polystyrene nanospheres with tunable gold dendritic patches. Nanoscale. 2013.

[58] Nhung TT, Bu Y, Lee S-W. Facile synthesis of chitosan-mediated gold nanoflowers as surface-enhanced Raman scattering (SERS) substrates. Journal of Crystal Growth. 2013;373:132-7.

[59] Homan KA, Chen J, Schiano A, Mohamed M, Willets KA, Murugesan S, et al. Silver–Polymer Composite Stars: Synthesis and Applications. Advanced Functional Materials. 2011;21:1673-80.

[60] Valenzuela K, Raghavan S, Deymier PA, Hoying J. Formation of Copper Nanowires by Electroless Deposition Using Microtubules as Templates. Journal of Nanoscience and Nanotechnology. 2008;8:3416-21.

[61] Perrault SD, Chan WCW. Synthesis and Surface Modification of Highly Monodispersed, Spherical Gold Nanoparticles of 50−200 nm. Journal of the American Chemical Society. 2009;131:17042-3.

[62] Xu D, Gu J, Wang W, Yu X, Xi K, Jia X. Development of chitosan-coated gold nanoflowers as SERS-active probes. Nanotechnology. 2010;21:375101.

[63] Boca S, Rugina D, Pintea A, Barbu-Tudoran L, Astilean S. Flower-shaped gold nanoparticles: synthesis, characterization and their application as SERS-active tags inside living cells. Nanotechnology. 2011;22:055702.

[64] Wang W, Cui H. Chitosan-Luminol Reduced Gold Nanoflowers: From One-Pot Synthesis to Morphology-Dependent SPR and Chemiluminescence Sensing. The Journal of Physical Chemistry C. 2008;112:10759-66.

[65] Wang W, Yang X, Cui H. Growth Mechanism of Flowerlike Gold Nanostructures: Surface Plasmon Resonance (SPR) and Resonance Rayleigh Scattering (RRS) Approaches to Growth Monitoring. The Journal of Physical Chemistry C. 2008;112:16348-53.

[66] Williams DB, Carter Barry C. Transmission Electron Microscopy: A Textbook for Materials Science. New York: Springer; 2009.

[67] Oldenburg SJ, Averitt RD, Westcott SL, Halas NJ. Nanoengineering of optical resonances. Chemical Physics Letters. 1998;288:243-7.

[68] Bode AM, Cunningham L, Rose RC. Spontaneous decay of oxidized ascorbic acid (dehydro-L-ascorbic acid) evaluated by high-pressure liquid chromatography. Clinical Chemistry. 1990;36:1807-9.

[69] Sau TK, Rogach AL, Döblinger M, Feldmann J. One-Step High-Yield Aqueous Synthesis of Size-Tunable Multispiked Gold Nanoparticles. Small. 2011;7:2188-94.

[70] Luty-Błocho M, Pacławski K, Wojnicki M, Fitzner K. The kinetics of redox reaction of gold(III) chloride complex ions with l-ascorbic acid. Inorganica Chimica Acta. 2013;395:189-96.

[71] Kuzmenko I, Kindermann M, Kjaer K, Howes PB, Als-Nielsen J, Granek R, et al. Crystalline Films of Interdigitated Structures Formed via Amidinium−Carboxylate Interactions at the Air−Water Interface. Journal of the American Chemical Society. 2001;123:3771-83.

[72] Li J, Wu J, Zhang X, Liu Y, Zhou D, Sun H, et al. Controllable Synthesis of Stable Urchin-like Gold Nanoparticles Using Hydroquinone to Tune the Reactivity of Gold Chloride. The Journal of Physical Chemistry C. 2011;115:3630-7.

[73] Song H-M, Wei Q, Ong QK, Wei A. Plasmon-Resonant Nanoparticles and Nanostars with Magnetic Cores: Synthesis and Magnetomotive Imaging. ACS Nano. 2010;4:5163-73.

[74] Chen S, Wang ZL, Ballato J, Foulger SH, Carroll DL. Monopod, Bipod, Tripod, and Tetrapod Gold Nanocrystals. Journal of the American Chemical Society. 2003;125:16186-7.

[75] Carbó-Argibay E, Rodríguez-González B, Pacifico J, Pastoriza-Santos I, Pérez-Juste J, Liz-Marzán LM. Chemical Sharpening of Gold Nanorods: The Rod-to-Octahedron Transition. Angewandte Chemie International Edition. 2007;46:8983-7.

[76] Sreeprasad TS, Samal AK, Pradeep T. Body- or Tip-Controlled Reactivity of Gold Nanorods and Their Conversion to Particles through Other Anisotropic Structures. Langmuir. 2007;23:9463-71.

[77] Wu H-Y, Liu M, Huang MH. Direct Synthesis of Branched Gold Nanocrystals and Their Transformation into Spherical Nanoparticles. The Journal of Physical Chemistry B. 2006;110:19291-4.

CHAPTER V - Polymeric-Gold Nanohybrids for Combined Imaging and Cancer Therapy

5.1 Summary

In this chapter, we report the use of folic acid (FA)-functionalized, doxorubicin (DOXO, a potent anticancer drug)/SPION-loaded poly(lactic-co-glycolic acid)-Au porous shell nanoparticles for simultaneous targeted delivery of localized hyperthermia in combination with magnetic resonance imaging in human cervical cancer (HeLa) cells. These polymeric-gold nanohybrids (PGNHs) were produced by a seeded-growth method using chitosan as an electrostatic "glue" to attach Au seeds to DOXO/SPION-PLGA NPs. In order to determine their potential as theranostic nanoplatforms, we have analyzed their physicochemical properties, cellular uptake and photothermal and chemotherapeutic efficiencies in vitro. In addition, the present nanoplatforms showed a NIR-light triggered release of cargo molecules under illumination. The capacity to induce localised cell death in a well-focused region was also demonstrated. The functionalization of our PGNHs with the targeting ligand folic acid improved their internalization efficiency and specificity. Furthermore, we have proved in vitro the possibility to guide our PGNHs to cancer cells by an external magnetic field, which additionally increased the cellular uptake and therapeutic efficiency.

5.2 Introduction

The outstanding physicochemical properties of nanomaterials and their clever combinations are allowing the development of multifunctional nanoplatform-based integration strategies for multimodal imaging [1-4], simultaneous real-time diagnosis and therapy (theranostics) [4-11] and multimodal therapy [12-16], which holds promise to be in the near future an alternative to current, conventional diagnosis and therapeutics for cancer, and are potentially offering new approaches for earlier detection and/or minimally invasive treatments [17, 18]. One advantage of these new approaches is multidiagnostic and/or multitherapeutic functions can be easily incorporated into the same nanoscale complex, with the potential to simultaneously combine these features in clinical applications.

This kind of biomedical nanosystems opens new windows to potentially overcome some of the different substantial impediments still unresolved in cancer therapeutics, such as for example the substantial toxicity to normal tissues of drug doses required to completely eliminate tumors, the poor effectiveness of drug

treatments against multi-drug resistant cancer cells, the impossibility of early detection of very small tumors or blood circulating malignant cells, or the temporal separation of diagnostics and therapeutic clinical phases [3-6].

Hence, the simultaneous combination of several different therapies in a single nanoplatform to enhance malignant cell cytotoxicity with targeted drug delivery and diagnostic imaging capabilities appears as a very attractive choice to solve, at least partially, these issues. In this regard, one treatment combined with chemotherapy which has shown promising results is thermo-chemotherapy [19-21]. Thermo-chemotherapy is the simultaneous application of a chemotherapeutic agent and hyperthermia (the therapeutic procedure used to raise the temperature above 42-43 ºC °C of a body area affected by maligniciency [22]). Despite the demonstrated enhanced cytotoxicity of some chemotherapeutic agents due to macroscopic temperature increases at low drug doses [21, 23-29], temperature increments can affect cell structure and/or function, such as membranes, cytoskeleton or the synthesis of macromolecules and DNA repair; therefore, refined temperature control (both and temporally) is required [22] in order to avoid undesirable side effects often caused due to non-targeted heating by conventional means (hot water baths, microwave or ultrasound [30-33]).

Recently, near-infrared (NIR) resonant nanomaterials such as gold (Au) nanoshells [7, 8, 34-37], Au nanocages [38], Au nanorods [39-43], and single-walled carbon nanotubes [44-47] have shown a great ability to absorb NIR light and convert it into cytotoxic local heat able to be used for tumor-selective treatments. Hence, if heat and drugs could be simultaneously delivered by nanoplatform at the tumor area, the therapeutic efficacy would be expected to be significantly improved with minimal side effects [42]. To additionally minimize administrated doses and maximize therapeutic efficacy, molecules such as antibodies, peptides or small ligands can be also attached to the surface of the former nanomaterials to provide improved targeted delivery through the recognition of overexpressed specific receptors on the surface of malignant cells [48, 49], although different *in vivo* studies have pointed to such surface modifcations only moderately enhance tumor/cell specificity, and passive tumour targeting dominates [50].

Finally, to provide the nanomaterial with diagnostic capabilities, the use of loaded/attached superparamagnetic iron oxide nanoparticles (SPIONs) in/to

nanoplatforms would allow their use as imaging T_2 contrast agents in magnetic resonance imaging (MRI) to obtain highly resolved 3D images of living organisms [51]. Through SPIONs manipulation by an external magnetic field, magnetically targeted drug delivery nanosytems for regulating drug release would be also expected [52].

Here, we report the use of folic acid (FA)-functionalized, doxorubicin (DOXO, a potent anticancer drug)/SPION-loaded poly(lactic-co-glycolic acid)-Au porous shell nanoparticles for simultaneous targeted specific delivery of localized cytotoxic heat and chemotherapy combined with MRI diagnosis in human cervical cancer (HeLa) cells. Previously, Halas *et al.* [35, 53] developed Au nanoshells with a silica core, in which SPIONs and the fluorescent dye indocyanine green (ICG) were encapsulated in a silica layer surrounding the metal shell for MRI and fluorescence imaging. The therapeutic response of the nanoconstruct was achieved through the NIR photothermal properties of the Au shell, and targeted delivery of the platform was pursued through the surface attachment of a human epidermal growth factor receptor 2 (HER2) antibody to target HER2 overexpressing cancer cells. A related system was developed by Hyeon *et al.* [54] but, in this case, SPIONs were directly embedded in the Au shell. This group also co-loaded SPIONs (or quantum dots, QDs) with DOXO inside PLGA NPs functionalized with FA ligands for simultaneous MRI (or fluorescence imaging) and targeted controlled delivery [55]. Dai *et al.* obtained Au nanoshell micelles composed of a cholesteryl succinyl silane core loaded with DOXO and SPIONs to achieve the simultaneous combination of MRI, magnetic targeted drug delivery, light triggered drug release, and photothermal therapy [56]. Yoo *et al*. [57-60] and Haam *et al.* [61] developed bare or antibody-functionalized DOXO-loaded PLGA-Au half and full nanoshells, respectively, to analyze the targeted and non-targeted simultaneous cytotoxic combination provided by NIR-induced hyperthermia and released drug on skin (A431), breast (SK-BR-3 and MCF7) and cervical (HeLa) cancer cells, and for rheumatoid arthritis treatment.

In this work, we present a polymeric-gold nanohybrid (PGNH) in which DOXO molecules and SPIONs are co-loaded to different extents inside the core of biocompatible and biodegradable PLGA NPs, and a complete porous gold layer is grown onto the surface of the polymeric NPs to provide NIR-light responsiveness to the PGNHs. FA attached to the surface of the Au layer allows PGNHs to be

specifically delivered *in vitro* to folic acid receptors overexpressed on the membrane surface of a HeLa cancer cell line to allow their internalization by receptor-mediated endocytosis, increasing cell accumulation [62, 63]. This is further enhanced when an external magnetic field is applied to the cultured cells by means of a magnetic-guiding effect [52]. Also, the presence of SPIONs allows increasing levels of magnetic contrast of cancerous cells by MRI. Since these nanoplatforms are NIR-resonant, the simultaneous effect of targeted NIR-induced hyperthermia and chemotherapy results in larger cell toxicities at lower drug concentrations. In comparison with the pairwise combinations, a synergistic effect is observed. Thus, the importance of our report lies in the simultaneous successful combination of chemotherapy with hyperthermia, magnetic and ligand assisted-targeted delivery and high-resolution imaging fulfilled in a single hybrid nanoconstruct.

5.3 Materials and methods

5.3.1Materials

Poly(D,L-lactide-*co*-glycolide) (PLGA) of 38-54 kDa with 50:50 lactide–glycolide ratio, Pluronic F127, $FeCl_2$, $FeCl_3$, $HAuCl_3 \cdot 3H_2O$, folic acid, N-(3-dimethylaminopropyl)-N'-ethylcarbodiimide hydrochloride (EDC), low molecular weight chitosan (LMW-chitosan, M_W = 111 kDa), ascorbic acid, trisodium citrate dihydrate, sodium borohydride ($NaBH_4$, 99%), $FeCl_2$, $FeCl_3$, crystal violet solution, and Nile Red (NR) were purchased from Sigma–Aldrich (St. Louis, MO, USA). N-hydroxysulfosuccinimide (sulfo-NHS) was purchased from ProteoChem (Cheyenne, USA). Calcein AM, propidium iodide, BODIPY® Phalloidin and ProLong® Gold antifade reagent with DAPI were purchased from Invitrogen (Carlsbad, USA). Oleic acid with 90% purity was purchased from Alfa Aesar (Karlshrue, Germany). DOXO·HCl and Dulbecco's Modified Eagle Medium, fetal bovine serum (FBS), L-glutamine, penicillin/streptomycin, sodium pyruvate, and MEM non-essential amino acids (NEAA) were purchased from Fisher Scientific (Pittsburgh, USA). SH-PEG_{5000}-NH_2 and SH-PEG_{5000}-OCH_3 were purchased from Laysan Bio, Inc. (Arab, USA). Dialysis membrane tubing (molecular weight cutoffs ~100-500 and ~3500 Da) was purchased from Spectrum Laboratories, Inc. (Rancho Dominguez, CA, USA). All

other chemicals and solvents were of reagent grade (purchased from Sigma–Aldrich). All glassware was washed with aqua regia and HF 5% (v/v) and extensively rinsed with water. Milli-Q water was used for preparation of aqueous solutions.

5.3.2 Synthesis of SPIONs

Oleic acid-stabilized Fe_3O_4 SPIONs were synthesized by a coprecipitation method [64, 65]. Briefly, aqueous solutions of 0.1 M of $FeCl_3$ (30 mL) and $FeCl_2$ (15 mL) prepared with N_2 purged-water were mixed; then, 3 mL of 5 M ammonia solution were added in small aliquots of 0.6 mL while stirring. A black precipitate was formed indicating the formation of SPIONs. After 20 min of stirring under N_2 atmosphere, 56.4 mg of oleic acid were added to the SPIONs and the temperature was raised to 80 °C and kept for 30 min while stirring to evaporate the ammonia. The magnetic NPs were washed twice by centrifugation at 9000 rpm for 20 min to eliminate excess of oleic acid, the supernatant was discarded and the precipitate was lyophilized and stored at 4 °C.

5.3.3 Preparation of DOXO/SPION-PLGA NPs

PLGA NPs containing SPIONs/DOXO or SPIONs/NR were prepared using a conventional emulsion-evaporation method with modifications. In a typical preparation, PLGA (25 mg) was dissolved in a sealed vial containing 2 mL of methylene chloride (MC), 2.5 mg of DOXO (previously converted to its hydrophobic base form by addition of triethylamine, as reported in literature [66] (or 2.5 mg of Nile Red, NR, when corresponding), and 2 mg of SPIONs dispersed in MC by sonication with a probe type sonicator (20 kHz, Bandelin Sonopuls, Bandelin GmbH, Berlin, Germany) at 20 W for 10 min in an ice bath. DOXO (NR) concentration was measured by UV-vis spectroscopy with a calibration curve (Figure 5.1a-b) Then, this organic solution was added in a single step to a Pluronic F127 aqueous solution (50 mL, 1% (w/v)) and was immediately sonicated at 100 W for 15 min in an ice bath. The organic solvent was completely evaporated under mechanical stirring overnight, the dispersion was subsequently centrifuged twice at 9000 rpm for 30 min and 20 ºC, the supernatant removed, and the final precipitate was resdispersed in 5 mL of water.

5.3.4 Synthesis of citrate-capped Au nanoseeds

Citrate-capped gold seeds were prepared based on a method previously reported by Jana et al. [67]. Briefly, 10 mL of $2.56 \cdot 10^{-4}$ M tri-sodium citrate were mixed with 0.125 mL of 0.010 M $HAuCl_3 \cdot H_2O$. Next, 0.300 mL of 0.1 M ice cold $NaBH_4$ solution was added all at once and mixed. The solution turned orange-pink immediately indicating particle formation. The average particle size obtained from Transmission electron microscopy (TEM) was 4 ± 2 nm.

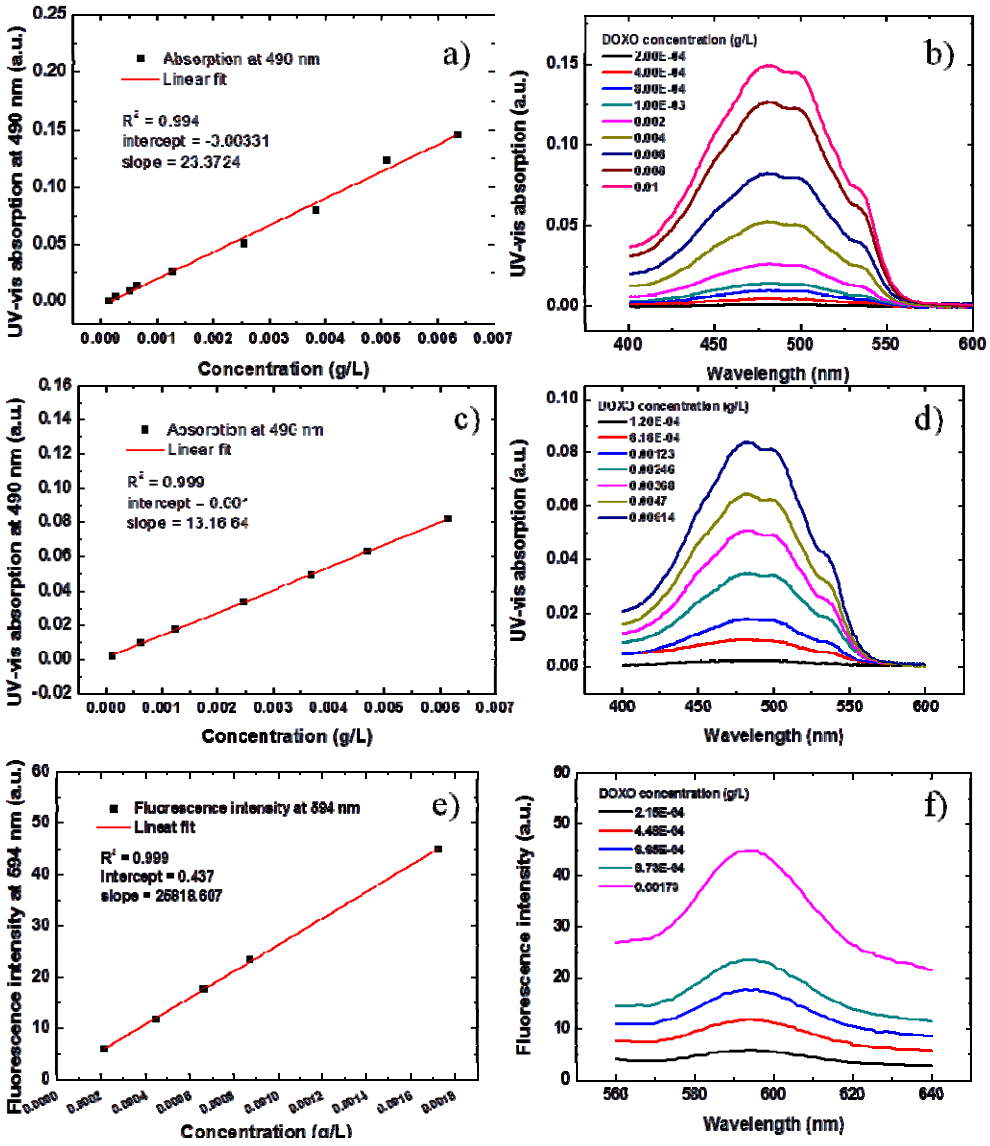

Figure 5.1: DOXO calibration curves and Uv-vis and fluorescence spectra of the standards used to build the curves: in methylene chloride, a) and b); in dimethyl sulfoxide, c) and d). DOXO fluorescence calibration curve e) and fluorescence spectra of DOXO standards f) in PBS (pH 7) used to prepare the curve.

5.3.5 Preparation of DXSP-PGNHs

Au citrated-capped nanoseeds were complexed to DOXO/SPION-PLGA NPs by means of electrostatic interactions between the positively charged chitosan on the surface of the NPs and negatively charged citrate-Au seeds. First, 5 mL of PLGA NPs suspension were mixed with 0.25 mL of 1 wt. % low molecular weight-chitosan previously dissolved in 1% (v/v) acetic acid. After stirring for 4 h, NPs were centrifuged twice at 9000 rpm for 30 min to eliminate free and loosely adsorbed chitosan. Then, the positively charged NPs were mixed with 1 mL of Au nanoseed solution and stirred 4 h at ambient temperature. The sample was centrifuged at 7000 rpm for 15 min and 20 °C. The supernatant was discharged and the precipitate was redispersed in 5 mL of water. To grow the gold nanoshells, 1 mL of the Au nanoseed decorated DOXO/SPION-PLGA NPs was mixed with 20 mL of an Au growth solution (0.05 wt.% K_2CO_3 and 0.02 wt.% $HAuCl_3 \cdot 3H_2O$ stored for 24 h prior use) and stirred 1 min; subsequently, 50 µL of ascorbic acid (0.5 M) were added. Immediately after the sample changed from clear to blue color, indicating the porous shell formation to give DOXO/SPION-PLGA NPs with a porous shell layer (DXSP-PGNHs). DXSP-PGNHs were left standing overnight for Ostwald rippening. Then, they were washed three times by centrifugation at 3500 rpm for 15 min and 20 °C, and finally redispersed by vortexing in water. High yields of DXSP-PGNHs were obtained with negligible generation of by-products such as small Au NPs. Despite sedimentation due to the high density of gold layer and SPIONs cargo, DXSP-PGNHs presented no large agglomeration in water, buffers or cell growth medium containing FBS, as observed by visual inspection and optical microscopy.

5.3.6 Characterization of DOXO/SPION-PLGA and DXSP-PGNHs NPs

NP sizes were obtained by dynamic light scattering (DLS) at 25 °C by means of an ALV-5000F (ALV-GmbH, Germany) instrument with vertically polarized incident light (λ = 488 nm) supplied by a diode-pumped Nd:YAG solid-state laser (Coherent Inc., CA, USA) operated at 2 W, and combined with an ALV SP-86 digital correlator (sampling time 25 ns to 100 ms). NP sizes and morphologies were also acquired by transmission and scanning electron microscopy (TEM and SEM,

respectively) by means of a Phillips CM-12 and a Carl Zeiss Libra 200 Fm Omega, and a FESEM ultra Plus electronic microscopes operating at 120 and 20 kV, respectively. Samples were prepared for analysis by evaporating a drop of the hybrid NP dispersion on a carbon-coated copper grid without staining (TEM) or on a silicon wafer (SEM). ζ-potentials were measured with a Zetasizer Nano ZS (Malvern, UK) using dispossable folded capillary cells. Samples were measured in triplicate in PBS (pH 7) at 25 °C. Optical characterization of the nanoconjugates was carried out by UV-vis-NIR and fluorescence spectroscopies with a Cary Bio 100 spectrophotometer and a Cary Eclipse spectrfluorometer, respectively (Agilent Technologies, USA). The concentration of PGNHs was determined by viscometry and UV-vis spectroscopy as reported previously in Chapters 3 and 4.

For DOXO loading capacity (LC) and encapsulation efficiency (EE) quantification, 1 mL of the DOXO/SPION-PLGA NP dispersion was lyophilized for 24 h, weighted and dissolved in 2 mL of dimethyl sulfoxide. The amount of DOXO was measured by UV-vis and/or fluorescence spectroscopy with a previously prepared calibration curve (Figure 5.1c-d). The LC and EE of the SPIONs were assessed by ICP-MS in a Varian 820-MS equipment (Agilent Technologies, USA). Drug loaded, D.L., and entrapment efficiency, E.E., in the DXSP- NPs were calculated as follows:

$$D.L.\% = \frac{weight\ of\ DOXO,SPIONs\ or\ ICG\ in\ NPs}{weight\ of\ NPs} \times 100 \qquad \text{(Eq 5.1)}$$

$$E.E.\% = \frac{weight\ of\ DOXO,SPIONs\ or\ ICG\ in\ NPs}{weight\ of\ DOXO,SPIONs\ or\ ICG\ initially\ loaded} \times 100 \qquad \text{(Eq 5.2)}$$

5.3.7 Conjugation of FA to DXSP-PGNHS NPs

5 mL of 11.33 mM FA solution in 130 mM $NaHCO_3$ buffer (pH 7.0) where mixed with 5 mL of 34 mM of N-(3-dimethylaminopropyl)-N'-ethylcarbodiimide hydrochloride (EDC) and 5 mL of 34 mM of N-hydroxisulfosuccinimide (sulfo-NHS), both dissolved in $NaHCO_3$ buffer. This mixture was reacted for 20 min at ambient temperature and protected from light [68]. Excess reagents were eliminated by extensive dialysis (membrane MWCO 0.1-0.5 kDa). The activated FA was mixed

with a 2.25 mM solution of SH-PEG_{5000}-NH_2 dissolved in the same buffer ([FA]:[PEG] = 5). This was reacted 4 h at ambient temperature in the dark. After reaction, the SH-PEG_{5000}-FA conjugate was dialyzed 24 h with a 3500 MWCO cellulose membrane against water to eliminate unreacted FA-NHS and by-products.

DXSP-PGNHs and BNK-PGNHs were pegylated with SH-PEG_{5000}-FA in a straightforward process. Briefly, 2 mL of PGNHs were mixed with 1 mL of 20 mM K_2CO_3 and 1 mL of SH-PEG_{5000}-FA (or SH-PEG_{5000}-OCH_3) and stirred 4 h in an ice bath. PGNHs were centrifuged at 3500 rpm for 10 min at 20ºC and washed three times to eliminate excess of SH-PEG_{5000}-FA. In order to determine the number of FA molecules attached to PGNHs, a control sample with water instead of PGNHs was subjected to the same procedure. A calibration curve of SH-PEG_{500}-FA was prepared (Figure 5.2a-b). Samples with 0, 5, 10, 15 and 25 µL of SH-PEG_{5000}-FA stock solution (0.56 mM) were prepared and left to a final volume of 500 µL with K_2CO_3 and water in the same proportions (1:3). A control sample (2 mL of deionized water, 1 mL of K_2CO_3 (20 mM) and 1 mL of SH-PEG_{5000}-FA) was made exactly the same as the PGNH-PEG_{5000}-FA one. Supernatants after pegylation of PGNHs and of control sample (supernatant was used to avoid error from possible aggregate formation and sedimentation) were extracted very carefully with a micropipette and used to calculate the concentration of SH-PEG_{5000}-FA attached to PGNHs using a calibration curve (Figure 5.2c). The concentration of non-attached SH-PEG_{5000}-FA was subtracted to the concentration of the processed control sample and this value was assumed to be the concentration of SH-PEG_{5000}-FA attached to PGNHs.

5.3.8 Laser induced temperature increase with NIR-continuous wave illumination (NIR-CW)

Temperature increment tests were performed with a continuous wave fiber-coupled diode laser source of 808 nm wavelength (50W, Oclaro Inc, San Jose, CA, USA). The laser was powered by a Newport 5700-80 regulated laser diode driver (Newport Corporation, Irvine, CA, USA). A 200-µm-core optical fiber was used to transfer laser power from the laser unit to the target solution, and equipped with a lens telescope mounting accessory at the output, which allowed for tuning of the laser spot size in the range 1-10 mm. The output power was independently calibrated using an

optical power meter (Newport 1916-C) and laser spot size was previously measured with a laser beam profiler (Newport LBP-1-USB), which was placed at the same distance (8 cm) between the lens telescope output and the quartz cuvette (or the 96-well plate). For measuring the temperature change mediated by the present DXSP-PGNHs, 2 mL of hybrid DXSP-PGNHs were placed in a quartz cuvette and irradiated for 10 min intervals and/or at different power intensities. The temperature of samples was measured with a type J thermocouple linked to a digital thermometer inserted into the solution.

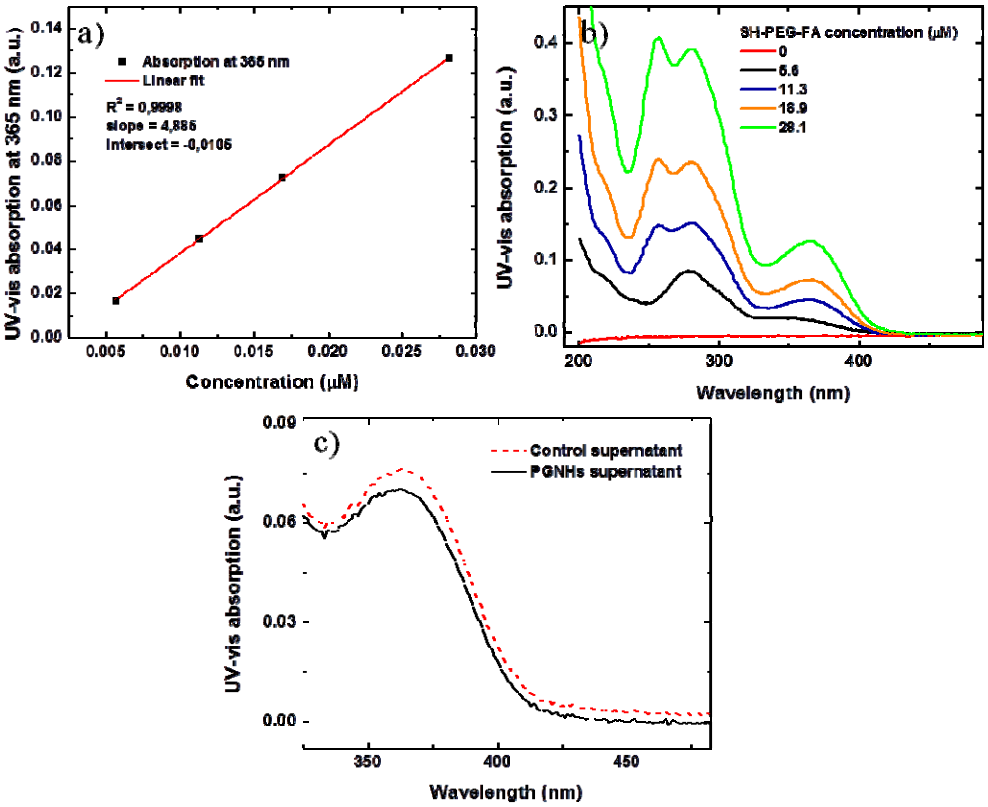

Figure 5.2: a) Calibration curve of SH-PEG_{5000}-FA. b) UV-vis spectra of the standards used to prepare the curve. c) UV-vis spectra of the PGNHs sample and control sample supernatantw after pegylation. The difference between both samples was assumed to be the conjugated SH-PEG_{5000}-FA.

5.3.9 *In vitro* NIR-laser triggered release of NR-PGNHs cargo in single cells with Near Infrared short pulsed illumination (NIR-SPI)

In vitro light-triggered release of cargo from NR-PGNHs was assayed with a wide field fluorescence microscope Axiovert 200M from Zeiss (Germany). The

microscope was coupled with an 830 nm IR laser diode via fiber optics and a beam-coupling device (Rapp-Opto DL-830 CW laser, 130 mW maximum output) and fixed spot illumination coupling. The maximum light power reaching the sample image plane on top of the used 63X/1.4 oil immersion Plan-Apochromat objective was measured to be ~30 mW (continuous output). The light energy was dispersed on a circular spot of ca. 6 μm^2. A tunable power supply output power of the laser could be varied smoothly from 0 to 30 mW effective light power on the sample plane. HeLa cells ($1 \cdot 10^5$ per dish) were seeded and cultured for 24 h in 35 mm Ibidi® µ-grid 500 dishes at standard culture conditions. Then, cells were washed with PBS and the medium was replaced with fresh medium containing NR-PGNHs ($1 \cdot 10^9$ NPs/mL) and incubated for 6 h. Subsequently, NP-containing cells were washed three times with PBS, and the medium containing NR-PGNHs was replaced with fresh medium and incubated for additional 18 h. The dishes were placed on the microscope stage within a controlled temperature and 5 % CO_2 atmosphere chamber. After localization and focusing, cells containing NR-PGNHs were illuminated for 1 s with a power of 0.3 mW/μm^2 or 0.6 mW/μm^2 (= 3.6 mW / 6 μm^2) (NIR-SPI) which correspond to laser fluences of $3 \cdot 10^4$ and $6 \cdot 10^4$ J/cm^2 and total deposited energies of 1.8 and 3.6 mJ, respectively. These laser intensities cause negligible damage to cells as it was demonstrated previously [69]. Confocal microscopy images of NR-PGNHs-containing cells were acquired with a LSM 510 META confocal microscope from Zeiss (Germany) before and after illumination with the laser-microscope in order to observe the laser-triggered release of cargo from NR-PGNHs. NR was excited with a 488 nm argon laser and light emission was acquired with a LP 590 nm filter.

5.3.10 Effect of NIR light on DXSP-PGNHs shape (with NIR-SPI)

In order to investigate the effect of laser illumination on the morphology of the NPs, 1 mL of SiO_2 beads (5 µm) with positive surface charge was mixed with 1 mL of negatively charged DXSP-PGNHs for 15 min and centrifuged at 1500 rpm for 10 minutes to discard non-attached NPs. A drop of the SiO_2/DXSP-PGNHs assembly was cast on a carbon-coated copper grid and left drying. TEM images of the assemblies placed in the center of the copper grid (easily detectable due to the large size of the SiO_2/DXSP-PGNHs) were acquired and, then, the grid was placed on a microscope glass slide and illuminated with the laser-microscope tandem at the same

powers previously used in release experiments. TEM images of the same SiO_2/DXSP-PGNHs assemblies previously analyzed were acquired after laser illumination. In this way, we were able to observe the effect of laser illumination on DXSP-PGNHs morphology.

5.3.11 NIR-laser triggered release of DOXO (with NIR-CI)

Release kinetics of DOXO from DOXO/SPION-PLGA NPs and from DXSP-PGNHs was assessed *in vitro* at 37 °C in PBS buffer (pH 7.2). Briefly, 5 mL of DOXO/SPION-PLGA NPs or DXSP-PGNHs with known DOXO concentrations were placed in centrifuge tubes. Samples were maintained in a 37 °C bath with constant stirring. The samples were irradiated repeatedly over a period of 5 min, followed by 1 h intervals with the laser turned off. Each hour, 500 µL of sample were taken and centrifuged at 3500 rpm (DXSP-PGNHs) or at 5000 rpm (DOXO/SPION-PLGA NPs) for 10 min at 20 °C. The supernatant was carefully extracted and its fluorescence at 594 nm was measured in a Cary Eclipse spectrophotometer (Agilent Technologies, Spain) for quantification of released DOXO with a calibration curve (Figure 5.1e-f). After centrifugation and supernatant extraction, the settled DOXO/SPION-PLGA NPs and DXSP-PGNHs were resuspended with fresh buffer and returned to the original sample.

5.3.12 Cellular uptake by confocal microscopy

DXSP-PGNHs uptake was followed by confocal microscopy by seeding HeLa cells on poly-L-lysine coated glass coverslips (12×12 mm^2) placed inside 6-well plates (3 mL, $5 \cdot 10^4$ cells/well) and grown for 24 h at standard culture conditions (5% CO_2 at 37 ºC in Dulbecco's Modified Eagle Medium (DMEM) supplemented with 10% (v/v) FBS, 2 mM L-glutamine, 1% penicillin/streptomycin, 1 mM sodium pyruvate, and 0.1 mM MEM Non-Essential Amino Acids (NEAA)). Then, 200 µL ($1 \cdot 10^9$ NPs/mL) were added to cells. After 6 h of incubation the NP-containing cells were washed three times with PBS pH 7.4 and, then, fixed with paraformaldehyde 4% (w/v) for 10 min, washed with PBS, permeabilized with 0.2% (w/v) Triton X-100, and stained with BODIPY® Phalloidin (Invitrogen). The cells were washed again

with PBS, mounted on glass slides stained with ProLong® Gold antifade DAPI (Invitrogen) and cured for 24 h at -20 °C. Samples were visualized with 20X and 63X objectives using a confocal spectral microscope Leica TCS-SP2 (Leica Microsystems GmbH, Heidelberg Mannheim, Germany), whereby the blue channel corresponds to DAPI (λ_{ex} 355 nm), the red channel to BODIPY® Phalloidin (λ_{ex} 633 nm), and the green channel to DOXO/SPION-PLGA-Au PS NPs as captured in reflection mode.

5.3.13 Cellular uptake by TEM

Uptake of DXSP-PGNHs by HeLa cells was also investigated by TEM. HeLa cells were seeded in 6-well plates (3 mL, $5 \cdot 10^4$ cells/well) and grown for 24 h at standard culture conditions. Then, 200 μL ($1 \cdot 10^9$ NPs/mL) were added to cells. After 6 h of incubation the NP-containing cells were washed three times with PBS, trypsinized and centrifuged at 1500 rpm for 4 min. Cell pellets were fixed with 500 μL of 2.5 wt.% glutaraldehyde. The pellet were then included in an agar pellet, post-fixed with osmium tetraoxide in 0.1 M cacodylate buffer (1% (w/v)), and finally pelletized with Eponate (Ted Pella Inc, Redding, CA, USA). Ultra-thin cuts were obtained with an ultramicrotome (UltraCut S, Leica Microsystems GmbH) and were analyzed with TEM (JEOL JEM 1011, Japan).

5.3.14 Cellular uptake by magnetic resonance imaging and magnetic susceptibility

Transverse relaxation times were measured at 9.4 T (400 MHz) with 440 mT m^{-1} gradients and 25 ºC with a Bruker Biospin USR94/20 instrument (Ettlingen, Germany). MRI phantoms were constructed in 1.6% (w/v) agarose solutions (Sigma–Aldrich) following a previously published experimental protocol [70]. Firstly, a 1.6% (w/v) agarose solution was heated and stirred at 80 ºC until complete dissolution of the solid agarose. Then, while the system was fluid, an arrangement of seven centrifuge tubes (1.5 mL) were placed within the agarose and allowed to cool to room temperature. After solidification, the tubes were removed and an agarose mold with seven holes was obtained. For cell imaging, HeLa cells ($2 \cdot 10^6$ cells) were seeded in 75 cm^2 flasks and cultured for 24 h at standard condition. Then, the medium was

replaced with fresh one containing a suitable amount of PGNHs (with or without FA) ($1 \cdot 10^9$ NPs/mL) and incubated for 6 h. Then, the medium with the NPs was removed and the cells were washed with PBS and incubated for 18 h. Cells were tripzinized and resuspended in 100 μL of PBS. In each hole of the phantom a mixture of cells labeled with NPs and agarose 2% (w/v) was placed. After a resting period, 1.6% (w/v) agarose was added to the mold to seal the phantom holes. Imaging of the phantoms was performed acquiring a 3D-Gradient echo image (T_2-weighting) with the following parameters: field of view: 80×80×40 mm, matrix size: 512×512×256 points giving a spatial resolution of 156×156×156 μm, echo time T_E = 7.89 ms and repetition time T_R = 100 ms, flip angle 20º and 2 averages. Magnetic susceptibility measurements were carried out with a SQUID magnetometer (Quantum Design MPMS5, San Diego, CA) at 5 K and 300 K.

5.3.15 Chemo-photothermal cytotoxicity (with NIR-CI)

The chemo-photothermal cytotoxic effect of non-functionalized, FA-functionalized and magnetically guided FA-functionalized PGNHs was qualitatively assessed on HeLa cells. Cells (3 mL, $5 \cdot 10^4$ cells/well) were seeded in 6-well plates and grown for 24 h at standard culture conditions. Then, 200 μL ($1 \cdot 10^9$ NPs/mL) were added to cells. After 6 h of incubation the NP-containing cells were washed three times with PBS pH 7.4 and illuminated with a laser (808 nm) at 2.5 W/cm^2 for 5 min. Cells were incubated for further 18 h. Right before analysis with a confocal microscope (Leica Microsystems GmbH) cells were washed three times with PBS to eliminate any residue of serum esterase that could cause interference [69]. Then, 3 mL of PBS with 1 wt.% of calcein AM (λ_{ex} = 495 nm, λ_{em} = 515 nm) and 1 wt.% of propidium iodide (λ_{ex} = 495 nm, λ_{em} = 515 nm) were added and incubated for 10 min.

5.3.16 *In vitro* cell growth cytotoxicity

Cytotoxicity induced by DXSP-PGNHs was determined by crystal violet staining [71, 72] as the inhibition of cellular growth. To this end, HeLa cells with an optical confluence of 80–90% were seeded into 96-well plates (100 μL, $1.5 \cdot 10^4$ cells/well) and grown for 24 h at standard culture conditions. Afterwards, the DXSP-

PGNHs and control samples were injected in the wells (100 μL) and incubated for 24 h and 48 h. After incubation, the culture medium was discarded and the cells were washed with 10 mM PBS, pH 7.4 several times. The cells were shaken at room temperature (300 rpm, 15 min) in the presence of 10 μL of a glutaraldehyde solution (11% (w/v) in water). The solution was discarded and cells were washed 3-4 times with milli-Q water. The cells were then shaken at room temperature (300 rpm, 15 min) in the presence of 100 μL of a crystal violet solution (0.1% (w/v) in 200 mM orthophosphoric acid, 200 mM formic acid, and 200 mM 2-N-morpholino-ethanesulfonic acid (MES), pH 6). The solution was discarded, and the cells were again washed 3-4 times with milli-Q water. Once washed, the cells were left for incubation at room temperature overnight for drying. Once dried, the cells were shaken at room temperature (300 rpm, 15 min) in the presence of 100 μL of acetic acid (10% (v/v) in water). Immediately after, the absorbance of the resulting solution was measured with a Microplate Reader (FLUOstar Optima, BMG Labtech GmbH, Germany) operating at 595 nm. All experiments were triplicate carried out. The growth inhibition was quantified as:

$$\%\ \text{Inhibition} = 100 - \frac{100 * \text{OA}}{\text{TA}} \qquad \text{(Eq 5.3)}$$

where OA and TA stand for the absorbance of studied samples and negative controls (cells in the absence of PGNHs), respectively.

5.4 Results and discussion

5.4.1 Preparation and characterization of the multifunctional nanoplatforms

Core-shell nanomaterials composed of iron oxide coated with a layer of a different inorganic material such as gold are very interesting since the resulting nanostructures can combine the magnetic and optical properties of the constituent elements while reducing the toxicity of the iron oxide, which opens the door to these

nanohybrid materials to be used as potential theranostic tools. To increase the effectiveness of these PGNHs, one must carefully control their physicochemical properties including size, shape, morphology, charge and surface chemistry.

Here, different kinds of core-shell multifunctional polymeric-gold nanohybrids were prepared for comparison purposes: PLGA-Au, PLGA-Au-FA, DOXO/SPION-PLGA-Au and DOXO/SPION-PLGA-Au-FA, named BNK-PGNH, BNK-PGNH-FA, DXSP-PGNH and DXSP-PGNH-FA, respectively. Configuration of each nanohybrid is detailed in Figure 5.3.

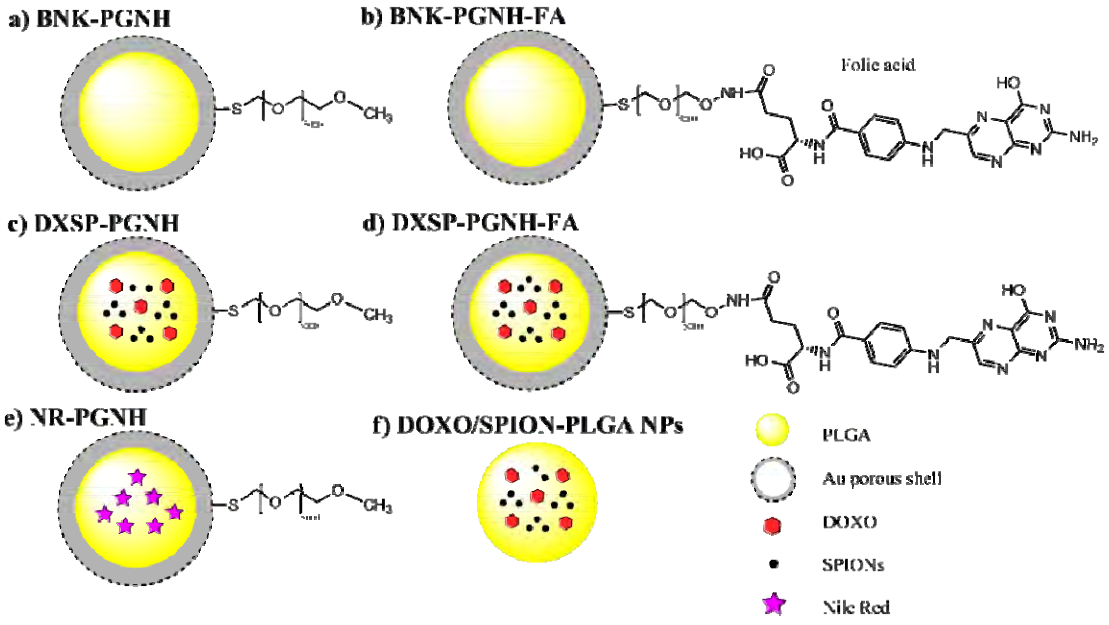

Figure 5.3: Sketches of polymeric-gold nanohybrids (PGNHs) and DOXO/SPION-PLGA NPs.

The synthesis of all these kinds of PGNHs was performed through a multistep procedure. PLGA NPs with (or without) the hydrophobic cargos (DOXO and SPIONs) were prepared by an oil-in-water (o/w) emulsion and subsequent solvent evaporation method, as previously described [60, 73]. In some experiments (NIR-triggered cargo release), the dye Nile Red (NR), (named NR-PGNH, Figure 5.3e) was also used as a model hydrophobic drug. When using the anticancer drug DOXO, DOXO·HCl was converted to its hydrophobic base form by addition of triethylamine [66] to favor its entrapment inside the hydrophobic polymeric matrix. With the same objective, oleic acid-stabilized SPIONs were synthesized by a coprecipitation method

[64], with an average inorganic core diameter of 9.8 ± 0.9 nm as measured by TEM (Figure 5.4a). It is worth mentioning that the size of the resulting PGNHs is largely determined by the size of the primary PLGA NPs. In this way, the molecular weight of the PLGA polymer as well as other external factors in the NP preparation procedure (polymer and stabilizer concentration, temperature, cargos concentration, ultrasonic power and duration, etc.) can be tuned to reach the desired final PGNHs size [74-77].

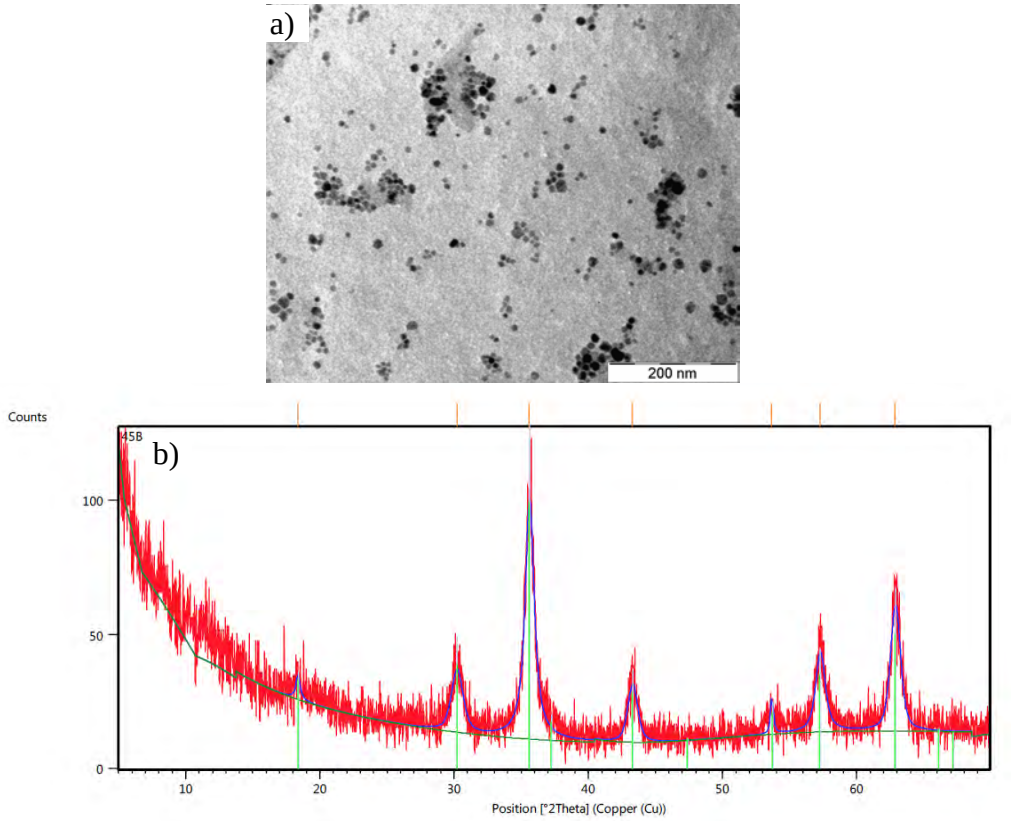

Figure 5.4: a) TEM image of oleic acid-stabilized Fe_3O_4 NPs; b) Powder X-ray diffractogram of as-synthesised oleci acid stabilized Fe_3O_4 NPs. Green lines indicate the position of the characteristic peaks in the diffractogram whereas orange vertical lines denote the characteristic peaks of magnetite X-ray diffraction at (from left to right) (111), (220), (311), (400), (422), (511), and (440) planes.

A mixed dispersion of SPIONs, DOXO (or NR when corresponding), and PLGA in methylene chloride, as detailed in the Experimental Section, was poured into an aqueous solution of block copolymer F127, $EO_{97}PO_{69}EO_{97}$ (where EO and PO are an oxyethlyene and an oxypropylene unit, respectively, and the subscripts denote

the block lengths), used as an emulsifier and stabilizer, and the resulting solution underwent strong sonication. After solvent evaporation DOXO/SPION-PLGA NPs displayed a mean hydrodynamic diameter of ca. 122 ± 11 nm as measured by dynamic light scattering (DLS) (Figure 5.5a), which was consistent with TEM and field emission electron microscopy (FEI-SEM) data (Figure 5.5e-f).

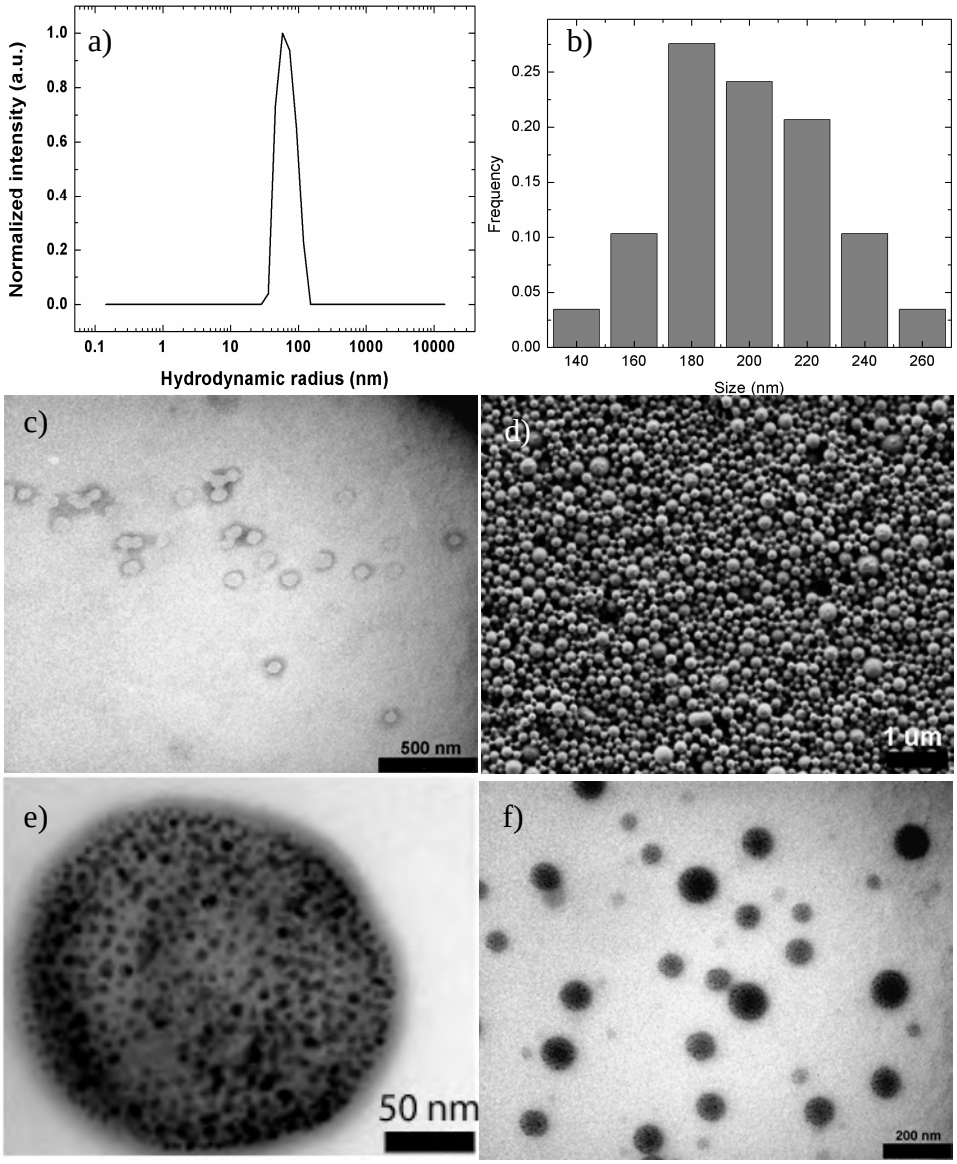

Figure 5.5: Size distribution of DOXO/SPION-PLGA NPs as obtained by a) DLS and b) TEM. c) TEM and d) FEI-SEM images of PLGA NPs. e) and f) TEM images of DOXO/SPION-PLGA NPs. In e) we can observe embedded SPIONs in a PLGA NP as homogenously distributed dark spots. DOXO/SPION-PLGA NPs were slightly heterogenous, which could account for the broad UV-vis absorption peaks of PGNHs.

Differences in sizes between these techniques arise from the dehydration underwent by the samples under the preparation procedure for TEM and SEM measurements [78]. TEM images of DOXO/SPION-PLGA NPs indicated that many SPIONs were successfully embedded into the matrix of each PLGA NP. The successful incorporation of DOXO inside the PLGA NPs was corroborated by the appearance of absorption and emission peaks at 490 and 591 nm, respectively, consistent with spectra of free DOXO (Figure 5.6).

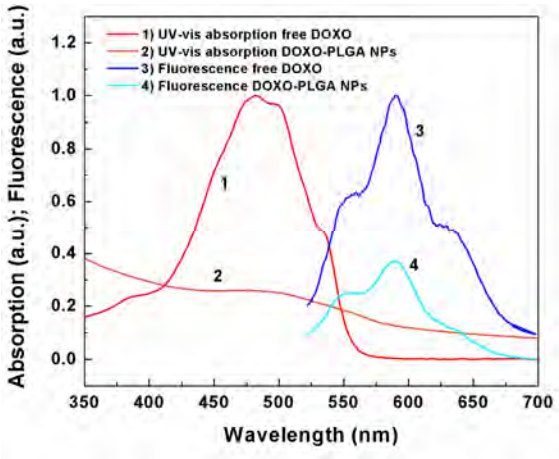

Figure 5.6: UV-vis absorption and fluorescence spectra of free DOXO (1 and 3) and DOXO-PLGA NPs (2 and 4).

The number density of SPIONs and DOXO could be easily tuned by varying the amount of SPIONs in the initial reaction mixture and the DOXO/PLGA molar ratio. In particular, when the mass ratio of DOXO to PLGA was 10 wt.%, the maximum drug encapsulation efficiency (EE) was ca. 95% and the loading capacity (LC) was 8.9 wt.% in the presence of 5 wt.% SPIONs (as measured by inductively coupled plasma mass spectrometry, ICP-MS) compared to 73% EE and 3.2 wt.% LC in their absence, which suggests a possible synergistic effect through additional hydrophobic interactions between DOXO molecules, oleic acid (OA) surfactant on the SPIONs surfaces and PLGA chains [56].

To grow the porous Au layer, low molecular weight chitosan chains were firstly adsorbed onto the surface of the negatively charged PLGA NPs derived from the terminal carboxyl groups of the PLGA chain (ζ-potential of ca. -35.3 ± 4.8 mV) [79] by electrostatic interactions. The ζ-potential of the PLGA NPs was increased from -35.3 ± 3.2 to +60.4 ± 3.9 mV by increasing the amounts of the coated chitosan

(Figure 5.7), confirming the successful coating of chitosan on the surface of the PLGA NPs. The hydrodynamic diameter changes from ca. 140 ± 14 to ca. 180 ± 17 nm after biopolymer coating, also denoting the absence of any severe agglomeration due to the electrostatic repulsions between the positively charged particles and the steric stabilization provided by the polyethylene oxide chains surrounding the PLGA NPs.

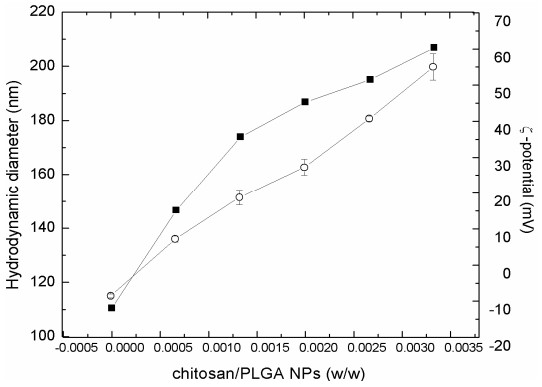

Figure 5.7: ζ-potential (■) and hydrodynamic diameter (○) of DOXO/SPION-PLGA NPs in deionized water after surface coating with increasing amounts of chitosan. After coating with the polycation, citrate-capped Au seeds were attached by electrostatic interactions, which subsequently acted as nucleation centers for Au shell growth.

Subsequently, negatively charged Au seeds with a diameter of about 2-3 nm were adsorbed onto the surface of the chitosan-coated PLGA NPs via electrostatic interactions. A ζ-potential of ca. -11.4 ± 2.1 mV indicated the successful deposition of Au seeds onto the surface of polymeric NPs (Figure 5.8a). Finally, the attached Au nanoseeds were used to nucleate the growth of a porous gold nanoshell by reduction of $HAuCl_4$ to bulk Au metal (Figure 5.8b-c). For PGNHs stabilization, a heterobifunctional polyethyleneglycol chain, SH-PEG_{5000}-OCH_3 or SH-PEG_{5000}-NH_2 when corresponding, was used by exploiting the strong bond formation between sulfhydryls groups and metal gold surfaces (final ζ-potential of ca. -4.8 ± 2.1 mV). PGNHs settled due to the high density of the Au shell and the SPION-loaded PLGA core; nevertheless, after vortexing no agglomerates in solution were observed by visual inspection and DLS for at least two weeks after pegylation when stored in PBS at 4 ºC.

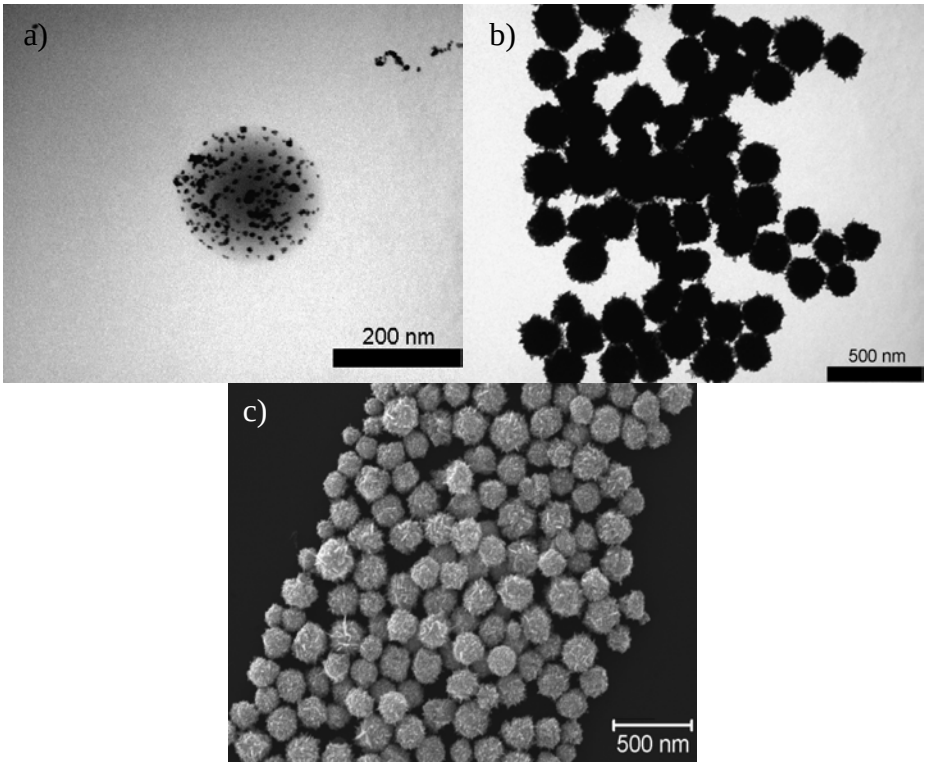

Figure 5.8: a) TEM image of Au nanoseeds decorating DOXO/SPION-PLGA NPs; b) TEM and c) SEM images of DXSP-PGNHs NPs.

To achieve targeted delivery of the nanoconstruct and enhance cellular acummulation inside cancerous cervical HeLa cells, FA was conjugated to the amino groups of PEG chains (Figure 5.9) to bind the FA-overexpressed receptors on cell membrane surfaces. The number of SH-PEG_{5000}-FA molecules conjugated to PGNHs was calculated to be $1.78 \cdot 10^6$ molecules/PGNH.

UV-vis spectra of DXSP-PGNHs at different stages of preparation are shown in Figure 5.10. The extinction spectrum of the blank PLGA NPs exhibited no obvious peak in the range from 400 nm to 800 nm (Figure 5.10a, plot 1) as a result of light scattering of the nanoparticles [80]. The peak at ca. 480 nm (Figure 5.10a, plot 2) was attributed to the absorbance of DOXO corroborating its successful loading into the PLGA NPs. After Au-seed adsorption, a plasmon resonance peak at ca. 535 nm for Au nanoparticles clustered at the surface of the PLGA NPs was present (Figure 5.10a, plot 3), and the metal seeds were observed as densely distributed dark spots by TEM (Figure 5.8a).

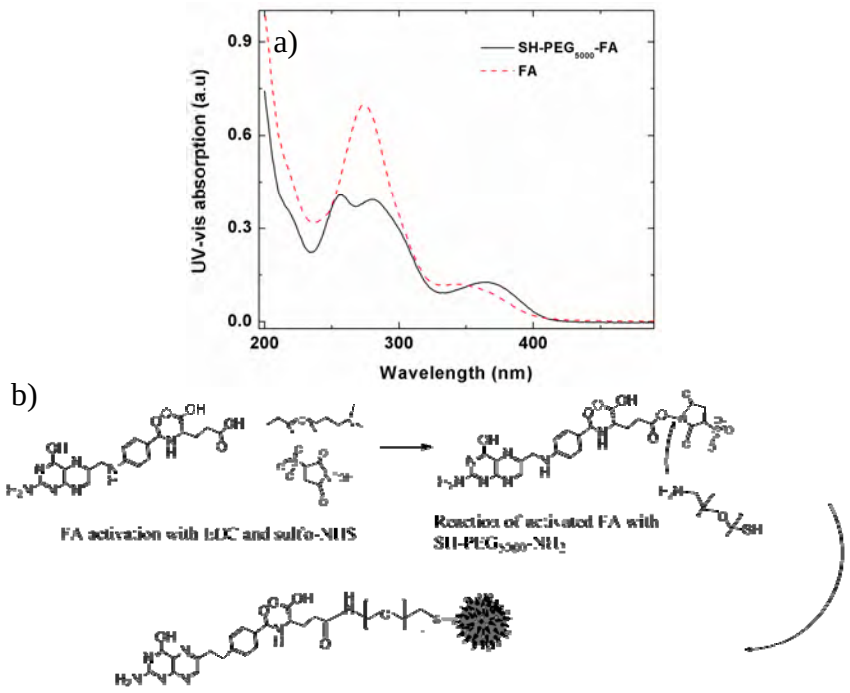

Figure 5.9: a) UV-Vis spectra of folic acid (FA) and SH-PEG-FA and, b) scheme of the conjugation protocol.

UV-vis spectra of DXSP-PGNHs at different stages of preparation are shown in Figure 5.10. The extinction spectrum of the blank PLGA NPs exhibited no obvious peak in the range from 400 nm to 800 nm (Figure 5.10a, plot 1) as a result of light scattering of the nanoparticles [80]. The peak at ca. 480 nm (Figure 5.10a, plot 2) was attributed to the absorbance of DOXO corroborating its successful loading into the PLGA NPs. After Au-seed adsorption, a plasmon resonance peak at ca. 535 nm for Au nanoparticles clustered at the surface of the PLGA NPs was present (Figure 5.10a, plot 3), and the metal seeds were observed as densely distributed dark spots by TEM (Figure 5.8a). The hydrodynamic diameter of PLGA-Au-seed NPs was evaluated to be around 170 ± 15 nm by DLS measurements. A new pronounced peak in the NIR range was observed after reduction of an Au growth solution onto the surface of the attached Au-seeds by ascorbic acid to give an Au shell layer (Figure 5.10a, plot 4). The absorption maximum of this new peak ranged between 750 to 900 nm depending on the thickness of the Au shell, which was controlled through both ascorbic acid concentration and volume of the added Au growth solution (Figure 5.11). Furthermore, the plasmon peak was not distorted nor broadened during the formation of the Au layer.

The structure of the metallic nanoshell could be also changed from a relatively smooth surface to a spiky structure depending on the synthetic conditions, the latter resembling the classical structure of a virus capside (Figure 5.10c inset). The Au nanoshell also seemed to be dense, multicrystalline and porous, which conveniently enables DOXO release through the gold pores (Figure 5.10d-e), and as additionally corroborated by electron diffraction X-ray (EDX) analysis (Figure 5.12). In this regard, EDX of PGNHs displayed Au and C peaks, the latter stemming from carbon atoms from the PLGA core; in addition, SEM maps for each element distribution coincide, which gives an additional confirmation that the Au shell is porous.

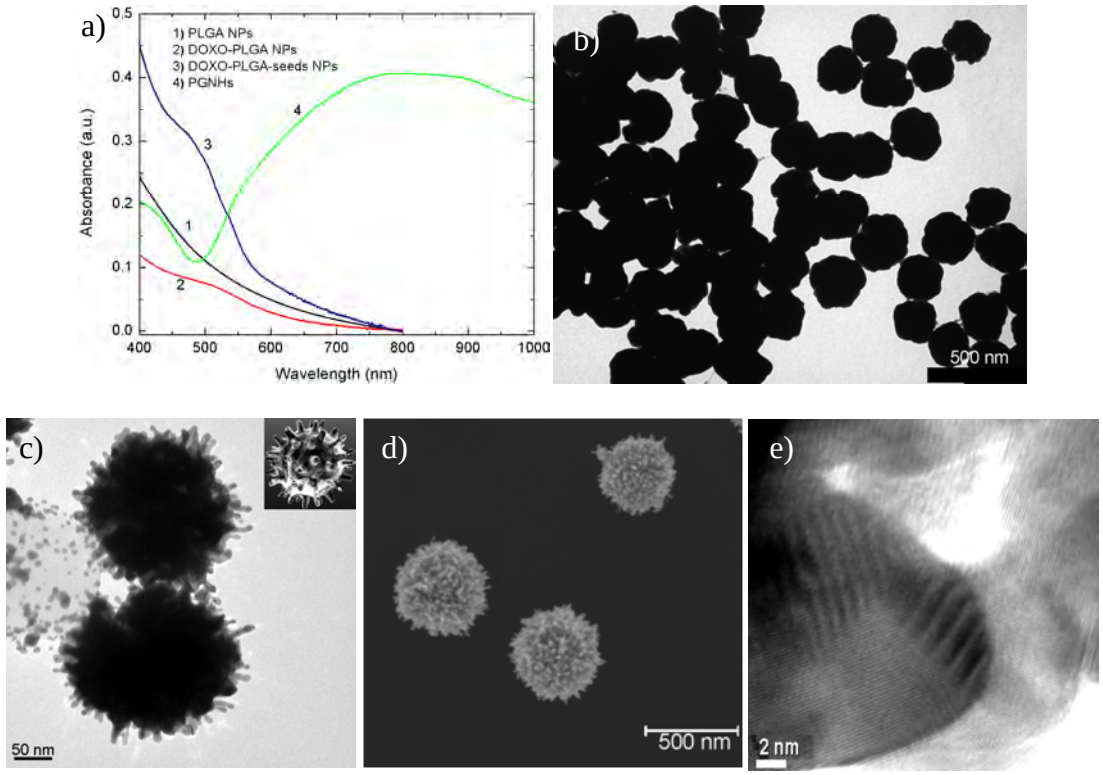

Figure 5.10: a) UV-vis absorption spectra of DXSP-PGNHs at different stages of their growth process. b) TEM images of PGNHs with a flat and c) a spiky surface mimicking a virus capside. d) SEM image of PGNHs showing their rough surface topology. e) High magnification TEM images showing the multicrystalline and porous structure of the Au shell.

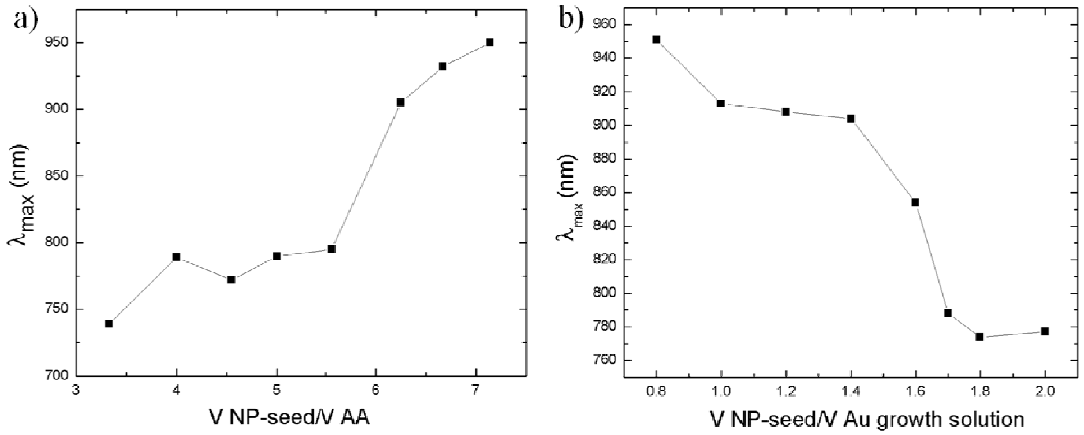

Figure 5.11: Tunability of the absorption maximum localization, λ_{max}, of DXSP-PGNHs with changes in $V_{NP\text{-}seed}/V_{ascorbic\ acid}$ and $V_{NP\text{-}seed}/V_{Au\ growth\ solution}$ ratios.

The final hydrodynamic diameter for DXSP-PGNH-FA was evaluated to be between 165 to 206 nm depending on the thickness of the Au shell by DLS measurements (Figure 5.12), which is consistent with TEM images.

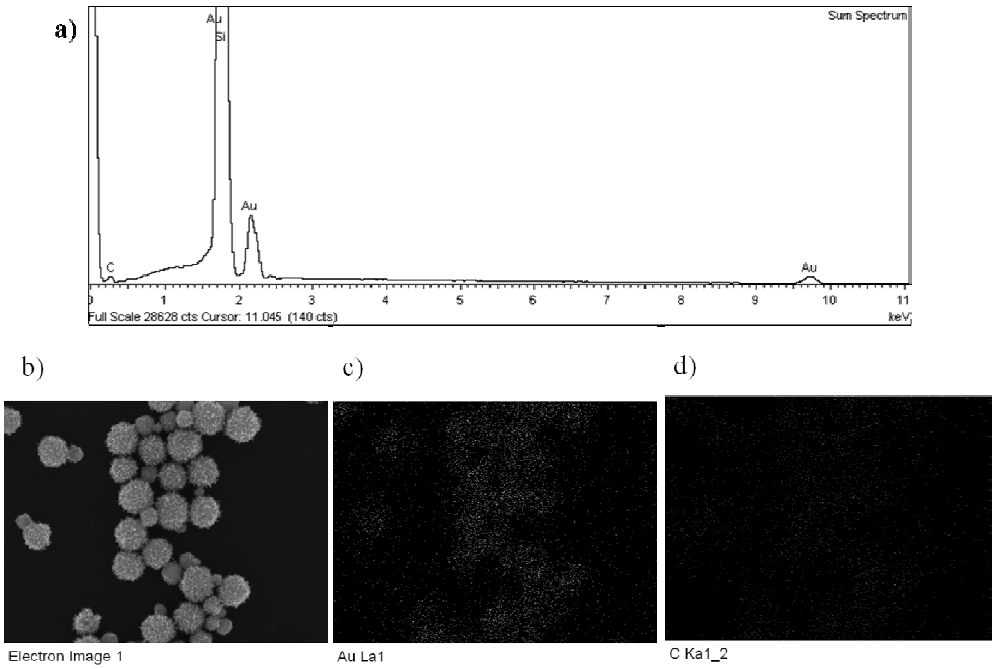

Figure 5.12: a) EDX spectrum of PGNHs with an Au peak from the shell and a small C peak form the PLGA core. A shoulder corresponding to O might be also present. b) SEM image and bit maps of c) Au and d) C. This maps show that both elements coincide at the same regions, which can be interpreted as the Au shell is porous.

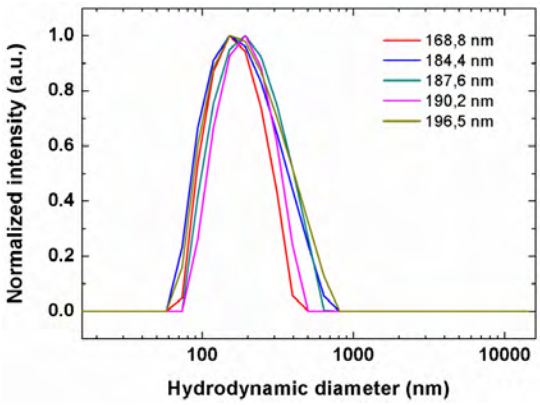

Figure 5.13: Hydrodynamic diameter of DXSP-PGNH-FA with different shell thickness, obtained by varying the $V_{NP\text{-}seed}/V_{ascorbic\ acid}$ ratio and keeping $V_{Au\ growth\ solution}$ constant at 20 mL.

5.4.2 Temperature Elevation Induced by NIR Laser Irradiation

The absorbance between 750 nm and 900 nm (Figure 5.10a) suggests that these hybrid nanoplatforms can be suitable for NIR light-triggered release of drugs and photothermal therapy [81] at relatively low laser output energies due to their enhanced absorption provided by their relatively large extinction cross-sections [82]. Exposure of aqueous suspensions of PGNHs to NIR-continuous wave illumination (NIR-CW setup at 808 nm) resulted in a rapid elevation of solution temperatures, which is an important feature for selective treatment of solid tumors. To investigate the hyperthermic potential of PGNHs, firstly the heat generated by NIR-CW at a laser power of 2.5 W/cm^2 over time (total illumination time = 10 min; total energy delivered = 188.6 J) on PGNHs solutions of different concentrations was measured. No obvious temperature change was observed when deionized water was exposed to NIR light (Figure 5.14a). By contrast, aqueous dispersions of PGNHs at concentrations $1\cdot10^8$-$1\cdot10^{10}$ NP/mL achieved temperature elevations of ca. 6, 8ºC, 11ºC, 13ºC, and 16ºC, respectively. Hence, at concentrations above $5\cdot10^8$ NP/mL, samples can be easily heated up above 43ºC, which is sufficient to kill tumor cells [83]. When changing the laser irradiation at a fixed NP concentration of $5\cdot10^8$ NP/mL, powers above 2.5 W/cm^2 overcome the required temperature threshold for thermal ablation of cancer cells (Figure 5.14b) with temperature elevations of up to 40 ºC, which can cause cargo release and cellular death (see below).

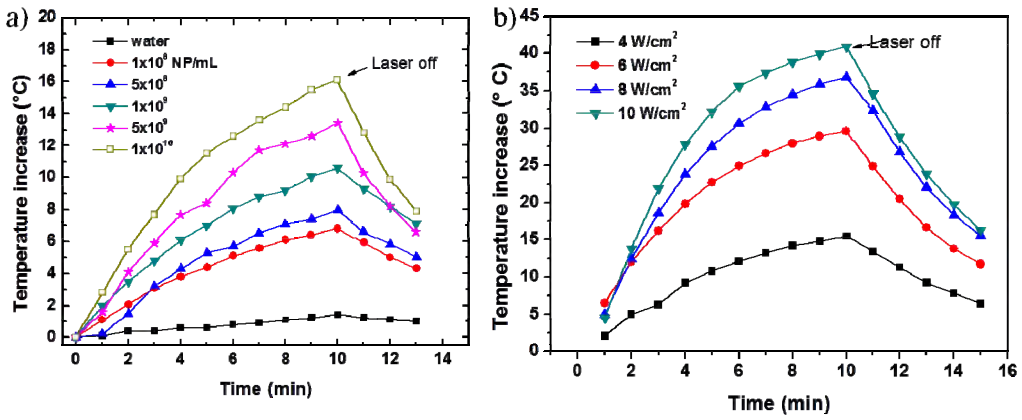

Figure 5.14: Temperature increases under NIR illumination of PGNHs at: a) $1{\cdot}10^8$, $5{\cdot}10^8$, $1{\cdot}10^9$, $5{\cdot}10^9$ and $1{\cdot}10^{10}$ NP/mL at a fixed laser power of 2.5 W/cm^2 (808 nm); b) at a fixed concentration of $5{\cdot}10^8$ NP/mL and laser powers of 4, 6, 8 and 10 W/cm^2 (808 nm). The solution temperature was set at 37 ºC.

5.4.3 NIR laser-triggered release of cargo inside cells

In order to know if NIR light excitation can affect and help to control cargo release from PGNHs, NR-PGNH where subjected to NIR-short pulsed illumination (NIR-SPI setup: laser wavelength = 830 nm; spot area = 6 μm^2; illumination time = 1 s). In principle, pulsed laser irradiation should allow a concentration of power density in small pulses, thus reducing the need of time exposure, which is advantageous for clinical practice. For this setup, the laser was coupled to a wide field optical microscope and the beam was focused through the microscope's objective. As observed in Figure 5.15, high light induced-temperature increases involved NR release from NR-PGNH inside the cells after 24 h of NIR-SPI as seen by the onset of NR fluorescence, and also some cells are observed to undergo membrane blebbling, a generally accepted sign of cell death [84, 85] (see Figure 5.15). At this respect, when cells were illuminated with NIR-SPI with a power intensity of 0.3 mW/μm^2 for 1 s (total energy delivered = 1.8 mJ) no damage or disruption of cells was observed but a diffusion of NR. After particle internalization, NIR-light irradiation led to an enhanced cargo diffusion inside the cells as observed from the increased fluorescence intensity from NR (Figure 5.16b,d), while it remained nearly unchanged in the absence of NIR irradiation (Figure 5.16a,c). This suggests that cargo molecules were released quickly upon illumination, diffused into the cell cytosol (as concluded by the diffuse instead of granular fluorescence NR pattern [86]), and eventually might enter

the cell nuclei, as in the case of DOXO which is known to interact with topoisomerase II to cause DNA cleavage and cytotoxicity [87]. When increasing the power light intensity to 0.6 mW/μm^2 for 1 s (total energy delivered = 3.6 mJ), NR release inside the cells was greatly enhanced. However, irradiated cells are observed to change their morphology probably due to the localized temperature increase due to NIR energy absorption by the nanoplatforms upon irradiation.

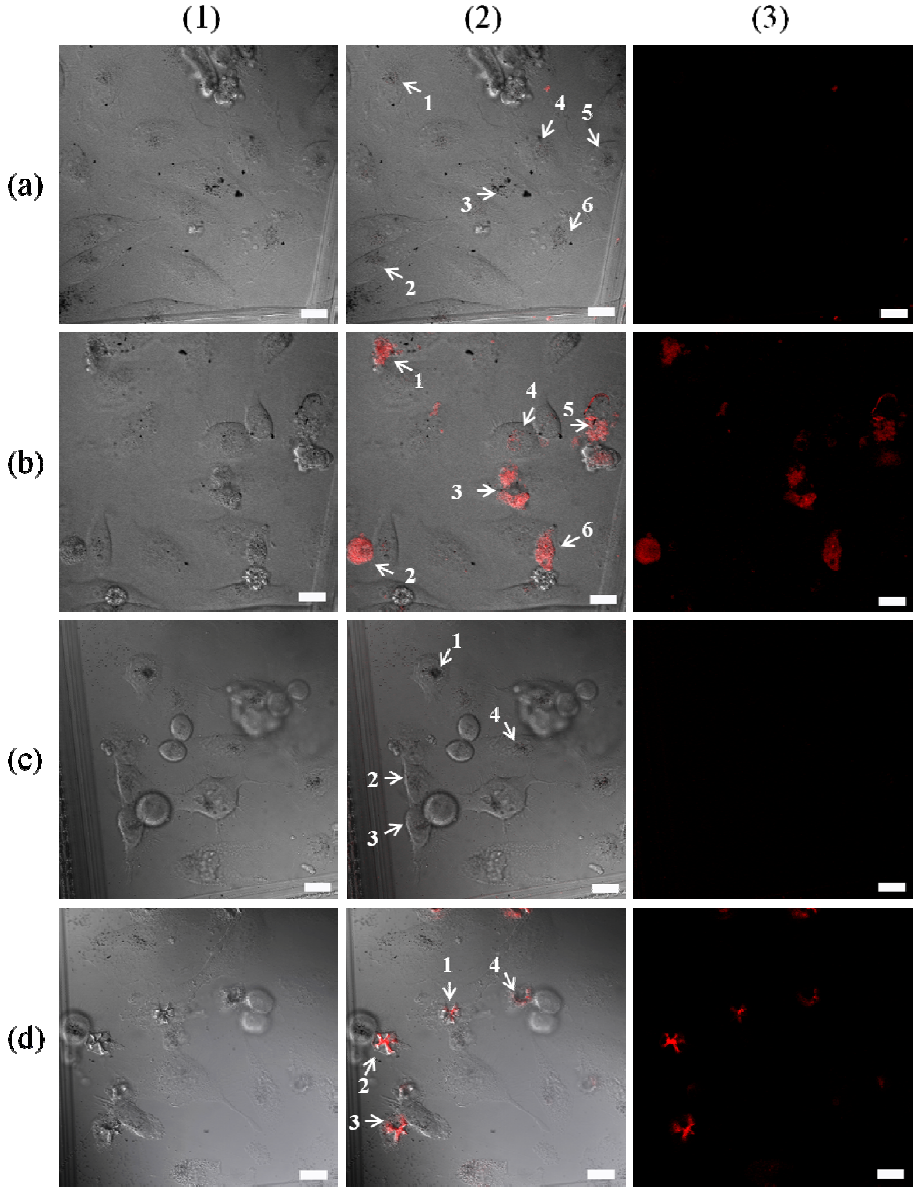

Figure 5.15: Confocal laser scanning microsocpy images of HeLa cells containing PGNH-5. Rows (a) and (c) represent cells before illumination, and (b) and (d) cells 24 h after NIR-SPI at 0.3 mW/μm^2 (b) and 0.6 mW/μm^2 (d), respectively. The arrows indicate illuminated cells. Images in column (1) are transmitted light (differential interference contrast, DIC channel), column (2) shows fluorescence emission images of NR (λ_{ex} = 510 nm, λ_{em} = 585 nm), and column (3) displays merged images. Scale bars = 20 μm.

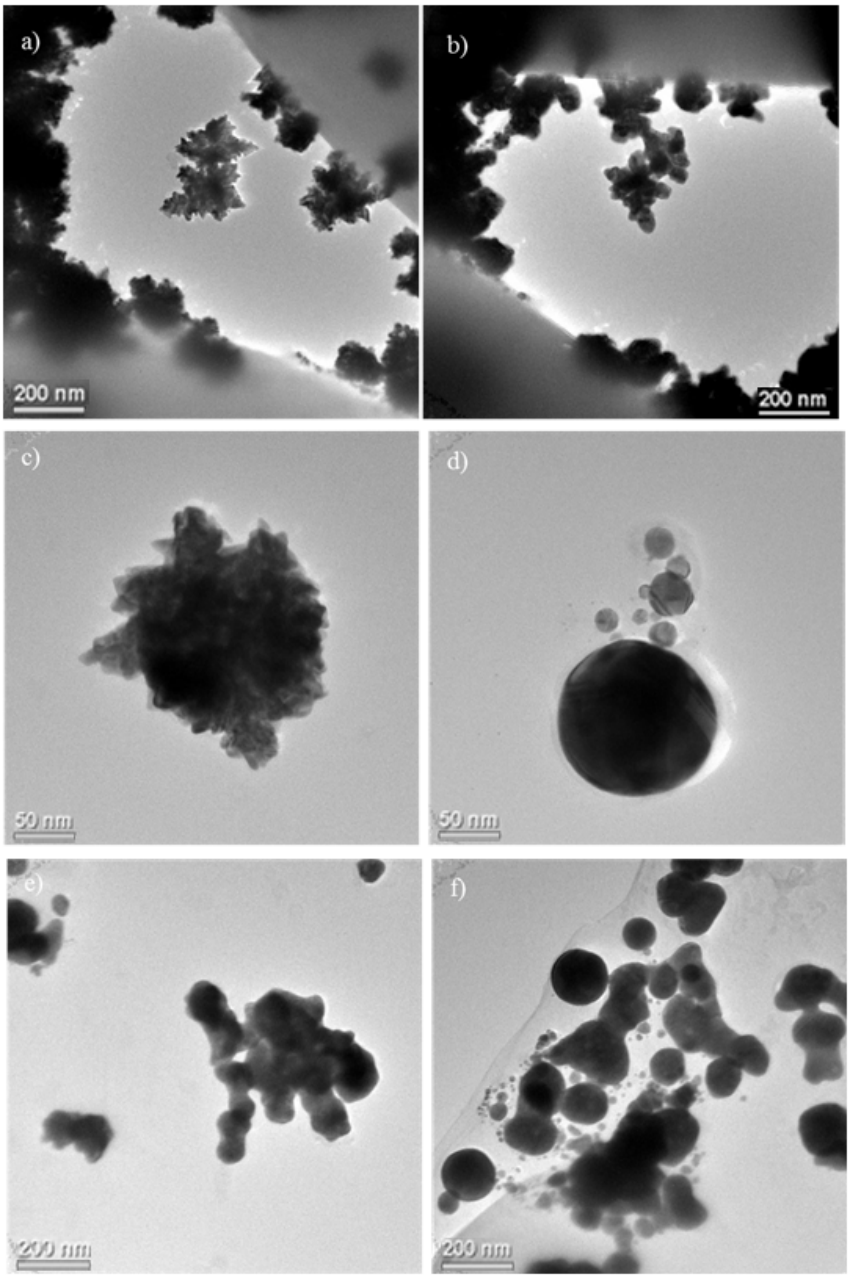

Figure 5.16: TEM images of DXSP-PGNHs supported on silica spheres of 5 μm size: a, c) before, and b, d) after NIR-SPI with a laser power of 0.3 and 0.6 mW/μm^2, respectively. In b), the spikes are smoothed but their shape is kept. d) At larger laser powers a re-shaping from a spiky morphology to a smoother sphere takes place. Also, e) detachment of some portions of the DXSP-PGNHs surface and f) complete nanoplatform rupture was observed.

The morphology of PGNHs upon NIR-SPI was studied by TEM. For this, DXSP-PGNHS were electrostatically attached to positively charged 5 μm SiO_2 beads. TEM images of DXSP-PGNH/SiO_2 assemblies were acquired before and after illumination with NIR light under NIR-SPI conditions. Figure 5.16 shows images of

the nanoplatforms irradiated under different intensities. The structure of the PGNHs was observed to be kept up to power intensities of ca. 0.3 mW/μm^2 (Figure 5.16b). Above such threshold, fusion of the Au layer with subsequent loss of spikes (when present) and nanoplatform rupture was observed when illuminated at 0.6 mW/μm^2 (Figure 5.16d-f), which is consistent with observations of single-cell *in vitro* NR release experiments.

These data corroborated that the photostability of the present nanostructures was not maintained under pulsed laser irradiation. Pulsed lasers can melt and reshape gold nanostructures to nanospheres even in picosenconds [88, 89]. This irreversible transformation of shape will dramatically deteriorate the heat producing ability [88]. Hence, in view of the present observations, we decided to use continuous wave (CW) illumination to perform the analysis of the drug light-triggered release *in vitro*. Also, CW irradiation was used to carry out the *in vitro* cytotoxicity tests of the DXSP-PGNH nanoplatforms, in this case, with the caution of maintaining the total energy light input per cell similar to that used in the pulsed laser-cargo release irradiation experiments (4.2 mJ/cell) (section 5.4.3).

5.4.4 Triggered Release of DOXO by NIR Light

The PLGA copolymer which configures the reservoir for DOXO drug molecules showed a glass-transition temperature (T_g) of ca. 45 ºC [90], which reduces the drug leakage during circulation and releases the drug when needed, that is, in the vicinity of tumor. However, the incorporation of the Au layer allows an additional light-triggered drug release mechanism by applying NIR laser irradiation, that is, the heat generated by DXSP-PGNHs under illumination is sufficiently higher to overcome the PLGA T_g inducing an enhanced release of the chemotherapeutic drug, as depicted by cell irradiation experiments (see Figure 5.15).

Figure 5.17a shows the characteristics of the DOXO release from bare DOXO/SPION PLGA NPs and DXSP-PGNHs solutions (PBS buffer pH 7.4 with 10% (v/v) FBS) in the absence and presence of NIR-CW irradiation. Samples were irradiated repeatedly over a period of 5 min, followed by 1 h intervals with the laser turned off. We observed that the release profile of the DXSP-PGNHs follows a similar trend as that of DOXO/SPION PLGA NPs, that is, an initial burst release

profile followed by a slower diffusion release phase. In the absence of irradiation, the release rate of the DXSP-PGNHs was much slower than that of bare PLGA NPs. This behaviour was adscribable to the presence of the Au layer but the concentrations released were still largely detectable, which supported the assumption of the porous nature of DXSP-PGNHs.

By contrast, a faster release was observed upon NIR irradiation of the DXSP-PGNHs solution. After the first NIR exposure for 5 min, the percentage of released DOXO steeply increased from 7.1% to 18.4%. This percentage increased to 29.7% over the whole period without NIR laser irradiation. When the samples were exposed to NIR light five times for 5 min, the accumulated released amount of DOXO over the whole experiment process was about three-fold greater than that without laser irradiation (79.5%). The enhanced drug release upon irradiation can be a consequence of the enhanced diffusion of the drug throughout the porous inorganic layer upon temperatures above the polymer T_g and some possible disruption of the DXSP-PGNHs structure (Figure 5.17b). Also, it was noted that DOXO release was particularly enhanced immediately upon irradiation. However, the released amount of DOXO after each irradiation cycle was progressively decreased due to the increased coverage of gold pores resulting from the melting effect of the metallic nanostructures [91] and the partial structural changes of some nanoplatforms.

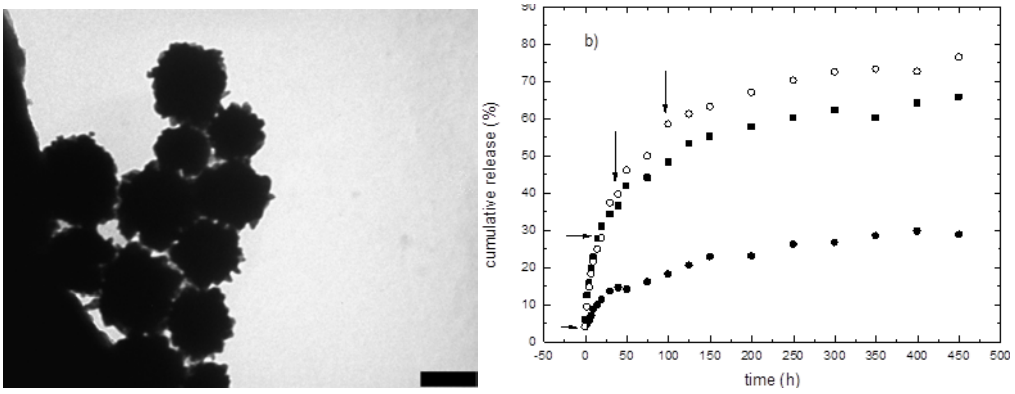

Figure 5.17: a) TEM image of DXSP-PGNHs after 10 minutes of NIR-CW, no substantial changes in the structure of nanoplatforms were observed. b) Release profile of DOXO from (■) bare DOXO/SPION PLGA NPs and DXSP-PGNHs nanoplatforms (●) in the absence (○) and presence of 2.5 W/cm^2 NIR-CW irradiation at 808 nm.

5.4.5 Magnetic properties and *in vitro* magnetic-resonance imaging

Due to the presence of SPIONs in their composition, the present DXSP-PGNHs also possess robust magnetic properties, as observed when placing a magnet near the nanoplatform solution (Figure 5.18a-b). The field-dependent magnetization curve of DXSP-PGNHs at 5 K showed hysteresis (Figure 5.19a), which is consistent with the thermal energy being insufficient to induce magnetic moment randomization, thus, the nanoconstructs showed typical ferromagnetic hysteresis loops with a remanence of 4.7 emu g^{-1} and a coercivity of 205 ± 6 Oe (Figure 5.19a). By contrast, the field-dependent magnetization curve of DXSP-PGNHs at 300 K shows no hysteresis (Figure 5.19b), which is consistent with superparamagnetic behavior arising from the embedded SPIONs.

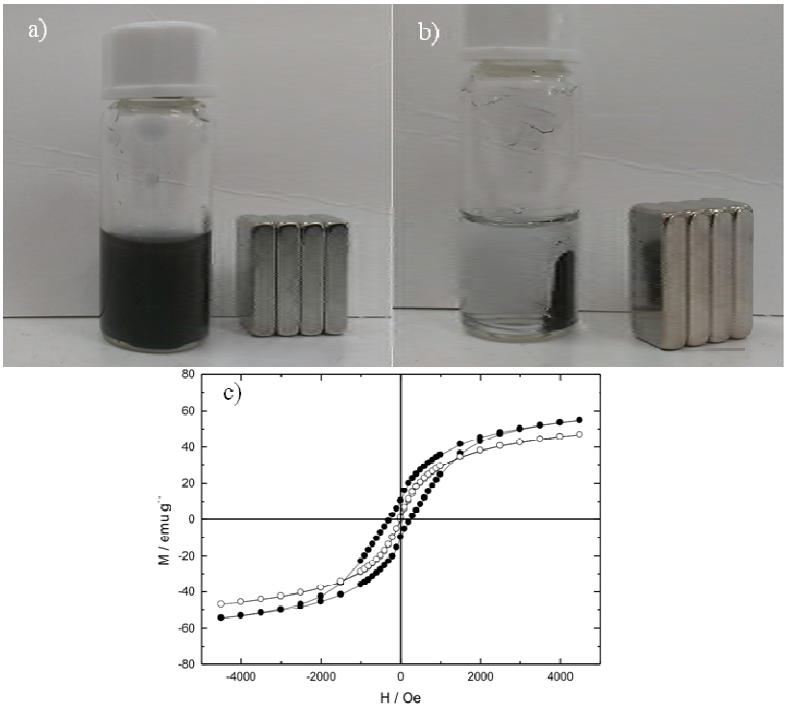

Figure 5.18: a) BNK-PGNHs and b) DXSP-PGNHs after 10 min exposure to an external applied magnetic field (0.5 T). c) Magnetization as a function of the applied external magnetic field of well dispersed SPIONs at (●) 5 and (○) 300 K.

The saturation magnetization at 300 K, M_{sat}, was determined to be 14.6 emu g^{-1}, similar to that observed previously for magnetic-Au coated silica nanoshells [35]. The M_{sat} of the nanoplatforms was observed to be lower than that of free SPIONs (Figure 5.18c) possibly due to the large diamagnetic mass of Au and PLGA contributing to

the total mass of the nanoplatforms. Additionally, the presence of canted or noncollinear surface spins, which has been observed in ferromagnetic materials with substituted diamagnetic neighboring cations, may also contribute to a decrease in M_{sat} since saturation of these spins usually requires higher magnetic fields [35].

SPIONs have received great attention as T_2 contrast agents due to their capability to shorten the spin-spin relaxation times, which results in a decrease in the MRI signal intensity and enables to differentiate between normal and abnormal tissues [92]. In addition, the specific weighted transverse-relaxivity (r_2) values can be greatly increased by clustering SPIONs in reservoirs, which leads to higher saturation magnetizations than that of individual ones owing to the interactions between the assembled nanocrystals [93-95].

In order to evaluate the T_2 contrast capabilities of the present hybrid nanoplatforms, DXSP-PGNHs with various Fe concentrations (as determined by ICP-MS) were investigated by T_2-weighted MRI at 9.4 T and 400 MHz. The signal intensity of the MR images decreased as the iron concentration increased, as expected for T_2 contrast agents due to the shortening of the spin-spin relaxation time of water, as commented previously [96]. The specific relaxivity, r_2, a measure of the change in spin-spin relaxation rate (T_2^{-1}) per unit Fe concentration, was determined to be 207 mM Fe^{-1} s^{-1} for our DXSP-PGNH (Figure 5.19c). This high r_2 value could be due to the large external magnetic field (9.4 T) applied to the nanoplatforms as well as their superior magnetic properties due to the enhanced magnetic interactions between clustered SPIONs inside the polymeric matrix of the nanoplatforms. It is worth mentioning that at high magnetic field strengths, the two contrast agents approved by the US Food and Drug Administration (FDA), AMI-25 and Resovist, have considerably lower r_2 values (160 and 151 mM $Fe^{-1}s^{-1}$, respectively) than the nanoplatforms here synthesized. Meanwhile, other types of hybrid particles embedding clustered SPIONs such as magnetic Au nanoshells, polymeric NPs or hybrid fibers have been reported with relaxivities comparable to our DXSP-PGNHs [35, 55, 97-101]. Hence, these data suggest that the present DXSP-PGNHs may be used in imaging diagnosis, in which the distribution of the particles depicted by MRI may be used to assist planning of chemo- and photothermal therapy and to predict the treatment outcome.

5.4.6 Cellular uptake and intracellular distribution

Because targeted delivery to specific cells is essential to systemic cancer therapy, we exploited the overexpression of FA receptors on the cellular membrane of HeLa cells by attaching this ligand on the surface of DXSP-PGNHs to investigate the cellular uptake *in vitro*, intracellular distribution, and cellular targeting efficacy of the present hybrid nanoplatforms through confocal and optical microscopy, TEM, and MRI.

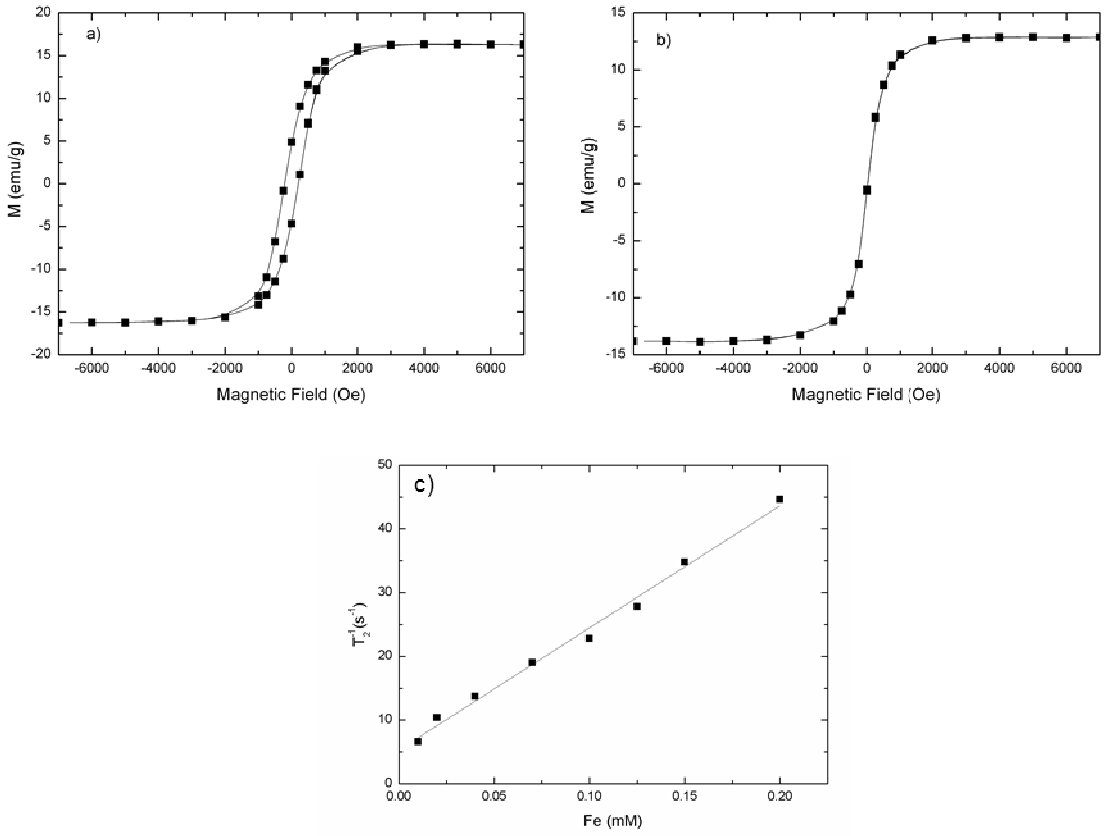

Figure 5.19: Magnetization as a function of applied external magnetic field of DXSP-PGNHs hybrid nanoplatforms at (●) 5 and (○) 300 K. c) T_2^{-1} *vs* [Fe] for DXSP-PGNHs. Specific relaxivity, a measure of the MRI contrasting ability, was r_2 = 207 mM Fe^{-1} s^{-1}.

From optical microscopy images it was possible to confirm that the present hybrid nanoplatforms are internalized inside the cells (the dark black spots in Figure 5.20a). In addition, when DXSP-PGNHs were illuminated light scattering occured as energy from the light stimulated electrons on the particle´s surfaces to oscillate and, subsequently, emitted photons at a single frequency which may be captured and used to determine the presence of particles *in vitro.* In this way, comparison of confocal

microscopy images of HeLa cells incubated with non-functionalized DXSP-PGNHs and functionalized DXSP-PGNHs-FA showed that the cellular uptake of the latter was enhanced compared to naked ones as denoted by the increased scattered light from the particles inside the cells [102-104] (denoted in green in Figure 5.20b-e by changing the color palette in the merged images shown).

After 4 h of incubation with HeLa cells, only a relative small amount of non-functionalized nanoplatforms appeared to be inside the cells (Figures 5.20b-c); in contrast, FA-functionalized nanoplatforms are more numerous inside the cells (larger number of green spots, Figure 5.20c-d) and appeared to be specifically bound to the cell membrane and within vesicular compartments inside cells (Figure 5.21). This demonstrated that the functionalized DXSP-PGNHs-FA are more easily internalized by cells than the non-functionalized ones, presumably through a receptor-mediated endocytosis process [105]. On the other hand, particle cell uptake was additionally enhanced upon application of an external magnetic field to cells by placing a magnet below the culture wells, as observed by fluorescence images (Figures 5.20f-g). This demonstrated that the simultaneous use of folate and magnetic field exhibited a synergistic effect on nanoplatform targeting to HeLa cells. The particles would remain in endosomal/lysosomal compartments and would not enter nuclei, as denoted by z-axis cross-sectional confocal microscopy and TEM images (Figure 5.20h and Figure 5.21).

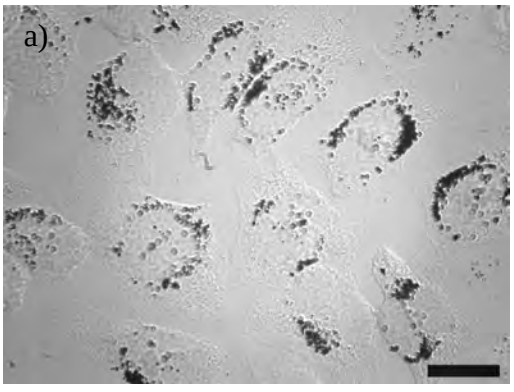

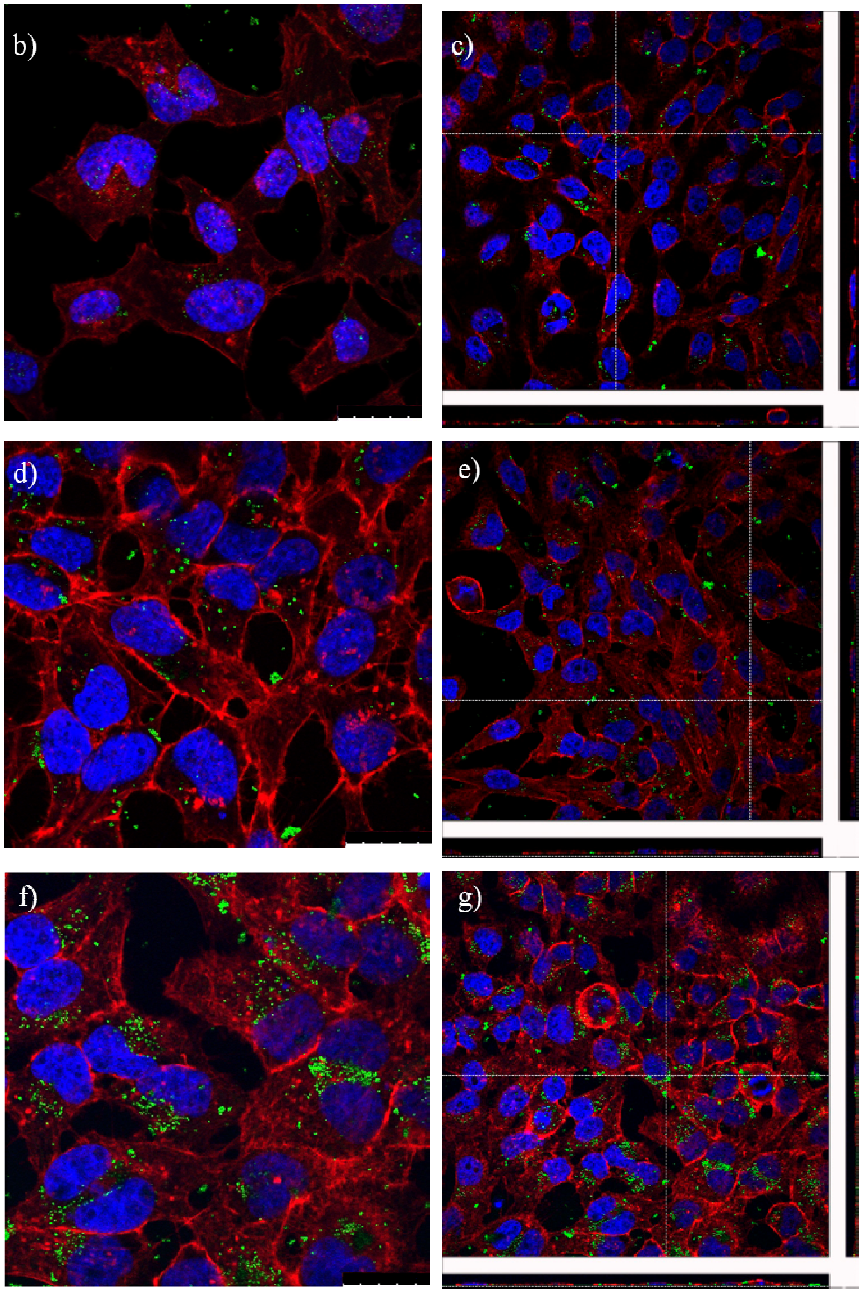
b)
c)
d)
e)
f)
g)

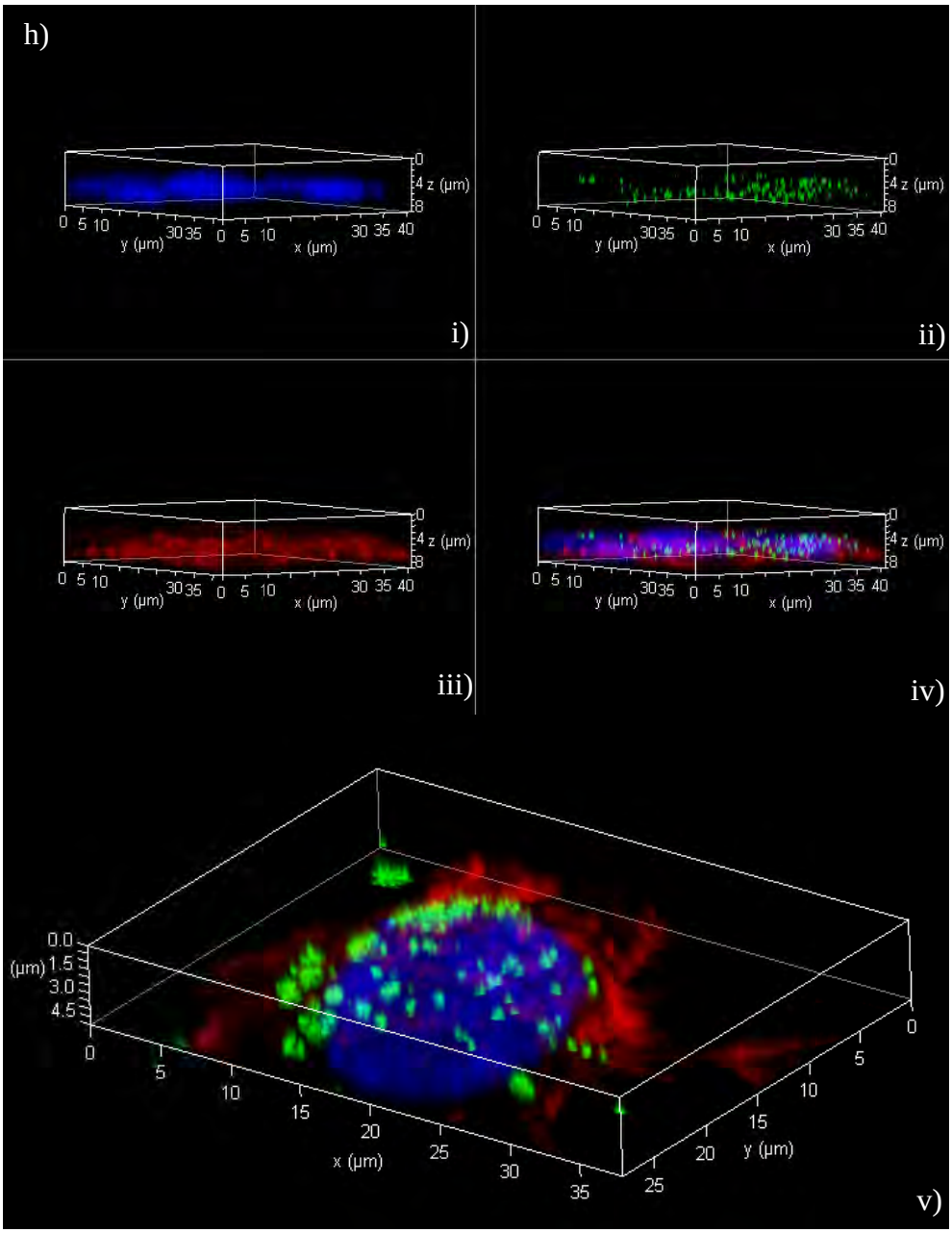

Figure 5.20: a) Optical microscopy image of HeLa cells with internalized DXSP-PGNHs. Confocal microscopy images of DXSP-PGNHs (b, c); DXSP-PGNHs-FA (d, e) and DXSP-PGNHs-FA with magnetic targeting (f, g). Nuclei were stained with DAPI (blue channel, λ_{exc} = 355 nm), the actin cytoskeleton with BODIPY Phalloidin (red channel, λ_{exc} = 633 nm) and reflected light for PGNHs (green channel). h) 3D images of cells incubated with DXSP-PGNH-FA: i) DAPI channel, ii) PGNHs reflected light, iii) BODIPY Phalloidin channel, iv) merged image of the three channels and v) crop of one cell. Scale bars are 20 µm.

Because our nanohybrids are multifunctional, we were able to evaluate the enhanced uptake due to the present hybrid NPs by TEM and MRI imaging. The cells labelled with the nanoplatforms clearly appear as hypointense spots in T_2-MR images of HeLa cells after being inoculated with DXSP-PGNHs and resuspended in 1.6% (w/v) agarose solution acquired with the 9.4 T MR scanner. Cells incubated with DXSP-PGNHs-FA (Figures 5.21d-e) were substantially darker than those incubated with non-functionalized DXSP-PGNHs (Figures 5.21b-c).

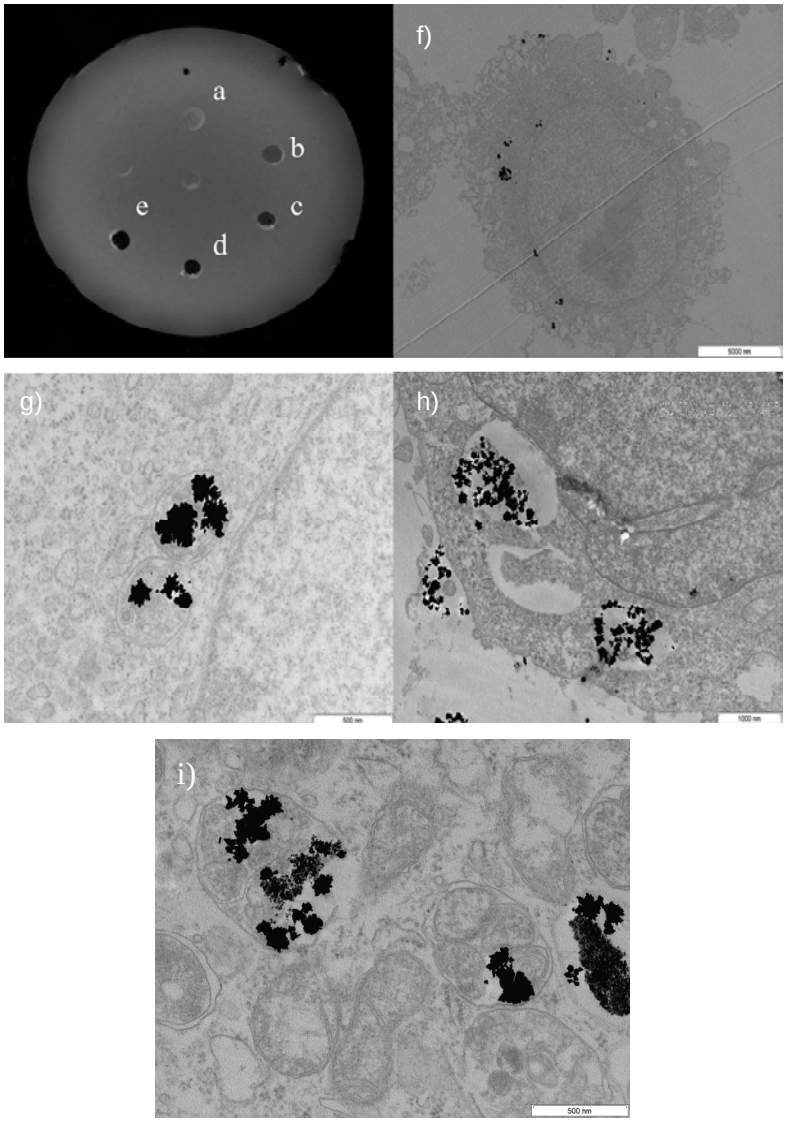

Figure 5.21: T_2-weighted MR image of HeLa cells. a) Control sample with unlabelled $1 \cdot 10^6$ cells; b, d) $1 \cdot 10^5$ and c, e) $1 \cdot 10^6$ cells labelled with DXSP-PGNHs and DXSP-PGNHs-FA, respectively. f) TEM image showing nanoplatform´s cellular uptake. In g), the encapsulation of nanoplatforms inside endocytosic vesicles is observed. h) DXSP-PGNHs entering the cells by endocytosis and subsequent formation of vesicles. i) DXSP-PGNHs inside and outside a broken vesicle upon light irradiation.

On the other hand, TEM images (Figures 5.21f-h) showed that DXSP-PGNH-FA NPs were endocytosed and the nanoplatforms seemed to be accumulated within vesicles (see arrows). However, some NPs were found free in the cytoplasm, which suggested that NPs may escape from vesicles (Figure 5.21i).

5.4.7 Chemo-photothermal cytotoxicity of nanoplatforms

In order to obtain a qualitative demonstration of the specificity and the enhanced localized cell cytotoxicity of our nanohybrids, a cell viability assay in the presence and absence of irradiation was performed by staining viable cells with calcein acetoxymethyl ester (calcein AM) and dead cells with propidium iodide (PI) in order to verify the chemo-photothermal effect of DXSP-PGNHs-FA.

Figure 5.22 shows a fluorescence microscope image of HeLa cells incubated with DXSP-PGNHs-FA for 24 h. The estimated amount of DOXO contained inside these nanoplatforms was ca. 1.3 μM. In the absence of NIR irradiation, cells (Figure 5.22a-b) showed a vivid green color over the entire area analyzed, suggesting that the nanohybrids alone did not induce cell death because of the low DOXO dose and the slow drug release. By contrast, after NIR-CW exposure (2.5 W cm^{-2} for 10 min), a well-marked red-fluorescent region was present, indicating that the cells exposed to NIR-CW were dead (Figure 5.22c), whereas those not exposed were mostly alive (green cells in the inset of Figure 5.22c). For comparison, cells containing BNK-PGNH-FA without loaded DOXO were also illuminated under the same conditions to elucidate whether the cell death was induced only through NIR-induced hyperthermia or by the combined effects of DOXO chemotoxicity and NIR-CW. As shown in Figure 5.22d, many of the cells still appeared alive; therefore, it is possible to conclude that the combined chemo- and phototherapy was more cytotoxic under the present conditions than chemo- or photo-treatments alone. The origin of such effect can be originated from the combination of an enhanced DOXO toxicity upon temperature elevation under NIR irradiation [21], the larger sensitivity to heat of cells exposed to DOXO and/or to intracellular protein denaturation which inhibits normal cellular growth and proliferation and possible induced some cell membrane damages [106].

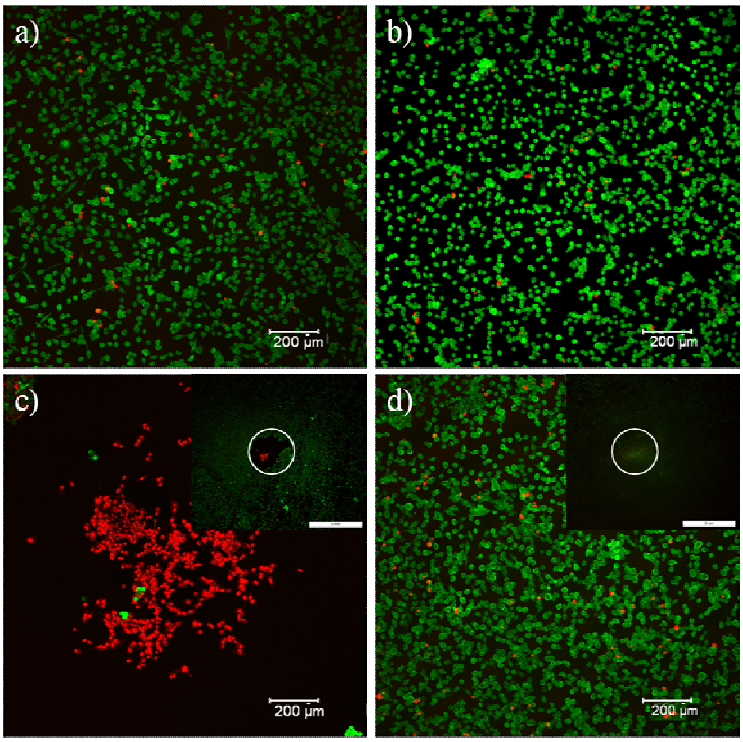

Figure 5.22: Confocal images of non-illuminated HeLa cells containing a) BNK-PGNHs-FA and b) DXSP-PGNHs-FA; HeLa cells containing c) DXSP-PGNHs-FA and d) BNK-PGNHs-FA illuminated at 2.5 W/cm^2 for 10 min. The inset points to the laser-illuminated area The black background color in c) stems from detachment of many dead cells after the washing step with PBS. Scale bars in insets are 5 mm.

5.4.8 *In Vitro* cell growth inhibition

We further quantitatively evaluated the multidimensional therapeutic potential of the present nanoplatforms based on the combination of localized hyperthermia under NIR-CW laser irradiation, DOXO chemotherapy and FA/magnetic targeting by means of the crystal violet assay [71] provided that DOXO can usually cause interferences with formazan crystals when using the standard MTT assay.

Cell viabilities (CV) of HeLa cells treated with BNK-PGNHs at different particle concentrations in the absence of NIR irradiation were almost negligible as observed in Figure 5.23a (black column), confirming that these particles are biocompatible. DXSP-PGNHs in the absence of irradiation possessed a slightly larger toxicity than the former ones, which depends on particle concentration (Figure 5.23a dark grey column), *i.e.* on loaded DOXO concentration inside the nanoplatforms and its subsequent release. This toxicity could result from the diffusion of the drug

through the pores of the metal layer in spite of this was not very significant since the amount of DOXO released should be low to inhibit tumor cell proliferation to large extents in the time scale of the experiment. In addition, some toxicity could be also caused by leakage of small amounts of non-encapsulated DOXO released during the FA functionalization process and washing steps and DOXO diffusion from some NPs with incomplete Au shells, which might be present in solution. All this is further supported when compared cytotoxicities of HeLa cells incubated with different concentrations of free DOXO, which resulted in lower viabilities compared with DXSP-PGNHs containing the same amount of drug.

Also, a slight enhanced free DOXO cytotoxicity was observed under NIR irradiation (2.5 W/cm^2 for 5 min). Moreover, when exposing the cells to NIR laser illumination CVs in the presence of BNK-PGNHs and DXSP-PGNHs decreases up to 67 and 39%, respectively. These larger cell mortalities appeared when the solution temperature raised above 43 ºC upon irradiation, at which tumor cells are damaged probably by denaturation of intracellular proteins, as mentioned previously [106]. Notably, DXSP-PGNHs exhibited an additional cytotoxic effect (($CV_{BNK\text{-}PGNHs} - CV_{DXSP\text{-}PGNHs}$)/ $CV_{BNK\text{-}PGNHs}$) of 42% compared to BNK-PGNHs due to the remote release of DOXO, which was more important as the amount of DOXO increased in solution. The mechanism is speculated to be caused by the altered kinetics, permeability and uptake of the chemotherapeutic agent during the heating process [42]. The photothermal effect of the Au nanolayer can partially melt the core of the polymeric matrix, releasing a larger amount of DOXO from DXSP-PGNHs.

On the other hand, the presence of the targeting ligand, folic acid, which favored an enhanced particle accumulation inside the cells as shown above, led to a further decreased in the cell viability up to 31% after 24 h (Figure 5.23b). The targeting efficacy of FA was further corroborated by adding an excess of FA to cells prior the addition of DXSP-PGNH-FA NPs. In this case, cell viability was similar to that observed for non functionalized DXSP-PGNH NPs.

On the other hand, cell cytotoxicity was additionally increased to larger extents when a magnetic field is applied to the cell culture for magnetic guiding of the particles, achieving a mortality of 82%. The targeting-induced tumoricidal effect was calculated to be 20% ($CV_{DXSP\text{-}PGNHs} - CV_{DXSP\text{-}PGNHs\text{-}FA}$)/ $CV_{BNK\text{-}PGNHs}$), and increased to 54% when magnetic targeting is also applied.

After 24 h of further incubation (48 h in total), the CVs with each nanostructure were also examined to reveal additional systemic cytotoxicity. Cell viability of HeLa cells treated with the functionalized nanoplatforms was additionally decreased due to the combined inhibitory effects of targeted hyperthermia and the sustained DOXO release (Figure 5.23b). In the case of DXSP-PGNHs-FA, the CV was 20%, and this nanoplatform exhibited an enhanced cytotoxic effect of 23% if compared to the non-functionalized ones. An additional enhancement of cell toxicity was observed when an external magnetic field was applied (93% cell toxicity). In this case, the targeting-induced tumoricidal effect was calculated to be 73% ($CV_{DXSP-PGNHs} - CV_{DXSP-PGNHs-FA+magnetic\ field}$)/ $CV_{BNK-PGNHs}$). These results demonstrated the improved cellular uptake by the combined effect of FA and magnetic targeting, and the synergistic chemotherapeutic and Au-shell driven hyperthermic efficacies of DXSP-PGNHs-FA.

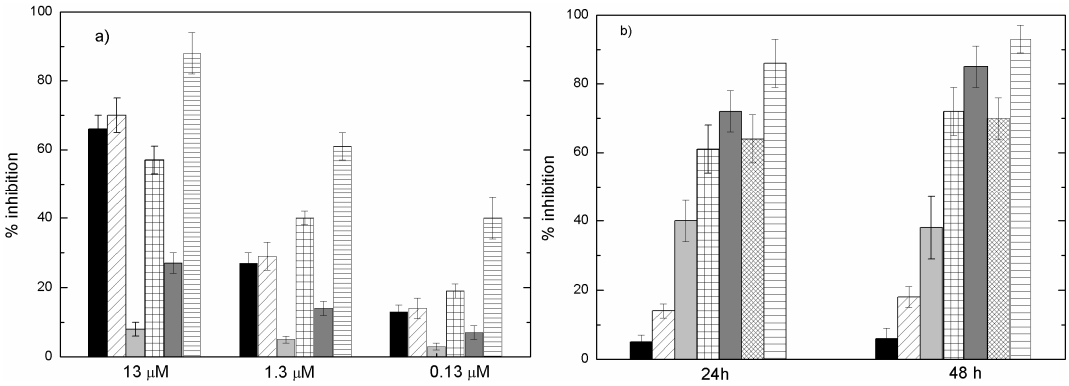

Figure 5.23: a) Cell growth inhibition of HeLa cells after incubation for 24 h in the presence of free DOXO in the absence (black columns) and presence (stripped columns) of NIR irradiation, 2.5 Wcm^{-2} for 5 min at 808 nm; BNK-PGNHs in the absence (light grey columns) and presence of NIR irradiation (squared columns); and DXSP-PGNHs in the absence (dark grey columns) and presence of NIR irradiation (dashed columns). Different free DOXO and equivalent DOXO loaded concentrations (13, 1.3 and 0.13 μM) inside the nanoplatforms were tested (when corresponding). b) Cell growth inhibition of HeLa cells after incubation for 24 and 48 h in the presence of BNK-PGNHs (black columns) and DXSP-PGNHs (stripped columns) in the absence of NIR irradiation; BNK-PGNHs (light grey columns), DXSP-PGNHs (squared columns), DXSP-PGNHs-FA (dark grey columns), DXSP-PGNHs-FA pretreated with free FA (dense quared columns), and DXSP-PGNHs-FA + applied magnetic field (dashed columns) in the presence of NIR-CI (2.5 Wcm^{-2} for 5 min). Equivalent DOXO concentration in DXSP-PGNHs and DXSP-PGNHs-FA was 1.3 μM.

5.5 Conclusions

We have synthesized polymeric core-coated Au nanoshells as a multifunctional platform to combine MR imaging, magnetic- and folic-acid targeted drug delivery, NIR light-triggered drug release, and photothermal therapy simultaneously into one system. The resulting nanoplatforms displayed enhanced T_2 -weighted MRI properties and surface plasmon absorbance in the NIR region, thus, exhibiting a NIR-induced temperature elevation and a NIR light-triggered and stepwise release behavior of doxorubicin.

The present nanoplatforms could be guided to the tumor area by the combination of ligand-induced and magnetic-assisted targeting, which enhanced their targeting effectiveness as observed *in vitro* by microscopies. In this regard, cell viability tests revealed that the combination of chemotherapy, magnetic and ligand-induced targeting, and NIR photothermal therapy through the use of DXSP-PGNH-FA increased the likelihood of cell killing significantly showing a synergistic effect, which potentially might help to overcome resistance to chemotherapeutic agents, making it a promising approach for cancer therapy. In this regard, the permeability of tumor vessels and the sensitivity of tumor cells toward chemotherapeutics should be greatly enhanced by hyperthemia, holding the promise of improving drug efficacy. In addition, photothermal therapy may facilitate triggered and enhanced drug release from the multifunctional nanoparticles, which is critical for achieving a high effective drug concentration in the tumor. Future studies employing more sophisticated nanoplatforms should perfectly allow both spatially and temporally improved hyperthermia, opto-magnetic-resonance imaging contrast agents for *in vivo* monitoring of tissue pharmacokinetics and cell tracking, and to enable a perfect and on-demand control of drug release dynamics for completely efficient chemotherapy.

5.6 Bibliography

[1] Ali Z, Abbasi AZ, Zhang F, Arosio P, Lascialfari A, Casula MF, et al. Multifunctional Nanoparticles for Dual Imaging. Analytical Chemistry. 2011;83:2877-82.

[2] Mulder WJM, Griffioen AW, Strijkers GJ, Cormode DP, Nicolay K, Fayad ZA. Magnetic and fluorescent nanoparticles for multimodality imaging. Nanomedicine. 2007;2:307-24.

[3] Lee D-E, Koo H, Sun I-C, Ryu JH, Kim K, Kwon IC. Multifunctional nanoparticles for multimodal imaging and theragnosis. Chemical Society Reviews. 2012;41:2656-72.

[4] Kim J, Piao Y, Hyeon T. Multifunctional nanostructured materials for multimodal imaging, and simultaneous imaging and therapy. Chemical Society Reviews. 2009;38:372-90.

[5] Caldorera-Moore ME, Liechty WB, Peppas NA. Responsive Theranostic Systems: Integration of Diagnostic Imaging Agents and Responsive Controlled Release Drug Delivery Carriers. Accounts of Chemical Research. 2011;44:1061-70.

[6] Bhojani MS, Van Dort M, Rehemtulla A, Ross BD. Targeted Imaging and Therapy of Brain Cancer Using Theranostic Nanoparticles. Molecular Pharmaceutics. 2010;7:1921-9.

[7] Gobin AM, Lee MH, Halas NJ, James WD, Drezek RA, West JL. Near-Infrared Resonant Nanoshells for Combined Optical Imaging and Photothermal Cancer Therapy. Nano Letters. 2007;7:1929-34.

[8] Hirsch LR, Stafford RJ, Bankson JA, Sershen SR, Rivera B, Price RE, et al. Nanoshell-mediated near-infrared thermal therapy of tumors under magnetic resonance guidance. Proceedings of the National Academy of Sciences. 2003;100:13549-54.

[9] Ke H, Wang J, Dai Z, Jin Y, Qu E, Xing Z, et al. Gold-Nanoshelled Microcapsules: A Theranostic Agent for Ultrasound Contrast Imaging and Photothermal Therapy. Angewandte Chemie International Edition. 2011;50:3017-21.

[10] Kievit FM, Zhang M. Cancer Nanotheranostics: Improving Imaging and Therapy by Targeted Delivery Across Biological Barriers. Advanced Materials. 2011;23:H217-H47.

[11] Sailor MJ, Park J-H. Hybrid Nanoparticles for Detection and Treatment of Cancer. Advanced Materials. 2012;24:3779-802.

[12] Liu H, Chen D, Li L, Liu T, Tan L, Wu X, et al. Multifunctional Gold Nanoshells on Silica Nanorattles: A Platform for the Combination of Photothermal Therapy and Chemotherapy with Low Systemic Toxicity. Angewandte Chemie International Edition. 2011;50:891-5.

[13] Ito A, Matsuoka F, Honda H, Kobayashi T. Antitumor effects of combined therapy of recombinant heat shock protein 70 and hyperthermia using magnetic nanoparticles in an experimental subcutaneous murine melanoma. Cancer Immunol Immunother. 2004;53:26-32.

[14] Hu C-MJ, Zhang L. Nanoparticle-based combination therapy toward overcoming drug resistance in cancer. Biochemical Pharmacology. 2012;83:1104-11.

[15] Chang M-Y, Shiau A-L, Chen Y-H, Chang C-J, Chen HHW, Wu C-L. Increased apoptotic potential and dose-enhancing effect of gold nanoparticles in combination with single-dose clinical electron beams on tumor-bearing mice. Cancer Science. 2008;99:1479-84.

[16] Atkinson RL, Zhang M, Diagaradjane P, Peddibhotla S, Contreras A, Hilsenbeck SG, et al. Thermal Enhancement with Optically Activated Gold Nanoshells Sensitizes Breast Cancer Stem Cells to Radiation Therapy. Science Translational Medicine. 2010;2:55ra79.

[17] Peer D, Karp JM, Hong S, Farokhzad OC, Margalit R, Langer R. Nanocarriers as an emerging platform for cancer therapy. Nat Nano. 2007;2:751-60.

[18] Hearty S, Leonard P, O'Kennedy R. Nanomedicine: Barcodes check out prostate cancer. Nat Nano. 2010;5:9-10.

[19] Heijden A, Hulsbergen- Van de Kaa C, Witjes JA. The influence of thermo-chemotherapy on bladder tumours: an immunohistochemical analysis. World J Urol. 2007;25:303-8.

[20] Nativ O, Witjes JA, Hendricksen K, Cohen M, Kedar D, Sidi A, et al. Combined Thermo-Chemotherapy for Recurrent Bladder Cancer After Bacillus Calmette-Guerin. The Journal of Urology. 2009;182:1313-7.

[21] Hahn GM, Braun J, Har-Kedar I. Thermochemotherapy: synergism between hyperthermia (42-43 degrees) and adriamycin (of bleomycin) in mammalian cell inactivation. Proceedings of the National Academy of Sciences. 1975;72:937-40.

[22] Wust P, Hildebrandt B, Sreenivasa G, Rau B, Gellermann J, Riess H, et al. Hyperthermia in combined treatment of cancer. The Lancet Oncology. 2002;3:487-97.

[23] Braun J, Hahn GM. Enhanced Cell Killing by Bleomycin and 43° Hyperthermia and the Inhibition of Recovery from Potentially Lethal Damage. Cancer Research. 1975;35:2921-7.

[24] Ning S, Hahn GM. Combination Therapy: Lonidamine, Hyperthermia, and Chemotherapy against the RIF-1 Tumor in Vivo. Cancer Research. 1991;51:5910-4.

[25] Overgaard J. Combined Adriamycin and Hyperthermia Treatment of a Murine Mammary Carcinoma in Vivo. Cancer Research. 1976;36:3077-81.

[26] Johnson HA, Pavelec M. Thermal Enhancement of Thio-TEPA Cytotoxicity. Journal of the National Cancer Institute. 1973;50:903-8.

[27] Kowal CD, Bertino JR. Possible Benefits of Hyperthermia to Chemotherapy. Cancer Research. 1979;39:2285-9.

[28] Cherukuri P, Glazer ES, Curley SA. Targeted hyperthermia using metal nanoparticles. Advanced Drug Delivery Reviews. 2010;62:339-45.

[29] Issels RD. Hyperthermia adds to chemotherapy. European Journal of Cancer. 2008;44:2546-54.

[30] Manthe RL, Foy SP, Krishnamurthy N, Sharma B, Labhasetwar V. Tumor Ablation and Nanotechnology. Molecular Pharmaceutics. 2010;7:1880-98.

[31] Eikesdal HP, Bjerkvig R, Raleigh JA, Mella O, Dahl O. Tumor vasculature is targeted by the combination of combretastatin A-4 and hyperthermia. Radiotherapy and oncology : journal of the European Society for Therapeutic Radiology and Oncology. 2001;61:313-20.

[32] Nelson BK, Conover DL, Krieg EF, Snyder DL, Edwards RM. Interactions of radiofrequency radiation-induced hyperthermia and 2-methoxyethanol teratogenicity in rats. Bioelectromagnetics. 1997;18:349-59.

[33] Diederich CJ, Hynynen K. Ultrasound technology for hyperthermia. Ultrasound in medicine & biology. 1999;25:871-87.

[34] Loo C, Lowery A, Halas N, West J, Drezek R. Immunotargeted Nanoshells for Integrated Cancer Imaging and Therapy. Nano Letters. 2005;5:709-11.

[35] Bardhan R, Chen W, Perez-Torres C, Bartels M, Huschka RM, Zhao LL, et al. Nanoshells with Targeted Simultaneous Enhancement of Magnetic and Optical Imaging and Photothermal Therapeutic Response. Advanced Functional Materials. 2009;19:3901-9.

[36] Schwartz JA, Shetty AM, Price RE, Stafford RJ, Wang JC, Uthamanthil RK, et al. Feasibility Study of Particle-Assisted Laser Ablation of Brain Tumors in Orthotopic Canine Model. Cancer Research. 2009;69:1659-67.

[37] Oldenburg SJ, Averitt RD, Westcott SL, Halas NJ. Nanoengineering of optical resonances. Chemical Physics Letters. 1998;288:243-7.

[38] Wang Y, Black KCL, Luehmann H, Li W, Zhang Y, Cai X, et al. Comparison Study of Gold Nanohexapods, Nanorods, and Nanocages for Photothermal Cancer Treatment. ACS Nano. 2013;7:2068-77.

[39] Sau TK, Murphy CJ. Room Temperature, High-Yield Synthesis of Multiple Shapes of Gold Nanoparticles in Aqueous Solution. Journal of the American Chemical Society. 2004;126:8648-9.

[40] Nikoobakht B, El-Sayed MA. Preparation and Growth Mechanism of Gold Nanorods (NRs) Using Seed-Mediated Growth Method. Chemistry of Materials. 2003;15:1957-62.

[41] Pérez-Juste J, Pastoriza-Santos I, Liz-Marzán LM, Mulvaney P. Gold nanorods: Synthesis, characterization and applications. Coordination Chemistry Reviews. 2005;249:1870-901.

[42] Hauck TS, Jennings TL, Yatsenko T, Kumaradas JC, Chan WCW. Enhancing the Toxicity of Cancer Chemotherapeutics with Gold Nanorod Hyperthermia. Advanced Materials. 2008;20:3832-8.

[43] Huang X, El-Sayed IH, Qian W, El-Sayed MA. Cancer Cell Imaging and Photothermal Therapy in the Near-Infrared Region by Using Gold Nanorods. Journal of the American Chemical Society. 2006;128:2115-20.

[44] Moon HK, Lee SH, Choi HC. In Vivo Near-Infrared Mediated Tumor Destruction by Photothermal Effect of Carbon Nanotubes. ACS Nano. 2009;3:3707-13.

[45] Tan A, Madani S, Rajadas J, Pastorin G, Seifalian A. Synergistic photothermal ablative effects of functionalizing carbon nanotubes with a POSS-PCU nanocomposite polymer. Journal of Nanobiotechnology. 2012;10:34.

[46] Zhou F, Wu S, Song S, Chen WR, Resasco DE, Xing D. Antitumor immunologically modified carbon nanotubes for photothermal therapy. Biomaterials. 2012;33:3235-42.

[47] Markovic ZM, Harhaji-Trajkovic LM, Todorovic-Markovic BM, Kepić DP, Arsikin KM, Jovanović SP, et al. In vitro comparison of the photothermal anticancer activity of graphene nanoparticles and carbon nanotubes. Biomaterials. 2011;32:1121-9.

[48] Farokhzad OC, Langer R. Impact of Nanotechnology on Drug Delivery. ACS Nano. 2009;3:16-20.

[49] Riehemann K, Schneider SW, Luger TA, Godin B, Ferrari M, Fuchs H. Nanomedicine—Challenge and Perspectives. Angewandte Chemie International Edition. 2009;48:872-97.

[50] Altınog lu EI, Russin TJ, Kaiser JM, Barth BM, Eklund PC, Kester M, et al. Near-Infrared Emitting Fluorophore-Doped Calcium Phosphate Nanoparticles for In Vivo Imaging of Human Breast Cancer. ACS Nano. 2008;2:2075-84.

[51] Alric C, Taleb J, Duc GL, Mandon C, Billotey C, Meur-Herland AL, et al. Gadolinium Chelate Coated Gold Nanoparticles As Contrast Agents for Both X-ray Computed Tomography and Magnetic Resonance Imaging. Journal of the American Chemical Society. 2008;130:5908-15.

[52] del Pino P, Munoz-Javier A, Vlaskou D, Rivera Gil P, Plank C, Parak WJ. Gene Silencing Mediated by Magnetic Liposphères Tagged with Small Interfering RNA. Nano Letters. 2010;10:3914-21.

[53] Bardhan R, Chen W, Bartels M, Perez-Torres C, Botero MF, McAninch RW, et al. Tracking of Multimodal Therapeutic Nanocomplexes Targeting Breast Cancer in Vivo. Nano Letters. 2010;10:4920-8.

[54] Kim J, Park S, Lee JE, Jin SM, Lee JH, Lee IS, et al. Designed Fabrication of Multifunctional Magnetic Gold Nanoshells and Their Application to Magnetic Resonance Imaging and Photothermal Therapy. Angewandte Chemie International Edition. 2006;45:7754-8.

[55] Kim J, Lee JE, Lee SH, Yu JH, Lee JH, Park TG, et al. Designed Fabrication of a Multifunctional Polymer Nanomedical Platform for Simultaneous Cancer- Targeted Imaging and Magnetically Guided Drug Delivery. Advanced Materials. 2008;20:478-83.

[56] Ma Y, Liang X, Tong S, Bao G, Ren Q, Dai Z. Gold Nanoshell Nanomicelles for Potential Magnetic Resonance Imaging, Light-Triggered Drug Release, and Photothermal Therapy. Advanced Functional Materials. 2013;23:815-22.

[57] Lee S-M, Kim HJ, Ha Y-J, Park YN, Lee S-K, Park Y-B, et al. Targeted Chemo-Photothermal Treatments of Rheumatoid Arthritis Using Gold Half-Shell Multifunctional Nanoparticles. ACS Nano. 2012;7:50-7.

[58] Lee S-M, Park H, Choi J-W, Park YN, Yun C-O, Yoo K-H. Multifunctional Nanoparticles for Targeted Chemophotothermal Treatment of Cancer Cells. Angewandte Chemie International Edition. 2011;50:7581-6.

[59] Lee S-M, Park H, Yoo K-H. Synergistic Cancer Therapeutic Effects of Locally Delivered Drug and Heat Using Multifunctional Nanoparticles. Advanced Materials. 2010;22:4049-53.

[60] Park H, Yang J, Lee J, Haam S, Choi I-H, Yoo K-H. Multifunctional Nanoparticles for Combined Doxorubicin and Photothermal Treatments. ACS Nano. 2009;3:2919-26.

[61] Yang J, Lee J, Kang J, Oh SJ, Ko H-J, Son J-H, et al. Smart Drug-Loaded Polymer Gold Nanoshells for Systemic and Localized Therapy of Human Epithelial Cancer. Advanced Materials. 2009;21:4339-42.

[62] Smith MW, Gumbleton M. Endocytosis at the blood–brain barrier: From basic understanding to drug delivery strategies. Journal of Drug Targeting. 2006;14:191-214.

[63] Mukherjee S, Ghosh RN, Maxfield FR. Endocytosis. Physiological Reviews. 1997;77:759-803.

[64] Li S, Ma Y, Yue X, Cao Z, Dai Z. One-pot construction of doxorubicin conjugated magnetic silica nanoparticles. New Journal of Chemistry. 2009;33:2414-8.

[65] Jain TK, Morales MA, Sahoo SK, Leslie-Pelecky DL, Labhasetwar V. Iron oxide nanoparticles for sustained delivery of anticancer agents. Mol Pharm. 2005;2:194-205.

[66] Jain TK, Richey J, Strand M, Leslie-Pelecky DL, Flask CA, Labhasetwar V. Magnetic nanoparticles with dual functional properties: Drug delivery and magnetic resonance imaging. Biomaterials. 2008;29:4012-21.

[67] Jana NR, Gearheart L, Murphy CJ. Wet Chemical Synthesis of High Aspect Ratio Cylindrical Gold Nanorods. The Journal of Physical Chemistry B. 2001;105:4065-7.

[68] Rollett A, Reiter T, Nogueira P, Cardinale M, Loureiro A, Gomes A, et al. Folic acid-functionalized human serum albumin nanocapsules for targeted drug delivery to chronically activated macrophages. International Journal of Pharmaceutics. 2012;427:460-6.

[69] Muñoz Javier A, del Pino P, Bedard MF, Ho D, Skirtach AG, Sukhorukov GB, et al. Photoactivated Release of Cargo from the Cavity of Polyelectrolyte Capsules to the Cytosol of Cells. Langmuir. 2008;24:12517-20.

[70] Trekker J, Hodenius M, Soenen S, Van Roy W, De Cuyper M, Lagae L, et al. The effect of intracellular clustering on the stability and contrast generating properties

of SPIOS: a comparison between PEGylated SPIOs and liposome SPIOs. Proc Intl Soc Mag Reson Med 2012. p. 4342.

[71] Cambon A, Rey-Rico A, Mistry D, Brea J, Loza MI, Attwood D, et al. Doxorubicin-loaded micelles of reverse poly(butylene oxide)-poly(ethylene oxide)-poly(butylene oxide) block copolymers as efficient "active" chemotherapeutic agents. Int J Pharm. 2013;445:47-57.

[72] Vega-Avila E, Pugsley MK. An overview of colorimetric assay methods used to assess survival or proliferation of mammalian cells. Proceedings of the Western Pharmacology Society. 2011;54:10-4.

[73] Park H, Yang J, Seo S, Kim K, Suh J, Kim D, et al. Multifunctional Nanoparticles for Photothermally Controlled Drug Delivery and Magnetic Resonance Imaging Enhancement. Small. 2008;4:192-6.

[74] Jain RA. The manufacturing techniques of various drug loaded biodegradable poly(lactide-co-glycolide) (PLGA) devices. Biomaterials. 2000;21:2475-90.

[75] Soppimath KS, Aminabhavi TM, Kulkarni AR, Rudzinski WE. Biodegradable polymeric nanoparticles as drug delivery devices. Journal of Controlled Release. 2001;70:1-20.

[76] Fraylich M, Wang W, Shakesheff K, Alexander C, Saunders B. Poly(d,l-lactide-co-glycolide) Dispersions Containing Pluronics: from Particle Preparation to Temperature-Triggered Aggregation. Langmuir. 2008;24:7761-8.

[77] Acharya S, Sahoo SK. PLGA nanoparticles containing various anticancer agents and tumour delivery by EPR effect. Advanced Drug Delivery Reviews. 2011;63:170-83.

[78] Rivera-Gil P, Jimenez De Aberasturi D, Wulf V, Pelaz B, Del Pino P, Zhao Y, et al. The Challenge To Relate the Physicochemical Properties of Colloidal Nanoparticles to Their Cytotoxicity. Accounts of Chemical Research. 2012;46:743-9.

[79] Kim SH, Jeong JH, Chun KW, Park TG. Target-Specific Cellular Uptake of PLGA Nanoparticles Coated with Poly(l-lysine)−Poly(ethylene glycol)−Folate Conjugate. Langmuir. 2005;21:8852-7.

[80] Ji T, Lirtsman VG, Avny Y, Davidov D. Preparation, Characterization, and Application of Au-Shell/Polystyrene Beads and Au-Shell/Magnetic Beads. Advanced Materials. 2001;13:1253-6.

[81] Ji X, Shao R, Elliott AM, Stafford RJ, Esparza-Coss E, Bankson JA, et al. Bifunctional Gold Nanoshells with a Superparamagnetic Iron Oxide−Silica Core

Suitable for Both MR Imaging and Photothermal Therapy. The Journal of Physical Chemistry C. 2007;111:6245-51.

[82] Melancon MP, Lu W, Zhong M, Zhou M, Liang G, Elliott AM, et al. Targeted multifunctional gold-based nanoshells for magnetic resonance-guided laser ablation of head and neck cancer. Biomaterials. 2011;32:7600-8.

[83] Paiva M, Castro DJ, Bublik M, Sercarz J. Laser-Induced Thermal Therapy for Recurrent Head and Neck Cancer: A Comprehensive Review.: 50. Journal of Investigative Medicine. 2006;54:S381-S2 10.2310/6650.2005.x0015.

[84] Tong L, Zhao Y, Huff TB, Hansen MN, Wei A, Cheng JX. Gold Nanorods Mediate Tumor Cell Death by Compromising Membrane Integrity. Advanced Materials. 2007;19:3136-41.

[85] Bisker G, Yeheskely-Hayon D, Minai L, Yelin D. Controlled release of Rituximab from gold nanoparticles for phototherapy of malignant cells. Journal of Controlled Release. 2012;162:303-9.

[86] Carregal-Romero S, Ochs M, Rivera-Gil P, Ganas C, Pavlov AM, Sukhorukov GB, et al. NIR-light triggered delivery of macromolecules into the cytosol. Journal of Controlled Release. 2012;159:120-7.

[87] Zunino F, Capranico G. DNA topoisomerase II as the primary target of anti-tumor anthracyclines. Anticancer Drug Des. 1990;5:307-17.

[88] Takahashi H, Niidome T, Nariai A, Niidome Y, Yamada S. Photothermal reshaping of gold nanorods prevents further cell death. Nanotechnology. 2006;17:4431.

[89] Link S, Burda C, Nikoobakht B, El-Sayed MA. Laser-Induced Shape Changes of Colloidal Gold Nanorods Using Femtosecond and Nanosecond Laser Pulses. The Journal of Physical Chemistry B. 2000;104:6152-63.

[90] Sigma-ALDRICH. http://www.sigmaaldrich.com/catalog/product/aldrich/739944?lang=de&region=DE.

[91] Guo C, Wang J, Dai Z. Selective content release from light-responsive microcapsules by tuning the surface plasmon resonance of gold nanorods. Microchim Acta. 2011;173:375-82.

[92] Weissleder R, Kelly K, Sun EY, Shtatland T, Josephson L. Cell-specific targeting of nanoparticles by multivalent attachment of small molecules. Nat Biotech. 2005;23:1418-23.

[93] Ai H, Flask C, Weinberg B, Shuai XT, Pagel MD, Farrell D, et al. Magnetite-Loaded Polymeric Micelles as Ultrasensitive Magnetic-Resonance Probes. Advanced Materials. 2005;17:1949-52.

[94] Ge J, Hu Y, Biasini M, Beyermann WP, Yin Y. Superparamagnetic Magnetite Colloidal Nanocrystal Clusters. Angewandte Chemie International Edition. 2007;46:4342-5.

[95] Abbasi AZ, Gutiérrez La, del Mercato LL, Herranz F, Chubykalo-Fesenko O, Veintemillas-Verdaguer S, et al. Magnetic Capsules for NMR Imaging: Effect of Magnetic Nanoparticles Spatial Distribution and Aggregation. The Journal of Physical Chemistry C. 2011;115:6257-64.

[96] Qiao R, Yang C, Gao M. Superparamagnetic iron oxide nanoparticles: from preparations to in vivo MRI applications. Journal of Materials Chemistry. 2009;19:6274-93.

[97] Yang J, Lee C-H, Ko H-J, Suh J-S, Yoon H-G, Lee K, et al. Multifunctional Magneto-Polymeric Nanohybrids for Targeted Detection and Synergistic Therapeutic Effects on Breast Cancer. Angewandte Chemie International Edition. 2007;46:8836-9.

[98] Juárez J, Cambón A, Topete A, Taboada P, Mosquera V. One-Dimensional Magnetic Nanowires Obtained by Protein Fibril Biotemplating. Chemistry – A European Journal. 2011;17:7366-73.

[99] Niu C, Wang Z, Lu G, Krupka TM, Sun Y, You Y, et al. Doxorubicin loaded superparamagnetic PLGA-iron oxide multifunctional microbubbles for dual-mode US/MR imaging and therapy of metastasis in lymph nodes. Biomaterials. 2013;34:2307-17.

[100] Schleich N, Sibret P, Danhier P, Ucakar B, Laurent S, Muller RN, et al. Dual anticancer drug/superparamagnetic iron oxide-loaded PLGA-based nanoparticles for cancer therapy and magnetic resonance imaging. International Journal of Pharmaceutics. 2013;447:94-101.

[101] Li K, Ding D, Huo D, Pu K-Y, Thao NNP, Hu Y, et al. Conjugated Polymer Based Nanoparticles as Dual-Modal Probes for Targeted In Vivo Fluorescence and Magnetic Resonance Imaging. Advanced Functional Materials. 2012;22:3107-15.

[102] Bhattacharya R, Patra CR, Earl A, Wang S, Katarya A, Lu L, et al. Attaching folic acid on gold nanoparticles using noncovalent interaction via different polyethylene glycol backbones and targeting of cancer cells. Nanomedicine: Nanotechnology, Biology and Medicine. 2007;3:224-38.

[103] Dixit V, Van den Bossche J, Sherman DM, Thompson DH, Andres RP. Synthesis and Grafting of Thioctic Acid PEG Folate Conjugates onto Au Nanoparticles for Selective Targeting of Folate Receptor-Positive Tumor Cells. Bioconjugate Chemistry. 2006;17:603-9.

[104] Li G, Li D, Zhang L, Zhai J, Wang E. One-Step Synthesis of Folic Acid Protected Gold Nanoparticles and Their Receptor-Mediated Intracellular Uptake. Chemistry – A European Journal. 2009;15:9868-73.

[105] Colombo M, Mazzucchelli S, Montenegro JM, Galbiati E, Corsi F, Parak WJ, et al. Protein Oriented Ligation on Nanoparticles Exploiting O6-Alkylguanine-DNA Transferase (SNAP) Genetically Encoded Fusion. Small. 2012;8:1492-7.

[106] Hanahan D, Weinberg RA. The Hallmarks of Cancer. Cell. 2000;100:57-70.

CHAPTER VI - Fluorescent Drug-loaded PLGA-based Branched Gold Nanoshells for Localized Multimodal Therapy and Imaging of Tumoral Cells

6.1 Summary

In this chapter, we report the synthesis of PLGA/DOXO-core Au-branched shell nanostructures (BGNSHs) functionalized with a human serum albumin/indocyanine green/folic acid complex (HSA-ICG-FA) to configure a multifunctional nanotheranostic platform. First, branched gold nanoshells (BGNSHs) were obtained through a seeded-growth surfactant-less method. These BGNSHs were loaded during the synthetic process with the chemotherapeutic drug doxorubicin, a DNA intercalating agent and topoisomerase II inhibitior. In parallel, the fluorescent near-infrared (NIR) dye isocyanine green (ICG) was conjugated to the proein human serum albumin (HSA) by electrostatic and hydrophobic interactions. Subsequently, folic acid was covalently attached to the HSA-ICG complex. In this eay, we created a protein complex with targeting specificity and fluorescent imaging capability. The resulting HSA-ICG-FA complex was adsorbed to the gold nanostructures surface (BGNSH-HSA-ICG-FA) in a straightforward incubation process thanks to the high affinity of HSA to gold surface. In this manner, BGNSH-HSA-ICG-FA platforms were featured with multifunctional abilities: the possibility of fluorescence imaging for diagnosis and therapy monitoring by exploiting the inherent fluorescence of the dye, and a multimodal therapy approach consisting of the simultaneous combination of chemotherapy, provided by the loaded drug, and the potential of photodynamic and photothermal therapies (provided by the dye and the gold nanolayer of the metallic hybrid structure, respectively) upon NIR light irradiation of suitable wavelength. The combination of this trimodal approach was observed to exert a synergistic effect on the cytotoxicity of tumora cells Furthermore, FA was proved to enhance the internalization of nanoplatform. The ability of the nanoplatforms as fluorescence imaging contrast was tested by preliminary analyzing their biodistribution in vivo in a tumor-bearing mice model.

6.2 Introduction

One of the areas of nanotechnology that has captured great interest by scientific community worldwide is the development of nanoengineered multifunctional systems which may be potentially used in a clinical strategy that simultaneously combine a (multi)diagnostic test and single or combined therapies based on the test results, the so-called nanotheranostic devices [1-7]. Nanoengineering of materials for this purpose involves the design, fabrication and testing of nanosystems that must combine several features such as biocompatibility, stealthness, long-circulating blood times, drug

transport and its triggerable release, imaging capabilities, and/or targeatibility, amongst others [8-12]. Improvement and suitable conjunction of all these characteristics would allow the early diagnosis of cancer and other diseases, the significant reduction of the therapeutic drug doses and subsequent reduction of adverse side effects, or the simultaneous combination of several therapeutic treatments with a real-time monitorization of their effectiveness [1, 3, 9, 10].

Amongst all the different diagnostic imaging techniques, fluorescence imaging offers a unique approach for visualizing morphological details in tissue with subcellular resolution, and becomes a powerful non-invasive tool for visualizing the full range of bio-species from living cells to animals. Most of the conventional fluorescence probes for bioimaging are based on single-photon excitation, emitting low energy fluorescence when excited by high energy light. These probes have some limitations: (i) DNA damage and cell death due to long-term exposure to high energy excitation; (ii) low signal-to-noise ratio caused by significant auto-fluorescence from the biological tissues; (iii) and low penetration depth in the biological tissues. Compared with visible light excitation, near-infrared (NIR) light excitation of NIR contrast agents for *in vivo* imaging provides several advantages such as deep penetration, weak autofluorescence, reduced photobleaching and low phototoxicity [13, 14]. In addition, these NIR probes can be simultaneously used under exposition to NIR light as phototherapeutic agents, acting as efficient photosensitizers transforming endogeneous oxygen to singlet oxygen ($^1O_2$) to kill cancer cells, the so-called photodynamic therapy (PDT) [15-17]. Because of this therapy is based on direct light administration to tumors/tissues, PDT treatment has remarkably improved tumor selectivity and reported side effects as compared to conventional chemo- and radio-therapies [18, 19]. However, PDT efficacy in tumors is largely limited by different factors such as the inadequeate selectivity and poor water solubility of most photosensitizers [18, 20-23], the self-destruction of photosensitizers upon light irradiation [24], and the depletion of tissue oxygen and disruption of tumor blood flow, which causes severe local hypoxia and cease the production of $^1O_2$ [25, 26], hindering the therapeutic efficacy of PDT and restricting its potential application in clinics [27].

On the other hand, novel plasmonic photothermal effects of gold nanostructures such as gold nanorods and nanostars [28-32], nanoshells [33-35], carbon nanotubes [36-

39] or graphene oxide [40-42] activated by NIR light illumination are being actively studied for their tumoricidal efficacies. Nevertheless, while these nanomaterials can certainly increase the local temperature around cancerous regions upon exposition to NIR light, it is not entirely evident that the photothermal effect is sufficient to achieve the desired level of cancer-cell cytotoxicity with a wide range [43, 44]. Thus, for patient compliance, the development of nanosystems for largely enhancing the tumorocidal efficacy by combination of different therapeutic approaches is vital and can allow to overcome current limitations of single available therapies and lead to synergisitc cytotoxic effects [45-48].

Hence, with the aim to simultaneously combine chemotherapy, photo- and thermotherapies with fluorescence imaging capability for diagnosis under NIR light illumination we here developed a multifunctional nanoplatform consisting of a poly(lactic-*co*-glycolic acid) biodegradable matrix loaded with the anticancer drug doxorubicin (DOXO). The polymeric PLGA nanoparticle (NP) was covered with a porous gold shell, which provides the nanoplatform the ability of NIR light absorption and subsequent efficient energy transduction in the form of localised heat due to NIR resonance of the metal shell, and also accelerates drug released from the nanoplatform [49].

The nanoshell surface was functionalized with human serum albumin (HSA) for stealthness, to which the fluorescent dye indocyanine green (ICG) was non-covalently conjugated to provide the nanoplatform with fluorescence imaging and singlet oxygen production capabilities. ICG is a tricarbocyanine dye with absorbing properties exclusively in the NIR electromagnetic spectrum, and currently used as a diagnostic agent for blood volume determination, ophtalmic angiography, cardiac output and hepatic function [50, 51]. In addition, folic acid was also covalently conjugated to the protein surface to provide the nanoplatofrm with specific targeability. In this way, heat, singlet oxygen species and drug could be simultaneosuly delivery to the selected tumor region. We demonstrated that the present nanoplatforms showed synergistic therapeutic effects *in vitro* by combination of chemo-, photo- and thermo-therapies, and can simultaneously act as effective contrast agents for *in vivo* optical imaging by exploiting the fluorescence enhancement of the dye upon positioned near the metal surface while

tuning the plasmon resonance of the nanoshell to the emission wavelength of the fluorophore [52].

6.3 Materials and Methods

6.3.1 Materials

Human serum albumin (HSA), indocyanine green (ICG), doxorubicin (DOXO), folic acid (FA), poly(D,L-lactide-*co*-glycolide) (PLGA) of 7-17 kDa with 50:50 lactide–glycolide ratio, Pluronic F127, hydrogen tetrachloroaureate (III) trihydrate ($HAuCl_3 \cdot 3H_2O$), N-(3-dimethylamniopropyl)-3-ethylcarbodiimide hydrochloride (EDC), sulfo-N-hydroxysuccinimide (Sulfo-NHS), 1,3-diphenylisobenzofuran (DPIBF), low molecular weight chitosan (LMW-chitosan, M_W = 111 kDa*)*, potassium carbonate anhydrous, sodium borohydride, sodium azide, sodium citrate tribasic and ascorbic acid were purchased from Sigma–Aldrich (St. Louis, MO, USA). ProLong® Gold antifade reagent with DAPI was purchased from Invitrogen (Carlsbad, USA). DOXO HCl, fetal bovine serum (FBS), Dulbecco's modified eagle medium (DMEM), fetal bovine serum (FBS), L-glutamine, penicillin/streptomycin, sodium pyruvate, and MEM non-essential amino acids (NEAA) were purchased from Fisher Scientific (Pittsburgh, PA, USA). Dialysis membrane tubing (molecular weight cutoff ~3500) was purchased from Spectrum Laboratories, Inc. (Rancho Dominguez, CA, USA). All other chemicals and solvents were of reagent grade (purchased from Sigma–Aldrich). Milli-Q water was used for all aqueous solutions. All glassware was washed with aqua regia and HF 5% (v/v) and extensively rinsed with water. All the chemicals were of analytical grade and used without further purification.

6.3.2 Synthesis of BGNSHs

PLGA-core gold-shell nanoconstructs (BGNSHs) were synthesized following a seeded-growth protocol based on previously protocols but with modifications [53].

First, PLGA NPs were synthesized by a nanoprecipitation process, using acetone as the organic solvent and F127 as a stabilizer agent. Briefly, in a typical preparation 25 mg of PLGA were dissolved in 2.5 mL of acetone. When corresponding, a suitable amount of DOXO (previously converted to its hydrophobic base form by addition of triethylamine, as reported in literature [54]) was added. This organic solution was added dropwise at 0.166 mL/min to 50 mL of F127 1% (w/v) in water at a 10 °C and moderate stirring at 250 rpm. The emulsion was homogenized with a sonicating tip at 100 W in an ice bath for 15 min. Acetone, non-encapsulated DOXO, and excess stabilizer were eliminated by stirring for 4 h and subsequent centrifugation twice at 9000 rpm for 30 min. DOXO concentration in the supernatant was measured by UV-vis spectroscopy by using a previously obtained-drug calibration curve. The final pellet was dispersed in 25 mL of water by vortexing for 30 s and filtered through 0.45 μm filters (Merck Millipore, USA). PLGA NPs had a hydrodynamic diameter and zeta potential of 100 ± 20 nm and -39 ± 8 mV, respectively.

In order to grow the gold nanolayer around the PLGA dielectric NP core, 5 mL of PLGA NPs were incubated for 4 h with 0.25 mL of chitosan. Chitosan, a biocompatible polycation, was adsorbed on the negative surface of PLGA NPs by electrostatic attraction, inverting the NPs surface charge to +4 mV. Excess of chitosan was eliminated by centrifugation twice at 9000 rpm for 15 min and 20 °C. Then, positively charged PLGA NPs were incubated for 4 h with 5 mL of citrate-capped Au seeds prepared following a methodology previously reported by Jana *et al.* [55]. Non-attached gold seeds were eliminated by centrifugation twice at 7000 rpm for 15 min at 20 °C. Subsequently, an Au growth solution was prepared by dissolving 0.05 g potassium carbonate and 2 mL of 0.025 M $HAuCl_4 \cdot 3H_2O$, and aged 24 h prior use. The growth of the Au shell was achieved by mixing 1 mL of PLGA NPs-seed precursor with 20 mL of the Au growth solution and subsequent reduction with 25 μL of 0.5 M ascorbic acid. PGNHs were immediately formed, as noticed by the blue coloration of the mixture solution. BGNSHs were left stand overnight and washed twice by centrifugation at 3500 rpm for 15 min and 20 °C

6.3.3 HSA-ICG complex

Indocyanine green (ICG) was non-covalently conjugated to human serum albumin (HSA) by mixing both reactants under ambient conditions. 10 mL of 5 μM HSA and 10 mL of 30 μM ICG both in 50 mM MES buffer at pH 6 were mixed and shaken for 4 h at ambient temperature. Then, in order to remove unbound ICG, the mixture was dialyzed 24 h against MES buffer with a cellulose dialysis membrane with MWCO of 3500 Da. Absorbance peaks of the protein-dye complex (λ_{max} = 780 nm) and bare protein (λ_{max} = 280 nm) were monitored to account for free-dye removal. The concentration of bound ICG was determined after subtraction of the ICG concentration in the supernantant to that initially added. The HSA-ICG complex was stored at 4 °C and protected from light before use.

6.3.4 Folic acid activation and conjugation to HSA-ICG complexes

Folic acid (FA) was reacted with EDC and sulfo-NHS to generate an active species, FA*, and covalently attached to the HSA-ICG complex. First, 1mL of 1 mM folic acid in MES 50 mM (pH 6) where mixed with 0.6 mg of N-(3-dimethylaminopropyl)-N'-ethylcarbodiimide hydrochloride (EDC) and 0.6 mg of N-hydroxisulfosuccinimide (sulfo-NHS). This mixture was reacted for 20 min at ambient temperature and protected from light. FA* was reacted with HSA-ICG in order to form a covalent bond between the activated FA* and amine groups of HSA. 50 μL of FA* and 10 mL of HSA-ICG (molar ratio 5:1) were mixed for 4 h at ambient temperature. The product was dialyzed 24 h against MES buffer with a cellulose membrane (MWCO 3500 Da) to eliminate unreacted FA* and remaining reaction by-products. The number of FA molecules conjugated to HSA was calculated with an UV-vis calibration curve of FA (Figure 6.1a-b). This curve was prepared by making dilutions of a stock solution of FA, and measuring their absorbance spectra. Absorbance at 280 nm was plotted against concentration and fitted to a linear curve.

Then, 50 μL of 5 μM FA* was mixed with 10 mL of 5 μM HSA-ICG in a 5:1 molar ratio. The initial concentration of FA* in the reacting mixture was 0.02487 mM. After 4 h of reaction and 24 h of dialysis to remove unreacted compounds, HSA-ICG complexes displayed two new peaks at ca. 275 and 360 nm which correspond to FA

(Figure 6.2) confirming the formation of HSA-ICG-FA complex. The concentration of FA in the complexes was found to be 3 molecules of FA per HSA-ICG complex entity.

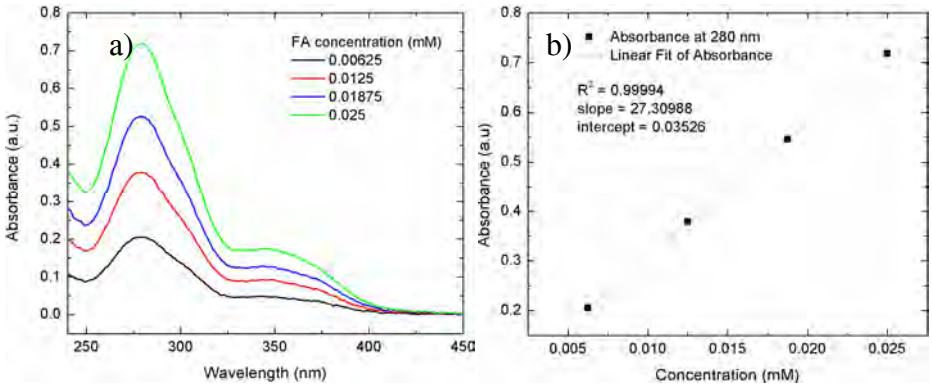

Figure 6.1: a) UV-vis spectra and calibration curve of FA, and b) linear fit of absorbance at 280 *vs* FA concentration.

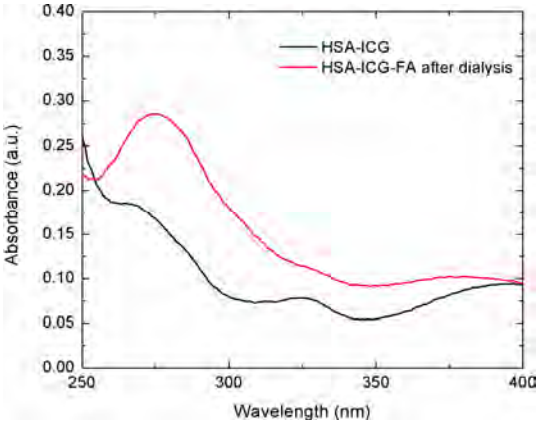

Figure 6.2: a) UV-vis spectra of HSA-ICG complexes before and b) after reaction with FA*.

6.3.5 Adsorption of HSA-ICG-FA on BGNSHs

2 mL of BGNSHs with an optical density of 1 at 800 nm were mixed with 0.500 mL of HSA-ICG-FA complex for 48 h under stirring in the dark. Afterwards, BGNSH-HSA-ICG-FA nanoconjugates were centrifuged three times for 15 min at 3500 rpm and 20 °C in order to eliminate non-adsorbed complexes and resuspended in PBS (pH 7.4) buffer solution. The absorbance of the supernatant was closely monitored to account for unbound HSA-ICG-FA concentration in the supernatant in order to calculate the amount

of ICG molecules on the nanoshells (~5.5 ± 0.4 μM). Finally, to further stabilize the protein coating, to 1 mL BGNSH-HSA-ICG-FA nanoconjugates in PBS (pH 7.4), N-(3-dimethylaminopropyl)-N-ethylcarbodiimide hydrochloride (5 mg, 25 mmol) and N-sulfo-hydroxysulfosuccinimide (5 mg, 25 mmol) were added. The reaction was carried out for 2 h at room temperature. Cross-linked BGNSH-HSA-ICG-FA complexes were purified with desalting zeba spin columns (Fisher Scientific, USA).

6.3.6 Nanoplatform characterization

NP sizes were obtained by dynamic light scattering (DLS) at 25 °C by means of an ALV-5000F (ALV-GmbH, Germany) instrument with vertically polarized incident light (λ = 488 nm) supplied by a diode-pumped Nd:YAG solid-state laser (Coherent Inc., CA, USA) operated at 2 W, and combined with an ALV SP-86 digital correlator (sampling time 25 ns to 100 ms). NP sizes and morphologies were also acquired by transmission and scanning electron microscopy (TEM and SEM, respectively) by means of a Phillips CM-12 and a Carl Zeiss Libra 200 Fm Omega (for TEM), and FESEM ultra Plus electronic microscopes (for SEM) operating at 120 and 20 kV, respectively. Elecron difracttion X-ray spectroscopy (EDX) was also performed using the same instrument as for SEM imaging. Samples were prepared for analysis by evaporating a drop of the hybrid NP dispersion on a carbon-coated copper grid without staining (TEM) or on a silicon wafer (SEM). ζ-potentials were measured with a Zetasizer Nano ZS (Malvern, UK) using dispossable folded capillary cells. Samples were measured in triplicate in PBS (pH 7.4) at 25 °C. The gold concentration in solution was determined by inductively coupling plasma-mass spectrometry (ICP-MS) in a Varian 820-MS equipment (Agilent Technologies, USA). The corresponding concentration of BGNSH-HSA-ICG-FA particles was calculated by assuming a sphere model of 100 nm diameter. UV-Vis spectra were measured in a Cary Bio 100 UV-Vis spectrophotometer (Agilent Technologies, USA). Fluorescence spectra were monitored in a Cary Eclipse spectrophotometer (Agilent Technologies, USA).

6.3.7 NIR-laser induced temperature increase

Temperature increment tests were performed with a continuous wave fiber-coupled diode laser source of 808 nm wavelength (50W, Oclaro Inc, San Jose, CA, USA). The laser was powered by a Newport 5700-80 regulated laser diode driver (Newport Corporation, Irvine, CA, USA). A 200-μm-core optical fiber was used to transfer laser power from the laser unit to the target solution, and equipped with a lens telescope mounting accessory at the output, which allowed for tuning of the laser spot size in the range 1-10 mm. The output power was independently calibrated using an optical power meter (Newport 1916-C) and laser spot size was previously measured with a laser beam profiler (Newport LBP-1-USB), which was placed at the same distance (8 cm) between the lens telescope output and the quartz cuvette (or the 96-well plate). For measuring the temperature change mediated by the present BGNSH-HSA-ICG-FA, 2 mL of BGNSH-HSA-ICG-FA conjugates, PBS buffer containing 10% (v/v) FBS, BGNSHS and free ICG samples were placed in a quartz cuvette and irradiated for 10 min at 2 W cm^{-2}. The temperature of samples was measured with a type J thermocouple linked to a digital thermometer inserted into the solution.

6.3.8 NIR-laser triggered release of DOXO

Release kinetics of DOXO from BGNSH-HSA-ICG-FA was assessed *in vitro* at 37 °C in PBS buffer (pH 7.4) containing 10% (v/v) fetal bovine serum. Briefly, 5 mL of DOXO-loaded BGNSH-HSA-ICG-FA with known DOXO concentration (3 μM) were placed in centrifuge tubes (in triplicate). Samples were maintained in a 37 °C bath with constant stirring. The samples were irradiated over a period of 10 min. Each hour, 500 μL of sample were taken and centrifuged at 3500 rpm for 10 min at 20 °C. The supernatant was carefully extracted and its fluorescence at 594 nm was measured in a Cary Eclipse spectrophotometer (Agilent Technologies, Spain) for quantification of released DOXO with a calibration curve. After centrifugation and supernatant extraction, the settled DOXO-loaded BGNSH-HSA-ICG-FA were resuspended in 500 μL with fresh buffer and returned to the original sample.

6.3.9 *In vitro* singlet oxygen generation

The generation of singlet oxygen *in vitro* was performed by following the decay of the absorbance peak at 420 nm of 1,3-diphenylisobenzofurane (DPIBF), which is a specific singlet oxygen trap [56]. Briefly, 2 mL of sample (deionized water, free ICG, BGNSH-HSA, or BGNSH-HSA-ICG-FA conjugates) were placed in a quartz cuvette, and 100 μL of 1 mM DPIBF in ethanol were added. Concentration of free ICG and ICG bound to BGNSH-HSA-ICG-FA was 5 μM. The UV-vis spectrum of samples before illumination was recorded and taken as the initial (100%) absorbance value. The sample was magnetically stirred and illuminated with NIR-light (808 nm) for 10 min; then, the UV-vis spectra recorded and the process was repeated twice. The total illumination time was 15 min. The singlet oxygen generation was qualitatively determined at three different laser powers densities: 2, 4 and 6 W/cm^2.

6.3.10 Tumor cells

MDA-MB-231 adenocarcinoma breast and HeLa cervical cancer cells from Cell Biolabs (San Diego, CA, USA) were used for *in vitro* studies. Cells were grown at standard culture conditions (5% CO_2 at 37 ºC) in Dulbecco's Modified Eagle Medium (DMEM) supplemented with 10% Fetal Bovine Serum (FBS), 2 mM L-glutamine, 1% penicillin/streptomycin, 1 mM sodium pyruvate, and 0.1 mM MEM Non-Essential Amino Acids (NEAA).

6.3.11 Cellular uptake by fluorescence microscopy

Cellular uptake of BGNSH-HSA-ICG-FA was followed by confocal fluorescence microscopy by seeding MDA-MB-231 and HeLa cells on poly-L-lysine coated glass coverslips (12 ×12 mm) placed inside 6-well plates ($1.5 \cdot 10^5$ cells/well with 3 mL of DMEM), and grown for 24 h at standard culture conditions. Then, the conjugates were added to cells (200 μL in PBS pH 7.4, $1 \cdot 10^{10}$ particles/mL). After 6 h of incubation, the NP-containing cells were washed three times with PBS, fixed with paraformaldehyde 4% (w/v) for 10 min, washed with PBS pH 7.4, treated with Triton X-100 (permeabilizer) for 10 min, and finally washed again with PBS pH 7.4. Then, coverslips were mounted on glass slides, stained with DAPI (Invitrogen) and cured for

24 h at -20 °C. Samples were visualized at 63X using a confocal fluorescence microscope (Leica DMI6000B**,** Leica Microsystems, Germany*)* using blue channel for DAPI, $\lambda_{exc.}$ 350 nm, red channel for ICG ($\lambda_{exc.}$ 760 nm), and transmitted light in differential interference contrast (DIC) mode.

6.3.12 *In vitro* cell cytotoxicity

Cytotoxicity of nanoplatforms was tested *in vitro* by the CCK-8 cytotoxicity assay. Breast MDA-MB-231 and cervical HeLa cancer cells with an optical confluence of 80–90% were seeded into 96-well plates (100 μL, $1.5 \cdot 10^4$ cells/well) and grown for 24 h at standard culture conditions in 100 μL growth medium. After 24 h of incubation at 37 °C and 5% CO_2, 50 μL of free DOXO (3 μM), free ICG (5 μM), BGNSH-HSA-FA, BGNSH-HSA-ICG (5 μM ICG), BGNSH-HSA-ICG-FA (5 μM ICG), DOXO-loaded BGNSH-HSA-FA (3 μM DOXO), and DOXO-loaded BGNSH-HSA-ICG-FA (3 μM DOXO, 5 μM ICG) were added to the wells. Some wells were left without particles as a negative control (blank) adding additional 50 μL of PBS. After 6 h of incubation, the culture medium was discarded, the cells washed with 10 mM PBS, pH 7.4 several times, new culture medium (100 μL) added (previously aerated for 2 min) and incubated for 1 h. A set of cells were illuminated with 808 nm laser at 2 W/cm^2 for 5 min and then incubated 15 min. This process was repeated twice more. Then, cells were left incubated for additional followed by incubation for 17 h. Another set of cells was left without illumination in order to determine the intrinsic cytotoxicity of the nanoplatforms. After 24 h total incubation, 10 μL of CCK-8 reagent was added to each well, and after 2 h the absorption at 450 nm of cell samples was measured with an UV-vis microplate absorbance reader (Bio Rad model 689, USA). Cell viability was calculated as:

$$\%CV = \frac{Abs_{sample}}{Abs_{blank}} x100 \qquad \text{(Eq 6.1)}$$

where Abs_{sample} is absorbance at 450 nm for samples and Abs_{blank} for controls without nanoplatforms and in the absence of illumination.

6.3.13 In vivo imaging and biodistribution

To assess the *in vivo* tracking of the nanoplatforms, $3 \cdot 10^6$ cells from a MDA-MB-231 cell line were injected in the dorsal flank of immunodeficient BALB/c nude mice [57]. One week upon injection, cell implantation was checked by registering the fluorescent activity of the cells. We next injected 10 mg/kg of either HSA-ICG-FA/NGHSH nanoplatforms or ICG-loaded PLGA NPs (as a control) in the mice tail vein and registered the *in vivo* fluorescent activity (λ_{exc} = 710 nm/λ_{em} = 840 nm) with a IVIS Spectrum imaging system (Caliper Life Sciences, Perkin-Elmer, USA) at different time intervals.

6.4 Results and discussion

The fabrication procedure of the hybrid nanoplatforms is represented in Figure 6.3. DOXO-loaded PLGA NPs were synthesized as previously described in Chapter 3 with some modifications. The drug loading capacity, defined as the amount of drug loaded inside the polymeric matrix regarding the amount of feeded drug and polymer particles, was estimated to be 3.9% (w/w). Next, citrated stabilized Au seeds (4 nm) were deposited onto the surface of chitosan-modified DOXO-loaded PLGA NPs, and a full and porous metal shell structure was obtained in the presence of a growth solution exclusively composed of $HAuCl_4$ and ascorbic acid (AA) [58].

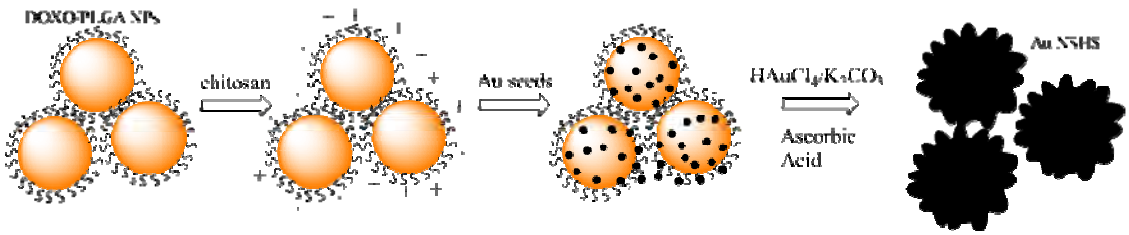

Figure 6.3: Scheme of the production of BGNSHs. First DOXO/PLGA NPs (~80 nm) were prepared by a nanoprecipitation method. These solid spheres were functionalized with chitosan

chains to bind negatively charged citrated-Au seeds. Finally, the PLGA NP-seed precursor was used as substrate to grow branched Au nanoshells, which resemble virus structures.

Trasmission and scanning electron microscopies confirmed the morphology of the hybrid gold nanoshells (BGNSHs), which resemble a virus capside (Figure 6.4a-b) with a size of ca. 85 ± 15 nm. The ultraviolet-visible/NIR absorption spectrum of BGNSHs exhibited a pronounced surface plasmon absorption in the NIR region ($\lambda \approx$ 770 nm, Figure 6.4c) consistent with a reticular Au shell formed around the dielectric polymeric core of the nanoplatform. In the absence of the metal shell, the DOXO-loaded PLGA NPs exhibited absorption maxima at $\lambda \approx 490$ nm, in agreement with the absorbance peak of free DOXO. Electron diffraction X-ray spectroscopy (EDX) showed traces of C and O elements from the polymeric inner components and Au corresponding to the metal shell, which was a first evidence of the porous nature of the metal shell, as observed previously in Chapter 4 and 5. This was additionally confirmed while examining high-resolution TEM (HR-TEM) images, where the existence of voids or pores on the metal layer could be observed (Figure 6.4d).

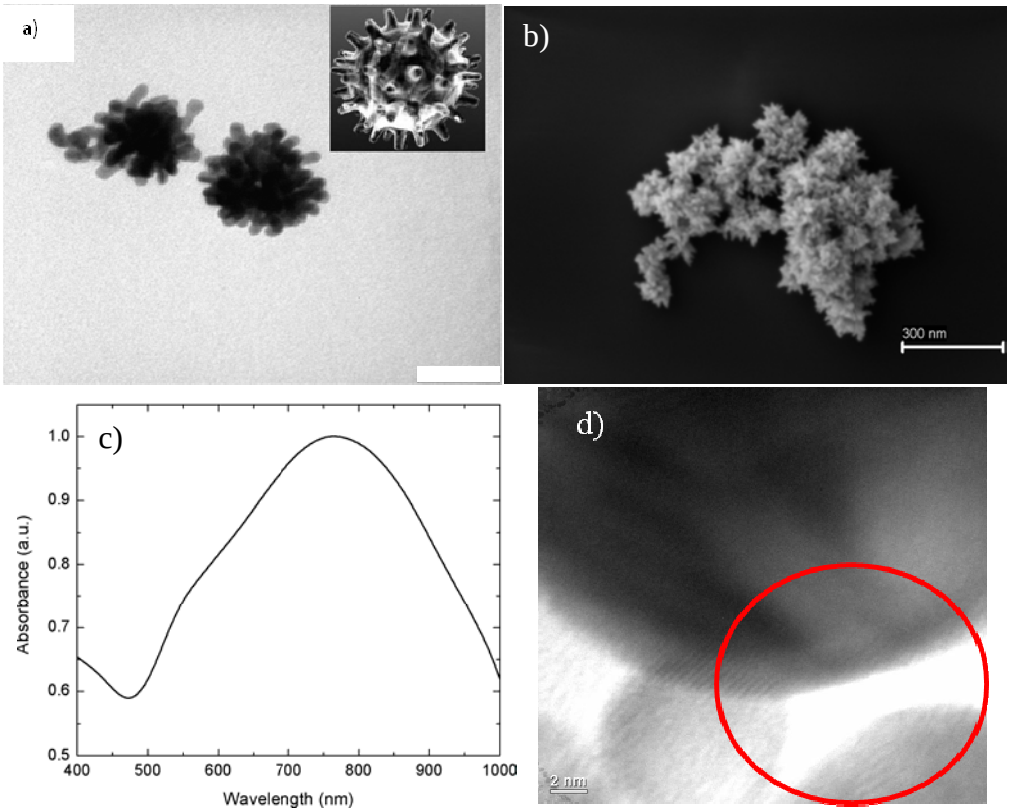

Figure 6.4: a) TEM image of BGNSHs nanoplatforms. The inset shows a virus particle confirming the biomimetic shape of the as-synthesized nanoplatforms; b) SEM image of BGNSHS. c) UV-vis absorption spectrum of BGNSHs. d) HRTEM image of BGNSHs showing the existence of voids in the Au shell structure. In a), the scale bar is 100 nm.

The Au surface of the hybrid BGNSHs was functionalized with HSA-ICG or HSA-ICG-FA (when corresponding) complexes to improve the stability and impart full stealthness to these nanoplatforms under physiological conditions [59]. HSA possess a great affinity for gold surfaces and it tends to spontaneously adsorb onto them. This strong adsorption can originate from combination of electrostatic, van der Waals and thiol-Au bonding provided by the thiol groups of the protein's cysteine residues. Besides the stabilizing effect, the protein layer can also act as a biocompatible coverage which reduces the non-specific adsorption of opsonines and macrophage recognition [60]. To configure the HSA-ICG-FA complexes ICG was non-covalently attached to the protein. Subsequently, FA was covalently conjugated by carbodiimide chemistry to the amine groups of the surface lysine residues of the protein molecules. The successful anchoring of ICG to HSA was evidenced by the presence of absorbance peaks for the

protein complex at ca. 780 nm (in the absence of BGNSHS), typical of the dye (Figure 6.5b), and at 278 and 385 nm (Figure 6.5c), corresponding to FA. Changes in zeta potential of the protein from -5.6 ± 2.3 to -27.6 ± 4.6 mV were observed at different stages of the conjugation process (Table 6.1).

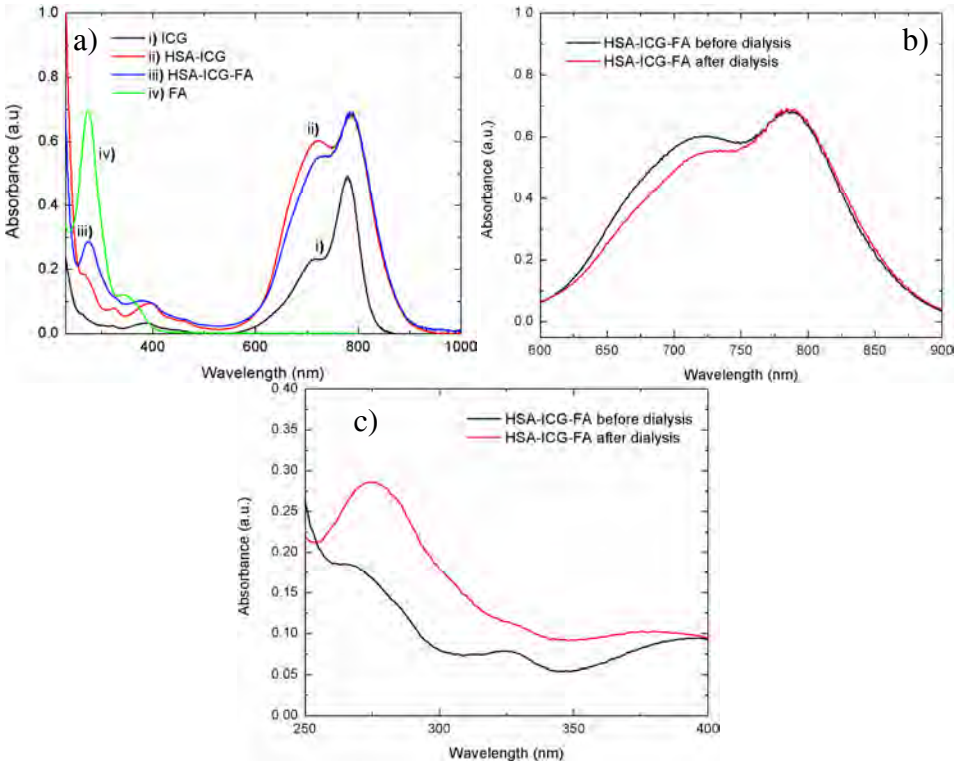

Figure 6.5: UV-vis spectra of free ICG, free FA, HSA-ICG and HSA-ICG-FA complexes after 24 h of dialysis. b) Change in ICG absorbance of HSA-ICG complexes before and after FA conjugation. c) UV-vis spectra of HSA-ICG-FA complexes showing the FA peaks before and after 24 h of dialysis.

Table 6.1: Zeta potential of HSA complexes in MES 50 ◘M (pH 6)

Sample	Zeta Potential (mV)
HSA	-5.6 ± 0.4
HSA-ICG	-1.0± 0.9

HSA-ICG-FA	-27.6 ± 1.7

Incubation of the protein complexes with the hybrid gold nanoshells led to the formation of BGNSH-HSA-ICG-FA nanoplatforms. Moreover, the succesfull conjugation of the HSA-ICG-FA complex to the BGNSHs was confirmed, on one hand, by a slight red-shift and broadening of the LSPR band of the metal nanoshell due to the higher refractive index of HSA than pure buffer (Figure 6.6a) [61, 62] and the peak absorbance positions of bounded ICG and, on the other, by the increase and blue-shift of the fluorescence peak of ICG upon protein complex adsorption onto the nanoplatform surface (Figure 6.6b).

The sizes of BGNSH-HSA-ICG-FA nanoplatforms were determined by dynamic light scattering (DLS) approximately to be ~ 135 ± 25 nm with and an effective zeta potential of -16.3 ± 1.7 mV (Table 6.2). The 30 nm increase in size regarding bare BGNSHs is consistent with the formation of a protein multilayer onto the gold surfaces, in agreement with previous reports [63]. We then determined the gold concentration of BGNSH-HSA-ICG (or BGNSH-HSA-ICG-FA) by inductively coupled plasma-mass spectroscopy (ICP-MS). Combined analysis by ICP-MS and UV-vis spectroscopy showed that about 450 ICG molecules were anchored per BGNSHS.

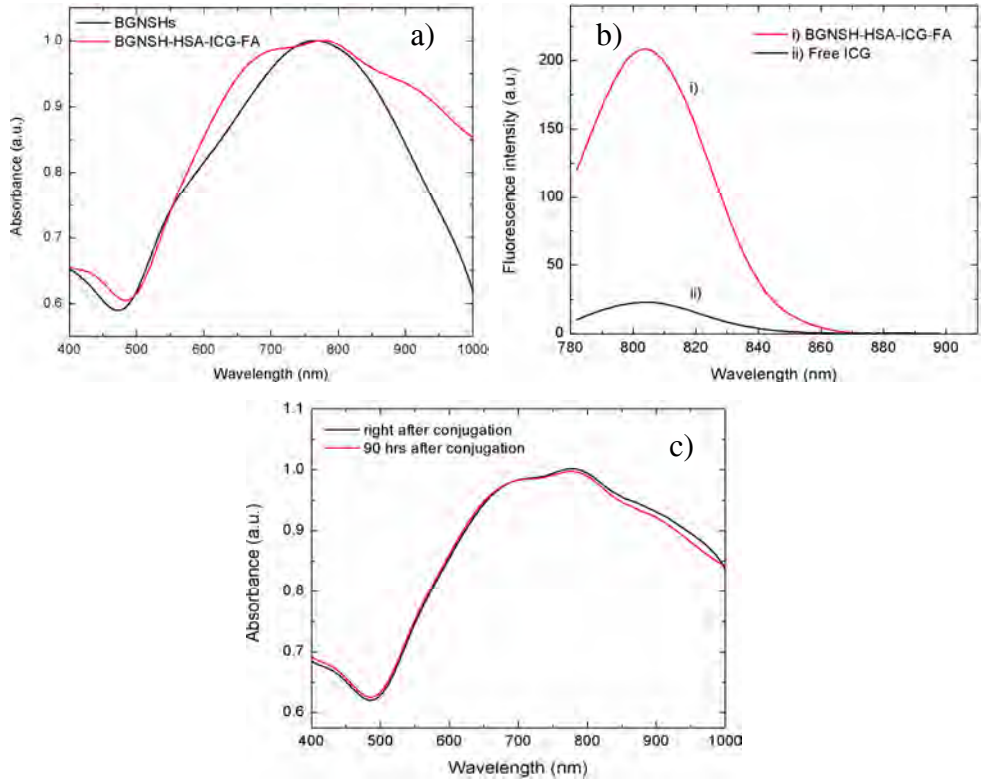

Figure 6.6: a) UV-vis spectra of bare BGNSHS and BGNSH-HSA-ICG-FA in PBS with 10% (v/v) FBS. b) Fluorescence spectra of free ICG (5 μM) and BGNSH-HSA-ICG-FA (with 5 μM of conjugated ICG). c) UV-vis spectra of BGNSH-HSA-ICG-FA in PBS with 10% (v/v) FBS right after incubation and after 96 h of storage at room temperature.

Table 6.2: Hydrodynamic radius and zeta potential of BGNSHs in PBS 10mM (pH 7.4)

Sample	**r_h (nm)**	**Zeta Potential (mV)**
Bare BGNSHs	55.2 ± 4.9	-24.6 ± 1.8
BGNSH-HSA	67.1 ± 8.9	-20.9 ± 2.4
BGNSH-HSA-ICG	68.1 ± 14.6	-16.6 ± 1.2
BGNSH-HSA-ICG-FA	68.3 ± 12.3	-16.3 ± 1.7

The BGNSH-HSA-ICG-FA platforms exhibited excellent dispersivity and stability in bare PBS and PBS containing 10% (v/v) FBS (Figure 6.6c), with no aggregates observed visually or by optical microscopy. Hence, the nanoplatform structure should enable for a simultaneous effective DOXO release through the porous Au layer and photodynamic- and photothermal-induced tumoricidal effect using NIR light because of minimal absorption by water and hemoglobin at this wavelength range.

To explore the photophysical and photochemical properties of BGNSH-HSA-ICG nanoplatforms, we first compared the fluorescence intensity of BGNSH-HSA-ICG and free ICG. We observed that the fluorescence of ICG was enhanced once it was adsorbed onto the metal shell surface as a part of the protein complex due to a metal enhanced fluorescence effect (Figure 6.6b). In this regard, it has been previously shown that ICG fluorescence enhancement takes place upon dye adsorption onto a metal surface at separation distances between the metal surface and the adsorbed dye between 7 and 50 nm [52]. This evidence suggested the existence of a multilayer protein structure on the BGNSHs surface which efficiently separated the dye molecules from the metal surface, avoiding their fluorescence quenching by the strong BGNSHs surface plasmonic effect.

To evaluate the potential hyperthermic potential of the nanoplatforms, the temperature increase generated by NIR laser irradiation (808 nm and 2 W cm^{-2} for 10 min) was measured (Figure 6.7a). The temperature of BGNSH-HSA-ICG solutions increased by ca. 19.5 ºC after 5 min of irradiation compared to ca. 15, 6 and 1 ºC of BGNSH-HSA, free ICG and buffer solutions, respectively. We also noted that the temperature rose rapidly within 3-4 min of irradiation, lying to a quasiplateau region afterwards. These results demonstrated the latent capability of the present nanoplatforms for hyperthermia or ablation of cancer cells, which was additionally enhanced thanks to the proper selection of the shell material and thickness (the HSA layer doped with ICG) with strong absorption in the NIR region [64]. Also, the heat generated by the nanoplatforms under NIR irradiation was sufficient to overcome the glass transition temperature of PLGA (45 ºC) to induce a sudden drug release of DOXO from nanoplatforms followed by a slower diffusion release phase. The amount of drug released was steeply increased (Figure 6.7b), coincident with NIR laser irradiation, which is certainly useful for increasing the tumoricidal effect of the nanoplatforms.

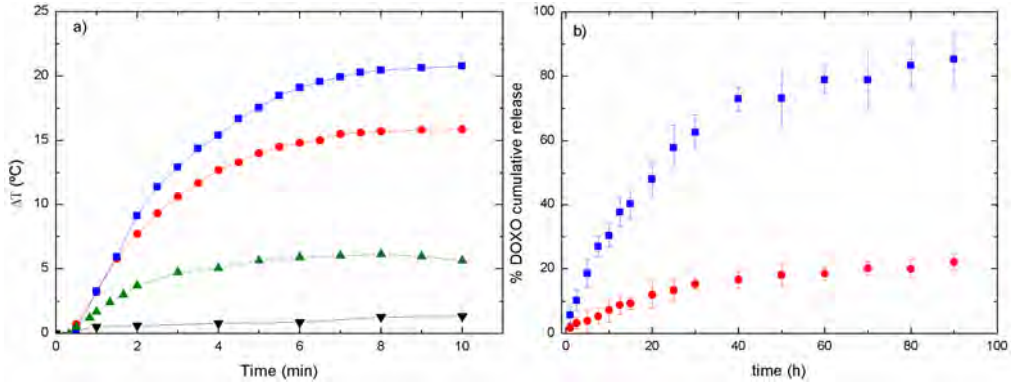

Figure 6.7: a) Temperature increases as a function of time under NIR light irradiation (808 nm at 2 W cm^{-2}) of (▼) PBS buffer solution with 10% (v/v) FBS, (●) BGNSHs, (▲) free ICG and (■) BGNSH-HSA-ICG-FA, respectively. b) Release profile of DOXO from BGNSH-HSA-ICG-FA nanoplatforms in the (●) absence and (■) presence of NIR irradiation (10 min).

The possibility of using the BGNSH-HSA-ICG-FA nanoplatforms as potential PDT agents was tested by measuring their $^1O_2$ generation capability under laser irradiation at 808 nm. Given that photodegradation may greatly restrict the efficiency of the nanoplatforms as potential PDT and PPT agents, we investigated the photostability of free ICG, BGNSH-HSA and BGNSH-HSA-ICG-FA nanoconstructs. First, the stability of the ICG fluorescence signal in the nanoplatform was greatly enhanced if compared with that of free ICG at similar concentration (5 μM) in the absence of irradiation, that is, whilst free ICG fluorescence decreases up to 50% in two days and 7% in one week, complexed ICG to the nanoplatform maintained ~ 55% of its original fluorescence after almost one month under storage (Figure 6.8a). On the other hand, fluorescence spectra after different time periods of laser irradiation showed that the fluorescence peak of ICG at ca. 810 nm decreased immediately after irradiation and almost dissapeared after 15 min under NIR light of 4 W/cm^2 and 6 W/cm^2 power density, while it barely changed after 30 min of persistent irradiation at 2 W/cm^2 (Figure 6.8b). It is worth noting that both LSPR of BGNSHs at 770 nm and the morphology of the nanoplatforms (Figure 6.8c) did not change under the latter irradiation conditions. These facts evidenced that BGNSHs were very stable upon continuous wave (CW) laser

irradiation at the selected NIR irradiation power, while complexed ICG molecules undergo certain photobleaching regardless anchoring on BGNSHs.

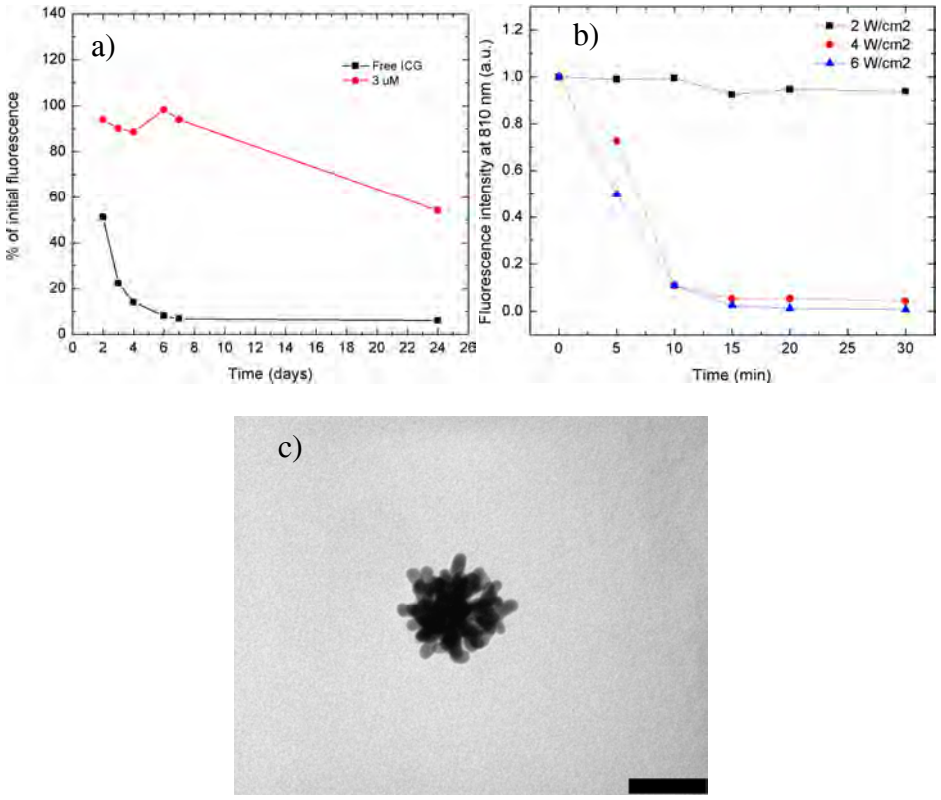

Figure 6.8: a) Fluorescence stability of (■) free ICG and (○) ICG complexed to BGNSH-HSA-ICG-FA nanoplatforms. Lines are to guide the eye. b) Photostability of BGNSH-HSA-ICG-FA nanoplatforms after continuous illumination with NIR-light. c) TEM image of one BGNSH-HSA-ICG-FA after 30 min of irradiation at 2 W/cm^2. Scale bar is 100 nm.

The generation of $^1O_2$ was determined quantitatively by following the absorbance intensity decay at 420 nm of 1,3-diphenylisobenzofurane (DPIBF), which is a specific singlet oxygen trap, as previously mentioned [56]. Based on the photostability results, we tested the $^1O_2$ production after 30 min of illumination. $^1O_2$ production was observed to increase up to 20 min oflaser irradiation and then, it reaches a quasi plateau region, which certainly indicates that a reduction in the singlet oxygen production took place (Figure 6.9). Also, the $^1O_2$ production was enhanced as the irradiated energy input was larger. Interestingly, the $^1O_2$ production of the BGNSH-HSA-ICG-FA nanoplatforms was slightly lower than that free ICG of similar concentration provided that the laser energy for the production of singlet oxygen was less in the former case

than in the latter (that is, for BNSH-HSA-ICG-FA nanoplatforms laser energy is simultaneously absorbed by ICG and the metal shell to produce singlet oxygen and heat), in agreement with previous works [32, 41, 46]. By contrastm, the $^1O_2$ generation ability of free ICG and BGNSH-HSA-ICG-FA nanoplatforms also obviously decreased after first 10 min of irradiation, which is consistent with the change in fluorescence intensity of ICG and HSA-ICG-FA complex (Figure 6.8b).

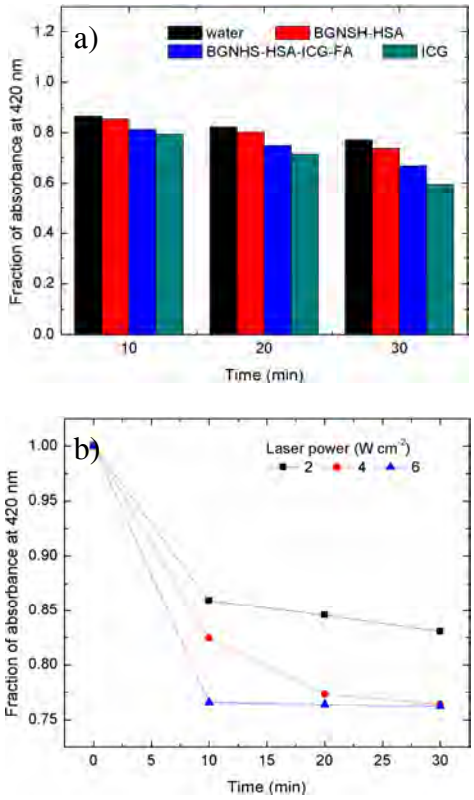

Figure 6.9: Decay of absorbance of DPIBF after illuminating with 2 W cm^{-2} in pure water, BGNSH-HSA, BGNSH-HSA-ICG-FA and ICG. b) Decay of DPIBF absorbance at 420 nm discarding the contribution of photodegradation by laser and the contribution of thermodegradation induced by BGNSH-HSA at 2, 4 and 6 W cm^{-2}.

To determine the potential use of this kind of nanoplatforms as a potential fluorescence imaging contrast agent, *in vitro* and *in vivo* localization experiments of the nanoplatforms were performed. Confocal NIR images provided by ICG fluorescence

showed internalization of the nanoplatforms with an homogeneous distribution in the cytoplasm of MDA-MB-231 breast (Figure 6.10a-c) and HeLa cervical cancer cells (Figure 6.10d-f), probably ocurring via a receptor-mediated endocytosis pathway provided that both kind of cells overexpressed folate receptors on their surface [65, 66]. *In vivo* targeting visualization of the nanoplatforms was tested by preparing tumor-bearing mice by implanting MDA-MB-231 cells into the subcutis of Balb/C nude mice.

When the tumor reached approximately 100 mm^3 in size, intravenous administration of 10 mg/kg of BGNSH-HSA-ICG-FA into the mouse tail vein was performed. For comparison, HSA/ICG-loaded PLGA NPs with the same dye concentration were also administered as a control.

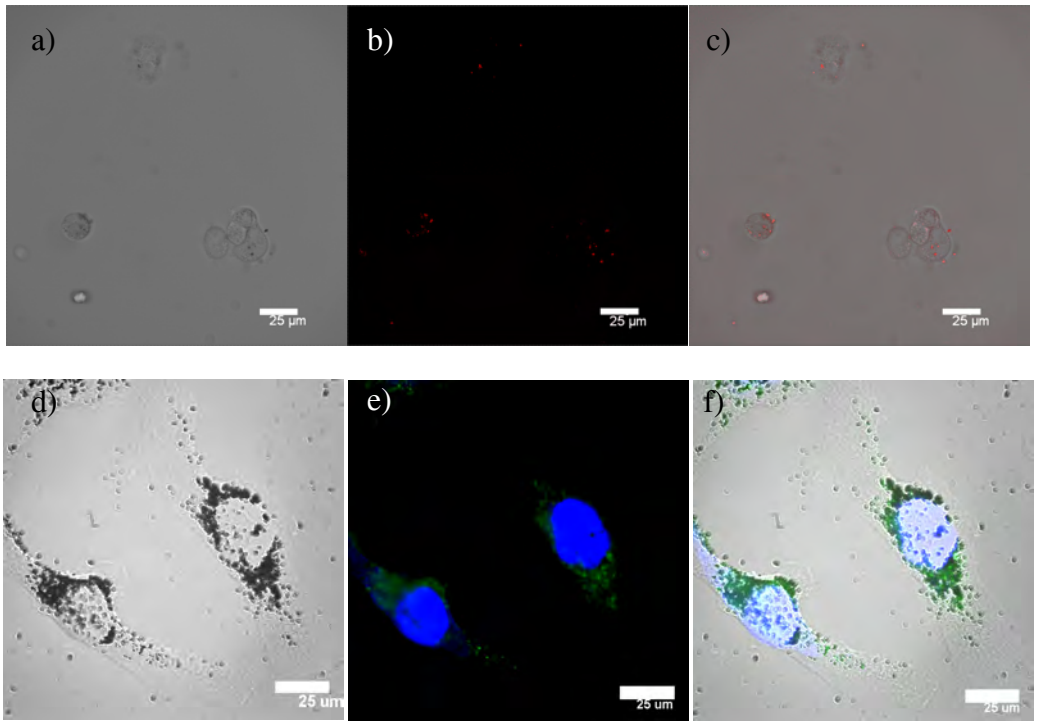

Figure 6.10: a) Transmission, b) fluorescence and c) merged confocal NIR images of BGNSH-HSA-ICG-FA nanoplatform internalization inside MDA-MB-231 cells. d) Transmission, e) fluorescence and f) merged images of fluorescence microscopy images of BGNSH-HSA-ICG-FA nanoplatform internalization inside HeLa cells. In d-e) nuclei were stained with DAPI (blue channel, λ_{exc} = 355 nm) and ICG localization around nuclei was coloured in green (λ_{exc} = 712 nm.

Monitoring of the nanoplatforms by measuring time-lapse *in vivo* NIR images with an IVIS Spectrum Imaging System revealed that the fluorescence intensity changed in the tumor region already after 2 h post-injection due to the localization of the nanoplatforms in the tumor by the combination of an enhanced permeation and retention effect (EPR effect) and a receptor-mediated endocytosis process. A gradual increase in fluorescence intensity observed in the tumor area with time indicated that the nanoplatforms progressively accumulated in such region but a full retention is such area seemed to be not completely achieved (Figure 6.11a), which suggested that intratumoral injection might be a more suitable route. Nevertheless, nanoplatforms were observed to extensively retained at the tumor area more than 48 h, as denoted by the larger fluorescence intensity if compared with that of HSA/ICG-loaded PLGA NPs used as a control (Figure 6.11b). In the latter case, the progressive decrease in fluorescence intensity in the tumor site came from the clearance of the HSA/ICG complex released from the PLGA NPs upon diffusion and matrix erosion [67].

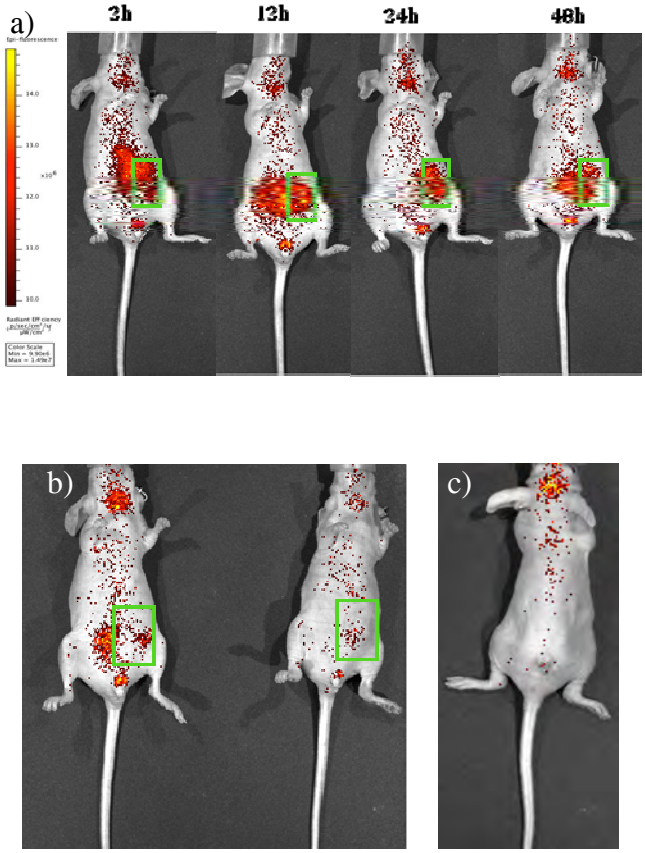

Figure 6.11: a) Biodistribution and localization of BGNSH-HSA-ICG-FA nanoplatforms at the tumor site (green-squeared region) at different times after injection. b) Biodistribution and

localization of BGNSH-HSA-ICG-FA nanoplatforms (left) and ICG-PLGA NPs (right) at the tumor site (green-squeared region) after 96 h of injection. c) Fluorescence image showing nanoplatform accumulation at the brain area. Fluorescence images were taken at λ_{exc} = 710 nm and λ_{em} = 840 nm.

On the other hand, 3-D image reconstruction of the fluorescence images also allowed to determine that the nanoplatforms are eliminated through the reticuloendothelial system (RES), in particular, nanoplatforms are observed to exclusively accumulated in the spleen with no traces apparently in liver or lungs after 12 h post-injection, much in the same way as the ICG-containing PLGA NPs examined previously in Chapter 3. At longer circulation times, the nanoplatform accumulation progressively reduced until completely dissapeared. In addition, it is worth mentioning that in the time scale of the experiments, these nanoplatforms were also observed to accumulate to a certain extent in the brain area (Figure 6.12). However, additional experiments are required to confirm this hypothesis which, if certain, would open up the possibility of using this type of nanomaterials as specific theranostic nanodevices for the treatment of brain pathologies.

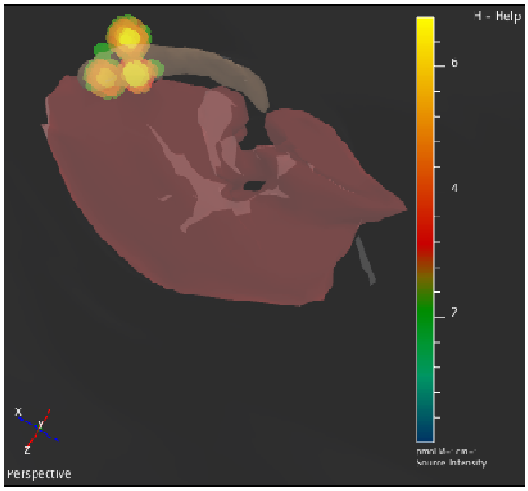

Figure 6.12: 3D-reconstructed fluorescence images of accummulation in the RES system after 12 h of incubation in a MDA-MB-231 tumor-bearing mouse after intravenous tail injection of BGNSH-HSA-ICG-FA nanoplatforms.

Finally, we further evaluated *in vitro* the multidimensional therapeutic potential of the present BGNSH-HSA-ICG-FA nanoplatforms on systemic chemotherapy (DOXO), localized hyperthermia from the Au shell and photodynamic activity provided by ICG molecules in the absence and presence of NIR laser irradiation by cell-counting kit-8 cell proliferation assay (CCK-8). This test is based on the bioreduction of 2-(2-methoxy-4-nitrophenyl)-3-(4-nitrophenyl)-5-(2,4-disulfophenyl)-2H-tetrazolium, monosodium salt (WST-8), which produces a water-soluble formazan dye in the presence of an electron carrier, 1-methoxy phenazine methosulfato (PMS).

Cell viabilities (CV) of HeLa and MDA-MB-231 cells treated with free DOXO, free ICG, BGNSH-HSA-FA, BGNSH-HSA-ICG, DOXO-loaded BGNSH-HSA-FA and DOXO-loaded BGNSH-HSA-ICG-FA in the absence and presence of laser illumination after 24 h are shown in Figure 6.13. The HSA-BGNSHs particles were completely non-toxic as denoted their very low cytotoxocity. In addition, DOXO-loaded BGNSH-HSA, and DOXO-loaded BGNHS-HSAICG nanoplatforms also displayed low toxicities due to, on one hand, the slow diffusion of drug through the metal shell which cannot inhibit tumor-cell proliferation (if compared with the largest cytoxicity of free DOXO) and, on the other, due to the low citotoxicity of ICG as observed from the cytotoxicity values of the free dye.

In comparison, NIR laser illumination (808 nm and 2 W cm^{-2} for 3 intervals of 5 min, see experimental section for details) led to a noticeable increased in cell cytotoxicity. BGNHS-HSA-FA nanoplatforms decreased cell viability upon NIR irradiation as a consequence of the generation of the hyperthermic effect from the metal nanolayer, which led to protein denaturation and subsequent inhibition of normal cellular growth and proliferation [68] if compared to the non-irradiated sample. Also, it should be noted that BGNSH-HSA-ICG-FA nanoplatforms killed more cells than either free ICG or BGNSH-HSA-ICG after irradiation (Figure 6.13). Given that the cytotoxicity of BGNSH-HSA was negligible at low concentrations, this improved efficiency might be attributed to a possible enhanced cellular uptake of BGNSH- HSA-ICG-FA and to a synergistic PDT/PTT effect. In order to confirm this point, we proceed to incubated BGNSH- HSA-ICG-FA with 100 mM sodium azide (NaN_3) for 30 min before irradiation provided that NaN_3 protect cells against PDT damage [32]. The

phototoxicity of BGNSH-HSA-ICG-FA with NaN_3 turned to be similar to that of BGNSH-HSA-FA particles.

Notably, for example, BGNSH-HSA-ICG-FA exhibited a synergistic cytotoxic effect in HeLa cells of 47.1% (($CV_{BGNSH\text{-}HSA+laser}$ - $CV_{BGNSH\text{-}HSA\text{-}ICG+laser}$)/ $CV_{BGNSH\text{-}HSA+laser}$) and 56.5% ($CV_{free\ ICG+laser}$ - $CV_{BGNSH\text{-}HSA\text{-}ICG+laser}$)/$CV_{free\ ICG+laser}$) if compared with BGNSH-HSA nanoplatforms and free ICG, respectively. On the other hand, the chemotherapuetic effect of DOXO also led to an enhanced citotoxicity when loaded inside BGNSH-HSA-ICG-FA if compared to free DOXO and unloaded BGNSH- HSA-ICG-FA particles as a consequence of the remote and sustained controlled release of the chemotherapeutic drug, which is favored by the partial meting of the polymeric core, for additional cytotoxic activity against the target cancer cell line. In this regard, DOXO-loaded BGNSH-HSA-ICG-FA nanoplatforms exhibited an additional cytotoxic effect of 74.0% (($CV_{BGNSH\text{-}HSA\text{-}ICG\text{-}FA+laser}$ - $CV_{DOXO\text{-}loaded\ BGNSH\text{-}HSA\text{-}ICG\text{-}FA+laser}$)/ $_{BGNSH\text{-}HSA\text{-}ICG\text{-}FA+laser}$) compared with unloaded BGNSH-HSA-ICG-FA nanoplatforms.

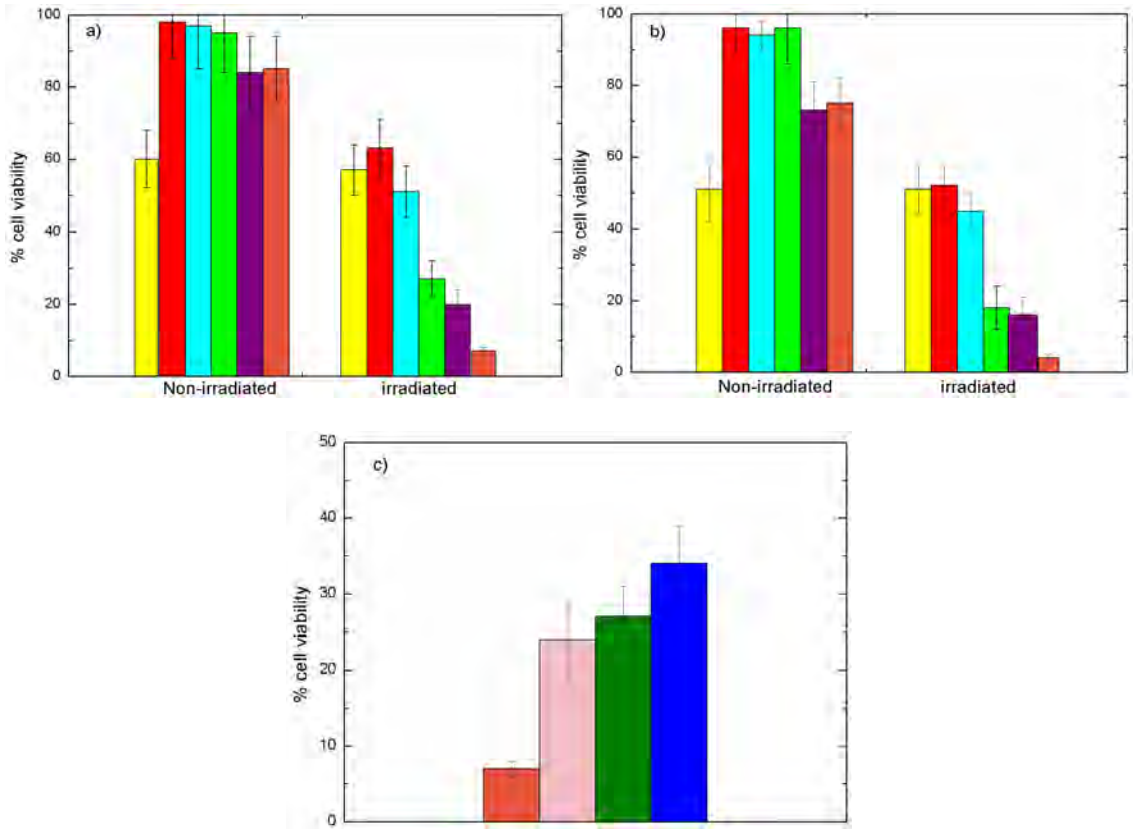

Figure 6.13: Cell viability of a) HeLa and b) MDA-MB-231cells after 24 h of incubation in the absence and presence of NIR light irradiation (2 W/cm^2 at 808 nm in 3 intervals of 5 min each). Colors code: Yellow, free DOXO; Red, free ICG; Cyan, BGNSH-HSA-FA; Green, BGNSH-HSA-ICG-FA; Violet, DOXO-loaded BGNSH-HSA-FA; Orange, DOXO-loaded BGNSH-HSA-ICG-FA nanoplatforms. c) Cell viabilty of HeLa cells under irradiation in the presence of DOXO-loaded BGNSH-HSA-ICG-FA (orange), BGNSH-HSA-ICG-FA (pink), BGNSH-HSA-ICG-FA + NaN_3 (dark green), and BGNSH-HSA-ICG (dark blue).

6.5 Conclusions

In summary, we have successfully fabricated a potential smart theranostic nanoplatform composed of a chemotherapeutic agent (DOXO) and a polymer-based gold shell which additionally combines localized photothermal activity provided by the metal shell and generation of singlet oxygen species by an incorporated ICG photosensitizer under NIR light illumination. The gold nanolayer was functionalized with an HSA-ICG-FA complex to provide, on one hand, stealthness to the nanoplatform and, on the other, photodynamic therapy, fluorescence-based imaging and targetability abilities In addition, the thickness of the protein layer was suitable to provide an enhancement of the dye fluorescence by the plasmonic coupling of the metal nanolayer. *In vitro* confocal fluorescence imaging confirmed the successful cell internalization of the hybrid nanoplatforms whilst *in vivo* fluorescence imaging demonstrated that nanoplatforms are highly localized and retained in the tumor region for long time. The simultaneous combination of chemotherapy, hyperthermia and oxygen reactive species led to an enhanced *in vitro* cell cytotoxicity, as measured in two different cancer cell lines. Further studies are being developed to minimize light irradiation doses and nanoplatform concentrations by optimization of the synthetic protocols , to add new functionalities and to quantify the cytotoxic potential of the nanoplatforms *in vivo*.

6.6 Bibliography

[1] Lammers T, Aime S, Hennink WE, Storm G, Kiessling F. Theranostic Nanomedicine. Accounts of Chemical Research. 2011;44:1029-38.

[2] Ryu JH, Koo H, Sun I-C, Yuk SH, Choi K, Kim K, et al. Tumor-targeting multi-functional nanoparticles for theragnosis: New paradigm for cancer therapy. Advanced Drug Delivery Reviews. 2012;64:1447-58.

[3] Mura S, Couvreur P. Nanotheranostics for personalized medicine. Advanced Drug Delivery Reviews. 2012;64:1394-416.

[4] Yang Z, Lee JH, Jeon HM, Han JH, Park N, He Y, et al. Folate-Based Near-Infrared Fluorescent Theranostic Gemcitabine Delivery. Journal of the American Chemical Society. 2013;135:11657-62.

[5] Bala V, Rao S, Boyd BJ, Prestidge CA. Prodrug and nanomedicine approaches for the delivery of the camptothecin analogue SN38. Journal of Controlled Release. 2013;172:48-61.

[6] Menon JU, Jadeja P, Tambe P, Vu K, Yuan B, Nguyen KT. Nanomaterials for Photo-Based Diagnostic and Therapeutic Applications. Theranostics. 2013;3:152-66.

[7] Pan D. Theranostic Nanomedicine with Functional Nanoarchitecture. Molecular Pharmaceutics. 2013;10:781-2.

[8] Caldorera-Moore ME, Liechty WB, Peppas NA. Responsive Theranostic Systems: Integration of Diagnostic Imaging Agents and Responsive Controlled Release Drug Delivery Carriers. Accounts of Chemical Research. 2011;44:1061-70.

[9] Doane TL, Burda C. The unique role of nanoparticles in nanomedicine: imaging, drug delivery and therapy. Chemical Society Reviews. 2012;41:2885-911.

[10] Ma X, Zhao Y, Liang X-J. Theranostic Nanoparticles Engineered for Clinic and Pharmaceutics. Accounts of Chemical Research. 2011;44:1114-22.

[11] Lee GY, Qian WP, Wang L, Wang YA, Staley CA, Satpathy M, et al. Theranostic Nanoparticles with Controlled Release of Gemcitabine for Targeted Therapy and MRI of Pancreatic Cancer. ACS Nano. 2013;7:2078-89.

[12] Khaletskaya K, Reboul J, Meilikhov M, Nakahama M, Diring S, Tsujimoto M, et al. Integration of Porous Coordination Polymers and Gold Nanorods into Core–Shell Mesoscopic Composites toward Light-Induced Molecular Release. Journal of the American Chemical Society. 2013;135:10998-1005.

[13] Hilderbrand SA, Weissleder R. Near-infrared fluorescence: application to in vivo molecular imaging. Current Opinion in Chemical Biology. 2010;14:71-9.

[14] Zhou J, Liu Z, Li F. Upconversion nanophosphors for small-animal imaging. Chemical Society Reviews. 2012;41:1323-49.

[15] Lovell JF, Liu TWB, Chen J, Zheng G. Activatable Photosensitizers for Imaging and Therapy. Chemical Reviews. 2010;110:2839-57.

[16] Celli JP, Spring BQ, Rizvi I, Evans CL, Samkoe KS, Verma S, et al. Imaging and Photodynamic Therapy: Mechanisms, Monitoring, and Optimization. Chemical Reviews. 2010;110:2795-838.

[17] Choi KY, Liu G, Lee S, Chen X. Theranostic nanoplatforms for simultaneous cancer imaging and therapy: current approaches and future perspectives. Nanoscale. 2012;4:330-42.

[18] Huang P, Cheng Xu, Lin J, Wang C, Wang X, Zhang C, et al. Folic Acid-conjugated Graphene Oxide loaded with Photosensitizers for Targeting Photodynamic Therapy. Theranostics. 2011;1:240-50.

[19] Huang P, Lin J, Wang X, Wang Z, Zhang C, He M, et al. Light-Triggered Theranostics Based on Photosensitizer-Conjugated Carbon Dots for Simultaneous Enhanced-Fluorescence Imaging and Photodynamic Therapy. Advanced Materials. 2012;24:5104-10.

[20] Bonnett R. Photosensitizers of the porphyrin and phthalocyanine series for photodynamic therapy. Chemical Society Reviews. 1995;24:19-33.

[21] Yun S, Zhi-long C, Xiao-xia Y, Peng H, Xin-ping Z, Xiao-xia D. Magnetic chitosan nanoparticles as a drug delivery system for targeting photodynamic therapy. Nanotechnology. 2009;20:135102.

[22] Huang P, Li Z, Lin J, Yang D, Gao G, Xu C, et al. Photosensitizer-conjugated magnetic nanoparticles for in vivo simultaneous magnetofluorescent imaging and targeting therapy. Biomaterials. 2011;32:3447-58.

[23] Huang P, Lin J, Yang D, Zhang C, Li Z, Cui D. Photosensitizer-loaded dendrimer-modified multi-walled carbon nanotubes for photodynamic therapy. Journal of Controlled Release. 2011;152, Supplement 1:e33-e4.

[24] Hongying Y, Fuyuan W, Zhiyi Z. Photobleaching of chlorins in homogeneous and heterogeneous media. Dyes and Pigments. 1999;43:109-17.

[25] Sitnik TM, Hampton JA, Henderson BW. Reduction of tumour oxygenation during and after photodynamic therapy in vivo: effects of fluence rate. Br J Cancer. 1998;77:1386-94.

[26] Coutier S, Mitra S, Bezdetnaya LN, Parache RM, Georgakoudi I, Foster TH, et al. Effects of Fluence Rate on Cell Survival and Photobleaching in Meta-Tetra-(hydroxyphenyl)chlorin–photosensitized Colo 26 Multicell Tumor Spheroids¶. Photochemistry and Photobiology. 2001;73:297-303.

[27] Agostinis P, Berg K, Cengel KA, Foster TH, Girotti AW, Gollnick SO, et al. Photodynamic therapy of cancer: An update. CA: A Cancer Journal for Clinicians. 2011;61:250-81.

[28] Alkilany AM, Thompson LB, Boulos SP, Sisco PN, Murphy CJ. Gold nanorods: Their potential for photothermal therapeutics and drug delivery, tempered by the complexity of their biological interactions. Advanced Drug Delivery Reviews. 2012;64:190-9.

[29] Choi J, Yang J, Bang D, Park J, Suh J-S, Huh Y-M, et al. Targetable Gold Nanorods for Epithelial Cancer Therapy Guided by Near-IR Absorption Imaging. Small. 2012;8:746-53.

[30] Zhang Z, Wang J, Chen C. Gold Nanorods Based Platforms for Light-Mediated Theranostics. Theranostics. 2013;3:223-38.

[31] Yuan H, Fales AM, Vo-Dinh T. TAT Peptide-Functionalized Gold Nanostars: Enhanced Intracellular Delivery and Efficient NIR Photothermal Therapy Using Ultralow Irradiance. Journal of the American Chemical Society. 2012;134:11358-61.

[32] Wang S, Huang P, Nie L, Xing R, Liu D, Wang Z, et al. Single Continuous Wave Laser Induced Photodynamic/Plasmonic Photothermal Therapy Using Photosensitizer-Functionalized Gold Nanostars. Advanced Materials. 2013;25:3055-61.

[33] Gobin AM, Lee MH, Halas NJ, James WD, Drezek RA, West JL. Near-Infrared Resonant Nanoshells for Combined Optical Imaging and Photothermal Cancer Therapy. Nano Letters. 2007;7:1929-34.

[34] Loo C, Lowery A, Halas N, West J, Drezek R. Immunotargeted Nanoshells for Integrated Cancer Imaging and Therapy. Nano Letters. 2005;5:709-11.

[35] Bardhan R, Chen W, Perez-Torres C, Bartels M, Huschka RM, Zhao LL, et al. Nanoshells with Targeted Simultaneous Enhancement of Magnetic and Optical Imaging and Photothermal Therapeutic Response. Advanced Functional Materials. 2009;19:3901-9.

[36] Hong C, Kang J, Kim H, Lee C. Photothermal Properties of Inorganic Nanomaterials as Therapeutic Agents for Cancer Thermotherapy. Journal of Nanoscience and Nanotechnology. 2012;12:4352-5.

[37] Murakami T, Nakatsuji H, Inada M, Matoba Y, Umeyama T, Tsujimoto M, et al. Photodynamic and Photothermal Effects of Semiconducting and Metallic-Enriched Single-Walled Carbon Nanotubes. Journal of the American Chemical Society. 2012;134:17862-5.

[38] Wang L, Shi J, Zhang H, Li H, Gao Y, Wang Z, et al. Synergistic anticancer effect of RNAi and photothermal therapy mediated by functionalized single-walled carbon nanotubes. Biomaterials. 2013;34:262-74.

[39] Singh R, Torti SV. Carbon nanotubes in hyperthermia therapy. Advanced Drug Delivery Reviews.

[40] Markovic ZM, Harhaji-Trajkovic LM, Todorovic-Markovic BM, Kepić DP, Arsikin KM, Jovanović SP, et al. In vitro comparison of the photothermal anticancer activity of graphene nanoparticles and carbon nanotubes. Biomaterials. 2011;32:1121-9.

[41] Tian B, Wang C, Zhang S, Feng L, Liu Z. Photothermally Enhanced Photodynamic Therapy Delivered by Nano-Graphene Oxide. ACS Nano. 2011;5:7000-9.

[42] Yang K, Hu L, Ma X, Ye S, Cheng L, Shi X, et al. Multimodal Imaging Guided Photothermal Therapy using Functionalized Graphene Nanosheets Anchored with Magnetic Nanoparticles. Advanced Materials. 2012;24:1868-72.

[43] He J, Huang X, Li Y-C, Liu Y, Babu T, Aronova MA, et al. Self-Assembly of Amphiphilic Plasmonic Micelle-Like Nanoparticles in Selective Solvents. Journal of the American Chemical Society. 2013;135:7974-84.

[44] Huang X, El-Sayed IH, Qian W, El-Sayed MA. Cancer Cell Imaging and Photothermal Therapy in the Near-Infrared Region by Using Gold Nanorods. Journal of the American Chemical Society. 2006;128:2115-20.

[45] Kuo W-S, Chang C-N, Chang Y-T, Yang M-H, Chien Y-H, Chen S-J, et al. Gold Nanorods in Photodynamic Therapy, as Hyperthermia Agents, and in Near-Infrared Optical Imaging. Angewandte Chemie. 2010;122:2771-5.

[46] Jang B, Park J-Y, Tung C-H, Kim I-H, Choi Y. Gold Nanorod−Photosensitizer Complex for Near-Infrared Fluorescence Imaging and Photodynamic/Photothermal Therapy In Vivo. ACS Nano. 2011;5:1086-94.

[47] Mi Y, Liu X, Zhao J, Ding J, Feng S-S. Multimodality treatment of cancer with herceptin conjugated, thermomagnetic iron oxides and docetaxel loaded nanoparticles of biodegradable polymers. Biomaterials. 2012;33:7519-29.

[48] Zheng M, Yue C, Ma Y, Gong P, Zhao P, Zheng C, et al. Single-Step Assembly of DOX/ICG Loaded Lipid–Polymer Nanoparticles for Highly Effective Chemo-photothermal Combination Therapy. ACS Nano. 2013;7:2056-67.

[49] Lee S-M, Park H, Choi J-W, Park YN, Yun C-O, Yoo K-H. Multifunctional Nanoparticles for Targeted Chemophotothermal Treatment of Cancer Cells. Angewandte Chemie International Edition. 2011;50:7581-6.

[50] Watanabe Y, Kumon K. Assessment by pulse dye-densitometry indocyanine green (ICG) clearance test of hepatic function of patients before cardiac surgery: Its value as a predictor of serious postoperative liver dysfunction. Journal of cardiothoracic and vascular anesthesia. 1999;13:299-303.

[51] Desmettre T, Devoisselle JM, Mordon S. Fluorescence Properties and Metabolic Features of Indocyanine Green (ICG) as Related to Angiography. Survey of Ophthalmology. 2000;45:15-27.

[52] Bardhan R, Grady NK, Halas NJ. Nanoscale Control of Near-Infrared Fluorescence Enhancement Using Au Nanoshells. Small. 2008;4:1716-22.

[53] Yang J, Lee J, Kang J, Oh SJ, Ko H-J, Son J-H, et al. Smart Drug-Loaded Polymer Gold Nanoshells for Systemic and Localized Therapy of Human Epithelial Cancer. Advanced Materials. 2009;21:4339-42.

[54] Jain TK, Richey J, Strand M, Leslie-Pelecky DL, Flask CA, Labhasetwar V. Magnetic nanoparticles with dual functional properties: Drug delivery and magnetic resonance imaging. Biomaterials. 2008;29:4012-21.

[55] Jana NR, Gearheart L, Murphy CJ. Wet Chemical Synthesis of High Aspect Ratio Cylindrical Gold Nanorods. The Journal of Physical Chemistry B. 2001;105:4065-7.

[56] Weishaupt KR, Gomer CJ, Dougherty TJ. Identification of Singlet Oxygen as the Cytotoxic Agent in Photo-inactivation of a Murine Tumor. Cancer Research. 1976;36:2326-9.

[57] Iglesias P, Fraga M, Costoya JA. Defining hypoxic microenvironments by non-invasive functional optical imaging. European journal of cancer (Oxford, England : 1990). 2013;49:264-71.

[58] Sanchez-Gaytan BL, Swanglap P, Lamkin TJ, Hickey RJ, Fakhraai Z, Link S, et al. Spiky Gold Nanoshells: Synthesis and Enhanced Scattering Properties. The Journal of Physical Chemistry C. 2012;116:10318-24.

[59] Choi J-s, Park JC, Nah H, Woo S, Oh J, Kim KM, et al. A Hybrid Nanoparticle Probe for Dual-Modality Positron Emission Tomography and Magnetic Resonance Imaging. Angewandte Chemie International Edition. 2008;47:6259-62.

[60] Sperling RA, Parak WJ. Surface modification, functionalization and bioconjugation of colloidal inorganic nanoparticles. Philosophical Transactions of the Royal Society A: Mathematical, Physical and Engineering Sciences. 2010;368:1333-83.

[61] Link S, El-Sayed MA. Size and Temperature Dependence of the Plasmon Absorption of Colloidal Gold Nanoparticles. The Journal of Physical Chemistry B. 1999;103:4212-7.

[62] Prodan E, Lee A, Nordlander P. The effect of a dielectric core and embedding medium on the polarizability of metallic nanoshells. Chemical Physics Letters. 2002;360:325-32.

[63] Goy-López S, Juárez J, Alatorre-Meda M, Casals E, Puntes VF, Taboada P, et al. Physicochemical Characteristics of Protein–NP Bioconjugates: The Role of Particle Curvature and Solution Conditions on Human Serum Albumin Conformation and Fibrillogenesis Inhibition. Langmuir. 2012;28:9113-26.

[64] Li J, Han J, Xu T, Guo C, Bu X, Zhang H, et al. Coating Urchinlike Gold Nanoparticles with Polypyrrole Thin Shells To Produce Photothermal Agents with High Stability and Photothermal Transduction Efficiency. Langmuir. 2013;29:7102-10.

[65] Meier R, Henning TD, Boddington S, Tavri S, Arora S, Piontek G, et al. Breast Cancers: MR Imaging of Folate-Receptor Expression with the Folate-Specific Nanoparticle P1133 1. Radiology. 2010;255:527-35.

[66] García-Díaz M, Kawakubo M, Mroz P, Sagristà ML, Mora M, Nonell S, et al. Cellular and vascular effects of the photodynamic agent temocene are modulated by the delivery vehicle. Journal of Controlled Release. 2012;162:355-63.

[67] Zolnik BS, Leary PE, Burgess DJ. Elevated temperature accelerated release testing of PLGA microspheres. Journal of Controlled Release. 2006;112:293-300.

[68] Hanahan D, Weinberg RA. The Hallmarks of Cancer. Cell. 2000;100:57-70.

CHAPTER VII - Targeted Combinatorial Therapy Using Gold Nanostars as Theranostic Platforms

7.1 Summary

In this chapter, we present the development of multimodal therapy nanoplatoform based on gold nanostars (Au NS) as core particles. These NS are functionalized the chemotherapeutic drug doxorubicin (DOXO), which is conjugated to the NS surface by means of a cleavable heterofunctional crosslinker (sulfo-LC-SPDP) to allow its relase under the action of reducting enzymes. To ensure a specific delivery of the chemotherapeutic drug, the nanoplatoform is additionally functionalized with folic acid (FA) as targeting ligand and cellular uptake adjuvant. By synthetically modifying the plasmon band of Au NS to the near infrared (NIR) region of the electromagnetic spectrum, the present nanoplatform are able to simultaneously combinethe capability of phototothermal therapy (PTT),through the conversion of absorbed light energy into localised heat, and chemotherapy, enabling their monitoringby means of optical fluorescence imaging thanks to DOXO autofluorescence. The cellular uptake was observed to be enhanced when the targeting ligand are bound to the nanoplatform. In addition, the therapeutic efficiency of the nanoplatformtested in HeLa cells demonstrated the larger cytotoxicity efficiency of the combined therapies if compared to individual ones.

7.2 Introduction

During last decades enormous efforts have been done to develop new effective methods for cancer therapy. Those relying on a single therapeutic treatment such as chemotherapy, radiotherapy, immunotherapy, gene therapy, thermotherapy or photodynamic therapy, although effective, still present different and important drawbacks such as inespecificity, very toxic side effects and/or development of cell resistances amongst others, which compromise many times the recovery of patients[1-4].In contrast to single treatments, the combination of several therapeutic approaches (the so-called multi-modality therapy) with different drugs and techniques may cooperatively supress cancer development with potential advantages (*e.g.*, synergistic efffects and reversal of drug resistance) and reduced side effects[5-9].

Gold-based nanomaterials have attracted great interest in the field of cancer diagnosis and treatment because of their enhanced optical properties including strong light absorption and scattering in the visible and near-infrared (NIR) wavelength regions related to their localised surface plasmon resonance (LPSR)[10-12],

biocompatibility, colloidal and chemical stability and ability to be functionalised through reactive groups of the capping agents (*e.g.* amino or carboxyl groups) or through thiol-mediated binding to the gold surface [13-15]. In particular, gold nanostructures have been investigated as suitable platforms for combinatorial therapeutics, especially for the conjunction of chemo- and phototherapy by exploiting the ease of gold functionalization and the possibility of matching the wavelength of irradiating light with the LPSR of the nanostructure; in this case, coherent oscillations of electrons in the conduction band will induce photothermal conversion by converting the absorbed light to heat [16-18].

A variety of gold anisotropic nanoparticles (NPs) such as gold nanorods[19-22], nanocages[23-25], hollow nanospheres[26, 27], nanoshells[28-31]or branched nanoparticles[32-35] typically exhibit LPSRs in the NIR region, the so-called “tissue therapeutic window” because of the lower optical attenuation from water and blood components in this spectral range (650-900 nm)[36] and their abilityto produce cytotoxic hyperthermia upon NIR laser irradiation when localised temperature is above 43 ºC, which kills malignant cells though apoptosis or necrosis[37].Also, these anisotropic NPs can be passively or actively concentrated in the tumor region due to an enhanced permemability and retention (EPR) effect or specific biotargeting, respectively, with long serum half-life circulation times[38-40].

Particularly, the use of branched AuNPs or gold nanostars (Au NS) with plasmon peaks tunable in the NIR range is of special interest thanks to their ease of synthesis for large scale production and size tunability, LPSR bands in the NIR window for deep bioimaging and great potential for NIR energy absorption due to high scattering cross-section ratios for efficient photothermal transduction, large surface-to-volume ratios useful for improving drug loading, and multiple sharp branches acting as “hot-spots” for Surface enhanced Raman spectroscopy (SERS)-based (bio)sensing[41-44].

Hence, apart from their great interest in biomedical fields such as plasmonic[45, 46]and SERS biosensors[42, 47-50]and bioimaging[33, 43, 51-53],this kind of nanoparticles have found important applicationsduring last years as single therapeutic probes to fight agains tumors by explotation of their light absorbing and binding properties in photodynamic (PDT)[44, 54], photothermal (PTT)[32, 35, 54,

55]; therapies, and photocontrolled-drug release[56] while using incident NIR light for irradition.

In contrast, to the best of our knowledge almost no works have exploited the potential role of Au NS as multitherapeutic nanoplatforms for multimodal treatment of tumors. In this regard, Wang *et al.*[57] constructed pegylated Au NS functionalized with the photosensitizer Ce6 for coordinated photodynamic/plasmonic photothermal therapies upon single continuous wave (CW) laser irradiation. Both *in vitro* and *in vivo*experiments demonstrated that the difference in photostability between photosensitizers and the gold nanostructure can be used to modulate PDT and PTT by adjusting the irradiation time. It is necessary to mention that while preparing the present work, Chen *et al*. [59] also reported *in vitro* and *in vivo* studies ofa multimodal chemo- and photothermal therapeutic system based on Au NS covalently functionalized with the peptide cyclic RGD as a targeting moiety.

In the present study, Au NS prepared by reducing Au^{3+} in N,N-dimethylformamide (DMF)[58] followed by pegylation. The chemotherapeutic drug doxorubicin (DOXO, an intercalating DNA agent and topoisomerase II inhibitor)[60] was grafted onto the surface of the polyethylene glycol (PEG)-functionalized Au NS through disulfide linkagesfor enzymatic-responsive controlled drug delivery, in contrast to the system developed by Chen *et al.*Folic acid, a targeting ligand which avidly binds to folate receptorsoverexpressed in different classes of tumors such as ovarian, breast, colon, renal or lung ones [61] was covalently linked to the surface of PEG-Au NS via carbodiimide chemistry to configure a multitherpautic nanconstruct integrating targeting, chemo- and photothermal therapies (folic acid-targeted Au NS, FA-DOXO/Au NS). The affinity of DOXO/Au NS and FA-DOXO/Au NS to a cervical cancer Hela cell line, which overexpresses folate receptors, was examined by fluorescence microscopy by using the inherent fluorescence of the drug. Furthermore, we also compared the chemo-photothermal therapeutic efficaciy of FA-DOXO/Au NS, DOXO/Au NS, FA/Au NS, Au NS and free DOXO in Hela cells under different concentrations and NIR light irradiation conditions, demonstrating the existence of a synergistic effect when applying the combinatorial treatments.

7.3 Materials and methods

7.3.1 Materials

Hydrogen tetrachloroaurate (III) trihydrate ($HAuCl_4$), N-(3-dimethylamniopropyl)-3-ethylcarbodiimide hydrochloride (EDC), sulfo-N-hydroxysuccinimide (Sulfo-NHS), trisodium citrate dihydrate, sodium borohydride ($NaBH_4$, 99%), ascorbic acid, potassium carbonate (K_2CO_3), doxorubicin hydrochloride (DOXO HCl), folic acid (FA), glutathione (GSH), PBS and HEPES bufferswere purchased from Sigma Aldrich Co (St. Louis, Missouri, USA). Sulfosuccinimidyl 6-(3´-[2-pirydildithio]-propiamido) hexanoate (Sulfo-LC-SPDP), Traut´s and Ellman´s reagents were purchased from Pierce (Rockford, Illinois, USA). Dialysis membrane tubing (molecular weight cutoff ~100-500 and ~3500 Da) was purchased from Spectrum Laboratories, Inc. (Rancho Dominguez, CA, USA).Thiol-PEG amine (HS-PEG-NH_2, molecular weight 5000 Da) was from Polymer Source (Ontario, Canada). Poly(vinylpyrrolidone) (PVP K15, 10000 Da) and DMF were from Fluka (St. Louis, Missouri, USA).ProLong® Gold antifade reagent with DAPI, Dulbecco's Modified Eagle Medium, crystal violet solution, fetal bovine serum (FBS), L-glutamine, penicillin/streptomycin, sodium pyruvate, and MEM Non-Essential Amino Acids (NEAA) were purchased from Invitrogen (Carlsbad, USA). HeLa cervical cancer cells were from Cell Biolabs (San Diego, CA, USA). All other chemicals and solvents were of reagent grade (purchased from Sigma–Aldrich). Milli-Q water was used for all aqueous solutions. All glassware was washed with aqua regia and HF 5% (v/v) and extensively rinsed with water. All the chemicals were of analytical grade and used without further purification.

7.3.2 Synthesis of pegylated Au NS

Au NS were prepared by a seed-mediated method as previously described[58]. Typically, gold nanoparticles (Au NPs) of 15 nm were prepared by standard citrate reduction and used as seeds[62]. Briefly, 5 mL of 1 wt.% sodium citrate aqueous solution was added under continuous stirring to a boiling aqueous solution of $HAuCl_4$ (100 mL, 0.5 mM) and allowed to react for 15 min. Then, Au particles were

transferred into ethanol through PVP modification. Thus, 5 mL of a PVP aqueous solution containing a sufficient amount to provide approximately 60 molecules of PVP per nm^2 of gold was added dropwise to the Au colloid and allowed to react overnight. Finally, the solution was centrifuged at 4000 rpmfor 90 min, the supernatant removed, and the particles redispersed in ethanol.

For obtention of Au NS, in a typical synthesis 82 μLofan aqueous solution of 50mM$HAuCl_4$ was mixed with 15 mL of10 mM PVP solution in DMF. After the complete disappearance of the Au^{3+}CTTS absorption band at 325 nm, acertain amount of preformed-seed dispersion was added undercontinuous stirring and allowed to react until completion of thereaction (no further changes in the UV-vis-NIR spectra). Theratio of [$HAuCl_4$] to [seed] was set to 90. Au NS solutions were centrifuged three times at 4500 rpm for 45 min, redispersed in water and stored.

Au NS were pegylated by mixing 1 mL of Au NS aqueous solution (1.65 mM), 2 mL of HS-PEG-NH_2 (4 mM) and 2 mL of K_2CO_3 (10 mM) under continuous stirring overnight. For removing the unattached HS-PEG-NH_2, the nanoparticle solution was centrifuged three times at 10500 rpm and redispersed at a concentration of 0.25 mM.

7.3.3 Preparation of SH-DOXO-SS

Firstly, 50 **μ**L of DOXO (3.4 mM), 50 **μ**L of Traut´s (34 mM) and 5 **μ**L EDTA in PBS (pH 7.4) were incubated for 1 h at room temperature. .The yield of the reaction (thiolated DOXO) was 80% as determined by Ellman´s reagent assay following manufacturer´s specifications. Afterwards, 14 **μ**L of this solution were reacted with 1 mL of sulfo-LC-SPDP (4 mM) in HEPES buffer (pH 7.4) for 24 h. Excess reagents were eliminated by centrifugation using Zeba spin columns .

7.3.4 Preparation of Au NS-PEG-SS-DOXO/FA nanoconjugates

In a first step, folic acid was activated by placing 1 mL of a folic acid solution (2 mM) in HEPES buffer reacting with EDC (4 mM) and sulfo-NHS (4 mM) for 6 h. Excess reagents where eliminated by extensive dialysis. Subsequently, 1 mL of SH-DOXO-SS, 1 mL of FA-EDC-Sulfo NHS and Au NS (0.25 mM) were mixed in HEPES

buffer overnight at room temperature. Excess DOXO and FA were removed by centrifugation (9000 rpm, 8 min) followed by dialysis when required. Nanoconjugates were redispersed in HEPES buffer. The conjugates were stored in Milli-Q water at 4°C.

7.3.5 Nanoconjugates characterization and drug loading

The Au NS size and morphology were characterized using transmission electron microscopy (TEM). TEM was performed on a Carl Zeiss Libra 200 Fm Omega electronic microscopes operating at 120 kV. Samples were prepared for analysis by evaporating a drop of the nanoconjugate dispersion on a carbon-coated copper grid without staining. A histogram of the particle size distribution and theaverage particle diameter was obtained by measuring about 200particles in an arbitrarily chosen area in the photomicrograph. Au NS conjugate hydrodynamic sizes were also measured by dynamic light scattering (DLS) at 25 °C by means of an ALV-5000F (ALV-GmbH, Germany) instrument with vertically polarized incident light (λ = 488 nm) supplied by a diode-pumped Nd:YAG solid-state laser (Coherent Inc., CA, USA) operated at 2 W, and combined with an ALV SP-86 digital correlator (sampling time 25 ns to 100 ms). ζ-potentials were measured with a Zetasizer Nano ZS (Malvern, UK) using dispossable folded capillary cells. Samples were measured in triplicate in PBS (pH 7) at 25 °C. Optical characterization of the nanoconjugates was carried out by UV-vis-NIR and fluorescence spectroscopies with a Cary Bio 100 spectrophotometer and a Cary Eclipse spectrfluorometer, respectively (Agilent Technologies, USA). The gold concentration in solution was determined by inductively coupling plasma-mass spectrometry (ICP-MS) in a Varian 820-MS equipment (Agilent Technologies, USA).The number of Au NS was calculated assuming a sphere model of 90 nm in diameter.

7.3.6 NIR-laser induced temperature increase

Temperature increment tests as a function of time were used to determine the phothotermal activity of the hybrid nanoconjugates. These tests were performed with a continuous wave fiber-coupled diode laser source of 808 nm wavelength (50W,

Oclaro Inc, San Jose, CA, USA). The laser was powered by a Newport 5700-80 regulated laser diode driver (Newport Corporation, Irvine, CA, USA). A 200-μm-core optical fiber was used to transfer laser power from the laser unit to the target solution, and equipped with a lens telescope mounting accessory at the output, which allowed for tuning of the laser spot size in the range 1-10 mm. The output power was independently calibrated using an optical power meter (Newport 1916-C) and laser spot size was previously measured with a laser beam profiler (Newport LBP-1-USB), which was placed at the same distance (8 cm) between the lens telescope output and the quartz cuvette (or the 96-well plate). For measuring the temperature change, 2 mL of Au NS-PEG nanoconjugatesin cell culture medium supplemented with 10% (v/v) FBS were placed in a quartz cuvette and irradiated for different times (0-10 min) at several laser power densities. The temperature of samples was measured with a type J thermocouple linked to a digital thermometer inserted into the solution.

7.3.7 Drug loading efficiency and release kinetics of DOXO

To calculate the DOXO loading efficiency, Au NS-PEG-SS-DOXO-FA nanoconjugates were collected by centrifugation and the unconjugated DOXO in the supernatant was quantified by using a DOXO UV-vis calibration curve at 490 nm. To corroborate DOXO concentration in some cases, this was also determined by fluorescence spectroscopy. Au-PEG-SS-DOX wasfirst treated with dithiothreitol (DTT) for 4 h, and the freeDOXO-SH was separated by dialysis. The fluorescenceintensity of DOXO-SH was calibrated, and the concentration ofbound DOXO was determined from known concentration of freeDOXO-SH in gold solution obtained after dialysis treatment.The DOXO loading was calculated according to the formula: drug loading (DL) = (mass of drug conjugated with Au NS / total mass of drug conjugated and Au NS).

To investigate the *in vitro* DOXO release profile, PBS containing 10% (v/v)FBS with or without GSH (10 mM) were used to release DOXO fromAu NS-PEG-SS-DOXO-FAby dialysis. Dislysate (2 mL) was withdrawn at different time intervals and an equal volume of PBS was added to the solution outside of the dialysis bag to maintain the net volume of the system. The absorbance peak (490 nm) of the solutions was detected, and the quantities of free drug were calculated by using a

standard calibration curve.

7.3.8 Cellular uptake by confocal microscopy

HeLa cervical cancer cells from Cell Biolabs (San Diego, CA, USA) were used for *in vitro* studies. Nanoconjugates(Au NS-PEG-SS-DOXO and Au NS-PEG-SS-DOXO-FA) uptake was followed by confocal microscopy by seeding HeLa cells on poly-L-lysine coated glass coverslips (12 × 12 mm) placed inside 6-well plates (3 mL, $1.5 \cdot 10^4$ cells/well) and grown for 24 h at standard culture conditions (5% CO_2 at 37 ºC in Dulbecco's Modified Eagle Medium (DMEM) supplemented with 10% (v/v) FBS, 2 mM L-glutamine, 1% penicillin/streptomycin, 1 mM sodium pyruvate, and 0.1 mM MEM Non-Essential Amino Acids (NEAA)). Then, nanoconjugates at the desired concentration were added to cells (100 μL). After 2 h of incubation the Au NS-containing cells were washed three times with PBS, then, fixed with paraformaldehyde 4% (w/v) for 10 min, washed again with PBS pH 7.4, mounted on glass slides and stained with ProLong® Gold antifade DAPI to stained nuclei, and cured for 24 h at -20 °C. Confocal images of DOXO were made using the autofluorescnece of DOXO with a confocal spectral microscope Leica TCS-SP2 **(**LEICA Microsystems Heidelberg GmbH, Mannheim, Germany*;* green channel for DOXO, $\lambda_{exc.}$ 488 nm; blue channel for DAPI, $\lambda_{exc.}$ 355 nm).Both bright-view differential interference contrastimages and confocalfluorescence images were obtained with a 40X (NA 1.2) and 63X (oilimmersion, NA 1.4) objectives.

7.3.9 In vitro cytotoxicity

To quantitatively evaluate the effect of the nanoconjugates on HeLa cells, cytotoxicity induced by the nanoconjugates was determined by the crystal violet assay. HeLa cells with an optical confluence of 80–90% were seeded into 96-well plates (100 μL, $1.5 \cdot 10^4$ cells/well) and grown for 24 h at standard culture conditions. The cells were treated with 100 μL of free DOXO, Au NS-PEG, Au NS-PEG-SS-DOXO, Au NS-PEG-SS-DOXO-FA. FA receptors of HeLa cells in several wells were previously blocked with excess FA prior addition of Au NS-PEG-SS-DOXO-FA. The dose of nanoconjugates was set according to the contained DOXO

concentrationin Au NS within a range of 0.2–5μM DOXO.After cells were incubated for 4h, the photothermal treatment was then performedusing a 808 nm laser. The beam diameter was 1.0 cmand the power density of the laser source was fixed at 2.0W/cm^2 . The cells were exposed under the 808 nmlaser for 10 min, and then incubated for another 18 h. Afterwards, the culture medium was discarded and the cells were washed with 10 mM PBS, pH 7.4 several times. The cells were shaken at room temperature (300 rpm, 15min) in the presence of 10 μL of a glutaraldehyde solution (11% (w/v) in water). The solution was discarded and cells were washed 3-4 times with PBS. The cells were then shaken at room temperature (300 rpm, 15 min) in the presence of 100 μL of a crystal violet solution (0.1% w/v in 200 mM orthophosphoric acid, 200 mM formic acid, and 200 mM 2-N-morpholino-ethanesulfonic acid (MES), pH 6). The solution was discarded, and the cells were again washed 3-4 times with milli-Q water. Once washed, the cells were left for incubation at room temperature overnight for drying. Once dried, the cells were shaken at room temperature (300 rpm, 15min) in the presence of 100 μL of acetic acid (10% w/w in water). Immediately after, the absorbance of the resulting solution was measured with a Microplate Reader (FLUOstar Optima, BMG Labtech GmbH, Germany) operating at 595 nm. All experiments were triplicate carried out. The growth inhibition was quantified as:

$$\%\ \text{Inhibition} = 100 - \frac{100 * \text{OA}}{\text{TA}} \qquad \text{(Eq. 7.1)}$$

where OA and TA stand for the absorbance of studied samples and negative controls (cells in the absence of NPs), respectively.

7.4 Results and discussion

7.4.1 Nanoconjugate characterization

The reaction for the synthesis of Au NS-PEG-SS-DOXO-FA is illustrated in Scheme 1. Au NS were prepared by a seed-mediated procedure in DMF in the

presence of PVP as the capping agent. Then, Au NS were modified by covalently thiol Au-S bonding of HS-PEG-NH_2onto Au NS surfaces. The biocompatible HS-PEG-NH_2 not only serves as a coating to reduce protein adsorption and nonspecific machrophage uptake, but also as a linking agent providing terminal functional groups for conjugation of ligands and biomolecules. Here, we followed a previously developed approach to incorporate a disulfide bond[63] onto the Au NS surfaces in order to achieve an enzyme-triggered release of a thiolated bounded chemotherapeutic drug (DOXO-SH) upon cell internalization of the hybrid nanoconjugate. To do this, a heterobifunctional cross-linker sulfo-LC-SPDP was used to obtain Au NS-PEG-SS conjugates. Then, a free sulfhydryl group was grafted to DOXO through modification of the drug witht Traut´s reagent to obtained DOXO-SH. The confirmation of DOXO thiolation was performed by an Ellman´s reagen assay, which confirmed a yield of ca. 80%. Upon combination of the DOXO-SH with Au NS-PEG-SS, stable disulfide linkages were formed between the Au NS and the drug. Finally, to provide targeability to the nanoconjugates folic acidwas covalently attached to the remaining amine-PEG chains by carbodiimide chemistry.

TEM images illustrated the morphology of the functionalized Au NS before and after DOXO conjugation.The average diameter of the Au NS before and after drug conjugation was rather similar (ca. 92 ±20 nm) indicating they were well dispersed after DOXO conjugation (Figure 7.1a-b). Dynamic light scattering was used to measure the hydrodynamic size of Au NS and confirmed that PEG, DOXO and FA were conjugated sequentially in the manner illustrated in Figure 7.2. The hydrodynamic diameter of PVP-functionalized Au NS was 112 ± 23 nm. After immobilization of PEG, Au NS diameter was rather similar to that of PVP-stabilized Au NS (107 ± 21), and was further increased to 129 ± 28 by subsequent coating with DOXO and FA through linkage with the LC-sulfo-SPDP linker (Figure 7.1c).

The modification of Au NS by DOXO and FA was monitored by UV-vis absorption fluorescence and Fourier Tranform infrared (FT-IR) spectra (Figure 7.3). Consistent with previous reports [55, 58], Au NS-PEG showed an absorbance peak at ca. 808 nm which is 18 nm red-shifted compared to that of PVP-stabilised Au NS (~ 790 nm). Free DOXO and FA displayed chaarcteriatic peaks at ca. 490 and 360 nm, respectively [64].

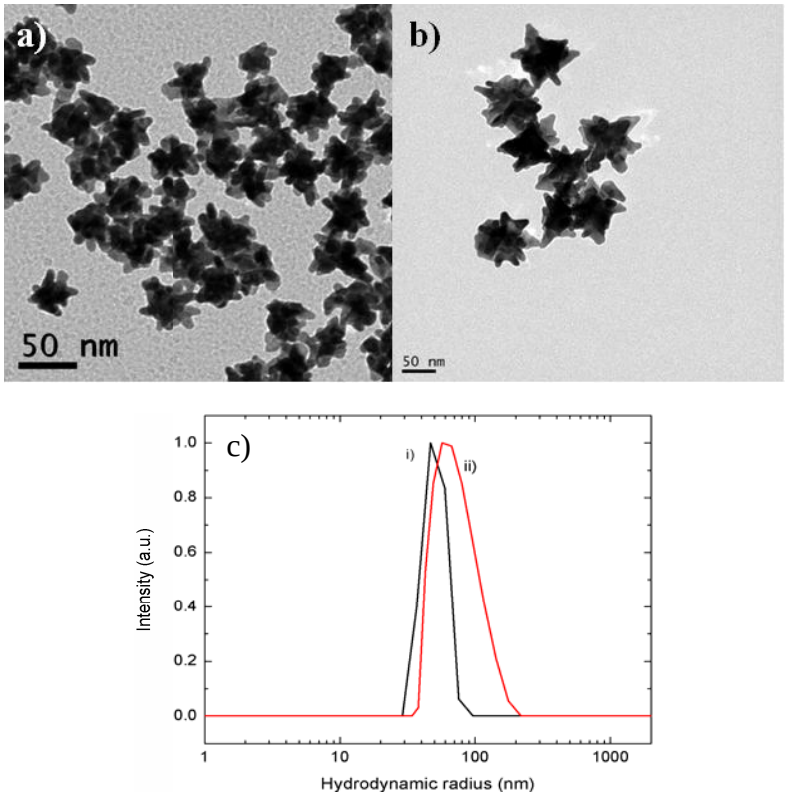

Figure 7.1: Au NS a) before and b) after conjugation of DOXO and FA. c) Hydrodynamic radii of Au NS i) after pegylation, and ii) after conjugation of FA and DOXO.

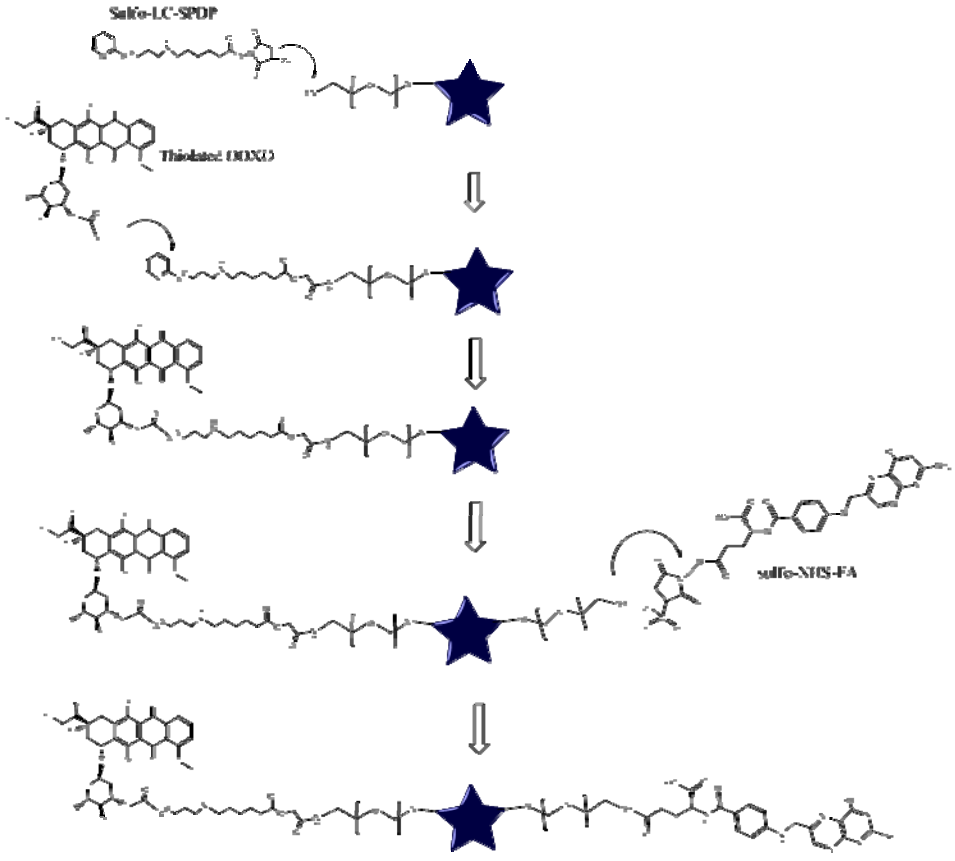

Figure 7.2: Scheme of the conjugation sequence of DOXO and FA to Au NS.

Au NS-PEG-SS-DOXO-FA nanoconjugates still exhibited the characterisitc absorption peaks of DOXO and FA, respectively, with an additional 9 nm red-shift in the plasmon band of Au NS as a consequence of the increase in the refractive index around the metal NP surface and the absence of aggregation, in agreement with TEM and DLS[58]. Fluorescence spectra also confirmed the successful attachment of DOXO to the Au NS. The fluorescence peak of DOXO did not shift after conjugation with Au NS (Figure 7.3b). Also, quenching of DOXO fluorescence was not observed, and if exists, this was minimaldue to the limited extent of overlap between absorption spectrum of Au NS and emission spectrum of DOXO. In this regard, linkers with long chains could be anchored on the surfaces of Au NS, which may perturb the energy transfer by increasing the distance between Au NS and the attached molecule; in addition, quenching efficiency decreases with increasing nanoparticle diameter, which is favored the relatively large size of Au NS[65-67].The estimated DOXO loading rate was 3.1% (w/w) by quantifying the unconjugated DOXO in the supernatant by both UV-vis and fluorescence data.

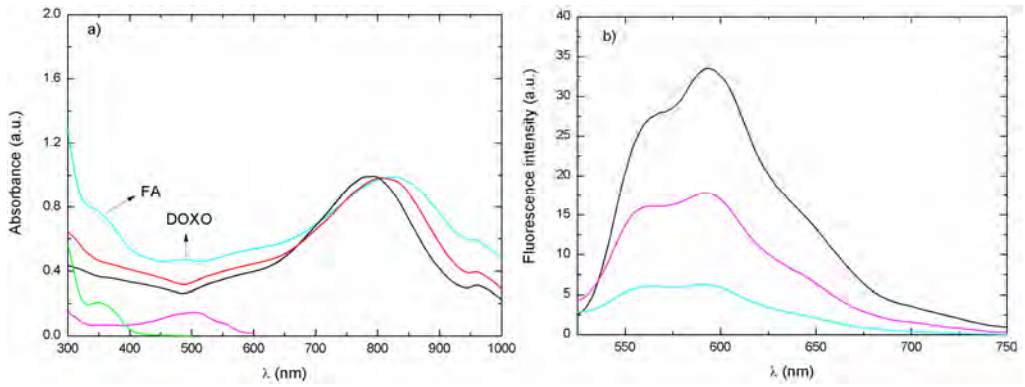

Figure 7.3: a) Normalized UV-Vis spectra of Au NS-PVP (—), Au NS-PEG (—), free DOXO (20 μM, —), free FA (—) and Au-NS-PEG-SS-DOXO-FA (—) in HEPES buffer (pH 7.4). Arrows denote the peaks corresponding to DOXO and FA in Au-NS-PEG-SS-DOXO-FA nanoconjugates. b) Fluorescence spectra of free DOXO initially added (20 μM, —), free DOXO in the supernatant (—), and Au-NS-PEG-SS-DOXO-FA (—) in HEPES buffer (pH 7.4).

To further verify the presence of the disulfide linkage in Au NS-PEG-SS-DOXO, DTT was added to a solution of these nanoconjugates provided that it cleaves and reduces disulfide linkages into free sulfhydryls[68]. We treated Au NS-PEG-SS-DOXO with an excess amount of DTT (10 mM) for cleaving and detaching DOXO

from Au NS, and separated DOXO-SH through dialysis. The resulting Au NS solution exhibited a drastic decrease in DOXO fluorescence after 2h of incubation, which confirmed the previous formation of disulfide bonds on nanocinjugate´s surfaces (Figure 7.4a).

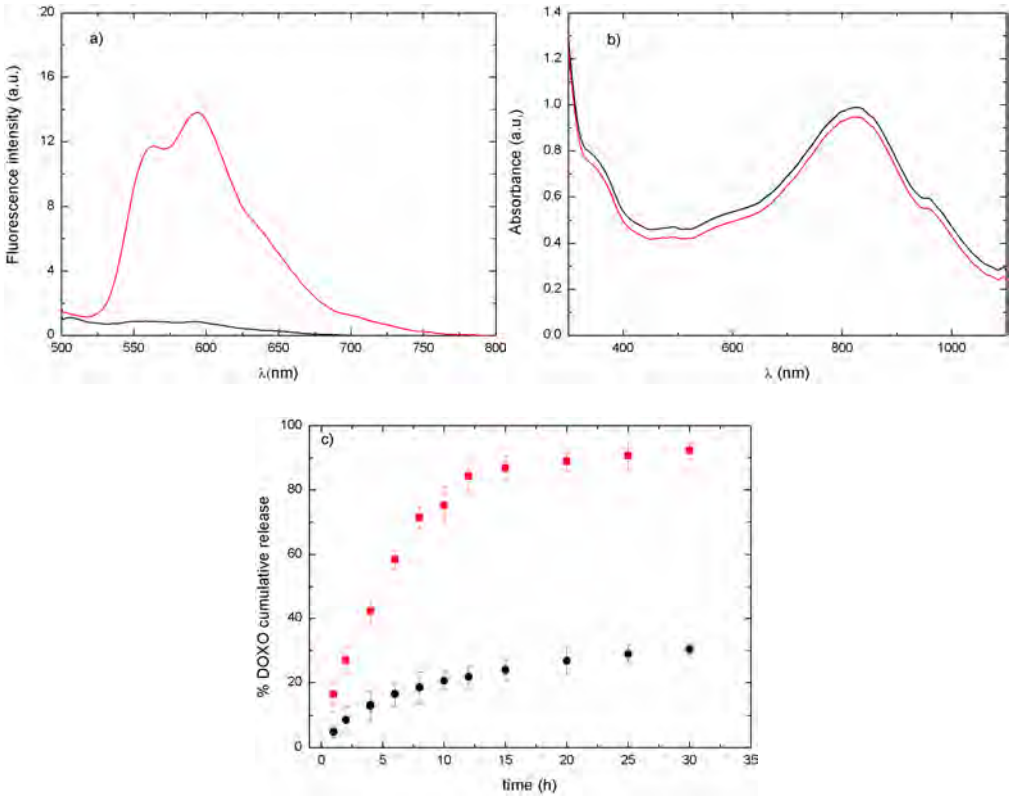

Figure 7.4: a) Decrease in DOXO fluorescence before (—) and after (—) DTT addition (15 mM) to Au NS-PEG-SS-DOXO-FA nanoconjugates dispersed in HEPES buffer (pH 7.4). b) Fluorescence spectra of Au NS-PEG-SS-DOXO-FA nanoconjugates dispersed in HEPES buffer (pH 7.4) immediately (—) and after 12 h (—) of incubation. c) *In vitro* DOXO release profile in HEPES buffer containing 10% (v/v) FBS (pH 7.4) in the absence (●) and presence (■) of glutathione (10 mM).

To investigate the stability of the nanoconjugates, UV-vis spectra of Au NS and Au NS-PEG-SS-DOXO-FA in cell culture medium with 10 % (v/v) fetal bovine serum immediately and after 12 h incubation were measured (Figure7.4b). Noshifts in the absorption spectra were detected and, in particular, in the plasmon peak of Au NS, which denoted the absence of particle aggregation upon incubation.

On the other hand, we analyzes the *in vitro* release profiles of DOXOAu NS-PEG-SS-DOXO nanoconjugates in the absence and presence of 10 mM glutathione

(GSH). In this way, we tried to simulate the reducing conditions inside cells provided that glutathione is a major endogenous antioxidant produced by the cells, participating directly in the neutralization of free radicals and reactive oxygen compounds, as well as maintaining exogenous antioxidants such as vitamins C and E in their reduced (active) forms[69]. It also reduces disulfide bonds formed within cytoplasmicproteins to cysteines by serving as an electron donor.

As would be expected, DOXO release was much faster in PBS buffer containing 10 % (v/v) FBS and glutathione (10 mM) than in its absence. Almost 42% of DOXO was release from Au NS-PEG-SS-DOXO in the initial 4 h when incubated with glutathione, and an almost complet release was achieved at 24 h incubation. In contrast, only ca. 30% of drug was released in the solution without the peptide upon incubation for more than 24 h.

On the other hand, Au NS have plasmon bands tunable in the NIRtissue optical window. These kind of nanoparticles are verystable, with a high potential to effectively transduceabsorbed laser light energy into heat[57]. Hence, the presence of the Au NS nanoconjugates in cell growth medium with 10% (v/v) FBS generated significant temperature increases upon NIR-light excitation which matches the plasmon resonance peak of the Au NS. The solution temperature increments depended on the energy input and/or the nanoconjugate concentration (Figure 7.5a-b). For example, Au NS-PEG nanoconjugates at the lowest concentration ($1 \cdot 10^8$ NP/mL) attained a maximum temperature increase of 12.5 ºC under a NIR irradiation of 3 W/cm^2 for 10 min. A similar temperature increment is achieved at the largest Au NS concentration tested ($1 \cdot 10^{11}$ NP/mL) but using an input energy three times lower (1 W/cm^2)for only 7 min.

It should be noted that the photostability of gold nanostructures is different under pulse laser and countinuous wave (CW)lasers. Femtosecond or nanosecond pulse lasers can melt andreshape gold nanostructures to nanospheres even in picoseconds[70-72]. This irreversible transformation of shape will dramaticallydeteriorate their heat producing ability[70, 73].On thecontrary, gold nanostructures are extremely stable under CWlaser in aqueous solutions or biological tissues[74]. To check this point, we recordedthe UV–vis spectra of Au NS($1 \cdot 10^{10}$ NP/mL) upon laser irradiation at 2 W/cm^2 for 1 h and 6 h. As shown in Figure 7.5c,only slight differencesare observed in the UV–vis spectra after 1 h of irradiation,

probably due to a lower surface rougheness of the Au NS as a consequence of less acute spikes due to localised melting of some apexes, as observed in TEM (Figure 7.5d). However, when increasing the irradiation time for 6 h an evident broadening of the plasmon peak of the Au NS was present due to shape transformation and some aggregation of the nanoparticles. Therefore, it is preferable to use CW laser instead of pulse laser, so that the therapeutic efficiency of photothermal treatment can accumulate to the desired level by simply adjusting the irradiation time and power.

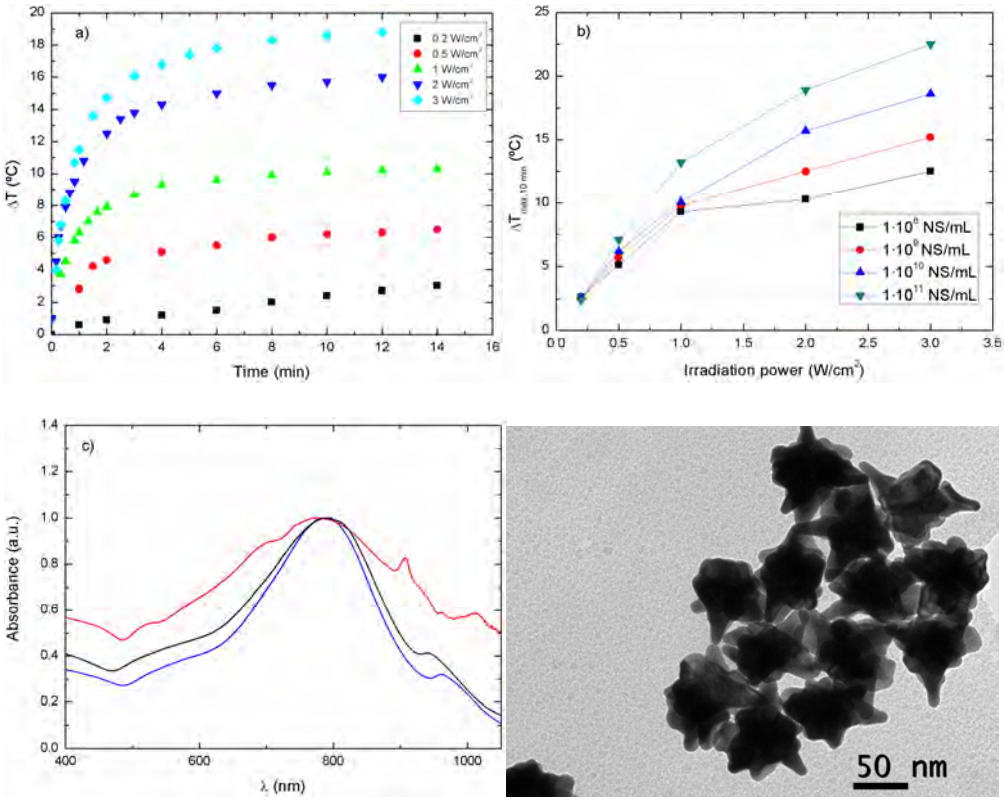

Figure 7.5: a) Temperature increments of Au NS-PEG particles ($1{\cdot}10^{10}$ NP/mL) in HEPES buffer with 10% (v/v) FBS (pH 7.4) upon NIR laser illumination of different intensities (808 nm). b) Temperature increments as a function of irradiation intensity of Au NS-PEG PBS solutuins (10% (v/v) FBS added) of different concentrations under NIR laser illumination (808 nm, 10 min). c) UV-vis spectra of Au NS in HEPES buffer (pH 7.4) before (—) and after 1 (—) and 8 h (—) of light irradiation at 808 nm and 2 W/cm^2. d) TEM image of Au NS after 1 h of irradiation at 2 W/cm^2.

7.4.2 Cellular uptake of nanoconjugates

To visualize the cellular uptake of the nanoconjugates, the red fluorescence emitted by DOXO from Au NS-PEG-SS-DOXO and Au NS-PEG-SS-DOXO-FA was

captured by laser confocal microscopy after incubation with cervical HeLa tumor cells which overexpressed folate receptors in their membrane surfaces (Figure 7.6). The weak red fluorescence of DOXO from Au NS-PEG-SS-DOXO in HeLa cells indicated that a low amount of nanoconjugates entered inside cells, and they were exclusively confined inside the cell cytoplasm (Figure 7.6a). By contrast, Au NS-PEG-SS-DOXO-FA uptakewas enhanced if compared to that of Au NS-PEG-SS-DOXO. In addition, certain incorporation of the drug inside the cell nuclei (as corresponds for DOXO acting as a DNA intercalating agent) could also be observed for Au NS-PEG-SS-DOXO-FA, which further proved the enhanced cell uptake of the FA-functionalized nanoconjugatesin the time scale analyzed (Figure 7.6b).

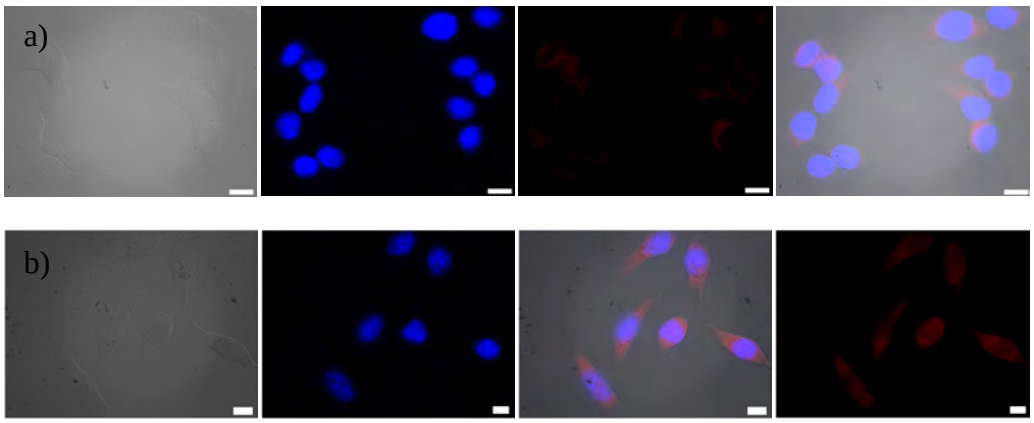

Figure 7.6: Transmission, fluorescence confocal and overlaid images of a) Au NS-PEG-DOXO and b) Au NS-PEG-SS-DOXO-FA (1 μM DOXO) after 2 h of incubation. Nuclei were stained with DAPI (blue channel, $\lambda_{exc.}$ = 365 nm); DOXO autofluorescence was registered by light excitation at $\lambda_{exc.}$ = 485 nm. Scale bars 10 μm.

In this regard, Dam *et al.*[56] designed a nanostructure composed of nucleolin-specific aptamer and Au NS which wereactively transported to the nucleus after 5 h incubation,and inducedmajor changes to the nuclear phenotype. In anotherstudy by Yuan *et al.*[54], TAT-peptide functionalizedAu NS were observed in the nuclear region bytwo-photon photoluminescence imaging. However,they did not find any true intranuclear TAT-NS exceptsome particles in the nuclear cleft. These resultssuggested that the red fluorescence observed from thenucleus in our study may be contributed by free DOXOreleased from Au NS-PEG-SS-DOXO-FA as a result of the disulfide bond breakage.On the other hand, 3D-reconstruction images of thin

optical sections allowed to observe fluorescence signals along the z-axis, which additionally confirmed the nanoconjugate uptake inside cells (Figure 7.7). Hence, these results clearly indicated that the presence of FA on the surface of Au NS increased its cellular uptake by HeLa cells, in agreement with previous reports [75, 76].

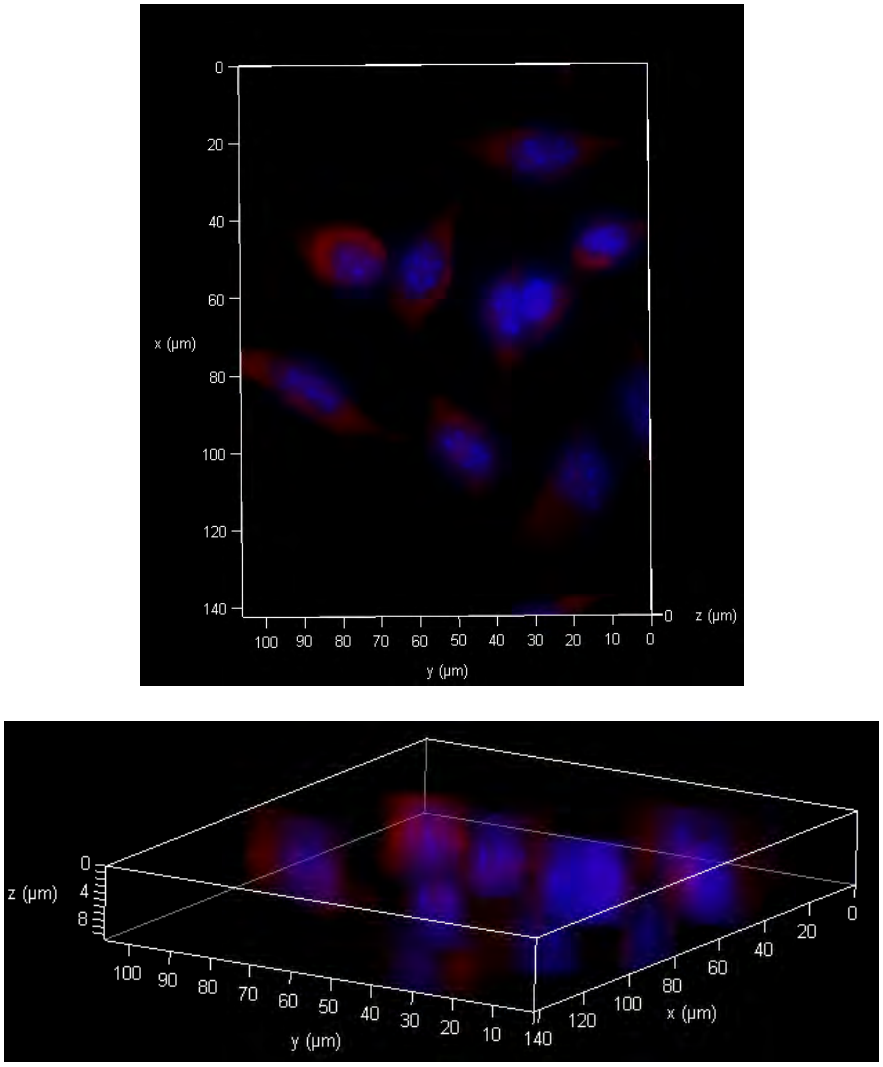

Figure 7.7: 3D images of HeLa cells with internalized Au NS-PEG-SS-DOXO-FA. Blue channel stands for DAPI (λ_{ex} = 365 nm) and the red one for DOXO (λ_{ex} = 485 nm).

7.4.3Therapeutic efficiency of nanoconjugates *in vitro*

To confirm the enhancement of anti-tumor efficacy of Au NS-PEG-SS-DOXO-FA nanoconjugates, cytotoxicity effects of Au NS, free DOXO, NIR-irradiated free DOXO, NIR-irradiated Au NS, and the combined chemo- and photothermal effects of Au-PEG-DOXO and Au NS-PEG-DOXO-FA under NIR laser irradiation for 10 min

were compared by using the crystal violet assay (Figure 7.8a).

All samples showed dose-dependent anti-tumor activity. At thehighest dose level, the inhibition ratio of Au NS PEG-SS-DOXO-FA was above 90 % of total cells, whichwas much higher than that of Au NS-PEG (67 %), DOXO (58%) and Au NS-PEG-SS-DOXO (86 %) at the same dose level.With the increase in concentration ofAu NS-PEG-SS-DOXO-FA nanoconjugates, the cell viability distinctively decreasedafter incubation for 24 h. The cell mortality could be directly observed by optical microcopy. Under the combination of NIR irradiation and selective chemotherapy, cells completely lost their integrity and only aggregates of membrane components were seen (Figure 7.8b-c).

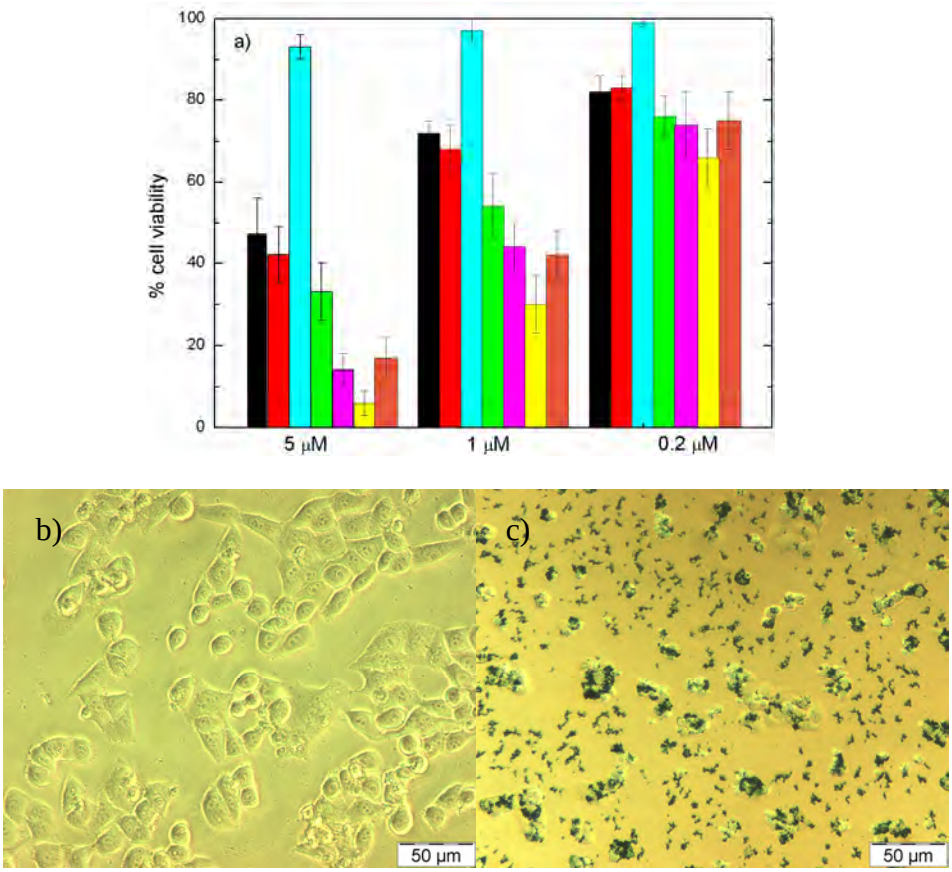

Figure 7.8: a) Cell viability of HeLa cells after 24 h of incubation in the absence and presence of NIR light irradiation (2 W cm^{-2} for 10 min at 808 nm) at different DOXO concentrations assayed by the crystal violet method. Colors code: Black, free DOXO; Red, free DOXO+NIR light; Cyan, Au NS-PEG; Green, Au-NS-PEG+NIR light; Magenta, Au NS-PEG-SS-DOXO+NIR; Yellow, Au NS-PEG-SS-DOXO-FA+NIR light; Orange, Au NS-PEG-SS-DOXO-FA+NIR light after saturating FA cell receptor by addition of an excess amount of free FA. b) Optical microscopy images of NIR-irradiated HeLa cells (808 nm, 2 W/cm^2 for 10 min) b) in the absence and c) presence of Au NS-PEG-SS-DOXO-FA (5 μM DOXO).

As observed from experimental data, most cellscould take up certain amounts of Au NS-PEG-SS-DOXO butthe resulting cytotoxicity was lowerthan that of Au NS PEG-SS-DOXO-FA. Thus, the FA molecular guideon the surface of Au NS recognizedfolate receptors and mediatedinternalization of the nanoconjugates in cells, as observed when previously adding free FA in excess to the sample cells, in agreement with results present in previous chapters.Subsequent endosomal transport and lysosomal degradationcould release the toxic DOXO from Au NS-PEG-SS-DOX-FA to induce apoptosis in cancer cells, which involed evident cellular morphological changes after the action of the nanoconjugates. Similarly, Nevell*et al.*[77]and Pandey et al [78]have demonstrated the improved photothermaleffect of combining FA-conjugated gold nanorodswith NIR irradiation.The results herein demonstrated the selective anti-tumor efficacy ofAu NS-PEG-SS-DOXO-FA combining chemotherapy andphotothermal therapy under NIR laser irradiation, that eclipsed that of DOXO, Au NS, or Au NS-PEG-SS-DOXO.

7.5 Conclusions

In summary, we have successfully developedtumor targeted Au NS-PEG-SS-DOXO nanoconjugates forcombinedphotothermal and chemo-therapy. Tumor-targeting ability of Au NS nanoconjugateswas further enhanced when a targeting molecule, FA, was attached to the nanoconjugate surface, and tested on FA-overexpressing cells such as HeLa by FA-mediated activetargeting. Au NS-PEG-SS-DOXO-FA enabledthe active delivery of the chemotherapeutic drug near the nucleus, allowing its subsquent incorporation upon further incubation. Tumor cellsshowed significant morphological changes upon the action of NIR light irradiation and the chemotherapeutic drug. In comparisonwith conventional hyperthermia or chemotherapy,the enhanced tumor therapy efficacy was demonstrated in Au NS-PEG-SS-DOXO-FA*in vitro* due to thecombination of the dual treatment. A synergistic effect between the chemotherapy and thermotherapy was confirmed by the therapeutic results of Au NS PEG-SS-DOXO-FA treated groups when compared with Au NS or free DOXO treated groups. Meanwhile, the nature of the targeting ligand could improve the cellular uptake of nanoconjugates, as demonstrated by experimental cytotoxicity data of Au NS-PEG-SS-DOXO, Au NS-PEG-SS-DOXO-FA, nad those when previously blocking celll FA receptors with free FA before addition of NS-PEG-SS DOXO-FA nanoconjugates. The above facts provide insight into thedevelopment of new strategies to design drug-loadednanoconstructs with increased therapeutic efficacy and prompt further exploration of these

nanoconstructsfor combined therapy of other related diseases. To the best of our knowledge, this is an innovation,only one recent work recently appeared while preparing this manuscript combined the photothermal therapeutic effect of gold nanostars and the chemotherapeutic effect of DOX for tumor-targeted therapy[61]. In contrast to this work, our nanoconjugates enabled the enzymatic-triggerable release of the chemotherapeutic drug inside the cells by breaking the disulfide bond through which the drug is bound to the Au Ns surface. In this way, our construction thenprovides additionalselectivity to the chemotherapeutic activity of the nanoconjugates.

7.6 Bibliography

[1] Farokhzad OC, Langer R. Nanomedicine: Developing smarter therapeutic and diagnostic modalities. Advanced Drug Delivery Reviews. 2006;58:1456-9.

[2] Lee PY, Wong KYK. Nanomedicine: a new frontier in cancer therapeutics. . Current Drug Deliv. 2011;8:245-53.

[3] Riehemann K, Schneider SW, Luger TA, Godin B, Ferrari M, Fuchs H. Nanomedicine—Challenge and Perspectives. Angewandte Chemie International Edition. 2009;48:872-97.

[4] Wagner V, Dullaart A, Bock A-K, Zweck A. The emerging nanomedicine landscape. Nat Biotech. 2006;24:1211-7.

[5] Lane D. Designer combination therapy for cancer. Nat Biotech. 2006;24:163-4.

[6] Sun T-M, Du J-Z, Yao Y-D, Mao C-Q, Dou S, Huang S-Y, et al. Simultaneous Delivery of siRNA and Paclitaxel via a “Two-in-One” Micelleplex Promotes Synergistic Tumor Suppression. ACS Nano. 2011;5:1483-94.

[7] Lee D-E, Koo H, Sun I-C, Ryu JH, Kim K, Kwon IC. Multifunctional nanoparticles for multimodal imaging and theragnosis. Chemical Society Reviews. 2012;41:2656-72.

[8] Mi Y, Guo Y, Feng S-S. Nanomedicine for multimodality treatment of cancer. Nanomedicine. 2012;7:1791-4.

[9] Ryu JH, Koo H, Sun I-C, Yuk SH, Choi K, Kim K, et al. Tumor-targeting multi-functional nanoparticles for theragnosis: New paradigm for cancer therapy. Advanced Drug Delivery Reviews. 2012;64:1447-58.

[10] Cobley CM, Chen J, Cho EC, Wang LV, Xia Y. Gold nanostructures: a class of multifunctional materials for biomedical applications. Chemical Society Reviews. 2011;40:44-56.

[11] Huang H-C, Barua S, Sharma G, Dey SK, Rege K. Inorganic nanoparticles for cancer imaging and therapy. Journal of Controlled Release. 2011;155:344-57.

[12] Llevot A, Astruc D. Applications of vectorized gold nanoparticles to the diagnosis and therapy of cancer. Chemical Society Reviews. 2012;41:242-57.

[13] Mout R, Moyano DF, Rana S, Rotello VM. Surface functionalization of nanoparticles for nanomedicine. Chemical Society Reviews. 2012;41:2539-44.

[14] Giljohann DA, Seferos DS, Daniel WL, Massich MD, Patel PC, Mirkin CA. Gold Nanoparticles for Biology and Medicine. Angewandte Chemie International Edition. 2010;49:3280-94.

[15] Dreaden EC, Alkilany AM, Huang X, Murphy CJ, El-Sayed MA. The golden age: gold nanoparticles for biomedicine. Chemical Society Reviews. 2012;41:2740-79.

[16] Kennedy LC, Bickford LR, Lewinski NA, Coughlin AJ, Hu Y, Day ES, et al. A New Era for Cancer Treatment: Gold-Nanoparticle-Mediated Thermal Therapies. Small. 2011;7:169-83.

[17] Melancon MP, Lu W, Zhong M, Zhou M, Liang G, Elliott AM, et al. Targeted multifunctional gold-based nanoshells for magnetic resonance-guided laser ablation of head and neck cancer. Biomaterials. 2011;32:7600-8.

[18] Qin Z, Bischof JC. Thermophysical and biological responses of gold nanoparticle laser heating. Chemical Society Reviews. 2012;41:1191-217.

[19] Huang X, El-Sayed IH, Qian W, El-Sayed MA. Cancer Cell Imaging and Photothermal Therapy in the Near-Infrared Region by Using Gold Nanorods. Journal of the American Chemical Society. 2006;128:2115-20.

[20] Choi J, Yang J, Bang D, Park J, Suh J-S, Huh Y-M, et al. Targetable Gold Nanorods for Epithelial Cancer Therapy Guided by Near-IR Absorption Imaging. Small. 2012;8:746-53.

[21] Alkilany AM, Thompson LB, Boulos SP, Sisco PN, Murphy CJ. Gold nanorods: Their potential for photothermal therapeutics and drug delivery, tempered by the complexity of their biological interactions. Advanced Drug Delivery Reviews. 2012;64:190-9.

[22] Tsai M-F, Chang S-HG, Cheng F-Y, Shanmugam V, Cheng Y-S, Su C-H, et al. Au Nanorod Design as Light-Absorber in the First and Second Biological Near-Infrared Windows for in Vivo Photothermal Therapy. ACS Nano. 2013;7:5330-42.

[23] Chen J, Glaus C, Laforest R, Zhang Q, Yang M, Gidding M, et al. Gold Nanocages as Photothermal Transducers for Cancer Treatment. Small. 2010;6:811-7.

[24] Xia Y, Li W, Cobley CM, Chen J, Xia X, Zhang Q, et al. Gold Nanocages: From Synthesis to Theranostic Applications. Accounts of Chemical Research. 2011;44:914-24.

[25] Wang Y, Black KCL, Luehmann H, Li W, Zhang Y, Cai X, et al. Comparison Study of Gold Nanohexapods, Nanorods, and Nanocages for Photothermal Cancer Treatment. ACS Nano. 2013;7:2068-77.

[26] Lu W, Xiong C, Zhang G, Huang Q, Zhang R, Zhang JZ, et al. Targeted Photothermal Ablation of Murine Melanomas with Melanocyte-Stimulating Hormone Analog–Conjugated Hollow Gold Nanospheres. Clinical Cancer Research. 2009;15:876-86.

[27] You J, Zhang G, Li C. Exceptionally High Payload of Doxorubicin in Hollow Gold Nanospheres for Near-Infrared Light-Triggered Drug Release. ACS Nano. 2010;4:1033-41.

[28] O'Neal DP, Hirsch LR, Halas NJ, Payne JD, West JL. Photo-thermal tumor ablation in mice using near infrared-absorbing nanoparticles. Cancer Letters. 2004;209:171-6.

[29] Choi M-R, Stanton-Maxey KJ, Stanley JK, Levin CS, Bardhan R, Akin D, et al. A Cellular Trojan Horse for Delivery of Therapeutic Nanoparticles into Tumors. Nano Letters. 2007;7:3759-65.

[30] Diagaradjane P, Shetty A, Wang JC, Elliott AM, Schwartz J, Shentu S, et al. Modulation of in Vivo Tumor Radiation Response via Gold Nanoshell-Mediated Vascular-Focused Hyperthermia: Characterizing an Integrated Antihypoxic and Localized Vascular Disrupting Targeting Strategy. Nano Letters. 2008;8:1492-500.

[31] Bardhan R, Lal S, Joshi A, Halas NJ. Theranostic Nanoshells: From Probe Design to Imaging and Treatment of Cancer. Accounts of Chemical Research. 2011;44:936-46.

[32] Van de Broek B, Devoogdt N, D'Hollander A, Gijs H-L, Jans K, Lagae L, et al. Specific Cell Targeting with Nanobody Conjugated Branched Gold Nanoparticles for Photothermal Therapy. ACS Nano. 2011;5:4319-28.

[33] Sironi L, Freddi S, Caccia M, Pozzi P, Rossetti L, Pallavicini P, et al. Gold Branched Nanoparticles for Cellular Treatments. The Journal of Physical Chemistry C. 2012;116:18407-18.

[34] Li J, Han J, Xu T, Guo C, Bu X, Zhang H, et al. Coating Urchinlike Gold Nanoparticles with Polypyrrole Thin Shells To Produce Photothermal Agents with High Stability and Photothermal Transduction Efficiency. Langmuir. 2013;29:7102-10.

[35] Baginskiy I, Lai T-C, Cheng L-C, Chan Y-C, Yang K-Y, Liu R-S, et al. Chitosan-Modified Stable Colloidal Gold Nanostars for the Photothermolysis of Cancer Cells. The Journal of Physical Chemistry C. 2013;117:2396-410.

[36] Weissleder R. A clearer vision for in vivo imaging. Nat Biotech. 2001;19:316-7.

[37] Dewhirst MW, Vujaskovic Z, Jones E, Thrall D. Re-setting the biologic rationale for thermal therapy. International Journal of Hyperthermia. 2005;21:779-90.

[38] Sapsford KE, Algar WR, Berti L, Gemmill KB, Casey BJ, Oh E, et al. Functionalizing Nanoparticles with Biological Molecules: Developing Chemistries that Facilitate Nanotechnology. Chemical Reviews. 2013;113:1904-2074.

[39] Huang X, Peng X, Wang Y, Wang Y, Shin DM, El-Sayed MA, et al. A Reexamination of Active and Passive Tumor Targeting by Using Rod-Shaped Gold Nanocrystals and Covalently Conjugated Peptide Ligands. ACS Nano. 2010;4:5887-96.

[40] Dufort S, Sancey L, Coll J-L. Physico-chemical parameters that govern nanoparticles fate also dictate rules for their molecular evolution. Advanced Drug Delivery Reviews. 2012;64:179-89.

[41] Guerrero-Martínez A, Barbosa S, Pastoriza-Santos I, Liz-Marzán LM. Nanostars shine bright for you: Colloidal synthesis, properties and applications of branched metallic nanoparticles. Current Opinion in Colloid & Interface Science. 2011;16:118-27.

[42] Rodriguez-Lorenzo L, Krpetic Z, Barbosa S, Alvarez-Puebla RA, Liz-Marzan LM, Prior IA, et al. Intracellular mapping with SERS-encoded gold nanostars. Integrative Biology. 2011;3:922-6.

[43] Hsiangkuo Y, Christopher GK, Hanjun H, Christy MW, Gerald AG, Tuan V-D. Gold nanostars: surfactant-free synthesis, 3D modelling, and two-photon photoluminescence imaging. Nanotechnology. 2012;23:075102.

[44] Fales AM, Yuan H, Vo-Dinh T. Cell-Penetrating Peptide Enhanced Intracellular Raman Imaging and Photodynamic Therapy. Molecular Pharmaceutics. 2013;10:2291-8.

[45] Dondapati SK, Sau TK, Hrelescu C, Klar TA, Stefani FD, Feldmann J. Label-free Biosensing Based on Single Gold Nanostars as Plasmonic Transducers. ACS Nano. 2010;4:6318-22.

[46] Shao L, Susha AS, Cheung LS, Sau TK, Rogach AL, Wang J. Plasmonic Properties of Single Multispiked Gold Nanostars: Correlating Modeling with Experiments. Langmuir. 2012;28:8979-84.

[47] Rodríguez-Lorenzo L, Álvarez-Puebla RnA, Pastoriza-Santos I, Mazzucco S, Stéphan O, Kociak M, et al. Zeptomol Detection Through Controlled Ultrasensitive Surface-Enhanced Raman Scattering. Journal of the American Chemical Society. 2009;131:4616-8.

[48] Yuan H, Fales AM, Khoury CG, Liu J, Vo-Dinh T. Spectral characterization and intracellular detection of Surface-Enhanced Raman Scattering (SERS)-encoded plasmonic gold nanostars. Journal of Raman Spectroscopy. 2013;44:234-9.

[49] Yuan H, Liu Y, Fales AM, Li YL, Liu J, Vo-Dinh T. Quantitative Surface-Enhanced Resonant Raman Scattering Multiplexing of Biocompatible Gold Nanostars for in Vitro and ex Vivo Detection. Analytical Chemistry. 2012;85:208-12.

[50] Pei Y, Wang Z, Zong S, Cui Y. Highly sensitive SERS-based immunoassay with simultaneous utilization of self-assembled substrates of gold nanostars and aggregates of gold nanostars. Journal of Materials Chemistry B. 2013;1:3992-8.

[51] Kim C, Song H-M, Cai X, Yao J, Wei A, Wang LV. In vivo photoacoustic mapping of lymphatic systems with plasmon-resonant nanostars. Journal of Materials Chemistry. 2011;21:2841-4.

[52] Schutz M, Steinigeweg D, Salehi M, Kompe K, Schlucker S. Hydrophilically stabilized gold nanostars as SERS labels for tissue imaging of the tumor suppressor p63 by immuno-SERS microscopy. Chemical Communications. 2011;47:4216-8.

[53] Song H-M, Wei Q, Ong QK, Wei A. Plasmon-Resonant Nanoparticles and Nanostars with Magnetic Cores: Synthesis and Magnetomotive Imaging. ACS Nano. 2010;4:5163-73.

[54] Yuan H, Fales AM, Vo-Dinh T. TAT Peptide-Functionalized Gold Nanostars: Enhanced Intracellular Delivery and Efficient NIR Photothermal Therapy Using Ultralow Irradiance. Journal of the American Chemical Society. 2012;134:11358-61.

[55] Yuan H, Khoury CG, Wilson CM, Grant GA, Bennett AJ, Vo-Dinh T. In vivo particle tracking and photothermal ablation using plasmon-resonant gold nanostars. Nanomedicine: Nanotechnology, Biology and Medicine. 2012;8:1355-63.

[56] Dam DHM, Lee JH, Sisco PN, Co DT, Zhang M, Wasielewski MR, et al. Direct Observation of Nanoparticle–Cancer Cell Nucleus Interactions. ACS Nano. 2012;6:3318-26.

[57] Wang S, Huang P, Nie L, Xing R, Liu D, Wang Z, et al. Single Continuous Wave Laser Induced Photodynamic/Plasmonic Photothermal Therapy Using Photosensitizer-Functionalized Gold Nanostars. Advanced Materials. 2013;25:3055-61.

[58] Barbosa S, Agrawal A, Rodríguez-Lorenzo L, Pastoriza-Santos I, Alvarez-Puebla RnA, Kornowski A, et al. Tuning Size and Sensing Properties in Colloidal Gold Nanostars. Langmuir. 2010;26:14943-50.

[59] Chen H, Zhang X, Dai S, Ma Y, Cui S, Achilefu S, et al. Multifunctional Gold Nanostar Conjugates for Tumor Imaging and Combined Photothermal and Chemo-therapy Theranostics. 2013;3:633-49.

[60] Frederick CA, Williams LD, Ughetto G, Van der Marel GA, Van Boom JH, Rich A, et al. Structural comparison of anticancer drug-DNA complexes: adriamycin and daunomycin. Biochemistry. 1990;29:2538-49.

[61] Parker N, Turk MJ, Westrick E, Lewis JD, Low PS, Leamon CP. Folate receptor expression in carcinomas and normal tissues determined by a quantitative radioligand binding assay. Analytical Biochemistry. 2005;338:284-93.

[62] Graf C, Vossen DLJ, Imhof A, van Blaaderen A. A General Method To Coat Colloidal Particles with Silica. Langmuir. 2003;19:6693-700.

[63] Gu Y-J, Cheng J, Man CW-Y, Wong W-T, Cheng SH. Gold-doxorubicin nanoconjugates for overcoming multidrug resistance. Nanomedicine : nanotechnology, biology, and medicine. 2012;8:204-11.

[64] Zhou J, Romero G, Rojas E, Ma L, Moya S, Gao C. Layer by layer chitosan/alginate coatings on poly(lactide-co-glycolide) nanoparticles for antifouling protection and Folic acid binding to achieve selective cell targeting. Journal of Colloid and Interface Science. 2010;345:241-7.

[65] Dulkeith E, Ringler M, Klar TA, Feldmann J, Muñoz Javier A, Parak WJ. Gold Nanoparticles Quench Fluorescence by Phase Induced Radiative Rate Suppression. Nano Letters. 2005;5:585-9.

[66] Kim CK, Rajamohan KR, Singh JP, Fortner A, Griffin J, Darbha GK, et al. Gold-nanoparticle-based miniaturized laser-induced fluorescence probe for specific DNA hybridization detection: studies on size-dependent optical properties. Nanotechnology. 2006;17:3085.

[67] Cobley CM, Au L, Chen J, Xia Y. Targeting gold nanocages to cancer cells for photothermal destruction and drug delivery. Expert Opinion on Drug Delivery. 2010;7:577-87.

[68] Kam NWS, Liu Z, Dai H. Functionalization of Carbon Nanotubes via Cleavable Disulfide Bonds for Efficient Intracellular Delivery of siRNA and Potent Gene Silencing. Journal of the American Chemical Society. 2005;127:12492-3.

[69] Scholz RW, Graham KS, Gumpricht E, Reddy CC. Mechanism of Interaction of Vitamin E and Glutathione in the Protection against Membrane Lipid Peroxidation. Annals of the New York Academy of Sciences. 1989;570:514-7.

[70] Takahashi H, Niidome T, Nariai A, Niidome Y, Yamada S. Photothermal reshaping of gold nanorods prevents further cell death. Nanotechnology. 2006;17:4431.

[71] Link S, Burda C, Nikoobakht B, El-Sayed MA. How long does it take to melt a gold nanorod?: A femtosecond pump–probe absorption spectroscopic study. Chemical Physics Letters. 1999;315:12-8.

[72] Link S, Burda C, Nikoobakht B, El-Sayed MA. Laser-Induced Shape Changes of Colloidal Gold Nanorods Using Femtosecond and Nanosecond Laser Pulses. The Journal of Physical Chemistry B. 2000;104:6152-63.

[73] Lal S, Clare SE, Halas NJ. Nanoshell-Enabled Photothermal Cancer Therapy: Impending Clinical Impact. Accounts of Chemical Research. 2008;41:1842-51.

[74] Ratto F, Matteini P, Cini A, Centi S, Rossi F, Fusi F, et al. CW laser-induced photothermal conversion and shape transformation of gold nanodogbones in hydrated chitosan films. J Nanopart Res. 2011;13:4337-48.

[75] Smith MW, Gumbleton M. Endocytosis at the blood–brain barrier: From basic understanding to drug delivery strategies. Journal of Drug Targeting. 2006;14:191-214.

[76] Mukherjee S, Ghosh RN, Maxfield FR. Endocytosis. Physiological Reviews. 1997;77:759-803.

[77] Book Newell B, Wang Y, Irudayaraj J. Multifunctional gold nanorod theragnostics probed by multi-photon imaging. European Journal of Medicinal Chemistry. 2012;48:330-7.

[78] Pandey S, Shah R, Mewada A, Thakur M, Oza G, Sharon M. Gold nanorods mediated controlled release of doxorubicin: nano-needles for efficient drug delivery. J Mater Sci: Mater Med. 2013;24:1671-81.

Conclusions

The results obtained reveal that the possible combination of chemotherapy, magnetic targeting, and photothermal therapy through polymeric NPs is expected to increase the likelihood of cell killing significantly, to improve the selectivity greatly and, potentially, to overcome resistance to chemotherapeutic agents, making it a promising approach not only for cancer therapy but also for other diseases as Alzheimer´s or Parkinson´s thanks to the ability of the present NPs to overcome the BBB. PLGA hybrid NPs could be guided to the tumor area by a magnetic field, followed by the combination of NIR laser irradiation at the tumor site, which should enhance the targeting effectiveness. The permeability of tumor vessels and the sensitivity of the tumor cells toward chemotherapeutics should be greatly enhanced by hyperthemia, holding the promise of improving drug efficacy. Photothermal ICG-mediated therapy may facilitate triggered and instant drug release from the NPs, which is critical for achieving a high effective drug concentration in the tumor. Moreover, one of the major advantages of NIR laser light as a source of hyperthermia is that the exposures are non-invasive and applied extracorporally, compared with other types of hyperthermia like radiofrequency or microwave ablation. In addition, the magnetic and luminescent properties of the hybrid NPs gained through the simultaneous incoporation of Fe_3O_4 NPs and the fluorescent ICG dye in their nanostructure also allows, at the same time, the use of these nanoplatforms as multimodal imaging diagnostic nanoconstructs able to follow their therapeutic response *in vivo*, configuring an example of fully biocompatible and biodegradable theranostic nanodevices.

We have synthesized branched gold nanoshells (BGNS) with PLGA cores by means of a surfactant-less method, using an $HAuCl_4/K_2CO_3$ growth solution and concentrated ascorbic acid as reductant. Size and structure (anisotropy) and, in consequence, the optical properties of nanostructures were tuned by modulating the synthetic conditions (feed ratios of Au growth solution, AA and NP-seed precursor). Both chitosan and AA played an important role as co-reductants and directing agents, resulting in the growth of highly branched structures resembling geometries found in nature, such as viruses, sea-urchins or bushes. Among the diverse experimental variables, the concentration of AA was dominant to enhance the reactivity of gold ions

by preferential reduction of Au^{I} to Au^{0} on the seed surfaces onto preferred facet via a kinetics-favored process. A excessive amount of AA promotes an instant reduction of the particles, decreasing their anisotropy by the isotropic deposition of the gold ions and the adsorption of excess AA on the surface of nanoshells. Meaningfully, the as-prepared BGNS were stable in aqueous solution for several months, and were found to be internalised by cells in the cytoplasm and fully biocompatible, as deduced from a cell viability test. The hollow and branched architecture of BGNS is also advantageous because it adds another control characteristic (i.e. core size) to tune the plasmon band position to the near infrared region of the electromagnetic spectrum, and allowing their potential use as photothermal agents and/or surface enhanced Raman scattering (SERS) probes. In addition, other functional materials and molecules can be incorporated into the core to fabricate multifunctional materials. In this way, these branched hollow NPs hold potential applicability as multifunctional nanoteranostic agents due to their optical properties and core-carrying capacity.

Likewise, we have synthesized polymeric core-Au coated nanoshells as a multifunctional platform to combine MR imaging, magnetic- and folic-acid targeted drug delivery, NIR light-triggered drug release, and photothermal therapy simultaneously into one system. The resulting nanoplatforms display enhanced T2 -weighted MRI properties and surface plasmon absorbance in the NIR region, thus exhibiting an NIR-induced temperature elevation and an NIR light-triggered and stepwise release behavior of doxorubicin.

Cell viability tests reveal that the combination of chemotherapy, magnetic, and ligand-induced targeting, and NIR photothermal therapy. DXSP-PLGA-PGNH-FA increased the likelihood of cell killing significantly and shoewd an improved cellular uptake driven by FA and magnetic targeting. Selectivity of DXSP-PGNHs-FA will be tested in further studies using a cell line without overexpressed FA receptors (FA-R) and co-cultures with FA-R non-overexpressing and overexpressing cellular lines. This potentially might help to overcome resistance to chemotherapeutic agents, making it a promising approach for future cancer therapy.

The nanoplatforms could be guided to the tumor area by the combination of ligand-induced and magnetic-assisted targeting, followed by NIR laser irradiation at the tumor site. This would enhance their targeting effectiveness as observed *in vitro* tests , in which a synergistic effect in killing cancer cells was found by the combined

photothermal therapy and the magnetic-field and ligand-guided drug delivery.

In this regard, the permeability of tumor vessels and the sensitivity of the tumor cells toward chemotherapeutics should be greatly enhanced by hyperthemia, holding the promise of improving drug efficacy. In addition, photothermal therapy may facilitate triggered and enhanced drug release from the multifunctional nanoparticles, which is critical for achieving a high effective drug concentration in the tumor.

Future studies employing more sophisticated nanoplatforms should perfectly allow both spatially and temporally improved hyperthermia, opto-magnetic-resonance imaging contrast agents for *in vivo* monitoring of tissue pharmacokinetics and cell tracking, and enable a perfect and on-demand control of drug release dynamics for completely efficient chemotherapy.

We have successfully fabricated a potential smart theranostic nanoplatform composed of a chemotherapeutic agent (DOXO) and a polymer-based gold shell which additionally combines localized photothermal activity provided by the metal shell and generation of singlet oxygen by the ICG photosensitizer under NIR light illumination. The gold nanolayer was functionalized with HSA-ICG-FA complex to provide, on one hand, stealthness to the nanoplatform and on the other hand photodynamic therapy and fluorescence based imaging capabilities and the targeting ligand (folic acid). In addition, the thickness of the protein layer was suitable to provide an enhancement of the dye fluorescence by the plasmonic coupling of the metal nanolayer. *In vitro* confocal fluorescence imaging confirmed the succesfull cell internalization of the hybrid nanoplatforms whilst *in vivo* fluorescence imaging demonstrated that the nanoplatforms are highly localized and retained in the tumor region for long time thanks. Certain accumulation of the nanoplatforms in the brain area is also observed, which might open up the utility of the present system to fight against diverse brain diseases. The simultaneous combination of chemotherapy hyperthermia and oxygen reactive species led to an enhanced *in vitro* cell cytotoxicity of the nanoplatforms, as measured in two different cancer cell lines. Further studies are being developed to minimize light irradiation doses and nanoplatform concentrations by optimization of the synthetic protocols while adding new functionalities and to quantify the cytotoxic potential of the nanoplatforms *in vivo*.

Finally, we have successfully developed tumor targeted gold nanostars functionalized with DOXO (Au NS-PEG-SS-DOXO) nanoconjugates for combined photothermal and chemo-

therapy. Tumor-targeting ability of Au NS nanoconjugates was further enhanced when a targeting molecule, FA, was attached to the nanoconjugate surface, and tested on FA-overexpressing cells such as HeLa by FA-mediated active targeting. Au NS-PEG-SS-DOXO-FA enabled the active delivery of the chemotherapeutic drug near the nucleus, allowing its subsquent incorporation upon further incubation.

Tumor cells showed significant morphological changes upon the action of NIR light irradiation and the chemotherapeutic drug. In comparison with conventional hyperthermia or chemotherapy, the enhanced tumor therapy efficacy was demonstrated in Au NS-PEG-SS-DOXO-FA *in vitro* due to the combination of the dual treatment.

A synergistic effect between the chemotherapy and thermotherapy was confirmed by the therapeutic results of Au NS PEG-SS-DOXO-FA treated groups when compared with Au NS or free DOXO treated groups. Meanwhile, the nature of the targeting ligand could improve the cellular uptake of nanoconjugates, as demonstrated by experimental cytotoxicity data of Au NS-PEG-SS-DOXO, Au NS-PEG-SS-DOXO-FA, nad those when previously blocking celll FA receptors with free FA before addition of NS-PEG-SS DOXO-FA nanoconjugates. The above facts provide insight into the development of new strategies to design drug-loaded nanoconstructs with increased therapeutic efficacy and prompt further exploration of these nanoconstructs for combined therapy of other related diseases. To the best of our knowledge, this is an innovation, only one recent work recently appeared while preparing this manuscript combined the photothermal therapeutic effect of gold nanostars and the chemotherapeutic effect of DOX for tumor-targeted therapy [61]. In contrast to this work, our nanoconjugates enabled the enzymatic-triggerable release of the chemotherapeutic drug inside the cells by breaking the disulfide bond through which the drug is bound to the Au Ns surface. In this way, our construction then provides additional selectivity to the chemotherapeutic activity of the nanoconjugates.

Index of Figures

Index of Tables